



HAL
open science

Synthesis and reactivity of $[\text{RhI}(\text{CO})_2(\text{L})]$ and $[\text{RL}][\text{RhI}_2(\text{CO})_2]$ rhodium complexes where L is a nitrogen-containing ligand for the methanol carbonylation reaction

Romain Adcock

► **To cite this version:**

Romain Adcock. Synthesis and reactivity of $[\text{RhI}(\text{CO})_2(\text{L})]$ and $[\text{RL}][\text{RhI}_2(\text{CO})_2]$ rhodium complexes where L is a nitrogen-containing ligand for the methanol carbonylation reaction. Coordination chemistry. Institut National Polytechnique de Toulouse - INPT, 2011. English. NNT : 2011INPT0123 . tel-04547017

HAL Id: tel-04547017

<https://theses.hal.science/tel-04547017>

Submitted on 15 Apr 2024

HAL is a multi-disciplinary open access archive for the deposit and dissemination of scientific research documents, whether they are published or not. The documents may come from teaching and research institutions in France or abroad, or from public or private research centers.

L'archive ouverte pluridisciplinaire **HAL**, est destinée au dépôt et à la diffusion de documents scientifiques de niveau recherche, publiés ou non, émanant des établissements d'enseignement et de recherche français ou étrangers, des laboratoires publics ou privés.



THÈSE

En vue de l'obtention du

DOCTORAT DE L'UNIVERSITÉ DE TOULOUSE

Délivré par *l'Institut National Polytechnique de Toulouse*
Discipline ou spécialité : *Chimie Organométallique et de Coordination*

Présentée et soutenue par *Romain James ADCOCK*
Le 10 Novembre 2011

Titre : *Synthesis and reactivity of $[\text{RhI}(\text{CO})_2(\text{L})]$ and $[\text{RL}][\text{RhI}_2(\text{CO})_2]$ rhodium complexes where L is a nitrogen-containing ligand for the methanol carbonylation reaction*

JURY

Dieter VOGT, Professeur, Université Science et Technique, Eindhoven, Pays-Bas
Jean-Cyrille HIERSON, Professeur, Université de Bourgogne, Dijon, France
Marc TAILLEFER, Directeur de Recherche CNRS, ENSCM, Montpellier, France
Romuald POTEAU, Professeur, Université Paul Sabatier, Toulouse, France
Philippe KALCK, Professeur Emérite, INP de Toulouse, France
Philippe SERP, Professeur, INP de Toulouse, France

Ecole doctorale : *Science de la Matière*
Unité de recherche : *Laboratoire de Chimie de Coordination UPR 8241 CNRS*
Directeurs de Thèse : Philippe KALCK/Philippe SERP
Rapporteurs : Dieter VOGT/Jean-Cyrille HIERSON

Abstract

This study focuses on the synthesis and reactivity of rhodium complexes bearing N-containing ligands or counter-cations for the [Rh]-catalyzed methanol carbonylation reaction to produce acetic acid under the industrial Celanese Acid Optimization (AO) process conditions.

In a first part, full synthesis and characterization of neutral Rh(I) square planar *cis*-[RhX(CO)₂(L)] (X = Cl or I) complexes have been described, for which L is an N-ligand belonging to the amine, imidazole or pyrazole family. For the [RhI(CO)₂(L)] complexes, variable-temperature ¹³C{¹H} NMR spectroscopy has put in evidence a fluxional behavior for the different sized L ligands involved. The rate of this fluxional process reveals to be related to both electronic and steric contributions brought by L to the Rh center. These parameters (mainly steric), supported by single-crystal X-ray analyses in the solid state, also influence significantly the kinetics of the methyl iodide oxidative addition reaction followed by rapid CO migratory insertion, the overall being the rate determining step of the [Rh]-catalyzed methanol carbonylation cycle. In absence of CO, this reaction gives rise to the corresponding neutral Rh(III) acetyl complex, which immediately dimerizes to afford [Rh(μ-I)I(COMe)(CO)(L)]₂ complex, for which several X-ray crystal structures have been obtained and studied. In addition, the surprising C-H activation in the case of a ^tBu-pyrazole ligand giving rise to a cyclometalated Rh dimer is reported.

In a second part, the reactivity of the latter neutral Rh(I) [RhI(CO)₂(L)] complexes as potential precursors has been investigated by batch experiments for the methanol carbonylation reaction. Mechanistic understanding via VT-HP-NMR experiments enabled to detect mainly anionic Rh(I) [RL][RhI₂(CO)₂] (R = H or CH₃ according to the working conditions) complexes formed by decoordination followed by quaternization of the L ligand. Despite this result, the pyrazole family ligands showed better stability under the harsh process conditions. Thus, it cannot be ruled out that equilibrium between neutral and anionic species co-exist in the reaction medium at high temperatures and that [RL]I salt dissociation occurs, restoring the L ligand into the Rh coordination sphere. At this stage we focused on the anionic Rh(I) complex and prepared a series of [XNR₃][RhI₂(CO)₂] (X = H or CH₃) species, which have been fully characterized. Infrared, NMR, conductivity experiments and DFT model calculations together put in evidence ion interactions according to the nature of the ammonium counter-cation. Protonated cations significantly impact on the kinetics of the methyl iodide oxidative addition presumably due to H-interactions with the Rh square plane.

The final part deals with the mechanism of the reductive elimination reaction, the last step of the [Rh]-catalyzed methanol carbonylation cycle, which from complex [RhI₃(COCH₃)(CO)₂], regenerates [RhI₂(CO)₂]⁻. In contrast to the classically admitted mechanism of reductive elimination of CH₃COI followed by subsequent hydrolysis to form AcOH and HI, we demonstrate from experimental DFT calculation that substitution of an iodo ligand by an acetate ion occurs to give rise to the [RhI₂(OAc)(COCH₃)(CO)₂]⁻ species. Thus, reductive elimination regenerates [RhI₂(CO)₂]⁻ and produces acetic anhydride, which after hydrolysis affords two molecules of acetic acid. Such a mechanism operates under process conditions at low water content with a significant amount of acetate ions.

Keywords: Rhodium - Methanol carbonylation - N-ligand (amine, imidazole, pyrazole) - MeI oxidative addition - Reductive elimination - Reaction mechanism - C-H activation

Résumé de thèse

Ce travail est centré sur la synthèse de complexes du rhodium contenant un ligand azoté et leur mise en œuvre dans la réaction catalytique de carbonylation du méthanol en acide acétique. Dans une première partie, nous nous intéressons à la préparation de complexes neutres de formule générale $[\text{RhI}_2(\text{CO})(\text{L})]$ (L = amines, imidazoles et pyrazoles) et à quelques homologues chlorés. Ces complexes plans carrés manifestent une réactivité directement liée à l'encombrement stérique du ligand azoté L dans la réaction d'addition oxydante de l'iodomethane suivie de la cis-migration du groupement méthyle pour former l'espèce acétyle.

Dans une deuxième partie, les complexes précédents ont été engagés dans des essais catalytiques de carbonylation du méthanol dans les conditions du procédé industriel. Comme il s'est avéré que les complexes neutres se transforment en espèce $[\text{RhI}_2(\text{CO})_2]^-$ pour laquelle les contre-cations associés sont constitués du ligand azoté protoné ou méthylé, nous avons effectué la préparation et la caractérisation des complexes $[\text{HNR}_3][\text{RhI}_2(\text{CO})_2]^-$ ou $[\text{MeNR}_3][\text{RhI}_2(\text{CO})_2]^-$. Par IR, RMN et électrochimie, nous nous sommes intéressés aux phénomènes d'appariement d'ions et nous montrons qu'il s'agit dans le meilleur des cas d'interactions hydrogènes. Celles-ci influent la vitesse de la réaction oxydante de CH_3I .

Dans la dernière partie, nous avons complété une étude, précédemment initiée au laboratoire, sur le mécanisme, qui dans la dernière étape du cycle catalytique permet de passer de l'espèce acétyle $[\text{RhI}_3(\text{COCH}_3)(\text{CO})_2]^-$ à l'espèce active $[\text{RhI}_2(\text{CO})_2]^-$ avec production de l'iodure d'acyle. A l'inverse du concept admis d'élimination réductrice de CH_3COI suivie de son hydrolyse immédiate en CH_3COOH et HI , nous montrons, avec l'appui de calculs théoriques (DFT) qu'en fait un ligand I^- est substitué par un ligand acetate pour conduire à l'espèce $[\text{RhI}_2(\text{OAc})(\text{COCH}_3)(\text{CO})_2]^-$. L'élimination réductrice produit alors l'anhydride acétique qui est hydrolysé en CH_3COOH régénérant $[\text{RhI}_2(\text{CO})_2]^-$. Un tel mécanisme opère en présence d'ions acetate dans les milieux faiblement hydratés visés par l'industriel.

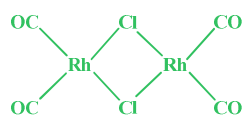
Mots clés : Ligands azotés – Rhodium – Carbonylation du méthanol – Addition oxydante – Elimination réductrice – Mécanisme réactionnel.

Abbreviations

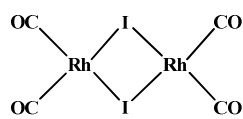
(Ac) ₂ O	acetic anhydride
Ac	Acetyl
AcOH	acetic acid
AcOMe	methyl acetate
Ar	aryl
BMIMI	1-butyl-3-methylimidazolium iodide
CO	carbon monoxide
DFT	density functional theory
dppe	1,2- <i>bis</i> (diphenylphosphino)ethane
dppm	<i>bis</i> (diphenylphosphino)methane
EMIMI	1-ethyl-3-methylimidazolium iodide
Et	ethyl
EtI	ethyl iodide
EtOH	ethanol
FT-IR	fourrier transformed infrared
H ₂ NEt ₂ I	diethylammonium iodide
H ₂ O	water
HHIMI	imidazolium iodide
HHPYI	pyrazolium iodide
HI	hydriodic acid
HNEt ₃ I	triethylammonium iodide
HP-IR	high pressure infrared
Ir	Iridium
LiI	Lithium iodide
Me	methyl
MeI	methyl iodide
MeOH	methanol
MePyI	1-methylpyridinium iodide
MHIMI	1-methylimidazolium iodide
MHPYI	1-methylpyrazolium iodide
MMIMI	1,3-dimethylimidazolium iodide
MMPYI	1,2-dimethylpyrazolium iodide
NEt ₄ I	tetraethylammonium iodide
NMe ₄ I	tetramethylammonium iodide
Ph	phenyl
PPNCl	bis-triphenylphosphoranylidene chloride
PrMMIMI	1-propyl-2,3-dimethylimidazolium iodide
PVP	polyvinylpyrrolidone
QAS	quaternary ammonium salt
Rh	Rhodium
RT	room temperature

SEt ₂ MeI	diethylmethylsulfonium iodide
^t Bu	<i>tert</i> -butyl
TEP	Tolman electronic parameter
TMS	tetramethylsilane
TSPSA	3-(trimethylsilyl)-1-propane sulfonic acid sodium salt
VT-HP-NMR	variable temperature-high pressure nuclear magnetic resonance
WGSR	water gas shift reaction
wt %	weight percent

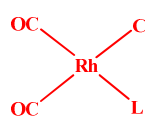
Glossary of Rhodium complexes



1



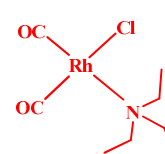
2



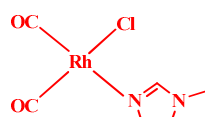
3



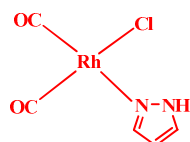
3a



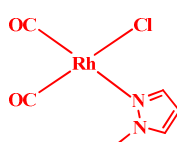
3b



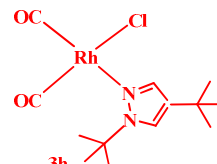
3d



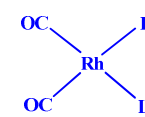
3e



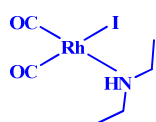
3f



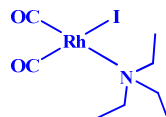
3h



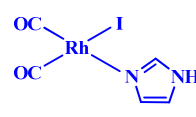
4



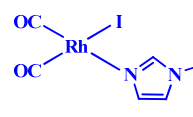
4a



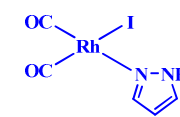
4b



4c



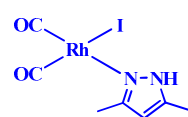
4d



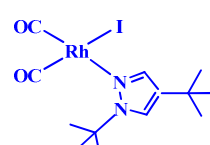
4e



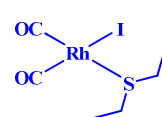
4f



4g



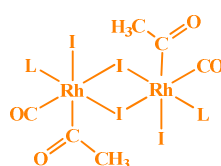
4h



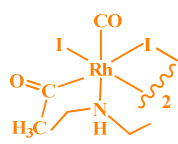
4i



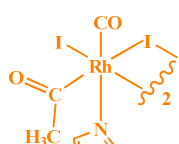
5



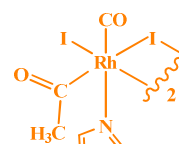
6



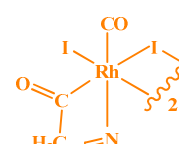
6a



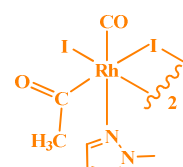
6c



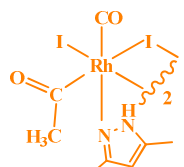
6d



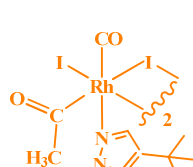
6e



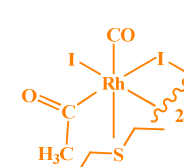
6f



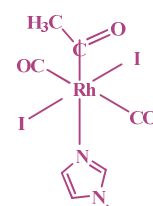
6g



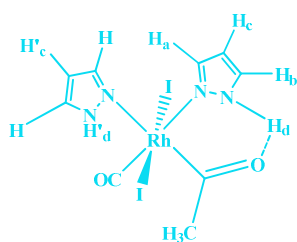
6h



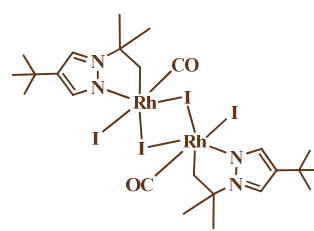
6i



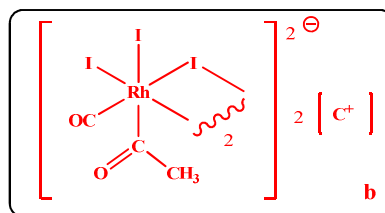
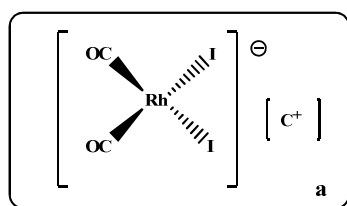
7d



8e

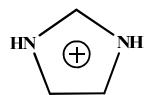


9h



WITH:

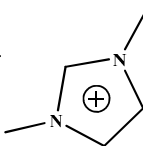
C⁺ =



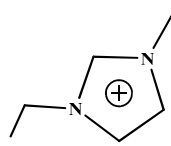
10a
HHIM



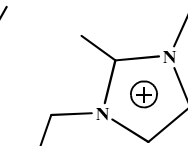
11a / 11b
MHIM



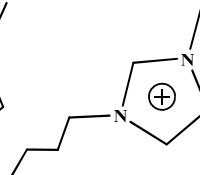
12a / 12b
MMIM



13a
EMIM

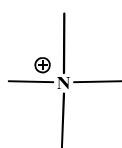


14a / 14b
Pr-MMIM

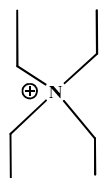


15a / 15b
BMIM

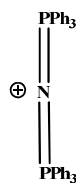
C⁺ =



16a / 16b
NMe₄



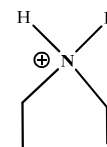
17a / 17b
NEt₄



18a / 18b
PPN

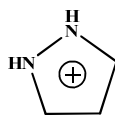


19a / 19b
HNEt₃

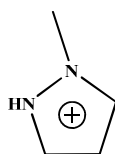


20a / 20b
H₂NEt₂

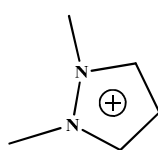
C⁺ =



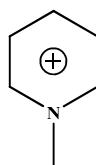
21a
HHPY



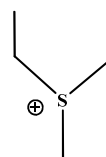
22a
MHPY



23a / 23b
MMPY



24a
MePy



25a
SEt₂Me

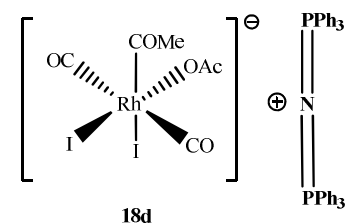
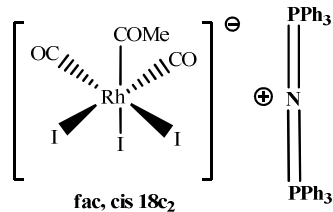
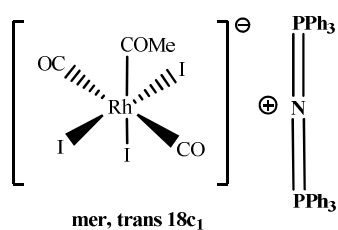


26a



27a

Complexes involved in Chapter IV:



Remerciements

Les travaux effectués et décrits dans ce manuscrit de thèse ont été réalisés au laboratoire de Chimie de Coordination, sous la direction du Pr. Philippe Kalck au sein de son équipe Catalyse et Chimie Fine, composante de l'Institut National Polytechnique de Toulouse de 2008-2010. Je tiens à le remercier sincèrement de m'avoir accueilli dans son groupe, de m'avoir apporté sa confiance, son soutien et son enthousiasme pour la recherche. Je tiens également à remercier le Pr. Philippe Serp, co-directeur de ma thèse et nouveau directeur de l'équipe depuis 2010. Les qualités, à la fois humaines et scientifiques de mes deux directeurs ont su me guider vers l'épanouissement de mon travail en tant que jeune chercheur.

J'aimerais exprimer également ma gratitude et un grand merci auprès du Dr. Carole Le Berre ainsi que le Dr. Duc Hanh Nguyen, étant des membres directement liés à mon sujet de thèse et dont leur participation active a contribué à l'aboutissement de ce travail scientifique d'équipe. Mme Dr. Carole Le Berre, coordonnatrice principale entre l'équipe et le partenaire industriel américain CELANESE. Par la suite je remercie profondément les membres de la société CELANESE pour le financement de ce projet et plus particulièrement les Dr. Paull Torrence, Dr. Grant Proulx et Dr. Ralph Gillespie de leurs expériences professionnelles. Je remercie également toutes les personnes précédentes pour avoir relu ce manuscrit avec attention. J'aimerais plus particulièrement remercier les rapporteurs et différents membres du Jury (Les Pr. Dieter Vogt, Pr. Jean-Cyrille Hierso, Dr. Marc Taillefer ainsi que le Pr. Romuald Poteau) pour avoir accepté de juger mes travaux de manière pertinente.

Je remercie chaleureusement les nombreuses personnes des différents services d'analyses scientifiques (RMN, MS, IR/RAMAN, RX, Electrochimie, microanalyse...) pour leur disponibilité et efficacité (Dr. Yannick Coppel, Dr. Christian Bijani, Francis Lacassin, David Paryl, Dr. Alix Saquet, Alain Moreau, Dr. Sonia Ladeira). Je remercie également le Pr. Gábor Laurency de

l'Ecole Polytechnique Fédérale de Lausanne pour son accueil et sa disponibilité lors d'un séjour dans son laboratoire pour effectuer de la HP-RMN.

J'adresse mes remerciements à toutes les différentes personnes de l'équipe C et autres équipes (G, A, O...) du LCC de Toulouse que j'ai côtoyé de près ou de loin lors de ces trois années bien remplies en expériences professionnelles et humaines. En particulier les différents permanents, doctorants, post-docteurs et techniciens (Pr. Martine Urrutigoïty, Dr. Odile Dechy-Cabaret, Dr. Jérôme Durand, Dr. Maryse Gouygou, Dr. Rosa Axet, Dr. Dominique Augustin, Dr. Duchanh Nguyen, Dr. Pavel Dub, Aurélien Berthegnies, Andrés Cardozo, Dr. Nadia Vujkovic, Katie Smart, Dr. Yann Champouret, Aurélie Morin, Dr. Julien Beausoleil, Pierre Lonchambon, Marc Guignard, Christelle Girardet, Kévin Fourmy, Jamal El Karroumi, Mustapha Oubenali, Meltem Tunckol, Marie-Noelle Garcia, Sylvie Pivato, Dr. Delphine Crozet, Dr. Revathi Bacsa, Ganna Gogolieva, Liping Zhang, Xiaojiang Li, Trang Nguyen, Abderrahim Elhaib, Dr. Jacques Teddy, Dr. Laura Rodriguez Perez, Lucie Orsoni, Boris Elbaum, Guillaume Bonnet, Dr. Amandine Fabrello...J'en oublie forcément !).

Enfin, je remercie tout particulièrement mes amis et mes proches dont le soutien a été plus qu'une aide pendant toutes ces années. A ce titre, j'ai une pensée particulière pour ma « belle-famille », mes parents, Cyril, Lauren, mimi et surtout Aurore.

Table of contents

General introduction	1
----------------------	---

CHAPTER I: BIBLIOGRAPHY

I-1 Introduction	5
I-2 Historical context	5
I-3 Process chemistry	8
I-4 [Rh]-complex-catalyzed methanol carbonylation	11
I-4-1 <i>Reaction mechanism</i>	11
I-4-2 <i>Reaction promotion by iodide salts</i>	15
I-4-3 <i>Supported rhodium catalysts</i>	17
I-4-4 <i>Ligand tuning for accelerated catalysis</i>	20
References	30

CHAPTER II: Reactivity of rhodium(I) complexes bearing nitrogen containing ligands towards CH₃I: Synthesis and full characterization of neutral *cis*-[RhX(CO)₂(L)] and acetyl [Rh(μ -I)(COMe)(CO)(L)]₂ complexes; Kinetic studies

Chapter II: Graphical synopsis	36
Chapter II abstract:	37
II-1 Introduction	38
II-2 Synthesis and characterization	39
II-2-1 <i>Synthesis and characterization of chloro rhodium(I) complexes [RhCl(CO)₂(L)] 3</i>	39
II-2-2 <i>Synthesis and characterization of iodo rhodium(I) complexes [RhI(CO)₂(L)] 4</i>	46
II-3 Variable temperature NMR studies of complexes 4	54
II-4- Synthesis and characterization of acetyl-Rh(III) complexes	66
II-5- IR-monitored kinetic study for 4a,c-h towards CH ₃ I	79
II-6 Specific reactivity obtained with 1,4-di- <i>tert</i> -butyl-pyrazole ligand h	87
II-6-1 <i>Unexpected C(sp³)-H bond activation starting from 4h</i>	87
II-7 Conclusion	94

References	96
<hr/>	
CHAPTER III: Reactivity of neutral <i>cis</i>-[RhI(CO)₂(L)] and anionic [XNR₃] <i>cis</i>-[RhI₂(CO)₂] (X = H, CH₃) complexes under methanol carbonylation conditions	
<hr/>	
III-1 Introduction	101
III-2 Catalytic reactivity of neutral complexes [RhI(CO) ₂ (L)]	101
III-3 Batch experiment study	102
III-4 Reactivity of 4e with hydriodic acid HI	105
III-5 HP-VT NMR study	106
III-5-1 <i>Experiment 1</i>	107
III-5-2 <i>Experiment 2</i>	117
III-6 Conclusion for reactivity under methanol carbonylation conditions	122
III-7 Nature of the counter-cation in anionic Rh(I) complexes: Ion pairing effect	123
III-7-1 <i>Background</i>	123
III-7-2 <i>Synthesis and characterization of anionic Rh(I) complexes</i>	124
III-7-3 <i>The role of solvent on ion-pairs</i>	128
III-7-4 <i>Single crystal X-ray structures for 12a and 18a</i>	131
III-7-5 <i>DFT modeling for selected complexes 19a, 20a and 27a</i>	133
III-7-6 <i>RT ¹H and ¹³C{¹H} NMR characterization of 11a-27a</i>	136
III-7-7 <i>Conductivity measurements for selected complexes 15a-20a and 27a</i>	136
III-8 Study of anionic Rh(I) complexes towards CH ₃ I oxidative addition	141
III-8-1 <i>Synthesis and characterization of anionic Rh(III) complexes</i>	141
III-8-2 <i>IR-monitored kinetic study for 14a, 16a and 18a-20a towards CH₃I</i>	144
III-9 Lithium iodide effect on <i>cis</i> -[RhI ₂ (CO) ₂] ⁻	148
III-10 Conclusion	151
References	153

CHAPTER IV: Direct involvement of an acetato ligand in the reductive elimination step of the rhodium-catalyzed methanol carbonylation

Chapter IV: Graphical synopsis	158
IV-1 Introduction	159
IV-2 Background	159
IV-3 New proposed mechanism for the formation of AcOH from $[\text{RhI}_3(\text{COCH}_3)(\text{CO})_2]$	153
IV-4 Synthesis and characterization	165
IV-5 Reactivity (<i>VT-HP-NMR and kinetics</i>)	170
IV-6 DFT calculations to investigate the reactivity of 18c	174
IV-7 Conclusion	179
References	180
General conclusion	182

CHAPTER V: EXPERIMENTAL SECTION

V-1 Experimental section: Chapter II	185
V-1-1 <i>Instrumentation and materials</i>	185
V-1-2 <i>Synthesis of precursor complexes 1 and 2</i>	186
V-1-3 <i>NMR data of starting ligands a-h</i>	189
V-1-4 <i>Synthesis of neutral cis-$[\text{RhCl}(\text{CO})_2(\text{L})]$ 3 complexes</i>	192
V-1-5 <i>Synthesis of neutral cis-$[\text{RhI}(\text{CO})_2(\text{L})]$ 4 complexes</i>	194
V-1-6 <i>Synthesis of neutral rhodium(III) complex $[\text{RhI}(\mu\text{-I})(\text{COMe})(\text{CO})(\text{NCMe})_2]$ 5</i>	201
V-1-7 <i>Synthesis of neutral rhodium(III) complexes $[\text{RhI}(\mu\text{-I})(\text{COMe})(\text{CO})(\text{L})_2]$ 6</i>	201
V-1-8 <i>Synthesis of neutral rhodium(III) complex $[\text{RhI}_2(\text{COMe})(\text{CO})_2(\text{N}_2\text{C}_3\text{H}_4)]$ 7d</i>	204
V-1-9 <i>Synthesis of neutral rhodium(III) complex $[\text{RhI}_2(\text{COMe})(\text{CO})(\text{N}_2\text{C}_3\text{H}_4)_2]$ 8e</i>	205
V-1-10 <i>Characterization of neutral cyclometalated dimeric rhodium(III) complex $[\text{RhI}(\mu\text{-I})(\text{CO})(\kappa^2\text{-N,C-h}\cap\text{CH}_2)]_2$ 9h</i>	206
V-1-11 <i>Kinetic measurements</i>	206
V-1-12 <i>X-ray crystal structure determination</i>	207

V-2 Experimental section: Chapter III	231
V-2-1 <i>Instrumentation and materials</i>	231
V-2-2 <i>Synthesis</i>	231
V-2-3 <i>Alkyl iodide NMR data</i>	232
V-2-4 <i>Synthesis of imidazolium and pyridinium iodide salt precursors</i>	232
V-2-5 <i>Synthesis of ammonium iodide salt precursors</i>	234
V-2-6 <i>Synthesis of pyrazolium and sulfonium iodide salt precursors</i>	235
V-2-7 <i>Synthesis of anionic cis-dicarbonyl-diiodo-rhodium(I) ammonium/sulfonium/lithium salt complexes</i>	236
V-2-8 <i>Synthesis of anionic dimeric rhodium(III) ammonium/sulfonium/lithium salt complexes</i>	242
V-2-9 <i>Catalytic batch experiments</i>	245
V-2-10 <i>High pressure variable temperature NMR experiments</i>	246
V-2-11 <i>Conductivity measurements</i>	248
V-2-12 <i>Ionic chromatography</i>	248
V-2-13 <i>X-ray structure determination (for complex 12a)</i>	248
V-3 Experimental section: Chapter IV	251
V-3-1 <i>Instrumentation and materials</i>	251
V-3-2 <i>Synthesis</i>	251
V-3-3 <i>High pressure NMR analyses</i>	252
V-3-4 <i>Kinetic experiments</i>	253
V-3-5 <i>Conductivity measurements</i>	253
V-3-6 <i>DFT calculations (computational details)</i>	254

SUPPORTING INFORMATION

Chapter II: FT-IR/ATR-IR, NMR spectra and kinetic activation parameters

Chapter IV: DFT computational details (Cartesian coordinates)

General introduction

The carbonylation of methanol to acetic acid is one of the most important and successful worldwide applications of homogeneous transition metal catalysis.¹ Acetic acid is an important bulk commodity chemical, with a world annual production capacity of ~ 9-10 million tones. Rh and Ir are the most active and preferred catalysts for carbonylation reactions to produce acetic acid.² Today, the main challenge for chemical industry is to develop productive, efficient and low-cost processes which are as clean as possible for the environment. In the Celanese Acid Optimization (AO) process, the use of a rhodium-complex catalyst with lithium iodide as a promoter enables to operate at low water concentration with a low capital investment and with a considerable saving from the major energy cost for water separation from acetic acid.³ Research efforts are still in progress to stabilize further the Rh catalyst by using different iodide promoters such as ammonium and/or phosphonium iodide salts. These promoters reveal high stability and at long term could replace LiI due to their unique combination of properties.⁴

For the [Rh]-catalyzed methanol carbonylation process, it is largely admitted that the classical well known anionic $[\text{RhI}_2(\text{CO})_2]^-$ complex is the main active species of the catalytic cycle. However, when an ammonium iodide co-promoter is involved, it cannot be ruled out that under the harsh requested working conditions, (HI/AcOH , $P_{\text{CO}} = 20\text{-}60$ bar, $T = 180\text{-}$

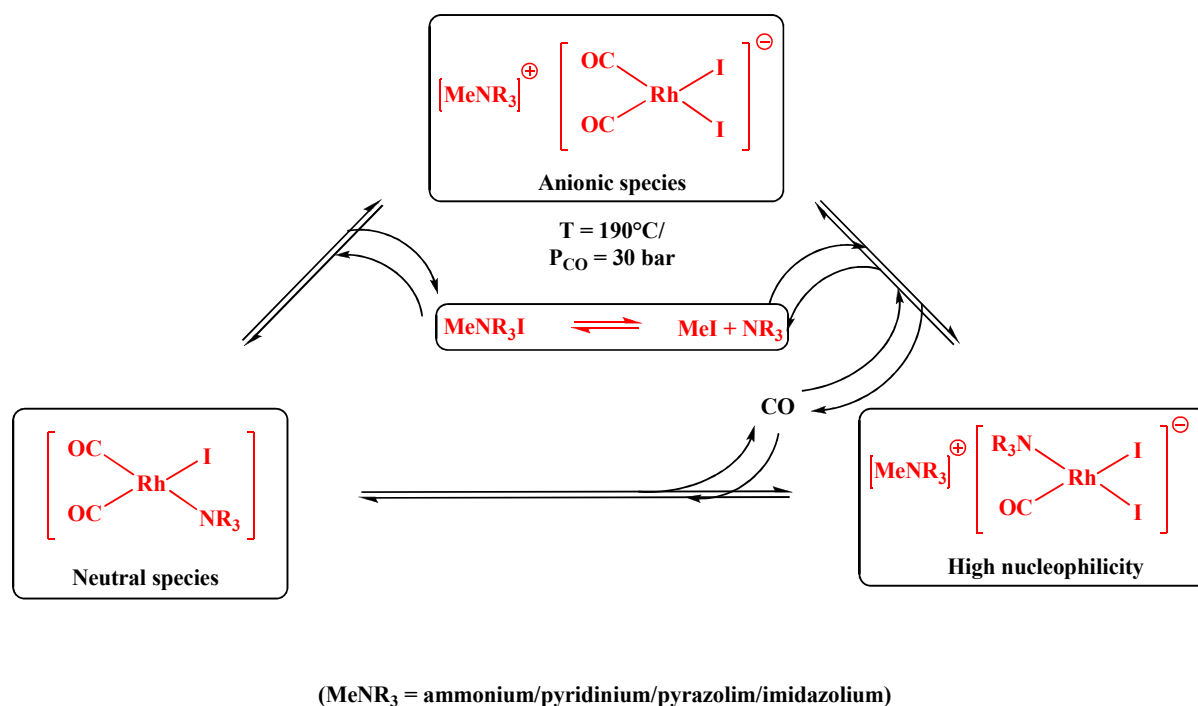
(1) (a) Howard, M. J.; Jones, M. D.; Roberts, M. S.; Taylor, S. A. *Catal. Today* **1993**, *18*, 325. (b) Maitlis, P. M.; Haynes, A.; Sunley, G. J.; Howard, M. J. *J. Chem. Soc. Dalton Trans.* **1996**, 2187. (c) Yoneda, N.; Kusano, S.; Yasui, M.; Pujado, P.; Wilcher, S. *Appl. Catal. A* **2001**, *221*, 253.

(2) (a) Cheung, H.; Tanke, R. S.; Torrence, G. P. *Ullmann's Encycl. Ind. Chem. 6th Ed.*, Wiley-VCH, **2000**. (b) Guerra, M. K. *Acetic Acid and Acetic Anhydride*, SRI International, Menlo Park, CA, **1994**, Report No. 37B. (c) Anonymous, *Eur. Chem. News* **2000**, Apr., 10.

(3) Torrence, P.; in: Cornils, B.; Herrmann, W. A. (Eds.), *Applied Homogeneous Catalysis with Organometallic Compounds*, second ed., Vol. 1, Wiley-VCH, Weinheim, **2002**, 104.

(4) (a) Lee, S. -Y.; Ogawa, A.; Kanno, M.; Nakamoto, H.; Yasuda, T.; Watanabe, M. *J. Am. Chem. Soc.* **2010**, *132*, 9764. (b) MacFarlane, D. R.; Forsyth, M.; Izgorodina, E. I.; Abbott, A. P.; Annat, G.; Fraser, K. *Phys. Chem. Chem. Phys.* **2009**, *11*, 4962. (c) MacFarlane, D. R.; Seddon, K. R. *Aust. J. Chem.* **2007**, *60*, 3.

220°C) organic salt dissociation takes place giving rise to the corresponding amine, which can further coordinate to the Rh species thus participating in the catalytic cycle (Scheme 1).



Scheme 1. Possible formation of different active Rh-species under catalytic conditions in the presence of organic N-containing iodide promoter.

In fact, investigations carried out in our group on $[\text{RhI}_2(\text{CO})_2]^-$ complex stabilized by the 1-methylimidazolium iodide promoter showed that in the reactant medium, under catalytic conditions, this salt was exposed to scrambling phenomena indicating a dissociative process and suggesting the formation of the methylimidazole before further quaternization by a different alkyl substituent.⁵ In addition, Eastman Chemical Company recently disclosed a process for the Rh-catalyzed carbonylation of methanol into acetic acid in ionic liquids, which operates in the absence of any added methyl iodide co-catalyst. Thus, it has very recently been

(5) Work under course for publish or patent: Nguyen, D. H, Leberre, C.; Serp, P, Kalck, P.; Torrence, G. P.

reported by Zoeller et al.⁶ that the use of Rh in methylpyridinium iodide (MePyI) as catalyst may lead to dissociation of MePyI to CH₃I and pyridine, followed by subsequent generation of [RhI₂(CO)(Py)]⁻ from [RhI₂(CO)₂]⁻ via a ligand exchange. Since [RhI₂(CO)(Py)]⁻ is much more nucleophilic than [RhI₂(CO)₂]⁻, the oxidative addition of CH₃I is much faster. In parallel, Haynes et al. have reported results raising the possibility that neutral Rh(III) methyl and acetyl complexes are significant intermediates in the Rh-catalyzed methanol carbonylation.⁷

In the case of neutral Rh-complexes bearing phosphorous-containing ligands such as phosphines, which have been largely explored in past studies, systematical ligand quaternization occurred and no evidence of any reversibility has been reported.⁸ In contrast, neutral N-containing iodo-Rh (I) complexes remain undescribed in the literature and consequently for methanol carbonylation catalysis although few examples have been studied by Dutta and co-workers for the chloro analogue complexes.⁹ In terms of reactivity, *cis*-[RhI(CO)₂(L)] (L = N-containing ligand) complex is of weaker nucleophilicity towards methyl iodide oxidative addition in comparison to an anionic Rh complex, yet CO *cis*-migration can occur faster. The oxidative addition of organic molecules to unsaturated transition metal complexes is a fundamental process in organometallic chemistry and it plays

(6) Zoeller, J. R.; Vetter, A. J.; Moore, M. K.; in: *Carbonylation in ionic liquids: Process and mechanism for the carbonylation of methanol to acetic acid using methyl pyridinium iodide and Rh in the absence of added methyl iodide*, ACS National Meeting, 08.28-09.01 **2011**, Embassy Suites Denver.

(7) Haynes, A.; Maitlis, P. M.; Stanbridge, I. A.; Haak, S.; Pearson, J. M.; Adams, H.; Bailey, N. A. *Inorg. Chim. Acta* **2004**, 357, 3027.

(8) (a) Rankin, J.; Poole, A. D.; Benyei, A. C.; Cole-Hamilton, D. J. *Chem. Commun.* **1997**, 1835. (b) Rankin, J.; Benyei, A. C.; Poole, A. D.; Cole-Hamilton, D. J. *J. Chem. Soc. Dalton Trans.* **1999**, 3771.

(9) (a) Borah, B. J.; Deb, B.; Sarmah, P. P.; Saikia, K.; Khound, P. P.; Dutta, D. K. *Inorg. Chim. Acta* **2011**, 370, 117. (b) Sarmah, P. P.; Deb, B.; Borah, B. J.; Fuller, A. L.; Slawin, A. M. Z.; Woollins, J. D.; Dutta, D. K. *J. Organomet. Chem.* **2010**, 695, 2603. (c) Borah, B. J.; Deb, B.; Sarmah, P. P.; Dutta, D. K. *J. Mol. Catal. A: Chemical* **2010**, 319, 66. (d) Dutta, D. K.; Chutia, P.; Sarmah, B. J.; Borah, B. J.; Deb, B.; Woollins, J. D. *J. Mol. Catal. A: Chemical* **2009**, 300, 29. (e) Srinivasan, A.; Toganoh, M.; Niino, T.; Osuka, A.; Furuta, H. *Inorg. Chem.* **2008**, 47, 11305. (f) Sarmah, B. J.; Borah, B. J.; Deb, B.; Dutta, D. K. *J. Mol. Catal. A: Chemical* **2008**, 289, 95. (g) Kumari, N.; Sarmah, B. J.; Dutta, D. K. *J. Mol. Catal. A: Chemical* **2007**, 266, 260. (h) Kumari, N.; Sharma, M.; Chutia, P.; Dutta, D. K. *J. Mol. Catal. A: Chemical* **2004**, 222, 53. (i) Kumari, N.; Sharma, M.; Das, P.; Dutta, D. K. *Appl. Organomet. Chem.* **2002**, 16, 258. (j) Dutta, D. K.; Singh, M. M. *Transition Met. Chem.* **1994**, 19, 290.

a key role in many important catalytic reactions¹⁰, in particular for Rh-catalyzed methanol carbonylation.

In this context, the following work will describe, in a first part, the preparation of new neutral Rh(I) square planar complexes $[\text{RhX}(\text{CO})_2(\text{L})]$ ($\text{X} = \text{Cl}, \text{I}$) bearing a series of N-containing ligands presenting different steric effects. Attention will be mainly focused on the reactivity of $[\text{RhI}(\text{CO})_2(\text{L})]$ complexes towards CH_3I leading to the corresponding dimeric Rh(III) acetyl $[\text{Rh}(\mu\text{-I})\text{I}(\text{COCH}_3)(\text{CO})(\text{L})_2]$ complexes.

In a second part, most of these Rh(I) complexes will be tested under catalytic conditions via batch experiments supported by a series of VT-HP-NMR experiments to investigate further their behavior. We will then focus on anionic $[\text{C}][\text{RhI}_2(\text{CO})_2]$ ($\text{C} = \text{N}$ -containing counter-cation) complexes and study the impact of the nature of the counter-cation on the CH_3I oxidative addition step.

Finally, a study on the reductive elimination, the last step of the methanol carbonylation reaction, for which experimental and theoretical evidences support a new alternative mechanism, will be presented.

(10) Collman, J. P.; Hegedus, L. S.; Norton, J. R.; Finke, R. G. *Principles and Applications of Organotransition Metal Chemistry*; University Science Books: Mill Valley, CA, **1987**.

CHAPTER I

BIBLIOGRAPHY

I-1 Introduction

Organometallic chemistry, which involves metal complexes containing direct metal-to-carbon bonds, has grown since the early 1950's at an incredible rate, mostly owing to the development of an impressive array of highly sophisticated apparatus of which in particular NMR and single-crystal X-ray equipments.¹ Additionally, theoretical studies of the bonding in metal complexes and of the course of reaction pathways have not only contributed to new knowledge, but also to the purposeful design of complexes and their use in stoichiometric and catalytic reactions.

This chapter will focus on the important recent advances in process development and mechanistic understanding of the methanol carbonylation reaction, principally to produce acetic acid, along with recent research efforts to identify new ligand-modified, supported, or promoted catalysts. Since the introduction of a rhodium-catalyzed process by Monsanto four decades ago, there has been almost continuous activity aimed toward improving the process and gaining a deeper understanding of the underlying chemistry. Strategies to improve catalyst performance and process economics have been developed, resulting in both rhodium- and iridium-catalyzed systems that operate with high activity at reduced water concentration, making product purification less costly.

I-2 Historical context

Homogeneous carbonylation catalysis is concerned with the transition-metal-assisted addition of carbon monoxide to organic compounds and involves a carbon-carbon coupling process to give higher molecular weight carbonyl-containing products. Carbonylation chemistry was pioneered by Otto Roelen (Ruhchemie) and Walther Reppe (IG Farben, later BASF) in the late 1930's.² Since then it has developed into the highest volume and most

important industrial process based on homogeneous catalysis to produce among others mainly acetic acid.

Acetic acid is mainly used (~ 40 %) in the manufacture of vinyl acetate, a monomer of great importance in the polymer sector. A range of other acetate esters are also significant derivatives, along with monochloroacetic acid which is an important intermediate in the production of pesticides. Dehydration of acetic acid can be used to make acetic anhydride, which is used as an acetylating agent, for example, in the production of cellulose acetate. Acetic acid also finds a major use as a solvent for the oxidation of xylene to terephthalic acid, which is required on a large scale for incorporation into polyethylene terephthalate. Industrial routes to acetic acid have included oxidation of ethanol derived from fermentation, hydrolysis of acetylene, and the oxidation of hydrocarbons such as butane (Celanese) or naphtha (BP Chemicals). However, these reactions also produce significant amounts of oxidation by-products, and their separation can be very complex and expensive.³

In the late 1950's, the development of the Wacker process (a PdCl₂/CuCl₂-catalyzed oxidation of ethylene) provided a route to acetaldehyde, which could be converted to acetic acid by subsequent oxidation. The production of acetic acid by carbonylation of methanol (Equation 1) can also be traced back to the 1950's when Reppe and coworkers at BASF developed a cobalt iodide catalyst that was effective for this reaction at relatively high temperatures and pressures (~ 250 °C, 600 bar).^{4,5}



The process based on the cobalt-catalyzed reaction was commercialized by BASF^{6,7} but proved not to be so selective as subsequent processes, with an acetic acid yield of 90 % based on methanol feedstock and 70 % based on CO. The major organic by-products were

higher alcohols, aldehydes, and carboxylic acids that required demanding and expensive separation procedures to give acetic acid of sufficient purity. Much higher catalytic activity and selectivity under milder conditions (~ 175 °C, 30 bar) was revealed by Paulik and Roth at Monsanto, who used an iodide-promoted rhodium complex catalyst.⁸ They started investigating the catalytic mechanism and in the same period of time, they identified iridium as having similar reactivity to rhodium. Monsanto selected the rhodium/iodide catalyst for commercialization, and the first plant based on this technology began production in Texas City in 1970. The so-called Monsanto process became the dominant method for acetic acid production during the 1970's and 1980's, such that by 1991 it accounted for ~ 55 % of global acetic acid production. It achieved selectivity of > 99 % (based on methanol) but only ~ 85% based on CO, which is also consumed by the water gas shift (WGS) reaction (Equation 2):



The process involving the rhodium/iodide combination was operated by other companies under license from Monsanto, including BP Chemicals and Hoechst-Celanese. In 1986, BP Chemicals acquired the licensing rights to the Monsanto process, and in the same year Hoechst-Celanese patented a modified process with a rhodium-complex catalyst that used lithium iodide as a promoter to enable operation at lower water concentration. Closely related rhodium-catalyzed processes were also commercialized for the anhydrous carbonylation of methyl acetate to acetic anhydride and the coproduction of acid and anhydride (Eastman as main example). During the early 1990's, BP Chemicals developed an iridium-complex catalyst that was competitive with the rhodium-complex catalyst, and the new technology was commercialized as the CativaTM process in 1995. Nowadays, approximately over 85 % of the total world acetic acid manufacturing capacity is covered by

the homogeneous catalytic carbonylation of methanol. The major commercial processes operating currently are displayed in Table 1.

Table 1. Commercial processes for methanol and methyl acetate carbonylation.

Original operator	Feedstock	Catalyst	Co-catalyst (promoter)	% H ₂ O (w/w)	% MeOAc (w/w)
Monsanto	MeOH	Rh/MeI	–	>15	1–2
Celanese	MeOH	Rh/MeI	LiI	<10	≥2
BP	MeOH	Ir/MeI	[Ru(CO) _x I _y]	<10	>10
Eastman	MeOAc	Rh/MeI	LiI	Anhydrous	≥10
BP	MeOAc/ MeOH	Rh/MeI	[QAS]I	Anhydrous	≥10

*QAS = quaternary ammonium salt

The following bibliographic reports will be concentrated on the manufacture of acetic acid by the **rhodium catalyzed** carbonylation of methanol, one of the most important industrial processes currently operating.

I-3 Process chemistry

Methanol carbonylation (Equation 1) involves formal insertion of carbon monoxide into the C–O bond of methanol. The transition metal catalyst does not activate methanol directly, therefore a more reactive methyl substrate (reactant) must be generated *in situ*. In this respect, a key role of the iodide promoter (HI) is to convert methanol into methyl iodide. (Equation 3).



For the continuous process, under industrial conditions, acetic acid is the main component of the reaction medium therefore, in a working catalytic system, esterification of

methanol leads to methyl acetate (Equation 4). Methyl acetate is then activated rather than methanol by the iodide co-catalyst (Equation 5). Equations 4 and 5 result globally in equation 3.



Methyl iodide undergoes carbonylation by the Rh transition metal catalyst to give (formally) acetyl iodide (Equation 6), which is rapidly hydrolyzed to the acetic acid product (Equation 7). The intermediacy of acetyl iodide is difficult to establish under aqueous conditions, and acetic acid may arise directly from hydrolysis of a metal-acetyl species.



A typical process flow diagram for methanol carbonylation is represented in Figure 1.

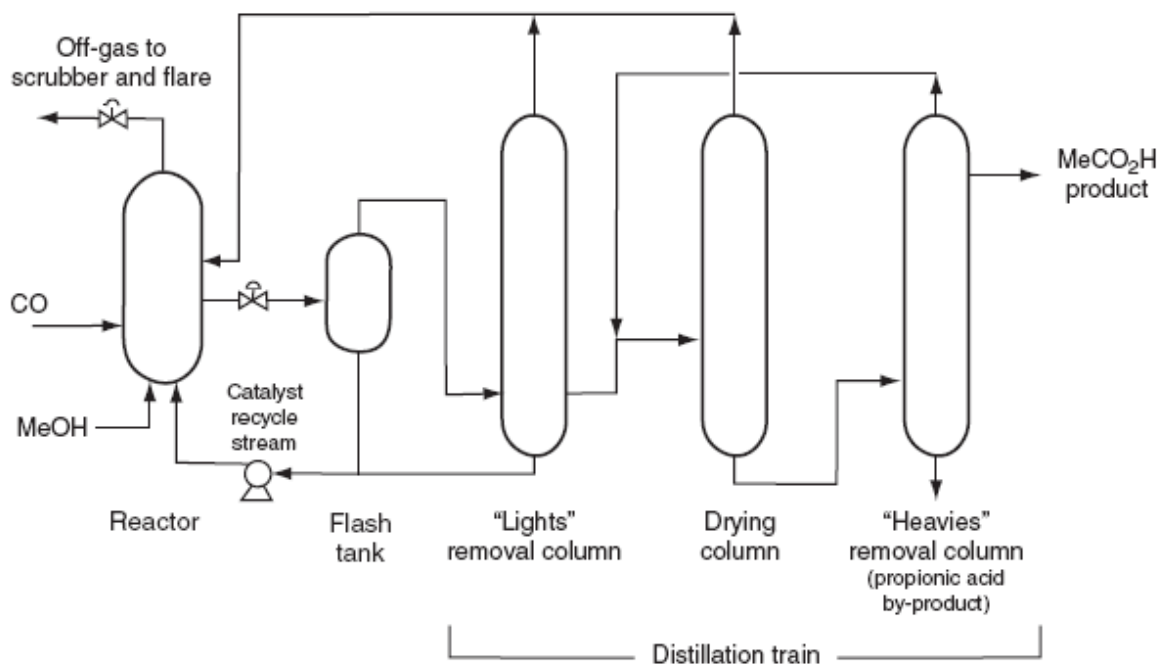


Figure 1. Process flow diagram for Rh-complex-catalyzed methanol carbonylation.

The process operates at 180-190 °C under ~ 30-40 bar of CO pressure for which feed stocks are introduced into a stirred reactor on a continuous basis and product solution flows from the reactor into a flash-tank where the initial separation of product from catalyst is achieved. Reduction of pressure in the flash-tank causes vaporization of most of the volatile components, while the catalyst remains dissolved in the liquid phase and is recycled back to the reactor. The product stream is directed into a distillation train to remove methyl iodide, water, and heavier by-products from the acetic acid product. These by-products include propionic acid and higher-molecular-weight organics, arising from condensation reactions of acetaldehyde. Higher alkyl iodides can also form, especially if iodide salts are added to the rhodium catalyst.

The relatively low partial pressure of CO in the flash-tank has implications for catalyst stability. Since the Rh catalyst exists principally as iodocarbonyl complexes ($[\text{RhI}_2(\text{CO})_2]^-$ and $[\text{RhI}_4(\text{CO})_2]^-$), loss of CO ligands and precipitation of insoluble species (RhI_3) can be

problematic. The conventional Monsanto process operates with a relatively high water concentration (10-15 wt %) that helps to maintain catalyst stability and solubility. Yet, this operation results in a costly separation process to dry the product, requiring three distillation columns. The presence of water also results in the occurrence of the WGS reaction (Equation 2), in competition with the desired carbonylation process, resulting in a lower amount of available CO. From a commercial point of view, methanol carbonylation operating at low water concentration with high activity and good catalyst stabilization is the main goal. Strategies to achieve this operation consist in:

- (1) Addition of iodide salt to promote and stabilize the Rh-complex-catalyst.
- (2) Anchoring the Rh-complex-catalyst to a polymer support to maintain the catalyst in the reactor.

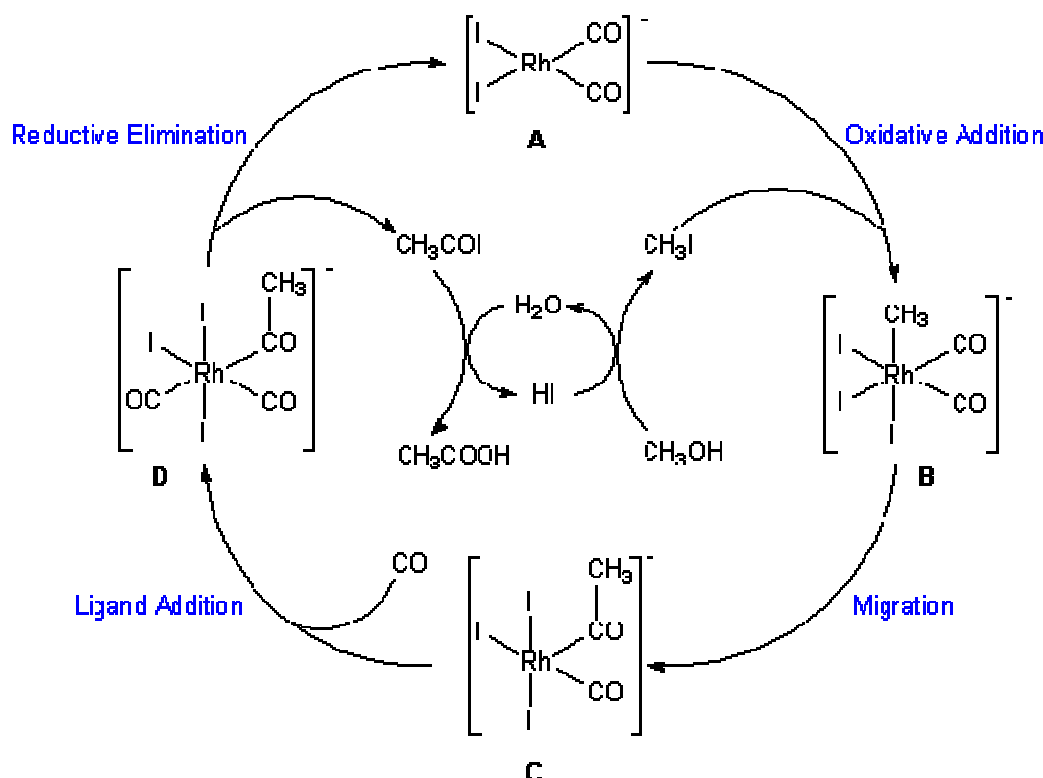
Along with long-term catalyst stability, the other key issues for any catalytic process are both activity and selectivity. Emphasis on attempts to improve activity by using **ligand-modified** Rh-catalysts is described in the following sections.

I-4 [Rh]-complex-catalyzed methanol carbonylation

I-4-1 *Reaction mechanism*

The Monsanto catalyst system has been the subject of numerous studies (leading references).^{9,10} The catalytic cycle of this classic example of a homogeneous catalytic reaction consists of six steps (Scheme 1).¹¹ The cycle includes several of the main reaction types known in organometallic chemistry¹², such as oxidative addition, ligand migration, CO insertion, and reductive elimination. These types of elementary steps have been examined separately in a number of experimental and theoretical studies.¹³ Systematic studies including

a detailed inspection of full catalytic cycles are scarce.¹⁴ The catalytic cycle of methanol carbonylation was proposed¹¹ on the basis of selected data on structures of reactants and intermediates which have been identified by X-ray crystallography,^{9a} infrared and NMR spectroscopy (Scheme 1).¹⁵



Scheme 1. Admitted catalytic cycle of the Rh-complex-catalyzed methanol carbonylation.

The rate of the overall carbonylation process is zero order in each of the reactants (MeOH and CO) but first order in the rhodium catalyst and in the methyl iodide cocatalyst, that is, $\text{Rate} = k[\text{Rh}][\text{MeI}]$, with k characterized by activation parameters $\Delta H^\ddagger = 63.6 \text{ kJ mol}^{-1}$ and $\Delta S^\ddagger = -116 \text{ J}\cdot\text{mol}^{-1}\cdot\text{K}^{-1}$.^{9b} Kinetic investigations have confirmed the catalytic cycle depicted in Scheme 1. The anion *cis*- $[\text{RhI}_2(\text{CO})_2]^-$ (**A**) was found to be the initial catalytically active species¹¹ and was identified as a Rh(I) square planar complex by *in situ* high pressure infrared (HPIR) spectroscopy¹⁶. Its interaction with the substrate CH_3I results in the formation of the hexacoordinated complex $[\text{RhI}_3(\text{CH}_3)(\text{CO})_2]^-$ (**B**),¹⁵ which is kinetically unstable.

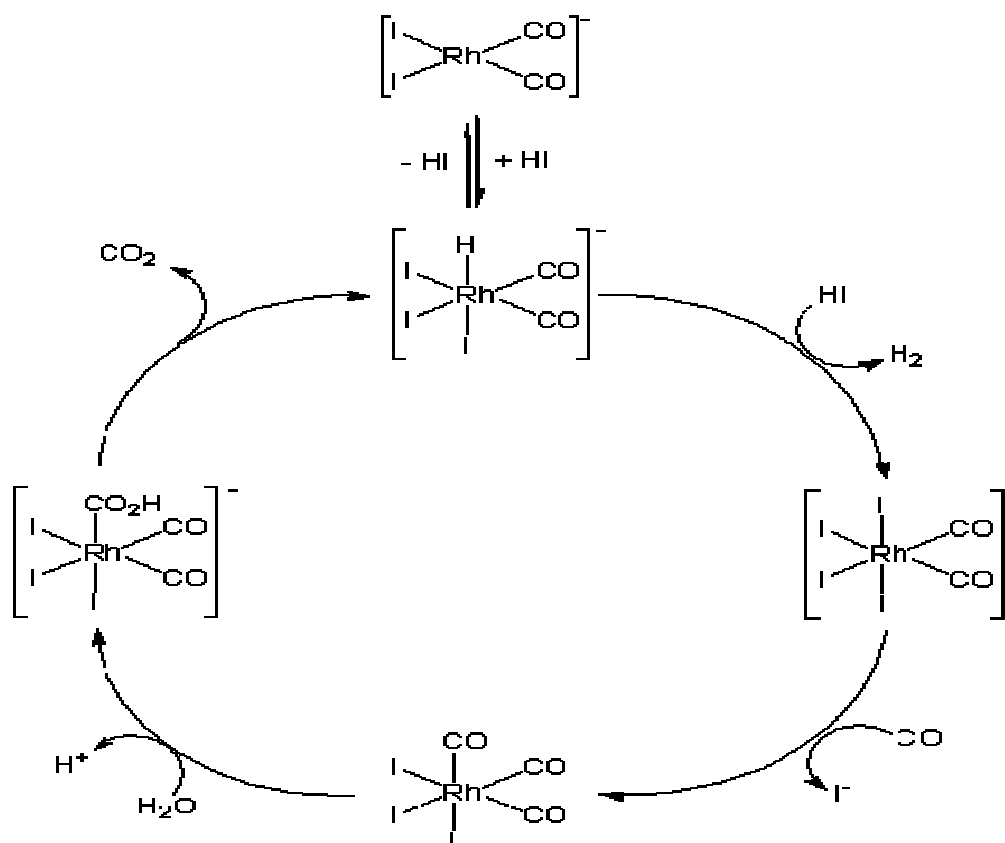
Oxidative addition of methyl iodide to *cis*-[RhI₂(CO)₂]⁻ (**A**) is the rate-determining step of the cycle, consistent with the observed kinetics. A large negative entropy of activation is consistent with initial nucleophilic attack by Rh on the carbon of methyl iodide, releasing I⁻ which coordinates to the metal center in a subsequent step. The reactive methyl complex, [RhI₃(CH₃)(CO)₂]⁻ (**B**), was not observed in the original work by Forster. However, Haynes et al.^{15,17} found that this key intermediate could be detected spectroscopically by using very high MeI concentrations to increase its near-steady-state concentration during the stoichiometric reaction of [RhI₂(CO)₂]⁻ (**A**) with MeI. IR and ¹³C NMR spectroscopic evidence supported a *fac,cis* geometry for [RhI₃(CH₃)(CO)₂]⁻ (**B**) and detection of this intermediate enabled estimates of the rate and activation parameters of the subsequent methyl migration reaction.

[RhI₃(CH₃)(CO)₂]⁻ (**B**) transforms into the isomeric pentacoordinated acetyl complex [RhI₃(CH₃CO)(CO)]⁻ (**C**) as a result of the migration of the methyl group to the CO ligand.¹⁸ The rhodium acetyl complex **C** is the only intermediate of the catalytic cycle which was isolated as a dimer^{9a} and its structure was determined by X-ray crystallography.^{19,20} The rhodium acetyl anion **C** was found to form a dianionic iodide-bridged dimer [Rh(μ-I)₂(COMe)(CO)]₂²⁻ through a very weak Rh-I-Rh bridge (with a rhodium-iodine distance of 3.0 Å, as compared to 2.7 Å commonly found for Rh-I bonds¹⁹). Complex dimer [{Rh(μ-I)₂(COMe)(CO)}₂]²⁻ exists in non-coordinating solvents, but is readily cleaved to monomeric species ([RhI₃(COMe)(CO)(sol)]⁻ or [RhI₂(COMe)(CO)(sol)₂]) in coordinating solvents.^{19,21} Complex **C** reacts rapidly with CO to form the six-coordinated dicarbonyl complex [RhI₃(COMe)(CO)₂]⁻ **D** with terminal CO ligands.¹⁹ This species has been characterized by IR and NMR spectroscopy as a *mer, trans*-isomer.²² An isomerization to a *fac,cis*-isomer was proposed to facilitate the subsequent elimination of CH₃COI.²² The *fac,cis*-isomer decomposes at room temperature to yield acetyl iodide CH₃COI and [RhI₂(CO)₂]⁻; the latter

species starts the next catalytic cycle. Finally, acetic acid is formed by acetyl iodide hydrolysis.

An alternative to sequential reductive elimination and hydrolysis of acetyl iodide is direct reaction of water with a rhodium acetyl complex to give acetic acid. The relative importance of these two alternative pathways has not yet been fully determined, although the catalytic mechanism is normally depicted as proceeding via reductive elimination of acetyl iodide from the rhodium center.

As mentioned earlier, the WGS reaction occurs in competition with methanol carbonylation. The mechanism of the WGS reaction, shown in Scheme 2, involves oxidation of Rh(I) to Rh(III) by reaction with HI.²³ Reaction of $[\text{RhI}_2(\text{CO})_2]^-$ with HI initially gives the hydride, $[\text{RhI}_3\text{H}(\text{CO})_2]^-$,²⁴ but this reacts readily with a second equivalent of HI to release H_2 and forms the Rh(III) anionic tetraiodide complex, $[\text{RhI}_4(\text{CO})_2]^-$. As in the case of the acetyl complex, $[\text{RhI}_3(\text{COMe})(\text{CO})_2]^-$, both the hydride and the tetraiodide are more stable as the *trans*-dicarbonyl isomers.



Scheme 2. Catalytic cycle of the Water-Gas Shift reaction as side-reaction in the Rh-complex-catalyzed methanol carbonylation.

Addition of I_2 to $\text{cis-}[\text{RhI}_2(\text{CO})_2]^-$ initially gives $\text{cis-}[\text{RhI}_4(\text{CO})_2]^-$ and a kinetic study of the *cis-trans* isomerization suggested a mechanism involving CO loss.²⁵ In situ HP-IR measurements of catalyst solutions revealed the presence of $\text{trans-}[\text{RhI}_4(\text{CO})_2]^-$ alongside $[\text{RhI}_2(\text{CO})_2]^-$ under conditions of low water concentration,²⁶ as well as during the anhydrous carbonylation of methyl acetate to acetic anhydride.²⁷ Complex $[\text{RhI}_4(\text{CO})_2]^-$ is an inactive form of the catalyst, so an accumulation of this species results in a decrease in the catalytic carbonylation rate.

In addition, loss of CO from $[\text{RhI}_4(\text{CO})_2]^-$, in regions of reduced CO pressure, can lead to $[\text{RhI}_4(\text{CO})(\text{sol})]^-$ and subsequent precipitation of insoluble rhodium (III) species (RhI_3).

Increasing the water concentration accelerates the reduction of $[\text{RhI}_4(\text{CO})_2]^-$ back to the active Rh(I) catalyst, completing the WGS reaction cycle, as depicted on Scheme 2.

Thus, high water concentrations help both to keep the rhodium-complex catalyst in its active form and to prevent catalyst precipitation. This situation leads to a characteristic dependence of rate on water concentration for the rhodium-complex-catalyzed process that attains a plateau when the solution contains more than ~ 10 wt % in water.

I-4-2 Reaction promotion by iodide salts

One approach that enables the use of lower water concentrations for rhodium-complex-catalyzed methanol carbonylation is the addition of iodide salts, as exemplified by the Celanese Acid Optimization (AO) technology.^{9f,28} A lithium iodide promoter allows to reach carbonylation rates that are comparable with those obtained in the conventional Monsanto process but at significantly lower water concentrations. The AO technology has been implemented to increase productivity at the Celanese facility in Clear Lake, Texas, and in a new 500 kT/year plant in Singapore.

Lowering the water concentration would normally result in a decrease in the proportion of rhodium existing as $[\text{RhI}_2(\text{CO})_2]^-$. However, the LiI-promoted process also employs a higher concentration of methyl acetate, which reacts with the other components as shown in Equations 8 and 9.



Thus, raising the methyl acetate concentration results in a lower HI concentration, which tends to inhibit oxidation of $[\text{RhI}_2(\text{CO})_2]^-$ to give $[\text{RhI}_4(\text{CO})_2]^-$, thus suppressing the WGS reaction significantly, which is beneficial for catalytic carbonylation activity.

It has also been proposed that iodide salts can promote the oxidative addition of MeI to $[\text{RhI}_2(\text{CO})_2]^-$, the rate-determining step in the cycle of the rhodium-complex-catalyzed methanol carbonylation reaction.²⁹ The precise mechanism of this promotion remains unclear and formation of a highly nucleophilic dianion, $[\text{RhI}_3(\text{CO})_2]^{2-}$, has been suggested, although there is no direct spectroscopic evidence of it. The possible participation of this dianion has been considered in a theoretical investigation.³⁰ An alternative nucleophilic dianion, $[\text{RhI}_2(\text{CO})_2(\text{OAc})]^{2-}$, has also been proposed^{31,32} on the basis that acetate salts (either added or generated in situ via Equation 8) are present in the medium.

Iodide salts are also efficient promoters and stabilizers for the anhydrous carbonylation of methyl acetate to acetic anhydride as for example the Eastman process that utilizes LiI or BP Chemicals throughout a process since 1988 that coproduces acetic anhydride and acetic acid using LiI and a quaternary ammonium iodide salt. These processes will not be described further.

Ionic liquids such as quaternary ammonium and phosphonium salts have also attracted attention as a means of immobilizing the rhodium catalyst. Processes for carbonylation of methanol with either gas-phase³³ or liquid-phase³⁴ reactants using $[\text{RhI}_2(\text{CO})_2]^-$ dissolved in an ionic liquid have been claimed. Ionic liquids are non-volatile, which aids in product separation, and the anionic rhodium complex is highly soluble in such solvents. However, ionic liquids are relatively expensive and their high viscosities can create mass-transfer limitations associated with slow diffusion of reactants. If the transport limitation is significant, the catalysis occurs predominantly near the surface of the ionic liquid, and the $[\text{RhI}_2(\text{CO})_2]^-$

dissolved in the bulk is not fully utilized. One attempt to address these issues was to use a supported ionic liquid phase (SILP) catalyst, as reported by Riisager et al.³⁵ In this system, the ionic liquid (1-butyl-3-methylimidazolium iodide) was supported as a thin film on solid silica (the thin film offers little mass-transport resistance) and used in a fixed-bed continuous reactor with gas-phase methanol. Rates were achieved that were comparable to those in Eastman's bubble column carbonylation reactor with gas phase reactants,³³ but using a much smaller amount of ionic liquid.

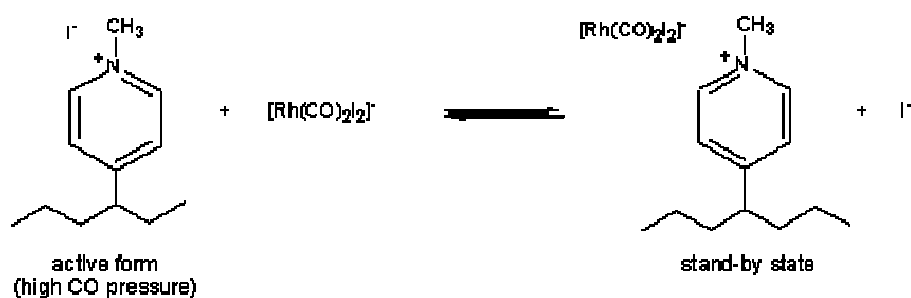
I-4-3 Supported rhodium catalysts

In all homogeneous catalytic processes, the catalyst must be separated from the liquid product and recycled properly to the reactor avoiding loss, especially when the metal is very expensive like rhodium. In order to overcome this situation, immobilization of the Rh-complex on a support has been the subject of considerable research. Active carbon was investigated as a possible support and proposed for vapor-phase operation.³⁶ However, reaction rate and selectivity were poorer than with homogeneous catalysts. Inorganic oxides and zeolites were also studied as catalyst supports for use in vapor-phase operation.³⁷

The catalyst immobilization can be made via covalent bonding, in which the support is modified to contain a pendant group (usually a phosphine) capable of acting as a ligand for the metal complex. However, metal-ligand bond cleavage makes irreversible leaching of the catalyst from the solid support a main drawback. This leaching is particularly problematic under the harsh conditions used for methanol carbonylation, as pendant phosphines are prone to degradation by the aqueous acidic medium and quaternization by methyl iodide. An alternative strategy for catalyst immobilization uses ion-pair interactions between ionic catalyst complexes and ion-exchange resins. All the rhodium complexes in the catalytic methanol carbonylation cycle are anionic making this method an attractive solution for ionic

immobilization. In 1981, Drago et al. described the effective immobilization of the rhodium catalyst on polymeric supports based on methylated polyvinylpyridines.³⁸ The activity was reported to be similar to that of the homogeneous system at 120 °C with minimal leaching of the supported catalyst. The ionically bound complex $[\text{RhI}_2(\text{CO})_2]^-$ was identified by IR spectra of the impregnated resin. DeBlasio et al.³⁹ reported the behavior of rhodium catalysts supported on zirconia, carbon, polyvinylpyrrolidone (PVP), and PPh_2 -modified crosslinked polystyrene. Leaching of rhodium catalyst into the liquid phase was found to occur in all cases. The PVP- and PPh_2 -modified cross-linked polystyrene supports were also investigated in methanol carbonylation with vapor-phase reactants, with the PVP system showing good activity and selectivity as well as negligible leaching of rhodium in long-term tests.⁴⁰ The better performance of the PVP-supported catalyst was attributed to strong ion-pair interactions between $[\text{RhI}_2(\text{CO})_2]^-$ and the quaternized pyrrolidone sites on the polymer.

The ionic immobilization method received considerable interest from industry.⁴¹ The best example is in 1998 with the AceticaTM process operated by Chiyoda and UOP (Universal Oil Products), which uses a polyvinylpyridine resin tolerant of elevated temperatures and pressures as the support.^{41c,d,f} They introduced novel pyridine resins and catalysts that exhibited high activity, long catalyst life, and no significant rhodium loss for methanol carbonylation reaction into acetic acid. Until the recent development of a commercial heterogeneous rhodium catalyst system by Chiyoda, no successful demonstration of such a catalyst had been known. Under the reaction conditions, the rhodium system is converted to its catalytically active anion form $[\text{RhI}_2(\text{CO})_2]^-$. Furthermore, the nitrogen atoms of the resin pyridine groups become positively charged after quaternization with methyl iodide. Thus, after counter-ion exchange, the active anionic rhodium complex $[\text{RhI}_2(\text{CO})_2]^-$ is maintained in the positive polymeric matrix by strong electrostatic interactions, as shown in Scheme 3.



Scheme 3. Equilibrium between the active form and the resting-state of the supported-catalyst in the Acetica™ process.

The concentration of rhodium on the solid phase is determined by the ion exchange equilibrium. Because equilibrium strongly favors the solid phase, virtually all the rhodium in the reaction mixture is immobilized. The catalyst exhibited no deactivation after continuous operation for more than 7000 h.

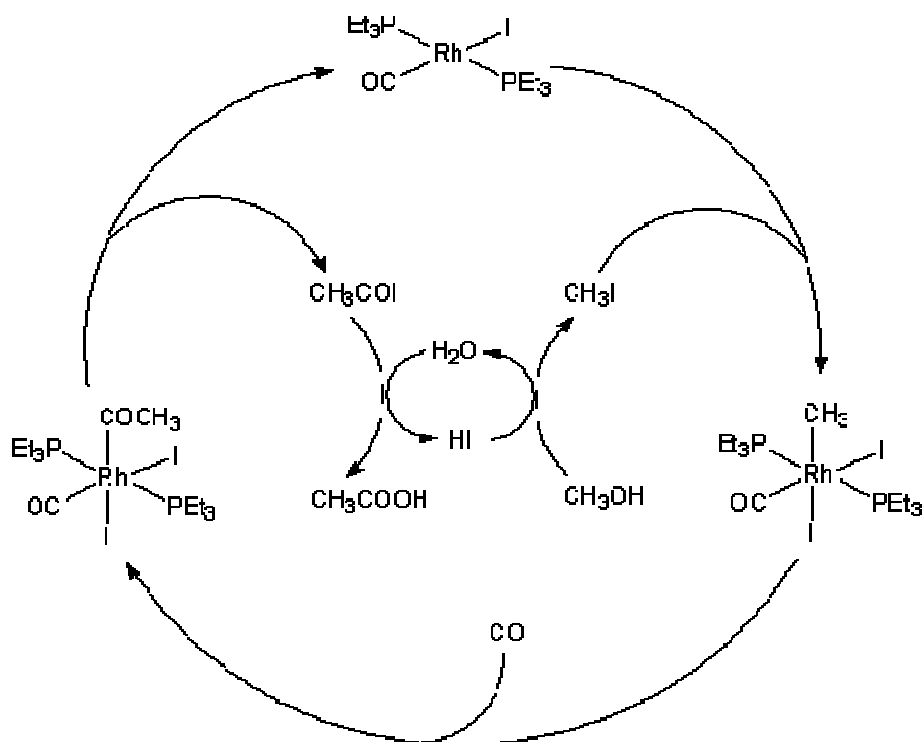
With homogeneous methanol carbonylation routes, acetic acid productivity is directly proportional to the catalyst concentration in the reaction liquid, and as a consequence, the acetic acid production is restricted by the solubility of the active metal. Only limited success has been achieved in improving the catalyst solubility by increasing the water concentration or by adding iodide salt stabilizers, because both additives give rise to increased recycling costs, higher corrosion rates and separation problems. Immobilization of the catalyst significantly reduces the loss of expensive rhodium metal, because the catalyst is confined to the reactor rather than circulating downstream, where reduced pressures may cause losses of the catalyst by precipitation of rhodium or evaporation of volatile rhodium carbonyl compounds.

I-4-4 Ligand tuning for accelerated catalysis

Significant research efforts are still devoted to explore and improve the Rh catalyst activity and stability, particularly by tuning the electron density brought to the metal center by the appropriate ligand for promoting the rate of the kinetically limiting oxidative addition step. Thus, the catalytic reaction rate can potentially be improved by the introduction of strong electron-donating ligands that increase the nucleophilicity. For this purpose, other rhodium compounds have been synthesized in recent years, and they have shown to be active catalysts of comparable or better performance as compared to the initial Monsanto catalyst. Most attempts to do this have employed phosphine ligands and their derivatives, commonly utilized in other homogeneous rhodium-catalyzed processes such as alkene hydrogenation or hydroformylation. In the original communication from Monsanto⁸, $[\text{RhCl}(\text{CO})(\text{PPh}_3)_2]$ was included among a list of viable catalyst precursors, and the promotion by phosphines, arsines, and stibines was later claimed in a patent.⁴² Brodzki et al.⁴³ also reported the use of rhodium complexes containing PPh_3 and dppe (1,2-*bis*(diphenylphosphino)ethane) in methanol carbonylation, and Moser et al.^{44,45} reported detailed in situ HP-IR spectroscopic investigations of PPh_3 -promoted nickel catalysts.

Cole-Hamilton et al.⁴⁶ investigated the use of trialkylphosphines as promoters for rhodium-based carbonylation catalysts, because they are strongly electron-donating. Complexes of the type $[\text{Rh}(\text{X})(\text{CO})(\text{PEt}_3)_2]$ ($\text{X} = \text{Cl}, \text{Br}$ or I) have a ν_{CO} absorption centered around 1960 cm^{-1} , as compared to 1988 and 2059 cm^{-1} for $[\text{RhI}_2(\text{CO})_2]^-$, suggesting that the rhodium center is more electron-rich in the triethylphosphine complexes. $[\text{RhCl}(\text{CO})(\text{PEt}_3)_2]$ turned out to be a very active catalyst precursor for acetic acid production: in the presence of 17.1 wt % of H_2O at 120 to 150 °C and 27 bar pressure, $[\text{RhI}(\text{CO})(\text{PEt}_3)_2]$ catalyzes the carbonylation of methanol at a rate nearly twice as high as that of $[\text{RhI}_2(\text{CO})_2]^-$. Water acts to

maintain the catalyst in its active form (as a Rh(I) complex) and decreases the formation of inactive Rh(III) complexes such as $[\text{RhI}_4(\text{CO})_2]^-$ or $[\text{RhI}_3(\text{CO})(\text{PEt}_3)_2]$. Thus, the rate of carbonylation is dramatically enhanced by a high water concentration. With low water concentrations, no appreciable benefit is obtained by using $[\text{RhCl}(\text{CO})(\text{PEt}_3)_2]$ instead of $[\text{Rh}(\text{CO})_2\text{Cl}]_2$ as catalyst precursor. Addition of methyl iodide to $[\text{RhI}(\text{CO})(\text{PEt}_3)_2]$ in CH_2Cl_2 resulted in the formation of $[\text{RhI}_2(\text{CO})(\text{CH}_3)(\text{PEt}_3)_2]$ (Scheme 4). The methyl group is *cis* with respect to the carbonyl ligand, as required for migratory insertion. There is no X-ray crystal structure analysis for complexes of the type $[\text{RhX}_2(\text{CO})(\text{CH}_3)(\text{PR}_3)_2]$. However, there are other six-coordinate Rh(III) complexes resulting from oxidative addition of CH_3I , most of them have iodide and methyl ligands in mutually *trans* positions.⁴⁷ The isolation of the methyl complex from a catalytically active system is rather unlikely, since the insertion of carbon monoxide into the Rh-C bond is extremely rapid. For $[\text{RhI}_2(\text{CO})_2]^-$, the methyl complex has a very short lifetime and was only detected as a transient by IR spectroscopy in neat methyl iodide,^{14c} while for the related $[\text{RhCl}(\text{CO})(\text{PPh}_3)_2]$ the oxidative addition of methyl iodide gives the six-coordinate complex $[\text{Rh}(\text{Cl})(\text{I})(\text{CH}_3)(\text{CO})(\text{PPh}_3)_2]$ in equilibrium with the five-coordinate insertion product, $[\text{Rh}(\text{Cl})(\text{I})(\text{COCH}_3)(\text{PPh}_3)_2]$. In the case of the triethylphosphine analogue, the higher electron density on the metal is responsible for the less facile methyl migration in $[\text{RhI}_2(\text{CO})(\text{CH}_3)(\text{PEt}_3)_2]$. Despite the stability of the methyl-Rh(III) complex, preliminary kinetic studies suggest that oxidative addition of CH_3I is still rate-determining.

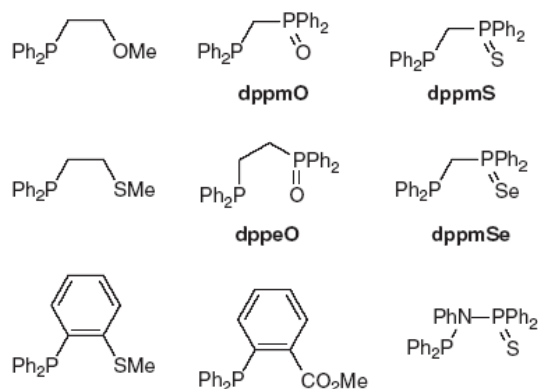


Scheme 4. Catalytic cycle of the methanol carbonylation catalyzed by the neutral complex $[\text{RhI}(\text{CO})(\text{PEt}_3)_2]$.

Notwithstanding the high initial activity of the Rh/PEt₃ system, catalyst degradation occurs via loss of the phosphine ligands, to give P(V) species such as Et₃PI⁺, Et₃PH⁺, Et₃PMe⁺, and Et₃PO. The rhodium complex catalyst reverts to $[\text{RhI}_2(\text{CO})_2]^-$, and so the enhanced activity is short-lived. The harsh conditions employed for methanol carbonylation (aqueous AcOH/HI, 150-200 °C, and CO at high pressure) mean that phosphine ligand dissociation and degradation is a common problem for phosphine-modified rhodium catalysts.

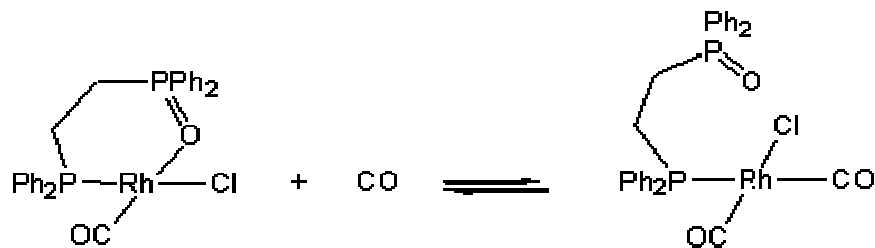
Heterodifunctional phosphine derivatives (Scheme 5) have also received considerable attention since the late 1980's. Bader and Lindner⁴⁸ investigated the use of ether-phosphines such as Ph₂PCH₂CH₂OMe, in which the ether oxygen can coordinate reversibly to the metal center. In a more recent variation on this theme, Dutta and coworkers⁴⁹ used a functionalized triarylphosphine ligand, PPh₂(C₆H₄-2-CO₂Me), that contains an *ortho*-ester substituent. A

number of other ligand types, including modified pyridines, phenols, and benzoic acids, have been tested by the group of Dutta⁵⁰ in the rhodium-complex-catalyzed methanol carbonylation.



Scheme 5. Examples of heterodifunctional ligands applied in methanol carbonylation.

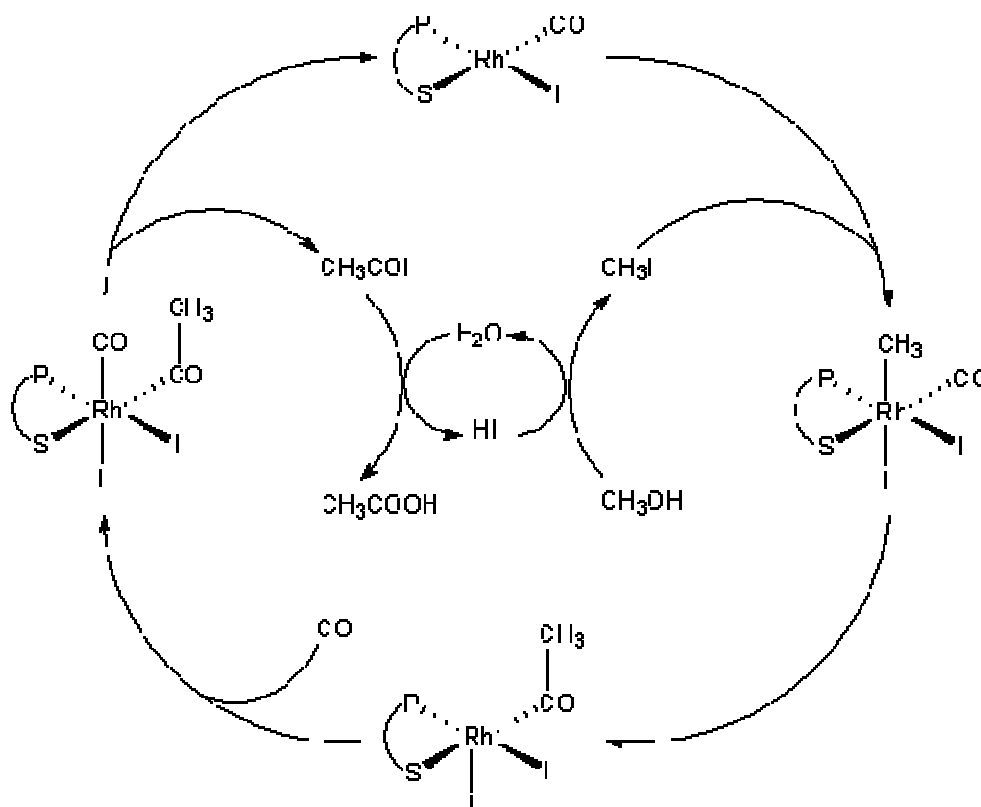
Wegman et al. have found that cis -[RhCl(CO){Ph₂P(CH₂)₂P(O)Ph₂}] is a precursor to a very active catalyst for the carbonylation of methanol under mild reaction conditions.⁵¹ Reaction of cis -[RhCl(CO){Ph₂P(CH₂)₂P(O)Ph₂}] with CO results in the displacement of the rhodium-oxygen bond and the formation of a new species (ν_{CO} 2096 and 2012 cm⁻¹) according to the equilibrium shown in Scheme 6.



Scheme 6. Equilibrium between [RhCl(CO){ κ^2 -Ph₂P(CH₂)₂P(O)Ph₂}] and [RhCl(CO){ κ^1 -Ph₂P(CH₂)₂P(O)Ph₂}]

The ratio of the κ^2 - and the κ^1 - complexes was determined to be approximately 1 : 1 (at 22 °C and 1 bar CO) by infrared spectroscopy. Infrared spectroscopic studies carried out under catalytic conditions at 80 °C and 3.5 bar CO (turnover frequency 400 h⁻¹) reveal only the κ^1 - coordinated phosphine oxide species. There is no indication of [RhI₂(CO)₂]⁻ which is the principal rhodium species present during catalysis with the Rh-I catalyst. In addition there is no induction period as might be expected if dissociation of Ph₂P(CH₂)₂P(O)Ph₂ and subsequent formation of [Rh(CO)₂I₂]⁻ is significant.

Baker et al. have found that the use of the diphosphinesulfide Ph₂PCH₂P(S)Ph₂ as a promoter for rhodium catalysed carbonylation of methanol allows a substantial rate increase under industrially feasible conditions (180 °C, 70 bar CO).⁵² The initial experiments were carried out using a ligand/rhodium ratio of 4 : 1, but the optimum rate enhancement was observed when the discrete complex *cis*-[RhCl(CO){ κ^2 -Ph₂PCH₂P(S)Ph₂}] was used as pre-catalyst. These authors showed that any additional phosphine quaternizes with CH₃I, and the addition of iodide inhibits the catalytic reaction (Scheme 7).

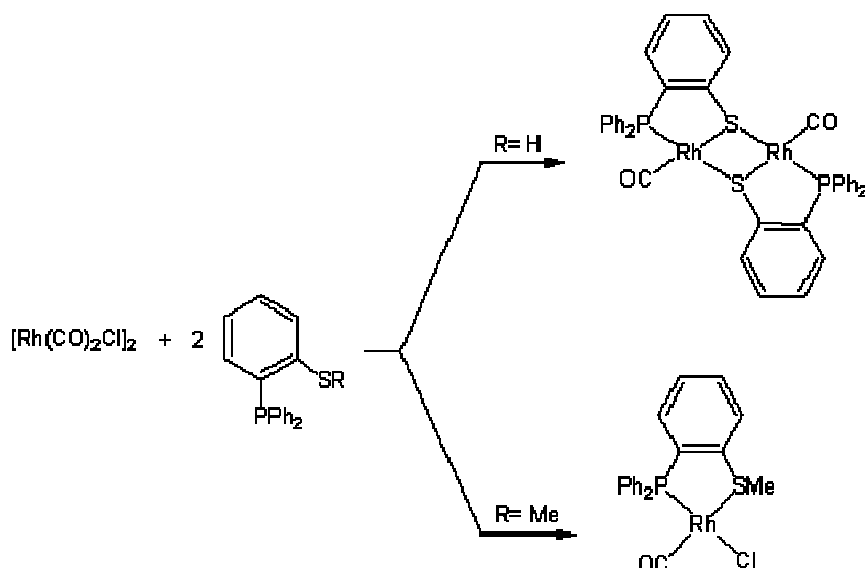


Scheme 7. Catalytic cycle of the methanol carbonylation catalyzed by the neutral complex $[\text{RhI}(\text{CO})\{\text{Ph}_2\text{PCH}_2\text{P}(\text{S})\text{Ph}_2\}]$

Addition of three equivalents of $[(\text{CH}_3)\text{PPh}_3]\text{I}$ causes a similar retardation in rate. $[\text{RhCl}(\text{CO})\{\text{Ph}_2\text{PCH}_2\text{P}(\text{S})\text{Ph}_2\}]$ is readily formed upon mixing $[\text{Rh}(\text{CO})_2\text{Cl}]_2$ with two equivalents of $\text{Ph}_2\text{PCH}_2\text{P}(\text{S})\text{Ph}_2$ in CH_3OH , and there is no evidence for the formation of dinuclear complexes in this reaction. The X-ray crystal structure analysis of $[\text{RhCl}(\text{CO})\{\text{Ph}_2\text{PCH}_2\text{P}(\text{S})\text{Ph}_2\}]$ confirms the stereochemistry regarding rhodium in which the phosphorus atom is *trans* with respect to the chloro ligand, while the sulfur atom is *trans* with respect to the carbonyl ligand; but the structure shows no unusual features to explain the unexpected stability of the catalyst at high temperatures. Unlike in the case of the oxygen analogue, in the case of $[\text{RhCl}(\text{CO})\{\text{Ph}_2\text{PCH}_2\text{P}(\text{S})\text{Ph}_2\}]$, there is no evidence for a hemilabile behavior of the P-S ligand, while it has been assumed to be important for catalysis employing mixed-donor ligands.⁴⁸ These results showed for the first time that a discrete rhodium-

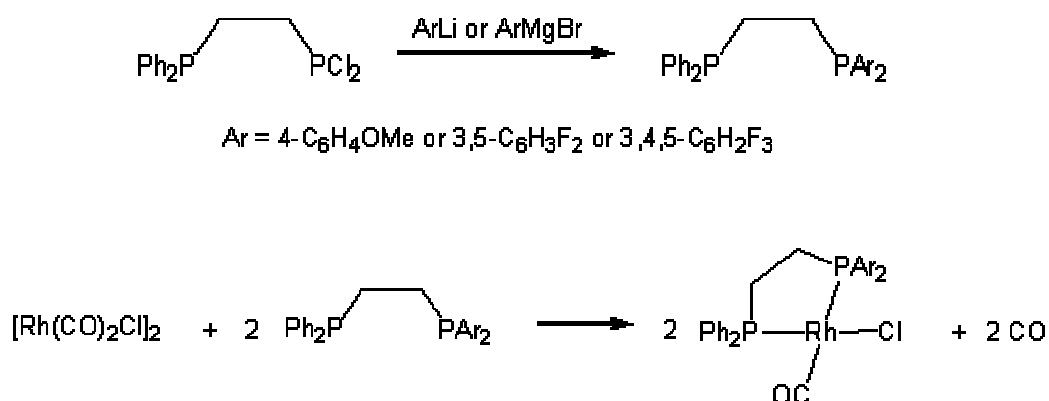
phosphine complex can give a significant improvement in carbonylation activity over $[\text{Rh}(\text{CO})_2\text{I}_2]^-$ under industrial conditions.

Dilworth et al. described other methanol carbonylation catalysts, which show significant improvements in absolute rates over those obtained with $[\text{RhI}_2(\text{CO})_2]^-$.⁵³ Both the dinuclear phosphinothiolate complex and the mononuclear phosphinothioether complex synthesized according to Scheme 8, efficiently catalyze the carbonylation of methanol with comparable rate. The authors proposed a mechanism similar to the cycle proposed for $[\text{RhI}(\text{CO})\{\text{Ph}_2\text{PCH}_2\text{P}(\text{S})\text{Ph}_2\}]$ (Scheme 7).^{52a}



Scheme 8. Synthesis of rhodium phosphinothiolate and phosphinothioether complexes.

Pringle et al. reported that rhodium complexes of unsymmetrical ethylene diphosphine ligands are more efficient catalysts than the symmetrical dppe analogues for methanol carbonylation and longer-lived than any other reported ligand-modified catalysts under industrial conditions.⁵⁴ The catalysts were prepared by addition of diphosphines to $[\text{Rh}(\text{CO})_2\text{Cl}]_2$ in methanol (Scheme 9).

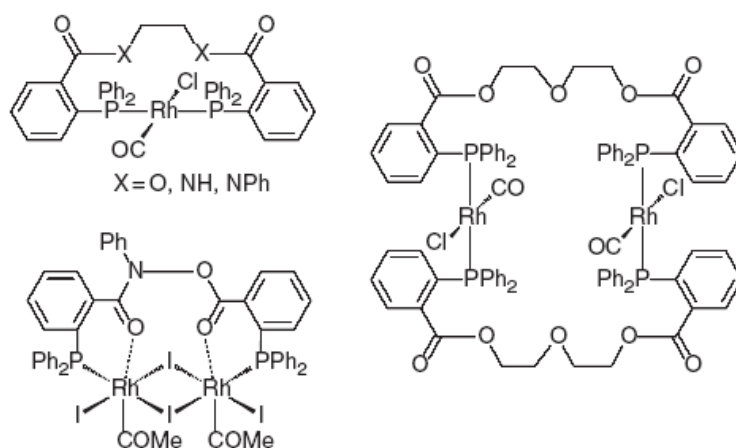


Scheme 9. Synthesis of rhodium complexes with unsymmetrical diphosphine ligands.

In each case the conversion of methanol was greater than 98%, and the selectivity for acetic acid was greater than 99%; however, the carbonylation rates are lower for these diphosphine complexes than for the $[\text{RhI}_2(\text{CO})_2]^-$ catalyst. The following observations suggest that the catalyst is indeed a diphosphine-rhodium complex throughout the catalytic reaction and not $[\text{Rh}(\text{CO})_2\text{I}_2]^-$. Infrared spectra obtained *in situ* during catalysis with $\text{Ph}_2\text{PCH}_2\text{CH}_2\text{P}(3,4,5\text{-C}_6\text{H}_2\text{F}_3)_2$ showed the absence of the intense ν_{CO} bands of $[\text{RhI}_2(\text{CO})_2]^-$ at 2059 and 1988 cm^{-1} . At the end of the catalytic reaction, ^{31}P NMR and IR spectra showed the presence of a mixture of diphosphine Rh(III) carbonyl complexes. The product *fac*- $[\text{RhI}_3(\text{CO})\{\text{Ph}_2\text{PCH}_2\text{CH}_2\text{P}(3,4,5\text{-C}_6\text{H}_2\text{F}_3)_2\}]$ was isolated from the reaction mixture, using the catalyst $[\text{RhCl}(\text{CO})\{\text{Ph}_2\text{PCH}_2\text{CH}_2\text{P}(3,4,5\text{-C}_6\text{H}_2\text{F}_3)_2\}]$.^{54a} The rate of catalysis is constant throughout a catalytic run and, after consumption of the entire methanol, a second aliquot of methanol was injected, the rate observed was the same as in the first run. This final observation not only confirms the integrity of the catalyst, but also shows its longevity to be greater than any previous rhodium-phosphine catalyst under these conditions, since every diphosphine complex executes over 500 turnovers without noticeable decrease of activity.

A number of recent studies were carried out with diphosphine ligands with the ability to act as *trans*-chelating ligands, rather than the *cis*-chelation commonly exhibited by the

bidentate ligands. A *trans*-chelating ligand can be considered to mimic the coordination geometry in Vaska-type complexes of monodentate phosphines, that is, *trans*-[Rh(CO)(PR₃)₂X]. Süß-Fink and coworkers⁵⁵ synthesized ligands using condensation reactions of 2-diphenyl-phosphinobenzoic acid with an appropriate diol, diamine, or amino alcohol. All the ligands having a simple C₂H₄ spacer in the backbone formed square-planar Rh(I) complexes containing a *trans*-chelating diphosphine, whereas a dinuclear complex was obtained for a diphosphine with a longer C₂H₄-O-C₂H₄ linker (Scheme 10). When tested in rhodium-complex-catalyzed methanol carbonylation, the complexes with these ligands all gave enhanced activity relative to [RhI₂(CO)₂].



Scheme 10. Rhodium complexes with diphosphine ligands developed by Süß-Fink et al.^{55b}.

All these reported phosphorous-containing ligand complexes enhance the oxidative addition step but as a consequence they usually retard the subsequent CO insertion step, because the increased electron density at the metal not only strengthens the Rh-alkyl bond but also leads to a stronger Rh-CO bond. Optimal parameters are required to achieve the delicate balance between these two factors, which will afford highly efficient catalysts. Indeed, for example in the case of PEt₃ ligands under CO pressure, the octahedral intermediate obtained from the square-planar precursor complex after CH₃I addition undergoes immediate migratory

insertion whereas it is relatively long-lived in the case of the $\text{PPh}_2\text{-CH}_2\text{-CH}_2\text{-PPh}_2$ ligand. On the other hand, for ligand $\text{PPh}_2\text{-CH}_2\text{-P(S)Ph}_2$ to which a sulfur atom is added to the framework, reactivity is also very immediate making detection of the alkyl intermediate difficult. The fact that both oxidative addition and CO insertion steps are accelerated with the latter ligand was quite unexpected. It has therefore been assumed that the steric requirements of the $\text{PPh}_2\text{-CH}_2\text{-P(S)Ph}_2$ ligand destabilize the octahedral intermediate giving rise to facile migratory insertion. This process is possible due to the important feature of the ligand framework as it can tune the reactivity by stabilizing the metal complex via chelate formation and also create a vacant coordination site at the metal center by the cleavage of the relatively weak metal-chalcogen bond which is a prerequisite criterion for catalytic reactions.

Based on these statements, and to understand further the impact of ligands on the catalytic reactivity of rhodium complexes in methanol carbonylation, we decided to introduce donating monodentate N-containing ligands (amines, imidazoles, pyrazoles) in the coordination sphere of the Rh center to form neutral $[\text{RhI}(\text{CO})_2(\text{L})]$ complexes with moderate steric hindrance. To the best of our knowledge, neither these iodo complexes nor their reactivity towards CH_3I had been previously investigated although several chloro $[\text{RhCl}(\text{CO})_2(\text{L})]$ analogues have been well characterized. Decoordination of such ligands in the harsh reaction medium of methanol carbonylation over the long-term can be anticipated. For this reason, the choice of the N-ligands involved has been carefully examined to ensure a corresponding stabilizing counter-cation. In addition, over time, the N-containing entity loaded in excess may enhance reactivity and selectivity generating neutral and anionic Rh-complex-catalysts co-existing in the mechanism cycle.

References

- (1) Van Leeuwen, P. W. N.; Morokuma, K.; Van Lenthe, J. H.; *Theoretical Aspects of Homogeneous Catalysis*; Kluwer Academic Publishers, **1995**.
- (2) Herrmann, W. A.; Cornils, B.; *Applied Homogeneous Catalysis with Organometallic Compounds*, VCH Weinheim, **1999**.
- (3) (a) Howard, M. J.; Jones, M. D.; Roberts, M. S.; Taylor, S. A. *Catal. Today*, **1993**, *18*, 325. (b) Gauss, M.; Seidel, A.; Torrence, P.; Heymanns, P. *Applied Homogeneous: Catalysis with Organometallic Compounds*, VHC, New York, **1996**, *vol. 1*, p. 104. (c) Agreda, V. H.; Zoeller, J. R. *Acetic Acid and Its Derivatives*, Marcel Dekker, New York, **1993**, *Chapters 1-6*, p. 3. (d) Wagner, F. S. *Kirk-Othmer Encyclopedia of Chemical Technology*, 4th Edition, **1991**, *vol. 1*, p. 121.
- (4) Reppe, W.; Friederich, H.; Von Kutepow, N.; Morsch, W. US2729651 (to BASF) **1956**.
- (5) Reppe, W.; Friederich, H. US2789137 (to BASF) **1957**.
- (6) Hohenschutz, H.; Von Kutepow, N.; Himmle, W. *Hydrocarbon Process* **1966**, *45*, 141.
- (7) Von Kutepow, N.; Himmle, W.; Hohenschutz, H. *Chem. Ing. Tech.* **1965**, *37*, 383.
- (8) Paulik, F. E.; Roth, J. F. *Chem. Commun.* **1968**, 1578.
- (9) (a) Forster, D. *Adv. Organomet. Chem.* **1979**, *17*, 255. (b) Dekleva, T. W.; Forster, D. *Adv. Catal.* **1986**, *34*, 81. (c) Howard, M. J.; Jones, M. D.; Roberts, M. S.; Taylor, S. A. *Catal. Today* **1993**, *18*, 325. (d) Maitlis, P. M. Haynes, A.; Sunley, G. J.; Howard, M. J.; *J. Chem. Soc. Dalton Trans.* **1996**, 2187. (e) Yoneda, N.; Kusano, S.; Yasui, M.; Pujado, P.; Wilcher,

S. Appl. Catal. A **2001**, *221*, 253. (f) Torrence, P. in: B. Cornils, W.A. Herrmann (Eds.), *Applied Homogeneous Catalysis with Organometallic Compounds*, second ed., Vol. 1, Wiley-VCH, Weinheim, **2002**, p. 104. (g) Thomas, C. M.; Süß-Fink, G. *Coord. Chem. Rev.* **2003**, *243*, 125.

(10) Haynes, A. *Top. Organomet. Chem.* **2006**, *18* 179.

(11) Forster, D. *J. Am. Chem. Soc.* **1976**, *98*, 846.

(12) Gates, B. C. *Catalytic Chemistry*, Wiley: New York **1992**.

(13) (a) Koga, N.; Morokuma, K. *J. Am. Chem. Soc.* **1993**, *115*, 6883. (b) Sakaki, S.; Ujino, Y.; Sugimoto, M. *Bull. Chem. Soc. Jpn.* **1996**, *69*, 3047. (c) Sakaki, S.; Ieki, M. *J. Am. Chem. Soc.* **1993**, *115*, 2373. (d) Albert, K.; Gisdakis, P.; Rösch, N.; *Organometallics* **1998**, *17*, 1608.

(14) (a) Matsubara, T.; Koga, N.; Ding, Y.; Musaeov, D. G.; Morokuma, K.; *Organometallics*, **1997**, *16*, 1065. (b) Dedieu, A. *Inorg. Chem.* **1980**, *19*, 375. (c) Margl, P.; Ziegler, T.; Blöchl, P. E. *J. Am. Chem. Soc.* **1996**, *118*, 5412.

(15) Haynes, A.; Mann, B. E.; Morris, G. E. Maitlis, P. M. *J. Am. Chem. Soc.*, **1993**, *115*, 4093.

(16) D. Forster, *Ann. N.Y. Acad. Sci.* **1977**, *295*, 79.

(17) Haynes, A.; Mann, B. E.; Gulliver, D. J. Morris, G. E.; Maitlis, P. M. *J. Am. Chem. Soc.* **1991**, *113*, 8567.

-
- (18) Bassetti, M.; Monti, D.; Haynes, A.; Pearson, J. M.; Stanbridge, I. A.; Maitlis, P. M.; *Gaz. Chim. Ital.* **1992**, *122*, 391.
- (19) Adams, H.; Bailey, N. A.; Mann, B. E.; Manuel, C. P.; Spencer, C. M.; Kent, A. G. J. *Chem. Soc., Dalton Trans.* **1988**, 489.
- (20) Adamson, G. W.; Daly, J. J.; Forster, D. J. *Organomet. Chem.* **1974**, *71*, C17.
- (21) (a) Cruise, N. A.; Evans, J. J. *Chem. Soc. Dalton Trans.* **1995**, 3089. (b) Haynes, A.; Maitlis, P. M.; Stanbridge, I. A.; Haak, S.; Pearson, J. M.; Adams, H. *Inorg. Chim. Acta* **2004**, *357*, 3027.
- (22) Howe, L. A.; Bunel, E. E.; *Polyhedron* **1995**, *14*, 167.
- (23) Baker, E. C.; Hendriksen, D. E.; Eisenberg, R. *J. Am. Chem. Soc.* **1980**, *102*, 1020.
- (24) Roe, D. C.; Sheridan, R. E.; Bunel, E. E. *J. Am. Chem. Soc.* **1994**, *116*, 1163.
- (25) Haynes, A.; McNish, J.; Pearson, J. M. *J. Organomet. Chem.* **1997**, *551*, 339.
- (26) Eby, R. T.; Singleton, T. C. *Appl. Ind. Catal.* **1983**, *1*, 275.
- (27) Schrod, M.; Luft, G.; Grobe, J. *J. Mol. Catal.* **1983**, *22*, 169.
- (28) Smith, B. L.; Torrence, G. P.; Aguilo, A.; Alder, J. S. US Patent 5001259 (to Hoechst Celanese) **1991**.
- (29) Fulford, A.; Hickey, C. E.; Maitlis, P. M. *J. Organomet. Chem.* **1990**, *398*, 311.
- (30) Kinnunen, T.; Laasonen, K. *J. Mol. Struct. (Theochem)* **2001**, *542*, 273.

-
- (31) Murphy, M. A.; Smith, B. L.; Torrence, G. P.; Aguilo, A. *J. Organomet. Chem.* **1986**, *303*, 257.
- (32) Smith, B. L.; Torrence, G. P.; Murphy, M. A.; Aguilo, A. *J. Mol. Catal.* **1987**, *39*, 115.
- (33) Tustin, G. C.; Moncier, R. M. US6916951 (to Eastman Chemical Company) **2005**.
- (34) Magna, L.; Olivier-Bourbigou, H.; Harry, S.; Commereuc, D. US Patent 7115774 (to IFP) **2006**.
- (35) Riisager, A.; Jorgensen, B.; Wasserscheid, P.; Fehrmann, R. *Chem. Commun.* **2006**, 994.
- (36) (a) Howard, M. J.; Jones, M. D.; Roberts, M. S.; Taylor, S. A. *Catal. Today*, **1993**, *18*, 325. (b) Schultz, R. G.; Montgomery, P. D. *J. Catal.* **1969**, *13*, 105.
- (37) (a) Krzywicki, A.; Marczewski, M. *J. Mol. Catal.* **1979**, *6*, 431. (b) Scurrall, M. S.; Howe, R. F. *J. Mol. Catal.* **1980**, *7*, 535.
- (38) Drago, R.S.; Nyberg, E. D.; El A'mma, A.; Zombeck, A. *Inorg. Chem.* **1981**, *3*, 641.
- (39) De Blasio, N.; Wright, M. R.; Tempesti, E.; Mazzocchia, C.; Cole-Hamilton, D. J. *J. Organomet. Chem.* **1998**, *551*, 229.
- (40) De Blasio, N.; Tempesti, E.; Kaddouri, A.; Mazzocchia, C.; Cole-Hamilton, D. J. *J. Catal.* **1998**, *176*, 253.
- (41) (a) Scates, M. O.; Warner, R. J.; Torrence, G. P. US Patent 5466874 (to Hoechst Celanese) **1995**. (b) Watson, D. J.; Williams, B. L.; Watt, R. J. European Patent 0612712 (to BP Chemicals) **1994**. (c) Minami, T.; Shimokawa, K.; Hamato, K.; Shiroto, Y.; Yoneda, N.

US Patent 5364963 (to Chiyoda) **1994**. (d) Shiroto, Y.; Hamato, K.; Asaoka, S.; Maejima, T. European Patent 0567331 (to Chiyoda) **1993**. (e) Marston, C. R.; Goe, G. L. European Patent 0277824 (to Reilly Tar) **1988**. (f) Yoneda, N.; Minami, T.; Weiszmann, J.; Spehlmann, B. *Stud. Surf. Sci. Catal.* **1999**, 121, 93.

(42) Paulik, F. E.; Hershman, A.; Knox, W. R.; Roth, J. F. US4690912 (to Monsanto) **1987**.

(43) Brodzki, D.; Leclere, C.; Denise, B.; Pannetier, G. *Bull. Soc. Chim. Fr.* **1976**, 61.

(44) Moser, W. R.; Marshik-Guerts, B. J.; Okrasinski, S. J. *J. Mol. Catal. A-Chem.* **1999**, 143, 57.

(45) Moser, W. R.; Marshik-Guerts, B. J.; Okrasinski, S. J. *J. Mol. Catal. A-Chem.* **1999**, 143, 71.

(46) (a) Rankin, J.; Poole, A. D.; Benyei, A. C.; Cole-Hamilton, D. J. *Chem. Commun.* **1997**, 1835. (b) Rankin, J.; Benyei, A. C.; Poole, A. D.; Cole-Hamilton, D. J. *J. Chem. Soc., Dalton Trans.* **1999**, 3771.

(47) (a) Schenck, T. G.; Milne, C. R. C.; Sawyer, J. F.; Bosnich, B. *Inorg. Chem.* **1985**, 24, 2338. (b) Lamprecht, G. J.; Van Zyl, G. J.; Leipoldt, J. G. *Inorg. Chim. Acta* **1989**, 164, 69. (c) Menu, M. J.; Desrosiers, P.; Darguenave, M.; Darguenave, Y. *Organometallics* **1987**, 6, 1822.

(48) Bader, A.; Lindner, E. *Coord. Chem. Rev.* **1991**, 108, 27.

(49) Dutta, D. K.; Woollins, J. D.; Slawin, A. M. Z.; Konwar, D.; Das, P.; Sharma, M. *Dalton Trans.* **2003**, 2674.

(50) (a) Das, P.; Sharma, M.; Kumari, N.; Konwar, D.; Dutta, D. K. *Appl. Organomet. Chem.* **2002**, *16*, 302. (b) Das, P.; Chutia, P.; Dutta, D. K. *Chem. Lett.* **2002**, 766. (c) Sharma, M.; Kumari, N.; Das, P.; Chutia, P.; Dutta, D. K. *J. Mol. Catal. A-Chem.* **2002**, *188*, 25. (d) Kumari, N.; Sharma, M.; Das, P.; Dutta, D. K. *Appl. Organomet. Chem.* **2002**, *16*, 258. (e) Kumari, N.; Sharma, M.; Chutia, P.; Dutta, D. K. *J. Mol. Catal. A Chem.* **2004**, *222*, 53. (f) Kumari, N.; Sarmah, B. J.; Dutta, D. K. *J. Mol. Catal. A Chem.* **2007**, *266*, 260. (g) Sharma, M.; Sarmah, B. J.; Bhattacharyya, P.; Deka, R. C.; Dutta, D. K. *Appl. Organomet. Chem.* **2007**, *21*, 255. (h) Sarmah, B.; Borah, B. J.; Deb, B.; Dutta, D. K. *J. Mol. Catal. A Chem.* **2008**, *289*, 95. (i) Dutta, D. K.; Chutia, P.; Sarmah, B. J.; Borah, B. J.; Deb, B.; Woollins, J. D. *J. Mol. Catal. A Chem.* **2009**, *300*, 29.

(51) (a) Wegman, R. W.; Abatjoglou, A. G. US Patent 4670570 (to Union Carbide Corporation) **1987**. (b) Wegman, R. W.; Abatjoglou, A. G.; Harrison, A. M. *J. Chem. Soc. Chem. Commun.* **1987**, 1891.

(52) (a) Baker, M. J.; Giles, M. F. Orpen, A. G.; Taylor, M. J.; Watt, R. J. *J. Chem. Soc. Chem. Commun.* **1995**, 197. (b) Baker, M. J.; Dilworth, J. R.; Sunley, J. G.; Wheatley, N. European Patent 0632006 (to BP Chemicals) **1995**.

(53) Dilworth, J. R.; Miller, J. R.; Wheatley, N.; Baker, M. J.; Sunley, J. G. *J. Chem. Soc., Chem. Commun.* **1995**, 1579.

(54) (a) Carraz, C. A.; Ditzel, E. J.; Orpen, A. G.; Ellis, D. D.; Pringle, P. G.; Sunley, G. J. *Chem. Commun.* **2000**, 1277. (b) Casey, C. P.; Paulsen, E. L.; Beuttenmueller, E. W.; Proft, B. R.; Matter, B. A.; Powell, D. R. *J. Am. Chem. Soc.* **1999**, *121*, 63. (c) Brunner, H.; Stumpf,

A. *J. Organomet. Chem.* **1993**, 459, 139. (d) Kapoor, P. N.; Pathak; D. D., Gaur, G.; Kutty, M. *J. Organomet. Chem.* **1984**, 276, 167.

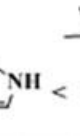
(55) (a) Thomas, C. M.; Süss-Fink, G. *Coord. Chem. Rev.* **2003**, 243, 125. (b) Thomas, C. M.; Mafua, R.; Therrien, B.; Rusanov, E.; Stoeckli-Evans, H.; G. Süss-Fink, G. *Chem. Eur. J.* **2002**, 8, 3343. (c) Burger, S.; Therrien, B.; Süss-Fink, G. *Helv. Chim. Acta* **2005**, 88, 478.

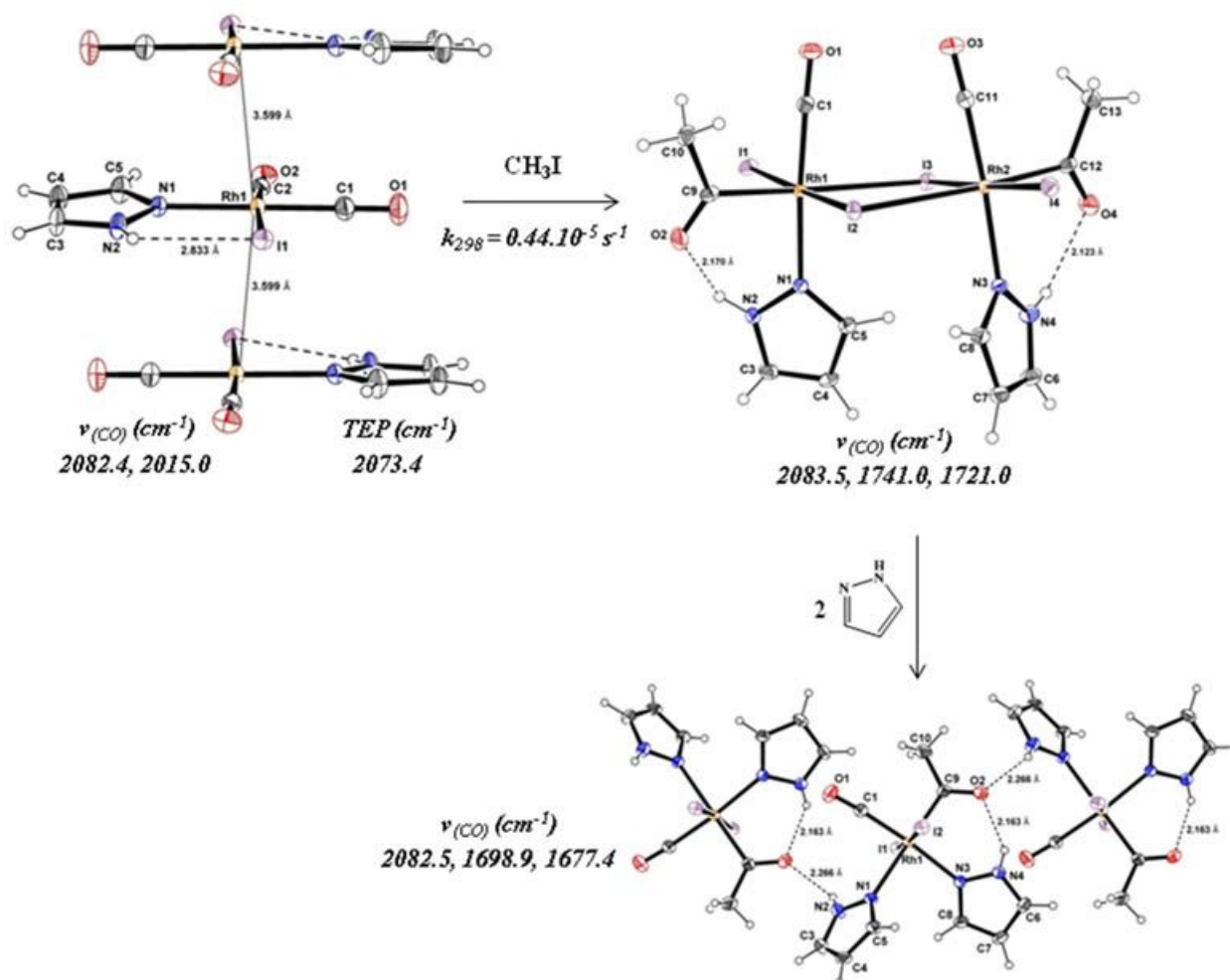
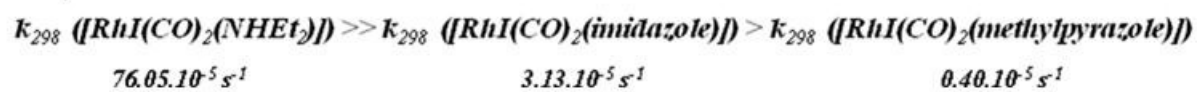
CHAPTER II

Reactivity of rhodium(I) complexes bearing nitrogen containing ligands towards CH₃I: Synthesis and full characterization of neutral *cis*-[RhX(CO)₂(L)] and acetyl [Rh(μ -I)I(COMe)(CO)(L)]₂ complexes; Kinetic studies

Chapter II: Graphical synopsis

CH₃I oxidative addition:

TEP (cm ⁻¹)									
E _a (KJ.mol ⁻¹)	-	57.5	65.3	81.3	-	-	89.6	-	70.6

**CH₃I oxidative addition:**

Chapter II abstract: The neutral Rh(I) square planar complexes $[\text{RhX}(\text{CO})_2(\text{L})]$ ($\text{X} = \text{Cl}$ **3**; $\text{X} = \text{I}$ **4**) bearing a nitrogen-containing ligand **L** (diethylamine **a**, triethylamine **b**, imidazole **c**, 1-methylimidazole **d**, pyrazole **e**, 1-methylpyrazole **f**, 3,5-dimethylpyrazole **g**, 1,4-di-*tert*-butyl-pyrazole **h**) have been straightforwardly obtained from **L** and standard $[\text{Rh}(\mu\text{-X})(\text{CO})_2]_2$ precursors. The synthesis was extended to the diethylsulfide ligand **i** for **4i**. The Tolman electronic parameter values (TEP) for **L** estimated from the CO stretching frequencies of **3** and **4** follow the order: $\mathbf{b} < \mathbf{a} \approx \mathbf{d} < \mathbf{c} < \mathbf{h} < \mathbf{g} < \mathbf{f} \approx \mathbf{i} < \mathbf{e}$. X-ray molecular structures of **3a,d-f,h** and **4a,d-f,h** were determined. Results from ^1H and $^{13}\text{C}\{^1\text{H}\}$ VT-NMR experiments suggest a fluxional dissociative ligand-exchange for **4c-i** and a supplementary intramolecular H-exchange process for **4e** and **4g**. The oxidative addition reaction of CH_3I to complexes **4** afforded the neutral dimeric iodo-bridged Rh(III)-acetyl complexes $[\text{RhI}(\mu\text{-I})(\text{COCH}_3)(\text{CO})(\text{L})]_2$ **6** in very good isolated yields. X-ray molecular structures for **6d₂** and **6e** reveal that the two apical CO ligands are in mutual *cis* position as are the two apical **d** and **e** ligands whereas isomer **6d₁** is centrosymmetric. Bridge-splitting reactions in **6d** and **6e** with CO or ligand **e** gave quantitatively the monomeric complexes $[\text{RhI}_2(\text{COCH}_3)(\text{CO})_2(\mathbf{d})]$ **7d** and $[\text{RhI}_2(\text{COCH}_3)(\text{CO})(\mathbf{e})_2]$ **8e**, as confirmed by its X-ray structure. The rate of CH_3I oxidative addition to **4** as determined by IR kinetic studies is strongly dependent on the nature of the N-containing ligand. The reaction rates are reduced significantly when using imidazole and pyrazole ligands. This rate reduction is primarily a steric effect as revealed by the X-ray structures. CH_3I oxidative addition to $[\text{RhI}(\text{CO})_2(\text{NHEt}_2)]$ **4a** bearing the sterically less hindered diethylamine ligand exhibits twice the reaction rate to that of the well known rhodium anionic $[\text{RhI}_2(\text{CO})_2]^-$ species and ca. 14 and 85 times faster than those obtained with complexes bearing imidazole (**c**, **d**) and pyrazole (**e**, **f**, **g**, **h**) ligands, respectively. Unexpected cyclometalated dimeric $[\text{RhI}(\mu\text{-I})(\text{CO})(\kappa^2\text{-N,C-h}\cap\text{CH}_2)]_2$ **9h** has been determined by X-ray diffraction resulting from a direct $\text{C}(\text{sp}^3)\text{-H}$ bond activation starting from **4h**.

II-1 Introduction

Significant research efforts continue to explore and improve the Rh catalyst activity and stability, particularly by tuning the electron density brought to the metal center by the appropriate donor ligand for promoting the rate of the kinetically limiting methyl iodide oxidative addition step although donor ligands generally retard the following CO-insertion step. On the other hand, steric effects must also be considered when tailoring the electron-donating character of a ligand. Indeed, the oxidative addition reaction rate can be significantly reduced using sterically hindered ligands. It is in this context that a series of N-containing ligands of different steric importance coordinated to the $\{\text{RhI}(\text{CO})_2\}$ moiety have been studied. Furthermore, this study is devoted to the introduction of nitrogen-containing ligands to obtain neutral iodo complexes with the goal that in further catalytic conditions, quaternization of the ligand is avoided and prevents the classical $[\text{RhI}_2(\text{CO})_2]^-$ catalyst to be restored.

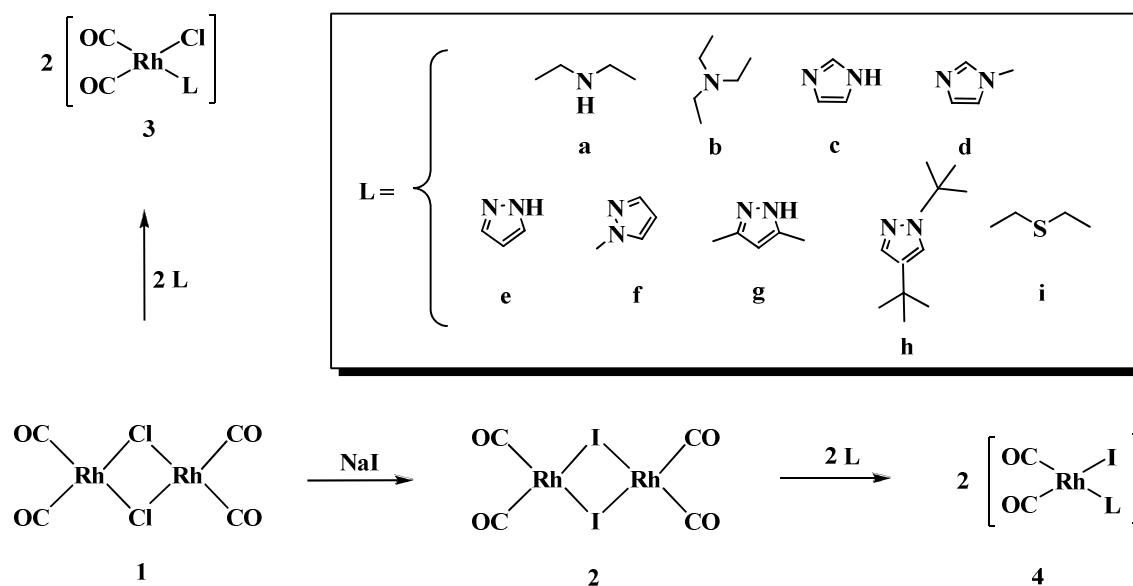
In this chapter we describe the synthesis and full characterization of $[\text{RhI}(\text{CO})_2(\text{L})]$ complexes together with a few chloro analogues in order to compare electronic parameters extracted from FT-IR and geometric features (ATR-IR, X-ray). ^1H and $^{13}\text{C}\{^1\text{H}\}$ VT-NMR experiments have shown that a fluxional dissociative ligand-exchange behavior occurs for **4c-i** and a supplementary intramolecular H-exchange process takes place in the case of **4e** and **4g**. Attention is also mainly focused on the reactivity of $[\text{RhI}(\text{CO})_2(\text{L})]$ towards CH_3I leading to the corresponding dimeric Rh(III) acetyl species where a few complexes have been structurally characterized. This reactivity is evaluated in terms of electronic and steric contributions on the behalf of the N-containing ligands: the oxidative addition of CH_3I to $[\text{RhI}(\text{CO})_2(\text{NHEt}_2)]$ bearing the sterically less hindered diethylamine ligand is twice as fast as

the well known anionic $[\text{RhI}_2(\text{CO})_2]^-$ species,¹ and ca. 14 and 85 times faster than that with imidazole (**c**, **d**) and pyrazole (**e**, **f**, **g**, **h**) ligands, respectively.

II-2 Synthesis and characterization

II-2-1 Synthesis and characterization of chloro rhodium(I) complexes $[\text{RhCl}(\text{CO})_2(\text{L})]$ **3**

The reaction of 1 molar eq. of the starting rhodium precursor $[\text{Rh}(\mu\text{-Cl})(\text{CO})_2]_2$ **1** with 2 eq. of nitrogen-containing ligand **L** (**L** = **a**, **b**, **d-f**, **h**) in dichloromethane at room temperature quantitatively afforded the neutral *cis*- $[\text{RhCl}(\text{CO})_2(\text{L})]$ d^8 complexes **3a,b,d-f,h** respectively, which are moderately air- and moisture stable (Scheme 1). These compounds have been fully characterized by FT-IR, multinuclear NMR spectroscopies, mass spectrometry, elemental analyses and single crystal X-ray crystallography. Since attempts to isolate complex **3b** in the solid state were unsuccessful, **3b** was only characterized *in-situ* by FT-IR.



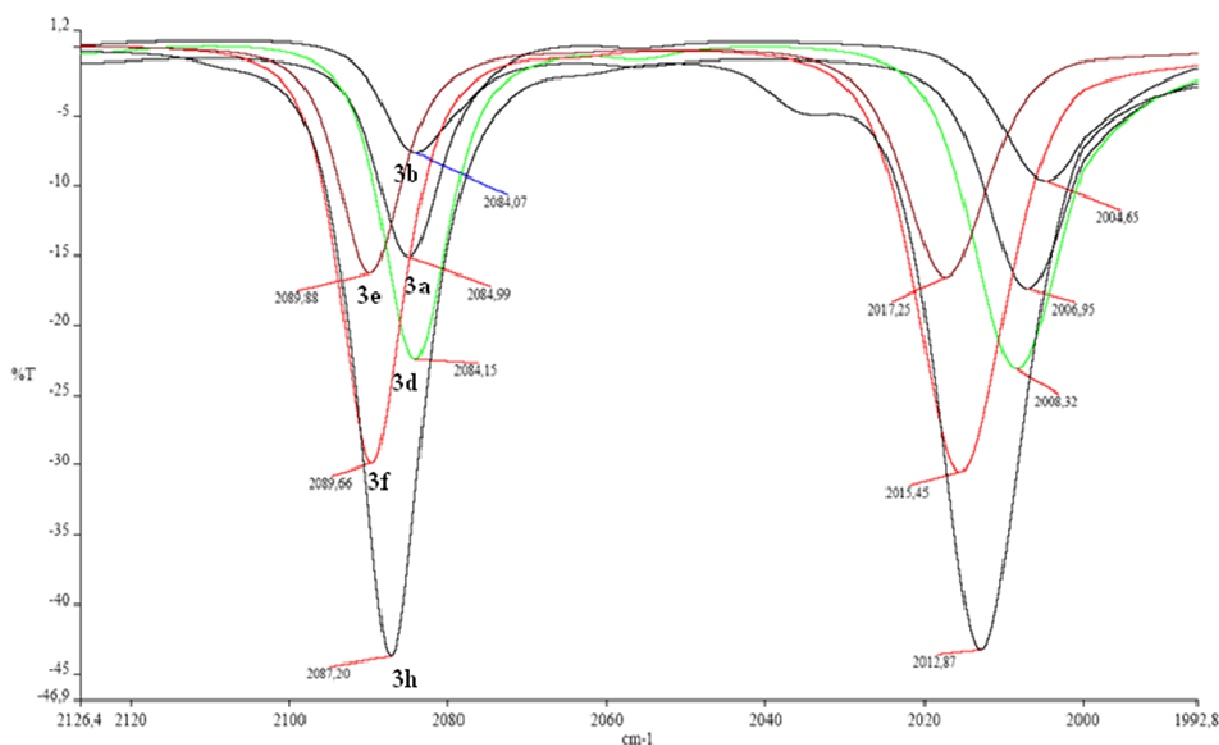
Scheme 1. General pathway for synthesis of *cis*- $[\text{Rh}(\text{X})(\text{CO})_2(\text{L})]$ **3** (X = Cl) and **4** (X = I).

Infrared data relevant to the characteristic ν_{CO} stretching frequencies of **3** in CH_2Cl_2 are displayed in Table 1 and corresponding spectra in the carbonyl region are depicted in Figure 1. As expected, two bands of the same intensity are observed in the carbonyl region, illustrating the typical behavior of CO ligands in mutual *cis* position in a square planar environment. The value of the ν_{CO} A_1 mode in the local C_{2v} symmetry varies over a very narrow range, when going from the two basic ligands diethylamine **a** ($\text{pK}_a = 10.84$) and triethylamine **b** ($\text{pK}_a = 10.75$) to the less basic 1-methylimidazole **d** ($\text{pK}_a = 7.13$). In the cases with further less basic 1-methylpyrazole **f** ($\text{pK}_a = 2.09$) and pyrazole **e** ($\text{pK}_a = 2.52$) ligands, this value shifts in the magnitude of ca. 5 cm^{-1} to higher frequency.² The difference of $73\text{-}79 \text{ cm}^{-1}$ between the two carbonyl stretching frequencies is large and therefore consistent with a significant coupling between the two CO vibrators.³ In fact, it is well established that the carbonyl stretching frequency can be used as an indicator of the electronic density on the metal center which was quantified first by Tolman, based on the so called Tolman electronic parameter (TEP).⁴ Initially, this value arises from the ν_{CO} A_1 mode for the $[\text{Ni}(\text{CO})_3(\text{L})]$ complex in CH_2Cl_2 . A method further developed by Crabtree⁵ and later refined by Nolan⁶ allows for the determination of the TEP by correlation of the average of the two CO stretching bands ($\nu_{\text{CO av}}$) of a given *cis*- $[\text{IrCl}(\text{CO})_2(\text{L})]$ complex. Herein, we chose to adopt the same methodology in order to gauge the influence of ligands (**a**, **b**, **d-f**, **h**) bound to the Rh center for *cis*- $[\text{RhCl}(\text{CO})_2(\text{L})]$. The TEP values for **3** are calculated according to Equation 1 (Eq. 1) (Table 5 and Figure 8) and follow the order: **b** < **a** \approx **d** < **h** < **f** < **e** (Table 1). Indeed, the estimated TEPs demonstrate that **a**, **b** and **d** clearly behave as better donors than **e**, **f** and **h** which is consistent with the observed trend via evaluation of the A_1 vibration mode.

$$\text{TEP} = 0.6214 \times (\nu_{\text{CO average}}) + 796.68 \quad (\text{Eq. 1})$$

Table 1. Infrared carbonyl stretching frequencies for $[\text{RhCl}(\text{CO})_2(\text{L})]$ **3**.

<i>Complexes</i>	$\nu(\text{CO})$ (cm^{-1}) (CH_2Cl_2)	$\Delta\nu_{\text{CO}}$ (cm^{-1})	$\nu_{\text{av}}(\text{CO})$ (cm^{-1})	<i>TEP</i> (cm^{-1})	<i>pKa</i> <i>ligand</i>
3a	2085.0; 2007.0	77.9	2046.0	2068.1	10.84
3b	2084.1; 2004.7	79.4	2044.4	2067.1	10.75
3d	2084.2; 2008.3	75.9	2046.3	2068.3	7.13
3e	2089.9; 2017.3	72.6	2053.6	2072.8	2.52
3f	2089.7; 2015.5	74.2	2052.6	2072.2	2.09
3h	2087.2; 2012.9	74.3	2050.0	2070.6	-

**Figure 1.** Infrared spectra in the carbonyl region in CH_2Cl_2 at 298 K for $[\text{RhCl}(\text{CO})_2(\text{L})]$ **3**.

Single X-ray structures of **3a,d-f,h** were resolved and their relevant bond length and angle parameters are listed in Table 2 (see S.I Chapter II for more details). The molecular views of **3a,h** and packing diagrams of **3d-f** are displayed in Figures 2-6, respectively. The crystal data for **3d** and **3e** are in very good agreement with those reported previously by Oro⁷ and Stobart⁸. In all cases, the C(2)-Rh-C(1) angle is $\sim 90^\circ$. The longest Rh-N(1) bond distance is 2.124(2) Å for **3a** which is consistent with the poor π -withdrawing of the very basic aliphatic diethylamine ligand. The Rh-N(1) bond lengths in the pyrazole complexes **3e,f**

are shorter than that in pyrazole complex **3h** and in 1-methylimidazole complex **3d**. The shorter Rh-N(1) bond length in **3e** (2.089(1) Å) when compared to **3f** (2.094(2) Å) and **3h** (2.108(3) Å) is consistent with the shorter angle between the pyrazole ring **e** and the Cl-Rh-(CO)₂ plane (14.9°) than that of **f** (66.9°) and **h** (89.5°). The Rh-C(1) bond distances of **3a,d** (1.857 Å) are slightly longer than those of **3e,f,h** (1.847(2), 1.844(2), 1.834(5) Å respectively) suggesting a stronger *trans* influence of the N-ligand.

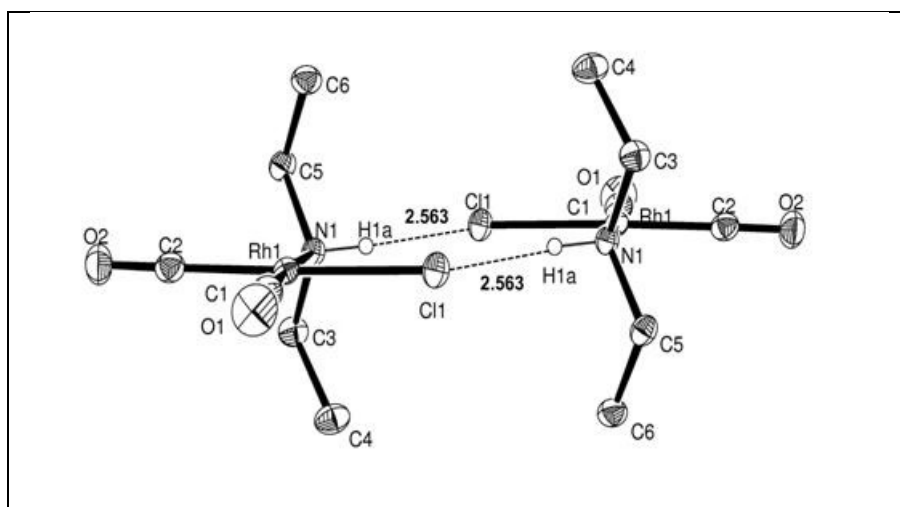


Figure 2. Molecular view putting in evidence an intermolecular H-bonding interaction (2.563 Å) between two molecules of **3a**. Thermal ellipsoids are shown at the 30% probability level and hydrogen atoms are omitted for clarity except for the amine group involved in the intermolecular H-bond.

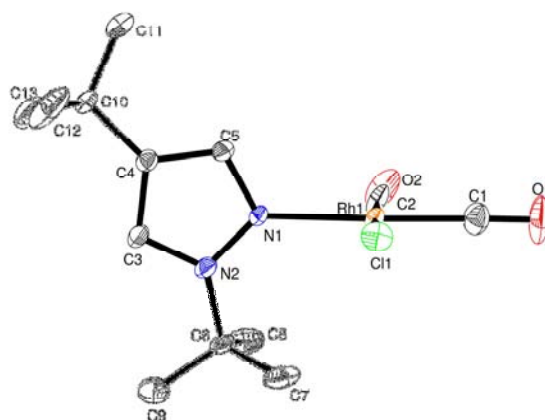
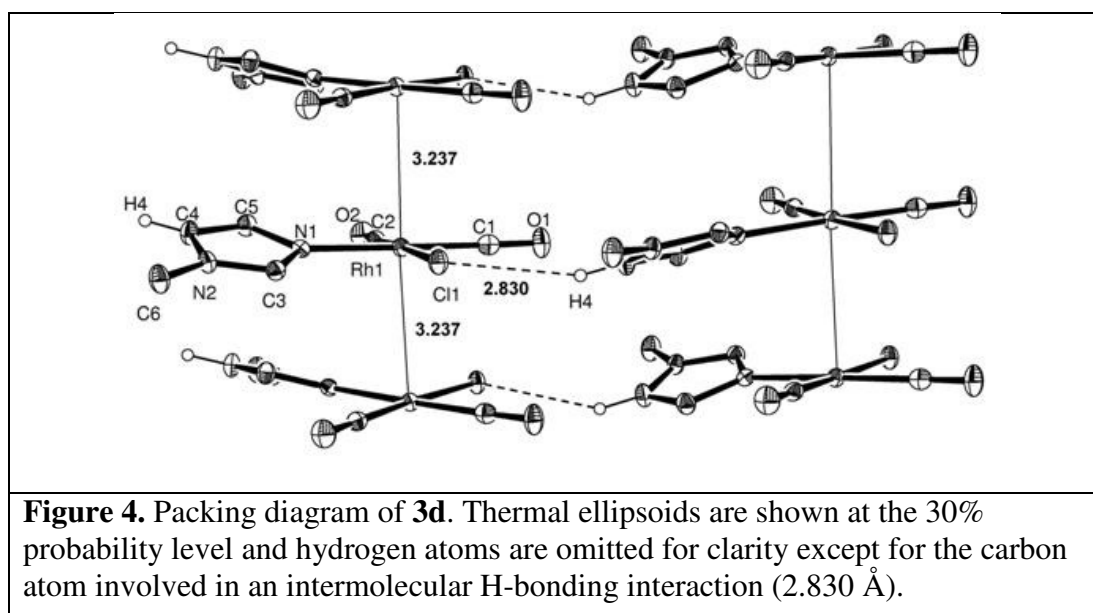
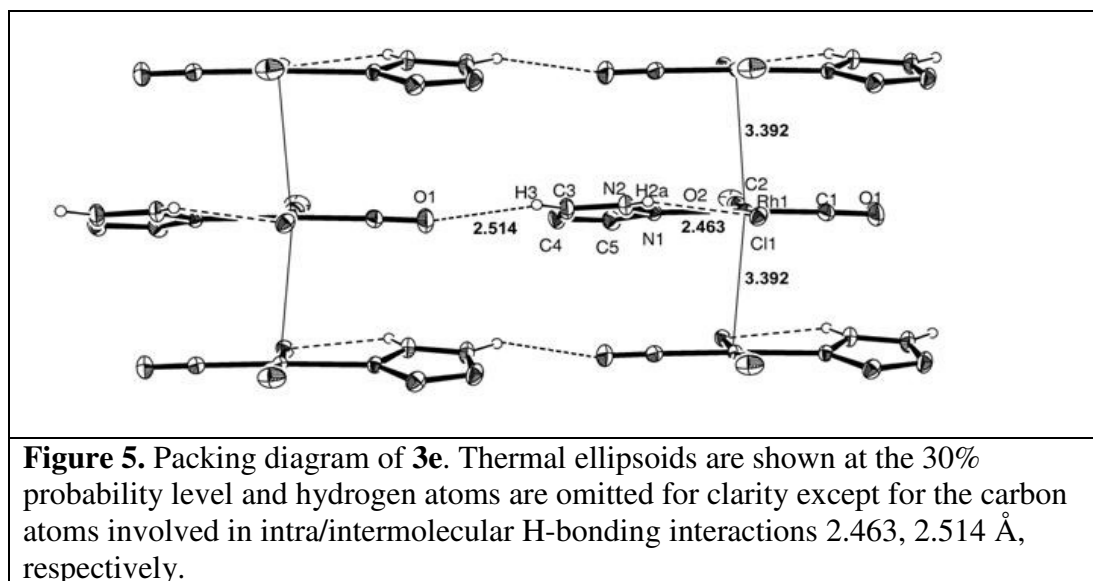


Figure 3. Molecular view of **3h**. Thermal ellipsoids are shown at the 30% probability level and hydrogen atoms are omitted for clarity.

Unlike the previously characterized chloro analogues **3d**⁷ and **3e**⁸ or $[\text{RhCl}(\text{CO})_2(\text{NH}_2\text{R})]^\text{9}$ (R = linear alkyl group), there are no molecular wires through intermolecular π - π Rh-Rh interactions for **3a**, **3f** and **3h**, most certainly due to the steric hindrance. Indeed, in **3a**, the two ethyl substituents are located above and below the Rh coordination plane, in **3f** ligand **f** is almost perpendicular (66.9°) to the coordination plane and in **3h**, ligand **h** is perpendicular (89.5°) to the coordination plane which result in a significantly longer Rh-Rh distance (3.237 and 3.392 Å for **3d** and **3e** vs. 7.475 , 13.092 and 14.114 Å for **3a**, **3f** and **3h**, respectively). For **3a**, an intramolecular N-H \cdots Cl distance (2.722 Å) is within the range expected for the H-bonding interaction (2.20 - 3.25 Å).¹⁰ However, the relatively small N-H \cdots Cl angle (106.73°) is not consistent with the definition of a proper H-bonding interaction: this short distance is more likely due to the somewhat closed N-H-Cl angle of 106.81° induced by solid state packing constraints so that it is not considered as a proper H-bonding interaction.¹¹

In contrast, the packing diagrams of **3a** and **3h** show (N)-H \cdots Cl and C(3)-H(3) \cdots Cl intermolecular interactions with corresponding distances and angles of 2.563 , 2.668 Å and 146.75° , 172.38° , respectively.





Noteworthy for **3e**, the intramolecular N-H \cdots Cl contact distance and angle of 2.463 Å and 130.13°, respectively are indicative of a H-interaction involving N-H \cdots Cl atoms which was not mentioned in the earlier published studies either for **3d**⁷ or **3e**.⁸ The packing diagram of **3f** shows an intermolecular C(3)-H \cdots Cl contact of 2.815 Å with a C(3)-H \cdots Cl angle of 138.73°.

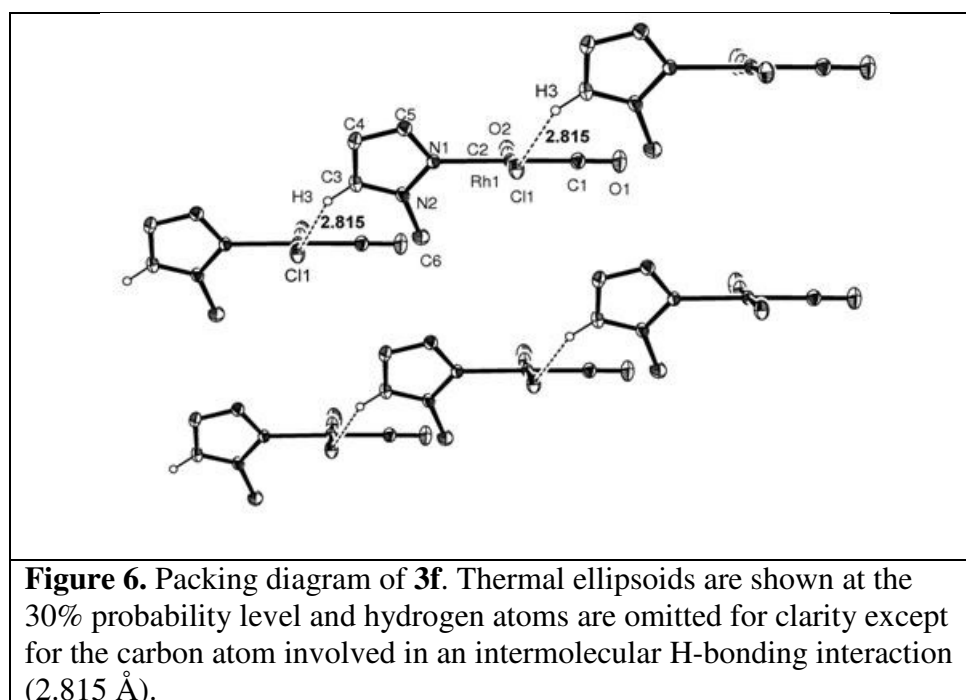


Table 2. Selected bond lengths (Å) and angles (deg) for *cis*-[RhCl(CO)₂(L)] **3**.

<i>Atoms</i>	<i>3a</i>	<i>3d</i>	<i>3e</i>	<i>3f</i>	<i>3h</i>
<i>Rh-N(1)</i>	2.124(2)	2.096(2)	2.089(1)	2.094(2)	2.108(3)
<i>Rh-Cl</i>	2.340(1)	2.374(1)	2.365(1)	2.333(1)	2.343(2)
<i>Rh-C(1)</i>	1.857(2)	1.857(4)	1.847(2)	1.844(2)	1.834(5)
<i>Rh-C(2)</i>	1.839(2)	1.843(4)	1.851(2)	1.847(2)	1.846(4)
<i>C(1)-O(1)</i>	1.132(2)	1.127(4)	1.130(2)	1.131(2)	1.125(5)
<i>C(2)-O(2)</i>	1.134(2)	1.134(4)	1.130(2)	1.132(3)	1.128(5)
<i>N(1)-H(1a)</i>	0.869(9)	-	-	-	-
<i>N(2)-H(2a)</i>	-	-	0.865(9)	-	-
<i>N(1)-H(1a)⋯Cl intra^b</i>	2.722	-	-	-	-
<i>N(2)-H(2a)⋯Cl intra^b</i>	-	-	2.463	-	-
<i>Rh⋯Rh (along b axis)</i>	7.475	3.237 ^a	3.392 ^a	13.092	14.114
<i>Rh⋯Rh (along c axis)</i>	10.771	8.670	13.976	14.981	10.188
<i>Other Rh⋯Rh distance</i>	4.988	-	7.229	5.808	5.847
<i>N(1)-H(1a)⋯Cl inter^c</i>	2.563	-	-	-	-
<i>C(4)-H(4)⋯Cl inter^c</i>	-	2.830	2.877	-	-
<i>C(3)-H(3)⋯Cl inter^c</i>	-	-	2.514	2.815	2.668
<i>Rh-C(1)-O(1)</i>	178.4(2)	178.3(3)	177.82(17)	178.2(2)	178.6(5)
<i>Rh-C(2)-O(2)</i>	179.23(2)	178.9(3)	178.91(12)	177.93(19)	176.6(4)
<i>Rh-N(1)-C(3)</i>	114.15(11)	126.7(2)	-	-	-
<i>Rh-N(1)-C(5)</i>	115.35(11)	127.6(2)	132.47(9)	127.43(12)	119.8(3)
<i>Rh-N(1)-H(1a)</i>	106.7(14)	-	-	-	-
<i>C(2)-Rh-C(1)</i>	91.20(9)	89.67(13)	90.08(7)	89.83(9)	89.65(2)
<i>C(1)-Rh-Cl</i>	89.65(7)	88.85(10)	89.02(6)	88.25(7)	87.46(2)
<i>C(2)-Rh-N(1)</i>	91.87(7)	91.80(11)	90.79(5)	93.59(7)	93.08(2)
<i>N(1)-Rh-Cl</i>	87.33(4)	89.70(7)	90.20(3)	88.32(4)	89.68(9)
<i>C(1)-Rh-N(1)</i>	176.58(8)	178.19(11)	177.89(5)	176.56(8)	176.54(2)
<i>C(2)-Rh-Cl</i>	178.22(6)	177.72(9)	177.45(4)	177.85(6)	175.34(2)
<i>Rh-Rh-Rh (zig-zag stacking)</i>	-	170.93	170.58	-	-
<i>Cl-Rh-(CO)₂ plane/N-ligand</i>	-	19.09	14.94	66.98	89.52

(^a): Stacking arrangement along the *b* axis, (^b): Intramolecular H⋯Cl distance, (^c): shortest intermolecular H⋯Cl distance.

The room temperature solution ¹H and ¹³C{¹H} NMR data are consistent with the molecular X-ray structures described above. The ¹³C{¹H} NMR spectra for **3a,d,f,h** feature a set of two doublets present in the carbonyl region, as expected. However, the ¹³C{¹H} NMR spectrum for **3e** displays only one sharp doublet, which is indicative of a fluxional behavior.¹²

Chemical shift and coupling constant data for carbonyl ligands are displayed in Table 3 (see S.I Chapter II for more details). The 1J coupling constant between Rh and C(1)O(1) in *trans*-position to the N-containing ligand is higher than that with *cis*-C(2)O(2), which is consistent with the somewhat shorter C(1)-O(1) bond length observed in the solid state in comparison with C(2)-O(2).

Table 3. Selected $^{13}\text{C}\{^1\text{H}\}$ NMR data for *cis*-[RhCl(CO)₂(L)] **3**.

Complexes	$\delta(^{13}\text{CO})$ (ppm)		$^1J_{(\text{CO-Rh})}$ (Hz)	
	<i>cis</i> C(2)O	<i>trans</i> C(1)O	<i>cis</i> C(2)O	<i>trans</i> C(1)O
3a	183.5 (d)	181.2 (d)	65.7	75.5
3d	184.4 (d)	181.2 (d)	64.5	73.9
3e	182.1 (d)		70.8	
3f	183.3 (br d)	180.0 (br d)	~51.4	~60.1
3h	183.4 (br d)	180.0 (br d)	68.2	76.8

NMR solvent = CD_2Cl_2 , 298 K, C(1)O in *trans* position with respect to the N-ligands, $^2J_{\text{C-C}}$ coupling is very small and therefore not detected.

II-2-2 Synthesis and characterization of iodo rhodium(I) complexes [RhI(CO)₂(L)] **4**

Starting from the iodo-bridged complex precursor **2**, the rhodium(I) complexes *cis*-[RhI(CO)₂(L)] **4a-i** were prepared in the same manner as the chloro analogues **3** (Scheme 1). Since the iodo complexes are usually more air- and moisture and/or thermally sensitive, synthesis of **4** was carried out at 263 K and warmed up gradually to RT. Complexes **4a,c-i** were fully characterized by FT-IR and conventional NMR spectroscopies, mass spectrometry, elemental analyses and single-crystal X-ray diffraction analyses (see S.I Chapter II + Chapter V for more details). Complex **4b** was only characterized *in-situ* by FT-IR since attempts to isolate it were unsuccessful.

FT-IR data of the characteristic ν_{CO} stretching frequencies of **4** in CH_2Cl_2 are displayed in Table 4 and corresponding spectra are depicted in Figure 7. As observed above for **3**, two bands of similar intensity are observed in the carbonyl region, illustrating the square planar configuration with two CO ligands in mutual *cis*-position.

Table 4. Infrared carbonyl stretching frequencies for *cis*-[RhI(CO)₂(L)] **4**.

Complexes	CH_2Cl_2			TEP^a (cm^{-1})	<i>pKa</i> ligand
	$\nu(\text{CO})$ (cm^{-1})	$\Delta\nu_{\text{CO}}$ (cm^{-1})	$\nu_{\text{av}}(\text{CO})$ (cm^{-1})		
4a	2077.6; 2005.8	71.8	2041.7	2069.5	10.84
4b	2076.4; 2003.5	72.9	2040.0	2068.5	10.75
4c	2077.9; 2008.1	69.8	2043.0	2070.2	6.95
4d	2077.0; 2007.1	69.9	2042.1	2069.7	7.13
4e	2082.4; 2015.0	67.4	2048.7	2073.4	2.52
4f	2082.0; 2013.4	68.6	2047.7	2072.8	2.09
4g	2080.2; 2011.9	68.3	2046.1	2071.9	4.12
4h^b	2096.2(w); 2079.6(s); 2027.1(w); 2010.5(s)	69.1	2045.1	2071.3	-
4i	2081.3; 2013.4	67.9	2047.4	2072.7	-

(^a): *TEP* was calculated by using the following correlation: $y(\text{TEP}) = 0.5576 x (\nu_{\text{CO}} \text{ average}) + 931.02$ (Figure 8), (^b): **4h** displays an unexpected distorted square planar geometry (see VI)

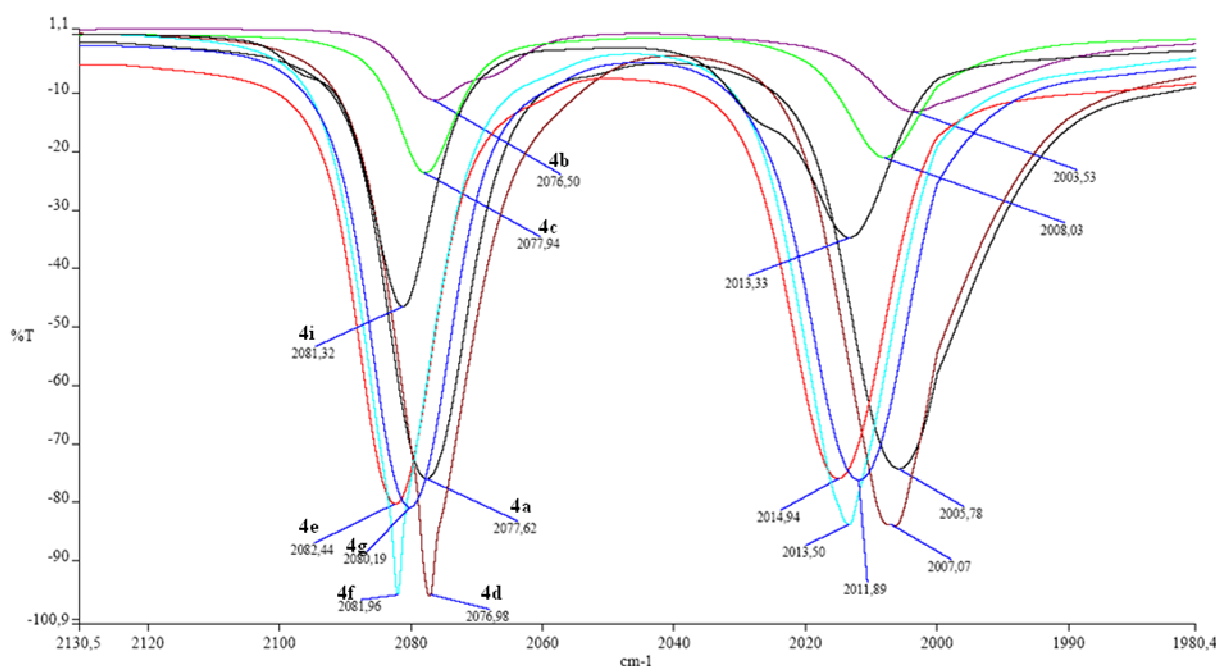


Figure 7. Infrared spectra in the carbonyl region in CH_2Cl_2 at 298 K for [RhI(CO)₂(L)] **4**.

The symmetric $A_1 \nu_{\text{CO}}$ band for complexes **4** appears at ca 7 cm^{-1} lower frequency than the corresponding chloro complexes **3** due to the stronger *trans* influence of the iodo ligand. Analysis of $A_1 \nu_{\text{CO}}$ values generally show a correlation with the ligand basicity. Ligands **a-d** of similar basicity exert almost the same electronic influence while the less basic **e-g** ligands increase the ν_{CO} 's by ca. $5\text{-}6 \text{ cm}^{-1}$ (Tables 1 and 4). Diethylsulfide ligand **i** shows similar electronic behavior as **e-g**. Interestingly, the Tolman electronic parameter (TEP) values for **L** estimated from the average CO stretching frequencies of *cis*-[RhI(CO)₂(L)] **4** follow a similar order to those calculated from the chloro analogues **3**: **b** < **a** \approx **d** < **c** < **h** < **g** < **f** \approx **i** < **e** (Table 5 and Figure 8).

Table 5. TEP values and carbonyl IR data for [Rh(CO)₂(X)(L)] (X = Cl, I) in CH₂Cl₂.

<i>L</i>	TEP	$\nu(\text{CO})$ for [Rh(CO) ₂ (X)(L)] in CH ₂ Cl ₂		$\nu(\text{CO})$ average		
		Cl	I	Cl	I	
<i>CH</i> ₃ <i>CN</i>	2077.2 ¹³	2095.0, 2026.0 ¹⁴	2087.3, 2023.8	2060.5	2055.6	
<i>NH</i> ₃	2073.6 ¹³	2093.0, 2014.0 ¹⁵	2081.5, 2010.8	2053.5	2046.1	
<i>Py</i>	2070.5 ¹³	2089.0, 2015.0 ^{12d}	2080.9, 2012.7	2052.0	2046.8	
<i>NMe</i> ₃	2069.4 ¹³	2086.9, 2007.9	2078.0, 2005.8	2047.4	2041.9	
	TEP _[RhCl]	TEP _[RhI]				
<i>a</i>	2068.1	2069.5	2085.0; 2007.0	2077.6; 2005.8	2046.0	2041.7
<i>b</i>	2067.1	2068.5	2084.1; 2004.7	2076.4; 2003.5	2044.4	2040.0
<i>c</i>	-	2070.2	-	2077.9; 2008.1	-	2043.0
<i>d</i>	2068.3	2069.7	2084.2; 2008.3	2077.0; 2007.1	2046.3	2042.1
<i>e</i>	2072.8	2073.4	2089.9; 2017.3	2082.4; 2015.0	2053.6	2048.7
<i>f</i>	2072.2	2072.8	2089.7; 2015.5	2082.0; 2013.4	2052.6	2047.7
<i>g</i>	-	2071.9	-	2080.2; 2011.9	-	2046.1
<i>h</i>	2070.6	2071.3	2087.2; 2012.9	2079.6; 2010.5	2050.0	2045.1
<i>i</i>	-	2072.7	-	2081.3; 2013.4	-	2047.4

Blue color: TEP values found in the literature

TEP_[RhCl]: calculated based on carbonyl IR data of [Rh(CO)₂(Cl)(L)],

TEP_[RhI]: calculated based on carbonyl IR data of [Rh(CO)₂(I)(L)]

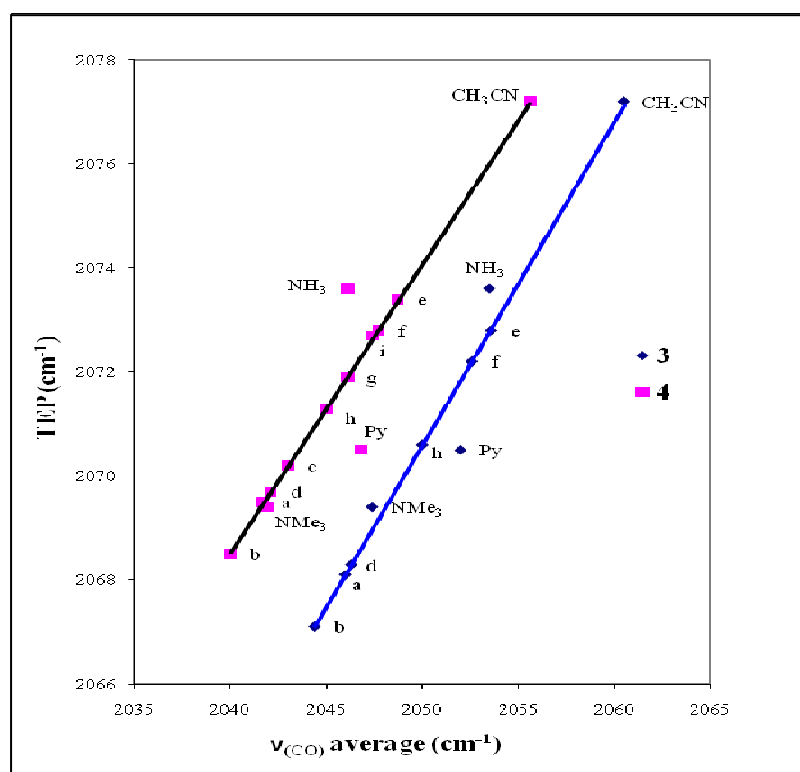


Figure 8. Plots illustrating the correlation of the average $\nu_{(\text{CO})}$ values for **3** and **4**.

The X-ray crystal structure ORTEP diagrams of complexes **4a,d-f,h** are depicted in Figures 9-13. Relevant bond lengths and angles are listed in Tables 6 and 7. The Rh-C(1) and C(1)-O(1) distances for CO *trans* to the ligand **L** are similar for both chloro and iodo complexes. A similar comparison prevails for the Rh-C(2) bond distances. However, the C(2)-O(2) bond distances are slightly shorter going from the chloro (ca. 1.132 Å) to the iodo analogues (ca. 1.125 Å), which reflects the slightly higher back-donation exerted in the former.¹⁶

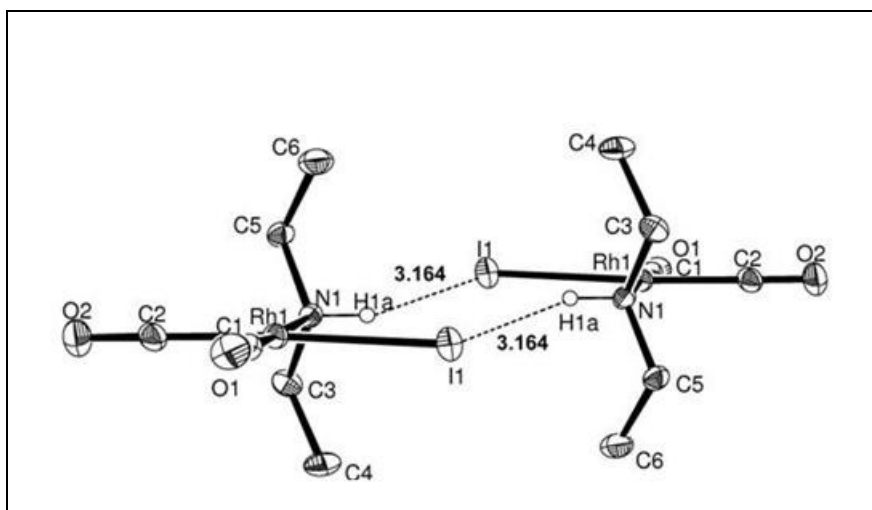


Figure 9. Molecular view putting in evidence an intermolecular H-bonding interaction (3.164 Å) between two molecules of **4a**. Thermal ellipsoids are shown at the 30% probability level and hydrogen atoms are omitted for clarity except for the amine group involved in the intermolecular H-bond.

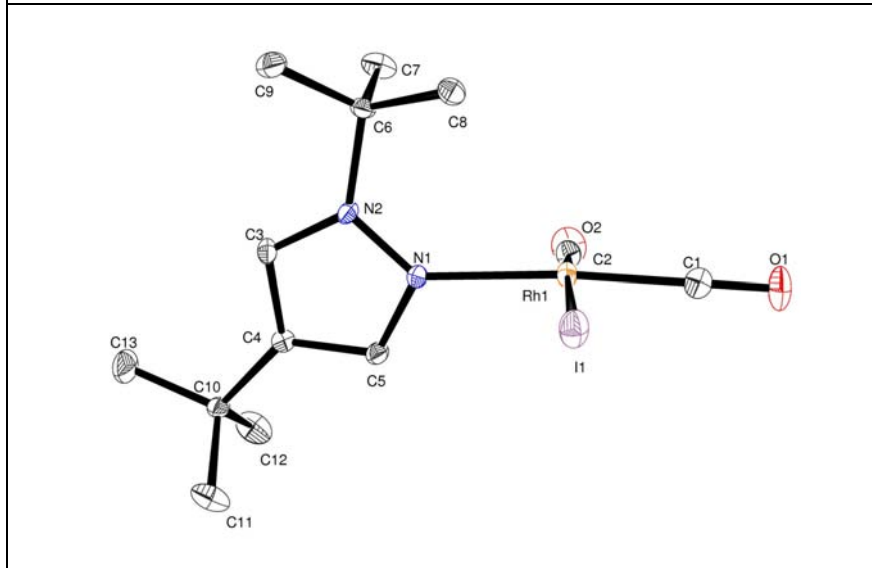


Figure 10. Molecular view of **4h**. Thermal ellipsoids are shown at the 30% probability level and hydrogen atoms are omitted for clarity.

For complexes **4d,e** the molecular packing diagrams dominantly adopt the stacking of square planar Rh-units along the *b* axis which result in slightly zig-zag wires of Rh atoms with Rh \cdots Rh \cdots Rh angles of 153.5° and 157.6°, and Rh \cdots Rh metal distances of 3.875 Å and 3.599 Å, respectively. This closer Rh \cdots Rh intermolecular approach for **4e** is consistent with the smaller angle formed by the Rh coordination plane with the N-heterocyclic ring (7.7° for

4e vs. 34.9° for **4d**). The separated wires of stacked units are staggered resulting in a Rh \cdots Rh distance of 7.246 Å for **4d** and 7.540 Å for **4e**. Such one-dimensional molecular chains formed via Rh \cdots Rh interaction were also observed for the chloro analogues **3d**^{7,e}⁸ (Figures 3 and 4) and other d⁸ Rh(I) complexes.^{17a,17b,18} For **4f,h**, the 1-methylpyrazole and 1,4-di-*tert*-butyl-pyrazole rings are almost perpendicular to the coordination plane (86.9 , 83.2° , respectively) so that the intermolecular Rh \cdots Rh distance are much longer (9.374, 16.222 Å, respectively).

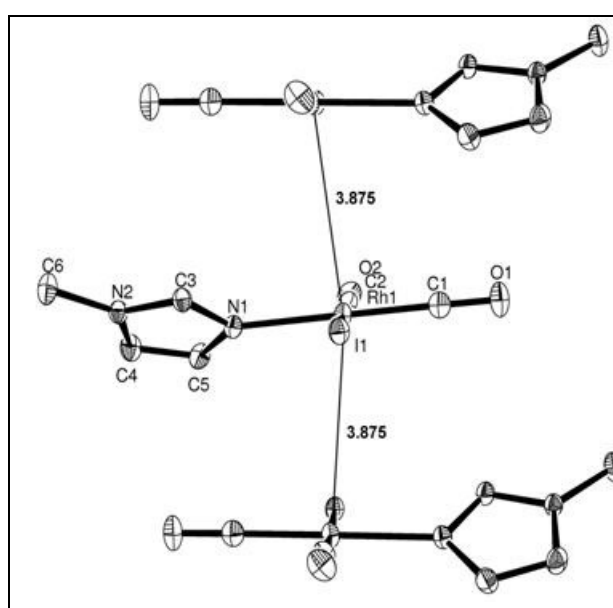


Figure 11. Packing arrangement of **4d** stacked parallel to the *b*-axis. Thermal ellipsoids are shown at the 30% probability level and hydrogen atoms are omitted for clarity.

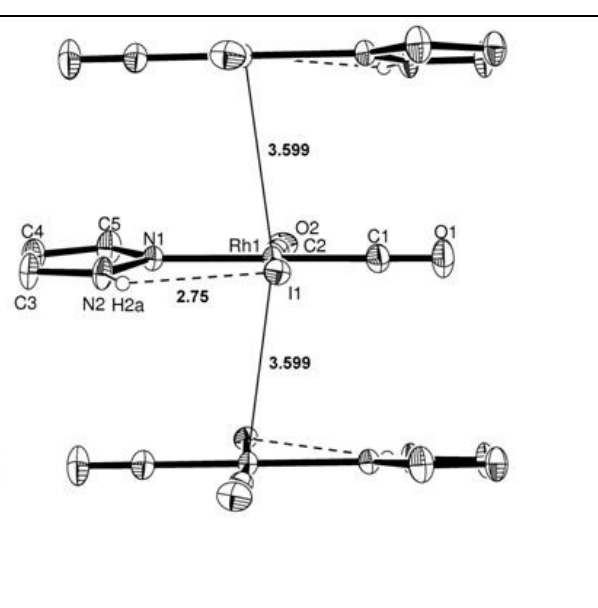


Figure 12. Packing arrangement of **4e** stacked parallel to the *b*-axis. Thermal ellipsoids are shown at the 30% probability level and hydrogen atoms are omitted for clarity except for the amine group involved in an intramolecular H-bonding interaction (2.75 Å).

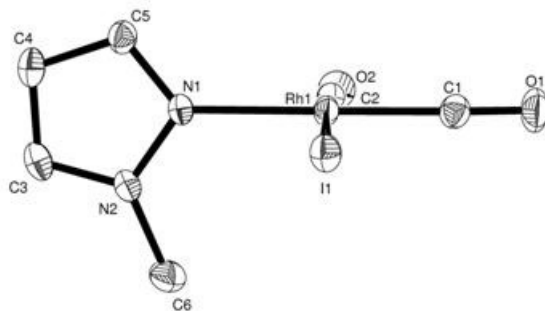


Figure 13. Representation of one molecule of **4f** from the asymmetric unit. Thermal ellipsoids are shown at the 30% probability level and hydrogen atoms are omitted for clarity.

An intramolecular H-bonding interaction has been detected for **4e**. The N-H \cdots I distance and angle are 2.750 Å and 134.36°, respectively. For **4a**, the N-H \cdots I distance of 2.900 Å and the N-H-I angle of 116.98°, which is larger than that in the chloro analogue **3a**, is still not considered as an intramolecular interaction.

In addition, the packing configurations lay out several different intermolecular H-bonding interactions for **4a,d-e**. For **4a**, the N-H \cdots I contact distance is 3.164 Å and the corresponding angle is 127.85°.¹⁹ For **4d** and **4e**, the C(4)-H(4) \cdots I contact distances are 3.214 Å and 3.223 Å with corresponding angles of 146.92° and 144.48°, respectively. In fact, for **3a,d,e** and **4a,c,d,e**, the observation of multiple CO bands on the IR-ATR spectra indicates that the strict local C_{2v} symmetry is lost, presumably due to the presence of strong intra or/and intermolecular interactions. By contrast, for **3f,h** and **4f,h** two neat ν_{CO} bands of almost the same intensity are observed which reflect the absence or weak intra- or/and intermolecular interactions (Figure 14).

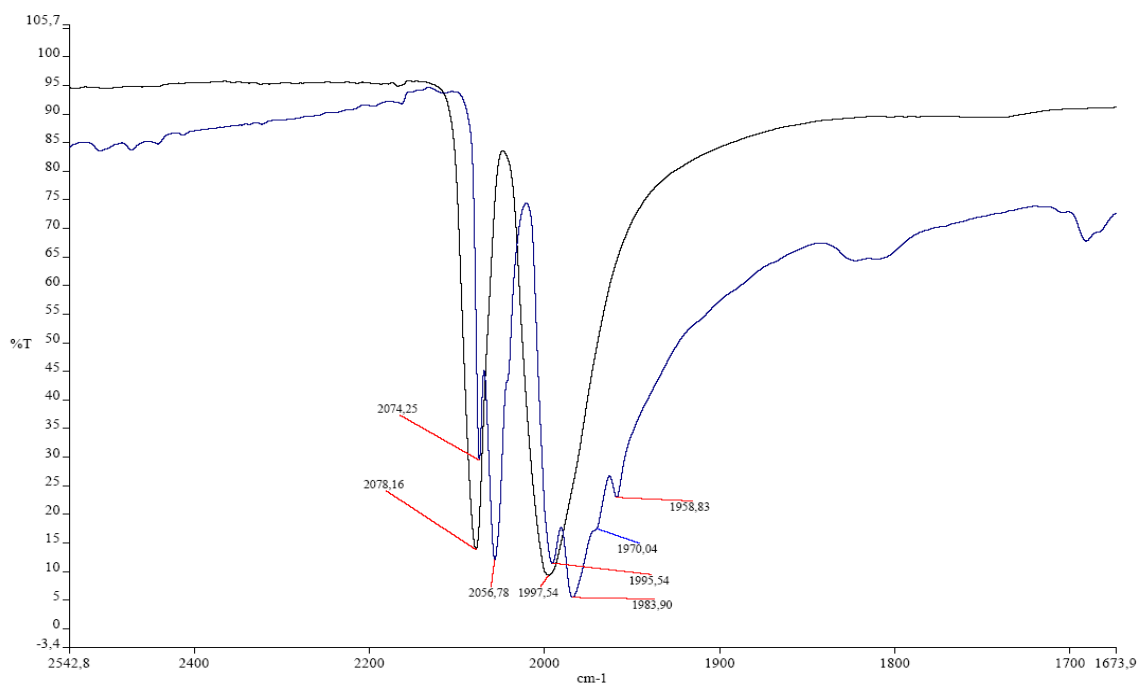


Figure 14. ATR-IR spectra at 298 K for **3d** (blue) and **3f** (black).

Table 6. Selected bond lengths (Å) and angles (deg) for *cis*-[RhI(CO)₂(L)] **4**.

<i>Atoms</i>	<i>4a</i>	<i>4d</i>	<i>4e</i>
<i>Rh-N(1)</i>	2.134(3)	2.102(2)	2.099(2)
<i>Rh-I</i>	2.645(1)	2.660(1)	2.662(1)
<i>Rh-C(1)</i>	1.862(5)	1.844(3)	1.838(3)
<i>Rh-C(2)</i>	1.857(4)	1.863(3)	1.862(3)
<i>C(1)-O(1)</i>	1.128(5)	1.138(3)	1.133(4)
<i>C(2)-O(2)</i>	1.120(5)	1.127(3)	1.134(3)
<i>N(1)-H(1a)</i>	0.879(10)	-	-
<i>N(2)-H(2a)</i>	-	-	0.871(10)
<i>N(1)-H(1a)⋯I intra^b</i>	2.898	-	-
<i>N(2)-H(2a)⋯I intra^b</i>	-	-	2.750
<i>Rh⋯Rh (along b axis)</i>	12.626	3.875 ^a	3.599 ^a
<i>Rh⋯Rh (along c axis)</i>	12.203	14.173	14.550
<i>Other Rh⋯Rh distance</i>	4.884	7.246	7.540
<i>N(1)-H(1a)⋯I inter^c</i>	3.164	-	-
<i>Rh-C(1)-O(1)</i>	177.7(4)	179.4(3)	179.8(3)
<i>Rh-C(2)-O(2)</i>	178.1(4)	178.6(3)	178.4(3)
<i>Rh-N(1)-N(2)</i>	-	-	124.63(16)
<i>Rh-N(1)-C(3)</i>	115.2(2)	126.79(18)	-
<i>Rh-N(1)-C(5)</i>	113.5(2)	127.30(17)	131.04(19)
<i>Rh-N(1)-H(1a)</i>	101(3)	-	-
<i>N(1)-Rh-I</i>	89.46(9)	92.25(6)	93.64(6)
<i>C(1)-Rh-N(1)</i>	175.30(15)	179.83(12)	179.40(11)
<i>C(2)-Rh-I</i>	176.99(13)	178.13(9)	175.40(9)
<i>Rh-Rh-Rh (zig-zag stacking)</i>	-	153.47	157.55
<i>I-Rh-(CO)₂ plane/N-ligand</i>	-	34.90	7.68

(^a): Stacking arrangement along the *b* axis, (^b): Intramolecular H⋯I distance, (^c): Shortest intermolecular H⋯I distance.

Table 7. Selected bond lengths (Å) and angles (deg) for *cis*-[RhI(CO)₂(L)] **4**.

Atoms	$4f^d$		4h
	Mol1	Mol2	
Rh-N(1)	2.099(3)	2.099(3)	2.127(3)
Rh-I	2.660(1)	2.660(1)	2.645(1)
Rh-C(1)	1.839(5)	1.841(4)	1.838(5)
Rh-C(2)	1.855(4)	1.847(5)	1.849(5)
C(1)-O(1)	1.135(5)	1.133(5)	1.123(5)
C(2)-O(2)	1.125(5)	1.140(5)	1.134(5)
Rh \cdots Rh (along b axis)	9.374	9.374	16.222
Rh \cdots Rh (along c axis)	14.609	14.609	17.644
Other Rh \cdots Rh distance	4.355	4.363	4.808
Rh-C(1)-O(1)	178.4(4)	178.9(4)	179.3(5)
Rh-C(2)-O(2)	177.2(4)	179.0(4)	177.1(5)
Rh-N(1)-N(2)	124.9(2)	126.4(2)	135.0(3)
Rh-N(1)-C(5)	129.1(3)	127.6(3)	118.6(3)
N(1)-Rh-I	90.91(8)	91.31(9)	92.54(9)
C(1)-Rh-N(1)	178.54(15)	177.59(15)	175.49(17)
C(2)-Rh-I	174.55(12)	177.64(12)	173.97(16)
I-Rh-(CO) ₂ plane/N-ligand	86.87	76.97	83.17

(^d): The crystal cell contains two molecules (Mol1 and Mol2).

II-3 Variable temperature NMR studies of complexes **4**

Complexes **4a,c-i** have been characterized by ¹H and ¹³C{¹H} NMR. The RT carbonyl region ¹³C{¹H} NMR spectrum of **4a** features two double doublets (Figure 15) whereas two larger doublets are observed for **4c, d**, which correspond to both CO in the mutual *cis* position.

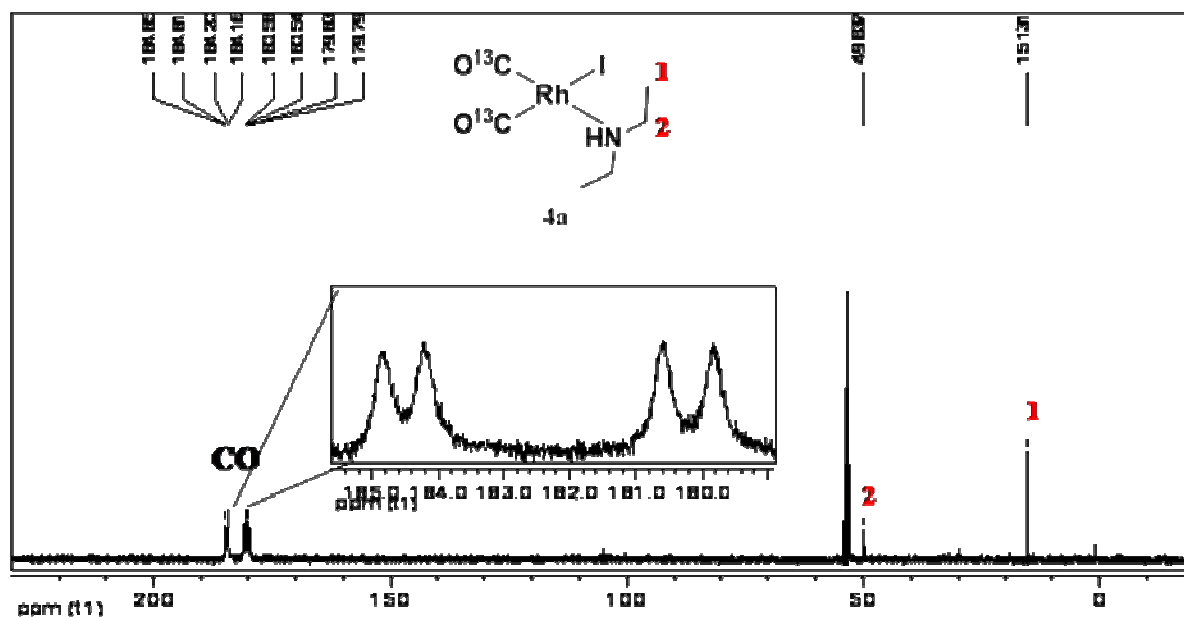


Figure 15. $^{13}\text{C}\{^1\text{H}\}$ NMR spectrum of **4a** at 298 K in CD_2Cl_2 .

The ^1H NMR spectrum of **4a** at RT consists of two sets of broad multiplets centered at δ 2.97 and 3.07 ppm in a 1:1 ratio for the methylene protons on the ethyl substituents of **a** while in the case of **3a**, only one broad multiplet centered at δ 3.02 ppm is observed (Figures 16 and 17). This indicates that in both cases the two H atoms of the CH_2 groups are diastereotopic as previously reported for $[\text{RhCl}(\text{CO})(\text{PPh}_3)(\mathbf{a})]$.^{10a}

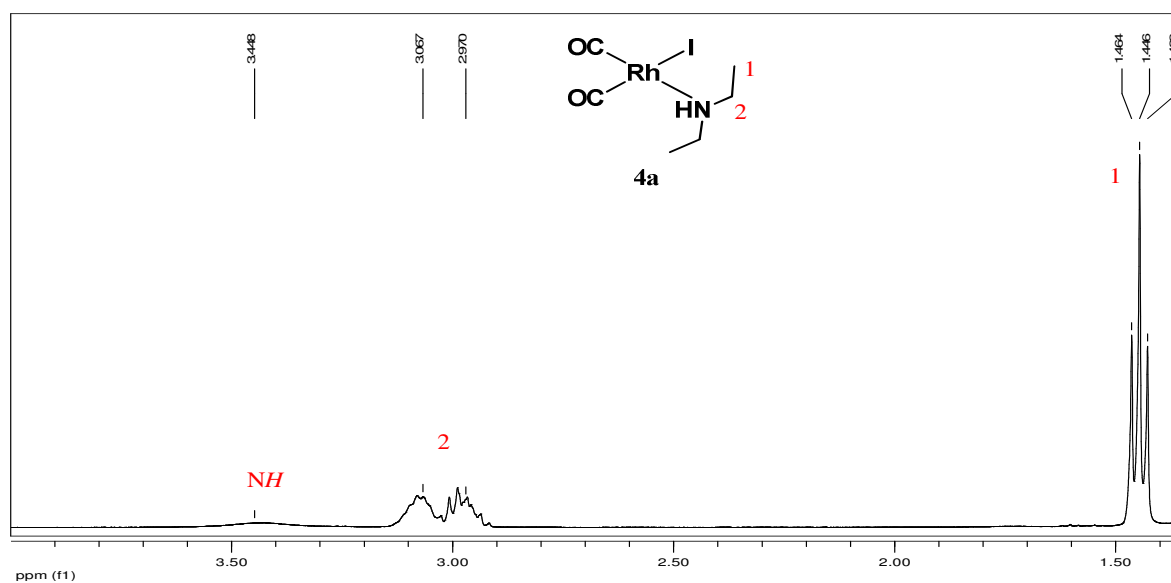


Figure 16. ^1H NMR spectrum of **4a** at 298 K in CD_2Cl_2 .

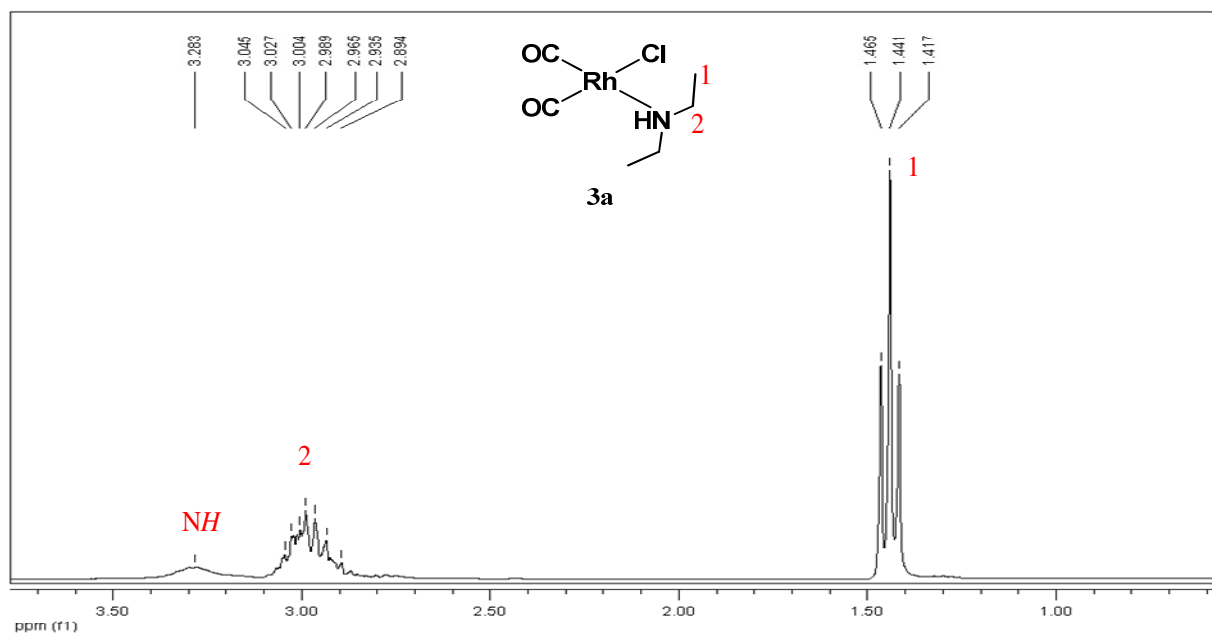


Figure 17. ^1H NMR spectrum of **3a** at 298 K in CD_2Cl_2 .

In contrast, $^{13}\text{C}\{^1\text{H}\}$ NMR spectra of **4e-i** recorded at RT exhibit only one broad singlet for the two CO's, which is indicative of a fluxional behavior (Figure 18).

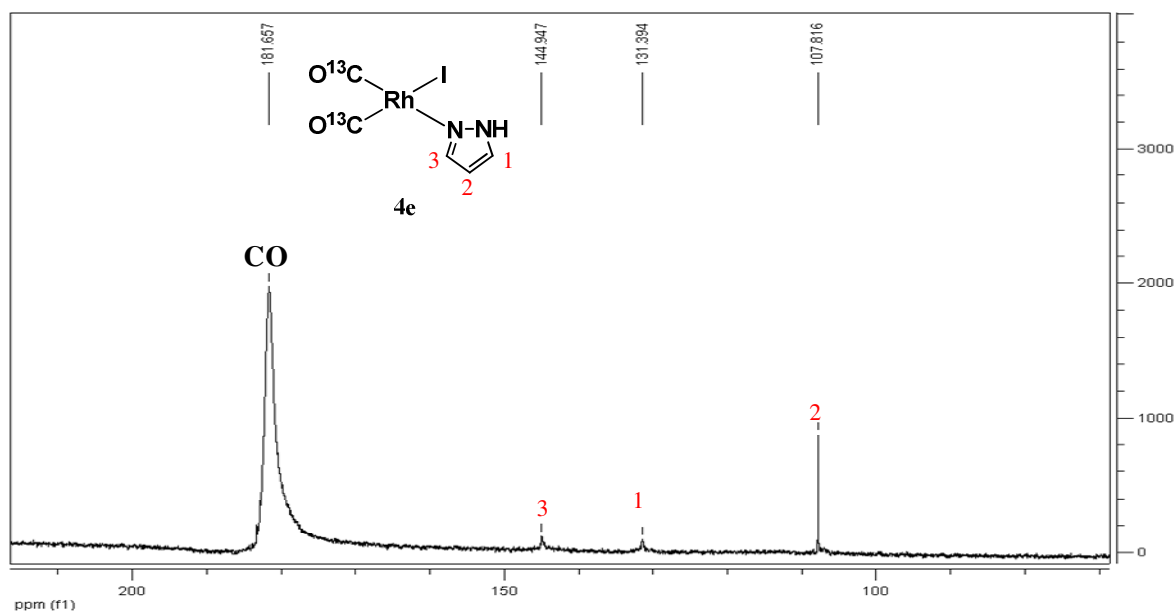


Figure 18. $^{13}\text{C}\{^1\text{H}\}$ NMR spectrum of **4e** at 298 K in CD_2Cl_2 .

For this reason ^1H and $^{13}\text{C}\{^1\text{H}\}$ NMR variable temperature (VT-NMR) experiments have been performed for **4c-i**. Selected chemical shifts and coupling constants are displayed in Table 8 (see Chapter V / S.I Chapter II for more details).

Table 8. Selected $^{13}\text{C}\{^1\text{H}\}$ VT-NMR data for *cis*-[RhI(CO)₂(L)] **4**.

Complexes	T (K)	$\delta(^{13}\text{CO})$ (ppm)		$^1J_{(\text{CO-Rh})}$ (Hz)		$^2J_{(\text{CO-CO})}$ (Hz)
		<i>cis</i> C(2)O	<i>trans</i> C(1)O	<i>cis</i> C(2)O	<i>trans</i> C(1)O	
4a	298	184.5 (dd)	180.2 (dd)	65.4	79.5	4.1
4c*	298	185.7 (br d)	180.0 (br d)	63.2	70.8	-
	233	186.1 (d)	179.9 (d)	61.9	76.5	-
4d	298	185.0 (br d)	180.1 (br d)	-	73.0	-
	243	185.4 (d)	179.8 (d)	62.4	77.9	-
4e	298	181.6 (br s)		-	-	-
	223	184.9 (d)	179.1 (d)	62.9	78.0	4.4
4f	298	182.0 (br s)		-	-	-
	203	185.2 (d)	178.9 (d)	59.1	75.5	4.8
4g	298	181.3 (br s)		-	-	-
	193	184.6 (d)	178.2 (d)	62.9	78.0	-
4h	298	181.2 (br s)		-	-	-
	193	184.9 (d)	178.9 (d)	65.9	77.0	-
4i	298	180.8 (br s)		-	-	-
	183	182.5 (d)	180.1	66.7	76.8	-

NMR Solvent = CD_2Cl_2 , (*): CD_3OD , C(1)O in *trans* position with respect to the ligands **a-i**.

The rapid dynamic site exchange of the coordinated ligands **e-i** on the NMR timescale gave rise to a time-averaged carbonyl chemical shift at RT as observed previously for **3f**.¹² At low temperature, the exchange-rate was slowed down and broad signals split into a couple of sharp double doublets, which is indicative of a static structure in solution. Figures 19 and 20 display a series of $^{13}\text{C}\{^1\text{H}\}$ VT-NMR spectra for **4e** and **4f** in the carbonyl region at 223-303 K and 203-298 K, respectively (see S.I Chapter II for more details).

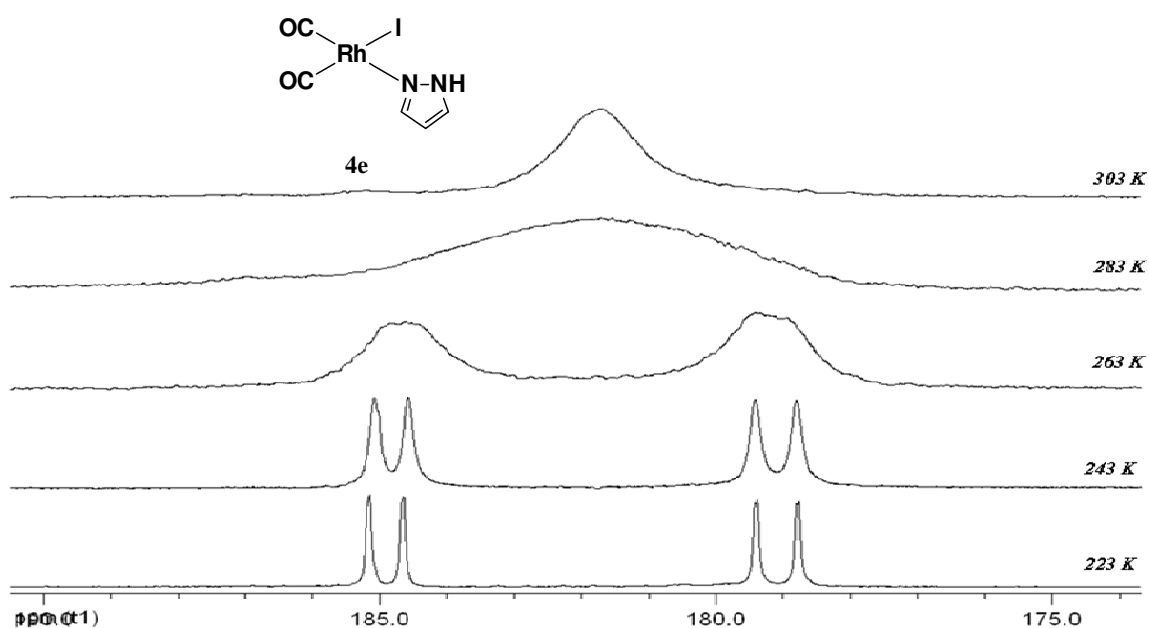


Figure 19. $^{13}\text{C}\{^1\text{H}\}$ VT-NMR stacked spectra of **4e** in the carbonyl region in CD_2Cl_2 .

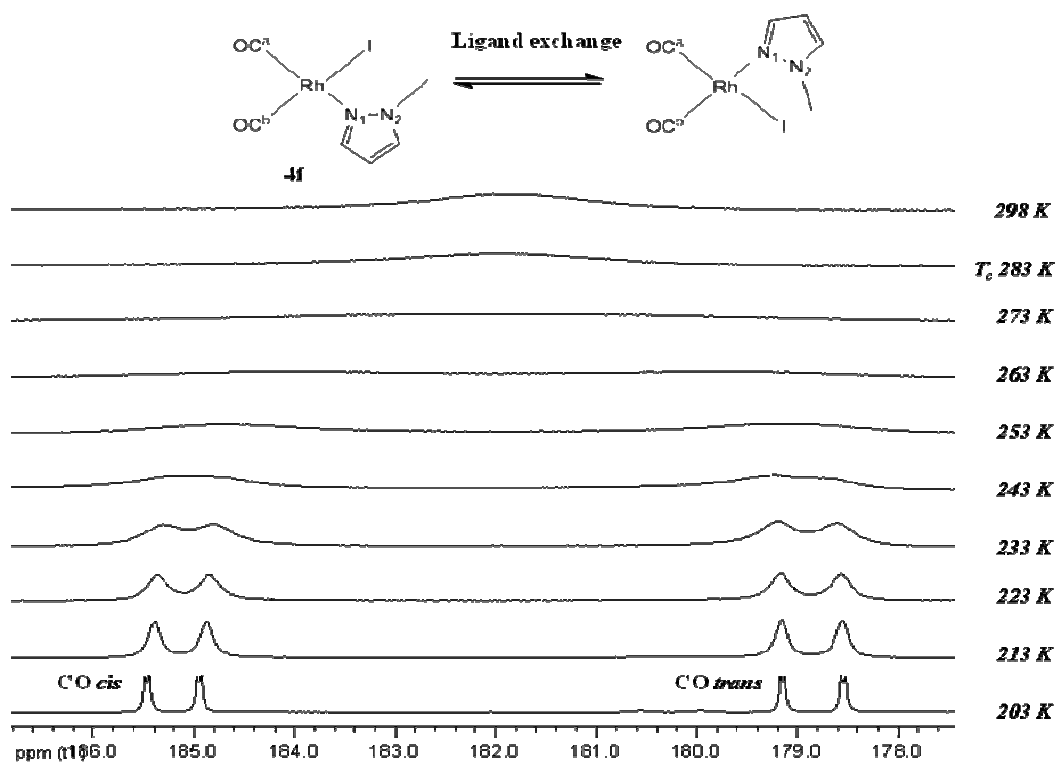
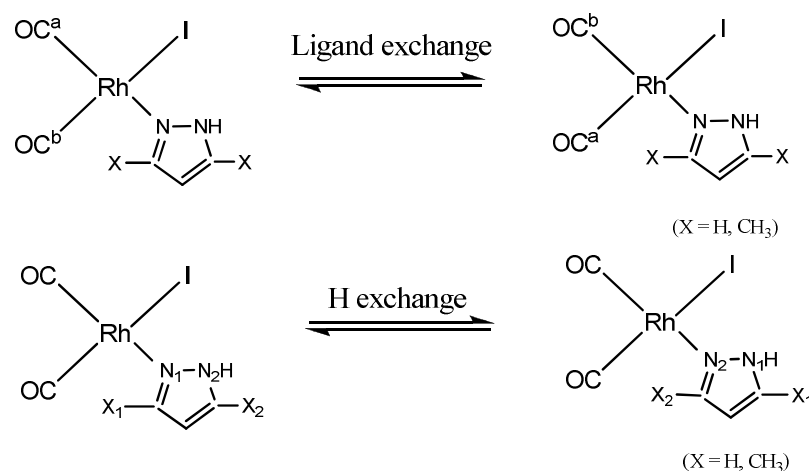


Figure 20. $^{13}\text{C}\{^1\text{H}\}$ VT-NMR stacking spectra in the carbonyl region of **4f** at 203-298 K in CD_2Cl_2 .

In addition, ^{15}N chemical shifts for **4d-f,h** have been determined throughout 2D ^1H - ^{15}N HMBC NMR experiments (see S.I Chapter II for more details). For **4d** at 298 K, a broad doublet which resonates at δ -189.8 ppm with a $^1J_{(\text{N-Rh})}$ of 23.5 Hz has been assigned to the none substituted N(1) atom and a broad signal that appears at δ -214.2 ppm higher field was assigned to the methyl substituted nitrogen atom N(2). In the same manner, ^{15}N chemical shifts corresponding to the Rh-N(1) and N(2) atoms for **4e,4f** and **4h** were determined at δ -158.7, -171.3 ppm (250 K), δ -153.9, -178.6 ppm (298 K) and δ -150.3, -166.4 ppm (193 K), respectively. $^1J_{\text{N-Rh}}$ values for **4e,f,h** have not been determined due to the too large signals obtained. For **4f**, a 1.8 ppm δ ($^{15}\text{N}(1)\text{-Rh}$) shift towards higher fields was observed whereas δ ($^{15}\text{N}(2)\text{-Me}$) was not affected in comparison with those of the corresponding free ligand **f** (δ ($^{15}\text{N}(1)$) = - 152.1 ppm, δ ($^{15}\text{N}(2)$) = - 178.9 ppm). Furthermore, (^1H - ^{103}Rh) 2D HMQC NMR measurements carried out at 243 K for **4e** and **4f** and at 193 K for **4h** present characteristic Rh(I) signals at δ - 8387, - 8334 ppm and - 8351 ppm, respectively.²⁰

In parallel to the ligand exchange phenomenon, it has been found by ^1H VT-NMR measurements that in the case of **4e,g**, a simultaneous H-exchange from one N atom to the other occurs (Scheme 2).



Scheme 2. Dynamic ligand and H exchange processes which occur in **4e** and **4g**.

A set of ^1H NMR spectra for **4e** and **4g** at variable temperatures (223-303 K and 263-298 K, respectively) are depicted in Figures 21 and 23. For **4e** at 303 K, a broad time-averaged signal at δ 7.78 ppm was assigned to the two H_a and H_b proton atoms in close vicinity to the N(1) and N(2) atoms of the pyrazole ring consistently with a fast H-exchange process on the NMR time-scale. This signal then splits into a separated couple of pseudo-triplets when decreasing the temperature. H_a slightly shifts downfield (7.77 ppm) in comparison with H_b (7.72 ppm) due to the electron withdrawing effect of the closer $\{\text{RhI}(\text{CO})_2\}$ moiety (Figure 22). Similarly, the two corresponding $^{13}\text{C}\{^1\text{H}\}$ NMR signals sharpened.

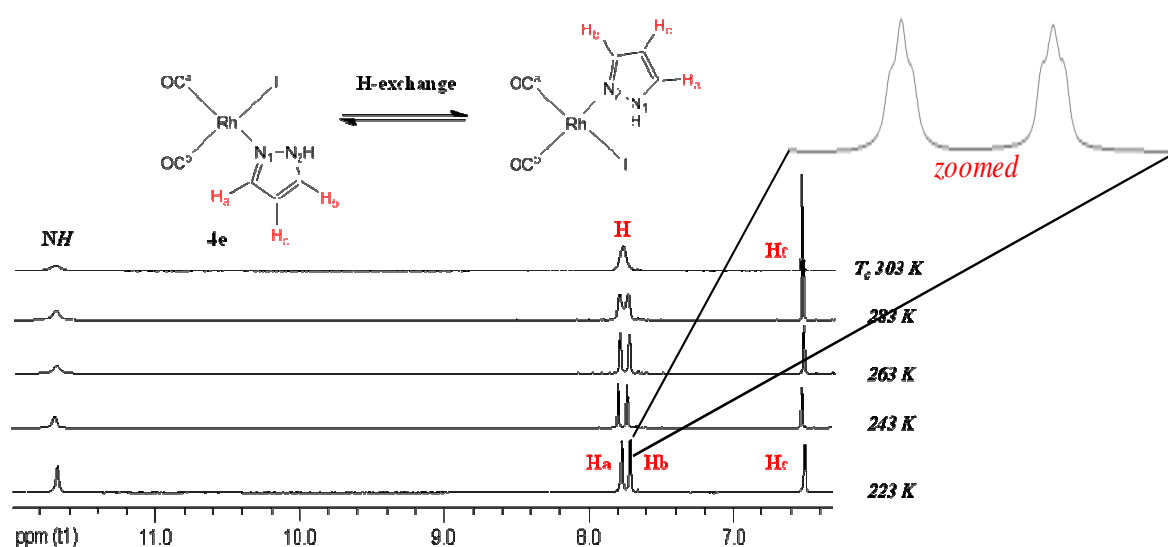


Figure 21. ^1H VT-NMR spectra of **4e** at 223-303 K in CD_2Cl_2 .

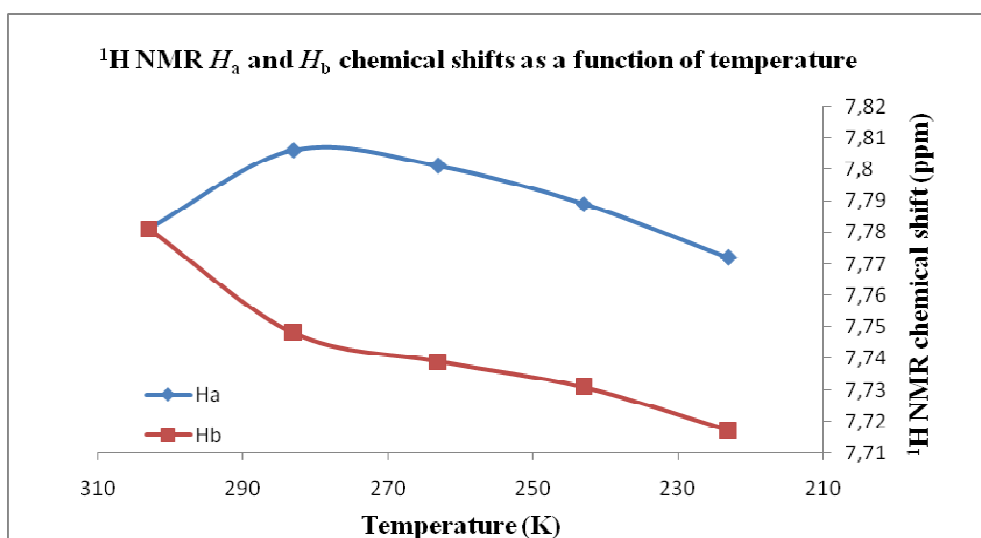


Figure 22. Plot of ^1H NMR chemical shifts for H_a and H_b in **4e** at 223-303 K in CD_2Cl_2 .

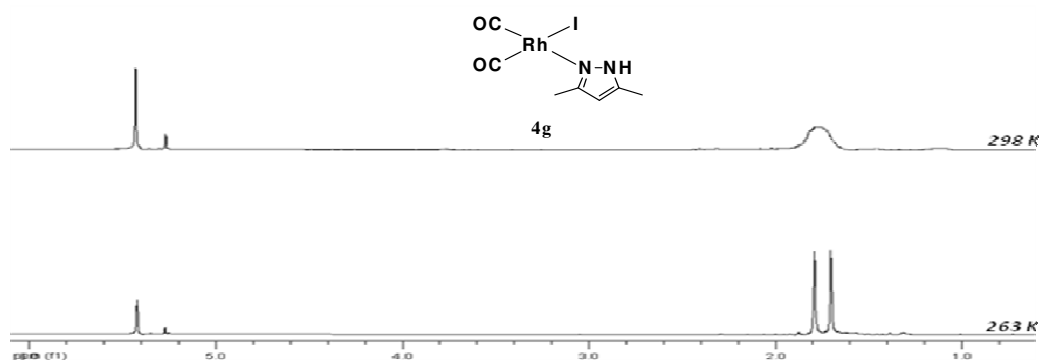


Figure 23. ^1H VT-NMR spectra of **4g** at 263-298 K in CD_2Cl_2 .

The following section briefly describes the determination of the activation parameters (ΔH^\ddagger , ΔS^\ddagger , E_a) relative to the VT-NMR exchange processes:

The Gibbs activation energy is determined from the Eyring-Polanyi equation (Eq. 2) as following:

$$k = \chi \frac{k_B T}{h} e^{-\Delta G^\ddagger/RT} \quad (\text{Eq. 2})$$

k = reaction exchange rate constant, T = absolute temperature, R = gas constant, k_B = Boltzmann constant, h = Planck constant, χ = Transmission coefficient²¹

The relationship between the Gibbs activation energy ΔG^\ddagger , the activation enthalpy ΔH^\ddagger and the activation entropy ΔS^\ddagger is given by equation (Eq. 3):

$$\Delta G^\ddagger = \Delta H^\ddagger - T \Delta S^\ddagger \quad (\text{Eq. 3})$$

Taking the log and fitting in (Eq. 3), the Eyring-Polanyi equation (Eq. 1) then becomes equation 4 (Eq. 4) as following:²¹

$$\log \frac{k}{T} = 10.32 - \frac{\Delta H^\ddagger}{4.58 T} + \frac{\Delta S^\ddagger}{4.58} \quad (\text{Eq. 4})$$

The Arrhenius equations (Eq. 5) and (Eq. 6) allow then to determine the Arrhenius activation energy E_a as following:

$$E_a = -RT \ln(k/A) \quad (\text{Eq. 5})$$

$$\ln(k) = \ln(A) - \frac{E_a}{RT} \quad (\text{Eq. 6})$$

The determination of the reaction exchange rate constant k at different temperatures was managed by the means of the WINDNMR software by Hans J. Reich. The following part describes the activation parameter determination relative to the H-exchange process for complex **4e** and the ligand exchange process for complex **4f** as examples. Eyring and Arrhenius plots are depicted in Figures 24-27 (see S.I Chapter II for more details):

T (K)	k (s ⁻¹)
303	151
283	83
263	40
243	19

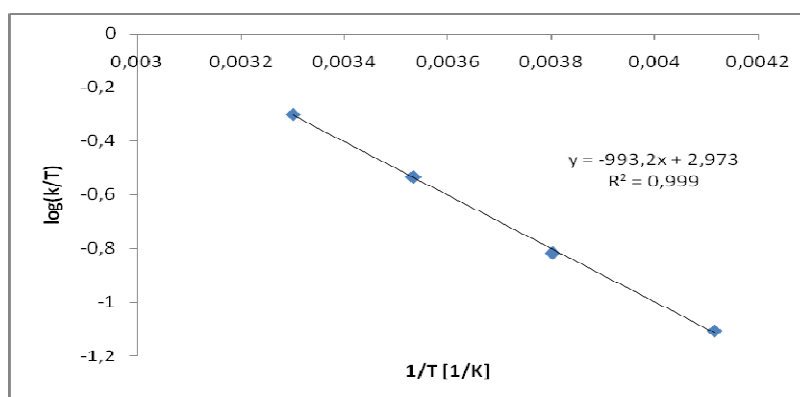


Figure 24. Eyring plot for the H-exchange process in 4e.

$$\Delta H \ddagger = 4549.3 \frac{\text{cal}}{\text{mol}} = 19034.27 \frac{\text{J}}{\text{mol}} = 19.034 \frac{\text{KJ}}{\text{mol}}$$

$$\Delta S \ddagger = -33.66 \frac{\text{cal}}{\text{K.mol}} = -140.83 \frac{\text{J}}{\text{K.mol}}$$

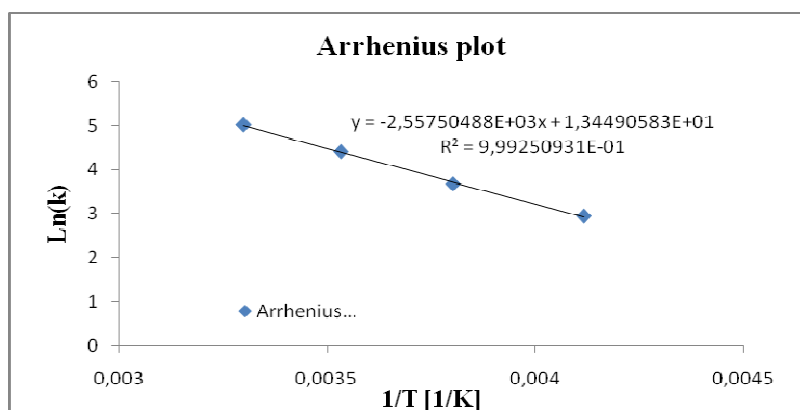


Figure 25. Arrhenius plot for the H-exchange process in 4e.

$$E_a = 21263.05 \text{ J.mol}^{-1} = 21.3 \text{ KJ.mol}^{-1}$$

T (K)	k (s ⁻¹)
305	4664
298	3364
283	2364
273	984
263	534
253	294
243	174
233	84
223	48

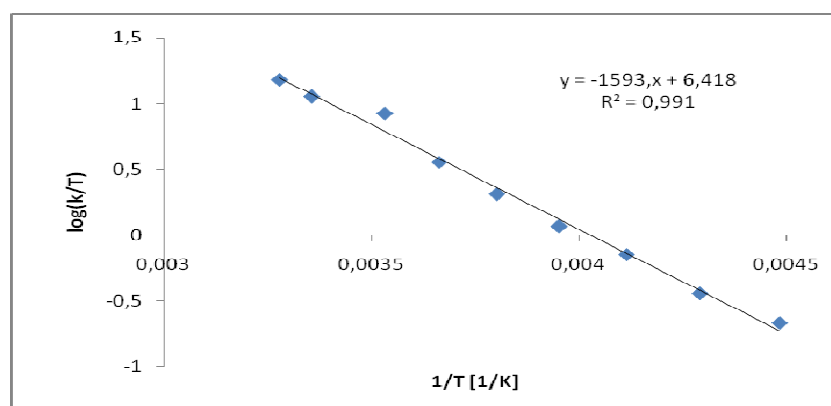


Figure 26. Eyring plot for the ligand exchange process in **4f**.

$$\Delta H^\ddagger = 7295.9 \frac{\text{cal}}{\text{mol}} = 30526.05 \frac{\text{J}}{\text{mol}} = 30.526 \frac{\text{KJ}}{\text{mol}}$$

$$\Delta S^\ddagger = -17.86 \frac{\text{cal}}{\text{K.mol}} = -74.726 \frac{\text{J}}{\text{K.mol}}$$

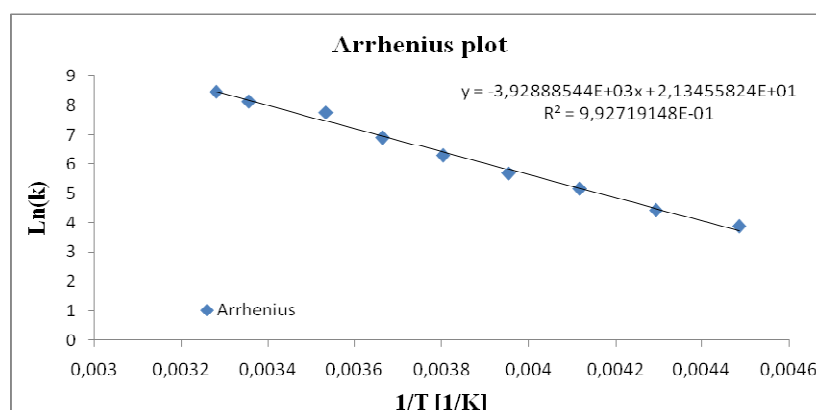


Figure 27. Arrhenius plot for the ligand exchange process in **4f**.

$$E_a = 32664.79 \text{ J.mol}^{-1} = 32.7 \text{ KJ.mol}^{-1}$$

Coalescence temperature (T_c) and activation parameters (ΔH^\ddagger , ΔS^\ddagger , E_a) for **4** have been determined and are listed in Table 9. The activation enthalpy ΔH^\ddagger is generally related to the lability of the ligands and therefore to their electronic and steric contributions.^{12c} The significantly lower T_c values for **4e-i** in comparison with those for **4c,d** indicates a higher labile character, thus a faster ligand-exchange, of pyrazole type ligands, which is consistent with their lower electron donating ability (higher TEP values). This observation suggests a

dissociative ligand-exchange mechanism being operative.^{12b} For **4c,d**, the coalescence temperatures were not reached even when working at RT in CD₂Cl₂ (low boiling point) that is why ¹H and ¹³C{¹H} VT-NMR experiments for determination of activation parameters were carried out and measured in CD₃OD solvent. Substitution of a H atom by a methyl group on the N(2) atom (ligand **f**) or on C(3)-C(5) atoms (ligand **g**) of the pyrazole ring results in an insignificant variation of E_a values. The lowest estimated Arrhenius activation energy E_a is 16.2 KJ.mol⁻¹ ($T_c = 223$ K) for **4i**, which reflects the high labile character of S-Et₂ compared to the amine derivatives. An additional experiment which supports this latter observation was carried out in parallel for the further less basic thiophene ligand. Indeed, the formation of the split monomeric complex [RhI(CO)₂(thiophene)] starting from **2** and 2 eq. of thiophene ligand was not detected by FT-IR spectroscopy which indicates a much higher labile character of this S-heterocyclic ligand.

It is noteworthy that for **4e**, the intramolecular mechanism is most probably due to the low value of the E_a compared to that of the ligand exchange^{12b, 12e}, although the nature of the H-exchange mechanism process still remains unclear. Indeed, the lower E_a (15 KJ.mol⁻¹) for [PdCl(PEt₃)₂(4-Br-**g**)] (4-bromo-3,5-dimethylpyrazole) is consistent with the rich electron donating contribution of the two PEt₃ ligands to the Pd center resulting in a stronger acidic character of N-H. In addition, the high electron donating P-ligands stabilize the Pd-N bond which agrees with the higher E_a value for the ligand exchange process (45 KJ.mol⁻¹) in comparison with our Rh-pyrazole complexes.

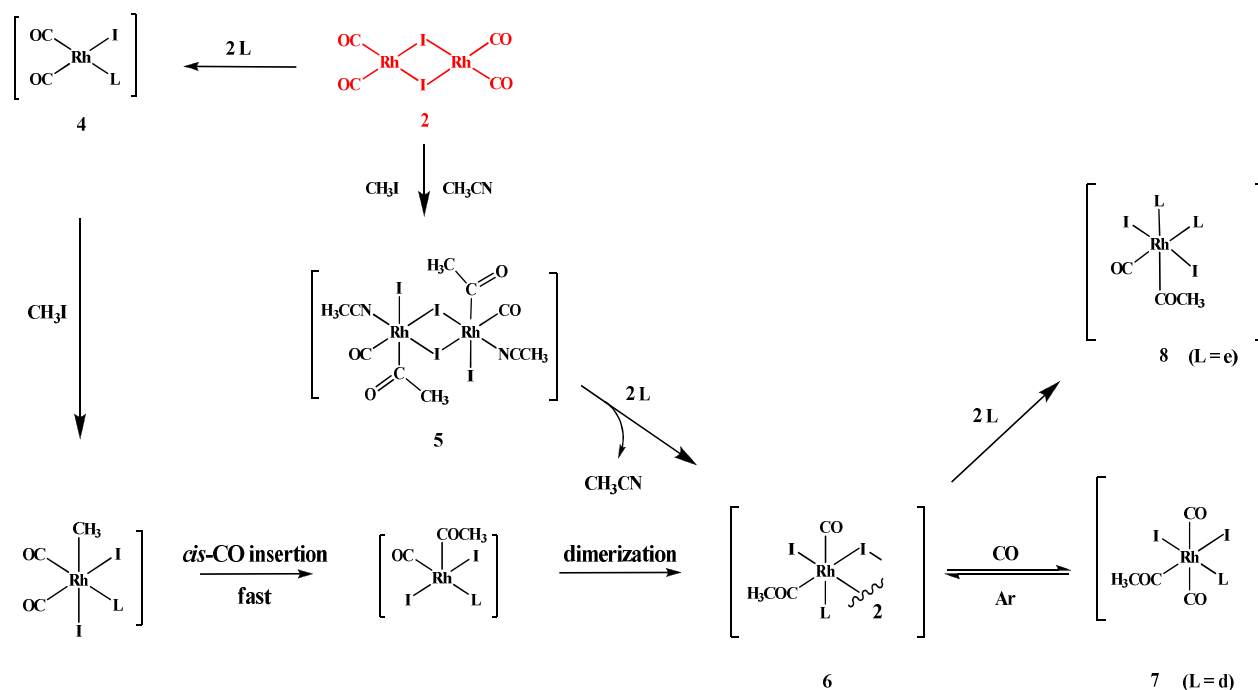
Table 9. Coalescence temperature T_c and activation parameters for *cis*-[RhI(CO)₂(L)] **4**.

<i>Complexes</i>	T_c (K)	E_a (kJ.mol ⁻¹)	ΔH^\ddagger (KJ.mol ⁻¹)	ΔS^\ddagger (J.K ⁻¹ .mol ⁻¹)
4a	>> 328	-	-	-
4c*	> 328	26.9 ± 1.6	24.7 ± 1.5	-117 ± 7.0
4d	> 295	29.0 ± 1.7	26.8 ± 1.6	-107 ± 6.4
4d*	328	26.7 ± 1.6	24.5 ± 1.5	-111 ± 6.7
4e	283	32.4 ± 1.9	30.2 ± 1.8	-76 ± 4.6
4e^a	303	21.3 ± 1.3	19.0 ± 1.1	-141 ± 8.5
4f	283	32.7 ± 2.0	30.5 ± 1.8	-75 ± 4.5
4g	273	28.3 ± 1.7	26.1 ± 1.6	-89 ± 5.3
4h	298	16.3 ± 1.0	14.3 ± 0.9	-135.5 ± 8.1
4i	223	16.2 ± 1.0	14.5 ± 0.9	-123 ± 7.4

NMR solvents = CD₂Cl₂, (*): CD₃OD, Ligand exchange process, (^a): H-exchange process, T_c : coalescence temperature.

II-4- Synthesis and characterization of acetyl-Rh(III) complexes

Complexes **4a,c-i** have been evaluated for the CH₃I oxidative addition reaction. Reaction of **4a,c-i** with neat CH₃I at RT afforded the corresponding neutral dimeric iodo-bridged Rh(III)-acetyl complexes [RhI(μ-I)(COMe)(CO)(L)]₂ **6a,c-i** (L = **a,c-i**) in high isolated yields. Alternatively, **6a,c-i** were also prepared according to the Haynes's method²² in a two step reaction: **2** was treated at RT with CH₃I in acetonitrile to produce the stable dimeric complex [RhI(μ-I)(COMe)(CO)(CH₃CN)]₂ **5**, which was further substituted with 2 molar eq. of ligands **a,c-i** (Scheme 3). In the range of working temperature conditions, no quaternization of Rh-ligated ligands **a,c-i** by CH₃I was detected for either synthetic methods.



Scheme 3. General reaction pathway leading to the Rh(III) acetyl complexes **5**, **6**, **7** and **8**.

Relevant FT-IR data of **6-8** in CH_2Cl_2 and neat CH_3I are summarized in Table 10 (see Annex Chapter II for more details).

Table 10. FT-IR carbonyl stretching frequencies for **6-8** at RT.

Complexes	CH_2Cl_2		CH_3I	
	$\nu(CO)$ (cm^{-1})	$\nu(COMe)$ (cm^{-1})	$\nu(CO)$ (cm^{-1})	$\nu(COMe)$ (cm^{-1})
6a	2072.6	1719.1	2063.3	1716.4
6c	2073.7	1734.9; 1707.0	2073.9	1719.2; 1705.2
6d	2073.1	1733.5	2068.0	1736.0
6e	2083.5	1741.0; 1721.0	2075.6	1736.7
6f	2076.6	1778.0	2072.3	1776.4; 1743.7
6g	2079.6	1753.8	2075.5	1749.6
6h	2081.9	1718.8	2076.7	1742.5; 1719.1
6i	2080.6	1720.8	2076.4	1743.6; 1721.1
7d*	2073.2	1735.9	-	-
8e	2082.5	1698.9; 1677.4	-	-

(*): Very weak symmetric band has been observed at 2155.6 cm^{-1} .

FT-IR spectra of the dimeric Rh(III) **6** showed a large and intense terminal ν_{CO} band at $\sim 2070 \text{ cm}^{-1}$, i.e. 35 cm^{-1} higher in frequency than the $\nu_{\text{CO, av}}$ of the starting complexes **4**, which is consistent with a [Rh(III)]-carbonyl fragment. In addition, a broad medium ν_{COMe} acetyl band appeared at $\sim 1700 \text{ cm}^{-1}$. Figure 28 illustrates these IR spectroscopic observations in the case of **6a**.

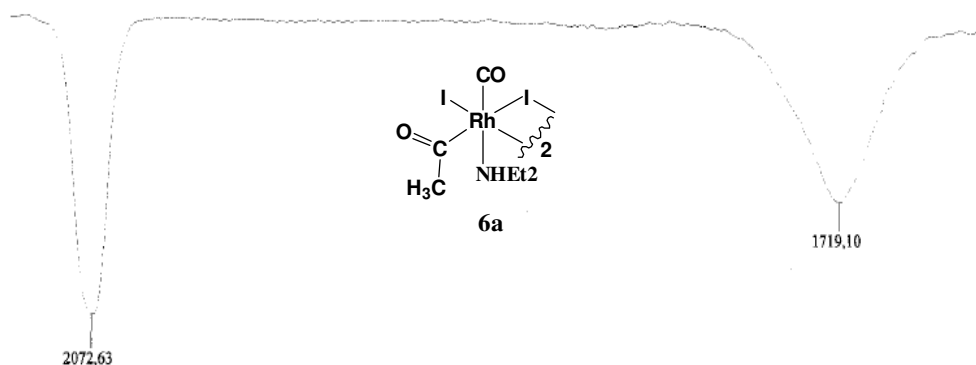


Figure 28. FT-IR spectrum of **6a** at 298 K in CH_2Cl_2 .

The ^1H and $^{13}\text{C}\{^1\text{H}\}$ NMR for **6** clearly identified the acetyl group with the proton signals at $\delta \sim 3.0 \text{ ppm}$ and the methyl carbon signal at $\delta \sim 48.0 \text{ ppm}$. The $^{13}\text{C}\{^1\text{H}\}$ NMR spectra in the carbonyl region for **6** exhibited a group of signals centered at $\delta \sim 212 \text{ ppm}$ which was assigned to [Rh]-COCH₃ and another group centered at higher field $\delta \sim 182 \text{ ppm}$, which was attributed to the terminal [Rh]-CO. Figure 29 illustrates these $^{13}\text{C}\{^1\text{H}\}$ NMR spectroscopic features in the case of **6d**.

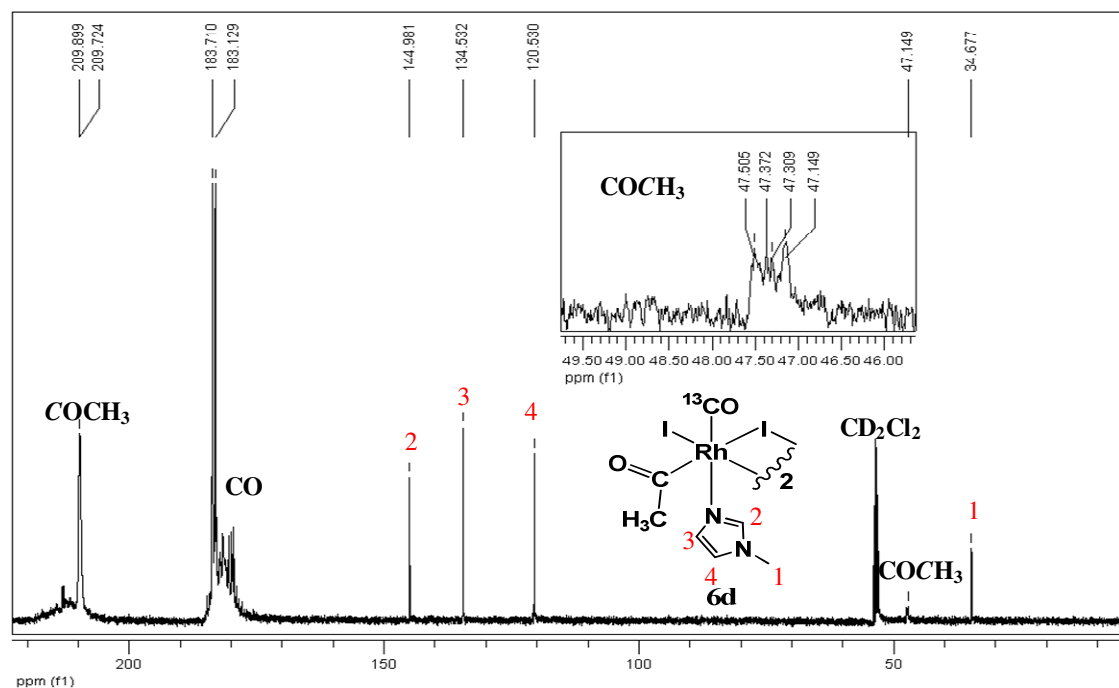


Figure 29. $^{13}\text{C}\{^1\text{H}\}$ NMR spectrum of ^{13}CO -6d at 298 K in CD_2Cl_2 .

The large carbonyl IR bands and ^{13}CO NMR pattern observed at RT for **6a,c-i** are consistent with the existence of several isomers in solution (Figure 29) based on results of an iodo-bridged Rh dimer.^{22,23} Even at low temperature (193 K), $^{13}\text{C}\{^1\text{H}\}$ NMR spectrum of **6e** still displayed very broad signals indicating that static structures in solution were still not observed. This should be due to both intra and intermolecular fluxional processes among the at least 18 possible isomers.²³

Further bridge-splitting reactions with CO or with an extra N-containing ligand **e** have been explored on complexes **6d** and **6e** (Figure 30). Brief CO bubbling (10 minutes) of a dichloromethane solution containing **6d** resulted in the sharpening of both characteristic infrared bands (ν_{CO} , ν_{COMe}) and corresponding $^{13}\text{C}\{^1\text{H}\}$ NMR signals ($\delta(\text{COMe}, \text{ppm}) = 210.2$ (d), $^1J_{\text{COMe-Rh}} = 21.6$ Hz; $\delta(\text{CO}, \text{ppm}) = 183.4$ (d), $^1J_{\text{CO-Rh}} = 58.5$ Hz). These data are consistent with the formation of the monomeric $[\text{RhI}_2(\text{COMe})(\text{CO})_2(\text{d})]$ **7d** complex, which

presents a much lower number of isomers in solution. In absence of CO atmosphere, **7d** gradually loses one CO which restores reversibly the initial dimeric **6d** species, as previously observed for the anionic $[\text{RhI}_3(\text{COMe})(\text{CO})_2]^-$ complex.²³ Furthermore, keeping the solution of **7d** in dichloromethane under CO atmosphere for a longer period of time (48 hours) affords the starting Rh(I) **4d** species (Figure 30). Under such reaction conditions, reductive elimination took place to give back the Rh(I) species **4d** and CH_3COI which further reacted with traces of adventitious water to give acetic acid ($\delta(\text{CH}_3\text{COOH}) = 175.9$ ppm) and HI. For **4d**, the large $^{13}\text{C}\{^1\text{H}\}$ carbonyl signal at 180 ppm observed at RT is presumably due to the fast exchange with free labeled ^{13}CO dissolved in the medium. Acetic anhydride has also been detected ($\delta((\text{CH}_3\text{CO})_2\text{O}) = 166.5$ ppm) presumably due to the reaction of CH_3COI with AcOH at low water concentration. Similar reaction has previously been observed for $[\text{RhI}_2(\text{COMe})_2(\text{CO})]_n$.²² In parallel, a small doublet centered at δ 179.3 ppm ($^1J_{\text{CO-Rh}} = 49.0$ Hz) has been tentatively assigned to $[\text{RhI}_3(\text{CO})_2(\mathbf{d})]$, which could be formed via HI oxidative addition upon **4d**. This reactivity has been explored in our group for the corresponding anionic $[\text{RhI}_2(\text{CO})_2]^-$ affording $[\text{RhI}_4(\text{CO})_2]^-$, for which CO resonated expectedly at higher field: $\delta(\text{CO}) = 173.1$ ppm, $^1J_{\text{CO-Rh}} = 48.1$ Hz (counter-cation: PPN^+ bis(triphenylphosphoranylidene)-ammonium).

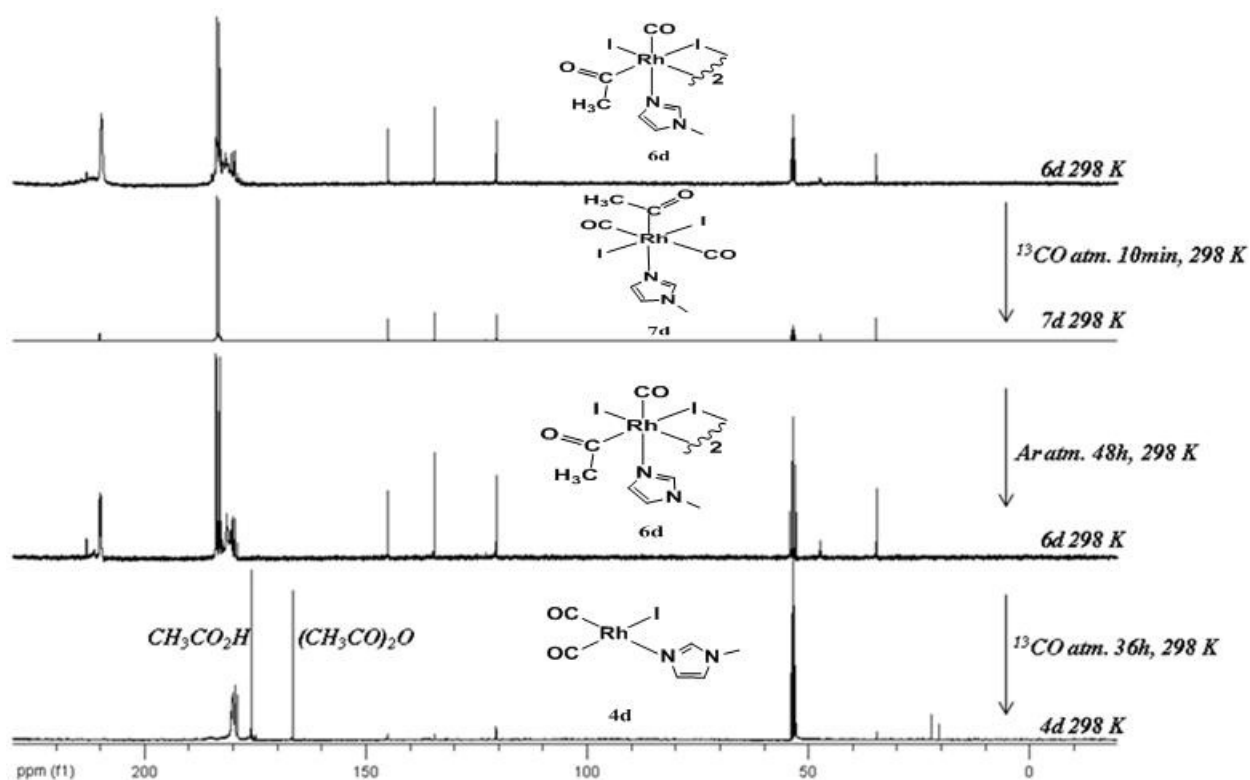


Figure 30. $^{13}\text{C}\{^1\text{H}\}$ NMR stacked spectra of **6d-7d-6d-4d** at 298 K in CD_2Cl_2 .

Treatment of **6e** with 2 eq. of ligand **e** quantitatively yielded monomeric $[\text{RhI}_2(\text{COMe})(\text{CO})(\text{e})_2]$ **8e** bearing two pyrazole ligands in the coordination sphere. In the FT-IR spectrum, the terminal ν_{CO} band at 2082.5 cm^{-1} shifted only slightly by 1 cm^{-1} , whereas the acetyl bands ($1698.9, 1677.4\text{ cm}^{-1}$) shifted drastically by more than 40 cm^{-1} at lower wavenumber with respect to the initial dimeric **6e** suggesting that **e** is coordinated in *trans* position to the acetyl ligand. Complete ^1H and ^{13}C chemical shift assignments for two distinctly bound pyrazole ligands have been determined from the interpretation of 2D ^1H - ^1H COSY and ^1H - ^{13}C HMQC NMR experiments (Figures 31-34). A broad time-averaged ^1H signal at RT for both C(3)-H and C(5)-H of one pyrazole ring was observed which agrees

with the fluxional H-exchange process. In contrast, for the other ring, the observation of two well separate ^1H signals suggests that N-H remains static on the NMR time-scale.

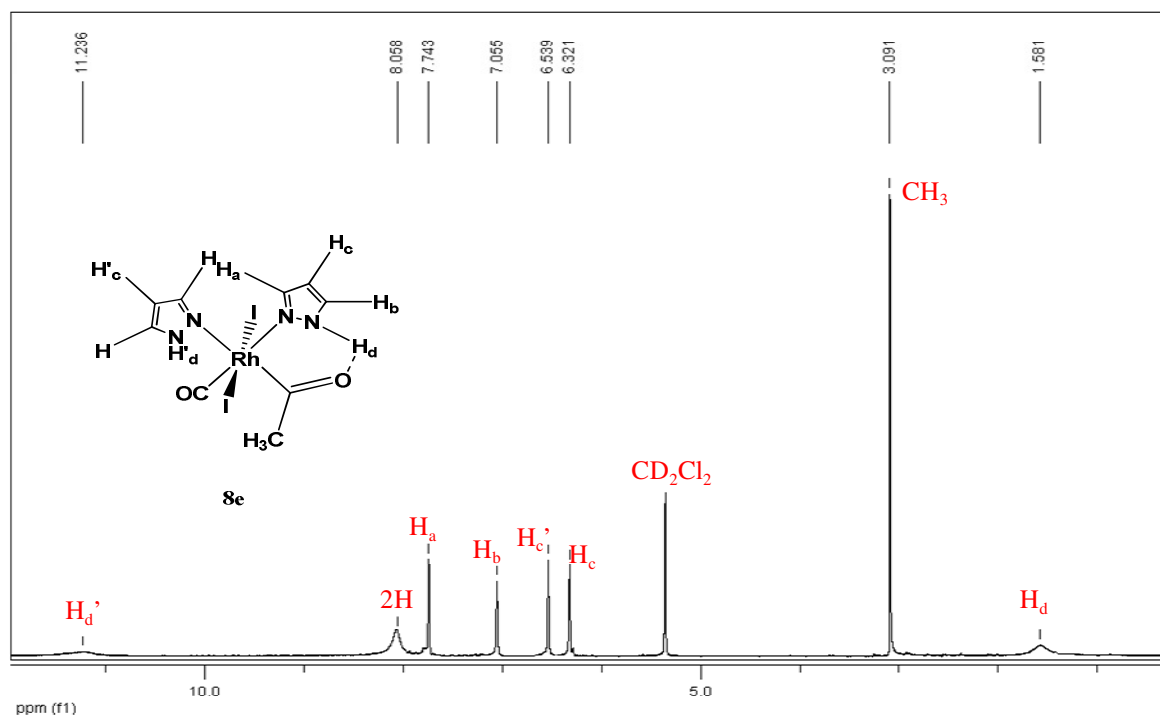


Figure 31. ^1H NMR spectrum of **8e** in the 1.00-12.00 ppm region at 298 K in CD_2Cl_2 .

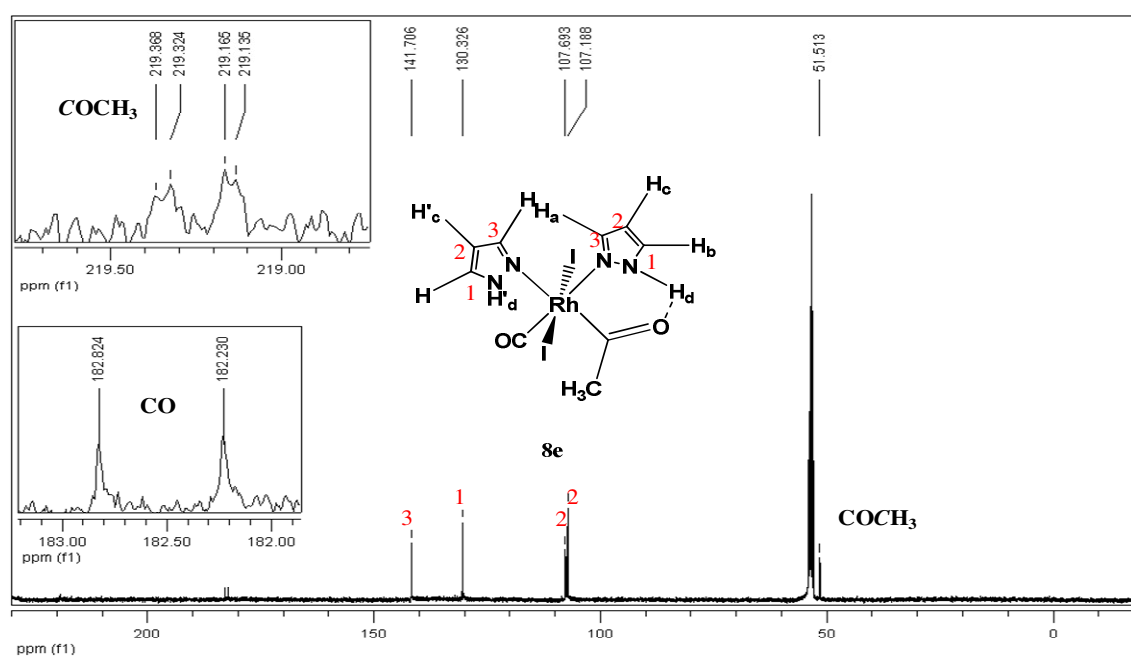


Figure 32. $^{13}\text{C}\{^1\text{H}\}$ NMR spectrum of **8e** at 298 K in CD_2Cl_2 .

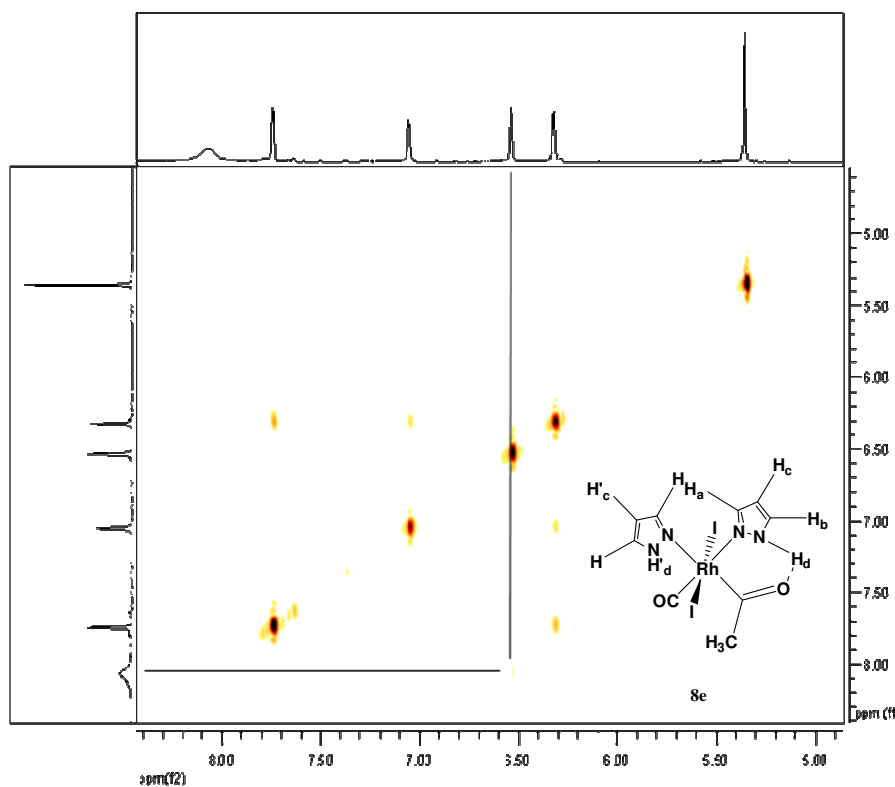


Figure 33. 2D ^1H - ^1H COSY NMR spectrum of **8e** in the 5.00-9.00 ppm region at 298 K in CD_2Cl_2 .

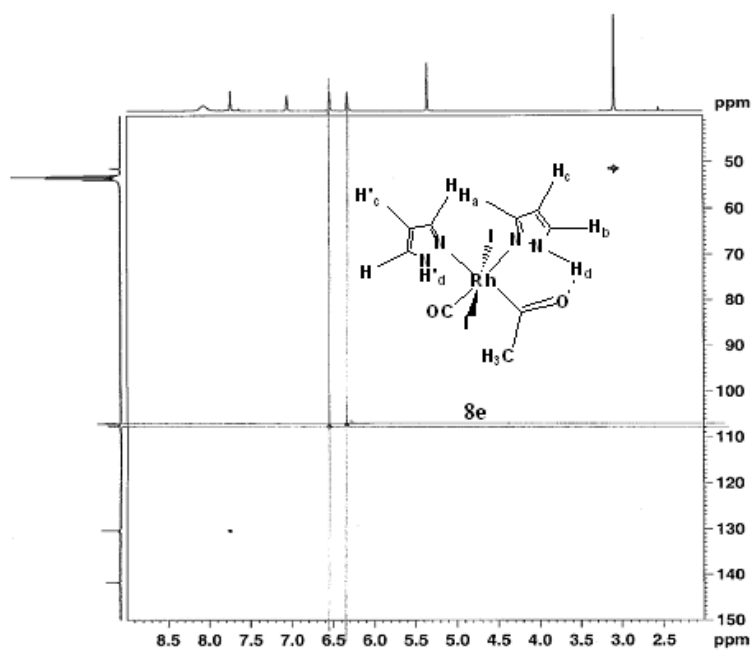


Figure 34. 2D ^1H - ^{13}C HMQC NMR spectrum of **8e** at 298 K in CD_2Cl_2 .

Suitable single crystals for X-ray analysis of **6d₁** and **6e** were grown in CH₂Cl₂ at 255 K and their molecular views are displayed in Figures 35 and 37. Attempts for crystallization of **7d** in CH₂Cl₂ gave another unexpected isomer **6d₂** (Figure 36). Selected bonds and angles are listed in Tables 11 and 12. The molecular structure of **6d₁** is centro-symmetric similarly to that of [RhI₂(COMe)(CO)(R)]²² (R = NCMe, NC^tBu) and [RhI₃(COMe)(CO)]₂²⁻²⁴ whereas **6d₂** and **6e** possess two apical terminal CO ligands in mutual *cis* position as well as two apical ligands **d** and **e**. In all cases the two acetyl moieties are located in the equatorial plane mutually *trans* to each other. The same arrangement prevails for the terminal iodo ligands which afford a local centro-symmetric structure for the {Rh₂(μ-I)₂I₂(COCH₃)₂} framework. The Rh(1)-I(3) bond length (2.96-3.00 Å) is much longer than the two mutually *trans* I(1)-Rh(1)-I(2) bonds (2.65-2.68 Å) indicating a large *trans* influence of the acetyl ligand. The non-bonded Rh(1)-Rh(2) distance is shorter for the centro-symmetric complex **6d₁** (4.010 Å) than for **6d₂** (4.105 Å) and **6e** (4.092 Å), which is consistent with a steric hindrance between the two N-ligands in the *cis* apical position. In fact, the angles formed between both heterocyclic rings are 67.4° and 71.4° for **6d₂** and **6e**, respectively whereas for **6d₁** they are almost parallel.

Further analysis of the packing diagram of **6e** shows the existence of both intra- and intermolecular H-bonding interactions: the two intramolecular N(2)-H(2a)⋯O(2), N(4)-H(H4a)⋯O(4) distances are 2.149 Å and 2.028 Å with corresponding angles of 127.9° and 136.1°, respectively.²⁵ The intermolecular N(2)-(H2a)⋯I(4) contact is 2.980 Å with an angle of 129.4°.

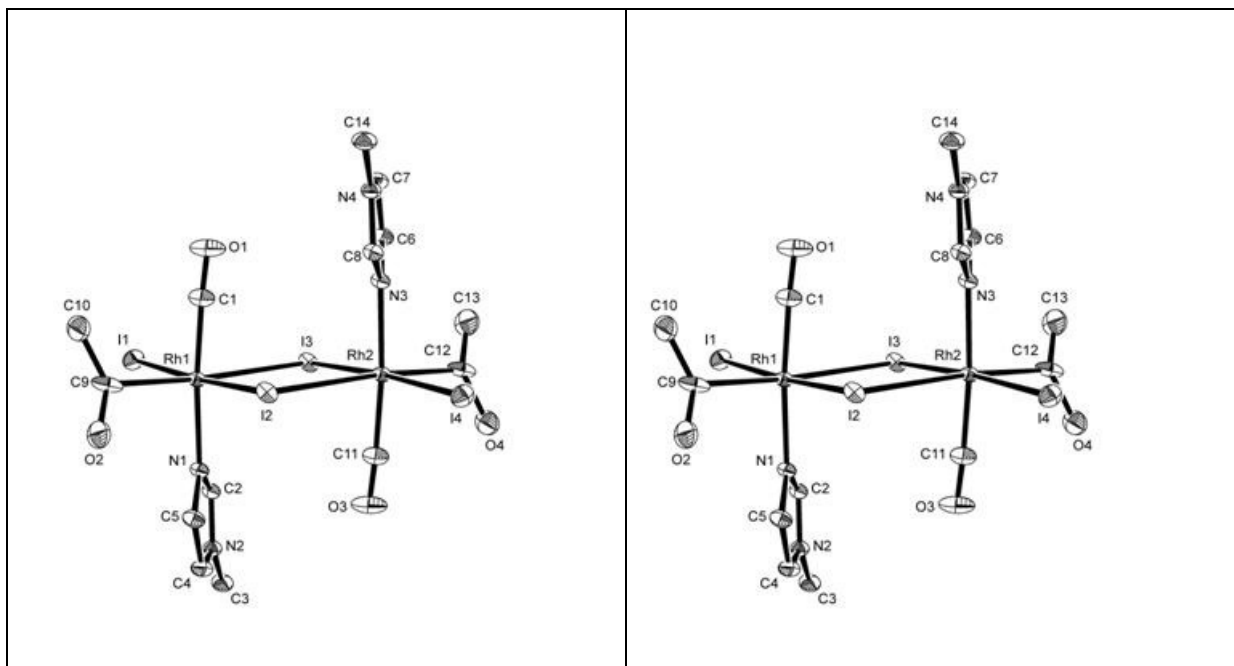


Figure 35. Molecular structure of one dimer $[\text{RhI}(\mu\text{-I})(\text{COMe})(\text{CO})(\mathbf{d})]_2$ **6d₁** from the asymmetric unit with the atom-labeling scheme. Thermal ellipsoids are shown at the 30% probability level and hydrogen atoms are omitted for clarity.

Figure 36. Molecular structure of dimer $[\text{RhI}(\mu\text{-I})(\text{COMe})(\text{CO})(\mathbf{d})]_2$ **6d₂** with the atom-labeling scheme. Thermal ellipsoids are shown at the 30% probability level and hydrogen atoms are omitted for clarity.

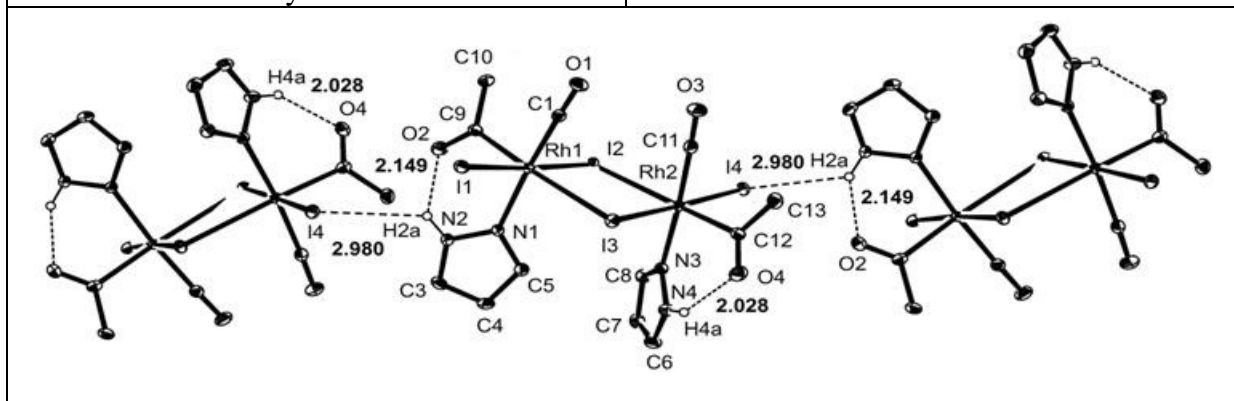


Figure 37. Molecular view of three molecules of dimer $[\text{RhI}(\mu\text{-I})(\text{COMe})(\text{CO})(\mathbf{e})]_2$ **6e**. Thermal ellipsoids are shown at the 30% probability level and hydrogen atoms are omitted for clarity except for the amine group putting in evidence intramolecular (2.028 Å, 2.149 Å) and intermolecular (2.980 Å) H-bonding interactions.

The X-ray crystal structure of $[\text{RhI}_2(\text{COMe})(\text{CO})(\mathbf{e})_2]$ **8e** was also solved (Figure 38, Tables 11 and 13). The two pyrazole ligands are in mutual *cis* position with the terminal carbonyl and acetyl ligands in the same plane, which is consistent with the NMR observations. The two iodo ligands occupy the apical positions of the octahedron. The two pyrazole rings *trans* and *cis* to the acetyl moiety are inclined towards the equatorial Rh-plane

by 57.5° and 29.6° , respectively. The longer Rh(1)-N(1) bond distance (2.245 \AA) in comparison with Rh(1)-N(3) bond (2.107 \AA) is in good agreement with the strong *trans*-influence of the acetyl ligand.

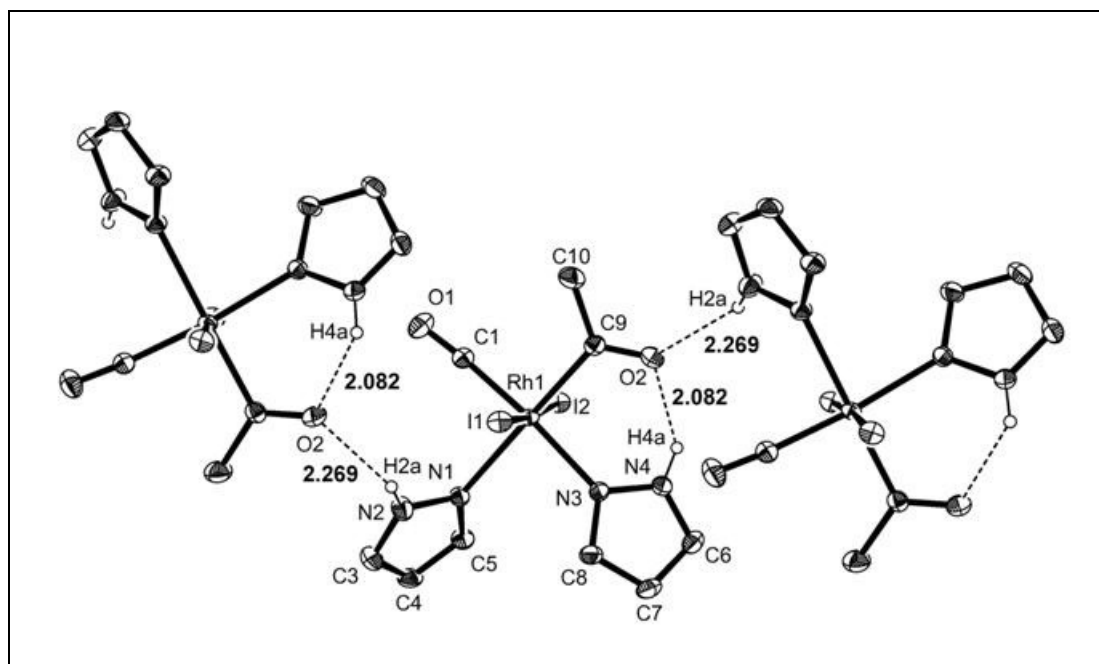


Figure 38. Molecular view of three molecules of $[\text{Rh}_2(\text{COMe})(\text{CO})(\text{e})_2]$ **8e**. Thermal ellipsoids are shown at the 30% probability level. Hydrogen atoms are omitted for clarity except for the amine group putting in evidence intramolecular (2.082 \AA) and intermolecular (2.269 \AA) H-bonding interactions.

Deeper analysis of the X-ray structure shows that both (N)-H atoms of each pyrazole ligands are involved in intramolecular N(4)-H(4a) \cdots O(2) (2.082 \AA , 128.1°) and intermolecular N(2)-H(2a) \cdots O(2) (2.269 \AA , 143.3°) interactions.²⁵ Indeed, the intramolecular contact results in the formation of a six-membered ring $[\text{Rh}(\text{I})-\text{N}(3)-\text{N}(4)-\text{H}(4a)\cdots\text{O}(2)-\text{C}(9)]$ which brings the *cis*-pyrazole plane closer to the equatorial Rh-plane in comparison with the *trans*-one (29.6° vs. 57.5°). It is very likely that this six-membered cycle is maintained in solution, preventing the H(4a)-exchange process to occur, as observed by the ^1H NMR study.

Table 11. Selected bond lengths (Å) for **6d₁**, **6d₂**, **6e** and **8e**.

<i>Atoms</i>	<i>6d₁</i> *		<i>6d₂</i>	<i>6e</i>	<i>8e</i>
	<i>Mol1</i>	<i>Mol2</i>			
<i>Rh(1)-I(1)</i>	2.653(1)	2.647(1)	2.662(1)	2.654(1)	2.674(1)
<i>Rh(1)-I(2)</i>	2.680(1)	2.669(1)	2.680(2)	2.671(1)	2.669(1)
<i>Rh(1)-I(3)</i>	2.958(1)	2.978(1)	2.960(2)	3.002(1)	-
<i>Rh(1)-C(1)</i>	1.854(4)	1.859(5)	1.863(6)	1.856(3)	1.864(4)
<i>Rh(1)-C(9)</i>	2.217(6)	2.057(5)	2.037(6)	2.064(3)	2.042(4)
<i>Rh(1)-N(1)</i>	2.100(3)	2.105(3)	2.106(4)	2.104(3)	2.245(3)
<i>Rh(1)-N(3)</i>	-	-	-	-	2.107(3)
<i>Rh(2)-I(2)</i>	2.958(1)	2.978(1)	3.067 (2)	2.956(1)	-
<i>Rh(2)-I(3)</i>	2.680(1)	2.669(1)	2.680(2)	2.682(1)	-
<i>Rh(2)-I(4)</i>	2.653(1)	2.647(1)	2.640(2)	2.647(1)	-
<i>Rh(2)-C(11)</i>	1.854(4)	1.859(5)	1.860(6)	1.868(3)	-
<i>Rh(2)-C(12)</i>	2.217(6)	2.057(5)	2.044(5)	2.088(3)	-
<i>Rh(2)-N(3)</i>	2.100(3)	2.105(3)	2.101(5)	2.107(3)	-
<i>N(2)-H(2a)···O(2) intra^a</i>	-	-	-	2.149	-
<i>N(2)-H(2a)···O(2) inter^b</i>	-	-	-	-	2.269
<i>N(4)-H(4a)···O(4) intra^a</i>	-	-	-	2.028	-
<i>N(4)-H(4a)···O(2) intra^a</i>	-	-	-	-	2.082
<i>Rh(1)···Rh(2) intra^a</i>	4.010	4.074	4.105	4.092	-

*The crystal cell contains two molecules (*Mol1* and *Mol2*).

Table 12. Selected angles (deg) for **6d₁**, **6d₂** and **6e**.

<i>Atoms</i>	<i>6d₁</i>		<i>6d₂</i>	<i>6e</i>
	<i>Mol1</i>	<i>Mol2</i>		
<i>Rh(1)-I(2)-Rh(2)</i>	90.53(2)-	92.12(2)	90.90(2)	93.18(1)
<i>Rh(1)-I(3)-Rh(2)</i>	90.53(2)-	92.12(2)	93.28(2)	91.94(1)
<i>Rh(1)-C(1)-O(1)</i>	176.7(5)	177.3(5)	176.5(5)	177.6(3)
<i>Rh(1)-C(9)-O(2)</i>	108.3(4)	119.1(4)	119.6(5)	118.1(2)
<i>Rh(1)-C(9)-C(10)</i>	112.9(4)	117.4(3)	118.2(4)	117.0(2)
<i>Rh(2)-C(11)-O(3)</i>	176.7(5)	177.3(5)	177.1(5)	177.2(3)
<i>Rh(2)-C(12)-O(4)</i>	108.3(4)	119.1(4)	118.2(4)	117.4(3)
<i>Rh(2)-C(12)-C(13)</i>	112.9(4)	117.4(3)	118.4(4)	117.1(2)
<i>C(1)-Rh(1)-I(2)</i>	87.21(16)	88.58(15)	86.52(18)	89.62(10)
<i>C(9)-Rh(1)-I(2)</i>	90.13(11)	90.59(12)	90.20(16)	90.21(9)
<i>N(1)-Rh(1)-I(2)</i>	91.76(10)	90.43(9)	93.93(12)	91.20(7)
<i>I(1)-Rh(1)-I(2)</i>	175.99(2)	177.40(2)	173.36(2)	176.42(1)
<i>C(1)-Rh(1)-I(3)</i>	83.93(16)	86.09(14)	88.95(18)	85.48(10)
<i>C(9)-Rh(1)-I(3)</i>	175.06(11)	178.06(12)	177.15(16)	176.13(9)
<i>N(1)-Rh(1)-I(3)</i>	90.85(9)	88.39(9)	86.39(12)	89.56(7)
<i>I(1)-Rh(1)-I(3)</i>	90.58(2)	90.60(2)	92.11(2)	95.24(1)
<i>I(2)-Rh(1)-I(3)</i>	89.47(2)	87.82(2)	88.55(2)	86.76(1)
<i>C(1)-Rh(1)-C(9)</i>	91.1(2)	92.78(19)	93.5(2)	92.11(13)
<i>C(1)-Rh(1)-N(1)</i>	174.69(19)	174.42(17)	175.3(2)	174.91(12)
<i>C(9)-Rh(1)-N(1)</i>	94.08(15)	92.73(16)	91.1(2)	92.91(11)
<i>C(1)-Rh(1)-I(1)</i>	88.81(16)	89.26(15)	86.89(18)	87.58(10)
<i>C(9)-Rh(1)-I(1)</i>	89.48(11)	90.96(12)	89.43(16)	87.66(9)
<i>N(1)-Rh(1)-I(1)</i>	92.25(10)	91.58(9)	92.71(12)	91.78(7)
<i>C(11)-Rh(2)-C(12)</i>	91.1(2)	92.78(19)	93.1(2)	92.33(13)
<i>C(11)-Rh(2)-N(3)</i>	174.69(19)	174.42(17)	173.9(2)	173.29(12)
<i>C(12)-Rh(2)-N(3)</i>	94.08(15)	92.73(16)	92.8(2)	93.72(11)
<i>C(11)-Rh(2)-I(4)</i>	88.81(16)	89.26(15)	88.11(18)	88.02(10)
<i>C(12)-Rh(2)-I(4)</i>	89.48(11)	90.96(12)	89.43(16)	91.31(8)
<i>N(3)-Rh(2)-I(4)</i>	92.25(10)	91.58(9)	90.61(13)	88.92(7)
<i>C(11)-Rh(2)-I(3)</i>	87.21(16)	88.58(15)	89.08(18)	89.61(10)
<i>C(12)-Rh(2)-I(3)</i>	90.13(11)	90.59(12)	91.01(16)	88.15(8)
<i>N(3)-Rh(2)-I(3)</i>	91.76(10)	90.43(9)	92.16(13)	93.50(7)
<i>I(4)-Rh(2)-I(3)</i>	175.99(2)	177.40(2)	177.18(2)	177.54(1)
<i>C(11)-Rh(2)-I(2)</i>	83.93(16)	86.09(14)	86.83(17)	84.49(10)
<i>C(12)-Rh(2)-I(2)</i>	175.06(11)	178.06(12)	177.34(16)	174.62(8)
<i>N(3)-Rh(2)-I(2)</i>	90.85(9)	88.39(9)	87.30(12)	89.70(7)
<i>I(4)-Rh(2)-I(2)</i>	90.58(2)	90.60(2)	93.23(2)	92.91(1)
<i>I(2)-Rh(2)-I(3)</i>	89.47(2)	87.815(16)	86.34(2)	87.50(1)
<i>N(2)-H(2a)···O(2) intra</i>	-	-	-	127.9
<i>N(4)-H(4a)···O(4) intra</i>	-	-	-	136.1

Table 13. Selected angles (deg) for **8e**.

<i>Atoms</i>	<i>8e</i>
<i>Rh(1)-C(1)-O(1)</i>	175.6(3)
<i>Rh(1)-C(9)-O(2)</i>	120.0(3)
<i>Rh(1)-C(9)-C(10)</i>	119.8(3)
<i>C(1)-Rh(1)-C(9)</i>	92.16(15)
<i>C(1)-Rh(1)-N(3)</i>	174.59(13)
<i>C(9)-Rh(1)-N(3)</i>	93.06(13)
<i>C(1)-Rh(1)-N(1)</i>	88.61(13)
<i>C(9)-Rh(1)-N(1)</i>	179.23(13)
<i>N(3)-Rh(1)-N(1)</i>	86.17(11)
<i>C(1)-Rh(1)-I(2)</i>	87.42(11)
<i>C(9)-Rh(1)-I(2)</i>	87.73(10)
<i>N(3)-Rh(1)-I(2)</i>	91.35(8)
<i>N(1)-Rh(1)-I(2)</i>	92.22(7)
<i>C(1)-Rh(1)-I(1)</i>	90.22(11)
<i>C(9)-Rh(1)-I(1)</i>	87.88(10)
<i>N(3)-Rh(1)-I(1)</i>	91.41(8)
<i>N(1)-Rh(1)-I(1)</i>	92.20(7)
<i>I(2)-Rh(1)-I(1)</i>	174.93(2)
<i>N(2)-H(2a)···O(2) inter</i>	143.3
<i>N(4)-H(4a)···O(2) intra</i>	128.1

II-5- IR-monitored kinetic study for **4a,c-h** towards **CH₃I**

In order to investigate the influence of electronic and steric effects of the N-containing ligands on the CH₃I oxidative addition, IR-monitored kinetic studies were performed in neat CH₃I, [4/CH₃I] = 17 mmol.L⁻¹. An example of stacking FT-IR spectra registered overtime (every one minute) in the 2200-1600 cm⁻¹ region for **4a** is displayed in Figure 39. It describes the decay of the initial characteristic bands for **4a** at 2074.0 and 2000.9 cm⁻¹ followed by the appearance of the ν_{CO} bands at 2063.3 and ν_{COMe} at 1716.4 cm⁻¹ for **6a**.

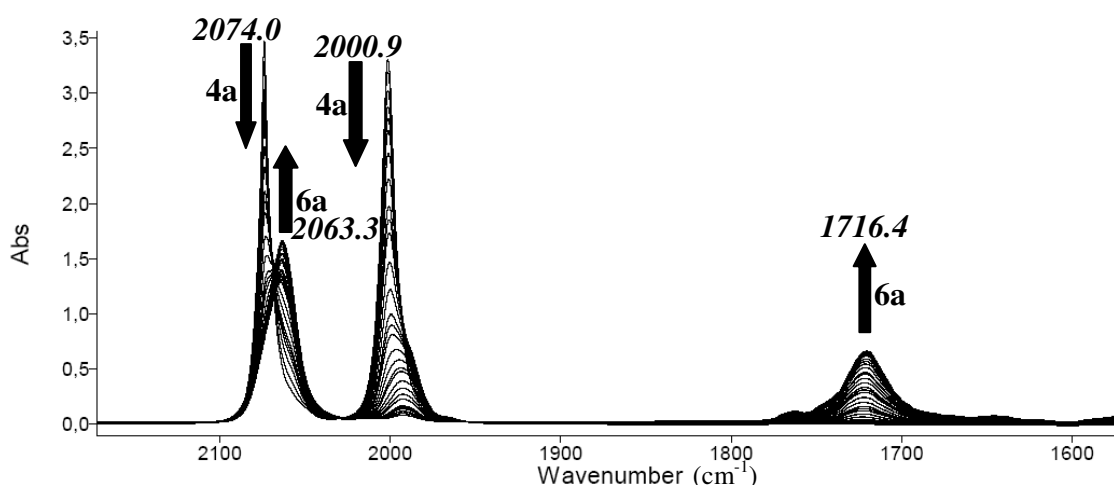
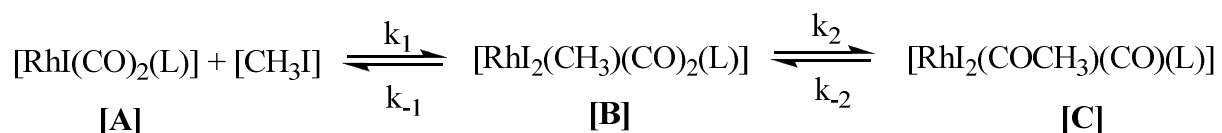


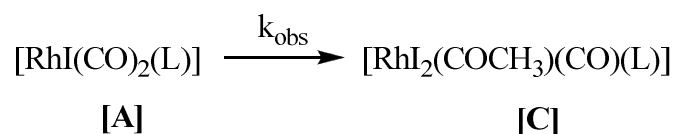
Figure 39. Series of FT-IR spectra for the reaction of **4a** (17 mmol.L⁻¹) with neat CH₃I at 298 K affording **6a**.

In all cases, the intermediate methyl-Rh(III) [RhI₂(CH₃)(CO)₂(L)] species (**L** = **a,c-h**) was not detected under our reaction conditions. The pseudo-order rate constants were found from the plot of Ln(A_t) versus time for which A_t is the anti-symmetric ν_{CO} absorbance of **4** at the time t and which is not affected by the ν_{CO} band of **6a**. To determine activation parameters, variable temperature kinetics were measured which generated reproducible linear Arrhenius plots. The following section briefly describes the determination of the activation parameters^{26,27} (ΔH[‡], ΔS[‡], E_a) relative to the IR-monitored kinetic study (see S.I Chapter II for more details):



Neat methyl iodide was used as a solvent, so that [CH₃I] >> [A], thus the system becomes:

It is noteworthy that species B was not observed by IR spectroscopy meaning that: $k_2 \gg k_1$



The reaction is first-order regarding [A] thus the following equation is considered:²⁸

$$[\text{A}] = [\text{A}]_0 e^{-k_{\text{obs}}t}$$

$$\text{Ln}([\text{A}]) = -k_{\text{obs}} t + \text{Ln}([\text{A}]_0)$$

For the overall oxidative addition reaction, all activation parameters (ΔH^\ddagger , ΔS^\ddagger , E_a) were determined based on the following Arrhenius equation:

$$E_a = -RT \ln(k/A)$$

$$\ln(k) = \ln(A) - \frac{E_a}{RT}$$

The following part describes the activation parameter determination for **4a** as an illustrative example (Parameters, Eyring and Arrhenius plots are depicted in Table 14, Figures 40 and 41, respectively):

Table 14. Different kinetic parameters for the CH_3I oxidative addition reaction of **4a**.

$T(^{\circ}\text{C})$	$T(\text{K})$	$1/T$	K	$\text{Ln}(k)$
15.4	288.4	0.00346741	0.00031436116300	-8.064968032
20	293	0.00341297	0.00044441733300	-7.718746498
25.2	298.2	0.003353454	0.0007605516590	-7.181466521
30	303	0.00330033	0.0009541425670	-6.954697456
$\text{Ln}(k/T)$	k/T	$(h/k_B) \cdot (k/T)$	$\text{Ln}[(h/k_B) \cdot (k/T)]$	$R \cdot (\text{Ln}[(h/k_B) \cdot (k/T)])$
-13.72931643780380	0.00000109001790222	$5.231261 \cdot 10^{-17}$	-37,4892942	-311,7036869
-13.39891910682620	0.00000151678270648	$7.279409 \cdot 10^{-17}$	-37,15889687	-308,9566076
-12.87923092322340	0.00000255047504695	$1.224035 \cdot 10^{-16}$	-36,63920869	-304,6356747
-12.66843026189080	0.00000314898536964	$1.511274 \cdot 10^{-16}$	-36,42840802	-302,8829785

h : Planck constant $6.62606957(29) \times 10^{-34} \text{ J}\cdot\text{s}^{-1}$; Boltzmann constant k_B : $1.3806488(13) \times 10^{-23} \text{ J}\cdot\text{K}^{-1}$; R : gas constant $8.314472 \text{ J}\cdot\text{mol}^{-1}\cdot\text{K}^{-1}$.

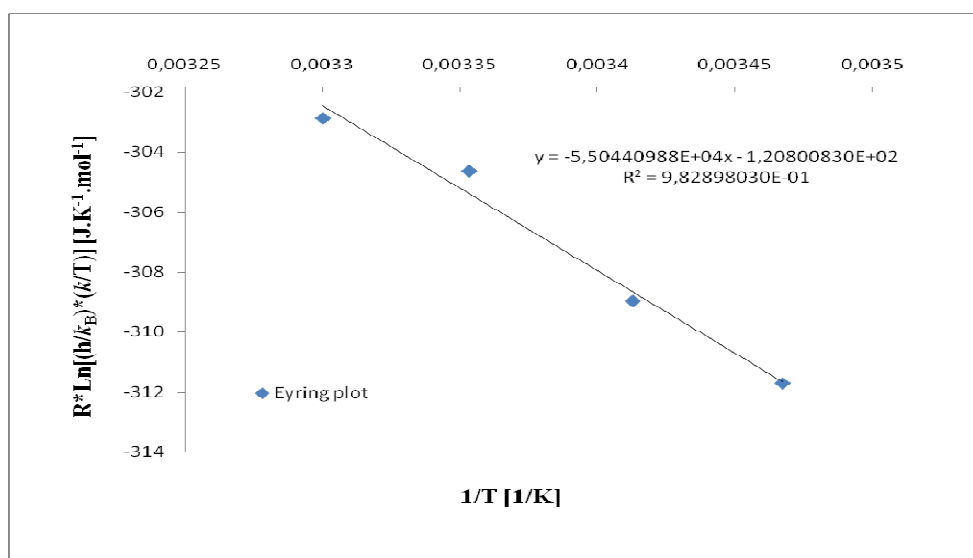


Figure 40. Eyring plot for **4a**: ΔH^\ddagger and ΔS^\ddagger determination.

$$\Delta H^\ddagger = 55044.0988 \text{ J.mol}^{-1} = 55.0440988 \text{ KJ.mol}^{-1}$$

$$\Delta S^\ddagger = -120.800830 \text{ J.K}^{-1}.\text{mol}^{-1}$$

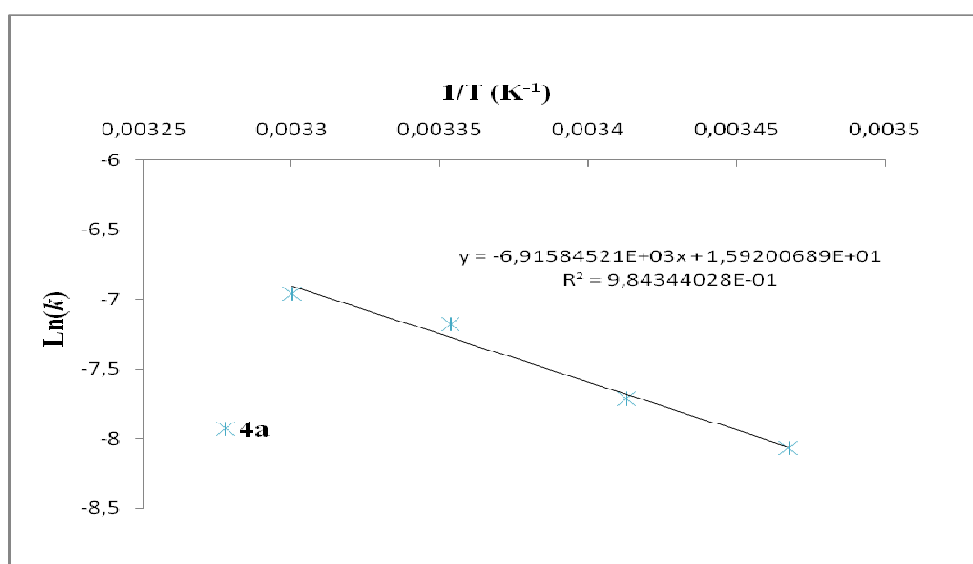


Figure 41. Arrhenius plot for **4a**: E_a determination.

$$E_a = 57498.33707594 \text{ J.mol}^{-1} = 57.49833707594 \text{ KJ.mol}^{-1}$$

Carbonyl infrared data in neat CH₃I, rate constants at 298 K ($k_{298\text{K}}$) and activation parameter values (E_a , ΔH^\ddagger , ΔS^\ddagger) for overall CH₃I oxidative addition reactions on **4a,c-h** are reported in Table 15. In addition, Figure 42 illustrates the different E_a values represented by the slopes of the different plots for **4a,c-h**. The very large negative values for the activation entropies ΔS^\ddagger are consistent with the associative S_N2 type mechanism commonly described for a nucleophilic [Rh(CO)₂I(L)] attack on the CH₃I carbon atom.^{29, 30}

Table 15. Reaction rate constants $k_{298\text{K}}$ and activation parameters for the overall CH₃I oxidative addition reaction of **4a,c-h** to **6a,c-h** (Figure 42).

<i>Entry</i>	<i>IR ν_{CO} (cm^{-1})</i>	<i>$\nu_{\text{av}}(\text{CO})$ (cm^{-1})</i>	<i>$k_{298\text{K}}$ (s^{-1}) $\times 10^5$</i>	<i>E_a (KJ.mol^{-1})</i>	<i>ΔH^\ddagger (KJ.mol^{-1})</i>	<i>ΔS^\ddagger ($\text{J.K}^{-1}.\text{mol}^{-1}$)</i>
4a	2074.0; 2000.9	2037.5	76.05 ± 1.5	57.5 ± 1.2	55.0 ± 1.1	-121 ± 2.4
4c	2073.3; 2002.8	2038.1	3.13 ± 0.06	81.3 ± 0.8	78.8 ± 0.8	-66 ± 1.3
4d	2072.4; 2002.0	2037.2	5.46 ± 0.1	65.3 ± 2.0	62.9 ± 1.3	-116 ± 2.3
4e	2078.0; 2010.3	2044.2	0.44 ± 0.009	70.6 ± 1.4	68.1 ± 1.4	-119 ± 2.4
4f	2077.6; 2009.2	2043.4	0.40 ± 0.008	89.6 ± 0.9	87.0 ± 0.9	-56 ± 1.1
4g	2075.6; 2007.1	2041.4	0.90 ± 0.02			
4h	2075.9; 2006.1	2041.0	0.49 ± 0.005			

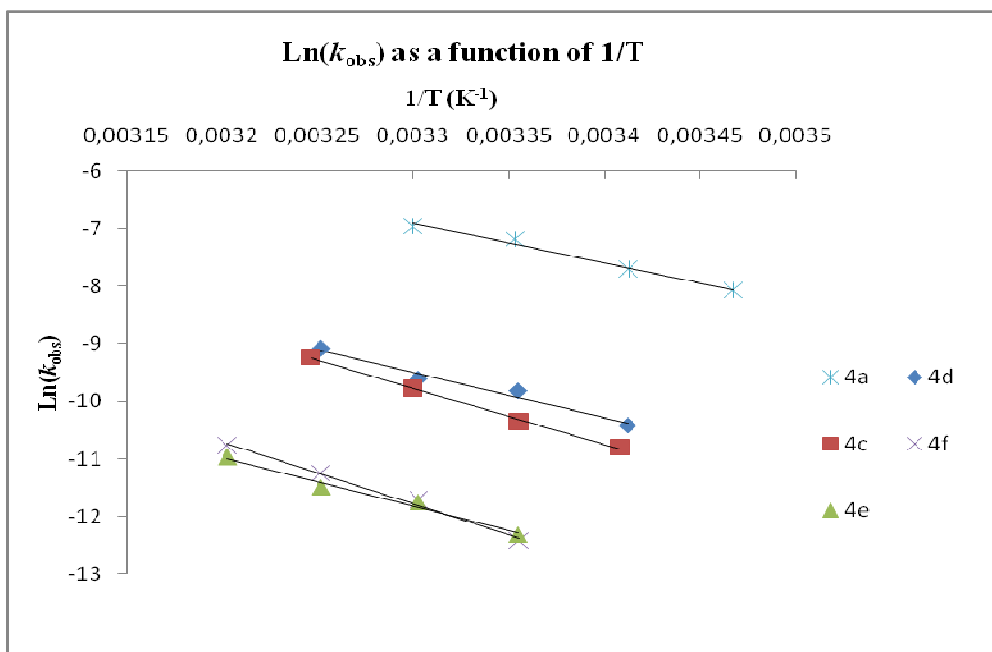


Figure 42. Kinetic data summary: E_a determination for **4a,c-f**.

The rate constant at 298 K for the CH_3I oxidative addition to **4a** ($76.1 \times 10^{-5} \text{ s}^{-1}$) is ca. 14 times larger than that to **4d** ($5.46 \times 10^{-5} \text{ s}^{-1}$), which is consistent with the lower activation energy E_a required (57.5 vs. 65.3 KJ.mol^{-1}). Thus, despite the very close TEP values of ligands **a** and **d** resulting in very close electronic density on the Rh(I) center, **4a** is more nucleophilic towards CH_3I than **4d**. However, complex **4d** is slightly more reactive than **4c** ($3.13 \times 10^{-5} \text{ s}^{-1}$), which is in good agreement with the lower TEP value of methylimidazole **d** compared to its derivative imidazole **c**. Similarly, the higher nucleophilicity towards CH_3I of **4g** and **4h** in comparison with that of **4e,f** follows similar order established by the TEP values which suggests the electronic influence as the main reaction driving force. This trend has been illustrated by plotting $k_{298\text{K}}$ as a function of the TEP values (Figure 43).

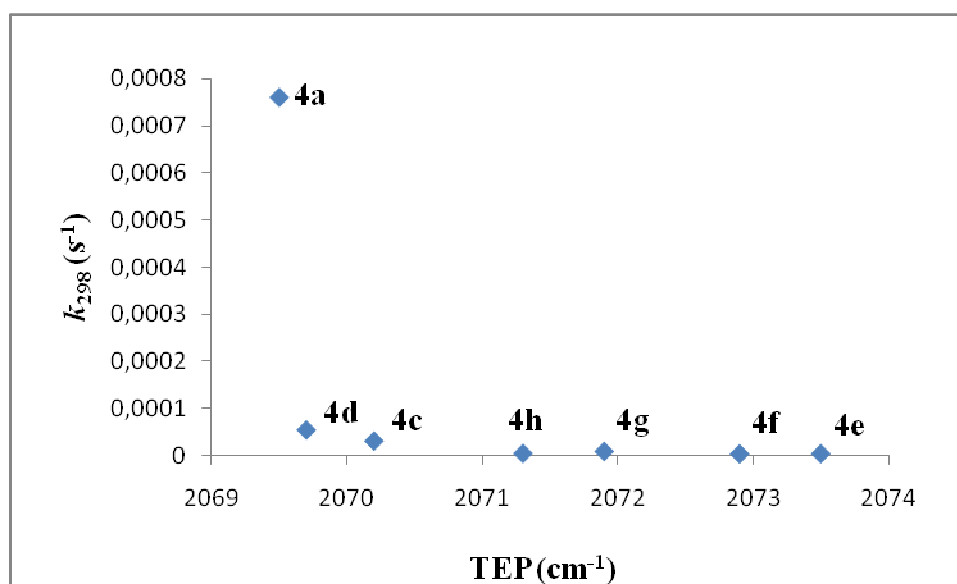


Figure 43. $k_{298\text{K}}$ (s⁻¹) as a function of TEP (cm⁻¹) plot for **4a,c-h**.

Surprisingly, the higher TEP values of **4e** compared to **4f** ($\Delta_{\text{TEP}} = 0.6 \text{ cm}^{-1}$) give significantly lower corresponding E_a values (70.6 KJ.mol⁻¹ vs. 89.6 KJ.mol⁻¹) whereas in the case of **4c,d** ($\Delta_{\text{TEP}} = 0.5 \text{ cm}^{-1}$) higher corresponding E_a values for **4c** (81.3 KJ.mol⁻¹ vs. 65.3 KJ.mol⁻¹) are obtained as expected. Assuming that the Arrhenius law is applicable over a large range of temperature, the weaker E_a value for **4e** (70.6 KJ.mol⁻¹) regardless to **4f** (89.6 KJ.mol⁻¹) reflects that at higher temperature the difference of k values becomes more pronounced. This observation can be explained by the steric effect exerted by the pyrazole ligands in the coordination sphere of the rhodium centers. CH₃I oxidative addition to a square planar complex is commonly accepted to proceed in two elemental steps: (i) nucleophilic attack by the rhodium center at the carbon atom to produce a cationic Rh-CH₃ intermediate and (ii) coordination of I⁻ to the five-coordinated cationic species to saturate the coordination sphere. On the other hand, as described above from X-ray structural analysis, 1-methylpyrazole ligand **f** adopts a conformation with its plane inclined significantly from the Rh coordination plane (torsion angle of ca. 77°) when compared to pyrazole **e** (with corresponding torsion angles of 7.7°). In **4f**, the N-methyl substituent of **f** is thus placed on one side of the metal coordination plane. During the oxidative addition, the CH₃I molecule

would preferentially approach the opposite less-hindered side. The S_N2 step takes place to generate an initial cationic intermediate $[\text{RhI}(\text{Me})(\text{CO})_2(\mathbf{f})]^+$ in which the vacant axial *trans* coordination site is sterically congested by the axial N-methyl group, which therefore presumably inhibits the next I approach to the Rh center in order to complete the oxidative addition. We predicted that this explanation would be even more verified in the case of **4h** (bulkier ligand and **h**-plane/Rh-plane angle of 83°). Indeed, the choice of the sterically hindered ligand **h** was made as we thought that with this type of ligand the rate of reactivity towards CH_3I would be further decreased or even completely inhibited despite its TEP value. It turns out that reactivity occurs and **4h** is not the slowest complex ($k_{298\text{K}} = 0.49 \times 10^{-5}$ vs. $0.40 \times 10^{-5} \text{ s}^{-1}$ for **4f**) although the result remains consistently in the range of the other pyrazole type ligands. Once again there is a balance between the steric and the electronic contribution, which is not negligible (TEP = 2071.3 vs. 2072.9 cm^{-1} for **4f**) despite the very bulky ligand.

Unlike the observation or isolation of methyl-Rh(III) intermediate species starting from $[\text{RhI}_2(\text{CO})_2]^-$ or $[\text{RhI}(\text{CO})(\text{P-L})]$,^{31,32} we did not detect any corresponding neutral $[\text{RhI}_2(\text{Me})(\text{CO})_2(\mathbf{L})]$ from **4** even in neat CH_3I . This can be possibly explained first by the lower electron density on the rhodium center brought by amine type ligands **L**, which results in the labilization of both $[\text{Rh}]-\text{Me}$ and $[\text{Rh}]-\text{CO}$ bonds and consequently favors the CO migratory insertion. Secondly, the steric hindrance of N-heterocycles can also positively impact on this step. The similar implication of steric effects on both oxidative addition and insertion reactions have been previously observed by Haynes et al. for Rh(I) N-heterocyclic carbene and α -diimine complexes.^{33,34}

In fact, the Rh(I) square planar complex **4a** bearing the aliphatic diethylamine, which does not possess any particular steric hindrance operates twice as fast as the well known

rhodium anionic $[C][RhI_2(CO)_2]$ ($C = \text{cation}$) species. The k_{298K} values are of 46.9 ($C^+ = \text{NBu}_4^+$) and $40 \times 10^{-5} \text{ s}^{-1}$ ($C^+ = \text{PPN}^+$) as measured by Maitlis³² and our group, respectively (see Chapter III section IV-3-2).

However, the imidazole and more especially the pyrazole ligands exert a steric constraint since the ligand rings tend to adopt a perpendicular geometry to the Rh square plane. This effect is enhanced by the presence of a methyl or *tert*-butyl group in close vicinity to the Rh center, as it is the case for **4f** and **4h**, respectively.

II-6 Specific reactivity obtained with 1,4-di-*tert*-butyl-pyrazole ligand **h**

II-6-1 Unexpected $C(\text{sp}^3)\text{-H}$ bond activation starting from **4h**

The selective and general transformation of unreactive C-H bonds to other functional groups is of great worldwide interest and importance.^{35,36} Agostic complexes are widely invoked as intermediates in the activation of C-H bonds in organometallic chemistry^{37,38} and have considerable precedent in the stabilization of coordinatively unsaturated metal centers. In the following section is described in more detail the behavior of complex **4h** in solution and in the solid state as an interesting $C(\text{sp}^3)\text{-H}$ agostic interaction (2.455 Å) forming an sp^3 cyclometalated ring has been evidenced (Figure 44).

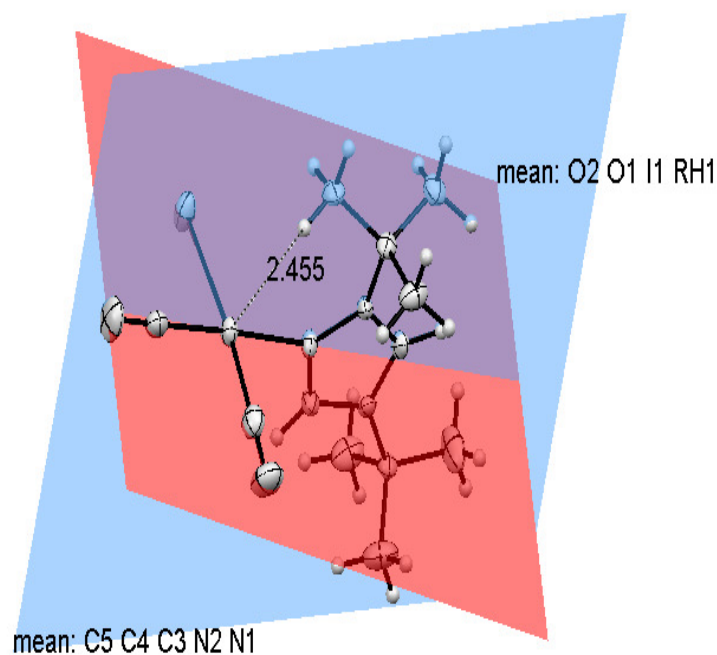


Figure 44. ORTEP view of **4h** putting in evidence the agostic interaction (2.455 Å).

Figure 45 displays the FT-IR spectra in the carbonyl region for **4h** in dichloromethane (ν_{CO} stretching frequencies: 2096.2(w), 2079.6(s), 2027.1(m) and 2010.5(s) cm^{-1}) and acetonitrile (2088.5(s), 2024.2(s) cm^{-1}). The agostic interaction induces the classical square planar geometry to be distorted in CH_2Cl_2 showing two weaker CO stretching bands at 2096.2 and 2027.1 cm^{-1} whereas in the more polar solvent CH_3CN , two neat bands are present consistent with the strict C_{2v} square planar configuration. This indicates that the polar solvent prevents the proton from the methyl group of the *tert*-butyl moiety substituted to the nitrogen of the pyrazole ring in ligand **h** to come in close proximity to the metal center.

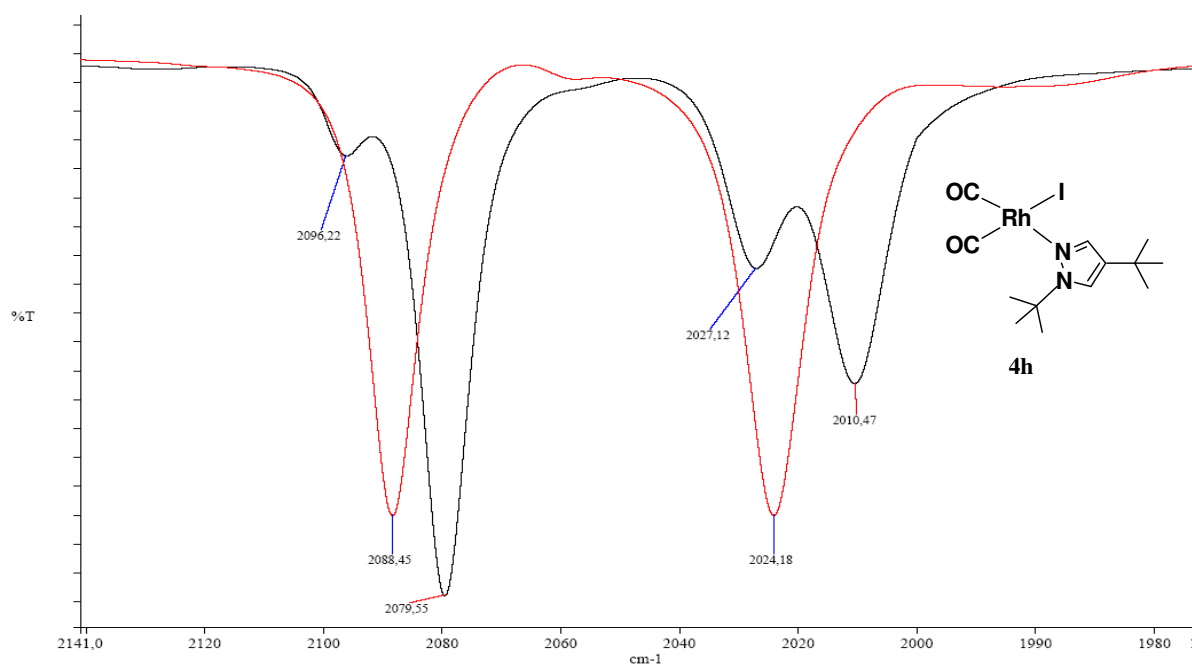


Figure 45. FT-IR $\nu(\text{CO})$ stretching frequencies for **4h** in CH_2Cl_2 (black) and CH_3CN (red).

Attempts to detect the agostic interaction throughout ^1H NMR at RT in CD_2Cl_2 revealed to be difficult although a large broad signal of low intensity (relative integral 9) attracted our attention. This signal resonated at δ 1.79 ppm and was assigned to the ^tBu group carried by the N(2) atom. **4h** exhibits a dynamic ligand exchange behavior which is detected by the $^{13}\text{C}\{^1\text{H}\}$ NMR in the carbonyl region as described earlier. This fluxional process cannot explain the broadness of the ^tBu ^1H NMR signal unless the hydrogens are in close proximity to the Rh center and therefore magnetically affected. A ^1H VT-NMR study was undertaken to check if this agostic interaction could be frozen out sufficiently for separate resonances to be observed for any of the hydrogens of the ^tBu . Even at 193 K in CD_2Cl_2 , only one sharp peak was observed for the ^tBu group, indicating a rapid exchange of the agostic interaction across all nine protons³⁹ (Figure 46).

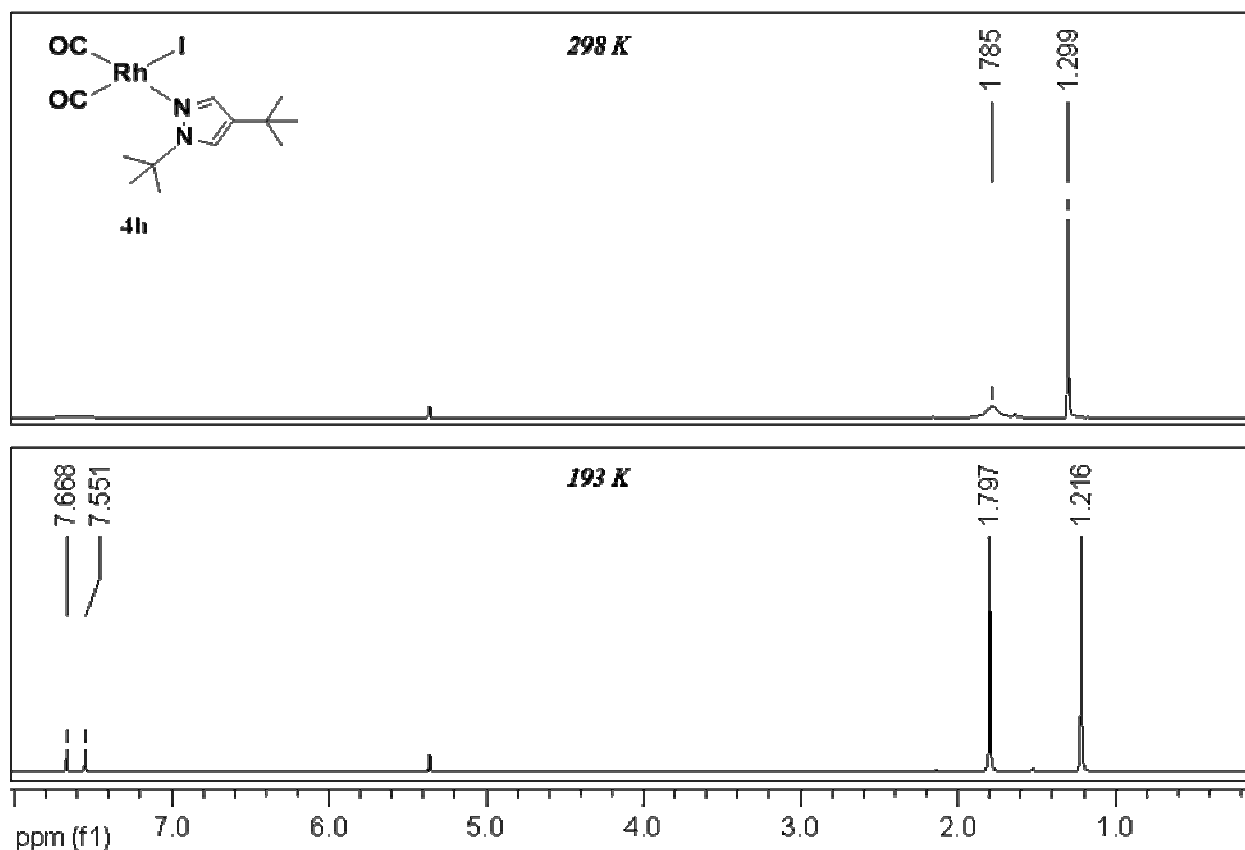


Figure 46. Stacked ^1H NMR spectra of **4h** at 298 and 193 K in CD_2Cl_2 .

It is noteworthy to point out that rare are the examples of this type of agostic interaction with late transition metals, especially with a dicarbonyl-Rh(I) framework where two strongly electron withdrawing CO ligands would be expected to disfavor or at least weaken the agostic interaction. Moreover, it is largely recognized that a preference exists for the activation of sp^2 over sp^3 C-H bonds.⁴⁰ It is in this context that is reported the unusual corresponding $\text{C}(\text{sp}^3)\text{-H}$ bond activated cyclometalated dimeric complex $[\text{RhI}(\mu\text{-I})(\text{CO})(\kappa^2\text{-N,C-h}\cap\text{CH}_2)]_2$ **9h** which has been determined by X-ray diffraction (Figure 47). Indeed, **9h** crystals were obtained together with **4h** crystals when attempts to crystallize **4h** were made. The two compounds were easily identified and separated as **4h** gave bright yellow crystals (Rh(I)) and **9h** red ones (Rh(III)). This indicates that the C-H activation mechanism self-operated at RT or even cooler temperature (crystals were grown at 255 K under shelter of

light) and therefore the mechanism yet remains unclear at this stage (see Scheme 4). ATR-IR spectrum (Figure 48) from the crystals of **9h** clearly shows one strong ν_{CO} band at 2061.8 cm^{-1} for the terminal CO ligands consistent with a *trans* configuration as confirmed by the X-ray structure.

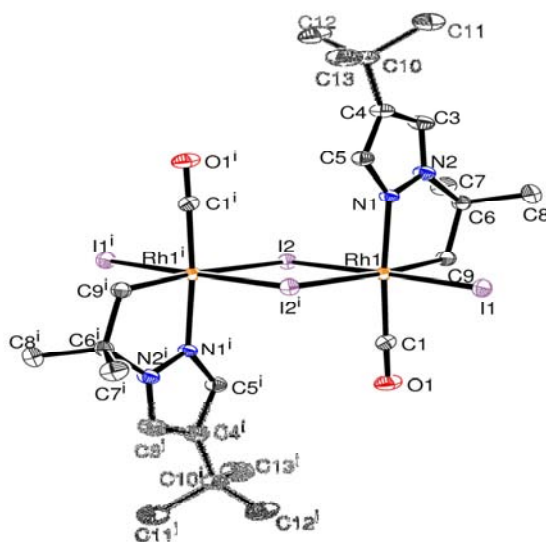


Figure 47. Single-crystal X-ray ORTEP view of **9h**. Thermal ellipsoids are shown at the 30% probability level. Selected bond lengths (Å) and angles (deg): Rh(1)-I(1) 2.6457(2), Rh(1)-I(2) 2.6683(2), Rh(1)-I(2)ⁱ 2.8148(2), Rh(1)-C(1) 1.860(2), Rh(1)-N(1) 2.0455(16), Rh(1)-C(9) 2.074(2), C(1)-O(1) 1.129(3), N(1)-N(2) 1.346(2), N(2)-C(6) 1.479(3), C(6)-C(9) 1.546(3), Rh \cdots Rh 3.969, I(1)-Rh(1)-I(2) 177.383(7), I(1)-Rh(1)-I(2)ⁱ 90.183(8), I(1)-Rh(1)-C(9) 92.30(7), I(1)-Rh(1)-N(1) 91.21(5), I(1)-Rh(1)-C(1) 88.89(7), I(2)-Rh(1)-C(9) 90.27(7), I(2)-Rh(1)-C(1) 90.59(7), I(2)-Rh(1)-N(1) 89.62(5), I(2)-Rh(1)-I(2)ⁱ 87.280(7), I(2)ⁱ-Rh(1)-C(1) 92.92(7), I(2)ⁱ-Rh(1)-C(9) 175.13(6), I(2)ⁱ-Rh(1)-N(1) 94.05(5), C(1)-Rh(1)-C(9) 91.31(9), C(1)-Rh(1)-N(1) 173.03(8), N(1)-Rh(1)-C(9) 81.72(7), Rh(1)-C(1)-O(1) 178.4(2), Rh(1)-N(1)-N(2) 115.28(12), Rh(1)-N(1)-C(5) 137.86(14), Rh(1)-C(9)-C(6) 112.70(14), Rh(1)-I(2)-Rh(1)ⁱ 92.721(8).

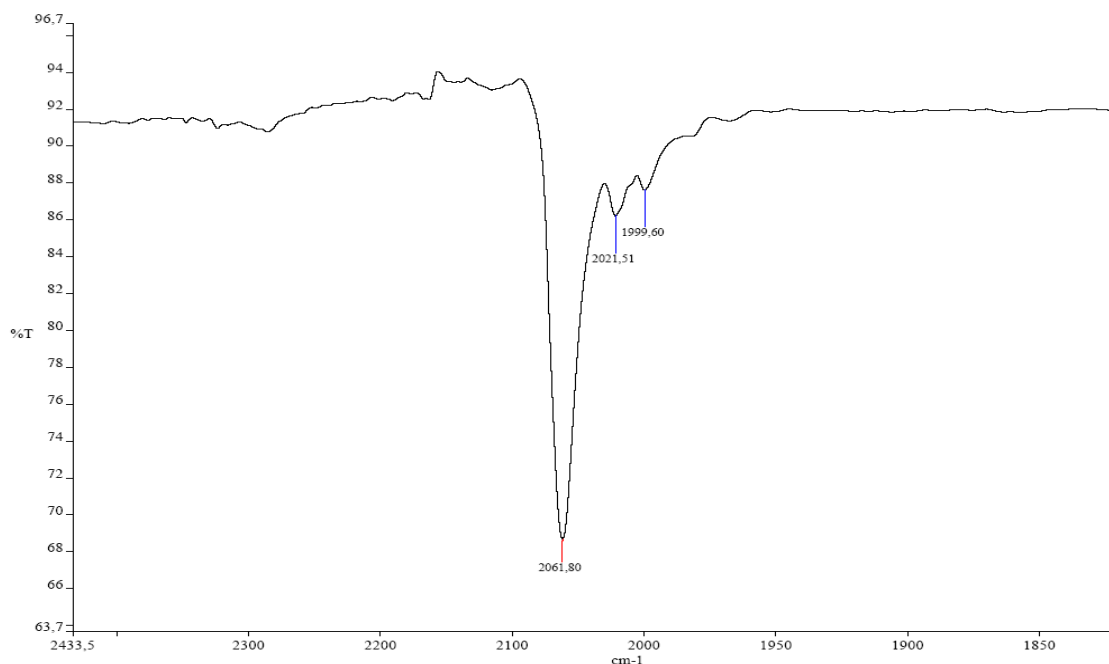
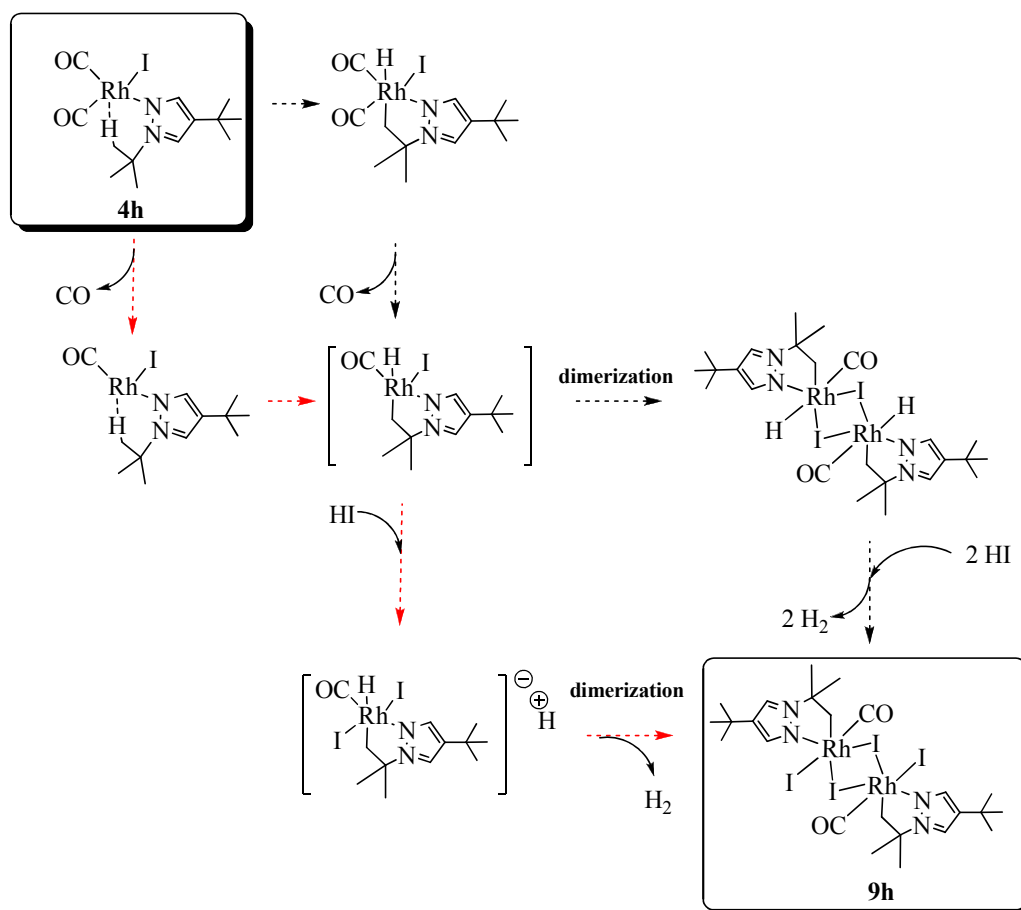


Figure 48. ATR-IR spectrum of **9h** at 298 K.

It is noteworthy that no CO migratory insertion occurs to afford the corresponding acyl complex. Attempts to reproduce the formation of **9h** and thus fully characterize the complex in solution have not yet been undertaken; the few characterizations were performed from the little amount of crystals obtained and therefore ^1H and $^{13}\text{C}\{^1\text{H}\}$ NMR was difficult (little amount of product and paraffin contamination due to the X-ray manipulation). Despite the poor quality ^1H NMR spectrum, **9h** was identified and all of the protons were slightly shifted to higher field in comparison with protons of **4h**. The CH_2 coupled to Rh were identified (δ_{A} 1.00, $^2J_{\text{Rh-H}} = 1.8$ Hz; δ_{B} 0.97, $^2J_{\text{Rh-H}} = 2.10$; $^2J_{\text{H-H}} = 6.8$ Hz) and the data agrees reasonably well with literature data.⁴¹



Scheme 4. Proposed mechanism for the formation of **9h**.

Different mechanism pathways to give **9h** starting from **4h** can be envisaged yet in all cases there has to be an unexplained source of iodide present in the medium. Traces of HI presumably come from another molecule of **4h** or a side-product especially as **9h** was produced with a 50% yield. The proposed mechanism depicted in scheme 4 most likely to occur is pointed out with red arrows. After the loss of a CO ligand, **4h** undergoes C-H activation to stabilize the complex and give a Rh-hydride intermediate which reacts with HI to eliminate hydrogen and after dimerization afford **9h**.

Although we focused more on **4h**, it is important to mention that the same chemistry applies to the chloro analogue **3h**, for which an agostic interaction yet weaker is also suspected (2.518 Å according to the X-ray structure). The same ^1H NMR observations were

made for the nine hydrogens of the ^tBu group carried by the N(2) atom (large and broad peak at 298 K and sharp and intense at 193 K) and the FT-IR spectrum also shows ν_{CO} side contributions indicating the distortion of the strict C_{2v} square planar configuration. These weaker bands are however much less pronounced than for **4h**, which confirms the X-ray analysis that a weaker agostic interaction takes place. Moreover, when **3h** was crystallized (yellow crystals) a minority of red crystals were present but unfortunately not suitable for diffraction, strongly suggesting the formation of the **9h** chloro analogue.

II-7 Conclusion

In summary, a series of mononuclear square planar rhodium(I) chloro and iodo dicarbonyl neutral complexes bearing diethylamine, imidazole and pyrazole derivatives have been synthesized. The iodo-Rh(I) N-heterocyclic complexes show a fluxional behavior as demonstrated by VT-NMR studies. In the solid state various intra and intermolecular $\text{H}\cdots\text{I}$, $\text{H}\cdots\text{O}$ interactions have been observed. The CH_3I oxidative addition has been performed on the iodo complexes **4** to form the corresponding dimeric acetyl-Rh(III) complexes **6**, among which two isomers were structurally determined for the first time. The iodo-bridged **6d,e** were further split by addition of either CO or **e** affording the corresponding monomeric Rh(III) **7d** and **8e** complexes, as confirmed by their X ray crystal structures. The different reactivity of **4** for the CH_3I oxidative addition is mainly attributed to the steric effect induced by the N-ligands rather than to the electronic effect. This study shows that a relative good donor ligand with moderate steric hindrance, such as NHEt_2 , can promote the limiting oxidative addition step and thus improve the catalytic process. To further understand the mechanism taking place in the alkyl halide addition followed by CO *cis*-migration involved in the square planar complex **4a**, investigations with NDEt_2 and CD_3I will be made. In this way, kinetic isotope

effects (KIEs) may help to give answers together with DFT calculations on how the mechanism operates.^{29a}

Furthermore, the design of a sterically hindered ligand **h** containing ^tBu groups substituted in the 1 and 3-positions on the pyrazole ring revealed an interesting agostic interaction when coordinated to the {RhX(CO)₂} (X = Cl, I) moiety (**3,4h**). **4h** nicely put in evidence a Csp³-H activation chemistry affording a dimeric cyclometalated complex **9h**. This result was unexpected and drives towards a different chemistry than the standard methyl iodide oxidative addition of methanol carbonylation nevertheless it remains highly interesting and needs to be further developed for a better understanding.

References

-
- (1) Haynes, A.; Mann, B. E.; Morris, G. E.; Maitlis, P. M. *J. Am. Chem. Soc.* **1993**, *115*, 4093.
- (2) For pKa values see: Catalan, J.; Elguero, J. *J. Chem. Soc. Perkin Trans.* **1983**, 1869.
- (3) Cotton, F. A. *Chemical Applications of Group Theory*, John Wiley & Sons: New York, **1990**.
- (4) Tolman, C. A. *Chem. Rev.* **1977**, *77*, 313.
- (5) Chianese, A. R.; Li, X.; Janzen, M. C.; Faller, J. W.; Crabtree, R. H. *Organometallics* **2003**, *22*, 1663.
- (6) (a) Kelly, R. A.; Clavier, H.; Giudice, S.; Scott, N. M.; Stevens, E. D.; Bordner, J.; Samardjiev, I.; Hoff, C. D.; Cavallo, Li.; Nolan, S. P. *Organometallics* **2008**, *27*, 202. (b) Diebolt, O.; Fortman, G. C.; Clavier, H.; Slawin, A. M. Z.; Escudero-Adan, E. C.; Benet-Buchholz, J.; Nolan, S. P. *Organometallics* **2011**, *30*, 1668.
- (7) Bonati, F.; Oro, L. A.; Pinillos, M. T.; Tejel, C.; Apreada, M. C.; Foces-Foces, C.; Cano, F. *H. J. Organomet. Chem.* **1989**, *369*, 253.
- (8) Decker, M. J.; Fjeldsted, D. O. K.; Stobart, S. R.; Zaworotko, M. J. *Chem. Commun.* **1983**, *24*, 1525.
- (9) Jang, K.; Jung, I. G.; Nam, H. J.; Jung, D. Y.; Son, S. U. *J. Am. Chem. Soc.* **2009**, *131*, 12046.
- (10) (a) Petrucci, M. G. L.; Lebuis, A. M.; Kakkar, A. K. *Organometallics* **1998**, *17*, 4966. (b) Garralda, M. A.; Hernandez, R.; Pinilla, E.; Torres, M. R. *J. Organomet. Chem.* **1999**, *586*, 150.
- (11) Jeffrey, G. A.; Saenger, W. *Hydrogen Bonding in Biological Structures*; Springer: Berlin, **1991**.

(12) (a) Borkett, N. F.; Bruce, M. I. *J. Organomet. Chem.* **1974**, *65*, C51. (b) Bushnell, G. W.; Dixon, K. R.; Eadie, D. T.; Stobart, S. R. *Inorg. Chem.* **1981**, *20*, 1545. (c) Atwood, J. L.; Dixon, K. R.; Eadie, D. T.; Stobart, S. R.; Zaworotko, M. J. *Inorg. Chem.* **1983**, *22*, 774. (d) Heaton, B. T.; Jacob, C.; Sampanthar, J. T. *J. Chem. Soc. Dalton Trans.* **1998**, 1403. (e) Brück, A.; Ruhland, K. *Organometallics* **2009**, *28*, 6383. (f) Litchman, W. M. *J. Am. Chem. Soc.* **1979**, *101*, 545.

(13) Gusev, D.G. *Organometallics* **2009**, *28*, 763.

(14) Epstein, R. A.; Geoffroy, G. L.; Keeney, M. E.; Mason, W. R. *Inorg. Chem.* **1979**, *18*, 478.

(15) Vallarino, L. M.; Sheargold, S. W. *Inorg. Chim. Acta* **1979**, *36*, 243.

(16) Zobi, F. *Inorg. Chem.* **2010**, *49*, 10370.

(17) (a) Conifer, C. M.; Taylor, R. A.; Law, D. J.; Sunley, G. J.; White, A. J. P.; Britovsek, G. J. P. *J. Chem. Soc. Dalton Trans.* **2011**, *40*, 1031. (b) Conifer, C. M.; Law, D. J.; Sunley, G. J.; Haynes, A.; Wells, J. R.; White, A. J. P.; Britovsek, G. J. P. *Eur. J. Inorg. Chem.* **2011**, 3511.

(18) (a) Mann, K. R.; Gordon II, J. G.; Gray, H. B. *J. Am. Chem. Soc.* **1975**, *97*, 3553. (b) Mann, K. R.; Lewis, N. S.; Williams, R. M.; Gray, H. B.; Gordon II, J. G. *Inorg. Chem.* **1978**, *17*, 828. (c) Bera, J. K.; Dunbar, K. R. *Angew. Chem. Int. Ed.* **2002**, *41*, 4453.

(19) Garcia-Seijo, M. I.; Habtemariam, A.; Fernandez-Anca, D.; Parsons, S.; Garcia-Fernandez, M. E. *Z. Anorg. Allg. Chem.* **2002**, *628*, 1075.

(20) (a) Fabrello, A.; Dinoi, C.; Perrin, L.; Kalck, P.; Maron, L.; Urrutigoity, M.; Dechy-Cabaret, O. *Magn. Reson. Chem.* **2010**, *48*, 448. (b) Nguyen, D. H.; Lauréano, H.; Jugé, S.; Kalck, P.; Daran, J. C.; Coppel, Y.; Urrutigoity, M.; Gouygou, M. *Organometallics* **2009**, *28*, 6288.

-
- (21) Friebolin, H. *Basic one- and two- dimensional NMR spectroscopy* VCH Verlags. Weinheim (Germany) **1991**, 270.
- (22) Haynes, A.; Maitlis, P. M.; Stanbridge, I. A.; Haak, S.; Pearson, J. M.; Adams, H.; Bailey, N. A. *Inorg. Chim. Acta* **2004**, 357, 3027.
- (23) Adams, H.; Bailey, N. A.; Mann, B. E.; Manuel, C. P.; Spencer, C. M.; Kent, A. G. J. *Chem. Soc. Dalton Trans.* **1988**, 489.
- (24) Adamson, G. W.; Daly, J. J.; Forster, D. J. *Organomet. Chem.* **1974**, 71, 17.
- (25) Ion, L.; Nieto, S.; Perez, J.; Riera, L., Riera, V., Diaz, J. Lopez, R.; Anderson, K. M.; Steed, J. W. *Inorg. Chem.* **2011**, 50, 8524.
- (26) Keitz, B. K.; Bouffard, J.; Bertrand, G.; Grubbs, R. H. *J. Am. Chem. Soc.* **2011**, 133, 8498.
- (27) Anderson, D. R.; Hickstein, D. D.; O'Leary, D. J.; Grubbs, R. H. *J. Am. Chem. Soc.* **2006**, 128, 8386.
- (28) Connors, K. A. *Chemical Kinetics (The Study of Reaction Rates in Solution)* VCH Verlags. Weinheim (Germany) **1990**, (chap. 2), 18.
- (29) (a) Griffin, T. R.; Cook, D. B.; Haynes, A.; Pearson, J. M.; Monti, D.; Morris, G. E. *J. Am. Chem. Soc.* **1996**, 118, 3029. (b) Fulford, A.; Hickey C. E.; Maitlis P. M. *J. Organomet. Chem.* **1990**, 398, 311.
- (30) Gonsalvi, L.; Adams, H.; Sunley, G. J.; Ditzel, E.; Haynes, A. *J. Am. Chem. Soc.* **1999**, 121, 11233.
- (31) Some selected examples: (a) Paulik, F. E.; Hershman, A.; Knox, W. R.; Roth, J. F. US4690912 (to Monsanto) **1987**. (b) Brodzki, D.; Leclere, C.; Denise, B.; Pannetier G. *Bull. Soc. Chim. Fr.* **1976**, 61. (c) Rankin, J.; Poole, A. D.; Benyei, A. C.; Cole-Hamilton, D. J. *Chem. Commun.* **1997**, 1835. (d) Rankin, J.; Benyei, A. C.; Poole, A. D.; Cole-Hamilton, D. J. *J. Chem. Soc. Dalton Trans.* **1999**, 3771. (e) Bader, A.; Lindner, E. *Coord. Chem. Rev.* **1991**,

- 108, 27. (f) Dutta, D. K.; Woollins, J. D.; Slawin, A. M. Z.; Konwar, D.; Das, P.; Sharma, M.; Bhattacharyya, P.; Aucott, S. M. *J. Chem. Soc. Dalton Trans.* **2003**, 2674. (g) Wegman, R. W.; Abatjoglou, A.G. US4670570 (to Union Carbide Corporation) **1987**. (h) Wegman, R. W.; Abatjoglou, A. G.; Harrison, A. M. *J. Chem. Soc. Chem. Commun.* **1987**, 1891. (i) Baker, M. J.; Giles, M. F.; Orpen, A. G.; Taylor, M. J.; Watt, R. J. *J. Chem. Soc. Chem. Commun.* **1995**, 197. (j) Baker, M. J.; Dilworth, J. R.; Sunley, J. G.; Wheatley, N. EU0632006 (to BP Chemicals) **1995**. (k) Dilworth, J. R.; Miller, J. R.; Wheatley, N.; Baker, M. J.; Sunley, J. G. *J. Chem. Soc. Chem. Commun.* **1995**, 1579. (l) Conifer, C. M.; Law, D. J.; Sunley, G. J.; White, A. J. P.; Britovsek, G. J. P. *Organometallics* **2011**, *30*, 4060. (m) Gonsalvi, L.; Adams, H.; Sunley, G. J.; Ditzel, E.; Haynes, A. *J. Am. Chem. Soc.* **2002**, *124*, 13597. (n) Thomas, C. M.; Süss-Fink, G. *Coord. Chem. Rev.* **2003**, *243*, 125. (o) Gonsalvi, L.; Adams, H.; Sunley, G. J.; Ditzel, E.; Haynes, A. *J. Am. Chem. Soc.* **1999**, *121*, 11233.
- (32) Haynes, A.; Mann, B. E.; Morris, G. E.; Maitlis, P. M. *J. Am. Chem. Soc.* **1993**, *115*, 4093.
- (33) Martin, H. C.; James, N. H.; Aitken, J.; Gaunt, J. A.; Adams, H.; Haynes, A. *Organometallics* **2003**, *22*, 4451.
- (34) Gonsalvi, L.; Gaunt, J. A.; Adams, H.; Castro, A.; Sunley, G. J., Haynes, A. *Organometallics* **2003**, *22*, 1047.
- (35) Labinger, J. A.; Bercaw, J. E. *Nature* **2002**, *417*, 507.
- (36) Bergman, R. G. *Nature* **2007**, *446*, 391.
- (37) Brookhart, M.; Green, M. L. H.; Parkin, G. *Proc. Nat. Acad. Sci. U.S.A.* **2007**, *104*, 6908.
- (38) Clot, E.; Eisenstein, O. in *Principles and Applications of Density Functional Theory in Inorganic Chemistry II*; Kaltsoyannis, N.; McGrady, J. E.; Eds.; Structure and Bonding; Springer: Berlin, **2004**, *Vol. 113*, pp 1-36.
- (39) Crosby, S. H.; Clarkson, G. J.; Rourke, J. P. *J. Am. Chem. Soc.* **2009**, *131*, 14142.

(40) Goldman, A. S.; Goldberg, K. I. In *Activation and Functionalization of C-H Bonds*; Goldberg, K. I.; Goldman, A. S.; Eds.; ACS Symposium Series 885; American Chemical Society: Washington, DC, **2004**.

(41) Zucca, A.; Stoccoro, S.; Agostina Cinellu, M.; Minghetti, G.; Manassero, M. *J. Chem. Soc. Dalton Trans.* **1999**, 3431.

CHAPTER III

**Reactivity of neutral *cis*-[RhI(CO)₂(L)] and anionic [XNR₃] *cis*-
[RhI₂(CO)₂] (X = H, CH₃) complexes under methanol
carbonylation conditions**

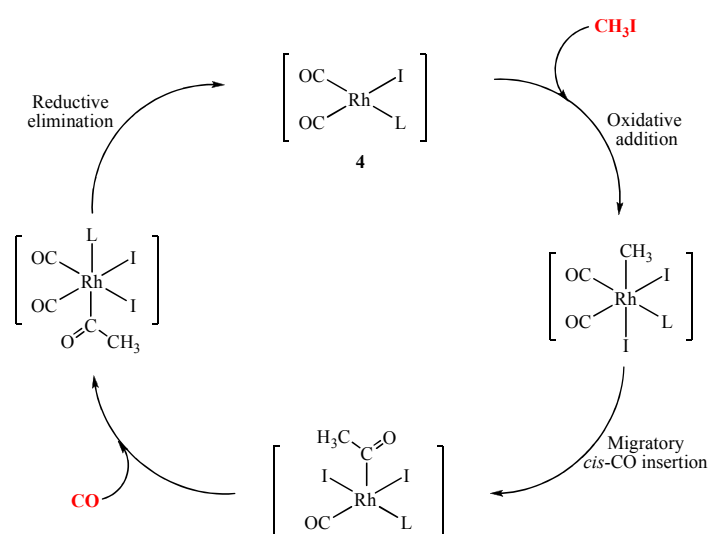
III-1 Introduction

In order to evaluate the catalytic performances (activity/stability) of $[\text{RhI}(\text{CO})_2(\text{L})]$ **4** complexes, selected neutral compounds **4a,d-g** bearing aliphatic diethylamine **a**, methylimidazole **d** or pyrazole **e-g** ligands (already described in chapter II) have been used as catalyst precursors for the carbonylation of methanol under industrial Celanese Acid Optimization (AO) process conditions.^{1,2,3}

The first part of the chapter will focus on batch experiments applied to complexes **4** followed by VT-HP-NMR investigations to understand their behavior on a mechanistic point of view. In a second part, we will present the synthesis and characterization of anionic Rh(I) $[\text{XNR}_3]$ *cis*- $[\text{RhI}_2(\text{CO})_2]$ ($\text{X} = \text{H}, \text{CH}_3$) complexes and study their reactivity towards CH_3I oxidative addition and will investigate the impact that can have the counter-cation on this reaction.

III-2 Catalytic reactivity of neutral complexes $[\text{RhI}(\text{CO})_2(\text{L})]$

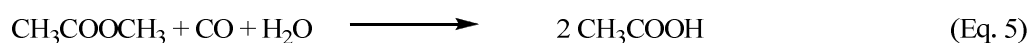
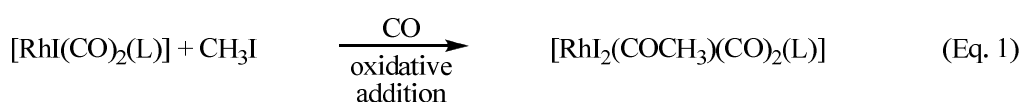
Scheme 1 represents the catalytic cycle involving a neutral catalytic precursor.



Scheme 1. Simplified catalytic cycle involving neutral complexes **4**.

III-3 Batch experiment study

All the catalytic tests have been carried out under the same conditions, close to the industrial AO process. The weight percent (wt %) of Rh catalyst **4**, water, methyl iodide and methyl acetate are 0.1, 5, 10 and 35, respectively. Acetic acid is introduced as the balance. For methyl acetate, a higher concentration is necessary in comparison with that of the industrial plant in order to keep the concentration of methyl iodide constant in the reactor. Indeed, it is considered that for one molecule of methyl iodide consumed during the oxidative addition reaction, one molecule of HI is released by the reaction of acetyl iodide with water, which can further react with one molecule of methyl acetate giving back a molecule of methyl iodide and acetic acid (Scheme 2).



Scheme 2. Consumption and production of the different products during a batch experiment.

Thus, the role of the high concentration of methyl acetate is to mimic the continuous feed of methanol under continuous working conditions. As a consequence, methyl acetate concentration decreases during the batch experiment. As shown in scheme 2, two molecules of acetic acid are produced, one arising from the real carbonylation reaction and the other from the reaction of methyl acetate with HI. Thus, acetic acid concentration increases during the batch experiment. The carbon monoxide pressure is kept constant at 30 bar during the

experiment via an over-pressurized CO reservoir, from which the CO consumption is measured. According to scheme 2, one molecule of CO is consumed whereas two molecules of acetic acid are produced. The carbonylation rate ($\text{mol}_{[\text{reactant}]} \cdot \text{L}^{-1} \cdot \text{h}^{-1}$) can be calculated from the consumption of either methyl acetate, water, carbon monoxide or the half-production of acetic acid (Scheme 2). Here, carbonylation rates were determined from the production of acetic acid. The concentration of all participating organic compounds was determined by GC analysis after 10 minutes of reaction. In all cases, the carbonylation rates measured are $\sim 13 \text{ mol} \cdot \text{L}^{-1} \cdot \text{h}^{-1}$ (Table 1). Thus, all these neutral precursors are less active than the standard AO technology involving $[\text{Li}][\text{RhI}_2(\text{CO})_2]$ precursor ($17.5 \text{ mol} \cdot \text{L}^{-1} \cdot \text{h}^{-1}$). It is worth mentioning that in these batch experiments, run 1 was carried out under slightly different conditions, in which 10 wt % [Li] salt was added to the medium in order to stabilize the $[\text{Li}][\text{RhI}_2(\text{CO})_2]$ catalytic species.

Table 1. Batch experiments for selected N-containing neutral *cis*- $[\text{RhI}(\text{CO})_2(\text{L})]$ **4** species.

<i>Run</i>	<i>Starting complex</i>	<i>Carb. rate (mol.L⁻¹.h⁻¹)</i>	<i>Observation (end of run)</i>	<i>Detected complexes, end of batch (IR analyses)</i>
1	A.O process*	17.5	No Rh(0) precipitation	$[\text{RhI}_4(\text{CO})_2][\text{Li}]$
2	4a (diethylamine)	14.0	Very little Rh(0) precipitation	$[\text{RhI}_4(\text{CO})_2][\mathbf{a}\text{-CH}_3]$
3	4d (1-methyl imidazole)	12.7	Little Rh(0) precipitation	$[\text{RhI}_4(\text{CO})_2][\mathbf{d}\text{-CH}_3]$
4	4e (pyrazole)	12.4	Little Rh(0) precipitation	$[\text{RhI}(\text{CO})_2(\mathbf{e})]$ (minor)/ $[\text{RhI}_4(\text{CO})_2][\mathbf{e}\text{-CH}_3]$ (major)
5	4f (1-methyl pyrazole)	12.6	Little Rh(0) precipitation	$[\text{RhI}(\text{CO})_2(\mathbf{f})]$ (minor)/ $[\text{RhI}_4(\text{CO})_2][\mathbf{f}\text{-CH}_3]$ (major)
6	4g (3,5-dimethyl pyrazole)	14.0	Very little Rh(0) precipitation	$[\text{RhI}(\text{CO})_2(\mathbf{g})]$ (minor)/ $[\text{RhI}_4(\text{CO})_2][\mathbf{g}\text{-CH}_3]$ (major)

Operating conditions: Rh metal: 1000 ppm, [H₂O]: 5 wt %, [AcOMe]: 35 wt %, [CH₃I]: 10 wt % and [AcOH]: balance. Reaction temperature: 190 °C, CO pressure: 30 bar. Batch run 1 was done starting from an in situ pre-formation of $[\text{Li}][\text{RhI}_2(\text{CO})_2]$ with [Li] 10 wt %.*

At the end of each batch experiments, the catalytic solution was evaporated under reduced pressure and the resulting solid products were systematically analyzed by FT-IR (Figure 1) and IC (ionic chromatography) analyses. For all experiments, the anionic Rh(III) complex $[\text{RhI}_4(\text{CO})_2]^-$ was detected as the major compound with a characteristic ν_{CO} stretching band detected at $\sim 2090 \text{ cm}^{-1}$.^{4,5} The corresponding methylated counter-cations $[\mathbf{a,d-g-CH}_3]^+$ were put in evidence by IC, which suggests that quaternization of these N-ligands occurred from methyl iodide under high temperature.

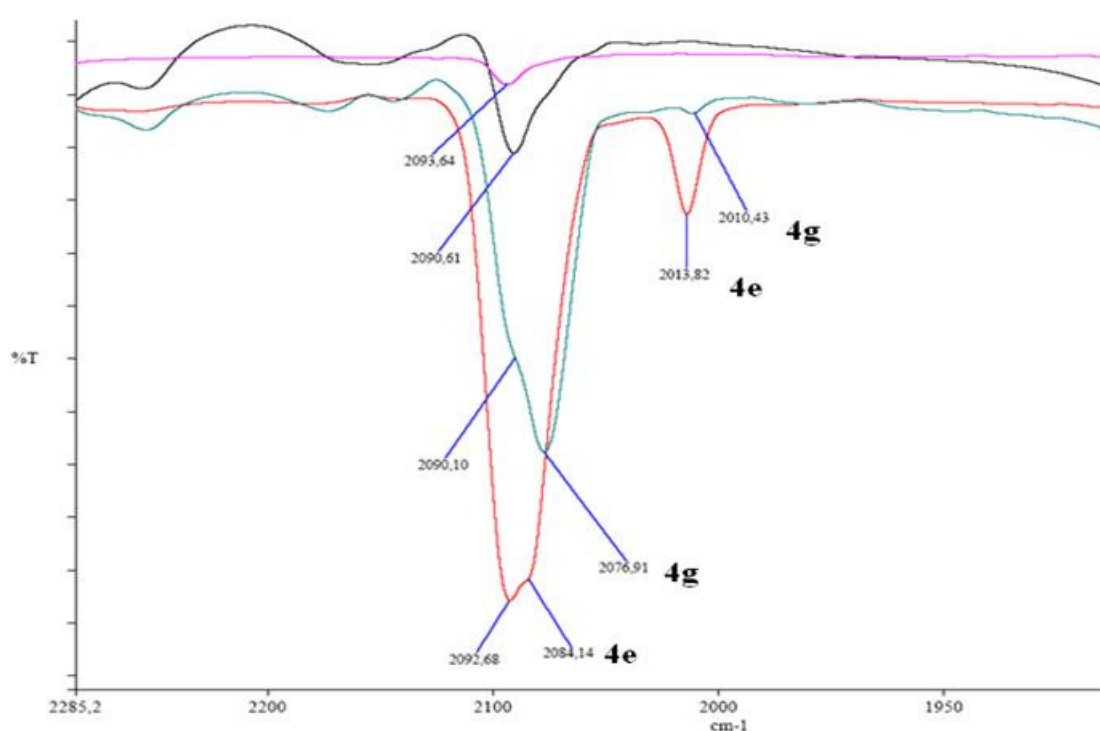
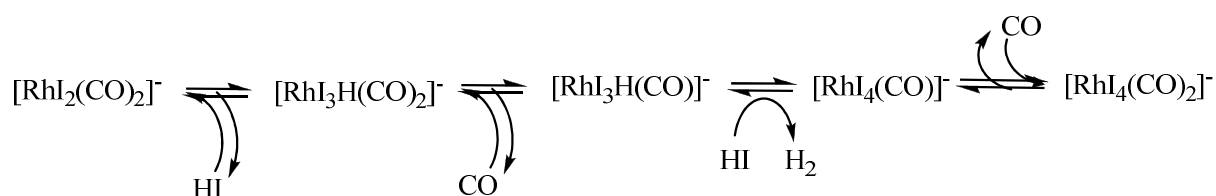


Figure 1. FT-IR spectra of the isolated solids after batch runs 4-6 in the CO region (CH_2Cl_2 , 298 K).

The formation of the stable anionic $[\text{RhI}_4(\text{CO})_2]^-$ species can be explained by two consecutive oxidative addition of HI on $[\text{RhI}_2(\text{CO})_2]^-$ with release of dihydrogen according to scheme 3.⁶ In fact, $[\text{RhI}_4(\text{CO})_2]^-$ is a resting state species (catalyst species that do not participate directly to the main reaction) and is predominantly detected after batch experiments.



Scheme 3. HI oxidative addition, first part of the WGS cycle.¹

It is noteworthy that for batch runs 4-6, small amounts of pyrazole ligated Rh(I) starting material were also detected at the end of the reaction with IR stretching ν_{CO} bands at 2084.1; 2013.8 cm^{-1} and 2076.9; 2010.4 cm^{-1} for **4e** and **4g**, respectively (Figure 1). In contrast, complexes **4a** and **4d** are not detected, which indicates their lower stability with respect to pyrazole type complexes.

Thus, the main results of the batch experiments described above indicate that under the harsh AO process conditions, the N-ligands of the neutral complexes **4** decoordinate, and are quaternized, resulting in the formation of the corresponding methylated ammonium salt. In the case of pyrazole catalysts **4e-g**, the batch experiment results raise the possibility that neutral complexes may be significant intermediates in Rh-catalyzed methanol carbonylation.⁷ This opens the perspective that dimethylpyrazolium iodide (MMPYI) salt was produced during the batch experiment and perhaps dissociated at high temperature to regenerate a neutral complex, in a similar manner to MePyI as previously reported by Zoeller et al.⁸

III-4 Reactivity of **4e** with hydriodic acid HI

To further understand the behavior of complexes **4** under acidic conditions, an additional experiment, which consists in the addition of 2 molar eq. of HI at 298 K on **4e** was carried out. FT-IR analysis in dichloromethane shows the coexistence of complexes **4e** and $[\text{RhI}_2(\text{CO})_2]^-$ with the corresponding protonated pyrazolium counter-cation HHPY (Figure 2). This observation underlines the impact of hydriodic acid and agrees with the previously

observed results at the end of batch reactions for which anionic species with quaternized counter-cations are mainly detected. It has been reported that for $[\text{IrI}_2(\text{CO})_2]^-$, HI kinetically reacts faster in comparison to methyl iodide. However, at high temperature and with high concentration of CH_3I , the oxidative addition of CH_3I is favored.⁹

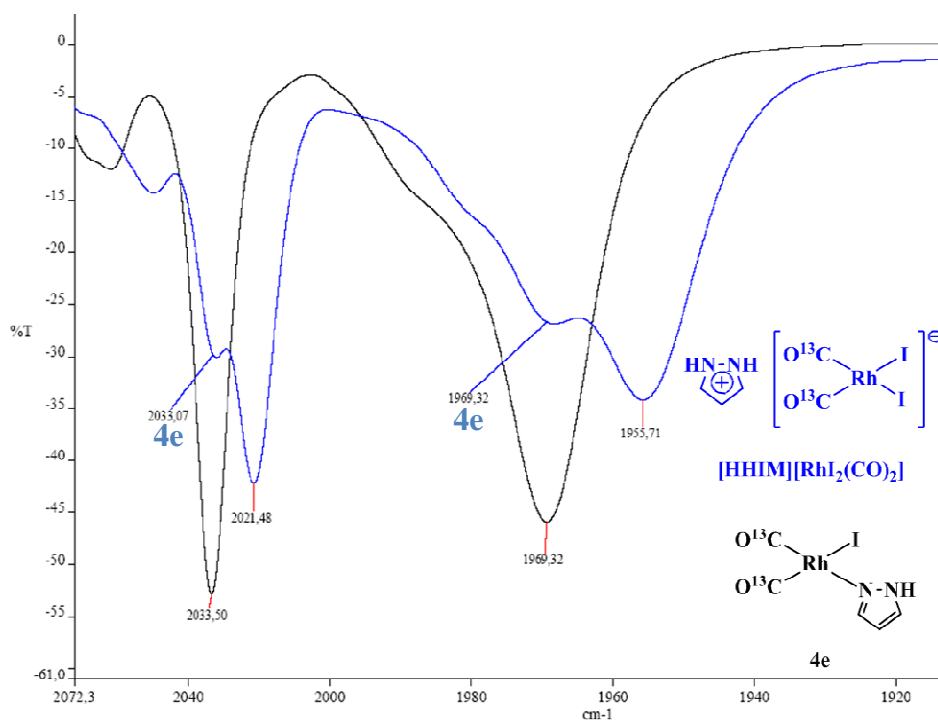


Figure 2. FT-IR spectra of $^{13}\text{CO-4e}$ (black) and $^{13}\text{CO-4e}/^{13}\text{CO-[HHPY][RhI}_2(\text{CO})_2]$ (blue) in CH_2Cl_2 at 298 K.

III-5 HP-VT NMR study

To deeper understand the behavior of complexes **4** under catalysis batch conditions, a set of ^1H , $^{13}\text{C}\{^1\text{H}\}$ HP-VT-NMR experiments were performed in specially designed sapphire NMR tubes, which could resist up to 100 bar of CO pressure and for which NMR characterizations were possible up to 373 K¹⁰ (see experimental chapter V for full details).

This technique is very useful to provide accurate structural information and have insight on mechanistic features under conditions similar to the ones requested in catalysis. Attention was mainly focused on complex $^{13}\text{CO-4d}$ for which a first set of NMR experiments (**Experiment 1**) were undertaken in a stepwise approach in order to investigate in detail on the effect of the following parameters: $[\text{CH}_3\text{I}]$, $T(\text{K})/P_{\text{CO}}(\text{bar})$ and $[\text{H}_2\text{O}]$. A second set of NMR experiments (**Experiment 2**) was then made on $^{13}\text{CO-4d}$ considering the entire catalytic medium in a one pot experiment, an approach closer to the catalytic process working conditions.

III-5-1 **Experiment 1** (see chapter V for full experimental details)

The first NMR experiment consisted in reaction of **4d** (3000 ppm of Rh) with 30 wt % of CH_3I in $\text{AcOH-}d_4$ (2 g total solution loaded in the sapphire tube) at 298 K in the absence of CO pressure.

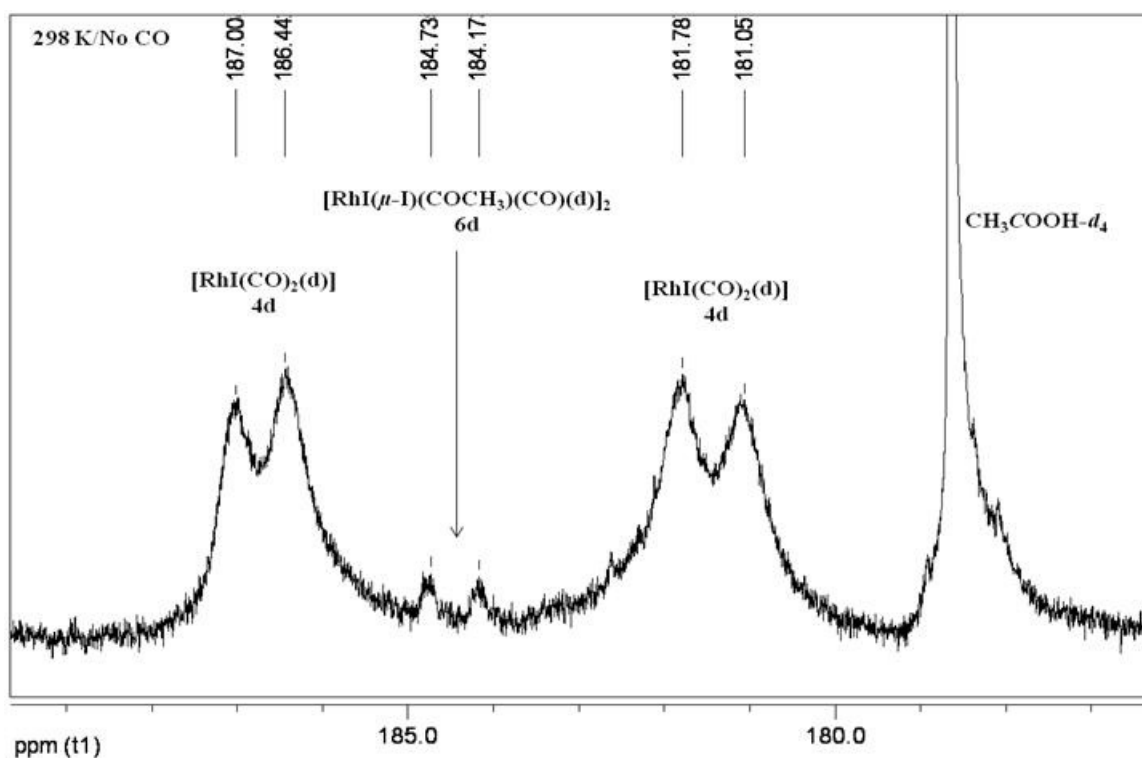
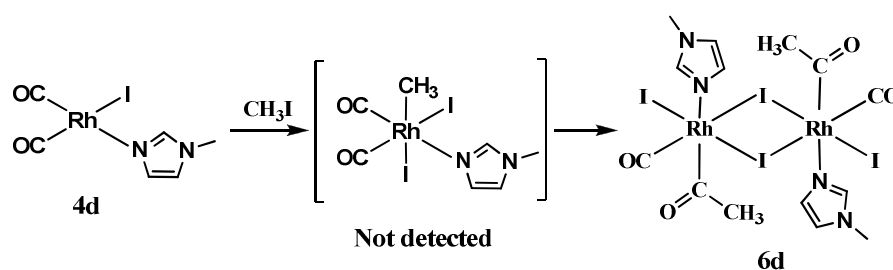


Figure 3. $^{13}\text{C}\{^1\text{H}\}$ NMR spectrum in the CO region at 298 K in the absence of CO.

$^{13}\text{C}\{^1\text{H}\}$ NMR spectrum recorded after 30 minutes of reaction (Figure 3) featured in the carbonyl region two broad doublets (δ 186.7 ppm, $^1J_{(\text{Rh}-\text{CO})}$ of 56.9 Hz; δ 181.4 ppm, $^1J_{(\text{Rh}-\text{CO})}$ of 73.4 Hz) for the starting complex **4d** and one weak broad doublet (δ 184.5 ppm, $^1J_{(\text{Rh}-\text{CO})}$ of 56.5 Hz) tentatively attributed to dimer **6d** resulting from CH_3I oxidative addition followed by CO *cis*-migration as described and characterized earlier in chapter II (Scheme 4). The Rh-methyl intermediate species $[\text{RhI}_2(\text{CH}_3)(\text{CO})_2(\text{d})]$ could not be detected under these conditions.



Scheme 4. CH_3I oxidative addition to **4d** followed by CO *cis*-migration affording **6d**.

$^{13}\text{C}\{^1\text{H}\}$ NMR was not accumulated long enough in order to detect the CO-acetyl signals at lower field. At this stage, the sapphire NMR tube was pressurized with CO (^{13}CO : 3 bar; ^{12}CO : 27 bar ratio), the sample was recorded for 30 minutes and temperature was maintained at 298 K. $^{13}\text{C}\{^1\text{H}\}$ NMR spectrum in the carbonyl region is displayed in Figure 4.

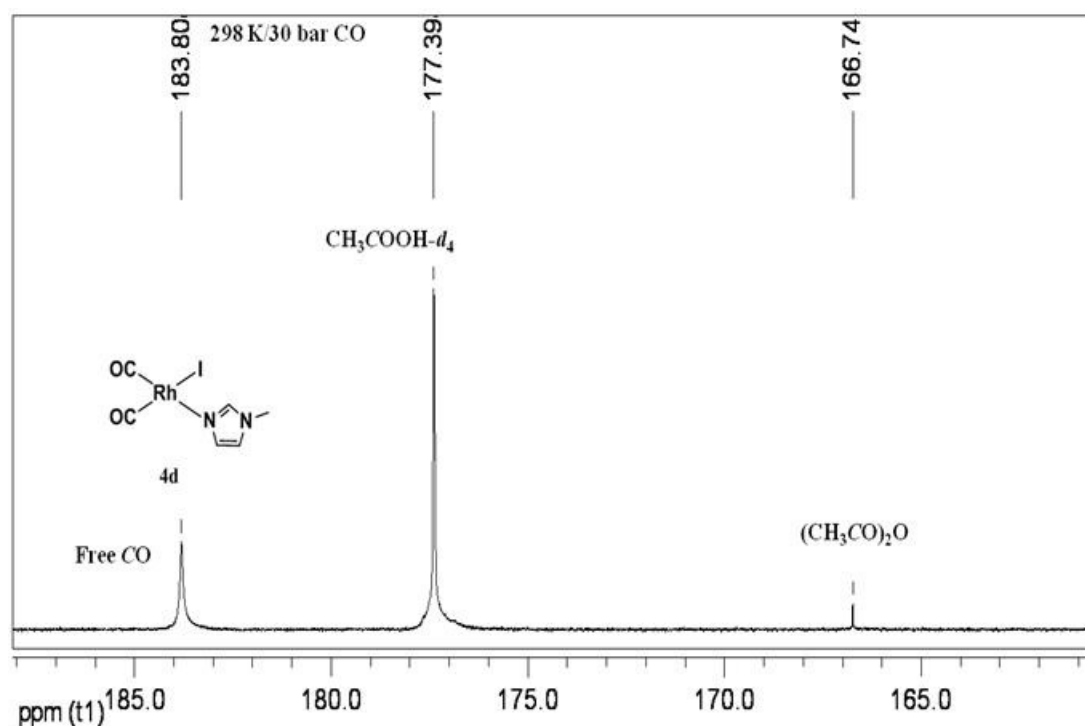
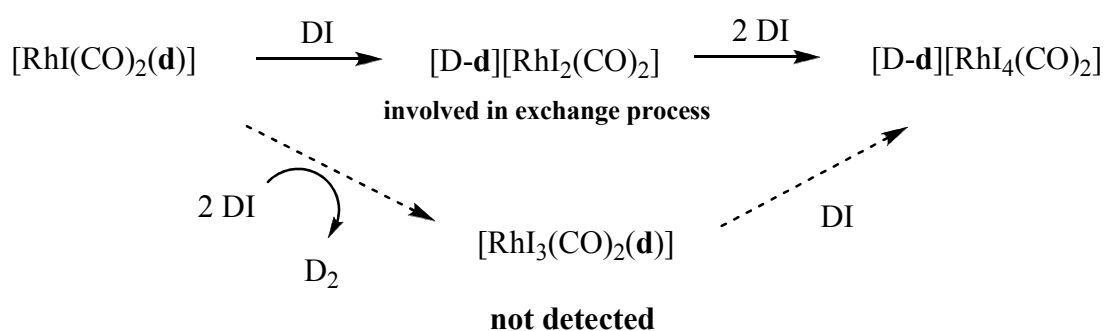


Figure 4. $^{13}\text{C}\{^1\text{H}\}$ NMR spectrum in the CO region at 298 K, ^{13}CO 3 bar + ^{12}CO 27 bar.

As CO (30 bar) is now present in the medium, bridge-splitting of **6d** giving rise to the formation of complex $[\text{RhI}_2(\text{COMe})(\text{CO})_2(\mathbf{d})]$ **7d** is expected. However, this species was not detected, presumably due to the very small amount of **7d**, which is consistent with a slow oxidative addition reaction rate (See chapter II). Moreover, it is strongly suspected that a rapid free CO/coordinated CO exchange for **4d** occurs, which results in one average-time large signal at δ 183.8 ppm.¹¹ This exchange process can also explain why detection of **7d** probably requires more accumulation time due to lower amount of ^{13}CO -**7d** (ratio ^{13}CO -**7d**/ ^{12}CO -**7d** *ca.* 1:9 according to the initial $^{13}\text{CO}/^{12}\text{CO}$ gas fill ratio of 3:27, respectively¹²). Besides, it cannot be ruled out that exchange process (here, in a dissociative manner) between free CO/coordinated CO also takes place for Rh(III) **7d**. It is worth mentioning that throughout ^1H and $^{13}\text{C}\{^1\text{H}\}$ NMR, the signals of coordinated methylimidazole were detected, which indicate that at low temperature the ligand is maintained coordinated. Furthermore, at this stage acetic anhydride was also detected (δ $(\text{CH}_3\text{CO})_2\text{O}$) = 166.7 ppm), which suggests that reductive

elimination took place to afford CH_3COI , which then immediately reacts with $\text{AcOH-}d_4$ releasing DI.¹³ This observation supports further the no detection of **7d**. It is noteworthy to mention that reaction of methyl iodide upon acetic acid also contributes to the formation of DI.

The next step was to study the impact of temperature. The solution was heated to 313 K. CO pressure was maintained under 30 bar with a $^{13}\text{CO}:^{12}\text{CO}:20$ ratio. The $^{13}\text{C}\{^1\text{H}\}$ NMR sample was recorded during 30 minutes (Figure 5). The peak intensity corresponding to acetic anhydride increased. A sharp doublet appeared in the carbonyl region at δ 172.8 ppm ($^1J_{\text{Rh-CO}} = 48.4$ Hz) which has been assigned to the Rh(III) complex $\text{trans-}[\text{RhI}_4(\text{CO})_2]^-$, the formation of which being explained on Scheme 5.



Scheme 5. Formation of Rh(III) complex $\text{trans-}[\text{RhI}_4(\text{CO})_2]^-$.

The proposed pathway leading to $[\text{MDIM}] \text{trans-}[\text{RhI}_4(\text{CO})_2]^-$ depicted above suggests decoordination of ligand **d** followed by its protonation, which results in the production of cation 1-methylimidazolium (MHIM, here **MDIM**). The alternative formation route via an intermediate neutral species $[\text{RhI}_3(\text{CO})_2(\mathbf{d})]$ cannot be excluded even if no spectroscopic evidence supports this proposal. A second sharp carbonyl doublet is also present at δ 177.5 ppm with associated coupling constant of $^1J_{\text{Rh-CO}} = 54.5$ Hz, which commonly are characteristic of a Rh(III) type species. In agreement with the medium composition, we

propose to assign it to complex $[\text{RhI}_3(\text{CO})_2(\text{AcO})]^-$. Despite the acidic medium, it is believed that there are always small amounts of acetate ions present in solution which could further substitute an iodo ligand to generate this species.

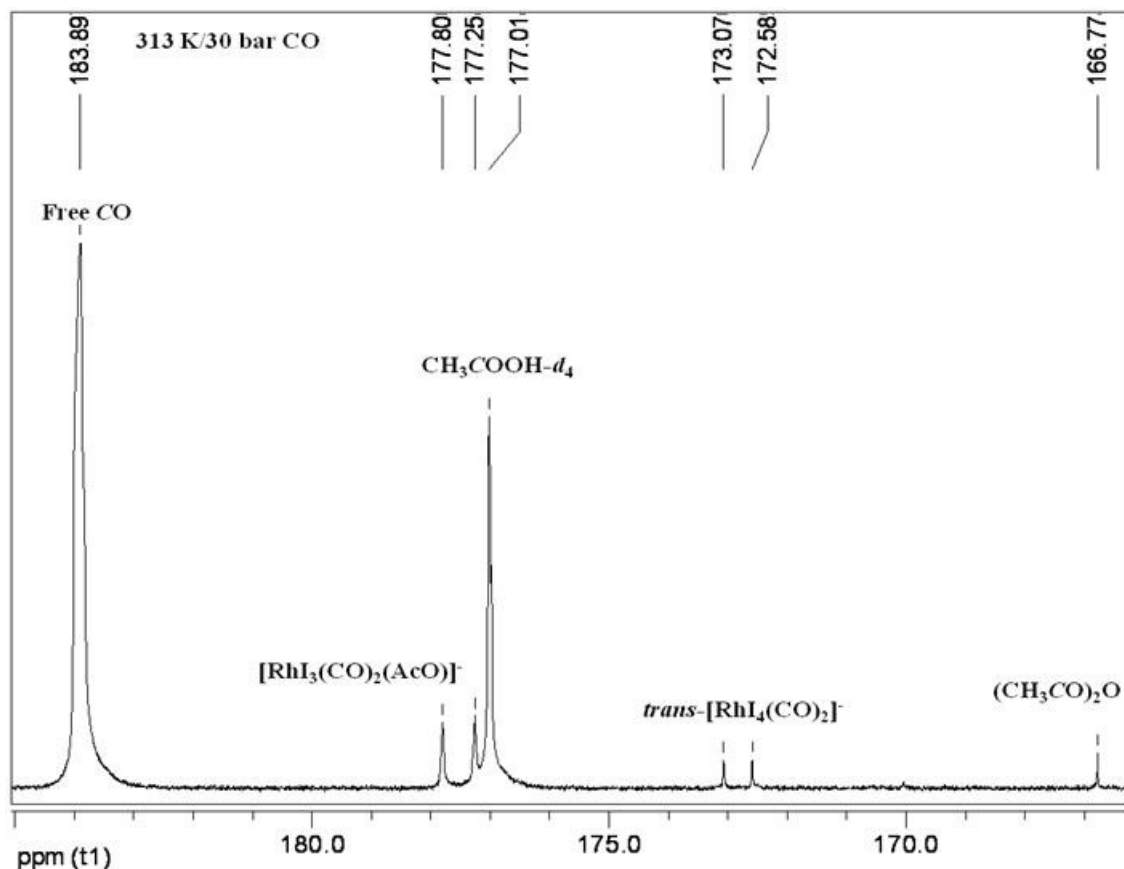


Figure 5. $^{13}\text{C}\{^1\text{H}\}$ NMR spectrum in the CO region at 313 K, ^{13}CO 10 bar + ^{12}CO 20 bar.

The sample was further heated to 333 K and maintained under 30 bar CO pressure. Under these conditions, imidazole ligand in **4d** processed via decoordination/protonation to form the corresponding 1-methylimidazolium rhodium salt. Indeed, the ^1H NMR spectrum, which shows the formation of MDIM⁺ is displayed in Figure 6 and compared to that of the former experiment carried out at 298 K in absence of CO. The $^{13}\text{C}\{^1\text{H}\}$ NMR spectrum in the carbonyl region (Figure 7) shows $[\text{RhI}_3(\text{CO})_2(\text{AcO})]^-$ still present, although the major product is now $[\text{MDIM}][\text{RhI}_4(\text{CO})_2]$ with a new sharp doublet (δ 170.3 ppm, $^1J_{(\text{Rh}-\text{CO})} = 53.4$ Hz) of weaker intensity assigned to the isomer *cis*- $[\text{RhI}_4(\text{CO})_2]^-$.^{5,6c}

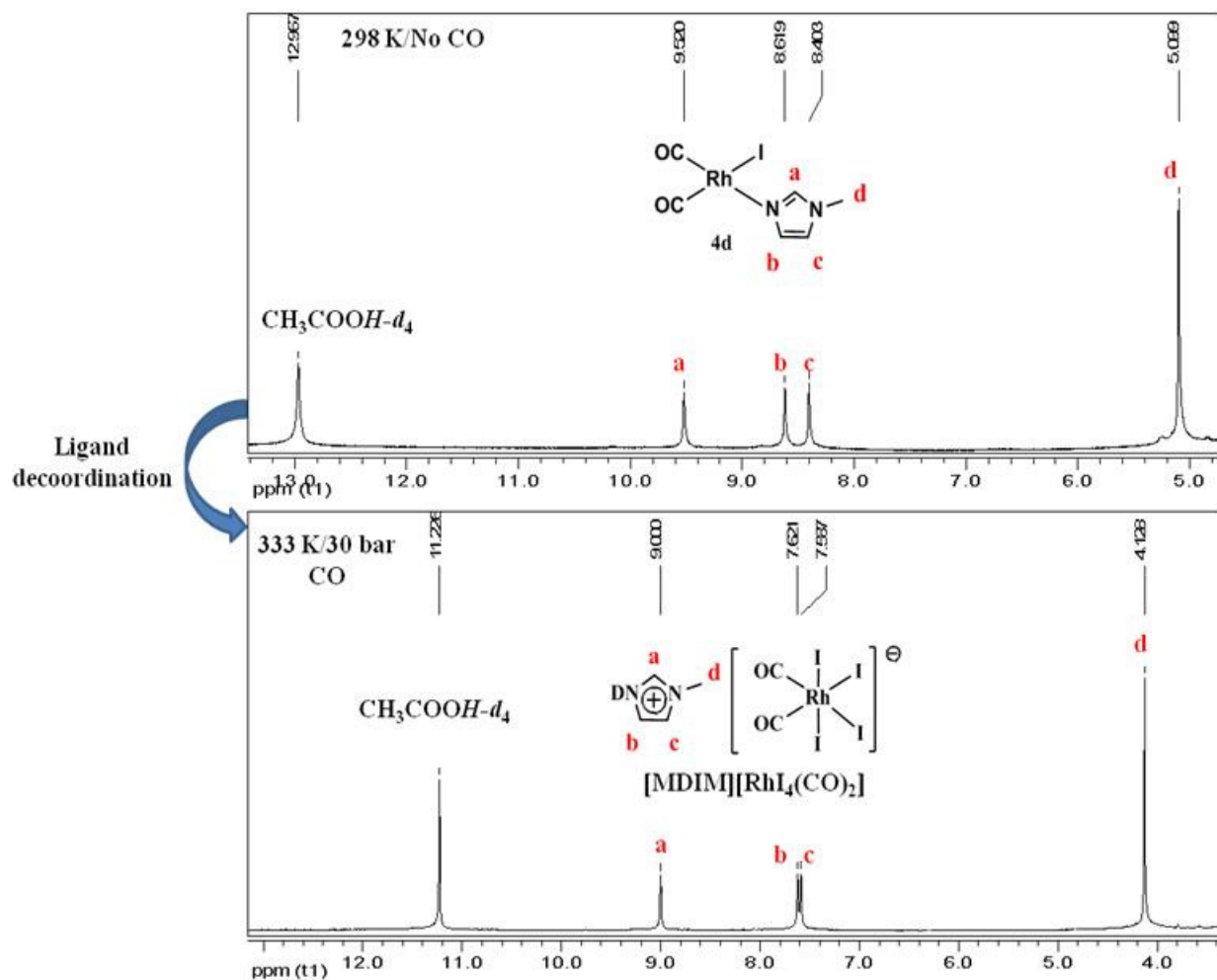


Figure 6. ^1H NMR spectra comparison between sample at 298 K in the absence of CO (**4d**) and sample at 333 K/ ^{13}CO 10 bar + ^{12}CO 20 bar ($[\text{MDIM}][\text{Rh}_4(\text{CO})_2]$).

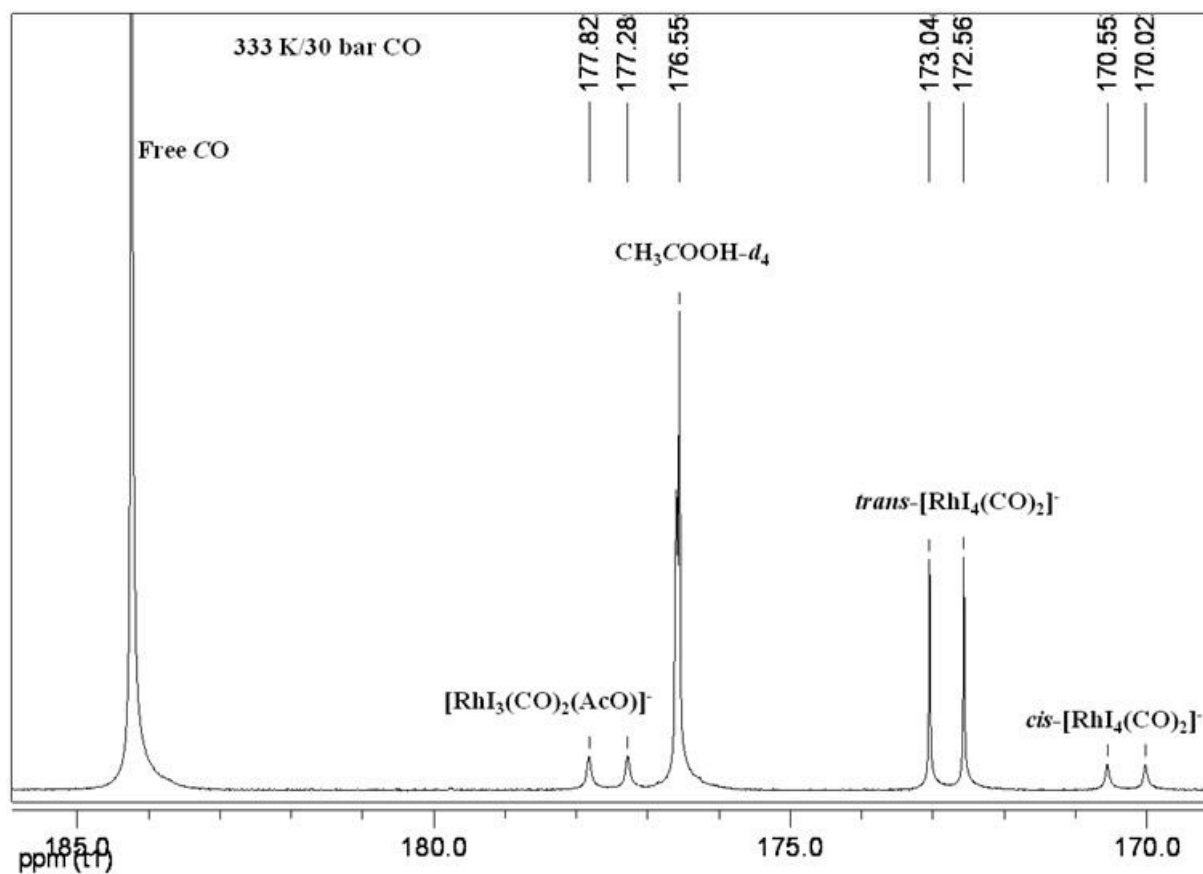


Figure 7. $^{13}\text{C}\{^1\text{H}\}$ NMR spectrum in the CO region at 333 K, ^{13}CO 10 bar + ^{12}CO 20 bar.

The sample was finally heated to 353 K under 30 bar of CO pressure. At this temperature the species presumably assigned to $[\text{RhI}_3(\text{CO})_2(\text{AcO})]^-$ vanishes and the only remaining carbonyl doublets detected belong to *cis* and *trans*- $[\text{RhI}_4(\text{CO})_2]^-$ (Figure 8).

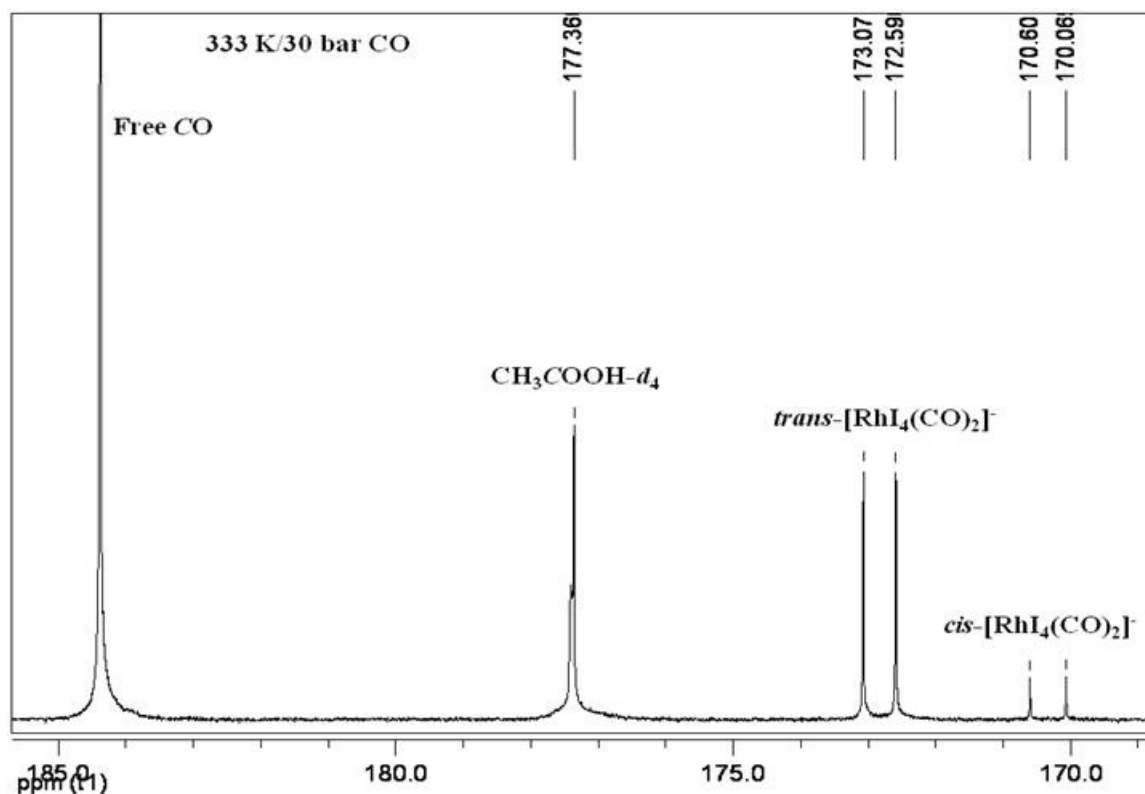
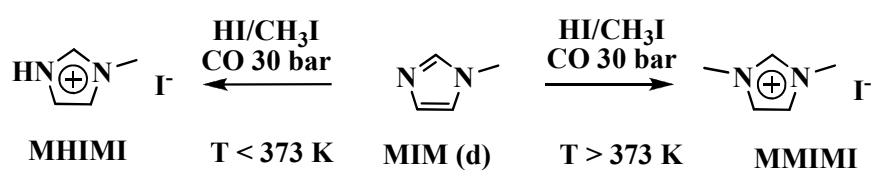


Figure 8. $^{13}\text{C}\{^1\text{H}\}$ NMR spectrum in the CO region at 353 K, ^{13}CO 10 bar + ^{12}CO 20 bar.

After 2 hours at 353 K, the spectra aspect remained unchanged. The sample was then brought back to room temperature under CO pressure and again the same spectrum as displayed in Figure 8 was obtained.

After this first set of VT-HP-NMR experiments, it seems that ligand **d** decoordinates from **4d** followed by hydriodic acid protonation to produce the anionic $[\text{MDIM}][\text{RhI}_2(\text{CO})_2]^-$ species, rapidly evolving to $[\text{MDIM}][\text{RhI}_4(\text{CO})_2]^-$ in the presence of DI, starts to take place at 313 K and is complete above 353 K. Initially introduced neutral complex **4d** behaves as active catalyst at low temperature (< 333 K) and is expected to evolve to the anionic rhodium salt $[\text{RhI}_2(\text{CO})_2]^-$ species in the presence of hydriodic acid. DI formation increases with time and with temperature to eventually lead to the only stable long living resting state species $[\text{RhI}_4(\text{CO})_2]^-$. It is worth mentioning that under the working conditions of these VT-HP-NMR experiments, we can affirm that the countercation formed is 1-methylimidazolium (MDIM)

and not dimethylimidazolium (MMIM) as observed after batch experiments. Batch experiments have been carried out in parallel to this work by Duc Hanh Nguyen, post-doc member in the group. He studied scrambling phenomena taking place under CO pressure between protonated and methylated imidazolium salts as a function of temperature and demonstrated that protonation occurred below 373 K, whereas above 373 K, quaternization by a methyl substituent provided by CH₃I was favored, as mentioned earlier in the chapter (Scheme 6).



Scheme 6. Protonation/methylation of **d** depending on T (K).

At this stage, the water impact on the stability of resting state [RhI₄(CO)₂]⁻ was investigated: 9 wt % H₂O was added under 10 bar CO pressure (¹³CO: 3 bar; ¹²CO: 7 bar ratio) at 298 K. It is worth mentioning that on the ¹³C{¹H} NMR spectrum, acetic anhydride was no longer observed due to the large presence of water which immediately reacted with the latter to give acetic acid.¹ The sample was then heated directly to 353 K, ¹³C{¹H} NMR is depicted in Figure 9.

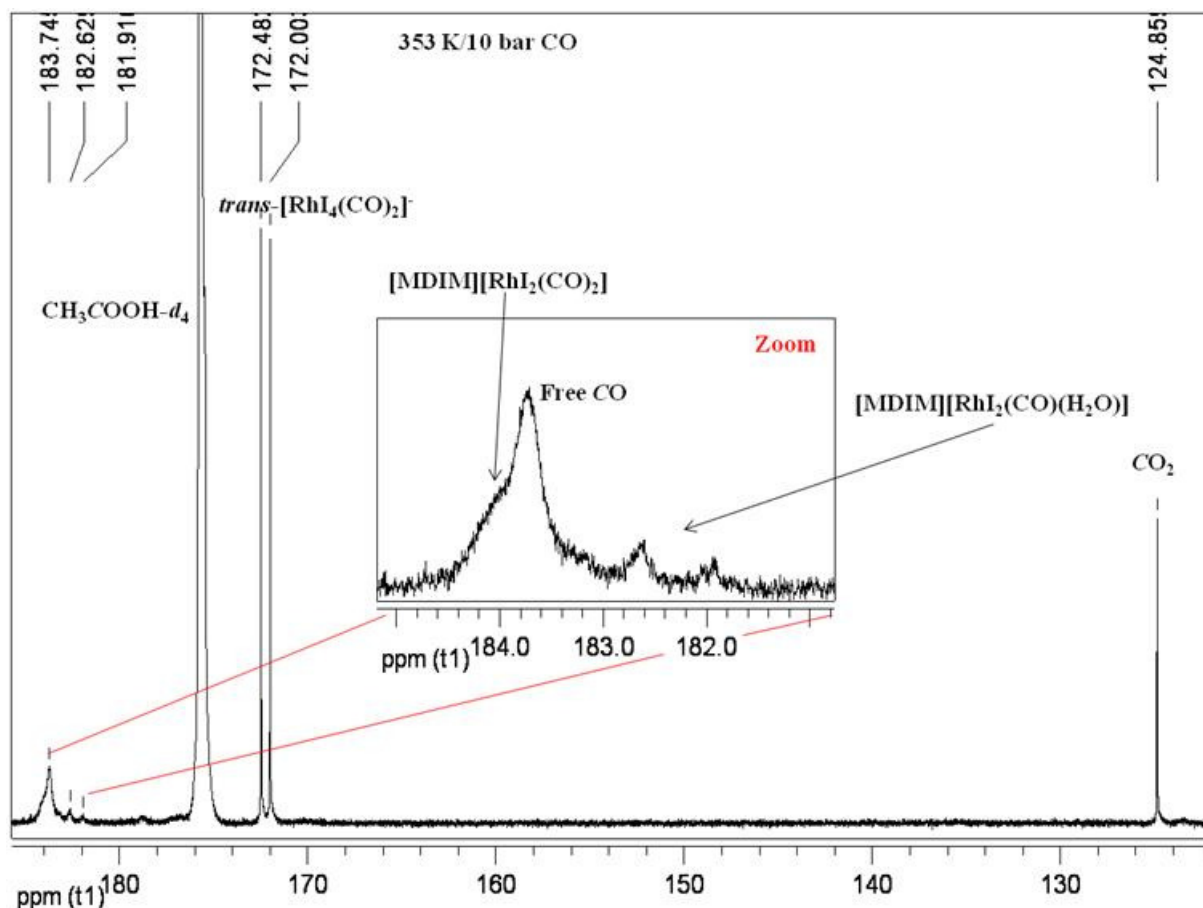
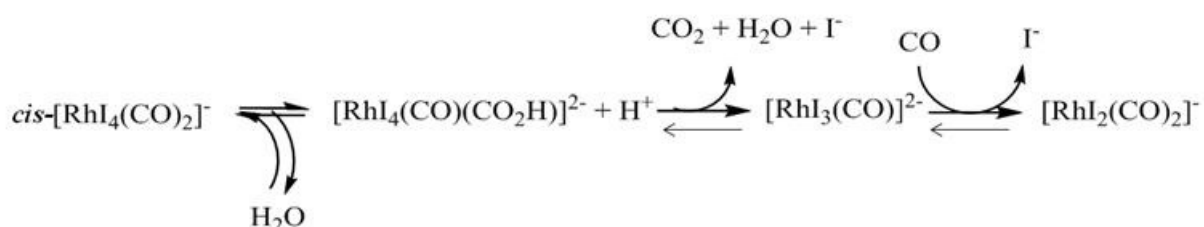


Figure 9. $^{13}\text{C}\{^1\text{H}\}$ NMR spectrum in the 100-190 ppm region at 353 K, ^{13}CO 7 bar + ^{12}CO 3 bar with H_2O addition.

The detection of a significant amount of CO_2 (δ 124.9 ppm) and the disappearance of the doublet assigned to $\text{cis-}[\text{RhI}_4(\text{CO})_2]^-$ (δ 170.3 ppm, $^1J_{(\text{Rh}-\text{CO})} = 53.4$ Hz) indicates that water reacted with CO generating CO_2 and H_2 , which further reduces $\text{cis-}[\text{RhI}_4(\text{CO})_2]^-$ to afford the active Rh(I) $[\text{RhI}_2(\text{CO})_2]^-$ species.⁹ This explains why a broad signal corresponding to the latter Rh(I) complex is masked by the free CO (exchange process) although slightly shifted in comparison to previous observations making it recognizable. This is presumably due to the better solubility of carbon dioxide in the medium in comparison with carbon monoxide. Partly replaced by CO_2 , the resulting lower amount of CO gives rise to a less marked free CO/coordinated CO exchange process. This reaction (scheme 7) constitutes the second part of the WGS cycle,^{1,6} the first part being displayed in scheme 3. In addition, a

weak intensity carbonyl doublet was also observed at δ 182.3 ppm, $^1J_{(\text{Rh-CO})} = 72.7$ Hz characteristic of a Rh(I) anionic type complex, which has been tentatively assigned to $[\text{RhI}_2(\text{CO})(\text{H}_2\text{O})]^-$, resulting from the large amount of water present in the medium. The analogue $[\text{RhI}_2(\text{CO})(\text{Py})]^-$ has been proposed by Zoeller et al.⁸



Scheme 7. Second part of the WGS cycle.

In fact dihydrogen released via WGSR plays a crucial role by regenerating the active Rh(I) $[\text{RhI}_2(\text{CO})_2]^-$ from inactive Rh(III) $[\text{RhI}_4(\text{CO})_2]^-$. The sample was then brought back to RT and the same spectrum as in Figure 9 was observed, showing the reappearance of the second doublet assigned to the *cis*- $[\text{RhI}_4(\text{CO})_2]^-$ isomer, which indicates the reversibility of this reaction at lower temperature.

III-5-2 *Experiment 2* (see chapter V for full experimental details)

$^{13}\text{CO-4d}$ was then studied by $^{13}\text{C}\{^1\text{H}\}$ VT-HP-NMR in the presence of the entire catalytic solution: Rh metal: ~ 1500 ppm, $[\text{H}_2\text{O}]$: 3 wt %, $[\text{AcOMe}]$: 35 wt %, $[\text{CH}_3\text{I}]$: 10 wt %, $[\text{HI}]$: 1 wt % and $[\text{AcOH-}d_4]$. Under these conditions a first sample was prepared at 298 K without CO pressure. The $^{13}\text{C}\{^1\text{H}\}$ NMR spectrum in the carbonyl region is displayed in Figure 10.

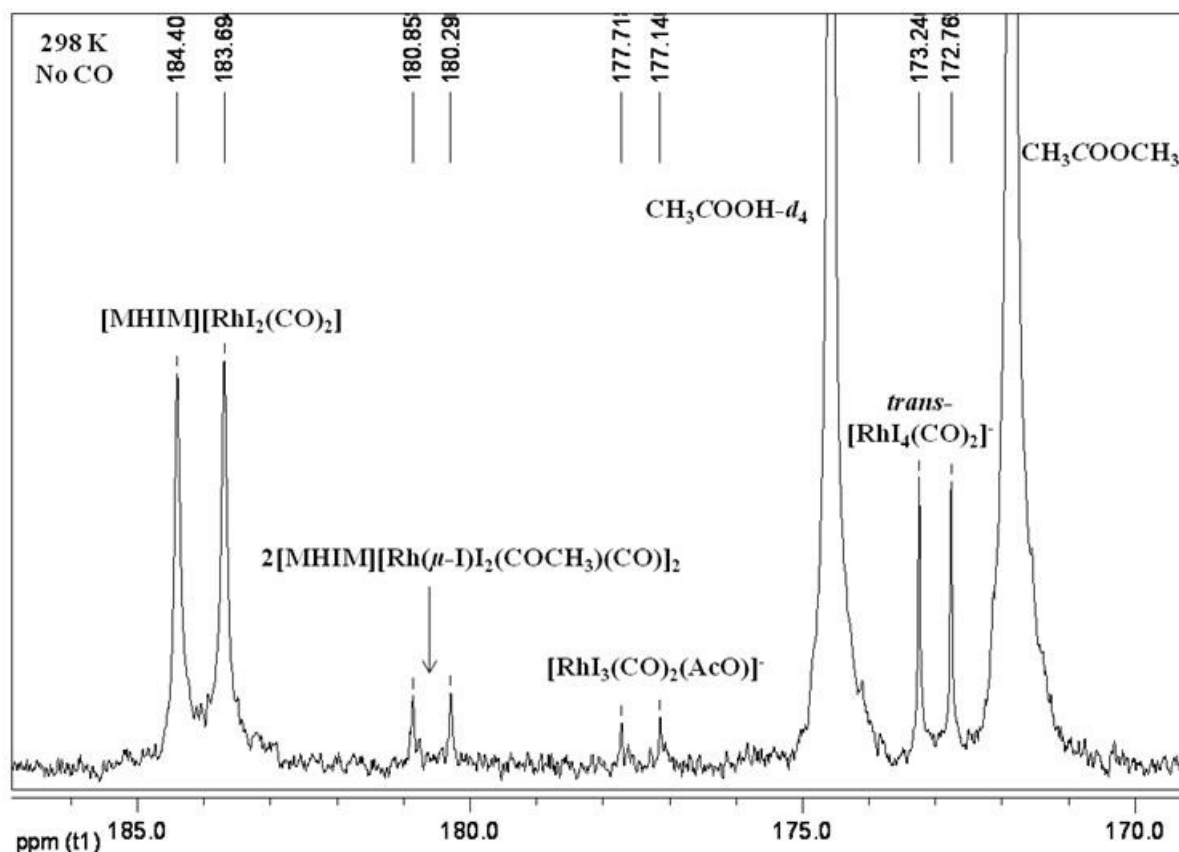


Figure 10. $^{13}\text{C}\{^1\text{H}\}$ NMR spectrum in the CO region at 298 K in the absence of CO.

A set of four terminal rhodium carbonyl doublets was detected and have been assigned to the following species: $[\text{MHIM}][\text{RhI}_2(\text{CO})_2]$ (δ 184.0 ppm, $^1J_{(\text{Rh}-\text{CO})} = 71.1$ Hz), $[\text{MHIM}]_2[\text{Rh}(\mu\text{-I})\text{I}_2(\text{COCH}_3)(\text{CO})]_2$ (δ 180.6 ppm, $^1J_{(\text{Rh}-\text{CO})} = 57.1$ Hz), $[\text{RhI}_3(\text{CO})_2(\text{AcO})]^-$ (δ 177.4 ppm, $^1J_{(\text{Rh}-\text{CO})} = 58.1$ Hz) and $\text{trans-}[\text{RhI}_4(\text{CO})_2]^-$ (δ 173.0 ppm, $^1J_{(\text{Rh}-\text{CO})} = 48.4$ Hz). As expected, under these conditions at RT without CO pressure, HI rapidly reacts with the starting neutral complex **4d** to give rise to rhodium anionic species. In the absence of CO, the CH_3I oxidative addition on $[\text{RhI}_2(\text{CO})_2]^-$, followed by CO *cis*-migration results in the formation of the $[\text{Rh}(\mu\text{-I})\text{I}_2(\text{COCH}_3)(\text{CO})]_2^{2-}$ dimer, although the acetyl species were once again not detected. Formation of acetic anhydride was again not observed here due to the presence of water, which immediately reacted with the latter to give acetic acid.¹

At 298 K, 30 bar CO pressure (^{13}CO 10 bar + ^{12}CO 20 bar) was added to the sample and the corresponding $^{13}\text{C}\{^1\text{H}\}$ NMR spectra show the terminal Rh-carbonyl doublet of $[\text{Rh}_4(\text{CO})_2]^-$ species broaden with a slight shift to lower field. The corresponding carbonyl signals are mainly hidden behind the methyl acetate peak. Carbonyl signal attributed to $[\text{RhI}_3(\text{CO})_2(\text{AcO})]^-$ species almost completely disappeared (Figure 11). Increasing NMR scanning period permitted the acetyl CO ligand of $[\text{MHIM}][\text{RhI}_3(\text{COCH}_3)(\text{CO})_2]$ (resulting from the CO bridge-splitting reaction of the corresponding dimer) to be detected with a broad signal at δ 215.4 ppm. The carbonyl ligands belonging to $[\text{MHIM}][\text{RhI}_2(\text{CO})_2]$ and $[\text{MHIM}][\text{RhI}_3(\text{COCH}_3)(\text{CO})_2]$ are most certainly involved in an exchange process with free CO present in the medium, as previously mentioned for Experiment 1.¹¹

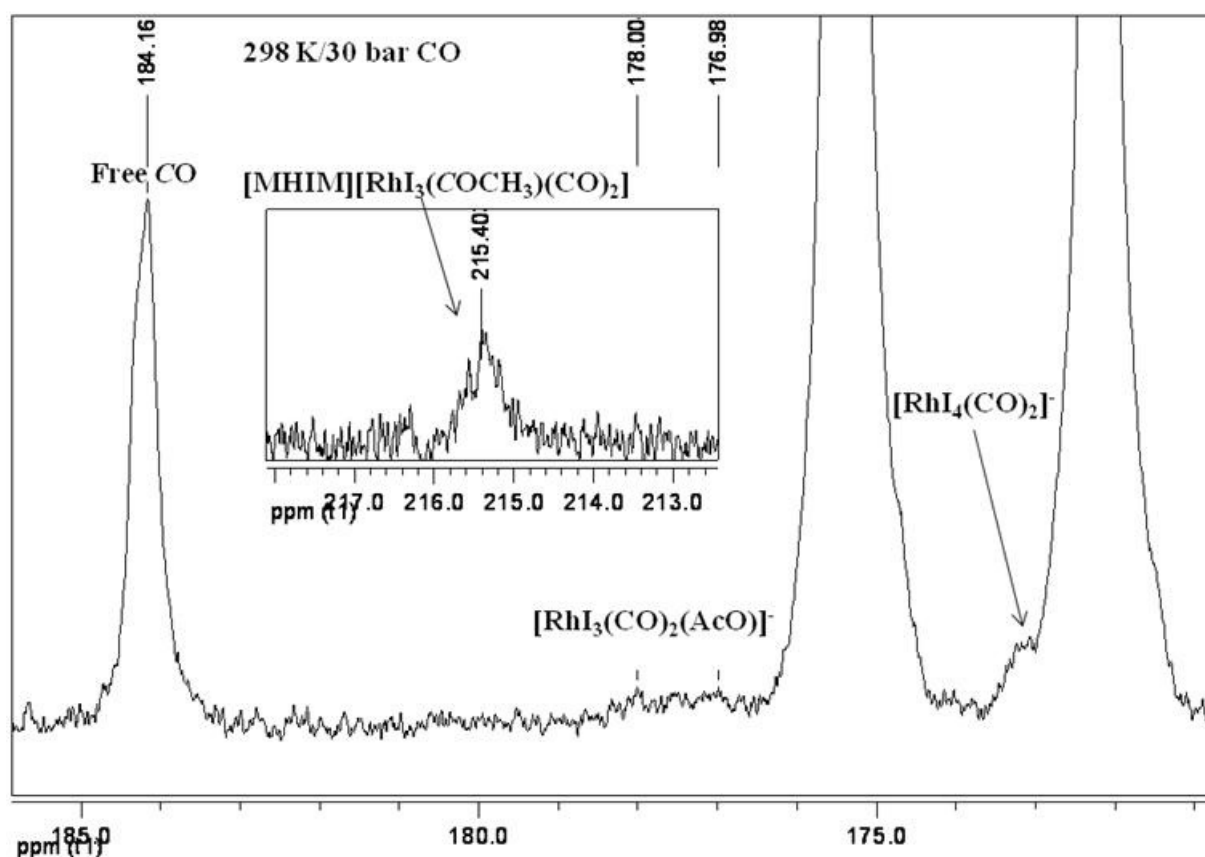


Figure 11. $^{13}\text{C}\{^1\text{H}\}$ NMR spectrum in the CO region at 298 K, ^{13}CO 10 bar + ^{12}CO 20 bar.

The sample was then brought directly to 353 K under 30 bar CO pressure. As previously observed earlier, under these conditions the WGS reaction operated, releasing CO₂ (δ 125.0 ppm) in the medium. (Figure 12).

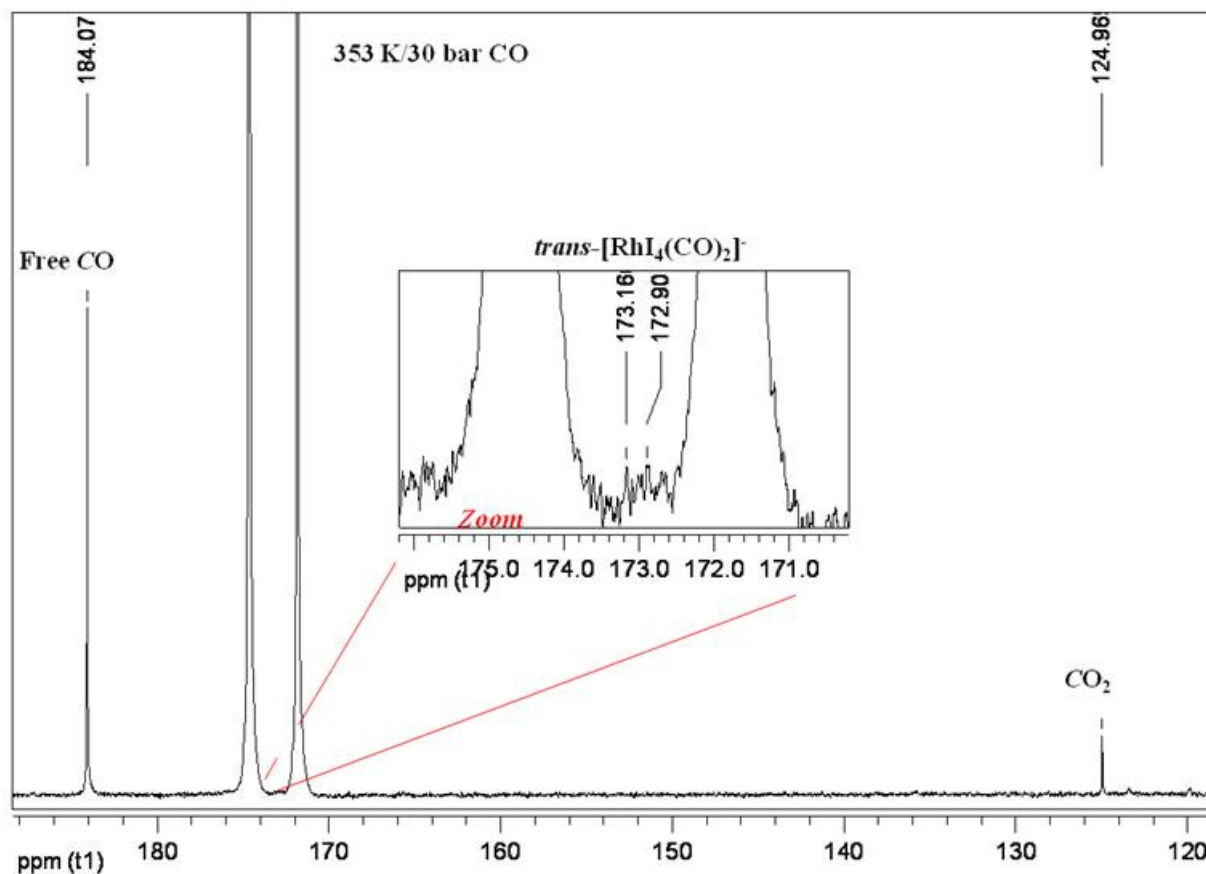


Figure 12. $^{13}\text{C}\{^1\text{H}\}$ NMR spectrum in the 120-190 ppm region at 353 K, ^{13}CO 10 bar + ^{12}CO 20 bar.

Cooling down to 298 K under 30 bar CO showed no difference in the $^{13}\text{C}\{^1\text{H}\}$ NMR spectrum compared to the one depicted in Figure 12.

Finally, the catalytic solution was recovered for evaporation of the major part of the volatile organic fraction under reduced pressure. The remaining concentrated solution was analyzed by $^{13}\text{C}\{^1\text{H}\}$ NMR at 298 K under 1 bar CO in AcOH-*d*₄ (Figure 13).

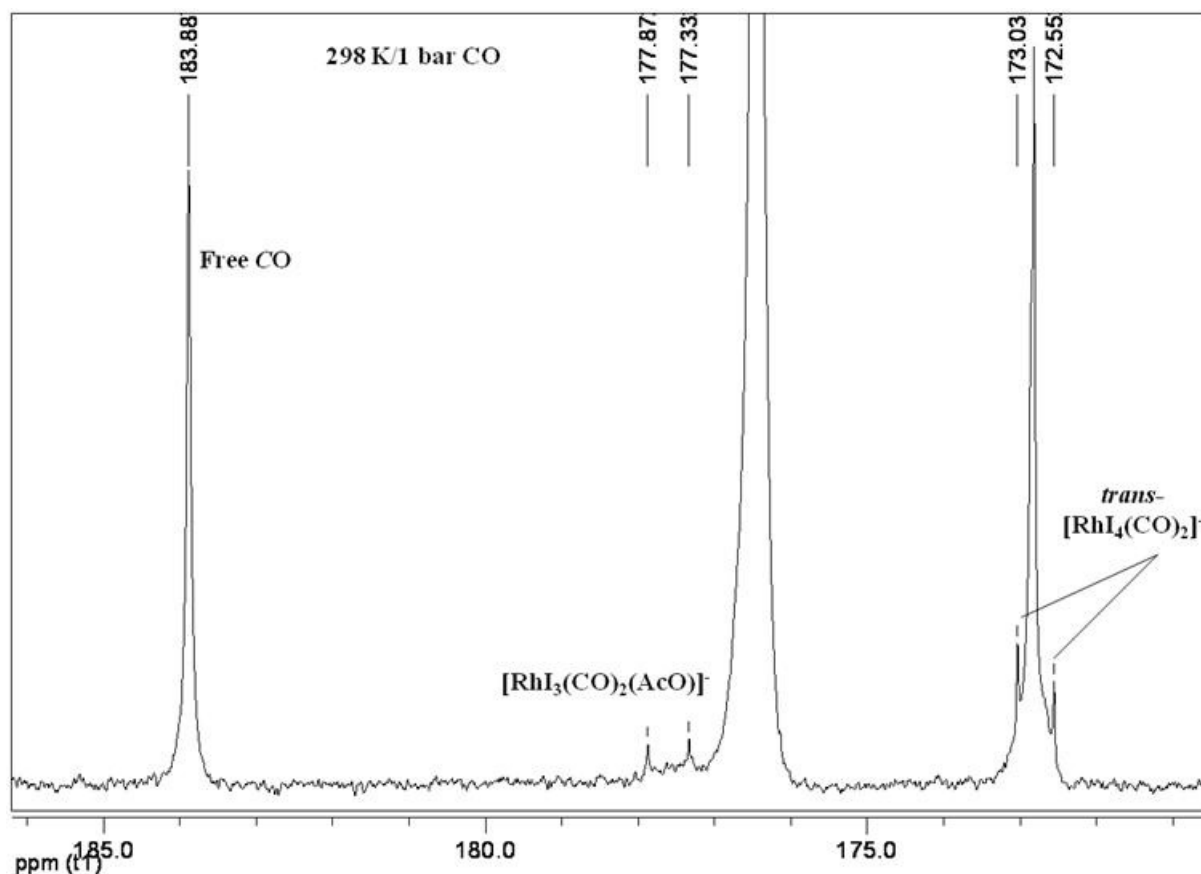


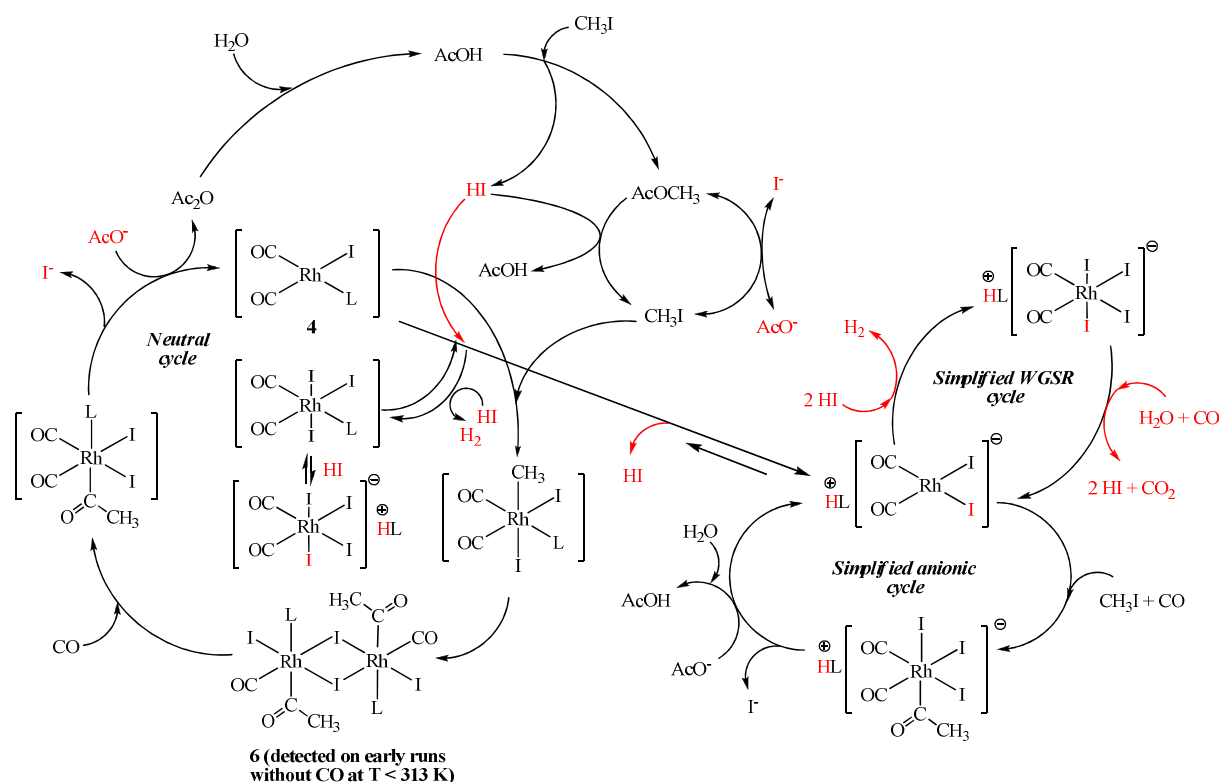
Figure 13. $^{13}\text{C}\{^1\text{H}\}$ NMR spectrum in the CO region at 298 K under 1 bar CO.

This last experiment shows that a small amount of $[\text{RhI}_3(\text{CO})_2(\text{AcO})]^-$ species (δ 177.6 ppm, $^1J_{(\text{Rh}-\text{CO})} = 54.3$ Hz) reappears in the medium along with *trans*- $[\text{RhI}_4(\text{CO})_2]^-$.

In summary, under catalytic conditions, the only detectable species is the resting state $[\text{RhI}_4(\text{CO})_2]^-$ species, all the other intermediate species are probably hidden by organic products or by solubilized free CO in the medium which is a major drawback for mechanistic investigations.

III-6 Conclusion for reactivity under methanol carbonylation conditions

It has been found throughout batch experiments and by *in situ* VT-HP-NMR experiments that neutral complexes **4** are very likely to run for a very short period of time at low temperature (< 313 K) in the absence of HI. Above this temperature increasing amounts of HI are generated provoking decoordination followed by protonation of the ligand. Above 353 K, it seems that the anionic catalytic system is favored to operate. In addition, above 373 K we believe that the counteraction is methylated rather than protonated. However, it cannot be completely ruled out that neutral species are still living in equilibrium with anionic species at higher temperatures.⁷ Indeed, small amounts of neutral rhodium complexes bearing pyrazole family ligands have been detected after batch experiments. A proposed mechanism is represented in scheme 8 for which both neutral and anionic species operate.



Scheme 8. Proposed mechanism involving both neutral and anionic species under catalytic conditions.

III-7 Nature of the counter-cation in anionic Rh(I) complexes: Ion pairing effect

III-7-1 Background

The results presented in the previous section concerning catalysis on neutral species led us to focus further attention on the anionic catalytic system and in particular on the role of the counter-cation during the CH_3I oxidative addition step followed by CO *cis*-migratory insertion.^{14,15}

Indeed, previous FT-IR work performed in our group on iridium chemistry showed in the carbonyl region the following ν_{CO} bands at 2046 (s) and 1967 (s) cm^{-1} (CH_2Cl_2) for complex $[\text{PPN}][\text{IrI}_2(\text{CO})_2]$. For complex $[\text{H}][\text{IrI}_2(\text{CO})_2]$, ν_{CO} bands were found at 2064 (s) and 1982 (s) cm^{-1} (CH_2Cl_2) with a striking 18 and 15 cm^{-1} shift to higher frequency for the symmetric and antisymmetric bands, respectively.⁹ This result indicates the effect brought by H^+ on the Ir metal. The small sized $[\text{H}^+]$ cation comes in close proximity with $[\text{IrI}_2(\text{CO})_2]^-$ and reduces the Ir electron density via an ion-pairing interaction. On the contrary, for $[\text{PPN}][\text{IrI}_2(\text{CO})_2]$, the bulky ammonium counter-cation interferes less with the $[\text{IrI}_2(\text{CO})_2]^-$ anion. In addition, Maitlis et al. established throughout spectroscopic and kinetic investigations that cations (in particular cations bearing protons) induced a lower effective charge on the metal center of anionic $[\text{RhI}_2(\text{CO})_2]^-$ species. This is presumably due to contact ion-pair formation, $\{\text{C}^+\cdots\text{RhI}_2(\text{CO})_2\}^-$.^{14,16}

These preliminary results initiated the idea to investigate further on the behavior of other N-containing counter-cations, and more particularly protonated cations, towards the $[\text{RhI}_2(\text{CO})_2]^-$ anion. It is also important to mention that most results achieved in this chapter take part in an important project belonging to the Celanese technology for which a liquid rhodium catalytic solution comprising an ionic liquid belonging to the ammonium,

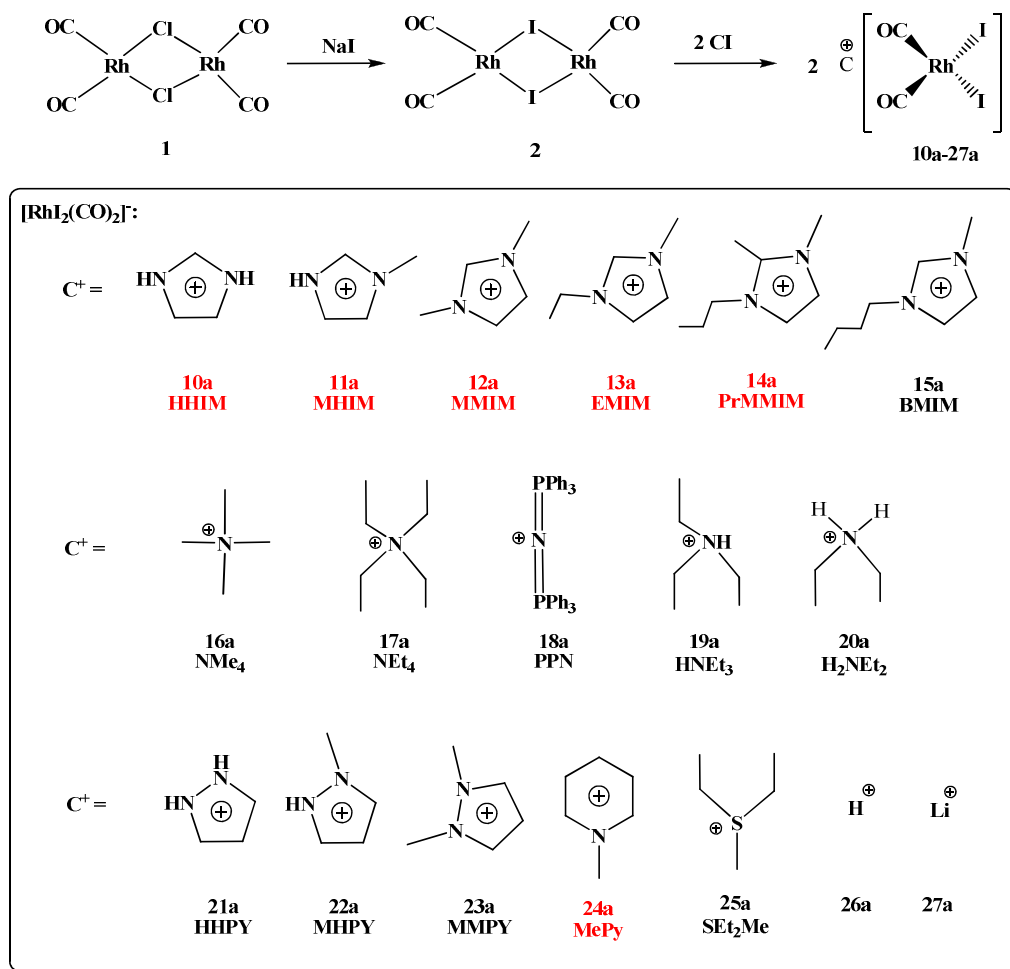
imidazolium or pyrazolium family is involved for stabilization concerns. Historically, the idea of ionic liquids was initially introduced by Eastman Chemical Company in 2002¹⁷ and currently adapted to the AO Celanese technology since.

The following work is directly related to chapter II as part of the counter-cations which will be studied result from protonation or methylation of the N-containing amine, imidazole or pyrazole ligands. It is in this context that a series of $[C][RhI_2(CO)_2]$ salts with ammonium, imidazolium or pyrazolium $[C^+]$ counter-cations has been prepared. In addition, the study was extended to the small sized $[H^+]$ and $[Li^+]$ cations¹⁴, these latter being mainly involved in the AO process technology.¹ The synthesis was also further extended to a pyridinium and a sulfonium Rh(I) complex. Duc Hanh Nguyen, post-doc in the team, participated in the synthesis of several complexes in the following section (red complexes in Scheme 9).

III-7-2 *Synthesis and characterization of anionic Rh(I) complexes*

The reaction of 1 molar eq. of the starting rhodium precursor $[Rh(\mu-I)(CO)_2]_2$ **2** with 2 eq. of imidazolium, ammonium, pyrazolium, pyridinium, sulfonium iodide salt precursor or hydriodic acid in dichloromethane at RT quantitatively afforded the corresponding *cis*- $[C][RhI_2(CO)_2]$ salt complexes **10a-15a**, **16a-20a**, **21a-23a**, **24a**, **25a** and **26a** (Scheme 9), which are air- and moisture unstable, most particularly **26a** which was only characterized *in situ* (Table 2). Complex **18a** was prepared differently starting from $PPNCl$ salt reacted with RhI_3 in DMF and water according to the literature.¹⁸ The reaction of 1 molar eq. of **2** with 2 eq. of lithium iodide in dichloromethane/methanol (minimum methanol to solubilize LiI) at RT afforded *cis*- $[Li][RhI_2(CO)_2]$ **27a** (Scheme 9). Most iodide salt precursors were synthesized (see chapter V for experimental details). These complexes have been fully characterized by FT-IR in solution (Table 2) and multinuclear NMR spectroscopies, except

for **26a** which was only detected via FT-IR ($\text{CH}_3\text{OH}/\text{CH}_2\text{Cl}_2$). Single crystal X-ray crystallography have been obtained for **12a** (Duc Hanh Nguyen, 2011) and **18a**¹⁹ (Nicolas Lassauque, PhD, 2006) by group members.



Scheme 9. Synthesis of anionic *cis*-[C][Rh₂(CO)₂] complexes **10a-27a**.

Table 2. Infrared carbonyl stretching frequencies for [C][Rh₂(CO)₂] **10a-27a** at 298 K.

Entries	$\nu(\text{CO})$ (cm^{-1}) (CH_2Cl_2)	$\Delta\nu_{\text{CO}}$ (cm^{-1})	$\nu_{\text{av}}(\text{CO})$ (cm^{-1})	Entries	$\nu(\text{CO})$ (cm^{-1}) (CH_2Cl_2)	$\Delta\nu_{\text{CO}}$ (cm^{-1})	$\nu_{\text{av}}(\text{CO})$ (cm^{-1})
10a	2068.0; 1998.4	69.6	2033.2	19a	2067.1; 1997.3	69.8	2032.2
11a	2066.8; 1996.9	69.9	2031.9	20a	2070.4; 2003.5	66.9	2037.0
12a	2062.5; 1991.6	70.9	2027.1	21a	2071.9; 2003.1	68.8	2037.5
13a	2062.4; 1991.5	70.9	2027.0	22a	2068.3; 1999.1	69.2	2033.7
14a	2062.0; 1989.6	72.4	2025.8	23a	2062.4; 1990.5	71.9	2026.5
15a	2062.7; 1991.8	70.9	2027.3	24a	2062.3; 1990.9	71.4	2026.6
16a	2062.4; 1991.4	71.0	2026.9	25a	2063.1; 1992.1	71.0	2027.6
17a	2060.7; 1988.8	71.9	2024.8	26a	2065.6; 1995.9	69.7	2030.8
18a	2058.0; 1986.1	71.9	2022.1	27a	2068.7; 1999.3	69.4	2034.0

The characteristic ν_{CO} stretching frequencies of **10a-27a** in CH_2Cl_2 are displayed in Table 2. As previously observed for neutral complexes **3** and **4**, two bands of similar strong intensity are observed in the carbonyl region, although shifted to lower frequency in comparison to neutral complexes, illustrating the square planar configuration with two CO ligands in mutual *cis*-position and a higher electron density on the Rh metal center, as expected for anionic species. For *cis*- $[\text{RhI}_2(\text{CO})_2]$ type complexes, analysis of the $\nu_{\text{CO, av}}$ value allows to compare the electronic parameter brought by each different cations in terms of electron density distributed around the anionic Rh moiety. These $\nu_{\text{CO, av}}$ values have been bar-charted in order to illustrate the frequency shift according to the counter-cation involved (Figure 14).

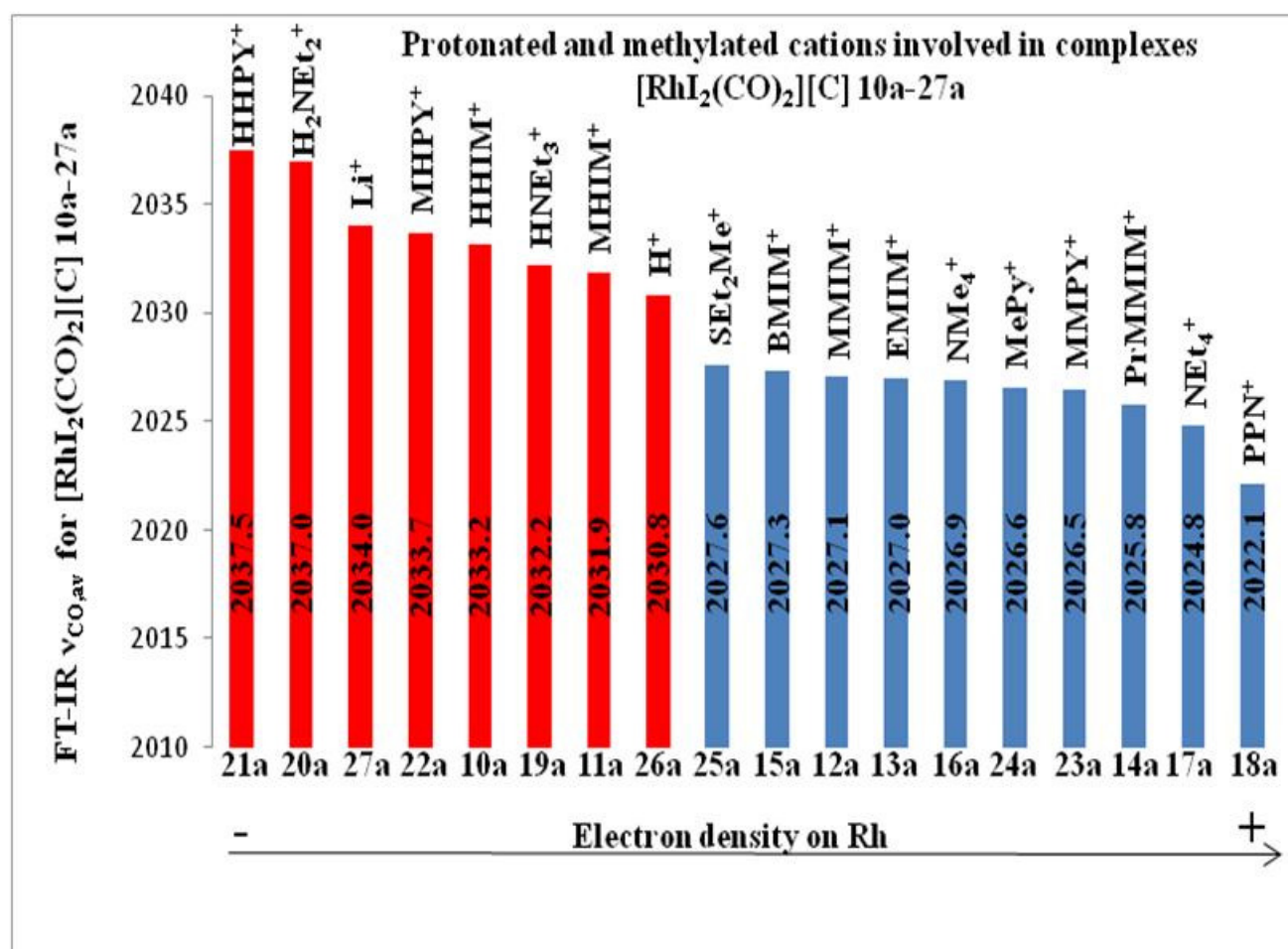


Figure 14. Bar-chart illustrating $\nu_{\text{CO, av}}$ values for $[\text{C}][\text{RhI}_2(\text{CO})_2]$ **10a-27a** complexes.

The $\nu_{\text{CO, av}}$ values for **10a-27a** are included in the range 2037.5 - 2022.1 cm^{-1} with a $\sim 15 \text{ cm}^{-1}$ difference between the two complexes **21a** (lower e^- density at the Rh center) and **18a** (higher e^- density at the Rh center) found at the extremities of this range. Indeed, for **10a-27a**, two sets of complexes have been identified and separated: complexes bearing protonated type cations (red bars in Figure 14) and complexes bearing unprotonated type cations (blue bars in Figure 14). All the protonated cations interestingly correspond to high $\nu_{\text{CO, av}}$ values in comparison to the unprotonated ones and are therefore suspected of more interaction with the Rh anionic metal center. This observation prevails even more for protonated pyrazolium cations (**21a**: 2037.5 cm^{-1} and **22a**: 2033.7 cm^{-1}) in comparison with the analogous protonated imidazolium cations (**10a**: 2033.2 cm^{-1} and **11a**: 2031.9 cm^{-1}). Complex **27a**, containing Li^+ as cation, has been included in the group of the protonated type cations due to its small size and presumed ability to ion pair with the anionic moiety according to its high $\nu_{\text{CO, av}}$ value (2034.0 cm^{-1}). Furthermore, the difference Δ between two CO vibrators of a given complex is of slightly smaller value for the protonated cations ($\sim 69 \text{ cm}^{-1}$) in comparison to that of the unprotonated cations ($\sim 71 \text{ cm}^{-1}$). Thus, indicates that the geometry of the classical square planar C_{2v} is slightly affected by the cationic interaction so that the CO-Rh-CO angle sharpens. In contrast, cations such as NMe_4^+ ($\nu_{\text{CO, av}} = 2026.9 \text{ cm}^{-1}$) or NEt_4^+ ($\nu_{\text{CO, av}} = 2024.8 \text{ cm}^{-1}$) are considered as true electrostatic ion-pairs according to the strict definition, for which absence of protons exclude contact ion-pairing interactions.²⁰ In the case of a large counter-cation such as PPN^+ ($\nu_{\text{CO, av}} = 2022.1 \text{ cm}^{-1}$) hardly any interaction with $[\text{RhI}_2(\text{CO})_2]^-$ is expected.

III-7-3 The role of solvent on ion-pairs

Ion pairs are defined as pairs of oppositely charged ions, with a common solvation shell, held together prevalently by Coulombic forces with lifetimes sufficiently longer than the correlation time of Brownian-motion (kinetic stability) and a binding energy higher than kT (thermodynamic stability).²¹

The FT-IR characterizations presented above were carried out in dichloromethane, a solvent of low relative permittivity and weak polarity which maximizes the electrostatic interaction. Thus, it favors ion pairing in the sense that no solvent molecule is thought to interpose between the two ions or at least very little. Therefore, we consider a contact, intimate or tight ion pair (Figure 15).

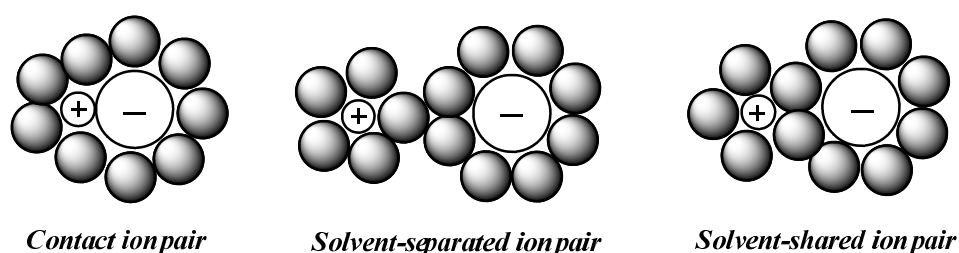
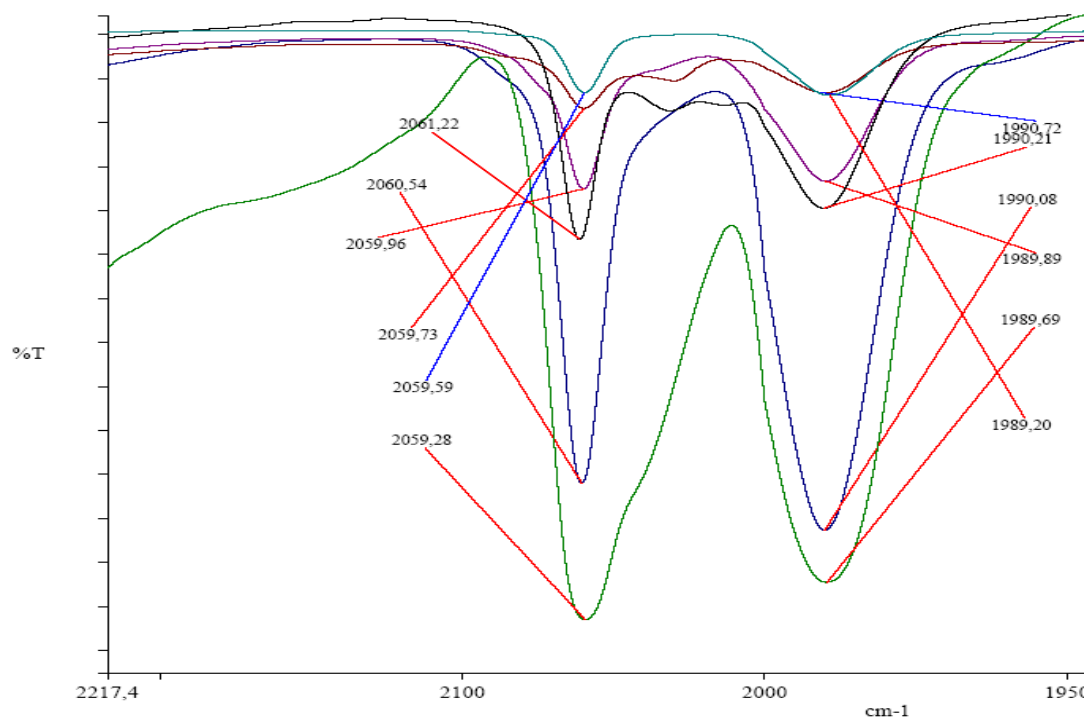


Figure 15. Different type of ion-pairs.

To confirm this solvent effect, selected complexes **16a-20a**, **26a**, **27a** were analyzed by FT-IR in methanol, a more polar solvent, which should favor solvent-separated ion-pairs. Carbonyl stretching frequencies are displayed in Table 3 and FT-IR spectra are shown in Figure 16.

Table 3. Infrared carbonyl stretching frequencies for **16a**, **18a-20a**, **26a-27a** at 298 K.

<i>Entries</i>	$\nu(\text{CO}) (\text{cm}^{-1}) (\text{CH}_3\text{OH})$	$\Delta\nu_{\text{CO}} (\text{cm}^{-1})$	$\nu_{\text{av}} (\text{CO}) (\text{cm}^{-1})$
16a	2060.5; 1990.1	70.4	2025.3
18a	2059.6; 1989.2	70.4	2024.4
19a	2059.7; 1990.7	69.0	2025.2
20a	2060.1; 1989.9	70.2	2025.0
26a	2059.3; 1989.7	69.6	2024.5
27a	2061.2; 1990.2	71.0	2025.7

**Figure 16.** FT-IR spectra in the carbonyl region in CH_3OH at 298 K for $[\text{C}][\text{RhI}_2(\text{CO})_2]$ (C = aliphatic cations) **16a**, **17a-20a**, **26a-27a**.

In methanol, the previously described interactions are no longer detected as all the complexes selected have roughly the same ν_{CO} bands at ~ 2060 , $\sim 1990 \text{ cm}^{-1}$ and $\nu_{\text{CO, av}}$ at $\sim 2025 \text{ cm}^{-1}$. In this situation, each ion has its own methanol solvation shell.²² The polar property of methanol separates the ions and eliminates the hydrogen interactions when they exist, resulting in longer distance in space between the ion pairs. An example of the effect of methanol is represented by the FT-IR-monitored experiment for **27a** in CH_2Cl_2 for which a series of **27a** samples have been prepared containing an increasing methanol concentration

(Table 4). Figure 17 illustrates the plot of $[\text{MeOH}] = f(A_1)$ with A_1 the symmetric ν_{CO} stretching mode for complex **27a**. The shift from higher to lower frequency as $[\text{MeOH}]$ increases is clearly observed.

Table 4. $A_1 \nu_{\text{CO}}$ stretching band shift as a function of $[\text{MeOH}]$ for **27a** at 298 K in CH_2Cl_2 .

27a/MeOH (molar ratio)	$[\text{MeOH}]$ (mol.L ⁻¹)	$A_1 \nu(\text{CO})$ band (cm ⁻¹)
1/1.87	0.01637	2067.2
1/3.74	0.03273	2066.7
1/5.61	0.04911	2066.5
1/14.98	0.13096	2065.2
1/24.35	0.21281	2064.6
1/33.71	0.29466	2063.7
1/43.08	0.37651	2063.0
1/52.45	0.45836	2062.7
1/241	2.1281	2061.2

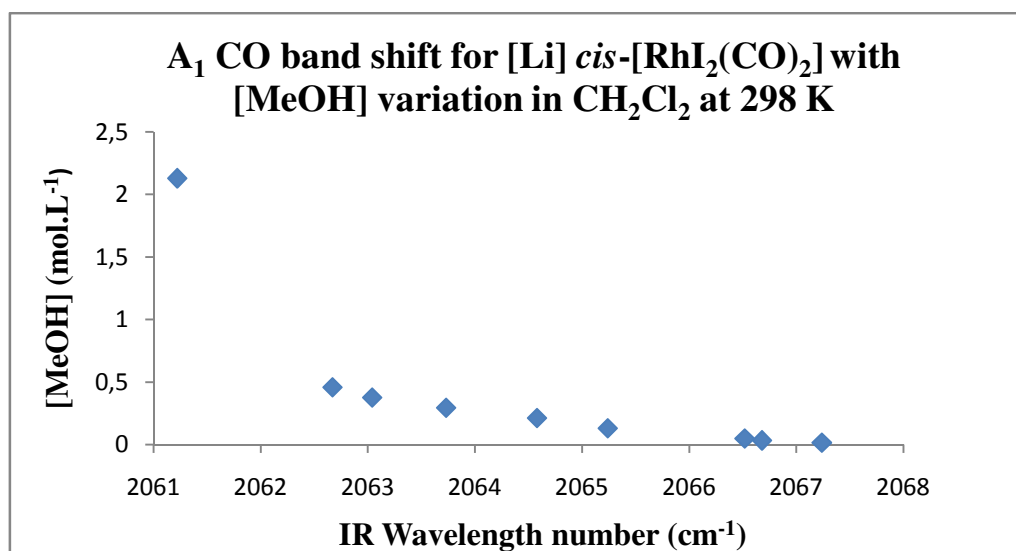


Figure 17. $[\text{MeOH}] = f(A_1)$ plot for **27a** in $\text{CH}_2\text{Cl}_2/\text{CH}_3\text{OH}$ at 298 K.

This experiment highlights the significant impact of the solvent nature for ion-pairing interactions and supports to demonstrate that intimate ion-pairing occurs in CH_2Cl_2 .

III-7-4 Single crystal X-ray structures for **12a** and **18a**

Single X-ray structures of **12a**, **18a**¹⁹ were resolved in our group and **24a** was reported in the literature.²³ The molecular view of **18a** and two different packing diagrams of **12a** are displayed in Figures 18, 19 and 20, respectively. Their selected bond length and angle parameters are listed in Table 5.

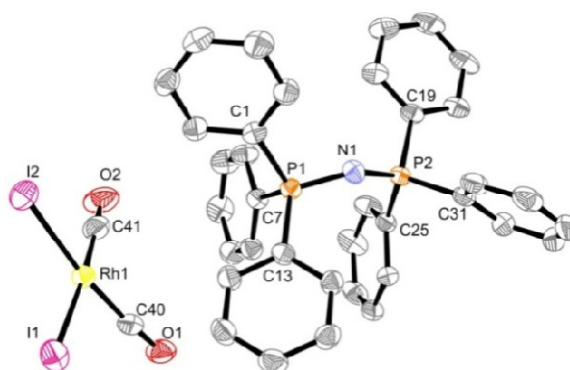


Figure 18. ORTEP molecular view of **18a**. Thermal ellipsoids are shown at the 30% probability level and hydrogen atoms are omitted for clarity.

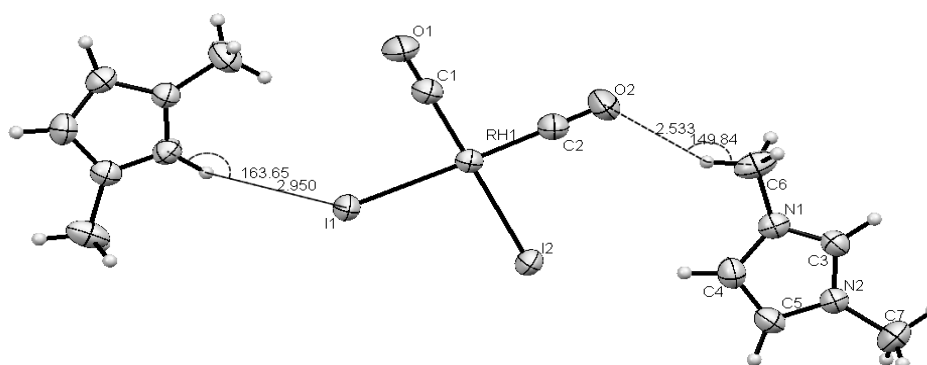


Figure 19. Packing diagram of **12a** putting in evidence intermolecular H-bonding interactions. Thermal ellipsoids are shown at the 30% probability level.

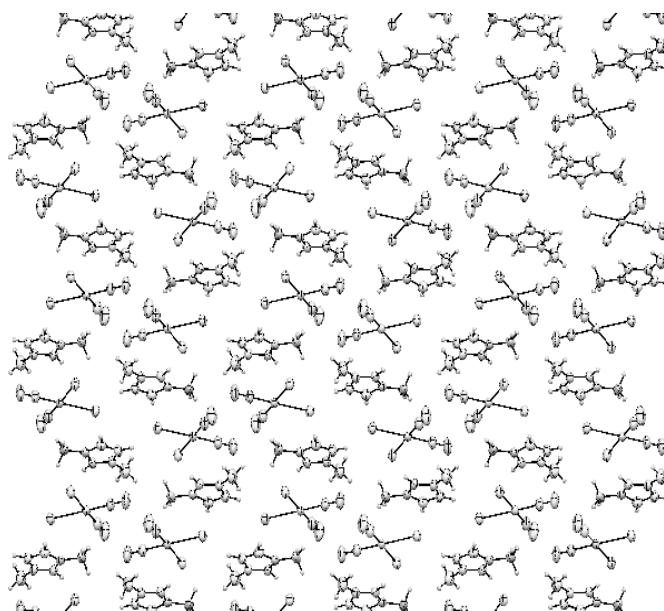


Figure 20. Packing diagram of **12a** showing the layered stacking pattern of ions. Thermal ellipsoids are shown at the 30% probability level.

Table 5. Selected bond lengths (Å) and angles (deg) for *cis*-[C][RhI₂(CO)₂] **12a**, **18a** and **24a**.

<i>Atoms</i>	<i>12a</i>	<i>18a</i>	<i>24a</i>
<i>Rh-I(1)</i>	2.6586(2)	2.6725(7)	2.6539(12)
<i>Rh-I(2)</i>	2.6560(2)	2.6515(11)	2.6606(8)
<i>Rh-C(1)</i>	1.842(2)	1.844(4)	1.864(5)
<i>Rh-C(2)</i>	1.837(2)	1.840(4)	1.846(5)
<i>C(1)-O(1)</i>	1.135(3)	1.140(4)	1.126(7)
<i>C(2)-O(2)</i>	1.129(3)	1.140(5)	1.132(7)
<i>Rh^{III}···P(1) (cation)</i>	-	5.484	-
<i>Rh^{III}···N(1) (cation)</i>	3.596	7.041	3.657(3)
<i>Rh^{III}···N(2) (cation)</i>	3.993	-	-
<i>Rh^{III}···ring (centroid)</i>	3.728	-	3.81
<i>C(3)-H(3)···I(1) inter</i>	2.950	-	-
<i>C(6)-H(6)···O(2) inter</i>	2.533	-	-
<i>I(1)-Rh-I(2)</i>	93.891(7)	94.48(3)	92.63(3)
<i>C(1)-Rh-C(2)</i>	92.92(10)	92.09(16)	93.4(2)
<i>I(1)-Rh-C(1)</i>	85.61(7)	88.49(10)	87.78(17)
<i>I(2)-Rh-C(2)</i>	87.58(7)	85.56(12)	86.18(16)
<i>Rh-C(1)-O(1)</i>	179.2(3)	176.0(3)	179.2(5)
<i>Rh-C(2)-O(2)</i>	178.6(2)	175.6(4)	178.8(5)
<i>C(3)-H(3)-I(1)</i>	163.65	-	-
<i>C(6)-H(6)-O(2)</i>	149.84	-	-

For crystal salts resolved above, the coordination geometry around the metal rhodium center is square planar with the two carbonyls in mutual *cis* position consistent with the FT-IR spectroscopic data. The packing of ions in the salt structures above shows some interesting features: $[\text{RhI}_2(\text{CO})_2]^-$ anions and MMIM cations are stacked in an alternating fashion with their planes almost parallel to each other, the angle between planes being $\sim 3.4^\circ$. This solid state behavior was described in the case of **24a**²³ (angle between planes is $\sim 4^\circ$). For **12a**, two intermolecular H-bonding interactions $\text{C}(3)\text{-H}(3)\cdots\text{I}(1)$ (2.950 Å, 163.65°) and $\text{C}(6)\text{-H}(6)\cdots\text{O}(2)$ (2.533 Å, 149.84°) have been found and the Rh-ring centroid distance (Table 4) is somewhat shorter (3.728 Å) in comparison to **24a** (3.81 Å) which is consistent with the FT-IR observations (Table 2 and Figure 14) although it is solution-analyzed data. As expected, $[\text{PPN}][\text{RhI}_2(\text{CO})_2]$ **18a** does not show any type of interaction between the bulky PPN^+ cation and the Rh anion. In fact, X-ray crystal structure for **18a** shows PPN^+ lying on the carbonyl side. As expected, the increasing ion pairing interaction effect follows the order: **18a** > **24a** > **12a**. Unfortunately, attempts to resolve single crystal X-ray structures for cations bearing protons with $[\text{RhI}_2(\text{CO})_2]^-$ anions, like for example **10a** or **11a**, were unsuccessful so far, presumably due to the more unstable character of these compounds.

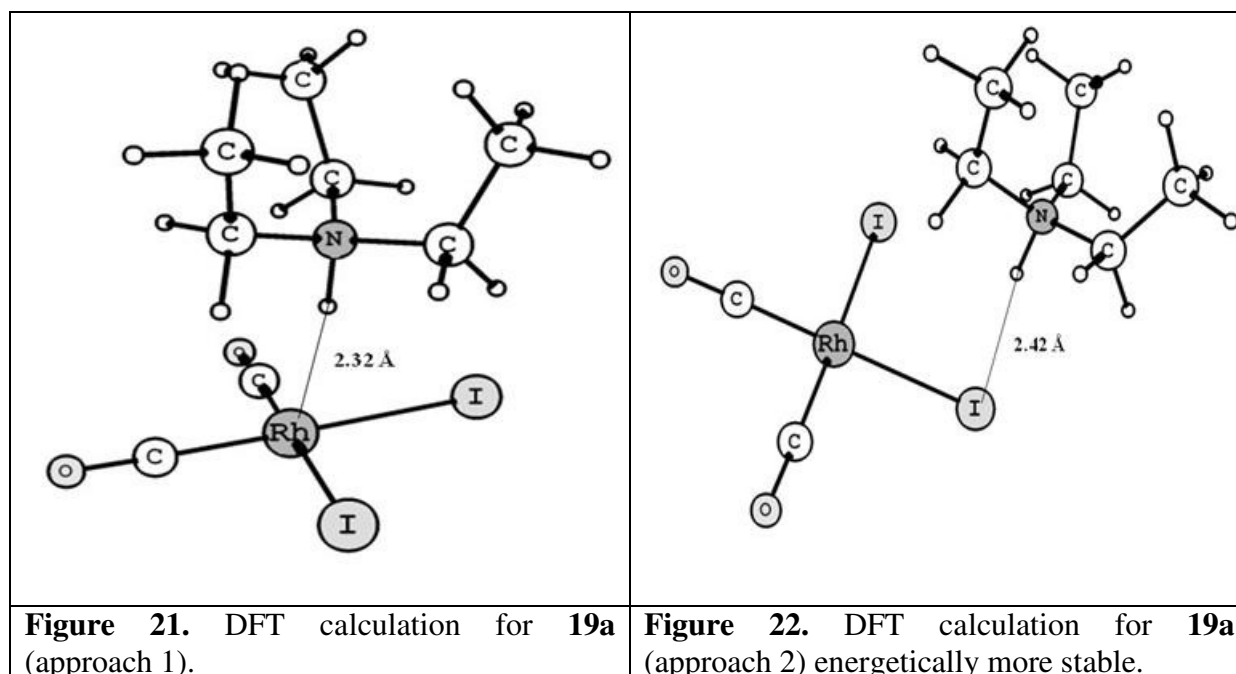
III-7-5 DFT modeling for selected complexes **19a**, **20a** and **27a**

To overcome the unsuccessful crystallization of some complexes and to obtain information on the geometry and position of the ions, rhodium salts **19a**, **20a** and **27a** were computed by density functional theory (DFT) by team colleagues (LCPNO-Toulouse). Table 6 exhibits the experimental FT-IR carbonyl stretching frequencies along with the calculated ones from which DFT-models were determined.²⁴ Calculated ν_{CO} stretching bands are overestimated values in comparison to the experimental data; however the shifting frequency difference from one complex to another is consistent.

Table 6. Experimental FT-IR ν_{CO} and calculated (DFT) ν_{CO} for **17a**, **19a**, **20a** and **27a**.

Entries	$\nu(\text{CO})$ (cm^{-1}) (CH_2Cl_2)	$\Delta\nu_{\text{CO}}$ (cm^{-1})	$\nu_{\text{av}}(\text{CO})$ (cm^{-1})	$\nu(\text{CO})$ (cm^{-1}) (DFT)	$\Delta\nu_{\text{CO}}$ (cm^{-1})	$\nu_{\text{av}}(\text{CO})$ (cm^{-1})
17a	2060.7; 1988.8	71.9	2024.8	2141; 2082	59	2111.5
19a	2067.1; 1997.3	69.8	2032.2	2148; 2089	59	2118.5
20a	2070.4; 2003.5	66.9	2037.0	2154; 2095	59	2124.5
27a	2068.7; 1999.3	69.4	2034.0	2166; 2106	60	2136.0

Two different geometries were calculated for the approach of the ammonium cation towards the Rh anion moiety for complex $[\text{HNEt}_3][\text{RhI}_2(\text{CO})_2]$ **19a**. The first approach is represented in Figure 21, where the hydrogen atom substituted on the nitrogen points directly to the Rh metal center with a 2.32 Å distance. The second approach was calculated with the hydrogen atom of the triethylammonium cation positioned in an interaction with one iodide atom (Figure 22). The distance separating them was found at 2.42 Å and this second situation was found to be the most probable in terms of energy and stability.



For **20a** and **27a** very stable geometries, represented in Figures 23 and 24, were determined by calculation. For **20a**, two interactions between the two hydrogen atoms of the

diethylammonium cation and the two iodide atoms belonging to the Rh anionic moiety have been found (2.43 Å, 2.51 Å). For **27a**. The Li⁺ cation interacts with both [RhI₂(CO)₂]⁻ iodine atoms (2.57 Å).

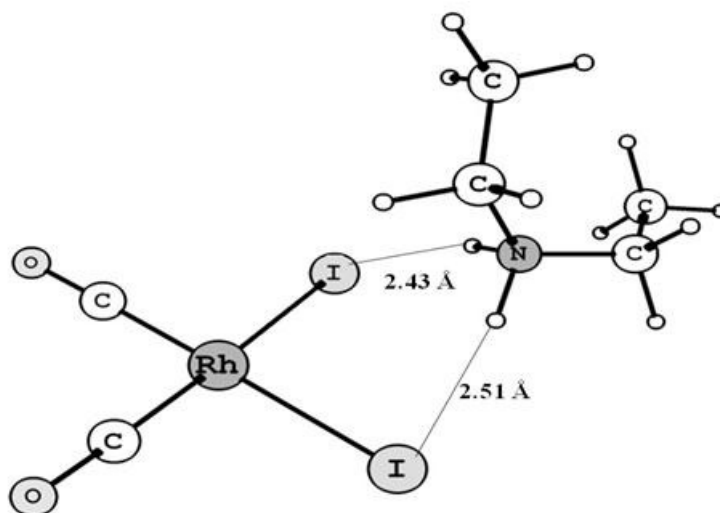


Figure 23. DFT calculation for **20a**.

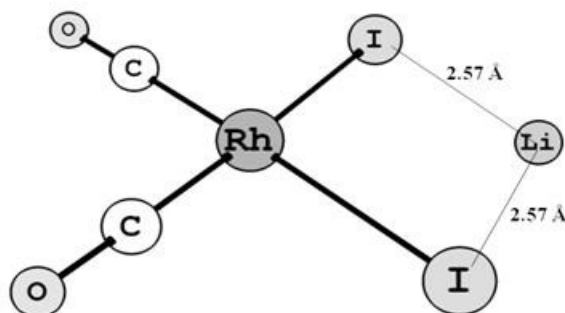


Figure 24. DFT calculation for **27a**.

These modeling DFT studies give more insight on the behavior of cations towards their anionic pair in solution. The results seem once again consistent with preceding data and it is clear that small cations bearing acidic hydrogen substituents interact with iodine atoms.

III-7-6 RT ^1H and $^{13}\text{C}\{^1\text{H}\}$ NMR characterization of **11a-27a**

The RT ^1H and $^{13}\text{C}\{^1\text{H}\}$ NMR data are consistent with the molecular X-ray structures described above. The $^{13}\text{C}\{^1\text{H}\}$ NMR spectra for **11a-27a** feature one sharp doublet present in the carbonyl region in the range 182.7-183.8 ppm and $^1J_{\text{CO-Rh}}$ coupling constants measured in the range 70.5-73.0 Hz.^{25,15} These data are displayed in Table 7 (See chapter V for experimental details).

Table 7. $^{13}\text{C}\{^1\text{H}\}$ NMR data for *cis*-[C][RhI₂(CO)₂] **11a-27a** complexes at 298 K.

<i>Entries</i>	$\delta(^{13}\text{CO})$ (ppm)	$^1J_{(\text{CO-Rh})}$ (Hz)	<i>Entries</i>	$\delta(^{13}\text{CO})$ (ppm)	$^1J_{(\text{CO-Rh})}$ (Hz)
11a	183.0 (d)	71.2	19a	183.1 (d)	73.0
12a	183.3 (d)	72.2	20a	182.7 (d)	73.0
13a	183.3 (d)	71.8	21a	182.9 (d)	72.1
14a	183.5 (d)	72.1	23a	183.3 (d)	71.7
15a	183.3 (d)	72.5	24a	183.3 (d)	71.7
16a	183.4 (d)	71.7	25a	183.3 (d)	72.1
17a	183.4 (d)	70.5	27a	182.4 (d)	73.0
18a	183.8 (d)	72.1			

III-7-7 Conductivity measurements for selected complexes **15a-20a** and **27a**

For further characterization, the measurement of the electrical conductivity for ionic rhodium salt solutions in methanol at 298 K is shown in Figure 26. The measurements were carried out at diluted Rh concentrations ($< 1.10^{-3}$ mol.L⁻¹) so that ion-pairing interactions did not occur. Indeed, the solution conducts electricity through motion of the ions under the effect of an electric field. At high concentrations, each ion is surrounded by other ions, both positive and negative. The electric field, affecting any particular ion, can change slightly due to surrounding ions. In our case, at infinite dilution, the distance between nearest neighbor ions is large, and only the effect of the applied electric field is felt by individual ions. The linear

plots (Figure 25) obtained as a function of concentration confirm that complete ion dissociation is reached and that in the case of dilute solutions, there is no effect of the surrounding ions on the mobility of any given ion. For ions with a single charge, the equivalent conductivity is equal to the molar conductivity Λ_m , obtained by dividing the conductivity by its molar concentration c as following: $\Lambda_m = \sigma / c$. The molar ionic conductivity of a solution is then given by the molar conductivities of the anion and the cation: $\Lambda_m = \Lambda_{m+} + \Lambda_{m-}$.²⁶

For **15a-20a**, **27a** and ammonium or lithium iodide salts, Λ_m corresponding values were determined by the slopes of the plots in Figures 25 and 26, respectively. Λ_m values are reported in Table 8.

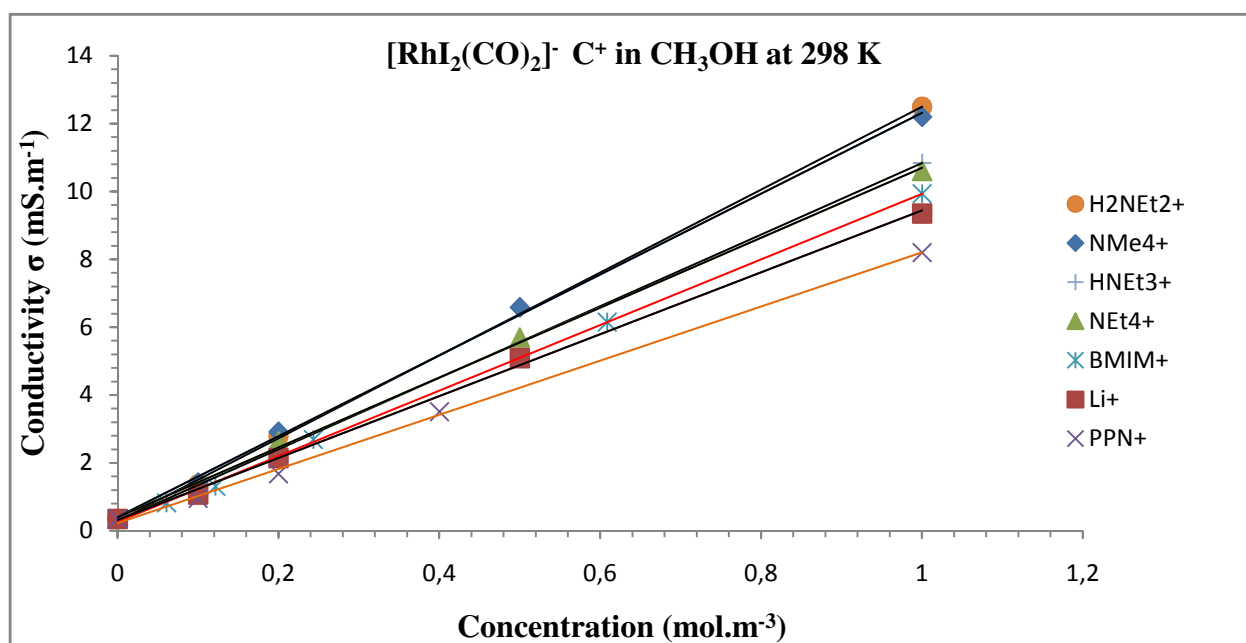


Figure 25. Conductivity as a function of concentration for **15a-20a** and **27a**.

The measurement in methanol at 298 K of the electrical conductivity for ionic iodide organic salt precursor solutions (Figure 26) allowed to obtain the respective ionic

conductivities of each single ions from which $[\text{Cl}^-]$ and $[\text{I}^-]$ conductivity values were found in the literature^{26,27} (Table 9).

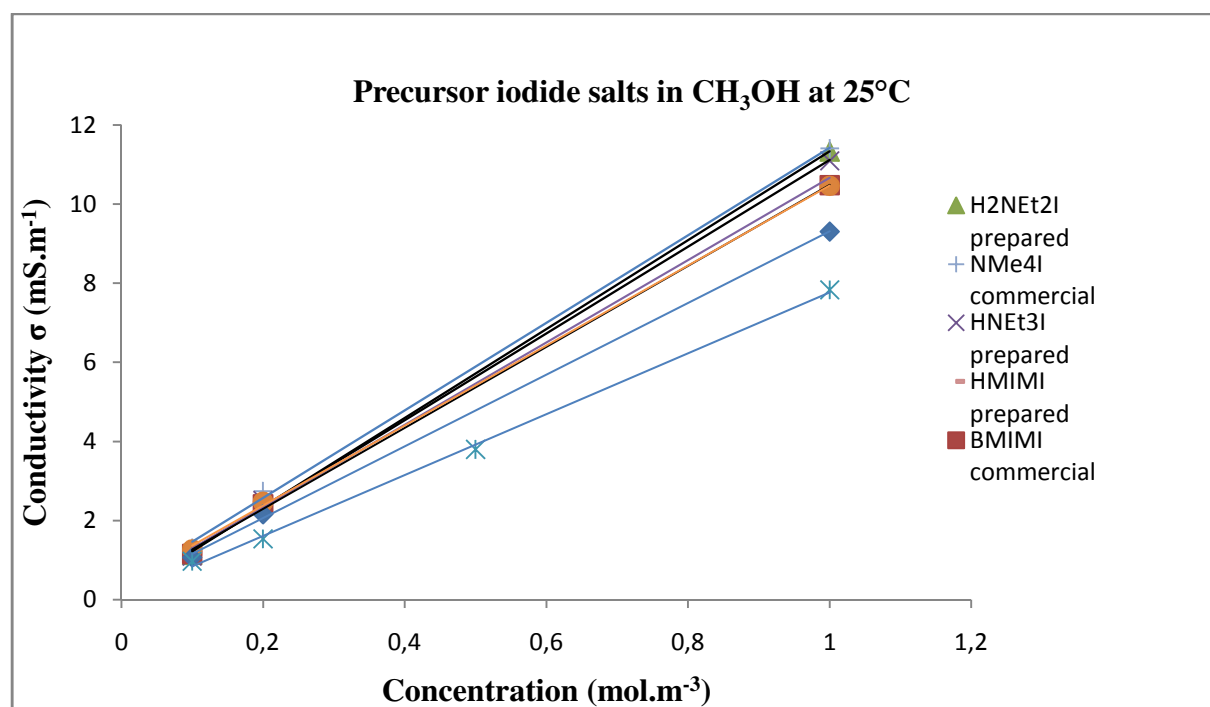


Figure 26. Conductivity as a function of concentration for precursor Cl iodide salts at 298 K.

This method finally permitted to estimate the single molar conductivity of the anion $[\text{RhI}_2(\text{CO})_2]^-$ for which $\Lambda_m([\text{RhI}_2(\text{CO})_2]^-) \sim 6.30 \cdot 10^{-3} \text{ S} \cdot \text{m}^2 \cdot \text{mol}^{-1}$.²⁸

Table 8. Ionic conductivities of selected salts in methanol at 298 K. Values read from plot slopes.

Precursor salts	$\Lambda_m (\text{S} \cdot \text{m}^2 \cdot \text{mol}^{-1}) \times 10^3$	Rh salts	$\Lambda_m (\text{S} \cdot \text{m}^2 \cdot \text{mol}^{-1}) \times 10^3$
[PPN][Cl]	7.70	[PPN][RhI ₂ (CO) ₂]	7.98
[BMIM][I]	10.24	[BMIM][RhI ₂ (CO) ₂]	9.68
[Li][I]	9.06	[Li][RhI ₂ (CO) ₂]	9.13
[H ₂ NEt ₂][I]	11.23	[H ₂ NEt ₂][RhI ₂ (CO) ₂]	12.21
[HNEt ₃][I]	10.96	[HNEt ₃][RhI ₂ (CO) ₂]	10.55
[NEt ₄][I]	10.12	[NEt ₄][RhI ₂ (CO) ₂]	10.30
[NMe ₄][I]	11.06	[NMe ₄][RhI ₂ (CO) ₂]	11.91

Table 9. Ionic conductivities of selected ions in methanol at 298 K. Values determined from corresponding salt conductivities (Table 8) and $[\text{Cl}^-]$, $[\text{I}^-]$ (literature).

<i>Cations/Anions</i>	$A_m (\text{S.m}^2.\text{mol}^{-1}) \times 10^3$	$\frac{[\text{RhI}_2(\text{CO})_2]^-}{A_m (\text{S.m}^2.\text{mol}^{-1}) \times 10^3}$
$[\text{PPN}^+]$	2.49	5.49
$[\text{BMIM}^+]$	3.98	5.70
$[\text{Li}^+]$	2.80	6.32
$[\text{H}_2\text{NEt}_2^+]$	4.97	7.24
$[\text{HNEt}_3^+]$	4.70	5.85
$[\text{NEt}_4^+]$	3.86	6.43
$[\text{NMe}_4^+]$	4.80	7.11
$[\text{Cl}^-]^{26}$	5.21	-
$[\text{I}^-]^{26}$	6.26	-
Average	-	6.31

The following equation (Eq. 1) relates conductivity to many other properties:²⁹

$$\sigma = (\alpha.F^2.d) / (6\pi.N_A.M_W.\eta).[(\zeta_a.r_a)^{-1} + (\zeta_c.r_c)^{-1}] \quad (\text{Eq. 1})$$

where is found: Viscosity (η), molar weight (M_W), Avogadro constant (N_A), Faraday constant (F), density (d), degree of ion dissociation ($0 < \alpha < 1$), anion and cation radii (r_a , r_c , respectively) and corrected microviscosity factor for the anion and cation (ζ_a , ζ_c , respectively).

The initial expectation was to think that the higher the conductivity values are, the more the ions are dissociated and the better the electric current flows through. For **15a-20a** and **27a**, conductivity measurements of each Rh salt constitute a method to probe and compare the behavior of the cations towards the $[\text{RhI}_2(\text{CO})_2]^-$ anion. The following order appears with increasing conductivity values:

$$\sigma \{[\text{PPN}][\text{RhI}_2(\text{CO})_2]\} < \sigma \{[\text{Li}][\text{RhI}_2(\text{CO})_2]\} < \sigma \{[\text{BMIM}][\text{RhI}_2(\text{CO})_2]\} < \sigma \{[\text{NEt}_4][\text{RhI}_2(\text{CO})_2]\} < \sigma \{[\text{HNEt}_3][\text{RhI}_2(\text{CO})_2]\} < \sigma \{[\text{NMe}_4][\text{RhI}_2(\text{CO})_2]\} < \sigma \{[\text{H}_2\text{NEt}_2][\text{RhI}_2(\text{CO})_2]\}$$

Conductivity is temperature dependant and increases with temperature (roughly proportional).²⁶ Experiments were also carried out at different temperatures and the same order as above was found. Under diluted working conditions, the viscosity parameter can be neglected; however molecular weight and ion size have a considerable importance.³⁰ The above order follows roughly the cation molecular weight except for lithium. For the small sized ammonium cations, methanol presumably solvates and dissociates the ions resulting in higher conductivity whereas for heavier and larger cations (BMIM⁺, PPN⁺), methanol solvates less so that σ decreases. Additionally, for BMIM⁺ and PPN⁺, the electronic delocalization along the aromatic rings attenuates somewhat the electronic charge which may also result in weaker conductivity. As for Li⁺ (in red for the above σ order), the very small size and located electronic charge may considerably favor strong methanol solvation resulting in altered size ion and therefore in a weaker than expected conductivity value.

Along with characterization, the other target of a conductivity study was to determine the degree of ion dissociation α in order to predict the concentration range of most intense ion-pairing interaction occurring for our Rh salts. For this purpose, a combination of diffusion ordered NMR spectroscopy (DOSY-NMR) and electric conductivity measurements was to be applied. DOSY-NMR is a powerful tool to determine the self-diffusion coefficients of the cation and anion in salts (D⁺ and D⁻) and was recently applied to several ionic liquids.³¹ From the fact that anion and cation have self-diffusion coefficients in the same order of magnitude one can conclude that they either diffuse independently from each other but with the same velocity (which is rather unlikely due to their different size and shape) or that they form an ion pair. From the self-diffusion coefficients and the conductivity data, it is possible to calculate the degree of dissociation α using a modified Stokes-Einstein equation (Eq. 2)^{31b} as following:

$$\sigma = (N.e^2/k.T).(D^+ + D^-).\alpha \quad (\text{Eq. 2})$$

for which σ is the conductivity, N the cations per volume, e the electric charge, D^+/D^- the self-diffusion coefficients and α the degree of dissociation.

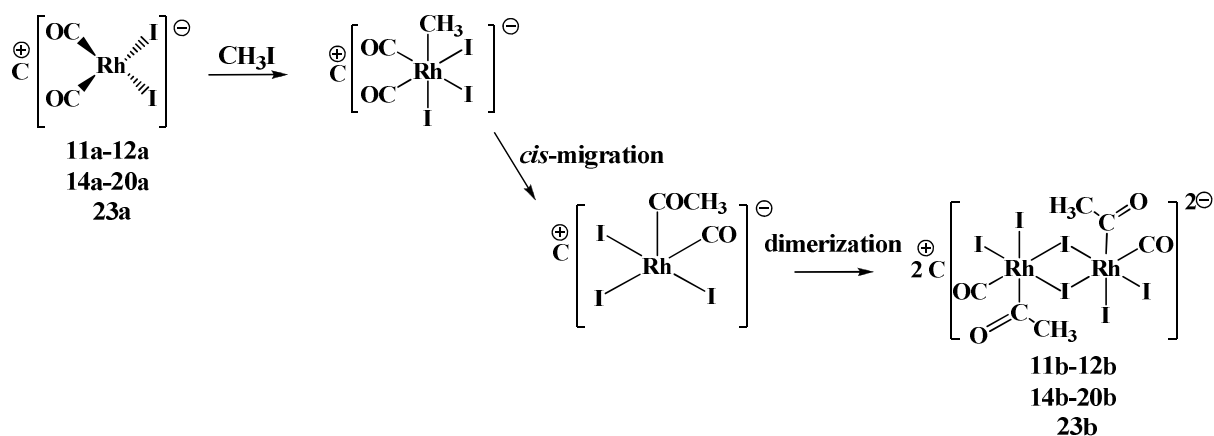
It should be mentioned here that the so-called degree of dissociation is not a measure of the number of ion pairs in solution, but reflects the organization of cations and anions. The smaller the value of α , the better ordered are the ions of the whole system. Unfortunately, our attempts to reach our goal were unsuccessful when it came to self-diffusion coefficient determination via DOSY-NMR. Indeed, the D^- values in our case were only possibly determined throughout $^{13}\text{C}\{^1\text{H}\}$ DOSY-NMR experiments as ^{13}C is the only viable magnetically active nuclei on the anionic $[\text{RhI}_2(^{13}\text{CO})_2]^-$ moiety. Very few $^{13}\text{C}\{^1\text{H}\}$ DOSY-NMR experiments have been reported in the literature.^{32,21a} During the $^{13}\text{C}\{^1\text{H}\}$ DOSY-NMR experiment a long scanning period is necessary and in our case, convection currents caused by small temperature gradients within the sample occurred, resulting in inaccurate self-diffusion values. One solution to the convection problem for the future, involves the use of a coaxial insert inside a normal 5 mm NMR tube. The inner and outer tubes are separated by a pyrex space. A space of *ca.* 2 mm is left between both tubes at the bottom.³²

III-8 Study of anionic Rh(I) complexes towards CH_3I oxidative addition

III-8-1 *Synthesis and characterization of anionic Rh(III) complexes*

Selected complexes **11a**, **12a**, **14a-20a** and **23a** have been evaluated for CH_3I oxidative addition reaction as previously done in chapter II for neutral complexes **4**. The reaction of **11a**, **12a**, **14a-20a** and **23a** with neat CH_3I at RT afforded the corresponding

anionic dimeric iodo-bridged Rh(III)-acetyl complexes $[C]_2[Rh(\mu-I)_2(COMe)(CO)]_2$ **11b**, **12b**, **14b-20b** and **23b** (Scheme 10).³³



Scheme 10. Synthesis of dianionic dimeric $[C]_2[Rh(\mu-I)_2(COCH_3)(CO)]_2$ complexes.

FT-IR data of **14b-20b** and **23b** in CH_2Cl_2 and neat CH_3I are summarized in Table 10.

Table 10. FT-IR carbonyl stretching frequencies for **14b-20b** and **23b** at RT.

Complexes	CH_2Cl_2		CH_3I	
	$\nu(CO) (cm^{-1})$	$\nu(COMe) (cm^{-1})$	$\nu(CO) (cm^{-1})$	$\nu(COMe) (cm^{-1})$
14b	2079.5	1737.1; 1720.4	2073.2; 2063.5	1737.7; 1719.6
15b	2076.4; 2064.3	1722.0	-	-
16b	2070.1	1719.6	2076.6; 2065.8	1736.0; 1720.2
17b	2078.1; 2049.3	1739.6; 1736.4	2074.5; 2059.7	1738.0; 1728.8
18b	2074.8; 2063.7	1736.5; 1714.8	2071.6; 2057.3	1735.7; 1715.3
19b	2075.3	1738.7; 1722.4; 1717.9	2077.2; 2066.6	1737.0; 1727.0
20b	-	-	2079.1; 2068.3	1739.9; 1733.1
23b	2065.8	1738.4; 1719.9	-	-

FT-IR spectra of the anionic dimeric Rh(III) complexes showed a large and intense terminal ν_{CO} band at $\sim 2074 \text{ cm}^{-1}$, i.e. 48 cm^{-1} higher in frequency than the $\nu_{CO, av}$ of the corresponding starting Rh(I) complexes **14b-20b** and **23b**, which is consistent with a

[Rh(III)]-carbonyl fragment. In addition, a broad medium ν_{COMe} acetyl band appeared at $\sim 1725 \text{ cm}^{-1}$.³³

The ^1H and $^{13}\text{C}\{^1\text{H}\}$ NMR for **14b-20b** and **23b** identified the acetyl group with the proton signals at $\delta \sim 3.1$ ppm and the methyl carbon signal at $\delta \sim 48.0$ ppm. The $^{13}\text{C}\{^1\text{H}\}$ NMR spectra in the carbonyl region exhibited a group of signals centered at $\delta \sim 212$ ppm which was assigned to [Rh]-COCH₃ and another group centered at higher field $\delta \sim 183$ ppm which was attributed to the terminal [Rh]-CO ligand. $^{13}\text{C}\{^1\text{H}\}$ NMR signals in the carbonyl region were not in all cases detected because synthesis was carried out with unlabeled ^{13}CO Rh(I) precursors and NMR scanning periods were not always sufficient. It is important to mention that many isomers are suspected to co-exist in solution for these type of dianionic dimeric Rh(III) species.³³ $^{13}\text{C}\{^1\text{H}\}$ NMR spectrum for **15b** complex is represented in Figure 27 as an illustrative example.

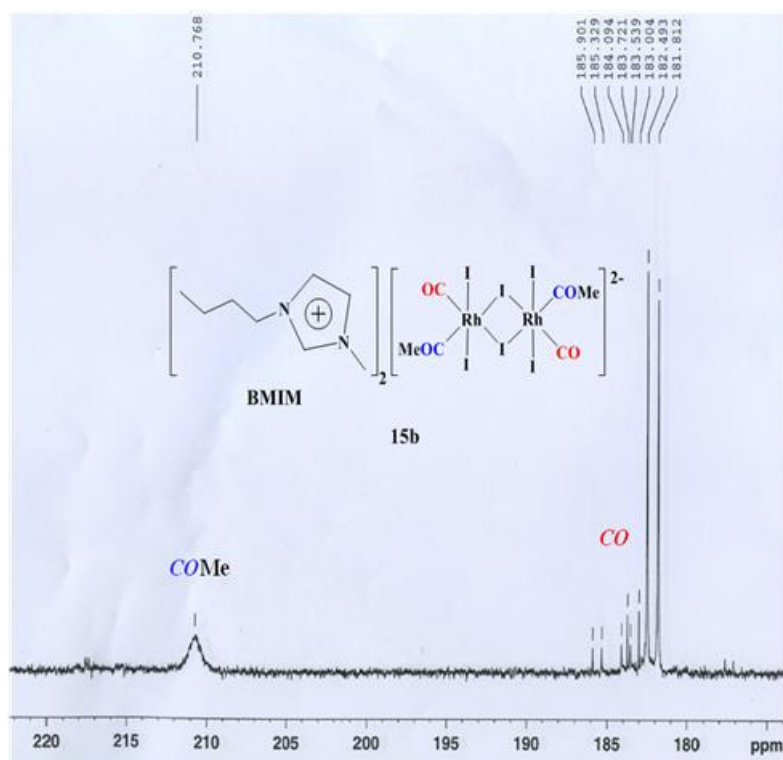


Figure 27. $^{13}\text{C}\{^1\text{H}\}$ NMR spectrum in the CO region at 298 K in CD_2Cl_2 for **15b**.

III-8-2 IR-monitored kinetic study for **14a**, **16a** and **18a-20a** towards CH_3I

In order to investigate the effect of ion-pairing interaction towards methyl iodide oxidative addition, IR-monitored kinetic studies were performed in neat CH_3I on selected anionic Rh(I) salts. Indeed, complexes **14a**, **16a**, and **18a-20a** are roughly comprised in the range (weak/high electron density brought to the Rh metal center in CH_2Cl_2) for the series of salts studied and methyl iodide is a reasonably apolar solvent which conserves the ion-pairing trend observed in CH_2Cl_2 (see Table 11). The working and operating conditions were the same as those previously described for the study on neutral complexes **4** in chapter II ([Rh-complex] = 17 mmol.L⁻¹).

An example of 3D stacking FT-IR spectra registered overtime (every one minute) in the 2200-1600 cm⁻¹ region for **18a** (PPN⁺) is displayed in Figure 28. It shows the decay of the initial characteristic bands for **18a** at 2051.2 and 1979.2 cm⁻¹ followed by the appearance of the ν_{CO} bands at 2071.6, 2057.3 cm⁻¹ and ν_{COMe} at 1735.7, 1715.3 cm⁻¹ for **18b**. Contrarily to the results observed in chapter II, the intermediate methyl-Rh(III) $[\text{RhI}_3(\text{CH}_3)(\text{CO})_2]^-$ species was also detected in very small quantities at the very beginning of IR-monitoring for **18a** (PPN⁺) with a ν_{CO} band at ~ 2096 cm⁻¹ (Figure 27) and very slightly detected for **16a** (NMe₄⁺) with a ν_{CO} band at ~ 2093 cm⁻¹ (Figure 29).^{25a} It is noteworthy that for the intermediate complex $[\text{RhI}_3(\text{CH}_3)(\text{CO})_2]^-$ only one band has been detected when two could be expected. This second band would be expected to appear at ~ 2023 cm⁻¹ and therefore possibly masked by the much more intense band of the Rh(I) **18a** starting complex or hidden by the baseline. The other possible explanation is that $[\text{RhI}_3(\text{CH}_3)(\text{CO})_2]^-$ CO ligands are in a *trans* configuration to one another which would result in one single ν_{CO} IR band.^{25a}

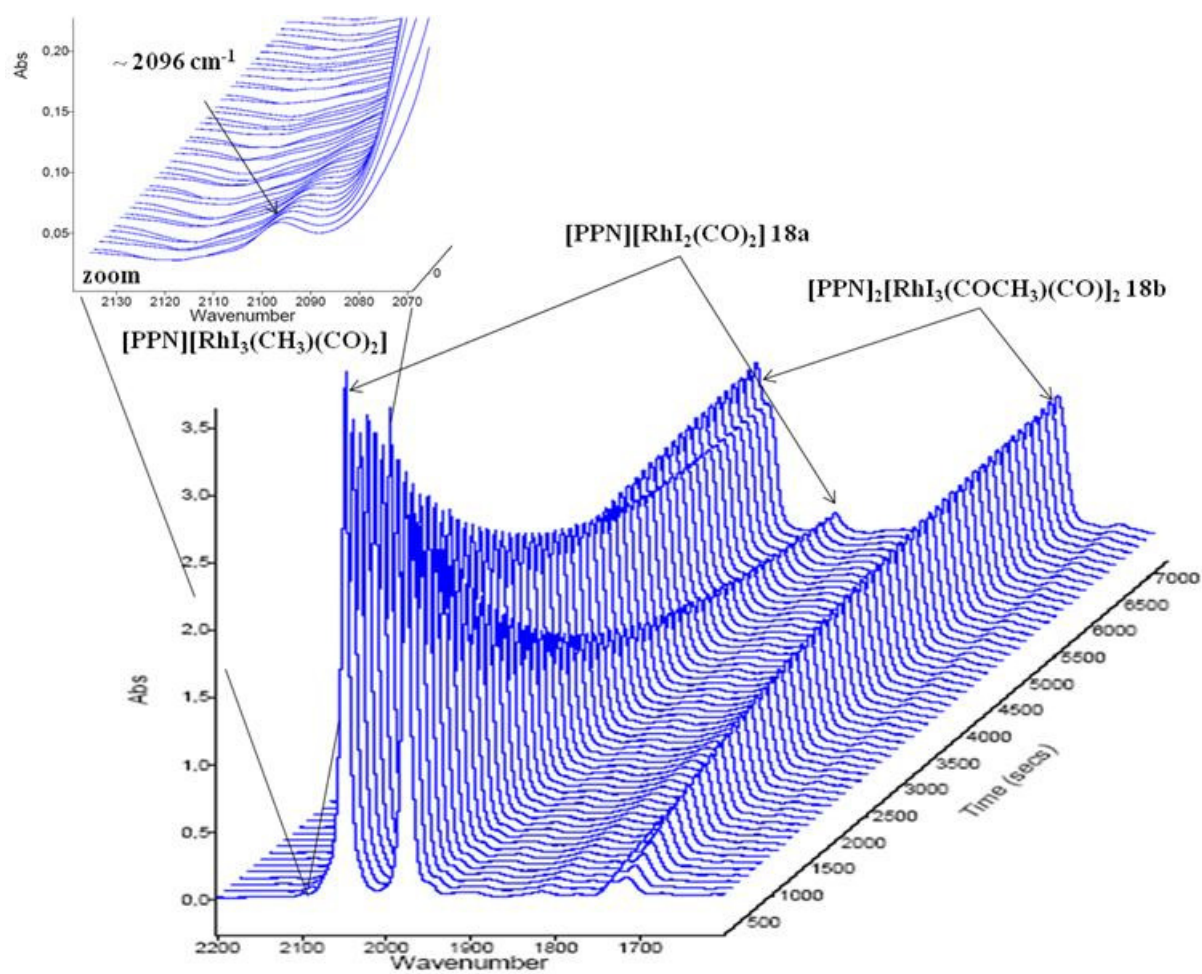


Figure 28. Series of FT-IR spectra for the reaction of **18a** with neat CH_3I at 298 K (17 mmol.L⁻¹) affording **18b** via the Rh(III)-methyl species.

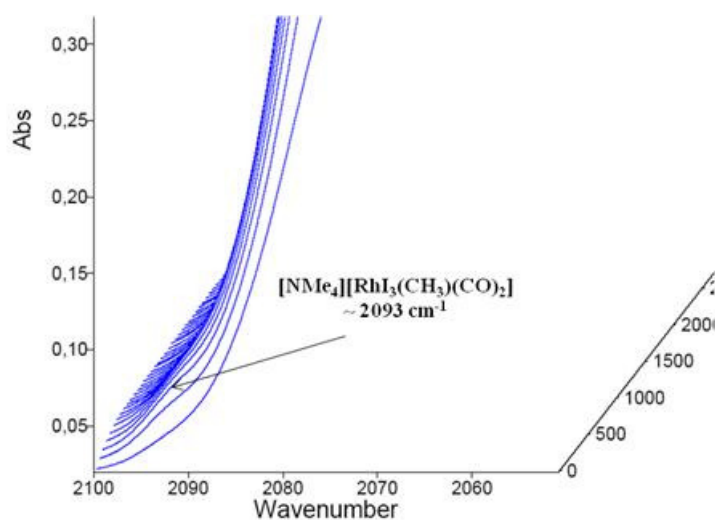


Figure 29. Detection of Rh(III)-methyl species in the case of **16a**.

The observation of the Rh(III)-methyl intermediate for **16a** and **18a** is explained by a similar nucleophilicity of the Rh metal towards the electrophilic carbon atom of CH₃I during the oxidative addition step in comparison to the neutral complexes **4**, yet a slightly slower *cis* CO-migration step occurs due to more strongly stabilized Rh-CO bond.

Under our working conditions and in the temperature range 298-338 K, the Rh(III)-methyl species were very present at a very low level (expanded ~ x70) and only for **16a**, **18a**. Therefore, these intermediate species were not taken into account for kinetic parameter determination. As in the previous study in chapter II, overall kinetic activation parameters have been determined taking only into account the disappearance of the ν_{CO} stretching bands of the Rh(I) starting complexes. Complete transformation of the anionic Rh(I) **a** salts into the final dimer anionic Rh(III) **b** species was achieved in ~ 2 hours for all studied complexes **14a**, **16a**, and **18a-20a**, which is much faster than what was found for neutral complexes **4** except for **4a**. Carbonyl infrared data in neat CH₃I, rate constants at 298 K ($k_{298\text{K}}$) and activation parameter values (E_a , ΔH^\ddagger , ΔS^\ddagger) for overall CH₃I oxidative addition reaction on **14a**, **16a**, and **18a-20a** are reported in Table 11. In addition, Figure 30 illustrates the different E_a values represented by the slopes of the different plots for **14a**, **16a**, and **18a-20a**.

Table 11. Reaction rate constants $k_{298\text{K}}$ and activation parameters for the overall CH₃I oxidative addition reaction on **14a**, **16a**, and **18a-20a**.

Entry	IR ν_{CO} (cm^{-1})	$\nu_{\text{av}}(\text{CO})$ (cm^{-1})	$k_{298\text{K}}$ (s^{-1}) $\times 10^5$	E_a (KJ.mol^{-1})	ΔH^\ddagger (KJ.mol^{-1})	ΔS^\ddagger ($\text{J.K}^{-1}.\text{mol}^{-1}$)
14a	2056.2; 1984.4	2020.3	107.06 \pm 2.1	58.0 \pm 0.6	55.4 \pm 1.1	-115 \pm 2.3
16a	2058.8; 1987.5	2023.2	93.14 \pm 1.9	56.1 \pm 0.6	53.5 \pm 1.1	-124 \pm 2.5
18a	2051.2; 1979.2	2015.2	40.00 \pm 0.8	64.7 \pm 0.6	61.9 \pm 1.2	-102 \pm 2.0
19a	2062.4; 1993.6	2028.0	35.58 \pm 0.7	86.7 \pm 0.9	84.1 \pm 1.7	-29 \pm 0.6
20a	2065.8; 2001.2	2033.5	38.58 \pm 0.8	69.2 \pm 0.7	66.7 \pm 1.3	-87 \pm 1.7

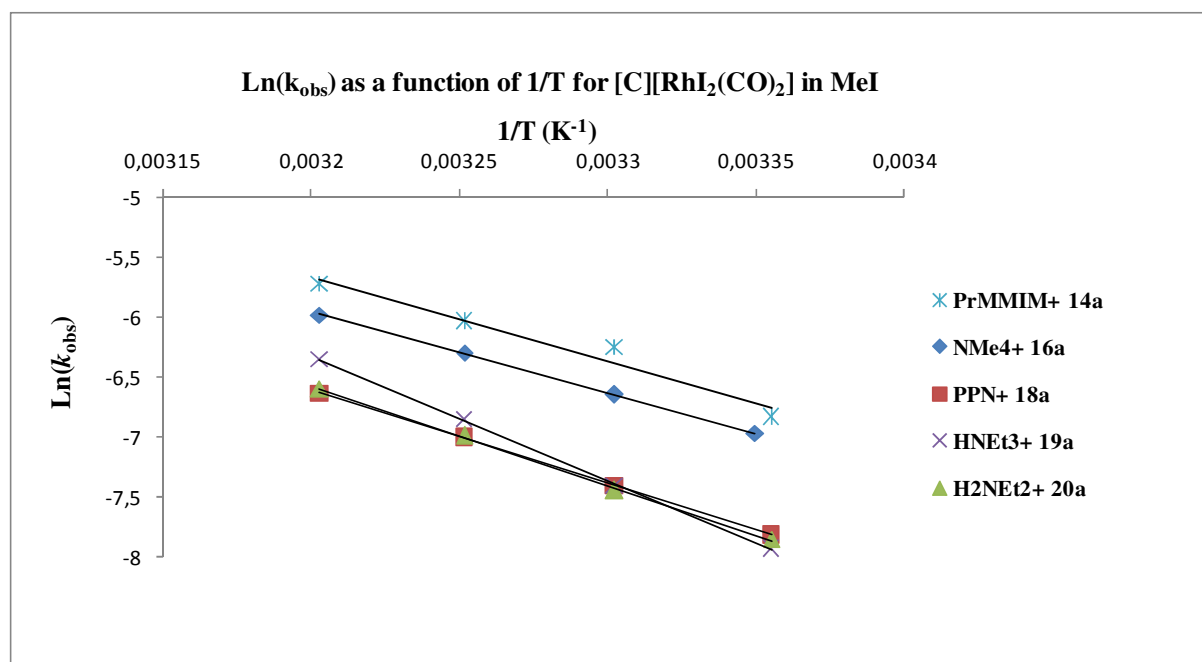


Figure 30. Kinetic data summary: E_a determination for **14a**, **16a**, and **18a-20a**.

Apart from **18a**, the k_{298} rate values for the CH_3I oxidative addition on **14a**, **16a**, and **18a-20a** complexes followed by CO *cis* migratory insertion, follow the nucleophilic character of the Rh metal center brought by the electron density, which has been gauged by the FT-IR CO stretching band shifts. Activation energies are also consistent with the kinetic rates determined. Complexes **14a** and **16a** share similar behavior in terms of electronic density and reactivity towards methyl iodide with $k_{298} = 107.1 \times 10^{-5}$ and $93.1 \times 10^{-5} s^{-1}$, respectively. **19a** and **20a** are slower with $k_{298} = 35.6 \times 10^{-5}$ and $38.6 \times 10^{-5} s^{-1}$, respectively. Complex **18a** is situated in between with $k_{298} = 40.0 \times 10^{-5} s^{-1}$, although according to the FT-IR data, we were expecting the fastest reactivity. According to the previous observation made for **18a**, for which the intermediate Rh(III)-methyl species was detected, we believe that the CO *cis* migratory insertion retards the overall reactivity and may be one of the reasons for this unexpected result. It is noteworthy that **19a** exhibits a higher activation energy of 86.7 KJ.mol^{-1} (Figure 30) in comparison with the other complexes. This may be due to the $HNEt_3^+$ position regarding $[RhI_2(CO)_2]^-$ in solution, for which previous DFT models showed two different possibilities (see § V-2-3). If the two proposed geometries (one with a H-interaction

on the Rh center and the other with a H \cdots I interaction) coexist during the methyl iodide nucleophilic attack, overall reaction kinetic rate and activation energy may be impacted, especially due to the fact that the models suggest the cation to be in an upright position regarding the *cis*-[RhI₂(CO)₂]⁻ square planar plane. Moreover, it can be assumed that in this context, the rather bulky ethyl groups belonging to HNEt₃⁺ cramps the attack towards CH₃I.

In summary, this study on [cation]^{+ \cdots} [RhI₂(CO)₂]⁻ behavior shows that throughout electronic features, the nature of the cation involved does impact reactivity towards methyl iodide oxidative addition/CO *cis*-migratory insertion steps. The nature of the interaction between the ions is difficult to define; a protonated type cation is suspected to interact via H-bonding whereas an unprotonated cation interacts throughout exclusive electrostatic Coulombic forces, consistent with the strict ion-pairing definition. Furthermore, the size of the cation may influence the nature of the electrostatic interaction and is not to be excluded. Finally, although this fundamental coordination chemistry study focused on one step of the methanol carbonylation, the aim is to gain insight on the behavior of Rh-salt species interacting together in the catalytic medium and investigate on the impact of an iodide salt promoter in terms of reactivity. The catalytic reaction medium is a fairly complex mixture of different solvents, which makes the study more challenging, as we have shown that the nature of the solvent also strongly impacts ion interactions.

III-9 Lithium iodide effect on *cis*-[RhI₂(CO)₂]⁻

This next section is devoted to a very short study on cation-anion interaction for the specific case of anionic Rh(I) [Li] *cis*-[RhI₂(CO)₂] complex **27a**, which is the main active species for the Celanese AO process. Indeed, as it has already been described in chapter I, LiI acts as a reaction promoter and evidence has been presented that it promotes also the CH₃I oxidative addition step.^{15,16a,34} The precise mechanism of this promotion remains unclear;

formation of a highly nucleophilic dianion, $[\text{RhI}_3(\text{CO})_2]^{2-}$, has been suggested, although there is no direct spectroscopic evidence for its detection. The possible participation of this dianion has been considered in a theoretical study.³⁵ An alternative nucleophilic dianion, $[\text{RhI}_2(\text{CO})_2(\text{OAc})]^{2-}$, has also been proposed^{3b,3c} on the bases that acetate salts (either added or generated *in situ* via Eq. 3) can promote the carbonylation.



In this context, to further investigate on the possible formation of this dianionic $[\text{RhI}_3(\text{CO})_2]^{2-}$ species, complex $^{13}\text{C}\text{-27a}$ was $^{13}\text{C}\{^1\text{H}\}$ NMR-monitored at 298 K in CD_3OD with 25 μL TMS as internal reference for a series of NMR experiments with samples containing increasing amounts of LiI. Figure 31 illustrates the plot $[\text{LiI}] = f(\delta_{\text{CO}})$. The $^{13}\text{C}\{^1\text{H}\}$ NMR $[\text{Rh}]\text{-CO}$ carbonyl chemical shifts have been plotted as a function of LiI salt concentration. The $^{13}\text{C}\{^1\text{H}\}$ NMR stacking spectra in the carbonyl region of four selected experiments (samples 3, 6, 8 and 10) are represented in Figure 32.

Table 12. $^{13}\text{C}\{^1\text{H}\}$ NMR data for $[\text{LiI}] = f(\delta_{\text{CO}})$ in CD_3OD at 298 K.

2/LiI molar eq.	δ CO (ppm)	$^1J_{\text{Rh-CO}}$ (Hz)	δ CO (ppm) TMS correction
Sample1 2eq: 27a	183.68	71.70	185.01
Sample2 4eq	183.67	71.77	184.96
Sample3 5eq	183.67	71.70	184.96
Sample4 10eq	183.64	71.70	184.82
Sample5 15eq	183.62	71.70	184.70
Sample6 25eq	183.56	71.55	184.38
Sample7 30eq	183.52	70.79	184.24
Sample8 35eq	183.51	70.72	184.09
Sample9 45eq	183.41	62.04	183.66
Sample10 55eq	183.36	58.94	183.54

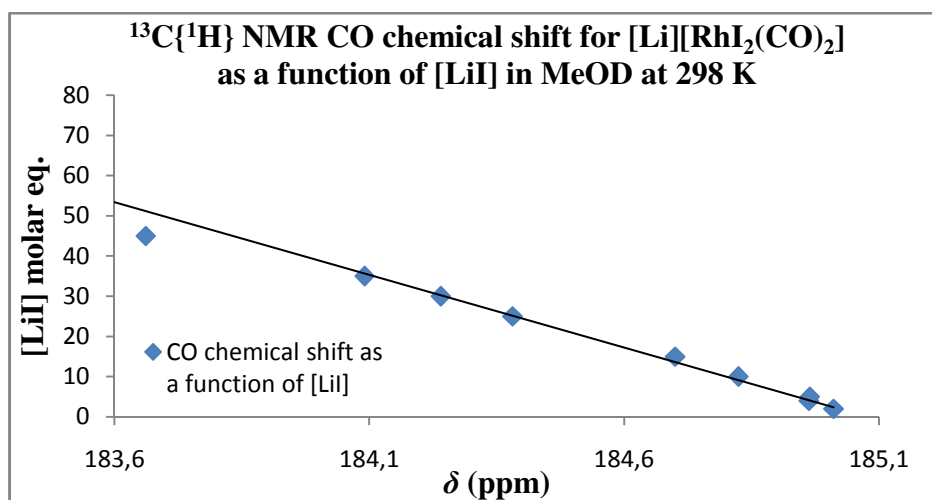


Figure 31. $[\text{LiI}] = f(\delta_{\text{CO}})$ plot for **27a** in CD_3OD at 298 K.

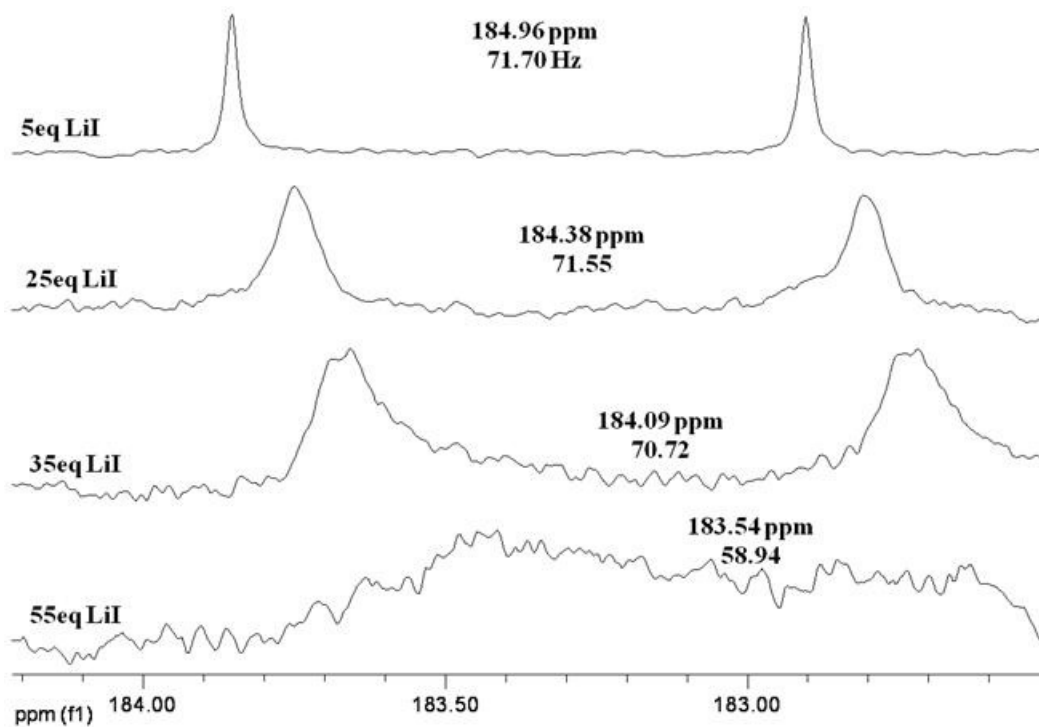


Figure 32. $^{13}\text{C}\{^1\text{H}\}$ NMR stacking spectra in the carbonyl region for **27a** + 5 eq LiI, 25 eq LiI, 35 eq LiI and 55 eq LiI at 298 K in CD_3OD .

In a range going from 2 to 55 molar equivalent of LiI regarding the dimeric precursor $^{13}\text{CO-2}$, the sharp [Rh]-CO associated doublet for **27a** (2 eq. LiI) resonated at δ 185.0 ppm with a coupling constant of $^1J_{\text{CO-Rh}} = 71.7$ Hz (CD_3OD). At 55 molar eq. of LiI, the initial doublet for **27a** broadened and was shifted to higher field at δ 183.5 ppm with a smaller coupling constant of $^1J_{\text{CO-Rh}} = 58.9$ Hz. This species could be suspected to be the dianionic $[\text{RhI}_3(\text{CO})_2]^{2-}$ complex. However, at 55eq LiI ($^{13}\text{CO-2}$:30 mg/LiI:386.4 mg) in a 0.5 mL NMR tube, the solution is highly saturated by LiI and solubility concerns explain the very broad signal obtained. A general salt effect provided by high LiI salt concentration in solution causing a chemical shift on **27a** cannot be excluded. It would be interesting to try and confirm this result by carrying out the same NMR experiment using poorly coordinating salts such as LiBF_4 or LiCF_3SO_3 and detect if they have an effect on the rhodium anion.¹

III-10 Conclusion

Batch experiments supported by *in situ* VT-HP-NMR experiments have shown that neutral complexes **4** were unlikely to run in the methanol carbonylation working conditions and were strongly affected by the highly acidic medium which resulted mainly in the formation of the anionic $[\text{RhI}_2(\text{CO})_2]^-$ active species. The neutral complexes **4** processed via their N-ligand decoordination followed by quaternization either by a proton (HI) or by a methyl group (CH_3I) according to the temperature. However, at this stage, batch experiments under process conditions have put in evidence complexes bearing pyrazole family ligands revealing better stability, thus not excluding the possibility to have neutral species living in equilibrium with anionic species at high temperatures.⁷ In a further fundamental study focused on $[\text{XNR}_3][\text{RhI}_2(\text{CO})_2]$ (X = H, Me) complexes, the nature of the counter-cation was

investigated and revealed that interactions (ion-pairs or contact H-bonding) occurred and affected the CH₃I oxidative addition rate.

Another type of interaction on complex [RhI₂(CO)₂]⁻ involving LiI or the organic compound AcOH, both largely present in the process medium has been invoked resulting in the possible formation of the pentacoordinated Rh(I) dianionic species [RhI₃(CO)₂]²⁻ or [RhI₂(CO)₂(AcO)]²⁻ due to acetate ions present in the medium. This latter suggestion, related to catalytic working conditions, has led us to a final study dealing with reductive elimination, the last step of the methanol carbonylation reaction, for which experimental and theoretical evidences support a new alternative mechanism.

References

- (1) Torrence, P.; in: Cornils, B.; Herrmann, W. A. (Eds.), *Applied Homogeneous Catalysis with Organometallic Compounds*, second ed., Vol. 1, Wiley-VCH, Weinheim, **2002**, 104.
- (2) Smith, B. L.; Torrence, G. P.; Aguilo, A.; Alder, J. S. US5001259 (to Hoechst Celanese) **1991**.
- (3) (a) Murphy, M. A.; Smith, B. L.; Torrence, G. P.; Aguilo, A. *Inorg. Chim. Acta* **1985**, *101*, L47. (b) Murphy, M. A.; Smith, B. L.; Torrence, G. P.; Aguilo, J. *Organomet. Chem.* **1986**, *303*, 257. (c) Smith, B. L.; Murphy, M. A.; Torrence, G. P.; Aguilo, J. *Mol. Catal.* **1987**, *39*, 115.
- (4) Haynes, A.; McNish, J.; Pearson, J. M. *J. Organomet. Chem.* **1998**, *551*, 339.
- (5) (a) Daly, J. J.; Sanz, F.; Forster, D. *J. Am. Chem. Soc.* **1975**, *97*, 2551. (b) Kumbhar, A. S.; Padhye, S. B.; Puranik, V. G.; Dhaneshwar, N. N.; Tavale, S. S.; Kelkar, A. A.; Chaudhari, R. *J. Mol. Catal.* **1992**, *75*, 187. (c) Heaton, B. T.; Jacob, C.; Moffet, S. *J. Organomet. Chem.* **1993**, *462*, 347.
- (6) (a) Eby, R. T.; Singleton, T. C. *Appl. Ind. Catal.* **1983**, *1*, 275. (b) Singleton, T. C.; Park, L. J.; Forster, D. *Prepr. Am. Chem. Soc. Div. Pet. Chem.* **1979**, *98*, 846. (c) Baker, E. C.; Hendriksen, D. E.; Eisenberg, R. *J. Am. Chem. Soc.* **1980**, *102*, 1020.
- (7) Haynes, A.; Maitlis, P. M.; Stanbridge, I. A.; Haak, S.; Pearson, J. M.; Adams, H.; Bailey, N. A. *Inorg. Chim. Acta* **2004**, *357*, 3027.
- (8) Zoeller, J. R.; Vetter, A. J.; Moore, M. K.; in: *Carbonylation in ionic liquids: Process and mechanism for the carbonylation of methanol to acetic acid using methyl pyridinium iodide and Rh in the absence of added methyl iodide*, ACS National Meeting, 08.28-09.01 **2011**, Embassy Suites Denver.

- (9) (a) Gautron, S.; Lassauque, N.; Le Berre, C.; Azam, L.; Giordano, R.; Serp, P.; Laurency, G.; Daran, J. C.; Duhayon, C.; Thiébaud, D.; Kalck, P. *Organometallics* **2006**, *25*, 5894. (b) Gautron, S.; in: *Nouveau procédé de carbonylation du méthanol en acide acétique catalysée par le système iridium-platine. Etude du mécanisme de la co-catalyse*, PhD manuscript, Paul Sabatier University, Toulouse, **2003**, *Chap. III*, 50.
- (10) Morris, G.; in: *Mechanism in Homogeneous Catalysis. A spectroscopic Approach*, Heaton B. Ed, Wiley-VCH Verlag, Weinheim, **2005**, 195.
- (11) The CO bound/free-exchange on **4d** operates very quickly as shown in: Churlaud R.; Frey U.; Metz, F.; Merbach A. E. *Inorg. Chem.* **2000**, *39*, 304.
- (12) It is admitted that part of the initially loaded free $^{13}\text{CO}/^{12}\text{CO}$ is involved in the exchange process with Rh(I), thus the total amount available is diluted and therefore reducing the ratio of labeled ^{13}CO for complex ^{13}CO -**7d**.
- (13) (a) Guerra, M. K. *Acetic Acid and Acetic Anhydride*, SRI International, Menlo Park, CA, **1994**, Report No. 37B. (b) Anonymous, *Eur. Chem. News* **2000**, Apr, 10. (c) Agreda, V. H. *CHEMTECH* **1992**, 172. (d) Hoechst AG (Erpenbach, H.; Gehrman, K.; Hörstermann, P.), DE 3.429.179 **1984**, EP 0.170.965 **1985**. (e) Hoechst (Kuckerts, H.), DE 24.50.965 **1974**.
- (14) Fulford, A.; Maitlis, P. M. *J. Organomet. Chem.* **1989**, *366*, C20.
- (15) Fulford, A.; Hickey, C. E.; Maitlis, P. M. *J. Organomet. Chem.* **1990**, *398*, 311.
- (16) (a) Hickey, C. E.; Maitlis, P. M.; *J. Chem. Soc. Chem. Commun.* **1984**, 1609. (b) Fulford, A.; Hickey, C. E.; Maitlis, P. M. *Abstr. 6th Intern. Symp. Homogeneous Catalysis*, Vancouver, **1988**, P99.
- (17) (a) Tustin, G. C.; Moncier, R. M. US0212295 (to Eastman Chemical Company) **2003**. (b) Tustin, G. C.; Moncier, R. M. US0212295, US 6,916,951 B2 (to Eastman Chemical Company) **2005**. (c) Tustin, G. C. *Prepr. Pap. Am. Chem. Soc. Div. Fuel. Chem.* **2005**, *50*, 594.

- (18) Serp. P.; Hernandez, M.; Richard, B.; Kalck, P. *Eur. J. Inorg. Chem.* **2001**, 2327.
- (19) Lassauque, N.; in: PhD manuscript, Paul Sabatier University, Toulouse, **2006**, *Chap. II*, 61.
- (20) Lacour, J.; Moraleda, D. *Chem. Commun.* **2009**, 7073.
- (21) (a) Macchioni, A. *Chem. Rev.* **2005**, *105*, 2039. (b) Swarc, M. *Ions and Ion Pairs in Organic Reactions*, Wiley-Interscience: New York, **1972**, Vol. 1. (c) Reichardt, C. *Solvents and Solvent Effect in Organic Chemistry*, Wiley-VCH: Weinheim, **2003**. (d) Swarc, M. *Acc. Chem. Res.* **1969**, *2*, 87. (e) Kraus, C. A. *J. Phys. Chem.* **1956**, *60*, 129. (f) Bjerrum, N. K. *Dan. Vidensk. Selsk. Math. Phys. Medd.* **1926**, *7*, 3. (g) Bjerrum, N. *Chem. Zentralbl.* **1926**, *II*, 1378. (h) Bjerrum, N. *Svensk Kem. Tidskr.* **1926**, *38*, 2. (i) Bjerrum, N. *Chem. Zentralbl.* **1926**, *I*, 2174.
- (22) (a) Yabe, T.; Kochi, J. K. *J. Am. Chem. Soc.* **1992**, *114*, 4491. (b) Ciccotti, G.; Ferrario, M.; Hynes, J. T.; Kapral, R. *Chem. Phys.* **1989**, *129*, 241. (c) Ciccotti, G.; Ferrario, M.; Hynes, J. T.; Kapral, R. *Chem. Phys.* **1990**, *93*, 7137. (d) Nakamura, K. *J. Am. Chem. Soc.* **1981**, *103*, 6973. (e) Jorgensen, W.; Buckner, J. K.; Huston, S. E.; Rossky, P. J. *J. Am. Chem. Soc.* **1987**, *109*, 1891.
- (23) Haynes, A.; Maitlis, P. M.; Quayoum, R.; Pulling, C.; Adams, H.; Spey, S. E.; Strange, R. *W. J. Chem. Soc. Dalton Trans.* **2002**, 2565.
- (24) (a) Andrae, D.; Haussermann, U.; Dolg, M.; Stoll, H.; Preuss, H. *Theor. Chim. Acta* **1990**, *77*, 123. (b) Moritz, A.; Cao, X.; Dolg, M. *Theor. Chem. Acc.* **2007**, *118*, 845. (c) Ehlers, A. W.; Bohme, M.; Dapprich, S.; Gobbi, A.; Hollwarth, A.; Jonas, V.; Kohler, K. F.; Stegmann, R.; Veldkamp, A.; Frenking, G. *Chem. Phys. Lett.* **1993**, *208*, 111. (d) Hehre, W. J.; Ditchfie, R.; Pople, J. A. *J. Chem. Phys.* **1972**, *56*, 2257. (e) Becke, A. D. *J. Chem. Phys.* **1993**, *98*, 5648. (f) Burke, K. P.; Yang, W. *Electronic Density Functional Theory: Recent*

Progress and New Directions, **1998**. (g) Frisch, M. J. et al. *Gaussian 03, Revision B.05*, Gaussian, Inc., Wallingford CT.

(25) (a) Haynes, A.; Mann, B. E.; Morris, G. E.; Maitlis, P. M. *J. Am. Chem. Soc.* **1993**, *115*, 4093. (b) Haynes, A.; Mann, B. E.; Gulliver, D. J.; Morris, G. E.; Maitlis, P. M. *J. Am. Chem. Soc.* **1991**, *113*, 8567. (c) Fulford, A.; Bailey, N. A.; Mann, B. E.; Manuel, C. P.; Spencer, C. M.; Kent, A. G. *J. Chem. Soc. Dalton Trans.* **1988**, 489.

(26) Zoski, G. in: Zoski, G. (Eds.), *Handbook of Electrochemistry*, Elsevier, Amsterdam, **2007**, 867.

(27) Bester-Rogac, M.; Hunger, J.; Stoppa, A.; Buchner, R. *J. Chem. Eng. Data* **2010**, *55*, 1799.

(28) Hagiwara, R.; Ito, Y. *Journal of Fluorine Chemistry* **2000**, *105*, 221.

(29) Bonhôte, P.; Dias, A. P.; Papageorgiou, N.; Kalyanasundaram, K.; Grätzel, M. *Inorg. Chem.* **1996**, *35*, 1168.

(30) Dorbritz, S.; Ruth, W.; Kragl, U. *Adv. Synth. Catal.* **2005**, *347*, 1273.

(31) (a) Schneiders, K.; Bösmann, A.; Schulz, P. S.; Wasserscheid, P. *Adv. Synth. Catal.* **2009**, *351*, 432. (b) Hayamizu, K.; Aihara, Y.; Arai, S.; Garcia Martinez, C.; *J. Phys. Chem. B* **1999**, *103*, 519. (c) Noda, A.; Hayamizu, K.; Watanabe, M. *J. Phys. Chem. B* **2001**, *105*, 4603. (d) Giernoth, R.; Bankmann, D. *Eur. J. Org. Chem.* **2005**, 4529. (e) Nama, D.; Kumar, P. G. A.; Pregosin, P. S.; Geldbach, T. J.; Dyson, P. J. *Inorg. Chim. Acta* **2006**, *359*, 1907. (f) Saito, Y.; Umecky, T.; Niwa, J.; Sakai, T.; Maeda, S. *J. Phys. Chem. B* **2007**, *111*, 11794. (g) Annat, G.; MacFarlane, D. F.; Forsyth, M. *J. Phys. Chem. B* **2007**, *111*, 9018.

(32) (a) Pregosin, P. S.; Kumar, P. G. A.; Fernández, I. *Chem. Rev.* **2005**, *105*, 2977. (b) Pregosin, P. S. *Progress in Nuclear Magnetic Resonance Spectroscopy* **2006**, *49*, 261.

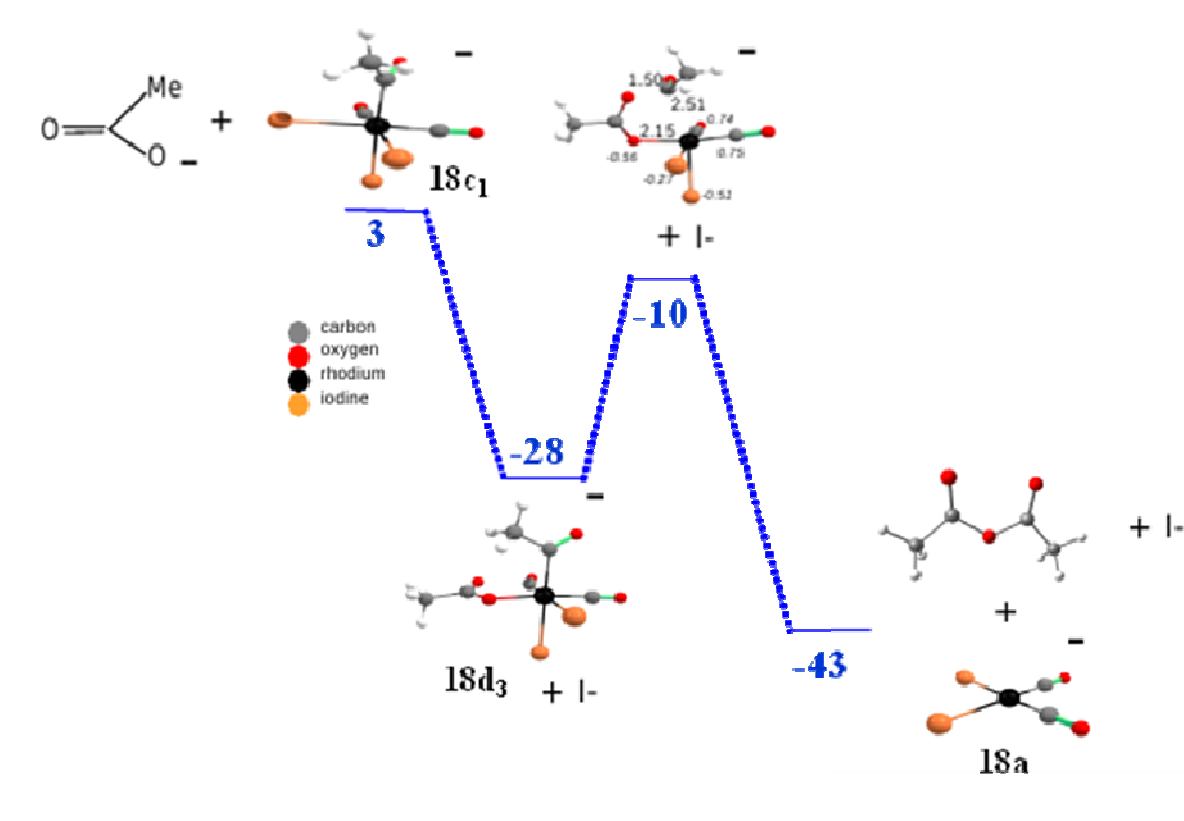
(33) Adams, H.; Bailey, N. A.; Mann, B. E.; Manuel, C. P.; Spencer, C. M.; Kent, A. G. *J. Chem. Soc. Dalton Trans.* **1988**, 489.

-
- (34) (a) Singleton, T. C.; Urry, W. H.; Paulik, F. E. (to Monsanto Chemicals), EP055.618 **1981**. (b) Kojima, H.; Koyama, H. (to Daicel Chem. Ind. Ltd.), JP60.214.756 **1985**. (c) Schreck, D. J. (to Union Carbide Corp), EP144.935 **1985**. (d) Schreck, D. J. (to Union Carbide Corp), EP144.936 **1985**. (e) Forster, D. *J. Am. Chem. Soc.* **1975**, *19*, 951. (f) Mizoroki, T.; Matsumoto, T.; Ozaki, A. *Bull. Chem. Soc. Jpn.* **1979**, *52*, 479.
- (35) Kinnunen, T.; Laasonen, K. *J. Mol. Struct. (Theochem)* **2001**, *542*, 273.

CHAPTER IV

**Direct involvement of an acetato ligand in the reductive
elimination step of the rhodium-catalyzed methanol carbonylation**

Chapter IV: Graphical synopsis



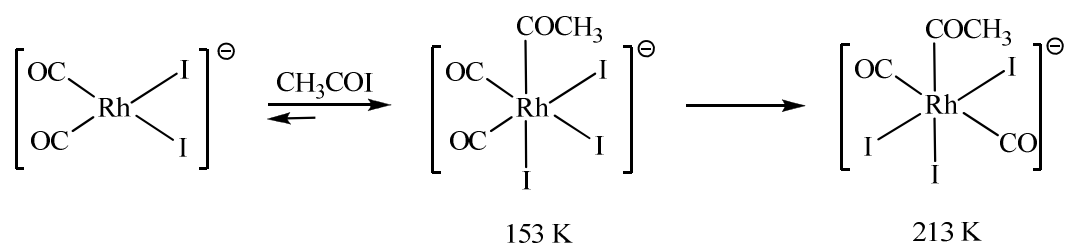
*Product formation from $[PPN][RhI_3(COCH_3)(CO)_2]$ **18c₁** involves a two-step process with initial iodide substitution by acetate followed by reductive elimination of acetic anhydride, which is then immediately hydrolyzed into acetic acid.*

IV-1 Introduction

This last chapter deals with the reductive elimination, last step of the rhodium-catalyzed methanol carbonylation, for which few investigations on the mechanism have been reported in the literature. Under the catalytic conditions of the AO Celanese process, an unexpected direct involvement of an acetato ligand operating in two steps is proposed. In order to collect spectroscopic data for the different rhodium intermediates involved in the catalytic cycle, we will focus throughout the entire study on complex [PPN][RhI₂(CO)₂] **18a**, previously introduced in chapter III.

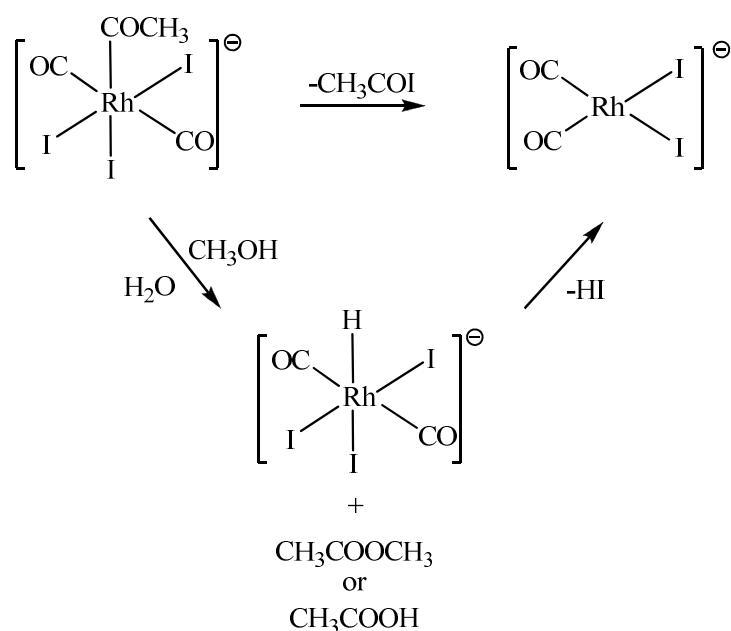
IV-2 Background

As previously described, CH₃I oxidative addition onto the anionic complex [RhI₂(CO)₂]⁻ followed by CO *cis*-migration results in the dianionic acetyl Rh(III) complex [Rh(μ-I)I₂(COCH₃)(CO)]₂²⁻. Under CO atmosphere, this dimer leads rapidly to the Rh(III) 18 e⁻ complex [RhI₃(COCH₃)(CO)₂]⁻ for which a CO ligand is weakly coordinated to the metal center since this complex rapidly restores complex [Rh(μ-I)I₂(COCH₃)(CO)]₂²⁻ in the absence of CO.¹ Infrared and NMR data² for the latter dicarbonyl acetyl rhodium complex suggests that its structure lies in an octahedral geometry with the two CO ligands in *trans* position, consistent with the crystal X-ray analysis reported.³ The complex *cis*-[RhI₃(COCH₃)(CO)₂]⁻ has previously been detected by ¹³C NMR at 153 K by direct reaction of acetyl iodide with [RhI₂(CO)₂]⁻, and then it isomerizes at 213 K to form the *trans*-acetyl complex (Scheme 1).⁴



Scheme 1. *cis-, trans-* isomerization of $[\text{RhI}_3(\text{COCH}_3)(\text{CO})_2]^-$.

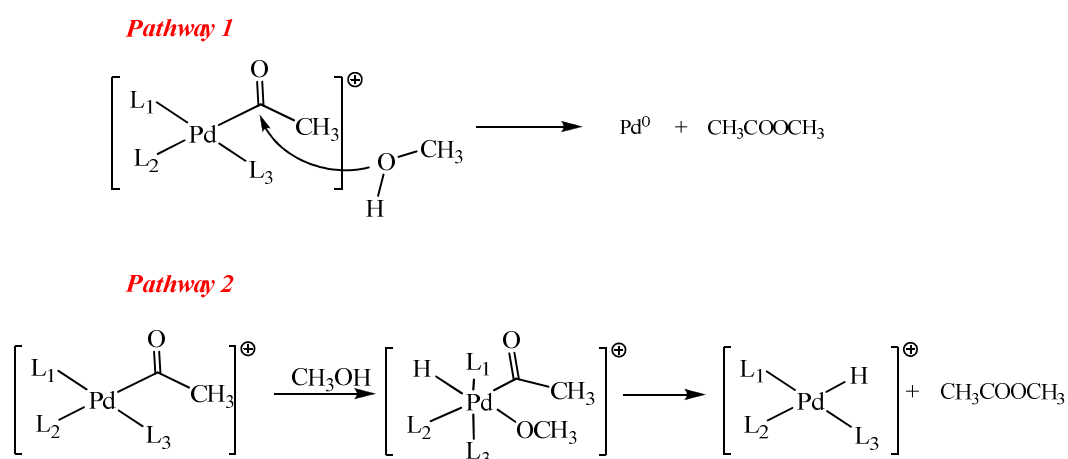
Complex $[\text{RhI}_3(\text{COCH}_3)(\text{CO})_2]^-$ can eliminate reductively acetyl iodide to give the starting active Rh(I) species $[\text{RhI}_2(\text{CO})_2]^-$ and thus, complete the catalytic cycle.⁵ It has been reported that slow decomposition of $[\text{RhI}_3(\text{COCH}_3)(\text{CO})_2]^-$ occurs under ambient conditions ($t_{1/2} = 12$ h at 298 K).⁶ In fact, Forster has proposed two different pathways for the reductive elimination reaction (Scheme 2).^{6a}



Scheme 2. Different pathways for the reductive elimination step.

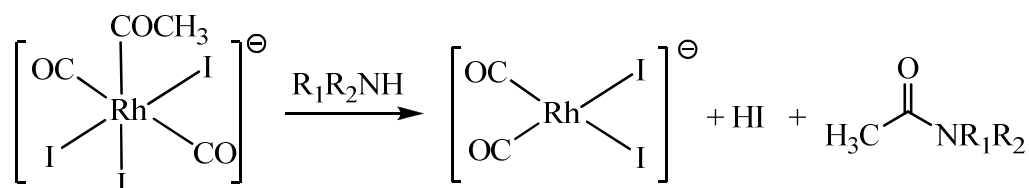
The first pathway is the direct reductive elimination of acetyl iodide mentioned above and the second involves methanol or water in a solvolytic mechanism via a Rh-hydride intermediate complex, which further eliminates HI to give back the starting catalyst $[\text{RhI}_2(\text{CO})_2]$. Forster however suggested that the acetyl iodide elimination is likely to be preferred since evidence of this pathway has been reported with Rh-phosphine complexes.⁷ It has also been proposed by Kilner et al. that water can react directly with the acetyl complex via a hydrolysis reaction to give acetic acid and the Rh(I) starting complex. These authors also observed that addition of acetic acid increased the rate of the elimination reaction.⁸

The solvolysis reaction can be closely compared to the reaction of methanol with cationic acetyl palladium complexes. Indeed, Van Leeuwen et al. proposed different mechanistic pathways for the formation of methyl acetate from acetyl palladium complexes in the presence of methanol.⁹ They reported that methanol could either attack the acetyl moiety (Pathway 1, Scheme 3) or could coordinate to the Pd metal centre to further undergo reductive elimination (Pathway 2, Scheme 3).



Scheme 3. Proposed pathways for methanolysis reaction on a Pd complex.

Moreover, Maitlis et al. have observed that addition of amines to the acetyl rhodium complex enhanced dramatically the elimination step affording an amide compound together with the starting Rh(I) complex. Preliminary kinetic studies on this reaction involving *N*-methylaniline suggested a nucleophilic attack of the amine on the acetyl ligand of the complex (Scheme 4).



Scheme 4. Reaction of Rh(III) acetyl complex with amines.

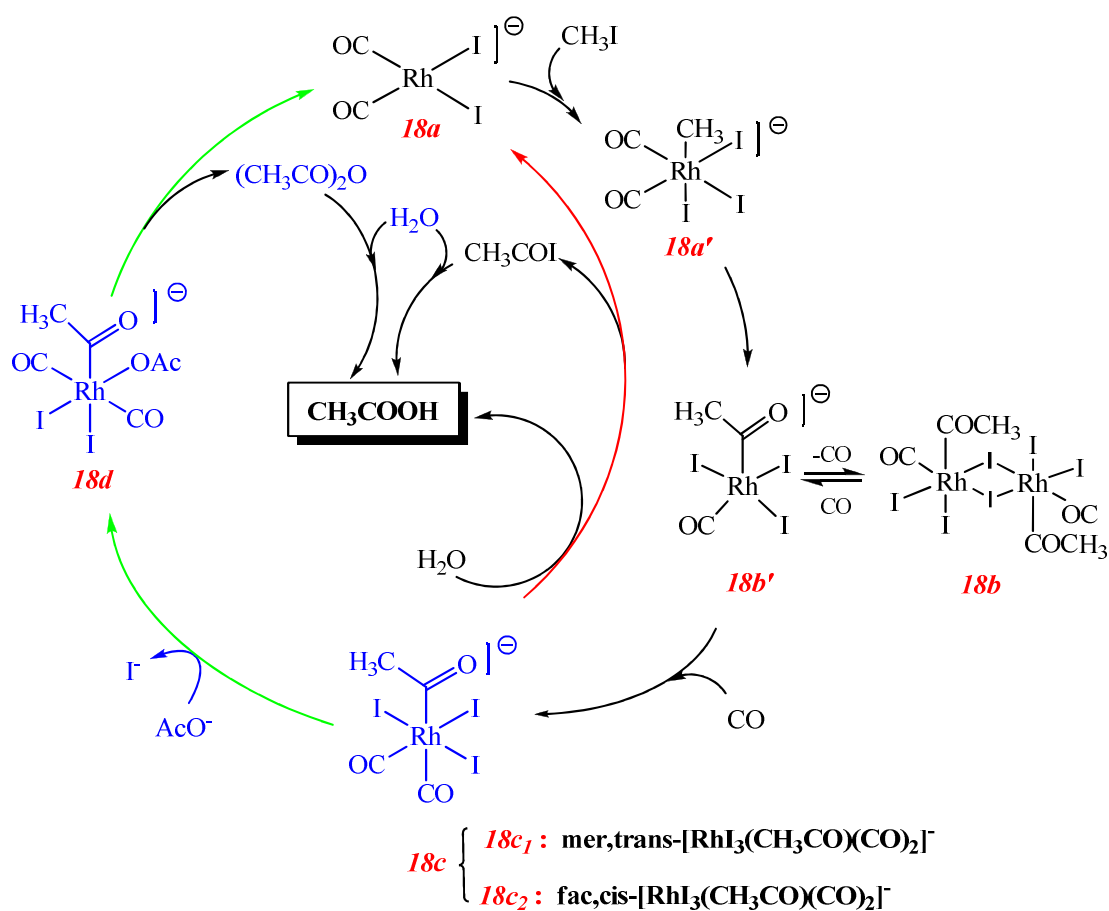
In the same study, they showed that reaction of the Rh(III) acetyl complex with tetrabutylammonium acetate resulted in immediate formation of Rh(I) $[\text{RhI}_2(\text{CO})_2]^-$ complex together with acetic anhydride.^{6b}

To the best of our knowledge, no further experimental study has been reported for the reductive elimination reaction of Rh-carbonyl species. Only a theoretical density functional study has been reported.¹⁰ Nevertheless, this reaction appears to be very important since Jones suggested that at 8 wt % of water concentration, it became the rate determining step of the Rh-catalyzed methanol carbonylation cycle.

The mechanism for the reductive elimination step has not been explored in detail unlike the other proposed steps in the catalytic cycle.⁶ Thus, the elimination of acetyl iodide from $[\text{RhI}_3(\text{COCH}_3)(\text{CO})_2]^-$ followed by its immediate hydrolysis to acetic acid is largely accepted as the final step of the catalytic cycle.^{11,12,6a} In this context other possible pathways can be proposed.

IV-3 New proposed mechanism for the formation of AcOH from $[\text{RhI}_3(\text{COCH}_3)(\text{CO})_2]^-$

$^{13}\text{C}\{^1\text{H}\}$ VT-HP-NMR experiments, IR-monitored kinetics and experimental data supported by DFT calculations, which are consistent with the substitution of an iodo ligand by an acetate ligand on the $[\text{RhI}_3(\text{COCH}_3)(\text{CO})_2]^-$ **18c** complex followed by reductive elimination of acetic anhydride, which immediately reacts with water to afford two molecules of acetic acid and the *cis*- $[\text{RhI}_2(\text{CO})_2]^-$ **18a** starting complex will be presented. Scheme 5 shows an overview of the different species that will be further discussed.



Scheme 5. Different proposed pathways for the reductive elimination reaction involving complex **18**.

As mentioned in the previous chapters, the rhodium-catalyzed process developed by Hoechst Celanese uses an inorganic iodide salt, such as LiI, as a co-promoter and stabilizer. LiI enhances the activity of the catalytic system and precludes the formation of insoluble inactive RhI_3 .^{11c} In chapter III, we mentioned that model reaction studies led some authors to suggest that the use of this salt allows the formation of a hypothetical pentacoordinated Rh(I) dianionic species $[\text{RhI}_3(\text{CO})_2]^{2-}$, which is more nucleophilic for the oxidative addition of methyl iodide. Furthermore, the presence of significant amounts of acetate ions (ca. 0.3 molar), due to the equilibrium of equation 1 (Eq. 1), could result in the formation of $[\text{RhI}_2(\text{OAc})(\text{CO})_2]^{2-}$.^{11c}



In the rhodium-catalyzed methanol carbonylation, the amount of water impacts the nature of the rate determining step (*rds*). At high water content, typically > 14 wt %, the *rds* is the oxidative addition of CH_3I on **18a**, producing the *cis*- $[\text{RhI}_3(\text{CH}_3)(\text{CO})_2]^-$ **18a'** intermediate, which evolves rapidly towards the acetyl species $[\text{RhI}_3(\text{COCH}_3)(\text{CO})]^-$ **18b'** by CO *cis*-migratory insertion and then by coordination of an external CO forms the acetyl complex $[\text{RhI}_3(\text{COCH}_3)(\text{CO})_2]^-$ **18c**.^{6a} In the absence of a CO atmosphere, complex **18b'** dimerizes into the dianionic complex $[\text{Rh}(\mu\text{-I})_2(\text{COCH}_3)(\text{CO})]_2^{2-}$ **18b**¹² (Scheme 5).

The elimination of acetyl iodide from complex **18c** followed by its immediate hydrolysis to AcOH, largely accepted as the final step of the catalytic cycle, added to the alternative mechanism proposed by Forster that involves the direct solvolysis of **18c** by water are represented in Scheme 5 (red arrow). The CH_3COI reductive elimination has also been proposed for the anhydrous carbonylation of methyl acetate to acetic anhydride (Eastman process) and carbonylation of MeOH/MeOAc mixture to AcOH/Ac₂O at low water content (BP-Chemicals

process). Both involve the active complex $[\text{RhI}_2(\text{CO})_2]^-$ and iodide salt stabilizers as for the Celanese process and lead to the formation of acetic anhydride Ac_2O from reaction of CH_3COI with LiOAc .

IV-4 Synthesis and characterization

Synthesis and characterization of complexes **18a** and **18b** have been described earlier in Chapter III. CO bubbling on a dichloromethane solution of **18b** afforded complex **18c**. This latter reversibly gives back **18b** if not kept under a CO atmosphere although at 273 K the reversibility to **18b** is slower and **18c** can live in solution for ~ 1 hour. The FT-IR ν_{CO} and ν_{COMe} stretching bands for **18a** (2058.0 and 1986.1 cm^{-1}), **18b** (2055.0 ; 1736.0 and 1720.1 cm^{-1}) and **18c** (2083.6 and 1705.5 cm^{-1}) are displayed in Figures 1, 2 and 3, respectively.

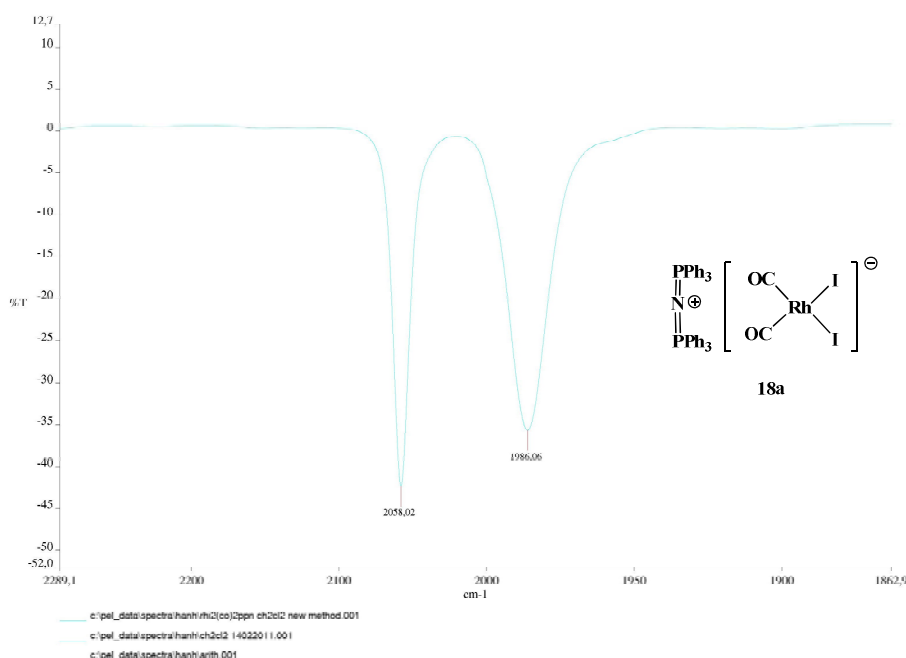


Figure 1. FT-IR ν_{CO} stretching bands for **18a** in CH_2Cl_2 at 298 K.

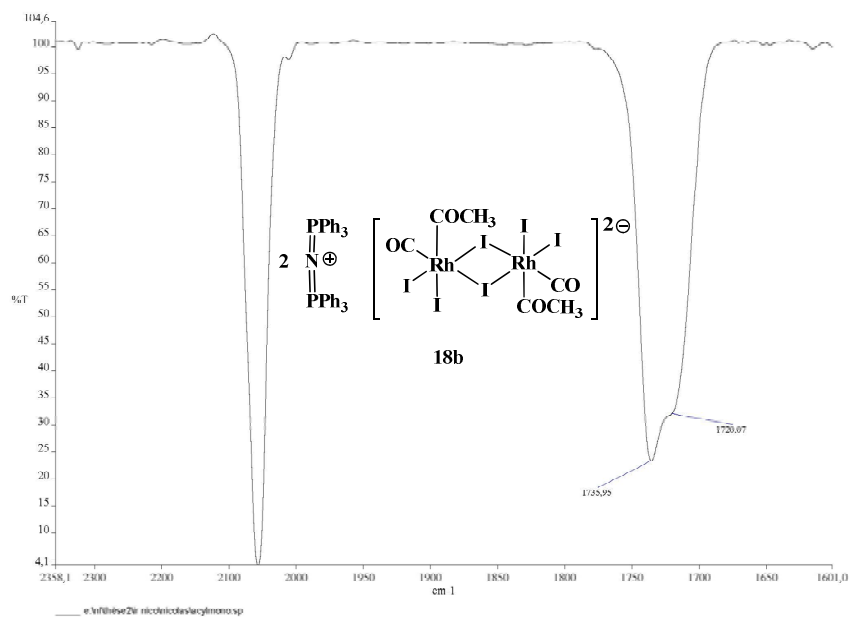


Figure 2. FT-IR ν_{CO} and ν_{COMe} stretching bands for **18b** in CH_2Cl_2 at 298 K.

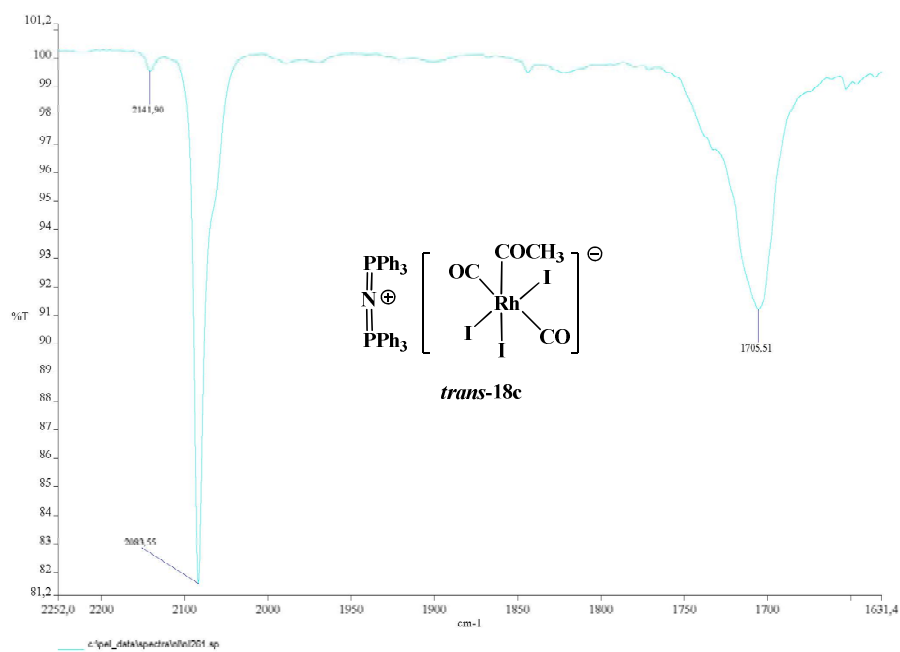


Figure 3. FT-IR ν_{CO} and ν_{COMe} stretching bands for *mer,trans*-**18c₁** in CH_2Cl_2 at 298 K.

It is noteworthy that Figure 3 shows a weak band at 2142 cm^{-1} for complex *mer,trans*-**18c₁**, which indicates that the CO ligands expected to be mutually in *trans* position are not exactly centro-symmetric in their local symmetry, so that the ν_{CO} Ag mode, which is expected to be inactive in IR (C_i group) produces a weak band at 2142 cm^{-1} . In addition, the ν_{CO} terminal band at 2083.6 cm^{-1} is slightly shouldered at lower frequency (2055.0 cm^{-1}), since traces of remaining dimer complex **18b** are expected. The single crystal X-ray structure of complex *mer,trans*-**18c₁** (Figure 4) was obtained in our laboratory (N. Lassauque, 2006) via synthesis of **18c** under CO in dichloromethane at 273 K and by addition of hexane in order to form a bilayered solution. The sample was sealed under CO and stored at 255 K.

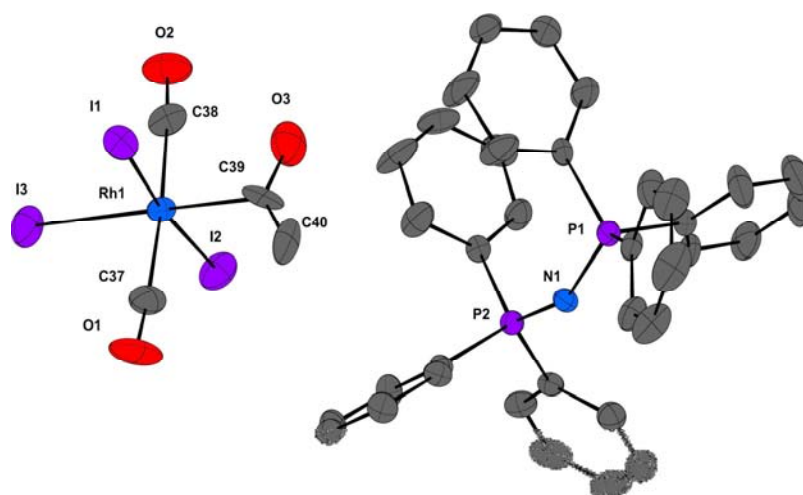


Figure 4. ORTEP view for the single crystal X-ray structure of *mer,trans*-**18c₁**. Ellipsoids are shown at the 30 % probability level. Selected bond lengths (Å) and angles (deg): C(37)-O(1): 1.092(6); C(37)-Rh(1): 1.945(7); C(38)-O(2): 1.108(6); C(38)-Rh(1): 1.926(7); C(39)-O(3): 1.201(6); C(39)-C(40): 1.234(8); C(39)-Rh(1): 2.152(7); Rh(1)-I(1): 2.6602(9); Rh(1)-I(3): 2.6702(9); Rh(1)-I(2): 2.8137(11).

O(1)-C(37)-Rh(1): 176.3(6); O(2)-C(38)-Rh(1): 175.6(6); O(3)-C(39)-C(40): 128.5(7); O(3)-C(39)-Rh(1): 110.8(5); C(40)-C(39)-Rh(1): 120.5(5); C(38)-Rh(1)-C(37): 174.7(2); C(38)-Rh(1)-C(39): 93.6(3); C(37)-Rh(1)-C(39): 91.5(3); C(38)-Rh(1)-I(1): 91.28(19); C(37)-Rh(1)-I(1): 90.08(16); C(39)-Rh(1)-I(1): 86.52(15); C(38)-Rh(1)-I(3): 91.02(19); C(37)-Rh(1)-I(3): 88.25(16); C(39)-Rh(1)-I(3): 86.38(15); I(1)-Rh(1)-I(3): 172.66(2); C(38)-Rh(1)-I(2): 84.94(17); C(37)-Rh(1)-I(2): 89.90(18); C(39)-Rh(1)-I(2): 178.31(19); I(1)-Rh(1)-I(2): 92.59(2); I(3)-Rh(1)-I(2): 94.56(2).

Complexes **18** were also synthesized starting from ^{13}C -labeled complex **18a** to facilitate the detection of carbonyl or acetyl signals for $^{13}\text{C}\{^1\text{H}\}$ NMR analyses. Figures 5 and 6 display the $^{13}\text{C}\{^1\text{H}\}$ NMR spectrum of complexes **18b** and *mer,trans*-**18c**₁, respectively.

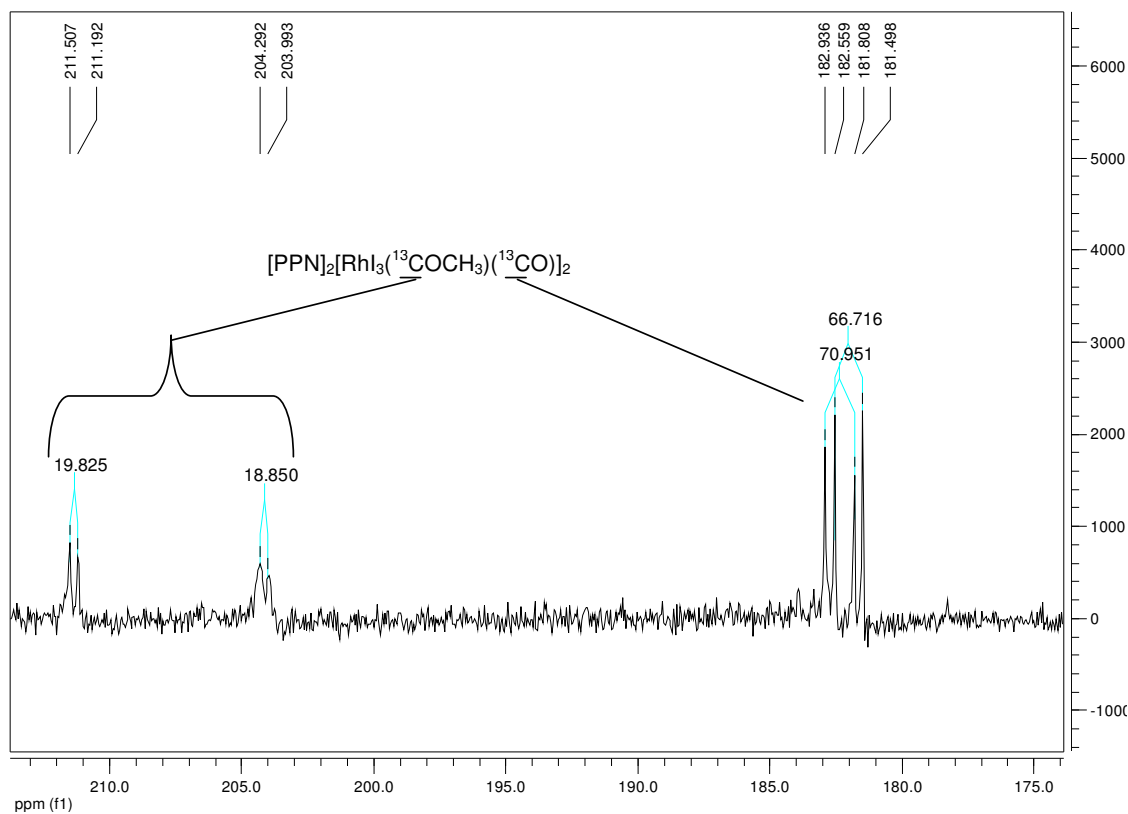


Figure 5. $^{13}\text{C}\{^1\text{H}\}$ NMR spectrum in the carbonyl region of **18b** in CD_2Cl_2 at 298 K.

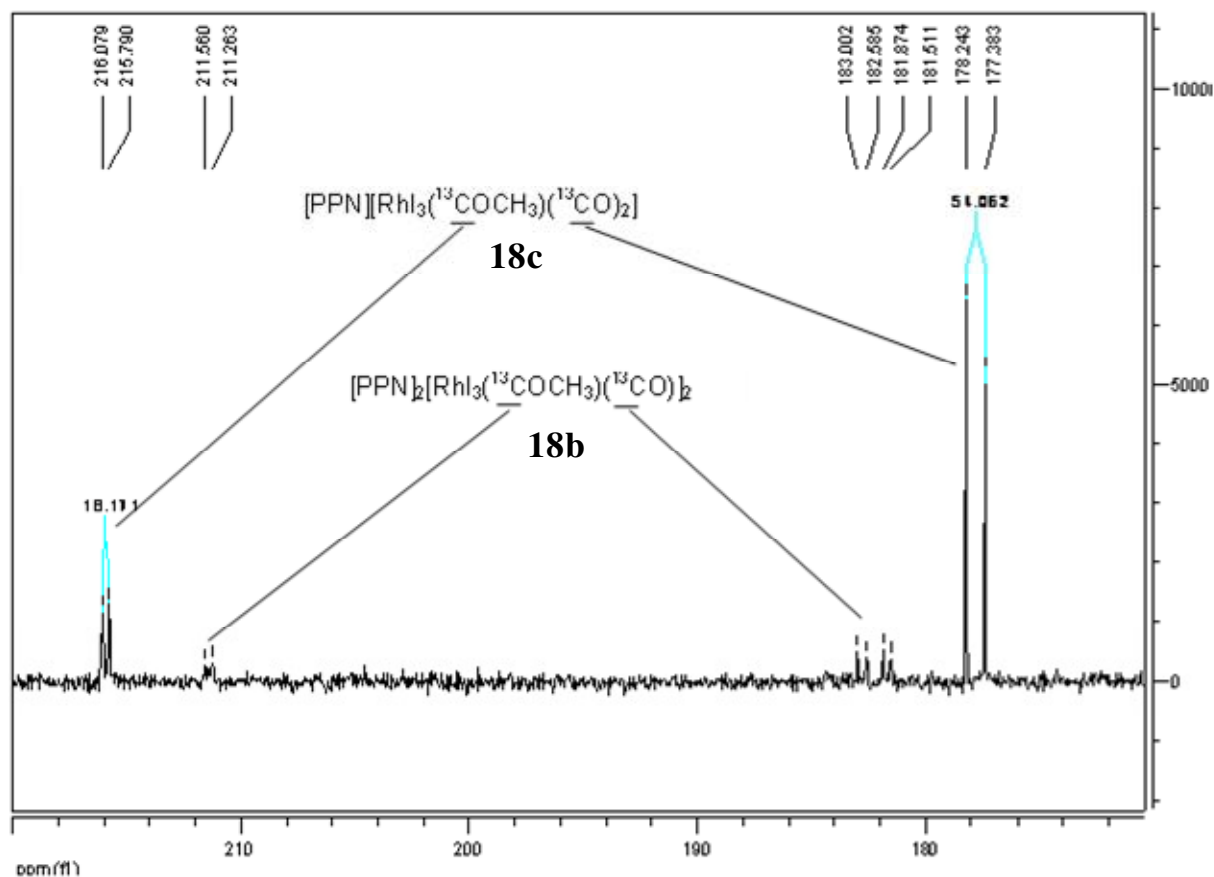


Figure 6. $^{13}\text{C}\{^1\text{H}\}$ NMR spectrum in the carbonyl region of *mer,trans*-**18c**₁ in CD_2Cl_2 at 298 K.

As previously described in chapter III, dimer complex **18b** exhibits at least two well distinct isomers as two sharp doublets for the terminal $[\text{Rh-CO}]$ CO ligands and two sharp doublets for the $[\text{Rh-COMe}]$ acetyl ligands are detected via $^{13}\text{C}\{^1\text{H}\}$ NMR (Figure 5) consistent with the FT-IR spectrum (Figure 2). Complex *mer,trans*-**18c**₁ exhibits a sharp doublet assigned to the two magnetically equivalent CO ligands (δ 177.7 ppm, $^1J_{\text{CO-Rh}} = 54.1$ Hz) consistent with a Rh(III) complex and with the mutual *trans* position of the CO ligands as observed already by FT-IR as well as with the X-ray structure. In addition, a sharp doublet at lower field (δ 216.9 ppm, $^1J_{\text{COMe-Rh}} = 18.2$ Hz) is attributed to the acetyl COCH_3 ligand. Weak doublets (COCH_3 ; δ 211.3

ppm, $^1J_{\text{COMe-Rh}} = 20.2$ Hz and CO: δ 182.4 and 182.0 ppm, $^1J_{\text{CO-Rh}} = 71.0$ and 66.7 Hz, respectively) are also detected indicating the small amounts of complex **18b** present in solution as previously mentioned above for the IR analysis.

IV-5 Reactivity (VT-HP-NMR and kinetics)

The impact of the water concentration on rhodium reactivity has been studied by a $^{13}\text{C}\{^1\text{H}\}$ VT-HP-NMR experiment giving rise to direct information on the nature of the *rdc* involved. The carbonylation reaction was studied at 363 K and under 15 bar ^{13}CO initial pressure.¹³ Figure 6 shows the most significant part of the $^{13}\text{C}\{^1\text{H}\}$ NMR spectra recorded for ^{13}CO -**18a** in a $\text{CD}_3\text{COOD}/\text{MeOAc}/\text{CH}_3\text{I}$ solution at three different water concentrations (5, 10 and 20 wt %).

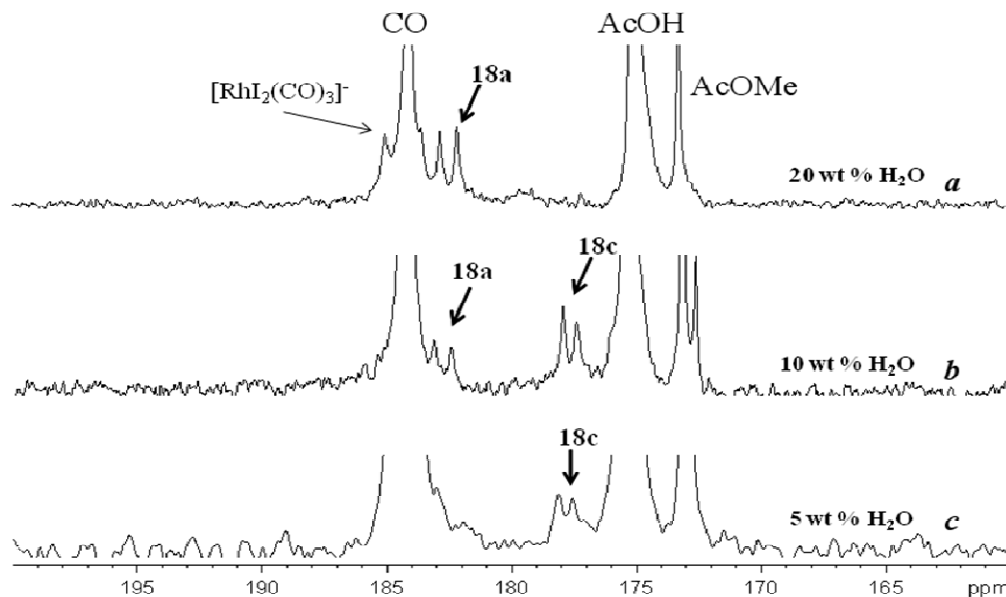


Figure 6. High pressure $^{13}\text{C}\{^1\text{H}\}$ NMR spectra of **18a** under methanol carbonylation conditions (15 bar ^{13}CO , 363 K, $[\mathbf{18a}] = 0.1$ %) at **a**) 20 wt % H_2O ; **b**) 10 wt % H_2O ; and **c**) 5 wt % H_2O .

At 20 wt % of water (Figure 1-*a*), the main detected rhodium species is **18a** ($\delta_{\text{CO}} = 182.8$ ppm, $^1J_{\text{CO-Rh}} = 69.5$ Hz) consistent with the *rds* being the methyl iodide oxidative addition step.^{6a,11} The signal at 186 ppm, close to the dissolved free ^{13}CO peak, is proposed to be the visible peak, part of the doublet of the species $[\text{RhI}_2(^{13}\text{CO})_3]^-$. This complex has not been isolated but as already discussed in chapter III, since we are in a slow exchange limit, we believe it is produced in small amounts.¹⁴ When the water content is decreased to 10 wt % (Figure 1-*b*), a new doublet appears which is assigned to the acetyl species **18c** ($\delta_{\text{CO}} = 177.8$ ppm, $^1J_{\text{CO-Rh}} = 54.6$ Hz; $\delta_{\text{COMe}} = 216.9$ ppm, $^1J_{\text{COMe-Rh}} = 18.2$ Hz). When the water content is reduced further to 5 wt % water (Figure 1-*c*), the sole rhodium carbonyl species detected is **18c**. This build-up of a steady state content of this acetyl rhodium species with a complete disappearance of **18a**, points to a shift of the *rds* as the reductive elimination from **18c**. These experimental observations could be interpreted as a direct involvement of water in the last step of the cycle. Since hydrolysis of acetyl iodide is very fast, then its classically proposed reductive elimination should be independent of water concentration. Thus, the solvolysis of **18c** seems more probable than the direct reductive elimination of CH_3COI . Furthermore, as different amounts of water should generate different concentrations of acetate anion arising from acetic acid dissociation, the possible role of acetate anions upon the reductive elimination step has to also be considered. The concentration of water in solution was successively increased by a stepwise addition of 0.10 or 1 mL of pure water to 50.0 mL of glacial acetic acid solvent being initially placed in a cell for conductivity measurements (Figure 7). As the water concentration increases, the conductivity increases due to acetic acid dissociation generating acetate ions.

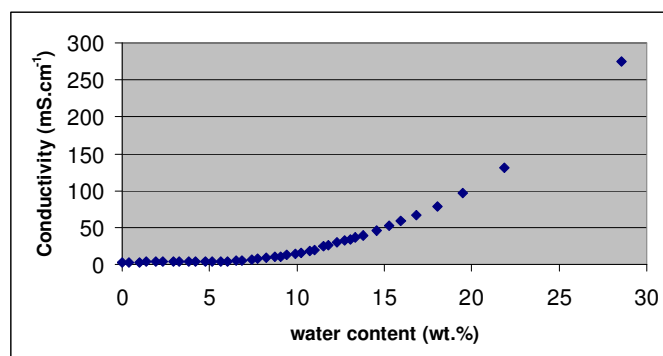


Figure 7. Plot of conductivity vs. wt % H₂O for glacial acetic acid.

The reductive elimination from **18a** was also monitored by FT-IR in dichloromethane at 298 K under 5 bar of CO in the presence and absence of water (Figures 8 and 9).

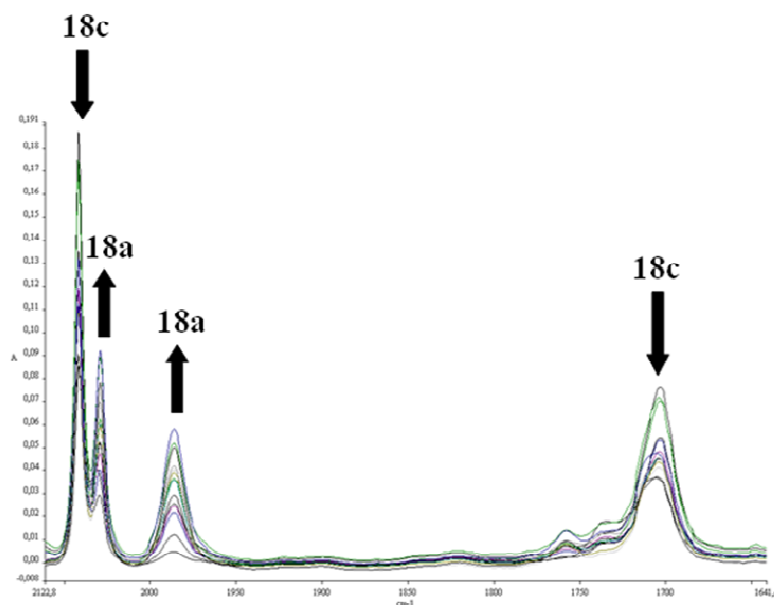


Figure 8. Series of FT-IR monitored spectra for the reductive elimination reaction of **18c** in dichloromethane at 298 K and under 5 bar of CO in the absence of water.

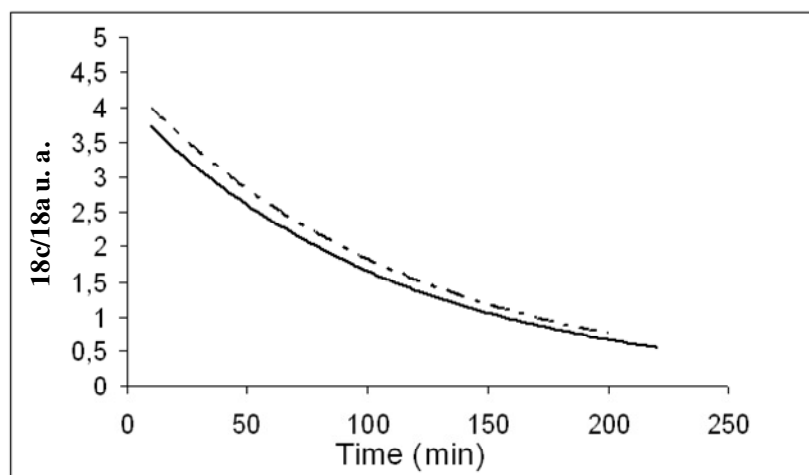


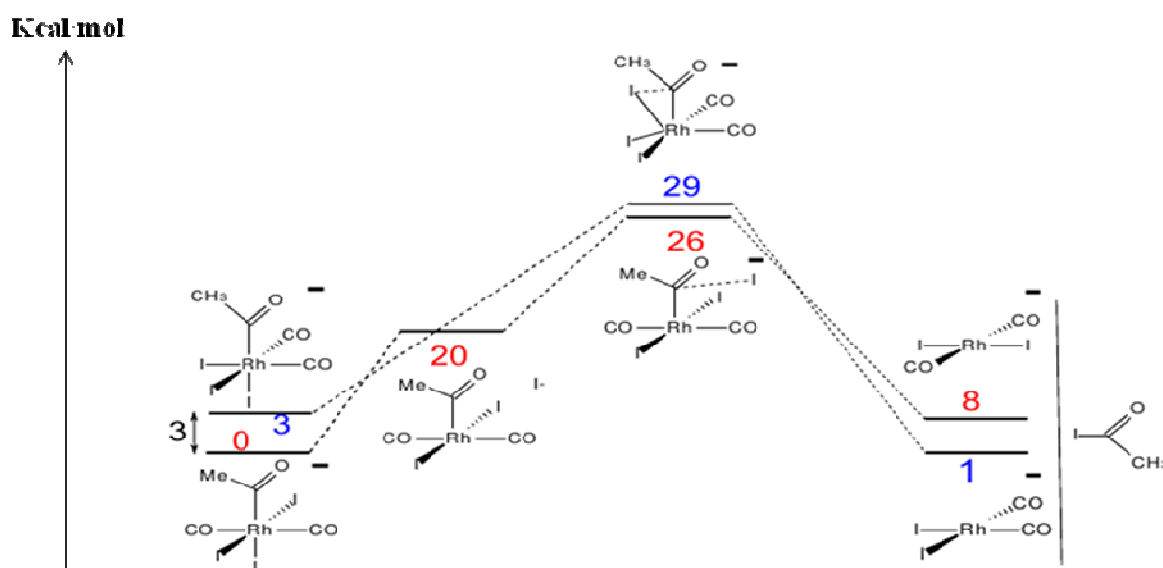
Figure 9. Infrared monitoring of the reaction of **18c** under 5 bar of CO at 298 K in CH₂Cl₂ under anhydrous conditions (full line) and in the presence of 5 wt % water (dotted line).

Under these conditions, the reaction operates slowly, independently of the water concentration. However, with 1 eq. of butylmethylimidazolium acetate under anhydrous conditions, the reductive elimination is immediate. As previously mentioned earlier, Maitlis et al. have shown that tetrabutylammonium acetate reacts immediately with [RhI₃(COCH₃)(CO)₂]⁻ to give [RhI₂(CO)₂]⁻ and acetic anhydride.^{6b}

Since these results are not consistent with neither a reductive elimination of CH₃COI nor the solvolysis of **18c**, DFT calculations, B3PW91 (Rh:SDD+f,I:SDD+d,CHO:6-31G(d,p)), (see [experimental chapter V for full details](#)) were performed to investigate the reactivity of **18c** under various conditions.

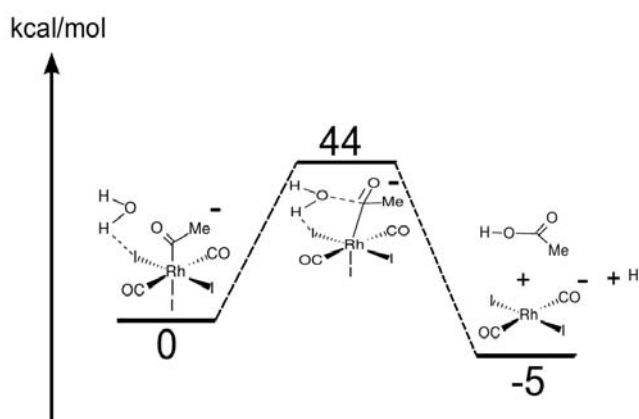
IV-6 DFT calculations to investigate the reactivity of **18c**

Initial computational studies probed the mechanism for the reductive elimination of CH_3COI from **18c** (Scheme 6). It can involve either *mer,trans*-**18c**₁ or its isomer *fac,cis*-**18c**₂. An endergonic pathway with a Gibbs free energy of $+8 \text{ kcal}\cdot\text{mol}^{-1}$ is obtained for **18c**₁ and a slightly exergonic pathway for **18c**₂ ($-1 \text{ kcal}\cdot\text{mol}^{-1}$). The corresponding energy barriers are $26 \text{ kcal}\cdot\text{mol}^{-1}$ for both pathways, which agree well with previous calculations reported by Kinnunen and Laasonen ($25 \text{ kcal}\cdot\text{mol}^{-1}$ for **18c**₁ and $23 \text{ kcal}\cdot\text{mol}^{-1}$ for **18c**₂).¹⁰



Scheme 6. Gibbs Free energy pathway computed for the internal rearrangement leading to the reductive elimination of CH_3OI . The energies are given in $\text{kcal}\cdot\text{mol}^{-1}$.

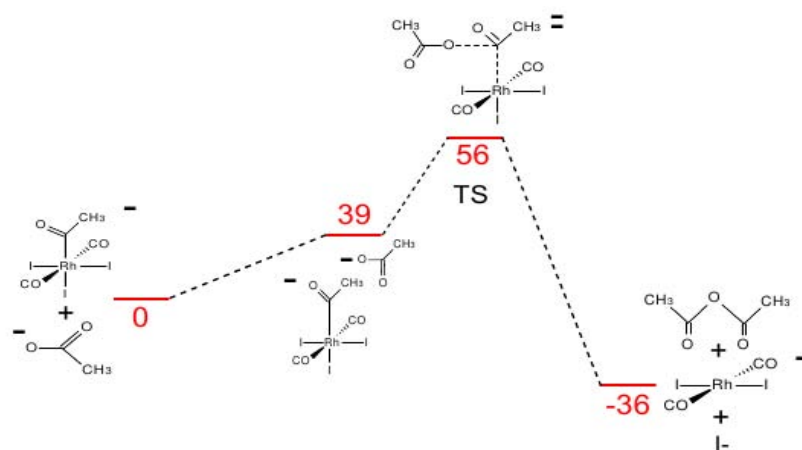
The two proposed mechanisms for the reductive elimination from **18c₂** and **18c₁** are different. The pathway for **18c₂** is a straightforward intra-molecular reaction involving the addition to the -COCH₃ group of an adjacent iodide, whereas **18c₁** requires a two step process. The decooordination of the iodide *trans* to -COCH₃ occurs first, followed by the attack of an iodo ligand I at the acetyl carbon. In both cases, CH₃COI is formed. Since these pathways are thermodynamically endergonic for **18c₁** and slightly exergonic or at best thermoneutral according to the precision of the calculations for **18c₂**, the possible involvement of water was investigated (Scheme 7).



Scheme 7. Gibbs Free energy pathway computed for the direct water-mediated reductive elimination. The energies are given in kcal.mol⁻¹.

Its direct attack on the acetyl group has been calculated. The reaction is exergonic by 5 kcal.mol⁻¹, but possesses an energy barrier of 44 kcal.mol⁻¹, making it kinetically improbable. Instead, the observed impact of water content on the rate of the reductive elimination from **18c₁** is

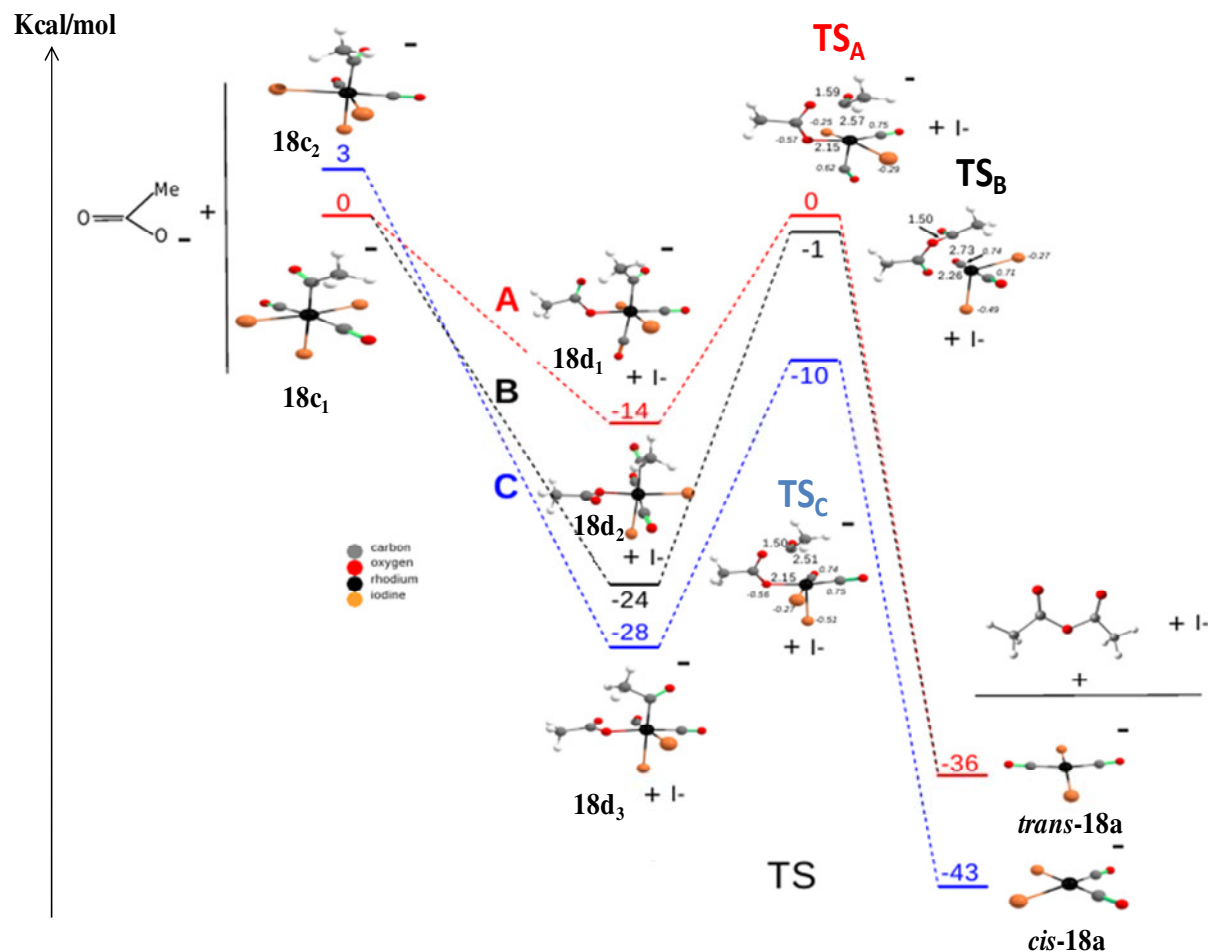
most likely due to the change in acetate anion concentration as a function of water content in an acetic acid medium. This statement is consistent with the experimental observation described above. Consequently, the direct attack of an AcO^- ligand on the acetyl group of **18c₁** must be considered as a probable pathway for the reductive elimination (Scheme 8).



Scheme 8. Gibbs Free energy pathway computed for the acetate-mediated reductive elimination.

The energies are given in kcal.mol^{-1} .

Although it is found to be highly exergonic, the energy barrier is far too high to be competitive (56 kcal.mol^{-1}). Therefore, an alternative pathway that involves an indirect acetate-mediated reaction appears to be more probable. This mechanism involves the replacement of an iodo ligand on **18c** by an acetate anion to form $[\text{RhI}_2(\text{COCH}_3)(\text{CO})_2(\text{CH}_3\text{COO})]^-$ **18d**. This species forms acetic anhydride upon reductive elimination that rapidly hydrolyzes to produce two acetic acid molecules (Scheme 9).



Scheme 9. Gibbs Free energy pathway computed for the acetate-mediated reductive elimination involving replacement of an iodo ligand. The energies are given in kcal.mol⁻¹.

There are three possible complexes that can form by substitution of I with AcO⁻ on **18c** to obtain an acetate ligand *cis* to the acetyl group without the highly endergonic replacement of a CO. The reaction of AcO⁻ with **18c₁** affords two possible rhodium carbonyl complexes. The first one **18d₁** conserves two iodo ligands *trans* to each other, with one CO moving *trans* to the acetyl ligand. The second complex **18d₂** conserves the two CO ligands *trans* to each other with no other ligand rearrangement. The reaction of AcO⁻ with **18c₂** affords only the structure **18d₃**, in which

the geometry of the I and the CO ligands relative to the acetyl ligand remains unchanged. For all of these cases, the replacement of I by AcO⁻ leads to a stabilization of **18d**₁, **18d**₂, and **18d**₃ by -14, -24, and -31 kcal.mol⁻¹, respectively.

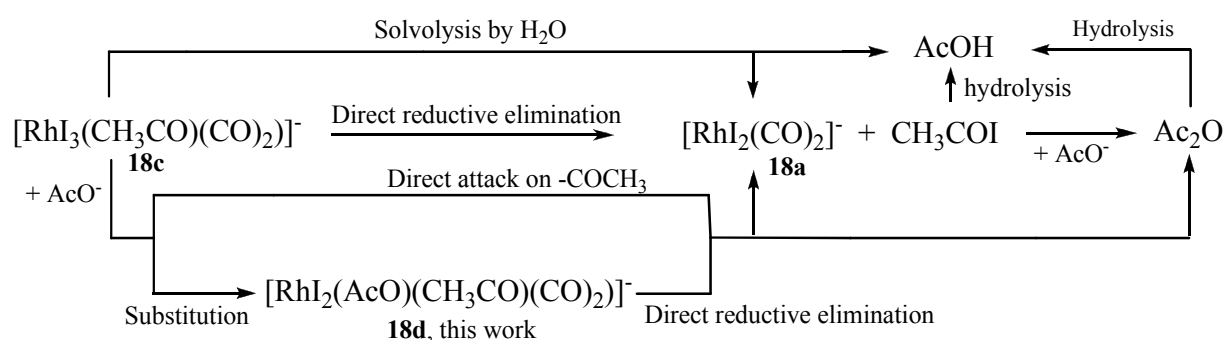
The comparative difference of these results for **18d**₁₋₃ can be explained primarily by a closer analysis of their geometries. Specifically, the predominant factor that impacts the stabilization energy of **18d** is the ligand type *trans* to the acetyl ligand (Scheme 9). As expected, a *trans* iodo to the acetyl ligand stabilizes **18d**₂ and **18d**₃ by strengthening the Rh-C bond of the acetyl group (push-pull effect). On the other hand, **18d**₁ is less stable due to the presence of two donor ligands *trans* to each other. Even though the three proposed isomers **18d**₁₋₃ produce a molecule of acetic anhydride and **18a**, the three corresponding transition states (TS) for **18d** lead to different energy barriers. As previously observed for **18d**, the nature of the ligand *trans* to the acetyl one of the TS complexes primarily impacts the relative energy barriers to form acetic anhydride. The calculated energy barriers of 14, 23, and 18 kcal.mol⁻¹ for TS_A, TS_B and TS_C, respectively, are consistent with kinetically facile reactions.

Although TS_A is the least stable structure, it leads to the lowest energy barrier because a CO ligand *trans* to the acetyl affords a weaker acetyl Rh-C bond due to the π -back bonding of CO. TS_B leads to the highest energy barrier (23 kcal.mol⁻¹). Indeed, at TS_B the anhydride moiety is already formed and the -COCH₃ and -OC(CH₃)O groups are loosely interacting with the Rh center (2.26 and 2.73 Å for Rh-O and Rh-C bonds, respectively). Both TS_A and TS_C exhibit short Rh-O bonds (2.15 Å). In addition, the Rh-C bond lengthens from 2.05 to 2.57-2.50 Å for **18d**₁/**18d**₃ and TS_A/TS_C, respectively. The two TS_A and TS_C are thus better prepared from **18d**₁ and **18d**₃ in line with a lower energy barrier. Finally, the formation of *cis*-[RhI₂(CO)₂]⁻ **18a** and acetic anhydride is more favorable than that of acetic anhydride and *trans*-[RhI₂(CO)₂]⁻ by 7

kcal.mol⁻¹. From the three possible pathways for the reductive elimination, A and C can be retained as the most probable mechanistic routes due to their lower energy barriers compared to pathway B. Furthermore, pathway C is far more exergonic than A thus making it the most feasible way to obtain acetic anhydride.

IV-7 Conclusion

In conclusion, the present experimental and theoretical studies support a new alternative acetate-mediated mechanism, for the reductive elimination step of the rhodium-catalyzed methanol as well as the methyl acetate carbonylation reactions. This proposed mechanism proceeds stepwise: the substitution of an iodo ligand by an acetate anion on the rhodium acetyl carbonyl complex followed by reductive elimination of acetic anhydride, which is immediately hydrolyzed to acetic acid (Scheme 10). This result contrasts with the classically proposed mechanism that involves the direct reductive elimination of CH₃COI followed by its hydrolysis or the direct solvolysis of the acetyl ligand of the rhodium complex.



Scheme 10. Summary of the different proposals for the reductive elimination step.

References

- (1) Roth, J. F.; Craddock, J. H.; Hershman, A.; Paulik, F. E. *Chem. Tech.* **1971**, 600.
- (2) Kent, A. G.; Mann, B. E.; Manuel, C. P. *J. Chem. Soc., Chem Commun.* **1985**, 728.
- (3) Cruise, N. A.; Evans, J. J. *Chem. Soc., Dalton Trans.* **1995**, 3089.
- (4) Howe, L. A.; Brunel, E. E. *Polyhedron* **1995**, *14*, 167.
- (5) This is the mechanism generally admitted in the literature for the Rh-catalyzed methanol carbonylation.
- (6) (a) Forster, D. *J. Am. Chem. Soc.* **1976**, *98*, 846. (b) Maitlis, P. M.; Haynes, A.; Sunley, G. J.; Howard, M. *J. Chem. Soc., Dalton Trans.* **1996**, 2187.
- (7) Baird, M. C.; Mague, J. T.; Osborn, J. A.; Wilkinson, G. *J. Chem. Soc.* **1967**, 1347.
- (8) Kilner, M.; Winter, N. J.; *J. Mol. Catal.* **1996**, *112*, 327.
- (9) Van Leeuwen, P. W. N.; Zuideveld, M. A.; Swennenhuis, B. H. G.; Freixa, Z.; Kamer, P. C. J.; Goubitz, K.; Fraanje, J.; Lutz, M.; Spek, A. L. *J. Am. Chem. Soc.* **2003**, *125*, 5523.
- (10) Kinnunen, T.; Laasonen, K. *J. Organomet. Chem.* **2001**, *628*, 222.
- (11) (a) Haynes, A. in *Top. Organomet. Chem.*, M. Beller (Ed), Springer-Verlag, Berlin Heidelberg, **2006**, 179. (b) Haynes, A. *In Adv. Catal.* **2010**, *53*, 1. (c) Torrence, P. in *Applied Homogeneous Catalysis with Organometallic Compounds* 2nd Ed, B. Cornils, W. A. Herrmann (Eds), Wiley-VCH, Weinheim, **2002**, 104.

(12) Adams, H.; Baily, N. A.; Mann, B. E.; Manuel C. P.; Spencer, C. M.; Kent, A. G. J. *J. Chem. Soc.; Dalton Trans.* **1988**, 489.

(13) Morris, G. in: *Mechanism in Homogeneous Catalysis. A spectroscopic Approach*, Heaton B. Ed, Wiley-VCH Verlag, Weinheim, **2005**, 195.

(14) The CO bound/free-exchange on **18a** in CH₂Cl₂ operates very quickly at 363 K as shown in Churlaud R., Frey U., Metz, F.; Merbach A. E. *Inorg. Chem.* **2000**, 39, 304. In our solvent/reactant mixture this exchange rate may operate slower, so that **18a** and dissolved ¹³CO present distinct signals. A peak at 186 ppm could be assigned to [RhI₂(CO)₃], the other component of the doublet being masked by the dissolved ¹³CO signal.

General conclusion

With the aim to enhance the reactivity (activity/stability) of the [Rh]-catalyzed methanol carbonylation reaction into acetic acid operating at low water content, we chose to introduce nitrogen containing ligands in the coordination sphere of the Rh-complex-catalyst. These moderately strong electron-donating ligands directly coordinate to the metal center affording neutral complexes or can act as counter-cations once protonated or methylated. Thus, we prepared a range of complexes of the type *cis*-[RhX(CO)₂(L)] (X = Cl or I and L = amine, imidazole or pyrazole family ligands containing various substituents) for which studies were mainly focused on iodo complexes. All these derivatives are square planar and for some of them, a fluxional behavior and/or H-interactions between the N-containing ligand and the halide take place. Except for the [RhI(CO)₂(NHEt₂)] complex, which reacts twice as fast as the classical Monsanto process active species [RhI₂(CO)₂]⁻ towards MeI oxidative addition reaction, the other neutral derivatives exhibit slower kinetics which is mainly related to the steric hindrance of the N-containing ligand.

Operating catalytic 10 minutes batch experiments under Celanese AO process conditions (190 °C/30 bar CO, large amounts of methyl acetate) but in the absence of lithium iodide, we put in evidence the formation of significant amounts of [RhI₄(CO)₂]⁻ for which the corresponding counter-cation is [MeNR₃]⁺ resulting from MeI methylation of the N-ligand. Thus, we focused on the corresponding anionic [XNR₃][RhI₂(CO)₂] (X = H or Me) complexes. They were fully characterized and their reactivity to the MeI oxidative addition reaction, which is the rate determining step of Rh-catalyzed methanol carbonylation process, was examined. Although we did not evidence a strict ion-pairing effect, we have some indirect indications that hydrogen interactions between the cation and the Rh square plane plays a role on the reaction rate. In addition, the cation size also impacts the kinetics. The

highest reaction rates have been obtained with tetramethyl ammonium and 1-propyl-2,3-dimethyl imidazolium cations which give rise to well separated ionic entities. On the contrary, diethyl and triethyl ammonium cations display lower rates for this oxidative addition reaction as they are involved in H-contact interactions with the Rh square plane. In fact, we observed the succession of two elementary catalytic steps: the oxidative addition giving rise to the $[\text{RhI}_3(\text{CH}_3)(\text{CO})_2]^-$ followed by the easier migratory CO insertion providing $[\text{RhI}_3(\text{COCH}_3)(\text{CO})]^-$ which in the absence of CO dimerizes immediately.

Finally we demonstrated that the reductive elimination step related to $[\text{RhI}_3(\text{COCH}_3)(\text{CO})_2]^-$ under low-water content process conditions, is not the direct loss of CH_3COI regenerating the Rh(I) active species $[\text{RhI}_2(\text{CO})_2]^-$ as generally admitted. For the catalytic medium containing large amounts of LiI salt which consequently generate significant amounts of acetate ions, we give evidence supported by DFT calculations that reductive elimination operates in a two step process. The first step consists in the direct substitution of an iodo I ligand with an acetate AcO^- giving rise to the $[\text{RhI}_2(\text{COCH}_3)(\text{OAc})(\text{CO})_2]^-$ complex. The second step is the reductive elimination of acetic anhydride restoring $[\text{RhI}_2(\text{CO})_2]^-$; Further hydrolysis of $(\text{AcO})_2$ affords two molecules of acetic acid. Such a mechanism can be extended to the manufacturing of acetic anhydride by methyl acetate carbonylation under anhydrous conditions as operated by the Eastman Kodak company.

Thus, it appears that the judicious choice of a robust nitrogen containing ligand, for which the equilibrium between the neutral coordinated state and the decoordination followed by quaternization resulting in a salt state, occurring under the harsh conditions required for the carbonylation process, could improve the activity, stability (presence of a large counter-cation) and selectivity during the reaction of CH_3I with carbon monoxide to produce *in fine* acetic acid. The aim would be to develop two catalytic cycles interplaying between neutral

and anionic species as for the CativaTM bimetallic [Ir-Ru] methanol carbonylation process. By such a strategy, it would be possible to combine the beneficial effects of both the neutral and anionic species on the three main catalytic steps: (i) the CH₃I oxidative addition, (ii) the CO migratory insertion and (iii) the CH₃COI / (AcO)₂O reductive elimination.

CHAPTER V

EXPERIMENTAL SECTION

V-1 Experimental section: Chapter II

V-1-1 Instrumentation and materials

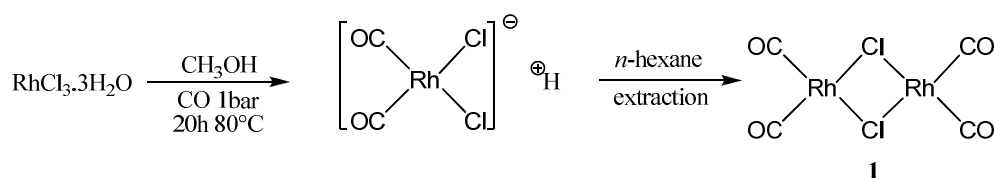
FT-IR spectra were collected on a Perkin-Elmer Spectrum One FT spectrophotometer with a 0.1 mm cell equipped with CaF₂ windows and ATR-IR. All NMR spectra data were recorded on Bruker DPX 300 or Avance 300-500 spectrometers with TMS as external reference for ¹H and ¹³C, [Rh(acac)₃] as external reference for ¹⁰³Rh and nitromethane for ¹⁵N. Chemical shifts are reported in ppm and coupling constants (*J*) are given in Hertz. Spectral assignments were made by means of routine one and two dimensional NMR experiments when appropriate. Mass spectra analyses were performed on a TSQ 7000 Thermo Electron spectrometer equipped with Electronic Impact (EI) and chemical ionization (DCI) sources. The major *m/z* peak was reported with the intensity as a percentage of the base peak in brackets. Elemental analyses were measured with a precision superior to 0.3% at the Microanalysis Laboratory of the LCC in Toulouse. All reactions were carried out using standard Schlenk techniques under an atmosphere of dry argon or in an MBraun glovebox containing dry argon and less than 1 ppm oxygen. All solvents used for synthetic experiments were obtained from a Solvent Purification System (MB SPS-800). CD₂Cl₂ (Eurisotop 99 %) was dried using activated molecular sieves. RhCl₃.xH₂O salt was supplied by Johnson Matthey and RhI₃ was provided by the Celanese plant in Clearlake (USA Texas). The reagents were procured from Aldrich Chemicals, France. Amine ligands were dried and distilled over KOH and degassed prior to use. N-heterocycle compounds were used as received. 1,4-di-*tert*-butyl-pyrazole ligand **h** was synthesized by adapting a method found in the literature¹ and then further purified by separating column chromatography techniques over silica Chromagel 60 A.C.C 35-70µm. Methyl iodide (Aldrich) was distilled over calcium

(1) Merkle, H. R.; Fretschner, E.; Schroder, J. WO96/27589 (to BASF AG), **1996**.

hydride and stored in foil-wrapped Schlenk tubes under argon to prevent formation of I₂. Labeled carbon monoxide ¹³CO (B1 99 %) gas was purchased at Air Liquide. The starting rhodium precursors [Rh(μ-Cl)(CO)₂]₂ **1**² and [Rh(μ-I)(CO)₂]₂ **2**^{3,4} were synthesized according to the literature procedures.

V-1-2 Synthesis of precursor complexes 1 and 2

[Rh(μ-Cl)(CO)₂]₂ **1**



RhCl₃·H₂O (8.32 mmol; 2 g) was loaded in a 250 mL flask in 120 mL of methanol. CO (1 bar) was bubbled in the solution mixture for 20 min under stirring. A cooling refrigerating column was connected to the flask neck and the solution was then heated to reflux (353 K) for 20 hours under stirring. A light yellow colored solution was obtained. After column removal and solvent evaporation by heating at 70°C under a stream of CO and with vigorous stirring, red needles appeared. When very little methanol remained, best was to cut the heating and remove the solvent by CO current under stirring. Indeed, the dimer could easily decompose exposed to heat. After n-hexane extraction, crystallization and filtration, the needles were dried under vacuum and recovered with a good yield. Storage was done under argon at 255 K. Red microcrystalline needles were obtained (Yield 90%). FT-IR (ν_{CO} , cm⁻¹): 2107.2, 2092.4, 2035.6, 2001.1 (CH₂Cl₂); 2097.6, 2084.2, 2035.1, 2021.2, 2001.8 (ATR).

(2) McCleverty, J.; Wilkinson, G. *Inorg. Synth.* **1966**, 8, 214.

(3) Fulford, A.; Hickey C. E.; Maitlis P. M. *J. Organomet. Chem.* **1990**, 398, 311.

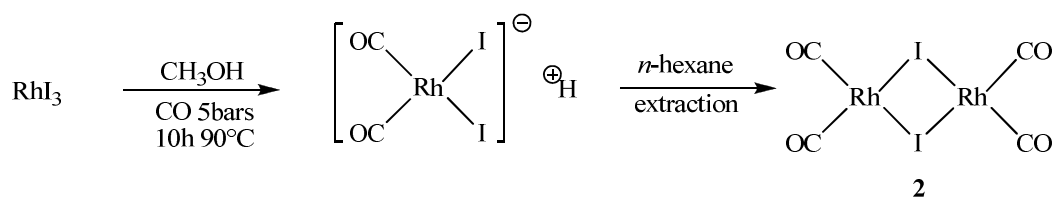
(4) Burger, S.; Therrien, B.; Süß-Fink, G. *Acta Cryst.* **2003**, E59, i53.

$^{13}\text{C}\{^1\text{H}\}$ NMR (298 K, 100.62 MHz, CD_2Cl_2 , ppm): δ 177.7 (d, 4C, CO, $^1J_{\text{CO-Rh}} = 76$ Hz).

Anal. Calcd. for $\text{C}_4\text{Cl}_2\text{O}_4\text{Rh}_2$ (%): C, 12.35. Found: C, 12.33.

$[\text{RhCl}_2(\text{CO})_2]\text{H}$ intermediate: Yellow colored methanol solution FT-IR (ν_{CO} , cm^{-1}): 2072.2, 2003.4 (CH_3OH).

$[\text{Rh}(\mu\text{-I})(\text{CO})_2]_2$ **2**



RhI_3 (4.14 mmol; 2g) was loaded in a 100 mL capacity vessel in 60 mL of methanol. The solution mixture was flushed three times with CO and the vessel pressurized with 5 bars of CO, heated at 363 K and stirred for 10 hours. A light yellow colored solution was obtained. After solvent evaporation in a flask by heating at 343 K under a stream of CO and with vigorous stirring, red-yellowish needles appeared. After *n*-hexane extraction and crystallization the needles were recovered, dried under vacuum with low yield (25%) and stored under argon at 255 K. Needles ready for X-ray analysis were obtained.

$[\text{RhI}_2(\text{CO})_2]\text{H}$ intermediate: Yellow colored methanol solution FT-IR (ν_{CO} , cm^{-1}): 2060.2, 1989.4 (CH_3OH).

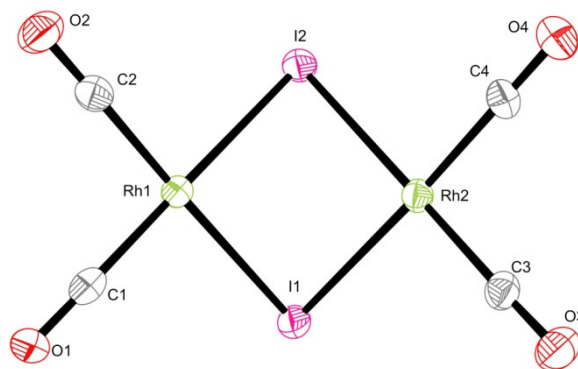
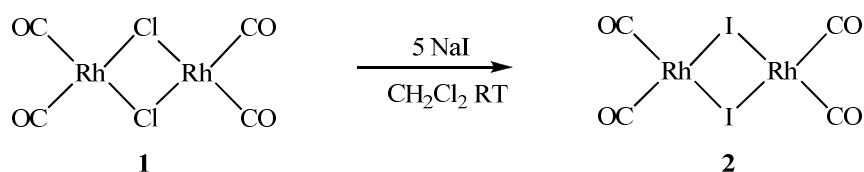


Figure 1. Single-crystal X-ray ORTEP view of **2** obtained in our group by N. Lassauque in 2006. Thermal ellipsoids are shown at the 30% probability level.⁵

Alternative method for synthesis of $[\text{Rh}(\mu\text{-I})(\text{CO})_2]_2$ **2**



$[\text{RhCl}(\text{CO})_2]_2$ **1** (5.14 mmol; 2 g) was loaded in a 100 mL schlenk tube to a 40 mL dichloromethane solution under stirring at RT. Sodium iodide was added with excess to the medium (25.7 mmol; 3.85 g). Although NaI was not soluble in CH_2Cl_2 , the reaction occurred in heterogeneous conditions under vigorous stirring for 5 hours. The reaction solution was then filtrated via canulation and the precipitate washed with CH_2Cl_2 . The dimer iodo bridged complex product **2** was obtained, after vacuum removal of the solvent, in a very good yield. A red powder was recovered and stored under argon at 255 K. Red microcrystalline powder (Yield 95%). FT-IR (ν_{CO} , cm^{-1}): 2096.2, 2080.6, 2027.1 (CH_2Cl_2); 2080.0, 2008.0 (CH_3OH bridge-splitting of **2** which leads to $[\text{RhI}(\text{CO})_2(\text{CH}_3\text{OH})]$); 2090.3, 2070.2, 2014.5, 1987.0 (ATR). $^{13}\text{C}\{^1\text{H}\}$ NMR (298 K, 100.62 MHz, CD_2Cl_2 , ppm): δ 179.3 (d, 4C, CO, $^1J_{\text{CO-Rh}} = 75$ Hz). Anal. Calcd. for $\text{C}_4\text{I}_2\text{O}_4\text{Rh}_2$ (%): C, 8.41. Found: C, 8.39.

(5) Lassauque, N.; in: PhD manuscript, Paul Sabatier University, Toulouse, **2006**, Chap. II, 61.

[RhI(CO)₂(CH₃OH)]: ¹³C{¹H} NMR (298 K, 75.47 MHz, CD₃OD, ppm): δ 180.5 (d, 2C, CO, ¹J_{CO-Rh} = 73.1 Hz).

¹³CO-labeling procedure for [Rh(μ-I)(CO)₂]₂ 2: A dichloromethane solution (V = 25 mL) containing **2** (500 mg, 0.87 mmol) was stirred vigorously at RT under ¹³CO atmosphere during 2 hours. The complete formation of labeled product **2-¹³CO** was monitored by FT-IR spectroscopy and the complex was isolated by solvent removal under reduced pressure.

V-1-3 NMR data of starting ligands a-h

Diethylamine a: ¹H NMR (298 K, 400.13 MHz, CD₂Cl₂, ppm): δ 2.65 (q, 4H, ³J_{H-H} = 7.15 Hz, CH₂), 1.51 (br s, 1H, NH), 1.10 (t, 6H, ³J_{H-H} = 7.15 Hz, CH₃). ¹³C{¹H} NMR (298 K, 100.62 MHz, CD₂Cl₂, ppm): δ 43.8 (s, 2C, CH₂), 15.0 (s, 2C, CH₃).

Triethylamine b: ¹H NMR (298 K, 400.13 MHz, CD₂Cl₂, ppm): δ 2.50 (q, 6H, ³J_{H-H} = 7.20 Hz, CH₂), 1.01 (t, 9H, ³J_{H-H} = 7.20 Hz, CH₃). ¹³C{¹H} NMR (298 K, 100.62 MHz, CD₂Cl₂, ppm): δ 46.3 (s, 3C, CH₂), 11.7 (s, 3C, CH₃).

Imidazole c: ¹H NMR (298 K, 400.13 MHz, CD₂Cl₂, ppm): δ 7.73 (s, 1H, ring-N=CH-NH), 7.13 (s, 2H, ring-N-CH=CH). ¹³C{¹H} NMR (298 K, 100.62 MHz, CD₂Cl₂, ppm) δ 135.4 (s, 1C, ring-N=CH-NH), 121.9 (s, 2C, ring-N-CH=CH).

1-methylimidazole d: ¹H NMR (298 K, 400.13 MHz, CD₂Cl₂, ppm): δ 7.39 (s, 1H, ring-N=CHN-CH₃), 6.99 (s, 1H, ring-NCH=CHN-CH₃), 6.91 (s, 1H, ring-NCH=CHN-CH₃), 3.66 (s, 3H, ring-NCH=CHN-CH₃). ¹³C{¹H} NMR (298 K, 100.62 MHz, CD₂Cl₂, ppm) δ 137.8 (s, 1C, ring-N=CHN-CH₃), 129.1 (s, 1C, ring-NCH=CHN-CH₃), 120.1 (s, 1C, ring-NCH=CHN-CH₃), 33.0 (s, 3H, ring-NCH=CHN-CH₃).

Pyrazole e: ^1H NMR (298 K, 400.13 MHz, CD_2Cl_2 , ppm): δ 12.90 (br s, 1H, ring-N-NH-CH), 7.72 (d, 2H, $^3J_{\text{H-H}} = 2.10$ Hz, ring-CH=N-NH-CH), 6.43 (t, 1H, $^3J_{\text{H-H}} = 2.0$ Hz, ring-NH-CH=CH). $^{13}\text{C}\{^1\text{H}\}$ NMR (298 K, 100.62 MHz, CD_2Cl_2 , ppm): δ 138.8 (s, 1C, ring-CH=N-NH), 129.7 (s, 1C, ring-N-NH-CH), 105.3 (s, 1C, ring-NH-CH=CH).

1-methylpyrazole f: ^1H NMR (298 K, 400.13 MHz, CD_2Cl_2 , ppm): δ 7.46 (d, 1H, $^3J_{\text{H-H}} = 2.00$ Hz, ring-N-CH_b), 7.40 (d, 1H, $^3J_{\text{H-H}} = 2.00$ Hz, ring-NCH₃-CH_a-CH_c), 6.26 (t, 1H, $^3J_{\text{H-H}} = 2.00$ Hz, ring-NCH₃-CH_a=CH_c), 3.91 (s, 3H, ring-NCH₃). $^{13}\text{C}\{^1\text{H}\}$ NMR (298 K, 100.62 MHz, CD_2Cl_2 , ppm): δ 138.8 (s, 1C, ring-N=CH), 129.7 (s, 1C, ring-NCH₃-CH), 105.3 (s, 1C, ring-NCH₃-CH=CH), 38.6 (s, 1C, ring-NCH₃-CH). 2D (^1H - ^{15}N) HMBC NMR (298 K, CD_2Cl_2 , 500.33 - 50.70 MHz, ppm): δ -178.9 (s, 1N, ring-N-NCH₃), -152.1 (s, 1N, ring-N-NCH₃).

3,5-dimethylpyrazole g: ^1H NMR (298 K, 400.13 MHz, CD_2Cl_2 , ppm): δ 12.29 (s 1H, ring-N-NH-C(CH₃)), 5.81 (s, 1H, ring-N=C(CH₃)-CH), 2.27 (s, 6H, ring-(CH₃)-C=N-NH-C(CH₃)). $^{13}\text{C}\{^1\text{H}\}$ NMR (298 K, 100.62 MHz, CD_2Cl_2 , ppm): δ 144.2 (s, 2C, ring-(CH₃)-C=N-NH-C(CH₃)), 103.9 (s, 1C, ring-N=C(CH₃)-CH), 12.1 (s, 2C, ring-(CH₃)-C=N-NH-C(CH₃)).

Synthesis of 1,4-di-tert-butyl-pyrazole, ligand h⁶

10.2 g (0.1 mol) of pyrazole followed by 35.6 g (0.32 mol) of *tert*-butanol and finally 0.77 g (0.005 mol) of sulfuric acid were added in an autoclave for 3 hours at 473 K under vigorous stirring. The vessel reached a total pressure of roughly 40 bar due to the *in situ* production of isobutene. The heating was then turned off and the reactor cooled down to RT under stirring for a further 12 hours period. This longer period of time in comparison with the initial protocol described in the literature must have favored a dehydration mechanism in the

(6) Merkle, H. R.; Fretschner, E.; Schroder, J. WO96/27589 (to BASF AG), **1996**.

4 position of the pyrazole ring so that an additional ^tBu group was substituted in that position. After gas release (depressurization), the medium was transferred for decantation and 15 mL of *tert*-butanol was added to the flask. The upper phase (organic phase) contained the expected product whereas unreacted pyrazole remained in the aqueous phase. The organic phase was collected and heated to 355 K under vacuum in a schlenk tube for over 4 hours in order to remove the alcohol. The white crude material left over was submitted to a silica column chromatography (Cyclohexane/Ethyl acetate, 9:1) for further purification. After the correct fractions collected and the solvents removed, white needles were obtained suitable for X-ray analysis. Ligand **h** was produced with an 89 % yield and stored at 255 K under argon prior to use, although the product is not air sensitive. ¹H NMR (298 K, 400.13 MHz, CD₂Cl₂, ppm): δ 7.37 (s, 1H, ring-N-C(CH₃)₃-N=CH), 7.34 (s, 1H, ring-N-C(CH₃)₃-CH), 1.57 (s, 9H, ring-N-C(CH₃)₃), 1.28 (s, 9H, ring-N-C=C-C(CH₃)₃). ¹³C{¹H} NMR (298 K, 100.62 MHz, CD₂Cl₂, ppm): δ 135.5 (s, 1C, ring-N-C(CH₃)₃-N=CH), 132.1 (s, 1C, ring-N-C(CH₃)₃-N=CH-C), 121.5 (s, 1C, ring-N-C(CH₃)₃-CH), 57.8 (s, 2C, ring-N-C=C-C(CH₃)₃, ring-N-C(CH₃)₃), 31.6 (s, 3C, ring-N-C(CH₃)₃), 29.6 (s, 3C, ring-N-C=C-C(CH₃)₃). Anal. Calcd. for C₁₁H₂₀N₂ (%): C, 73.33; H, 11.11; N, 15.55. Found: C, 73.21; H, 11.05; N, 15.48. MS (DCI⁺): *m/z* (%) 181.1 [M + H]⁺ (100%).

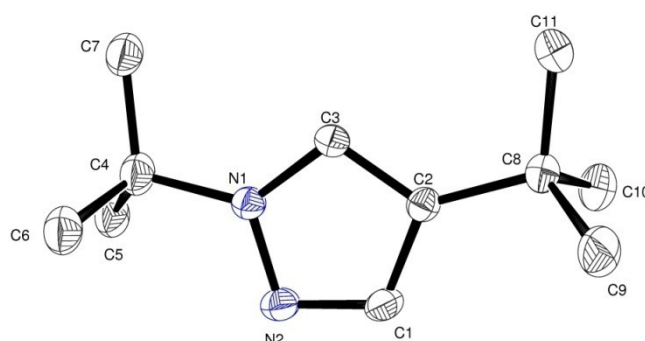


Figure 2. Single-crystal X-ray ORTEP view of **h**. Thermal ellipsoids are shown at the 30% probability level.

Diethylsulfide i: ^1H NMR (298 K, 400.13 MHz, CD_2Cl_2 , ppm): δ 2.56 (q, 4H, $^3J_{\text{H-H}} = 7.50$ Hz, CH_2), 1.26 (t, 6H, $^3J_{\text{H-H}} = 7.20$ Hz, CH_3). $^{13}\text{C}\{^1\text{H}\}$ NMR (298 K, 100.62 MHz, CD_2Cl_2 , ppm): δ 46.3 (s, 2C, CH_2), 11.7 (s, 2C, CH_3).

V-1-4 Synthesis of neutral *cis*-[RhCl(CO)₂(L)] 3 complexes

To a dichloromethane solution ($V = 25$ mL) of **1** (500 mg, 1.28 mmol) under stirring was added via cannulation a solution of 2 molar eq. of ligand (**a**, **b**, **d**, **e**, **f** or **h**) in dichloromethane ($V = 5$ mL). The reaction mixture was vigorously stirred at room temperature for 6 hours. After solvent removal under vacuum (or evaporation under CO flux), the compounds **3** obtained were washed with pentane, dried under vacuum and stored under argon at 255 K prior to use.

Chloro(dicarbonyl)(diethylamine)rhodium(I) complex [RhCl(CO)₂{(HN(CH₂CH₃)₂)}]

3a: Light orange-brown microcrystalline product (Yield 95%). Crystals ready for X-ray analysis were obtained in CH_2Cl_2 /pentane at 255 K. FT-IR (ν_{CO} , cm^{-1}): 2085.0 (s), 2007.0 (s) (CH_2Cl_2); 2075.0 (m br), 2062.5 (sh), 1987.3 (s), 1970.6 (sh), 1959.7 (sh) (ATR). ^1H NMR (298 K, 400.13 MHz, CD_2Cl_2 , ppm): δ 3.28 (br s, NH), 2.99 (m, 4H, CH_2CH_3), 1.47 (t, 6H, CH_2CH_3 , $^2J_{\text{H-H}} = 7.2$ Hz). $^{13}\text{C}\{^1\text{H}\}$ NMR (298 K, 100.62 MHz, CD_2Cl_2 , ppm): δ 183.5 (d, 1C, CO, $^1J_{\text{CO-Rh}} = 65.7$ Hz), 181.2 (d, 1C, CO, $^1J_{\text{CO-Rh}} = 75.5$ Hz), 49.4 (s, 1C, CH_2CH_3), 15.1 (s, 1C, CH_2CH_3). Anal. Calcd. For $\text{C}_6\text{H}_{11}\text{ClNO}_2\text{Rh}$ (%): C, 26.92; H, 4.11; N, 5.23. Found: C, 27.01; H, 4.19; N, 5.24. MS (DCI^+): m/z (%) 285.0 [$\text{M} + \text{NH}_4$]⁺ (100%).

Chloro(dicarbonyl)(triethylamine)rhodium(I) complex [RhCl(CO)₂{(N(CH₂CH₃)₃)}] **3b:**

Dark oil (Yield 78%). FT-IR (ν_{CO} , cm^{-1}): 2084.1 (s), 2004.7 (s) (CH_2Cl_2).

Chloro(dicarbonyl)(1-methylimidazole)rhodium(I) complex [RhCl(CO)₂{(N₂C₄H₆)}] **3d:**

Green-golden microcrystalline product (Yield 93%). Crystals ready for X-ray analysis were

obtained in CH₂Cl₂/pentane at 255 K. FT-IR (ν_{CO} , cm⁻¹): 2084.2 (s), 2008.3 (s) (CH₂Cl₂); 2074.2 (m), 2056.5 (s), 1995.5 (sh), 1983.8 (vs), 1970.7 (sh), 1958.7 (sh) (ATR). ¹H NMR (298 K, 400.13 MHz, CD₂Cl₂, ppm): δ 8.07 (s, 1H, ring-N=CHN-CH₃), 7.21 (s, 1H, ring-NCH=CHN-CH₃), 7.05 (s, 1H, ring-NCH=CHN-CH₃), 3.77 (s, 3H, ring-NCH=CHN-CH₃). ¹³C{¹H} NMR (298 K, 100.62 MHz, CD₂Cl₂, ppm): δ 184.4 (d, 1C, CO, ¹J_{CO-Rh} = 64.5 Hz), 181.2 (d, 1C, CO, ¹J_{CO-Rh} = 73.9 Hz), 140.1 (s, 1C, ring-N=CHN-CH₃), 130.4 (s, 1C, ring-NCH=CHN-CH₃), 121.4 (s, 1C, ring-NCH=CHN-CH₃), 34.8 (s, 1C, ring-NCH=CHN-CH₃). Anal. Calcd. For C₆H₆ClN₂O₂Rh (%): C, 26.05; H, 2.17; N, 10.13. Found: C, 26.10; H, 2.19; N, 10.15. MS (DCI⁺): *m/z* (%) 294.4 [M + NH₄]⁺ (100%).

Chloro(dicarbonyl)(pyrazole)rhodium(I) complex [RhCl(CO)₂{(N₂C₃H₄)}] 3e: Red microcrystalline product (Yield 92%). Crystals ready for X-ray analysis were obtained in CH₂Cl₂/pentane at 255 K. FT-IR (ν_{CO} , cm⁻¹): 2089.9 (s), 2017.3 (s) (CH₂Cl₂); 2067.6 (s), 2009.0 (vs br), 1981.0 (sh) (ATR). ¹H NMR (298 K, CD₂Cl₂, 400.13 MHz, ppm): δ 9.18 (br s, 1H, ring-N-NH-CH), 7.74 (s, 2H, ring-CH_a=N-NH-CH_b), 6.56 (t, 1H, ring-NH-CH=CH_c, ³J_{Hc-Ha} = ³J_{Hc-Hb} = 2.0 Hz). ¹³C{¹H} NMR (298 K, 100.62 MHz, CD₂Cl₂, ppm): δ 182.1 (d, 2C, CO, ¹J_{CO-Rh} = 70.8 Hz), 136.9 (br s, 2C, ring-CH=N-NH-CH), 107.5 (s, 1C, ring-NH-CH=CH). Anal. Calcd. For C₅H₄ClN₂O₂Rh (%): C, 22.86; H, 1.52; N, 10.67. Found: C, 22.94; H, 1.60; N, 10.72. MS (DCI⁺): *m/z* (%) 280.4 [M + NH₄]⁺ (100%).

Chloro(dicarbonyl)(1-methylpyrazole)rhodium(I) complex [RhCl(CO)₂{(N₂C₄H₆)}] 3f: Red-orange microcrystalline product (Yield 96%). Crystals ready for X-ray analysis were obtained in CH₂Cl₂/pentane at 255 K. FT-IR (ν_{CO} , cm⁻¹): 2089.7 (s), 2015.5 (s) (CH₂Cl₂); 2078.0 (vs), 1997.2 (vs) (ATR). ¹H NMR (298 K, CD₂Cl₂, 400.13 MHz, ppm): δ 7.69 (br d, 1H, ring-N=CH_b-CH_c, ³J_{Hb-Hc} = 2.0 Hz), 7.67 (br d, 1H, ring-NCH₃-CH_a-CH_c, ³J_{Ha-Hc} = 2.0 Hz), 6.45 (t, 1H, ring-NCH₃-CH_a=CH_c, ³J_{H-H} = 2.4 Hz), 4.16 (s, 3H, ring-NCH₃). ¹³C{¹H}

NMR (298 K, 100.62 MHz, CD₂Cl₂, ppm): δ 183.3 (br d, 1C, CO, $^1J_{\text{CO-Rh}} = 51.4$ Hz), δ 180.0 (br d, 1C, CO, $^1J_{\text{CO-Rh}} = 60.1$ Hz), 142.4 (s, 1C, ring-N=CH), 134.3 (s, 1C, ring-NCH₃-CH), 107.5 (s, 1C, ring-NCH₃-CH=CH), 40.8 (s, 1C, ring-NCH₃-CH). Anal. Calcd. For C₆H₆ClN₂O₂Rh (%): C, 26.05; H, 2.17; N, 10.13. Found: C, 26.08; H, 2.18; N, 10.16. MS (DCI⁺): m/z (%) 294.3 [M + NH₄]⁺ (100%).

Chloro(dicarbonyl)(1,4-di-*tert*-butyl-pyrazole)rhodium(I)complex

[RhI(CO)₂{(N₂C₁₁H₂₀)}] **3h**: Bright yellow microcrystalline product (96%). Crystals ready for X-ray analysis were obtained in CH₂Cl₂ at 255 K. FT-IR (ν_{CO} cm⁻¹): 2087.2 (s), 2012.9 (s) (CH₂Cl₂); 2075.5 (vs), 1993.2 (vs) (ATR). ¹H NMR (298 K, 500.33 MHz, CD₂Cl₂, ppm): δ 7.76 (br s, 1H, ring-N-C(CH₃)₃-N=CH), 7.60 (br s, 1H, ring-N-C(CH₃)₃-CH), 1.88 (br s, 9H, ring-N-C(CH₃)₃), 1.31 (s, 9H, ring-N-CH=C-C(CH₃)₃). ¹³C{¹H} NMR (298 K, 125.82 MHz, CD₂Cl₂, ppm): δ 183.4 (br d, 1C, CO, $^1J_{\text{Rh-CO}} = 68.2$ Hz), 180.0 (br d, 1C, CO, $^1J_{\text{Rh-CO}} = 76.8$ Hz), 139.4 (s, 1C, ring-N-C(CH₃)₃-N=CH), 133.1 (s, 1C, ring-N-C(CH₃)₃-N=CH-C), 127.4 (s, 1C, ring-N-C(CH₃)₃-CH), 60.5 (s, 2C, ring-N-C=C-C(CH₃)₃, ring-N-C(CH₃)₃), 31.2 (br s, 3C, ring-N-C(CH₃)₃), 30.9 (s, 3C, ring-N-CH=C-C(CH₃)₃). ¹H NMR (193 K, 500.33 MHz, CD₂Cl₂, ppm): δ 7.69 (s, 1H, ring-N-C(CH₃)₃-N=CH), 7.55 (s, 1H, ring-N-C(CH₃)₃-CH), 1.81 (s, 9H, ring-N-C(CH₃)₃), 1.22 (s, 9H, ring-N-CH=C-C(CH₃)₃). Anal. Calcd. For C₁₃H₂₀ClN₂O₂Rh (%): C, 41.67; H, 5.34; N, 7.48. Found: C, 41.44; H, 5.38; N, 7.38. MS (DCI⁺): m/z (%) 392.3 [M + NH₄]⁺ (100%).

V-1-5 Synthesis of neutral *cis*-[RhI(CO)₂(L)] 4 complexes

To a dichloromethane solution (V = 25 mL) of **2** (500 mg, 0.87 mmol) under stirring was added via cannulation a solution of 2 molar eq. of ligand (**a-i**) in dichloromethane (V = 5 mL) at 263 K. The reaction mixture was slowly warmed to room temperature and vigorously stirred during 6 hours. After solvent removal under vacuum, the compounds **4** were washed

with pentane, dried under vacuum and stored under argon at 255 K prior to use. For $^{13}\text{C}\{^1\text{H}\}$ NMR measurements of **4** and **6** ^{13}C -labeled $[\text{Rh}(\mu\text{-I})(\text{CO})_2]_2$ was used as the precursor.

Iodo(dicarbonyl)(diethylamine)rhodium(I) complex $[\text{RhI}(\text{CO})_2\{\text{HN}(\text{CH}_2\text{CH}_3)_2\}]$ **4a:**

Brown green microcrystalline product (Yield 92%). Crystals ready for X-ray analysis were obtained in pentane at 255 K. FT-IR (ν_{CO} , cm^{-1}): 2077.6 (s), 2005.8 (s) (CH_2Cl_2); 2074.0 (s), 2000.9 (s) (CH_3I); 2068.1 (m br), 1998.3 (vs) (ATR). **4a**- ^{13}C : ^1H NMR (298 K, 400.13 MHz, CD_2Cl_2 , ppm): δ 3.45 (br s, 1H, NH), 3.07 (m, 2H, CH_2CH_3 , $^2J_{\text{H-H}} = 4.0$ Hz), 2.97 (m, 2H, CH_2CH_3 , $^2J_{\text{H-H}} = 4.0$ Hz), 1.45 (t, 6H, CH_2CH_3 , $^2J_{\text{H-H}} = 6.4$ Hz). $^{13}\text{C}\{^1\text{H}\}$ NMR (298 K, 100.62 MHz, CD_2Cl_2 , ppm): δ 184.5 (dd, 1C, CO, $^1J_{\text{CO-Rh}} = 65.4$ Hz, $^2J_{\text{CO-CO}} = 4.0$ Hz), 180.2 (dd, 1C, CO, $^1J_{\text{CO-Rh}} = 79.5$ Hz, $^2J_{\text{CO-CO}} = 4.1$ Hz), 49.8 (s, 1C, CH_2CH_3), 15.1 (s, 1C, CH_2CH_3). Anal. Calcd. for $\text{C}_6\text{H}_{11}\text{INO}_2\text{Rh}$ (%): C, 20.05; H, 3.06; N, 3.90. Found: C, 20.20; H, 3.22; N, 3.70. MS (DCI^+): m/z (%) 376.9 $[\text{M} + \text{NH}_4]^+$ (100%).

Iodo(dicarbonyl)(triethylamine)rhodium(I) complex $[\text{RhI}(\text{CO})_2\{\text{N}(\text{CH}_2\text{CH}_3)_3\}]$ **4b:**

Dark brown oil (Yield 80%). FT-IR (ν_{CO} , cm^{-1}): 2076.4 (s), 2003.5 (s) (CH_2Cl_2); 2057.4, 1984.7 (ATR).

Iodo(dicarbonyl)(imidazole)rhodium(I) complex $[\text{RhI}(\text{CO})_2\{\text{N}_2\text{C}_3\text{H}_4\}]$ **4c:**

Brown microcrystalline product (Yield 89%). FT-IR (ν_{CO} , cm^{-1}): 2077.9 (s), 2008.1 (s) (CH_2Cl_2); 2073.3 (s), 2002.8 (s) (CH_3I); 2076.0 (sh), 2059.5 (vs), 1996.1 (vs br), 1970.6 (sh) (ATR). **4c**- ^{13}C : ^1H NMR (298 K, 500.33 MHz, CD_3OD , ppm): δ 8.26 (s, 1H, ring-N=CH-NH), 7.33 (br s, 1H, ring-N-CH=CH), 7.24 (br s, 1H, ring-N-CH=CH). $^{13}\text{C}\{^1\text{H}\}$ NMR (298 K, 125.82 MHz, CD_3OD , ppm) δ 185.7 (br d, 1C, CO, $^1J_{\text{CO-Rh}} = 63.2$ Hz), 180.0 (br d, 1C, CO, $^1J_{\text{CO-Rh}} = 70.8$ Hz), 140.3 (s, 1C, ring-N=CH-NH), 130.5 (s, 1C, ring-N-CH=CH), 117.1 (s, 1C, ring-N-CH=CH). ^1H NMR (233 K, 500.33 MHz, CD_3OD , ppm): δ 8.36 (s, 1H, ring-N=CH_a-NH), 7.40 (s, 1H, ring-N-CH_b=CH_c), 7.28 (t, 1H, ring-N-CH_b=CH_c, $^3J_{\text{Hc-Hb}} = ^4J_{\text{Hc-Ha}} = 1.5$ Hz).

$^{13}\text{C}\{^1\text{H}\}$ NMR (233 K, 125.82 MHz, CD_3OD , ppm) δ 186.1 (d, 1C, CO, $^1J_{\text{CO-Rh}} = 61.9$ Hz), 179.9 (d, 1C, CO, $^1J_{\text{CO-Rh}} = 76.5$ Hz), 140.6 (s, 1C, ring-N=CH-NH), 130.8 (s, 1C, ring-N-CH=CH), 117.2 (s, 1C, ring-N-CH=CH). Anal. Calcd. for $\text{C}_5\text{H}_4\text{IN}_2\text{O}_2\text{Rh}$ (%): C, 18.75; H, 1.25; N, 8.75. Found: C, 18.74; H, 1.22; N, 8.74. MS (DCI⁺): m/z (%) 371.8 [$\text{M} + \text{NH}_4$]⁺ (100%).

Iodo(dicarbonyl)(1-methylimidazole)rhodium(I) complex $[\text{RhI}(\text{CO})_2\{(\text{N}_2\text{C}_4\text{H}_6)\}]$ **4d:**

Brown microcrystalline product (Yield 92%). Crystals ready for X-ray analysis were obtained in CH_2Cl_2 /pentane at 255 K. FT-IR (ν_{CO} , cm^{-1}): 2077.0 (s), 2007.1 (s) (CH_2Cl_2); 2072.4 (s), 2002.0 (s) (CH_3I); 2052.2 (s), 1994.6 (vs br) (ATR). **4d- ^{13}C** : ^1H NMR (298 K, CD_2Cl_2 , 500.33 MHz, ppm): δ 8.14 (s, 1H, ring-N=CHN- CH_3), 7.30 (s, 1H, ring-NCH=CHN- CH_3), 7.03 (s, 1H, ring-NCH=CHN- CH_3), 3.78 (s, 3H, ring-NCH=CHN- CH_3). $^{13}\text{C}\{^1\text{H}\}$ NMR (298 K, 125.82 MHz, CD_2Cl_2 , ppm): δ 185.0 (br d, 1C, CO), 180.1 (br d, 1C, CO, $^1J_{\text{CO-Rh}} = 73.0$ Hz), 142.3 (s, 1C, ring-N=CHN- CH_3), 131.9 (s, 1C, ring-NCH=CHN- CH_3), 121.4 (s, 1C, ring-NCH=CHN- CH_3), 34.7 (s, 1C, ring-NCH=CHN- CH_3). ^1H NMR (235 K, CD_2Cl_2 , 500.33 MHz, ppm): δ 8.12 (s, 1H, ring-N=CHN- CH_3), 7.25 (s, 1H, ring-NCH=CHN- CH_3), 7.04 (d, 1H, ring-NCH=CHN- CH_3 , $^3J_{\text{H-H}} = 1.5$ Hz), 3.76 (br s, 3H, ring-NCH=CHN- CH_3 , $^2J_{\text{H-N}} = 3.5$ Hz). $^{13}\text{C}\{^1\text{H}\}$ NMR (235 K, 125.82 MHz, CD_2Cl_2 , ppm): δ 185.4 (d, 1C, CO, $^1J_{\text{CO-Rh}} = 62.4$ Hz), 179.8 (d, 1C, CO, $^1J_{\text{CO-Rh}} = 77.9$ Hz), 142.3 (s, 1C, ring-N=CHN- CH_3), 131.9 (s, 1C, ring-NCH=CHN- CH_3), 121.6 (s, 1C, ring-NCH=CHN- CH_3), 35.0 (s, 1C, ring-NCH=CHN- CH_3). ^1H NMR (298 K, CD_3OD , 500.33 MHz, ppm): δ 8.22 (s, 1H, ring-N=CHN- CH_3), 7.31 (s, 1H, ring-NCH=CHN- CH_3), 7.22 (s, 1H, ring-NCH=CHN- CH_3), 3.80 (s, 3H, ring-NCH=CHN- CH_3). $^{13}\text{C}\{^1\text{H}\}$ NMR (298 K, 125.82 MHz, CD_3OD , ppm): δ 185.5 (br d, 1C, CO), 180.1 (br d, 1C, CO), 142.3 (s, 1C, ring-N=CHN- CH_3), 131.2 (s, 1C, ring-NCH=CHN- CH_3), 121.6 (s, 1C, ring-NCH=CHN- CH_3), 33.4 (s, 1C, ring-NCH=CHN- CH_3). ^1H NMR (243 K, CD_3OD , 500.33 MHz, ppm): δ 8.30 (s, 1H, ring-N=CHN- CH_3), 7.38 (s, 1H, ring-

NCH=CHN-CH₃), 7.26 (d, 1H, ring-NCH=CHN-CH₃), 3.81 (br s, 3H, ring-NCH=CHN-CH₃). ¹³C{¹H} NMR (243 K, 125.82 MHz, CD₃OD, ppm): δ 185.9 (d, 1C, CO, ¹J_{CO-Rh} = 62.0 Hz), 179.9 (d, 1C, CO, ¹J_{CO-Rh} = 76.5 Hz), 142.6 (s, 1C, ring-N=CHN-CH₃), 131.5 (s, 1C, ring-NCH=CHN-CH₃), 121.5 (s, 1C, ring-NCH=CHN-CH₃), 33.4 (s, 1C, ring-NCH=CHN-CH₃). ¹H NMR (298 K, AcOH-*d*₄, 300.13 MHz, ppm): δ 8.19 (s, 1H, ring-N=CHN-CH₃), 7.32 (s, 1H, ring-NCH=CHN-CH₃), 7.14 (s, 1H, ring-NCH=CHN-CH₃), 3.81 (s, 3H, ring-NCH=CHN-CH₃). ¹³C{¹H} NMR (298 K, AcOH-*d*₄, 75.47 MHz, ppm): δ 184.7 (br s, 1C, CO), 181.0 (br s, 1C, CO), 142.3 (s, 1C, ring-N=CHN-CH₃), 131.2 (s, 1C, ring-NCH=CHN-CH₃), 121.5 (s, 1C, ring-NCH=CHN-CH₃), 33.7 (s, 1C, ring-NCH=CHN-CH₃). 2D (¹H-¹⁵N) HMBC NMR (298 K, CD₂Cl₂, 500.33 - 50.70 MHz, ppm): δ -214.2 (br s, 1N, ring-N=CHN-CH₃, ²J_{N-H} = 6.6 Hz), -189.8 (br d, 1N, ring-N=CHN-CH₃, ¹J_{Rh-N} = 23.5 Hz). Anal. Calcd. for C₆H₆IN₂O₂Rh (%): C, 19.57; H, 1.64; N, 7.55. Found: C, 19.17; H, 1.63; N, 7.61. MS (DCI⁺): *m/z* (%) 385.9 [M + NH₄]⁺ (100%).

Iodo(dicarbonyl)(pyrazole)rhodium(I) complex [RhI(CO)₂{(N₂C₃H₄)}] **4e:** Brown-orange microcrystalline product (Yield 95%). Crystals ready for X-ray analysis were obtained in CH₂Cl₂/pentane at 255 K. FT-IR (ν_{CO}, cm⁻¹): 2082.4 (s), 2015.0 (s) (CH₂Cl₂); 2078.0 (s), 2010.3 (s) (CH₃I); 2060.2 (s), 1999.4 (vs br), 1976.8 (sh), 1967.7 (sh), 1904.4 (sh) (ATR). **4e**-¹³CO: ¹H NMR (298 K, CD₂Cl₂, 500.33 MHz, ppm): δ 11.71 (br s, 1H, ring-N-NH-CH), 7.78 (br s, 2H, ring-CH_a=N-NH-CH_b), 6.54 (t, 1H, ring-NH-CH=CH_c, ³J_{Hc-Ha} = ³J_{Hc-Hb} = 2.5 Hz). ¹³C{¹H} NMR (298 K, 125.82 MHz, CD₂Cl₂, ppm): δ 181.7 (br s, 2C, CO), 144.9 (br s, 1C, ring-CH=N-NH), 131.4 (br s, 1C, ring-N-NH-CH), 107.8 (s, 1C, ring-NH-CH=CH). ¹H NMR (223 K, CD₂Cl₂, 500.33 MHz, ppm): δ 11.68 (br s, 1H, ring-N-NH-CH), 7.77 (s, 1H, ring-CH_a=N-NH), 7.72 (s, 1H, ring-N-NH-CH_b), 6.51 (s, 1H, ring-NH-CH=CH_c). ¹³C{¹H} NMR (223 K, 125.82 MHz, CD₂Cl₂, ppm): δ 184.9 (dd, 1C, CO, ¹J_{CO-Rh} = 62.9 Hz, ²J_{CO-CO} = 4.4 Hz), 179.1 (dd, 1C, CO, ¹J_{CO-Rh} = 78.0 Hz, ²J_{CO-CO} = 5.2 Hz), 145.2 (s, 1C, ring-CH=N-

NH), 131.8 (s, 1C, ring- N-NH-CH), 108.1 (s, 1C, ring- NH-CH=CH). 2D (^1H - ^{15}N) HMBC NMR (250 K, CD_2Cl_2 , 500.33 - 50.70 MHz, ppm): δ -171.3 (br s, 1N, ring-N-NH-CH), -158.7 (br d, 1N, ring-N-NH-CH). 2D (^1H - ^{103}Rh) HMQC NMR (243 K, CD_2Cl_2 , 500.33 - 15.82 MHz, ppm): δ -8387 (br s, *Rh*). Anal. Calcd. for $\text{C}_5\text{H}_4\text{IN}_2\text{O}_2\text{Rh}$ (%): C, 16.87; H, 1.06; N, 8.01. Found: C, 16.95; H, 1.13; N, 7.91. MS (DCI^+): m/z (%) 371.9 [$\text{M} + \text{NH}_4$] $^+$ (100%).

Iodo(dicarbonyl)(1-methylpyrazole)rhodium(I) complex $[\text{RhI}(\text{CO})_2\{(\text{N}_2\text{C}_4\text{H}_6)\}]$ **4f:**

Bright yellow microcrystalline product (Yield 94%). Crystals ready for X-ray analysis were obtained in CH_2Cl_2 /pentane at 255 K. FT-IR (ν_{CO} , cm^{-1}): 2082.0 (s), 2013.4 (s) (CH_2Cl_2); 2077.6 (s), 2009.2 (s) (CH_3I); 2056.3 (vs), 1986.4 (vs), 1971.0 (sh), 1963.5 (sh) (ATR). **4f**- $^{13}\text{C}\text{O}$: ^1H NMR (298 K, CD_2Cl_2 , 500.33 MHz, ppm): δ 7.69 (br d, 1H, ring-N= CH_b - CH_c , $^3J_{\text{H}_b\text{-H}_c} = 2.0$ Hz), 7.65 (br d, 1H, ring-N CH_3 - CH_a - CH_c , $^3J_{\text{H}_a\text{-H}_c} = 2.0$ Hz), 6.50 (t, 1H, ring-N CH_3 - CH_a = CH_c , $^3J_{\text{H-H}} = 2.5$ Hz), 4.16 (s, 3H, ring-N CH_3). $^{13}\text{C}\{^1\text{H}\}$ NMR (298 K, 125.82 MHz, CD_2Cl_2 , ppm): δ 182.0 (br s, 1C, CO), 142.8 (s, 1C, ring-N=CH), 134.2 (s, 1C, ring-N CH_3 -CH), 107.8 (s, 1C, ring-N CH_3 -CH=CH), 41.3 (s, 1C, ring-N CH_3 -CH). ^1H NMR (203 K, CD_2Cl_2 , 500.33 MHz, ppm): δ 7.66 (br d, 1H, ring-N CH_3 - CH_a = CH_c , $^3J_{\text{H}_a\text{-H}_c} = 2.0$ Hz), 7.65 (br d, 1H, ring-N= CH_b - CH_c , $^3J_{\text{H}_b\text{-H}_c} = 2.0$ Hz), 6.47 (t, 1H, ring-N CH_3 - CH_a = CH_c , $^3J_{\text{H-H}} = 2.5$ Hz), 4.10 (s, 3H, ring-N CH_3). $^{13}\text{C}\{^1\text{H}\}$ NMR (203 K, 125.82 MHz, CD_2Cl_2 , ppm): δ 185.2 (dd, 1C, CO, $^1J_{\text{CO-Rh}} = 59.1$ Hz, $^2J_{\text{CO-CO}} = 4.8$ Hz), 178.9 (dd, 1C, CO, $^1J_{\text{CO-Rh}} = 75.5$ Hz, $^2J_{\text{CO-CO}} = 4.8$ Hz), 142.7 (s, 1C, ring-N=CH), 134.5 (s, 1C, ring-N CH_3 -CH), 107.9 (s, 1C, ring-N CH_3 -CH=CH), 41.7 (s, 1C, ring-N CH_3 -CH). 2D (^1H - ^{15}N) HMBC NMR (298 K, CD_2Cl_2 , 500.33 - 50.70 MHz, ppm): δ -178.6 (br s, 1N, ring-N-N CH_3), -153.9 (br d, 1N, ring-N-N CH_3). 2D (^1H - ^{103}Rh) HMQC NMR (243 K, CD_2Cl_2 , 500.33 - 15.82 MHz, ppm): δ -8334 (br s, *Rh*). Anal. Calcd. for $\text{C}_6\text{H}_6\text{IN}_2\text{O}_2\text{Rh}$ (%): C, 19.36; H, 1.65; N, 7.43. Found: C, 19.57; H, 1.63; N, 7.61. MS (DCI^+): m/z (%) 385.9 [$\text{M} + \text{NH}_4$] $^+$ (100%).

Iodo(dicarbonyl)(3,5-dimethylpyrazole)rhodium(I) complex [RhI(CO)₂{(N₂C₅H₈)}] **4g:**

Dark green microcrystalline product (Yield 96%). FT-IR (ν_{CO} , cm^{-1}): 2080.2 (s), 2011.9 (s) (CH_2Cl_2); 2075.6 (s), 2007.1 (s) (CH_3I); 2070.0 (vs), 2005.8 (vs br) (ATR). **4g-¹³C**: ¹H NMR (298 K, 500.33 MHz, CD_2Cl_2 , ppm): δ 9.83 (br s 1H, ring-N-NH-C(CH_3)), 5.43 (s, 1H, ring-N=C(CH_3)-CH), 1.72 (br s, 6H, ring-(CH_3)-C=N-NH-C(CH_3)). ¹³C{¹H} NMR (298 K, 125.82 MHz, CD_2Cl_2 , ppm): δ 181.4 (br s, 2C, CO), 142.6 (br s, 2C, ring-(CH_3)-C=N-NH-C(CH_3)), 106.0 (s, 1C, ring-N=C(CH_3)-CH), 13.6 (s, 1C, ring-(CH_3)-C=N-NH-C(CH_3)), 10.3 (s, 1C, ring-(CH_3)-C=N-NH-C(CH_3)). ¹H NMR (193 K, 500.33 MHz, CD_2Cl_2 , ppm): δ 9.97 (s 1H, ring-N-NH-C(CH_3)), 5.41 (s, 1H, ring-N=C(CH_3)-CH), 1.76 (s, 3H, ring-(CH_3)-C=N-NH-C(CH_3)), 1.65 (s, 3H, ring-(CH_3)-C=N-NH-C(CH_3)). ¹³C{¹H} NMR (193 K, 125.82 MHz, CD_2Cl_2 , ppm): δ 184.6 (d, 1C, CO, $^1J_{\text{CO-Rh}} = 62.9$ Hz), 178.2 (d, 1C, CO, $^1J_{\text{CO-Rh}} = 78.0$ Hz), 151.7 (s, 1C, ring-(CH_3)-C=N-NH-C(CH_3)), 142.8 (s, 1C, ring-(CH_3)-C=N-NH-C(CH_3)), 105.9 (s, 1C, ring-N=C(CH_3)-CH), 15.3 (s, 1C, ring-(CH_3)-C=N-NH-C(CH_3)), 10.7 (s, 1C, ring-(CH_3)-C=N-NH-C(CH_3)). Anal. Calcd. for $\text{C}_7\text{H}_8\text{IN}_2\text{O}_2\text{Rh}$ (%): C, 21.89; H, 1.97; N, 7.27. Found: C, 21.99; H, 2.09; N, 7.33. MS (DCI⁺): m/z (%) 399.9 [$\text{M} + \text{NH}_4$]⁺ (100%).

Iodo(dicarbonyl)(1,4-di-tert-butyl-pyrazole)rhodium(I) complex [RhI(CO)₂{(N₂C₁₁H₂₀)}] **4h:**

Bright yellow microcrystalline product (92%). Crystals ready for X-ray analysis were obtained in CH_2Cl_2 at 255 K. FT-IR (ν_{CO} cm^{-1}): 2096.0 (w), 2079.6 (s), 2027.1 (m), 2010.5 (s) (CH_2Cl_2); 2075.9 (s), 2006.1 (s) (CH_3I); 2067.5 (vs), 2055.7 (sh), 2011.2 (vs), 1972.8 (sh) (ATR). ¹H NMR (298 K, 500.33 MHz, CD_2Cl_2 , ppm): δ 7.70 (br s, 1H, ring-N-C(CH_3)₃-N=CH), 7.58 (br s, 1H, ring-N-C(CH_3)₃-CH), 1.82 (br s, 9H, ring-N-C(CH_3)₃), 1.31 (s, 9H, ring-N-CH=C-C(CH_3)₃). ¹³C{¹H} NMR (298 K, 125.82 MHz, CD_2Cl_2 , ppm): δ 181.2 (br s, 2C, CO), 139.3 (s, 1C, ring-N-C(CH_3)₃-N=CH), 133.0 (s, 1C, ring-N-C(CH_3)₃-N=CH-C), 126.9 (s, 1C, ring-N-C(CH_3)₃-CH), 60.1 (s, 2C, ring-N-C=C-C(CH_3)₃, ring-N-C(CH_3)₃), 31.3 (br s, 3C, ring-N-C(CH_3)₃), 31.0 (s, 3C, ring-N-CH=C-C(CH_3)₃). ¹H NMR (193 K, 500.33

MHz, CD₂Cl₂, ppm): δ 7.68 (s, 1H, ring-N-C(CH₃)₃-N=CH), 7.57 (s, 1H, ring-N-C(CH₃)₃-CH), 1.80 (s, 9H, ring-N-C(CH₃)₃), 1.22 (s, 9H, ring-N-CH=C-C(CH₃)₃). ¹³C {¹H} NMR (193 K, 125.82 MHz, CD₂Cl₂, ppm): δ 184.9 (d, 1C, CO, ¹J_{Rh-CO} = 65.9 Hz), 178.9 (d, 1C, CO, ¹J_{Rh-CO} = 77.1 Hz), 139.7 (s, 1C, ring-N-C(CH₃)₃-N=CH), 132.4 (s, 1C, ring-N-C(CH₃)₃-N=CH-C), 128.0 (s, 1C, ring-N-C(CH₃)₃-CH), 60.5 (s, 2C, ring-N-CH=C-C(CH₃)₃, ring-N-C(CH₃)₃), 31.4 (s, 3C, ring-N-C(CH₃)₃), 31.3 (s, 3C, ring-N-CH=C-C(CH₃)₃). 2D (¹H-¹⁵N) HMBC NMR (193 K, CD₂Cl₂, 500.33 - 50.70 MHz, ppm): δ -166.4 (br s, 1N, ring- N-N-C(CH₃)₃), -150.3 (br d, 1N, ring- N-N-C(CH₃)₃). 2D (¹H-¹⁰³Rh) HMQC NMR (193 K, CD₂Cl₂, 500.33 - 15.82 MHz, ppm): δ -8351 (br s, Rh). Anal. Calcd. for C₁₃H₂₀IN₂O₂Rh (%): C, 33.49; H, 4.29; N, 6.01. Found: C, 33.52; H, 4.31; N, 6.03. MS (DCI⁺): *m/z* (%) 483.8 [M + NH₄]⁺ (100%).

Iodo(dicarbonyl)(diethylsulfide)rhodium(I) complex [RhI(CO)₂{S(CH₂CH₃)₂}] **4i:** Dark brown oil (Yield 87%). FT-IR (ν_{CO} , cm⁻¹): 2081.3 (s), 2013.4 (s) (CH₂Cl₂); 2076.8 (s), 2008.6 (s) (CH₃I); 2067.0 (vs), 1997.7 (vs), 1968.5 (sh) (ATR). **4h-¹³CO**: ¹H NMR (298 K, 500.33 MHz, CD₂Cl₂, ppm): δ 3.08 (q, 4H, S(CH₂-CH₃)₂, ³J_{H-H} = 7.5 Hz), 1.45 (t, 6H, S(CH₂-CH₃)₂, ³J_{H-H} = 7.5 Hz). ¹³C{¹H} NMR (298 K, 125.82 MHz, CD₂Cl₂, ppm): δ 180.8 (br d, 2C, CO, ¹J_{CO-Rh} = 67.4 Hz), 31.6 (s, 2C, S(CH₂-CH₃)₂), 13.8 (s, 2C, S(CH₂-CH₃)₂). ¹H NMR (183 K, 500.33 MHz, CD₂Cl₂, ppm): δ 3.06 (br d, 4H, S(CH₂-CH₃)₂, ³J_{H-H} = 6.0 Hz), 1.36 (t, 6H, S(CH₂-CH₃)₂, ³J_{H-H} = 7.5 Hz). ¹³C{¹H} NMR (183 K, 125.82 MHz, CD₂Cl₂, ppm): δ 182.5 (d, 1C, CO, ¹J_{CO-Rh} = 66.7 Hz), 180.1 (d, 1C, CO, ¹J_{CO-Rh} = 76.8 Hz), 30.2 (s, 2C, S(CH₂-CH₃)₂), 14.2 (s, 2C, S(CH₂-CH₃)₂). Anal. Calcd. for C₆H₁₀SIO₂Rh (%): C, 19.15; H, 2.66; S, 8.51. Found: C, 19.30; H, 2.70; S, 8.62. MS (DCI⁺): *m/z* (%) 393.99 [M + NH₄]⁺ (100%).

V-1-6 Synthesis of neutral rhodium(III) complex $[Rh(\mu-I)(COMe)(CO)(NCMe)]_2$ **5⁷**

$[Rh(\mu-I)(CO)_2]_2$ **2** (0.46 g, 0.80 mmol) was dissolved in MeCN/MeI (50 mL, 2:1 v/v) and stirred at room temperature under argon for 6 hours. The volatile phase was removed under vacuum and the resulting orange-red precipitate was dried and stored under argon at 255 K prior to use. (Yield 90%). FT-IR (ν_{CO} , ν_{COMe} , cm^{-1}): 2090.8 (s), 1749.2 (m, br), 1730.7 (m, br) (CH_2Cl_2); 2080.1 (s), 1702.3 (m, br) (ATR). 1H NMR (298 K, 400.13 MHz, CD_2Cl_2 , ppm): δ 2.92 (br s, 6H, $COCH_3$), 2.65 (br s, 6H, $NC-CH_3$). $^{13}C\{^1H\}$ NMR (298 K, 100.62 MHz, CD_2Cl_2 , ppm): δ 207.9 (d, 2C, $COCH_3$, $^1J_{COMe-Rh} = 18.9$ Hz), 182.1 (d, 2C, CO, $^1J_{CO-Rh} = 63.7$ Hz), 58.7 (s, 2C, $NC-CH_3$), 45.6 (s, 2C, $COCH_3$), 29.7 (s, 2C, $NC-CH_3$). Anal. Calcd. for $C_5H_6I_2NO_2Rh$ (%): C, 12.80; H, 1.28; N, 2.98. Found: C, 12.91; H, 1.32; N, 2.92.

V-1-7 Synthesis of neutral rhodium(III) complexes $[Rh(\mu-I)(COMe)(CO)(L)]_2$ **6**

To a solution of MeI (12 mL) was added *cis*- $[RhI(CO)_2(L)]$ **4** (200 mg) at room temperature. The solution was allowed to react at RT under vigorous stirring for 5 days (in order to make sure that the oxidative addition was complete). During this time, all solutions turned dark red. After removal of MeI excess under vacuum, the compounds **6a** and **6c-i** obtained were washed with pentane or ether, dried under vacuum and stored under argon at 255 K prior to use.

$[Rh(\mu-I)(COMe)(CO)(HN(CH_2CH_3)_2)]_2$ **6a**: Dark brown oil (87%). FT-IR (ν_{CO} , ν_{COMe} , cm^{-1}): 2072.6 (s), 1719.1 (m, br) (CH_2Cl_2); 2063.3 (s), 1716.4 (m, br) (CH_3I). 1H NMR (298 K, 400.13 MHz, CD_2Cl_2 , ppm): δ 7.68 (br s, 2H, *NH*), 3.18 (q, 8H, CH_2CH_3 , $^2J_{H-H} = 6.2$ Hz), 3.15 (s, 6H, $COCH_3$), 1.44 (t, 12H, CH_2CH_3 , $^2J_{H-H} = 7.2$ Hz). $^{13}C\{^1H\}$ NMR (298 K, 100.62 MHz, CD_2Cl_2 , ppm): δ not observed (*COMe*), 188-182 (br m, main d at 183.4, CO, $^1J_{CO-Rh} =$

(7) Haynes, A.; Maitlis, P. M.; Stanbridge, I. A.; Haak, S.; Pearson, J. M.; Adams, H.; Bailey, N. A. *Inorg. Chim. Acta* **2004**, 357, 3027.

72.9 Hz), 49.7 (br s, 2C, COCH₃), 42.9 (s, 4C, CH₂CH₃), 11.1 (s, 4C, CH₂CH₃). Anal. Calcd. for C₇H₁₃I₂NO₂Rh (%): C, 16.81; H, 2.60; N, 2.80. Found: C, 16.96; H, 2.80; N, 2.81.

[RhI(μ-I)(COMe)(CO)(N₂C₃H₄)₂ 6c: Dark brown powder poorly soluble in CH₂Cl₂ (Yield 86%). FT-IR (ν_{CO}, ν_{COMe}, cm⁻¹): 2073.7 (s), 1734.9 (m, br), 1707.0 (m, br) (CH₂Cl₂); 2073.9 (s), 1719.2 (m, br), 1705.2 (m, br) (CH₃I). ¹H NMR (298 K, 300.13 MHz, CD₂Cl₂, ppm): δ 9.66 (br s, 2H, ring-N=CH-NH), 8.77 (s, 2H, ring-N=CH-NH), 8.02 (s, 2H, ring-N-CH=CH), 7.14 (s, 2H, ring-N-CH=CH). Anal. Calcd. for C₆H₇I₂N₂O₂Rh (%): C, 14.52; H, 1.41; N, 5.64. Found: C, 14.68; H, 1.60; N, 5.52.

[RhI(μ-I)(COMe)(CO)(N₂C₄H₆)₂ 6d: Red microcrystalline product (Yield 88%). Crystals suitable for X-ray analysis were obtained in CH₂Cl₂ at 255 K. FT-IR (ν_{CO}, ν_{COMe}, cm⁻¹): 2073.1 (s), 1733.5 (m, br) (CH₂Cl₂); 2068.0 (s), 1736.0 (m, br) (CH₃I). **6d-¹³CO:** ¹H NMR (298 K, CD₂Cl₂, 400.13 MHz, ppm): δ 8.58 (s, 2H, ring-N=CHN-CH₃), 7.96 (s, 2H, ring-NCH=CHN-CH₃), 6.98 (s, 2H, ring-NCH=CHN-CH₃), 3.85 (br s, 6H, ring-NCH=CHN-CH₃), 2.84 (br s, 6H, COCH₃). ¹³C{¹H} NMR (298 K, 100.62 MHz, CD₂Cl₂, ppm): δ 216-208 (br m, COMe, main pseudo-d at 209.8, ¹J_{COMe-Rh} = 17.6 Hz), 185-179 (br m, CO, main d at 183.4, ¹J_{CO-Rh} = 58.3 Hz), 145.0 (s, 1C, ring-N=CHN-CH₃), 134.5 (s, 1C, ring-NCH=CHN-CH₃), 120.5 (s, 1C, ring-NCH=CHN-CH₃), 47.3 (m, 2C, COCH₃), 34.7 (s, 2C, ring-NCH=CHN-CH₃). Anal. Calcd. for C₇H₉I₂N₂O₂Rh (%): C, 16.48; H, 1.76; N, 5.49. Found: C, 16.82; H, 1.90; N, 5.39.

[RhI(μ-I)(COMe)(CO)(N₂C₃H₄)₂ 6e: Red microcrystalline product (Yield 90%). Crystals ready for X-ray analysis were obtained in CH₂Cl₂ at 255 K. FT-IR (ν_{CO}, ν_{COMe}, cm⁻¹): 2083.5 (s), 1741.0 (m, br), 1721.0 (m, br) (CH₂Cl₂); 2075.6 (s), 1736.7 (m, br) (CH₃I). **6e-¹³CO:** ¹H NMR (298 K, CD₂Cl₂, 300.13 MHz, ppm): δ 11.84 (br s, 2H, ring-N-NH-CH), 7.81 (br s, 2H, ring-CH=N-NH-CH), 7.75 (s, 2H, ring-CH=N-NH-CH), 6.55 (t, 2H, ring-NH-CH=CH ³J_{H-H} =

2.4 Hz), 2.95, 2.94 (6H, COCH₃). ¹³C{¹H} NMR (298 K, 75.47 MHz, CD₂Cl₂, ppm): δ 213.2 (br s, COMe), 186-178 (br m, main d at 182.8 CO, ¹J_{CO-Rh} = 60.6 Hz), 146.1 (s, 2C, ring-CH=N-NH), 131.3 (s, 2C, ring- N-NH-CH), 107.6 (s, 2C, ring- NH-CH=CH), 48.0 (br s 2C, COCH₃). Anal. Calcd. for C₆H₇I₂N₂O₂Rh (%): C, 14.52; H, 1.41; N, 5.64. Found: C, 14.41; H, 1.43; N, 5.59.

[RhI(μ-I)(COMe)(CO)(N₂C₄H₆)₂ 6f: Dark brown powder (Yield 84%). FT-IR (ν_{CO}, ν_{COMe}, cm⁻¹): 2076.6 (s), 1778.0 (m, br) (CH₂Cl₂); 2072.3 (s), 1776.4 (m, br), 1743.7 (m, br) (CH₃I). ¹H NMR (298 K, CD₂Cl₂, 300.13 MHz, ppm): δ 8.21 (br s, 1H, ring-N=CH-CH), 7.89 (br s, 1H, ring-N=CH-CH), 7.73 (br s, 1H, ring-NCH₃-CH-CH), 7.60 (br s, 1H, ring-NCH₃-CH-CH), 6.59 (br s, 1H, ring-NCH₃-CH=CH), 6.44 (br s, 1H, ring-NCH₃-CH=CH), 3.97 (s, 6H, ring-NCH₃), 3.75 (s, 3H, COCH₃), 3.17 (s, 3H, COCH₃). ¹³C{¹H} NMR (298 K, 75.47 MHz, CD₂Cl₂, ppm): δ n. d. (COMe), 182.0 (br d, CO, ¹J_{CO-Rh} = 65.7 Hz), 148.7 (s, 1C, ring-N=CH), 145.3 (s, 1C, ring-N=CH), 138.1 (s, 1C, ring-NCH₃-CH), 135.2 (s, 1C, ring-NCH₃-CH), 107.7 (s, 1C, ring-NCH₃-CH=CH), 106.6 (s, 1C, ring-NCH₃-CH=CH), 45.5 (br s, 2C, COCH₃), 37.8 (s, 2C, ring-NCH₃-CH). Anal. Calcd. for C₇H₉I₂N₂O₂Rh (%): C, 16.48; H, 1.76; N, 5.49. Found: C, 16.64; H, 1.83; N, 5.41.

[RhI(μ-I)(COMe)(CO)(N₂C₅H₈)₂ 6g: Dark brown powder (Yield 86%). FT-IR (ν_{CO}, ν_{COMe}, cm⁻¹): 2079.6 (s), 1753.8 (m, br) (CH₂Cl₂); 2075.5 (s), 1749.6 (m, br) (CH₃I). ¹H NMR (298 K, 300.13 MHz, CD₂Cl₂, ppm): δ 10.82 (br s 2H, ring-N-NH-C(CH₃)), 6.08 (br s, 2H, ring-N=C(CH₃)-CH), 3.18 (s, 6H, COCH₃), 2.44 (s, 6H, ring1-(CH₃)-C=N-NH-C(CH₃)), 2.25 (s, 6H, ring2-(CH₃)-C=N-NH-C(CH₃)). ¹³C{¹H} NMR (298 K, 100.62 MHz, CD₂Cl₂, ppm): δ 212.5 (d, COMe, ¹J_{COMe-Rh} = 19.0 Hz), 204.6 (br m, COMe), 183.6 (d, CO, ¹J_{CO-Rh} = 63.1 Hz), 150.9 (s, 2C, ring-(CH₃)-C=N-NH-C(CH₃)), 142.5 (s, 2C, ring-(CH₃)-C=N-NH-C(CH₃)), 107.6 (s, 2C, ring-N=C(CH₃)-CH), 46.5 (br s, 2C, COCH₃), 16.2 (s, 2C, ring-(CH₃)-C=N-NH-

C(CH₃)), 11.1 (s, 2C, ring-(CH₃)-C=N-NH-C(CH₃)). Anal. Calcd. for C₈H₁₁I₂N₂O₂Rh (%): C, 18.33; H, 2.10; N, 5.34. Found: C, 18.60; H, 2.37; N, 5.21.

[RhI(μ-I)(COMe)(CO)(N₂C₁₁H₂₀)]₂ 6h: Only characterized in solution. FT-IR (ν_{CO} , ν_{COMe} , cm⁻¹): 2081.9 (s), 2057.2 (sh), 1718.8 (br s) (CH₂Cl₂); 2076.7 (s), 1742.5 (sh), 1719.1 (br s) (CH₃I).

[RhI(μ-I)(COMe)(CO)(S(CH₂CH₃)₂)₂]₂ 6i: Dark brown oil (Yield 85%). FT-IR (ν_{CO} , ν_{COMe} , cm⁻¹): 2080.6 (s), 1720.8 (m, br) (CH₂Cl₂); 2076.4 (s), 1743.6 (m, br), 1721.1 (m, br) (CH₃I). ¹H NMR (298 K, 300.13 MHz, CD₂Cl₂, ppm): δ 3.14 (m, 8H, S(CH₂-CH₃)₂), 3.01 (s, 3H, COCH₃), 2.89 (s, 3H, COCH₃), 1.41 (t, 12H, S(CH₂-CH₃)₂, ³J_{H-H} = 6.9 Hz). ¹³C{¹H} NMR (298 K, 75.47 MHz, CD₂Cl₂, ppm): δ n.d (COMe), 181.9 (br d, CO, ¹J_{CO-Rh} = 81.4 Hz), 49.6 (br s, 2C, COCH₃), 36.1 (s, 2C, S(CH₂-CH₃)₂), 29.6 (s, 2C, S(CH₂-CH₃)₂), 21.9 (s, 2C, S(CH₂-CH₃)₂), 9.0 (s, 2C, S(CH₂-CH₃)₂). Anal. Calcd. for C₇H₁₃I₂SO₂Rh (%): C, 16.22; H, 2.51; S, 6.19. Found: C, 16.41; H, 2.71; S, 6.01.

V-1-8 Synthesis of neutral rhodium(III) complex [RhI₂(COMe)(CO)₂(N₂C₃H₄)] 7d

In situ characterization of CO bridge-splitting reaction: To a CD₂Cl₂ solution of **6d** (100 mg, 0.098 mmol) under stirring was fed a CO bubbling (1 bar) for 2 minutes. The reaction mixture turned dark red and was analyzed by FT-IR spectroscopy. For ¹³C{¹H} characterization, the reaction was carried out with **6d**-¹³CO under ¹³CO atmosphere. When not kept under CO atmosphere the reaction was reversible and dimer **6d** was recovered. FT-IR (ν_{CO} , ν_{COMe} , cm⁻¹): 2155.6 (w), 2073.2 (s), 1735.9 (s) (CH₂Cl₂). **7d**-¹³CO: ¹H NMR (298 K, CD₂Cl₂, 400.13 MHz, ppm): δ 8.58 (s, 1H, ring-N=CHN-CH₃), 7.95 (d, 1H, ring-NCH=CHN-CH₃, ³J_{H-H} = 1.2 Hz), 6.98 (d, 1H, ring-NCH=CHN-CH₃, ³J_{H-H} = 1.2 Hz), 3.84 (s, 3H, ring-NCH=CHN-CH₃), 2.82 (s, 3H, COCH₃). ¹³C{¹H} NMR (298 K, 100.62 MHz,

CD₂Cl₂, ppm): δ 210.2 (d, 1C, COMe, $^1J_{\text{COMe-Rh}} = 21.6$ Hz), 183.4 (d, 2C, CO, $^1J_{\text{CO-Rh}} = 58.5$ Hz), 145.0 (s, 1C, ring-N=CHN-CH₃), 134.5 (s, 1C, ring-NCH=CHN-CH₃), 120.5 (s, 1C, ring-NCH=CHN-CH₃), 47.4 (s, 1C, COCH₃), 34.7 (s, 1C, ring-NCH=CHN-CH₃).

V-1-9 Synthesis of neutral rhodium(III) complex [RhI₂(COMe)(CO)(N₂C₃H₄)₂] **8e**

To a dichloromethane solution (V = 10 mL) of **6e** (100 mg, 0.100 mmol) under stirring was added a solution of 2 molar eq. of ligand **e** in dichloromethane (V= 2 mL). The reaction mixture was vigorously stirred at room temperature for 6 hours. After solvent removal under vacuum, the compound **8e** obtained was washed with ether and extracted with pentane, dried under vacuum and stored under argon at 255 K prior to use. Red microcrystalline product (Yield 94%). Crystals ready for X-ray analysis were obtained in pentane at 255 K. FT-IR (ν_{CO} , ν_{COMe} , cm⁻¹): 2082.5 (s), 1698.9 (m, br), 1677.4 (m, br) (CH₂Cl₂). ¹H NMR (298 K, CD₂Cl₂, 400.13 MHz, ppm): δ 11.24 (br s, 1H, ring1-N-NH-CH), 8.06 (br s, 2H, ring1-CH=N-NH-CH), 7.74 (s, 1H, ring2-CH=N-NH-CH), 7.05 (s, 1H, ring2-CH=N-NH-CH), 6.54 (s, 1H, ring1-NH-CH=CH), (s, 1H, ring2-NH-CH=CH), 3.09 (s, 3H, COCH₃), 1.58 (br s, 1H, ring2-N-NH-CH). ¹³C{¹H} NMR (298 K, 100.62 MHz, CD₂Cl₂, ppm): δ 219.3 (dd 1C, COMe, $^1J_{\text{COMe-Rh}} = 19.7$ Hz, $^2J_{\text{C-C}} = 3.7$ Hz), 182.5 (d, 1C, CO, $^1J_{\text{CO-Rh}} = 59.8$ Hz), 141.7 (s, 2C, ring1-CH=N-NH, ring2-CH=N-NH), 130.3 (s, 2C, ring1- N-NH-CH, ring2- N-NH-CH), 107.7 (s, 1C, ring1- NH-CH=CH), 107.2 (s, 1C, ring2- NH-CH=CH), 51.5 (s 1C, COCH₃). Anal. Calcd. for C₉H₁₁IN₄O₂Rh (%): C, 24.72; H, 2.52; N, 12.82. Found: C, 24.74; H, 2.54; N, 12.75.

V-1-10 Characterization of neutral cyclometalated dimeric rhodium(III) complex $[RhI(\mu-I)(CO)(\kappa^2-N,C-h\cap CH_2)]_2$ **9h**

Red crystals ready for X-ray analysis were obtained in pentane at 255 K. ATR-IR (ν_{CO} , cm^{-1}): 2061.6 (s), 2021.8 (vw), 1999.6 (vw). 1H NMR (298 K, 300.13 MHz, CD_2Cl_2 , ppm): δ 7.13 (br m, 2H, ring-N-C(CH₃)₃-N=CH), 7.00 (br m, 2H, ring-N-C(CH₃)₃-CH), 1.58 (s, 12H, ring-N-C(CH₃)₂-CH₂), 1.48 (s, 18H, ring-N-CH=C-C(CH₃)₃), 1.00 (d, 2H, Rh-CH₂-C(CH₃)₂-N, $^2J_{Rh-H} = 1.8$ Hz), 0.97 (d, 2H, Rh-CH₂-C(CH₃)₂-N, $^2J_{Rh-H} = 2.10$; $^2J_{H-H} = 6.8$ Hz).

V-1-11 Kinetic measurements

In a typical experiment, to a Schlenk tube containing the complex was added MeI (5 mL), which was previously adjusted at desired temperature. The total methyl iodide/complex solution was prepared at 17 mmol.L⁻¹ concentration for all experiments. Immediately after mixing under stirring, the stopwatch was switched on and a sample of the reaction solution was rapidly transferred by syringe to an infrared cell (CaF₂ window, 1.00 mm path length) fitted with a thermostatic jacket and placed in the sample compartment. FT-IR spectra (4.0 cm^{-1} resolution) were scanned in the region 4000-450 cm^{-1} and saved at regular time interval using spectrum software TIMEBASE. Absorbance (A_t) versus time data for the appropriate ν_{CO} frequencies were extracted by subtracting the solvent spectrum. Kinetic measurements were made by following the decay of the lower antisymmetric frequency ν_{CO} band of the Rh(I) starting complexes **4**. The pseudo-order rate constants were found from the gradient of the plot of $\ln(A_t)$ versus time where $A(t)$ is the absorbance at the time t .

V-1-12 X-ray crystal structure determination

X-ray structures were determined on an Oxford Diffraction Xcalibur CCd diffractometer. The crystallographic data were collected at low temperature 180(2) K on a Bruker Kappa APEX II diffractometer (**h**, **3e**, **3f**, **4d**, **4e**, **4h** and **6e**) or a Gemini Oxford Diffraction diffractometer (**3a**, **3d**, **3h**, **4a**, **4f**, **6d₁**, **6d₂**, **8e** and **9h**), both equipped with an Oxford Cryosystems Cryostream cooler device and using the Mo K α radiation ($\lambda=0.71073$ Å). The structures were solved by direct methods using SHELXS-97⁸ or SIR92⁹ and all non-hydrogen atoms were refined anisotropically using the least-squares method on F^2 with the aid of the program SHELXL-97.¹⁰ Drawing of molecules was performed with the program ORTEP.¹¹

(8) Sheldrick, G. M. *Acta Crystallogr.* **1990**, A46, 467.

(9) Altomare, A.; Casciarano, G.; Giacovazzo, C.; Guagliardi, A. *J. Appl. Crystallogr.* **1993**, 26, 343.

(10) SHELXL-97, Program for Crystal Structure Refinement, Sheldrick, G. M. *University of Göttingen*, **1997**.

(11) Farrugia, L. J. *J. Appl. Crystallogr.* **1997**, 30, 565.

Table 1. Crystal data and details of collection and refinement for the following *cis*-[RhCl(CO)₂(L)] **3** single crystal structures.

<i>Parameters</i>	<i>3a</i>	<i>3d</i>	<i>3e</i>
Chemical Formula	C ₆ H ₁₁ ClNO ₂ Rh	C ₆ H ₆ ClN ₂ O ₂ Rh	C ₅ H ₄ ClN ₂ O ₂ Rh
Formula weight	267.52	276.49	262.46
Crystal system	triclinic	orthorhombic	monoclinic
Space group	P-1	P bca	P 2 ₁ /c
a (Å)	7.2049(3)	16.4534(5)	10.4119(11)
b (Å)	7.4749(3)	6.4536(2)	6.7619(7)
c (Å)	10.7705(4)	17.3250(5)	13.9762(11)
α (°)	79.193(3)	90	90
β (°)	76.434(3)	90	125.835(5)
γ (°)	61.200(4)	90	90
V (Å ³)	492.23(4)	1839.63(10)	797.72(14)
Z	2	8	4
<i>ρ</i> _{calc} (mg.m ⁻³)	1.805	1.997	2.185
Temperature (K)	180(2)	180(2)	180(2)
Crystal dimension (mm)	0.15 x 0.15 x 0.1	0.16 x 0.08 x 0.04	0.24 x 0.14 x 0.1
μ Mo Kα (mm ⁻¹)	1.962	2.107	2.423
θ range (°)	3.33 - 27.87	3.59 - 25.34	2.93 - 30.52
Reflections collected	10786	9624	10111
Independent reflections	2279	1685	2445
<i>R</i> _{int}	0.0272	0.0408	0.0185
Goodness-of-fit on F ²	1.163	1.06	1.074
<i>R</i> _I (I > 2σ (I))	0.0158	0.0232	0.0134
<i>wR</i> ² (all data)	0.0377	0.0487	0.0363
Largest difference peak and hole (e Å ⁻³)	0.337 and -0.349	0.441 and -0.442	0.400 and -0.354

$$R_I = \frac{\sum ||F_{ol} - |F_c||}{\sum |F_{ol}|}, wR^2 = \frac{[\sum w(|F_o|^2 - |F_c|^2)^2 / \sum w|F_o|^2]}{1/2}$$

Table 2. Crystal data and details of collection and refinement for the following *cis*-[RhCl(CO)₂(L)] **3** and ligand **h** single crystal structures.

<i>Parameters</i>	3f	h	3h
Chemical Formula	C ₆ H ₆ ClN ₂ O ₂ Rh	C ₁₁ H ₂₀ N ₂	C ₁₃ H ₂₀ ClN ₂ O ₂ Rh
Formula weight	276.49	180.29	374.67
Crystal system	monoclinic	orthorhombic	monoclinic
Space group	C 2/c	P b c a	P 2 ₁
a (Å)	9.3891(10)	11.7986(8)	5.8465(2)
b (Å)	13.0923(16)	10.6288(8)	14.1141(4)
c (Å)	14.9814(18)	18.6090(14)	10.1884(2))
α (°)	90	90	90
β (°)	95.963(6)	90	103.712(2)
γ (°)	90	90	90
V (Å ³)	1831.6(4)	2333.7(3)	816.77(4)
Z	8	8	2
<i>ρ</i> _{calc} (mg.m ⁻³)	2.005	1.026	1.523
Temperature (K)	180(2)	180(2)	180(2)
Crystal dimension (mm)	0.2 x 0.08 x 0.04	0.16 x 0.08 x 0.04	0.16 x 0.1 x 0.08
μ Mo Kα (mm ⁻¹)	2.116	0.061	1.208
θ range (°)	2.68 - 30.52	2.19 - 25.35	3.59 - 25.35
Reflections collected	12171	25871	8163
Independent reflections	2808	2131	2966
<i>R</i> _{int}	0.0248	0.0535	0.0354
Goodness-of-fit on F ²	1.017	1.061	1.040
<i>R</i> _I (I > 2 σ(I))	0.0209	0.0734	0.0272
<i>wR</i> ² (all data)	0.0461	0.2391	0.0575
Largest difference peak and hole (e Å ⁻³)	0.516 and -0.653	0.561 and -0.345	0.354 and -0.222

Table 3. Crystal data and details of collection and refinement for the following *cis*-[RhI(CO)₂(L)] **4** single crystal structures.

<i>Parameters</i>	<i>4a</i>	<i>4d</i>	<i>4e</i>
Chemical Formula	C ₆ H ₁₁ INO ₂ Rh	C ₆ H ₆ IN ₂ O ₂ Rh	C ₅ H ₄ IN ₂ O ₂ Rh
Formula weight	358.97	367.94	353.91
Crystal system	monoclinic	monoclinic	monoclinic
Space group	P 2 ₁ /c	P 2 ₁ /c	P 2 ₁ /c
a (Å)	7.928(5)	11.2116(10)	10.3601(3)
b (Å)	12.626(5)	7.5428(6)	7.0604(2)
c (Å)	12.203(5)	14.1730(11)	14.5503(4)
α (deg)	90	90	90
β (deg)	117.84(3)	126.628(5)	121.741(2)
γ (deg)	90	90	90
V (Å ³)	1080.1(10)	961.88(15)	905.12(5)
Z	4	4	4
<i>ρ</i> _{calc} (mg m ⁻³)	2.207	2.541	2.597
Temperature (K)	180(2)	180(2)	180(2)
Crystal dimension (mm)	0.22 x 0.16 x 0.04	0.12 x 0.08 x 0.04	0.14 x 0.04 x 0.02
μ Mo Kα (mm ⁻¹)	4.400	4.947	5.252
θ range (°)	3.32 - 26.37	2.26 - 30.46	2.86 - 30.61
Reflections collected	6460	10584	12040
Independent reflections	2178	2914	2777
<i>R</i> _{int}	0.0338	0.0262	0.0326
Goodness-of-fit on F ²	1.052	0.985	1.008
<i>R</i> _I (I > 2 σ(I))	0.0268	0.0211	0.021
<i>wR</i> ² (all data)	0.068	0.0423	0.0498
Largest difference peak and hole (e Å ⁻³)	0.795 and -0.633	0.488 and -0.511	1.103 and -0.541

Table 4. Crystal data and details of collection and refinement for the following *cis*-[RhI(CO)₂(L)] **4** single crystal structures and [RhI(μ -I)(COMe)(CO)(e)]₂ **6e**.

<i>Parameters</i>	4f	4h	6e
Chemical Formula	C ₆ H ₆ IN ₂ O ₂ Rh	C ₁₃ H ₂₀ IN ₂ O ₂ Rh	C ₁₂ H ₁₄ I ₄ N ₄ O ₄ Rh ₂
Formula weight	367.94	466.12	991.69
Crystal system	triclinic	monoclinic	monoclinic
Space group	P -1	P 2 ₁ /c	P 2 ₁ /c
a (Å)	8.1648(4)	6.0795(15)	7.19570(10)
b (Å)	9.3741(4)	16.222(5)	21.5950(5)
c (Å)	14.6087(7)	17.644(4)	15.1380(3)
α (deg)	86.941(4)	90	90
β (deg)	85.400(4)	108.932(13)	106.1480(10)
γ (deg)	64.642(5)	90	90
V (Å ³)	1006.91(9)	1646.0(8)	2259.50(8)
Z	4	4	4
ρ_{calc} (mg m ⁻³)	2.427	1.881	2.915
Temperature (K)	180(2)	180(2)	180(2)
Crystal dimension (mm)	0.18 x 0.12 x 0.08	0.2 x 0.04 x 0.04	0.12 x 0.06 x 0.04
μ Mo K α (mm ⁻¹)	4.726	2.913	6.949
θ range (°)	3.65 - 25.35	2.44 - 30.65	1.69 - 30.49
Reflections collected	15125	17047	27483
Independent reflections	3675	4957	6845
R_{int}	0.0356	0.0803	0.0263
Goodness-of-fit on F ²	1.034	0.949	1.061
R_1 (I > 2 σ (I))	0.0238	0.0473	0.0214
wR^2 (all data)	0.0521	0.0661	0.044
Largest difference peak and hole (e Å ⁻³)	0.571 and -0.449	0.694 and -0.744	0.974 and -0.508

Table 5. Crystal data and details of collection and refinement for the following **[RhI(μ -I)(COMe)(CO)(L)]₂ **6**, **[RhI₂(COMe)(CO)(e)₂] **8e** and **[RhI(μ -I)(CO)(κ^2 -N,C-h \cap CH₂)]₂ **9h** single crystal structures.******

<i>Parameters</i>	6d₁	6d₂	8e	9h
Chemical Formula	C ₁₄ H ₁₈ I ₄ N ₄ O ₄ Rh ₂	C ₁₄ H ₁₈ I ₄ N ₄ O ₄ Rh ₂	C ₉ H ₁₁ I ₂ N ₄ O ₂ Rh	C ₂₄ H ₃₈ I ₄ N ₄ O ₂ Rh ₂
Formula weight	1019.74	1019.74	563.93	1127.41
Crystal system	triclinic	orthorhombic	monoclinic	monoclinic
Space group	P -1	P na ₂ ₁	P 2 ₁ /c	P 2 ₁ /c
a (Å)	10.1933(15)	15.9689(2)	7.4412(3)	10.9826(8)
b (Å)	11.5069(17)	20.4498(3)	12.9941(6)	10.5471(7)
c (Å)	12.3739(18)	7.5262(1)	16.3518(8)	17.4959(11)
α (deg)	105.633(6)	90	90	90
β (deg)	93.540(7)	90	107.686(4)	110.590(4)
γ (deg)	112.887(5)	90	90	90
V (Å ³)	1264.8(3)	2457.76(6)	1506.36(12)	1897.2(2)
Z	2	4	4	2
ρ_{calc} (mg m ⁻³)	2.678	2.756	2.487	2.123
Temperature (K)	180(2)	180(2)	180(2)	180(2)
Crystal dimension (mm)	0.12 x 0.08 x 0.08	0.38 x 0.23 x 0.10	0.2 x 0.14 x 0.08	0.18 x 0.16 x 0.1
μ Mo K α (mm ⁻¹)	6.212	6.393	5.232	4.292
θ range (°)	2.21 - 30.66	3.6 - 25.35	3.6 - 26,37	2.30 - 30.51
Reflections collected	30995	23523	16325	74844
Independent reflections	7757	4494	3077	5781
R_{int}	0.0338	0.0253	0.0370	0.0177
Goodness-of-fit on F ²	1.041	1.048	1.05	1.068
R_1 (I > 2 σ (I))	0.0287	0.0219	0.0213	0.0178
wR^2 (all data)	0.0772	0.0551	0.0478	0.0421
Largest difference peak and hole (e Å ⁻³)	3.675 and -1.930	0.918 and -0.423	0.670 and -0.418	0.914 and -0.505

CRYSTALLOGRAPHY DATA (ORTEP VIEWS)

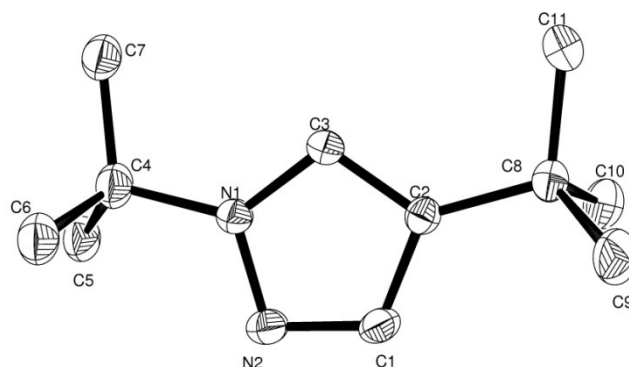


Figure 3. Single crystal X-ray structure of **h**.

Table 6. Bond lengths (Å) and angles (°) for **h**.

C(1)-N(2) 1.330(4), C(1)-C(2) 1.391(4), C(1)-H(1) 0.9500, C(2)-C(3) 1.371(4), C(2)-C(8) 1.514(4), C(3)-N(1) 1.356(3), C(3)-H(3) 0.9500, N(1)-N(2) 1.352(3), N(1)-C(4) 1.479(4), C(4)-C(5) 1.513(6), C(4)-C(7) 1.514(7), C(4)-C(6) 1.565(7), C(4)-C(5') 1.582(7), C(5)-H(5A) 0.9800, C(5)-H(5B) 0.9800, C(5)-H(5C) 0.9800, C(6)-H(6A) 0.9800, C(6)-H(6B) 0.9800, C(6)-H(6C) 0.9800, C(7)-H(7A) 0.9800, C(7)-H(7B) 0.9800, C(7)-H(7C) 0.9800, C(8)-C(9) 1.520(4), C(8)-C(11) 1.524(4), C(8)-C(10) 1.540(4), C(9)-H(9A) 0.9800, C(9)-H(9B) 0.9800, C(9)-H(9C) 0.9800, C(10)-H(10A) 0.9800, C(10)-H(10B) 0.9800, C(10)-H(10C) 0.9800, C(11)-H(11A) 0.9800, C(11)-H(11B) 0.9800, C(11)-H(11C) 0.9800.

N(2)-C(1)-C(2) 113.3(2), N(2)-C(1)-H(1) 123.3, C(2)-C(1)-H(1) 123.3, C(3)-C(2)-C(1) 103.1(2), C(3)-C(2)-C(8) 129.5(2), C(1)-C(2)-C(8) 127.3(2), N(1)-C(3)-C(2) 108.4(2), N(1)-C(3)-H(3) 125.8, C(2)-C(3)-H(3) 125.8, N(2)-N(1)-C(3) 111.0(2), N(2)-N(1)-C(4) 119.2(2), C(3)-N(1)-C(4) 129.7(2), N(1)-C(4)-C(5) 109.8(3), N(1)-C(4)-C(7) 110.0(4), C(5)-C(4)-C(7) 111.2(4), N(1)-C(4)-C(6) 104.5(3), C(5)-C(4)-C(6) 110.0(4), C(7)-C(4)-C(6) 111.2(4), C(4)-C(5)-H(5A) 109.5, C(4)-C(5)-H(5B) 109.5, H(5A)-C(5)-H(5B) 109.5, C(4)-C(5)-H(5C) 109.5, H(5A)-C(5)-H(5C) 109.5, H(5B)-C(5)-H(5C) 109.5, C(4)-C(6)-H(6A) 109.5, C(4)-C(6)-H(6B) 109.5, H(6A)-C(6)-H(6B) 109.5, C(4)-C(6)-H(6C) 109.5, H(6A)-C(6)-H(6C) 109.5, H(6B)-C(6)-H(6C) 109.5, C(4)-C(7)-H(7A) 109.5, C(4)-C(7)-H(7B) 109.5, H(7A)-C(7)-H(7B) 109.5, C(4)-C(7)-H(7C) 109.5, H(7A)-C(7)-H(7C) 109.5, H(7B)-C(7)-H(7C) 109.5, C(2)-C(8)-C(9) 109.5(2), C(2)-C(8)-C(11) 110.9(2), C(9)-C(8)-C(11) 109.9(3), C(2)-C(8)-C(10) 108.2(2), C(9)-C(8)-C(10) 109.6(3), C(11)-C(8)-C(10) 108.7(3), C(8)-C(9)-H(9A) 109.5, C(8)-C(9)-H(9B) 109.5, H(9A)-C(9)-H(9B) 109.5, C(8)-C(9)-H(9C) 109.5, H(9A)-C(9)-H(9C) 109.5, H(9B)-C(9)-H(9C) 109.5, C(8)-C(10)-H(10A) 109.5, C(8)-C(10)-H(10B) 109.5, H(10A)-C(10)-H(10B) 109.5, C(8)-C(10)-H(10C) 109.5, H(10A)-C(10)-H(10C) 109.5, H(10B)-C(10)-H(10C) 109.5, C(8)-C(11)-H(11A) 109.5, C(8)-C(11)-H(11B) 109.5, H(11A)-C(11)-H(11B) 109.5, C(8)-C(11)-H(11C) 109.5, H(11A)-C(11)-H(11C) 109.5, H(11B)-C(11)-H(11C) 109.5, C(1)-N(2)-N(1) 104.1(2).

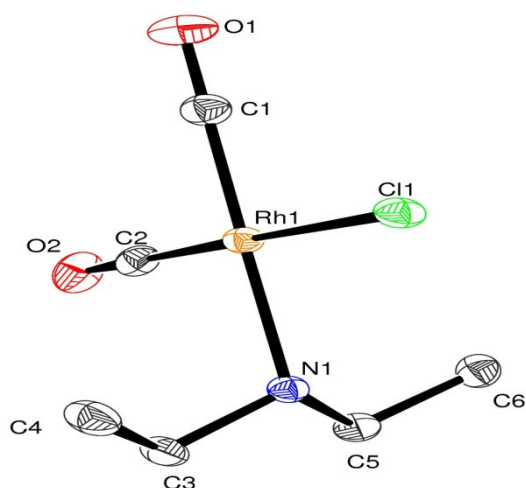


Figure 4. Single crystal X-ray structure of **3a**.

Table 7. Bond lengths (Å) and angles (°) for **3a**.

C(1)-O(1) 1.132(2), C(1)-Rh(1) 1.857(2), C(2)-O(2) 1.134(2), C(2)-Rh(1) 1.839(2), C(3)-N(1) 1.491(2), C(3)-C(4) 1.510(3), C(3)-H(3A) 0.9900, C(3)-H(3B) 0.9900, C(4)-H(4A) 0.9800, C(4)-H(4B) 0.9800, C(4)-H(4C) 0.9800, C(5)-N(1) 1.491(2), C(5)-C(6) 1.511(3), C(5)-H(5A) 0.9900, C(5)-H(5B) 0.9900, C(6)-H(6A) 0.9800, C(6)-H(6B) 0.9800, C(6)-H(6C) 0.9800, N(1)-Rh(1) 2.1237(15), N(1)-H(1A) 0.869(9), Cl(1)-Rh(1) 2.3404(5).

O(1)-C(1)-Rh(1) 178.4(2), O(2)-C(2)-Rh(1) 179.23(19), N(1)-C(3)-C(4) 111.44(15), N(1)-C(3)-H(3A) 109.3, C(4)-C(3)-H(3A) 109.3, N(1)-C(3)-H(3B) 109.3, C(4)-C(3)-H(3B) 109.3, H(3A)-C(3)-H(3B) 108.0, C(3)-C(4)-H(4A) 109.5, C(3)-C(4)-H(4B) 109.5, H(4A)-C(4)-H(4B) 109.5, C(3)-C(4)-H(4C) 109.5, H(4A)-C(4)-H(4C) 109.5, H(4B)-C(4)-H(4C) 109.5, N(1)-C(5)-C(6) 111.23(15), N(1)-C(5)-H(5A) 109.4, C(6)-C(5)-H(5A) 109.4, N(1)-C(5)-H(5B) 109.4, C(6)-C(5)-H(5B) 109.4, H(5A)-C(5)-H(5B) 108.0, C(5)-C(6)-H(6A) 109.5, C(5)-C(6)-H(6B) 109.5, H(6A)-C(6)-H(6B) 109.5, C(5)-C(6)-H(6C) 109.5, H(6A)-C(6)-H(6C) 109.5, H(6B)-C(6)-H(6C) 109.5, C(3)-N(1)-C(5) 111.26(14), C(3)-N(1)-Rh(1) 115.35(11), C(5)-N(1)-Rh(1) 114.15(11), C(3)-N(1)-H(1A) 103.2(13), C(5)-N(1)-H(1A) 104.8(13), Rh(1)-N(1)-H(1A) 106.7(14), C(2)-Rh(1)-C(1) 91.20(9), C(2)-Rh(1)-N(1) 91.87(7), C(1)-Rh(1)-N(1) 176.58(8), C(2)-Rh(1)-Cl(1) 178.22(6), C(1)-Rh(1)-Cl(1) 89.65(7), N(1)-Rh(1)-Cl(1) 87.33(4).

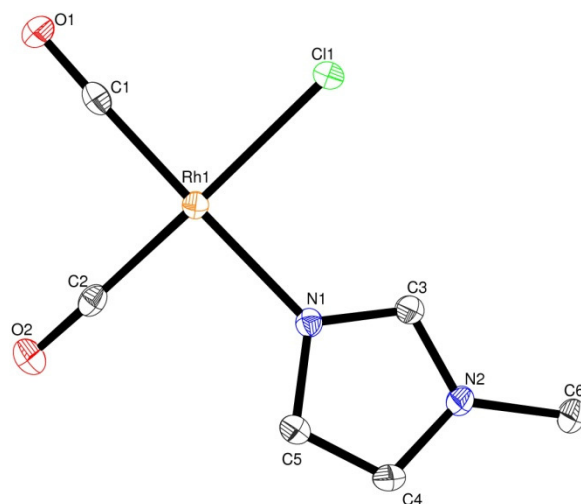


Figure 5. Single crystal X-ray structure of **3d**.

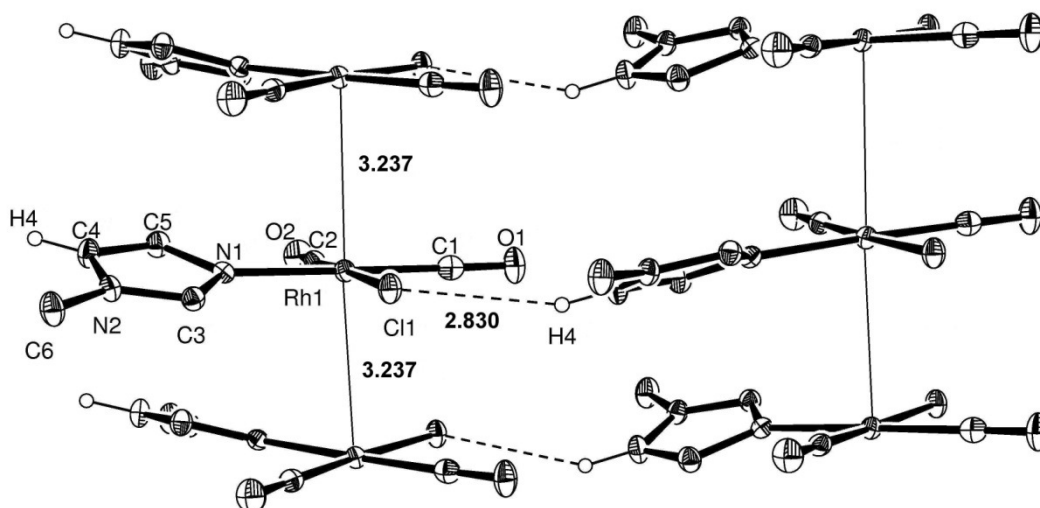


Figure 6. Packing arrangement of *cis*-[RhCl(CO)₂(N₂C₄H₆)] **3d** stacked parallel to the *b*-axis. Thermal ellipsoids are shown at the 30% probability level. Hydrogen atoms are omitted for clarity except on carbon atom involved in an intermolecular H-bonding interaction (2.830 Å).

Table 8. Bond lengths (Å) and angles (°) for **3d**.

C(1)-O(1) 1.127(4), C(1)-Rh(1) 1.857(4), C(2)-O(2) 1.134(4), C(2)-Rh(1) 1.843(4), C(3)-N(1) 1.322(4), C(3)-N(2) 1.337(4), C(3)-H(3) 0.9500, C(4)-C(5) 1.348(4), C(4)-N(2) 1.362(4), C(4)-H(4) 0.9500, C(5)-N(1) 1.384(4), C(5)-H(5) 0.9500, C(6)-N(2) 1.461(4), C(6)-H(6A) 0.9800, C(6)-H(6B) 0.9800, C(6)-H(6C) 0.9800, N(1)-Rh(1) 2.096(2), Cl(1)-Rh(1) 2.3740(8).

O(1)-C(1)-Rh(1) 178.3(3), O(2)-C(2)-Rh(1) 178.9(3), N(1)-C(3)-N(2) 111.1(3), N(1)-C(3)-H(3) 124.5, N(2)-C(3)-H(3) 124.5, C(5)-C(4)-N(2) 106.8(3), C(5)-C(4)-H(4) 126.6, N(2)-C(4)-H(4) 126.6, C(4)-C(5)-N(1) 109.0(3), C(4)-C(5)-H(5) 125.5, N(1)-C(5)-H(5) 125.5, N(2)-C(6)-H(6A) 109.5, N(2)-C(6)-H(6B) 109.5, H(6A)-C(6)-H(6B) 109.5, N(2)-C(6)-H(6C) 109.5, H(6A)-C(6)-H(6C) 109.5, H(6B)-C(6)-H(6C) 109.5, C(3)-N(1)-C(5) 105.6(2), C(3)-

N(1)-Rh(1) 126.7(2), C(5)-N(1)-Rh(1) 127.6(2), C(3)-N(2)-C(4) 107.5(3), C(3)-N(2)-C(6) 126.3(3), C(4)-N(2)-C(6) 126.1(3), C(2)-Rh(1)-C(1) 89.67(13), C(2)-Rh(1)-N(1) 91.80(11), C(1)-Rh(1)-N(1) 178.19(11), C(2)-Rh(1)-Cl(1) 177.72(9), C(1)-Rh(1)-Cl(1) 88.85(10), N(1)-Rh(1)-Cl(1) 89.70(7).

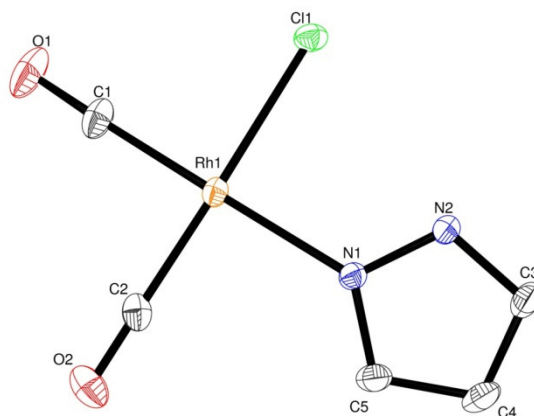


Figure 7. Single crystal X-ray structure of **3e**.

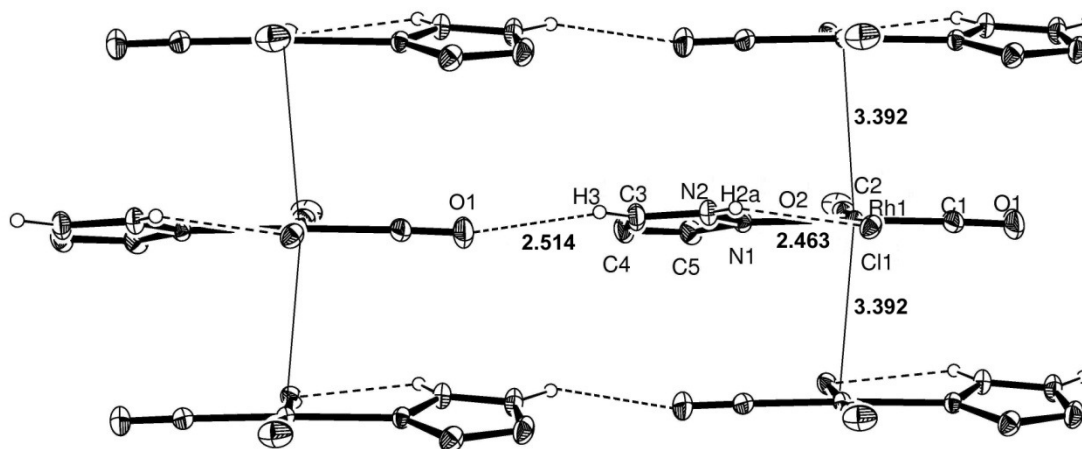


Figure 8. Packing arrangement of *cis*-[RhCl(CO)₂(N₂C₃H₄)] **3e** stacked parallel to the b-axis. Thermal ellipsoids are shown at the 30% probability level. Hydrogen atoms are omitted for clarity except on carbon atom and amine group involved in intramolecular (2.463 Å) and intermolecular (2.514 Å) H-bonding interactions.

Table 9. Bond lengths (Å) and angles (°) for **3e**.

Rh(1)-C(1) 1.8468(15), Rh(1)-C(2) 1.8508(14), Rh(1)-N(1) 2.0887(11), Rh(1)-Cl(1) 2.3649(4), O(2)-C(2) 1.1296(18), O(1)-C(1) 1.1295(19), N(1)-C(5) 1.3373(16), N(1)-N(2) 1.3417(14), N(2)-C(3) 1.3386(16), N(2)-H(2A) 0.865(9), C(5)-C(4) 1.388(2), C(5)-H(5) 0.9500, C(4)-C(3) 1.367(2), C(4)-H(4) 0.9500, C(3)-H(3) 0.9500.

C(1)-Rh(1)-C(2) 90.08(7), C(1)-Rh(1)-N(1) 177.89(5), C(2)-Rh(1)-N(1) 90.79(5), C(1)-Rh(1)-Cl(1) 89.02(6), C(2)-Rh(1)-Cl(1) 177.45(4), N(1)-Rh(1)-Cl(1) 90.20(3), C(5)-N(1)-N(2) 105.19(11), C(5)-N(1)-Rh(1) 132.47(9), N(2)-N(1)-Rh(1) 122.34(8), C(3)-N(2)-N(1) 111.72(11), C(3)-N(2)-H(2A) 130.5(10), N(1)-N(2)-H(2A) 117.6(10), N(1)-C(5)-C(4) 110.65(12), N(1)-C(5)-H(5) 124.7, C(4)-C(5)-H(5) 124.7, C(3)-C(4)-C(5) 105.18(11), C(3)-C(4)-H(4) 127.4, C(5)-C(4)-H(4) 127.4, N(2)-C(3)-C(4) 107.26(13), N(2)-C(3)-H(3) 126.4, C(4)-C(3)-H(3) 126.4, O(2)-C(2)-Rh(1) 178.91(12), O(1)-C(1)-Rh(1) 177.82(17).

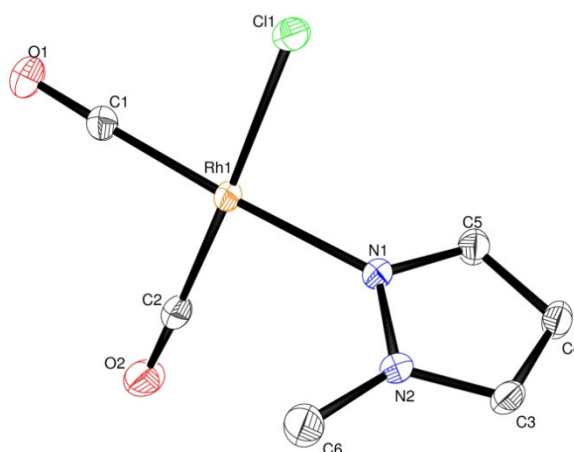


Figure 9. Single crystal X-ray structure of **3f**.

Table 10. Bond lengths (Å) and angles (°) for **3f**.

C(1)-O(1) 1.131(2), C(1)-Rh(1) 1.844(2), C(2)-O(2) 1.132(3), C(2)-Rh(1) 1.847(2), C(3)-N(2) 1.342(2), C(3)-C(4) 1.363(3), C(3)-H(3) 0.9500, C(4)-C(5) 1.388(3), C(4)-H(4) 0.9500, C(5)-N(1) 1.331(2), C(5)-H(5) 0.9500, C(6)-N(2) 1.448(2), C(6)-H(6A) 0.9800, C(6)-H(6B) 0.9800, C(6)-H(6C) 0.9800, N(1)-N(2) 1.351(2), N(1)-Rh(1) 2.0937(15), Cl(1)-Rh(1) 2.3328(6).

O(1)-C(1)-Rh(1) 178.2(2), O(2)-C(2)-Rh(1) 177.93(19), N(2)-C(3)-C(4) 108.10(17), N(2)-C(3)-H(3) 125.9, C(4)-C(3)-H(3) 125.9, C(3)-C(4)-C(5) 104.92(17), C(3)-C(4)-H(4) 127.5, C(5)-C(4)-H(4) 127.5, N(1)-C(5)-C(4) 110.80(17), N(1)-C(5)-H(5) 124.6, C(4)-C(5)-H(5) 124.6, N(2)-C(6)-H(6A) 109.5, N(2)-C(6)-H(6B) 109.5, H(6A)-C(6)-H(6B) 109.5, N(2)-C(6)-H(6C) 109.5, H(6A)-C(6)-H(6C) 109.5, H(6B)-C(6)-H(6C) 109.5, C(5)-N(1)-N(2) 105.71(15), C(5)-N(1)-Rh(1) 127.43(12), N(2)-N(1)-Rh(1) 126.85(11), C(3)-N(2)-N(1) 110.46(15), C(3)-N(2)-C(6) 127.77(17), N(1)-N(2)-C(6) 121.64(16), C(1)-Rh(1)-C(2) 89.83(9), C(1)-Rh(1)-N(1) 176.56(8), C(2)-Rh(1)-N(1) 93.59(7), C(1)-Rh(1)-Cl(1) 88.25(7), C(2)-Rh(1)-Cl(1) 177.85(6), N(1)-Rh(1)-Cl(1) 88.32(4).

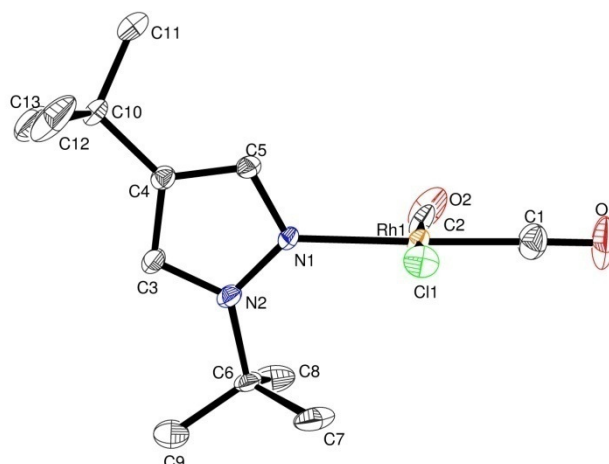


Figure 10. Single crystal X-ray structure of **3h**.

Table11. Bond lengths (Å) and angles (°) for **3h**.

C(1)-O(1) 1.125(5), C(1)-Rh(1) 1.834(5), C(2)-O(2) 1.128(5), C(2)-Rh(1) 1.846(4), C(3)-N(2) 1.361(5), C(3)-C(4) 1.374(5), C(3)-H(3) 0.9500, C(4)-C(5) 1.384(5), C(4)-C(10) 1.517(5), C(10)-C(12) 1.505(7), C(10)-C(11) 1.508(6), C(10)-C(13) 1.511(6), C(5)-N(1) 1.337(5), C(5)-H(5) 0.9500, C(11)-H(11A) 0.9800, C(11)-H(11B) 0.9800, C(11)-H(11C) 0.9800, C(13)-H(13A) 0.9800, C(13)-H(13B) 0.9800, C(13)-H(13C) 0.9800, C(12)-H(12A) 0.9800, C(12)-H(12B) 0.9800, C(12)-H(12C) 0.9800, C(6)-N(2) 1.496(5), C(6)-C(7) 1.508(6), C(6)-C(8) 1.514(6), C(6)-C(9) 1.525(6), C(8)-H(8A) 0.9800, C(8)-H(8B) 0.9800, C(8)-H(8C) 0.9800, C(7)-H(7A) 0.9800, C(7)-H(7B) 0.9800, C(7)-H(7C) 0.9800, C(9)-H(9A) 0.9800, C(9)-H(9B) 0.9800, C(9)-H(9C) 0.9800, N(1)-N(2) 1.355(4), N(1)-Rh(1) 2.108(3), Cl(1)-Rh(1) 2.3432(10).

O(1)-C(1)-Rh(1) 178.6(5), O(2)-C(2)-Rh(1) 176.6(4), N(2)-C(3)-C(4) 108.7(3), N(2)-C(3)-H(3) 125.6, C(4)-C(3)-H(3) 125.6, C(3)-C(4)-C(5) 104.1(3), C(3)-C(4)-C(10) 127.9(3), C(5)-C(4)-C(10) 127.9(3), C(12)-C(10)-C(11) 108.3(4), C(12)-C(10)-C(13) 110.5(4), C(11)-C(10)-C(13) 108.8(4), C(12)-C(10)-C(4) 109.1(3), C(11)-C(10)-C(4) 109.9(3), C(13)-C(10)-C(4) 110.3(3), N(1)-C(5)-C(4) 111.8(3), N(1)-C(5)-H(5) 124.1, C(4)-C(5)-H(5) 124.1, C(10)-C(11)-H(11A) 109.5, C(10)-C(11)-H(11B) 109.5, H(11A)-C(11)-H(11B) 109.5, C(10)-C(11)-H(11C) 109.5, H(11A)-C(11)-H(11C) 109.5, H(11B)-C(11)-H(11C) 109.5, C(10)-C(13)-H(13A) 109.5, C(10)-C(13)-H(13B) 109.5, H(13A)-C(13)-H(13B) 109.5, C(10)-C(13)-H(13C) 109.5, H(13A)-C(13)-H(13C) 109.5, H(13B)-C(13)-H(13C) 109.5, C(10)-C(12)-H(12A) 109.5, C(10)-C(12)-H(12B) 109.5, H(12A)-C(12)-H(12B) 109.5, C(10)-C(12)-H(12C) 109.5, H(12A)-C(12)-H(12C) 109.5, H(12B)-C(12)-H(12C) 109.5, N(2)-C(6)-C(7) 109.5(3), N(2)-C(6)-C(8) 108.6(3), C(7)-C(6)-C(8) 112.4(4), N(2)-C(6)-C(9) 109.2(3), C(7)-C(6)-C(9) 107.8(4), C(8)-C(6)-C(9) 109.3(4), C(6)-C(8)-H(8A) 109.5, C(6)-C(8)-H(8B) 109.5, H(8A)-C(8)-H(8B) 109.5, C(6)-C(8)-H(8C) 109.5, H(8A)-C(8)-H(8C) 109.5, H(8B)-C(8)-H(8C) 109.5, C(6)-C(7)-H(7A) 109.5, C(6)-C(7)-H(7B) 109.5, H(7A)-C(7)-H(7B) 109.5, C(6)-C(7)-H(7C) 109.5, H(7A)-C(7)-H(7C) 109.5, H(7B)-C(7)-H(7C) 109.5, C(6)-C(9)-H(9A) 109.5, C(6)-C(9)-H(9B) 109.5, H(9A)-C(9)-H(9B) 109.5, C(6)-C(9)-H(9C) 109.5, H(9A)-C(9)-H(9C) 109.5, H(9B)-C(9)-H(9C) 109.5, C(5)-N(1)-N(2) 105.9(3), C(5)-N(1)-Rh(1) 119.8(3), N(2)-N(1)-Rh(1) 134.0(2), N(1)-N(2)-C(3) 109.5(3), N(1)-N(2)-C(6) 122.9(3), C(3)-N(2)-C(6) 127.4(3), C(1)-Rh(1)-C(2) 89.65(19), C(1)-Rh(1)-N(1) 176.54(18),

C(2)-Rh(1)-N(1) 93.08(15), C(1)-Rh(1)-Cl(1) 87.46(15), C(2)-Rh(1)-Cl(1) 175.34(15), N(1)-Rh(1)-Cl(1) 89.68(9).

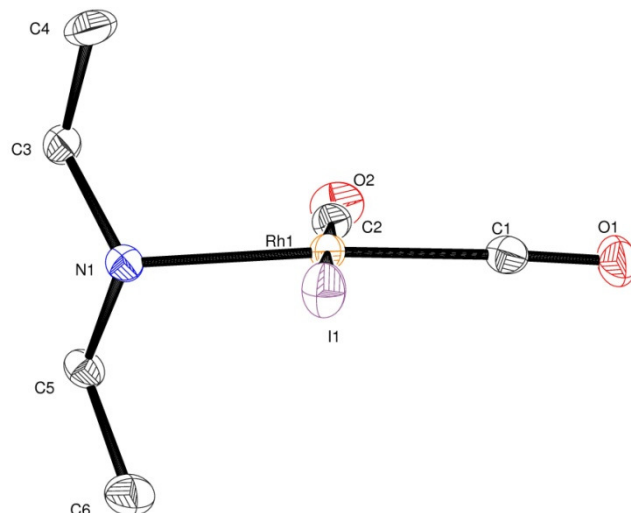


Figure 11. Single crystal X-ray structure of **4a**.

Table 12. Bond lengths (Å) and angles (°) for **4a**.

I(1)-Rh(1) 2.6450(10), Rh(1)-C(2) 1.857(4), Rh(1)-C(1) 1.862(5), Rh(1)-N(1) 2.134(3), O(1)-C(1) 1.128(5), O(2)-C(2) 1.120(5), N(1)-C(5) 1.490(5), N(1)-C(3) 1.498(5), N(1)-H(1A) 0.879(10), C(3)-C(4) 1.488(6), C(3)-H(3A) 0.9900, C(3)-H(3B) 0.9900, C(4)-H(4A) 0.9800, C(4)-H(4B) 0.9800, C(4)-H(4C) 0.9800, C(5)-C(6) 1.510(6), C(5)-H(5A) 0.9900, C(5)-H(5B) 0.9900, C(6)-H(6A) 0.9800, C(6)-H(6B) 0.9800, C(6)-H(6C) 0.9800.

C(2)-Rh(1)-C(1) 91.30(19), C(2)-Rh(1)-N(1) 91.44(16), C(1)-Rh(1)-N(1) 175.30(15), C(2)-Rh(1)-I(1) 176.99(13), C(1)-Rh(1)-I(1) 88.01(13), N(1)-Rh(1)-I(1) 89.46(9), C(5)-N(1)-C(3) 110.7(3), C(5)-N(1)-Rh(1) 113.5(2), C(3)-N(1)-Rh(1) 115.2(2), C(5)-N(1)-H(1A) 108(3), C(3)-N(1)-H(1A) 107(3), Rh(1)-N(1)-H(1A) 101(3), O(1)-C(1)-Rh(1) 177.7(4), O(2)-C(2)-Rh(1) 178.1(4), C(4)-C(3)-N(1) 112.2(3), C(4)-C(3)-H(3A) 109.2, N(1)-C(3)-H(3A) 109.2, C(4)-C(3)-H(3B) 109.2, N(1)-C(3)-H(3B) 109.2, H(3A)-C(3)-H(3B) 107.9, C(3)-C(4)-H(4A) 109.5, C(3)-C(4)-H(4B) 109.5, H(4A)-C(4)-H(4B) 109.5, C(3)-C(4)-H(4C) 109.5, H(4A)-C(4)-H(4C) 109.5, H(4B)-C(4)-H(4C) 109.5, N(1)-C(5)-C(6) 111.2(4), N(1)-C(5)-H(5A) 109.4, C(6)-C(5)-H(5A) 109.4, N(1)-C(5)-H(5B) 109.4, C(6)-C(5)-H(5B) 109.4, H(5A)-C(5)-H(5B) 108.0, C(5)-C(6)-H(6A) 109.5, C(5)-C(6)-H(6B) 109.5, H(6A)-C(6)-H(6B) 109.5, C(5)-C(6)-H(6C) 109.5, H(6A)-C(6)-H(6C) 109.5, H(6B)-C(6)-H(6C) 109.5.

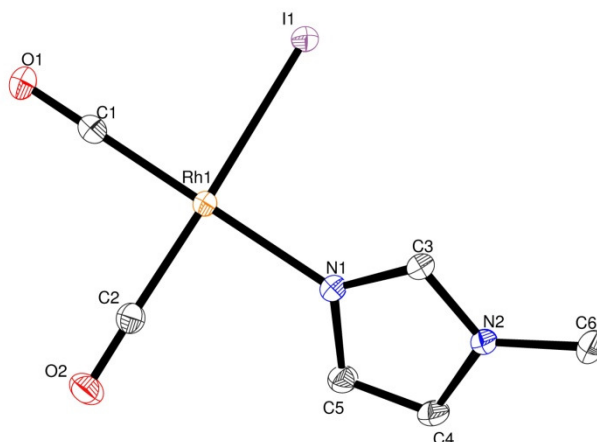


Figure 12. Single crystal X-ray structure of **4d**.

Table 13. Bond lengths (Å) and angles (°) for **4d**.

I(1)-Rh(1) 2.6599(3), Rh(1)-C(1) 1.844(3), Rh(1)-C(2) 1.863(3), Rh(1)-N(1) 2.102(2), O(1)-C(1) 1.138(3), O(2)-C(2) 1.127(3), N(1)-C(3) 1.323(3), N(1)-C(5) 1.372(3), N(2)-C(3) 1.338(3), N(2)-C(4) 1.370(3), N(2)-C(6) 1.458(3), C(3)-H(3) 0.9500, C(4)-C(5) 1.349(4), C(4)-H(4) 0.9500, C(5)-H(5) 0.9500, C(6)-H(6A) 0.9800, C(6)-H(6B) 0.9800, C(6)-H(6C) 0.9800.

C(1)-Rh(1)-C(2) 90.67(12), C(1)-Rh(1)-N(1) 179.83(12), C(2)-Rh(1)-N(1) 89.41(10), C(1)-Rh(1)-I(1) 87.67(8), C(2)-Rh(1)-I(1) 178.13(9), N(1)-Rh(1)-I(1) 92.25(6), C(3)-N(1)-C(5) 105.6(2), C(3)-N(1)-Rh(1) 126.79(18), C(5)-N(1)-Rh(1) 127.30(17), C(3)-N(2)-C(4) 107.5(2), C(3)-N(2)-C(6) 126.8(2), C(4)-N(2)-C(6) 125.7(2), O(1)-C(1)-Rh(1) 179.4(3), O(2)-C(2)-Rh(1) 178.6(3), N(1)-C(3)-N(2) 111.0(2), N(1)-C(3)-H(3) 124.5, N(2)-C(3)-H(3) 124.5, C(5)-C(4)-N(2) 106.1(2), C(5)-C(4)-H(4) 126.9, N(2)-C(4)-H(4) 126.9, C(4)-C(5)-N(1) 109.7(2), C(4)-C(5)-H(5) 125.1, N(1)-C(5)-H(5) 125.1, N(2)-C(6)-H(6A) 109.5, N(2)-C(6)-H(6B) 109.5, H(6A)-C(6)-H(6B) 109.5, N(2)-C(6)-H(6C) 109.5, H(6A)-C(6)-H(6C) 109.5, H(6B)-C(6)-H(6C) 109.5.

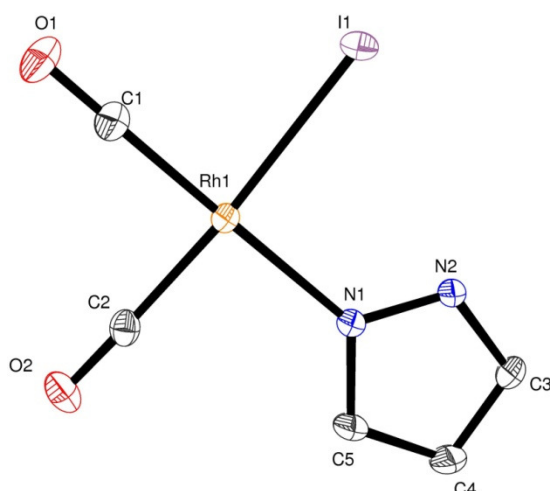


Figure 13. Single crystal X-ray structure of **4e**.

Table 14. Bond lengths (Å) and angles (°) for **4e**.

I(1)-Rh(1) 2.6623(3), Rh(1)-C(1) 1.838(3), Rh(1)-C(2) 1.862(3), Rh(1)-N(1) 2.099(2), O(2)-C(2) 1.134(3), O(1)-C(1) 1.133(4), N(1)-C(5) 1.335(3), N(1)-N(2) 1.341(3), N(2)-C(3) 1.332(4), N(2)-H(2A) 0.871(10), C(3)-C(4) 1.365(4), C(3)-H(3) 0.9500, C(4)-C(5) 1.377(4), C(4)-H(4) 0.9500, C(5)-H(5) 0.9500.

C(1)-Rh(1)-C(2) 89.65(13), C(1)-Rh(1)-N(1) 179.40(11), C(2)-Rh(1)-N(1) 90.95(10), C(1)-Rh(1)-I(1) 85.76(10), C(2)-Rh(1)-I(1) 175.40(9), N(1)-Rh(1)-I(1) 93.64(6), C(5)-N(1)-N(2) 104.3(2), C(5)-N(1)-Rh(1) 131.04(19), N(2)-N(1)-Rh(1) 124.63(16), C(3)-N(2)-N(1) 112.2(2), C(3)-N(2)-H(2A) 131(2), N(1)-N(2)-H(2A) 117(2), O(2)-C(2)-Rh(1) 178.4(3), O(1)-C(1)-Rh(1) 179.8(3), N(2)-C(3)-C(4) 107.1(3), N(2)-C(3)-H(3) 126.5, C(4)-C(3)-H(3) 126.5, C(3)-C(4)-C(5) 105.0(2), C(3)-C(4)-H(4) 127.5, C(5)-C(4)-H(4) 127.5, N(1)-C(5)-C(4) 111.4(3), N(1)-C(5)-H(5) 124.3, C(4)-C(5)-H(5) 124.3.

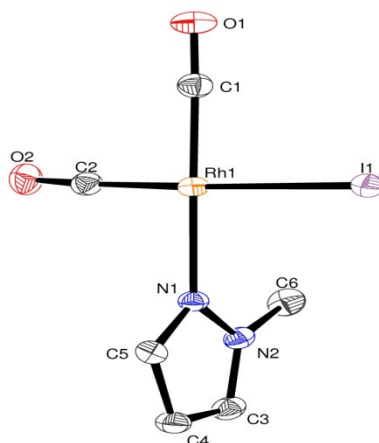


Figure 14. Single crystal X-ray structure of **4f**.

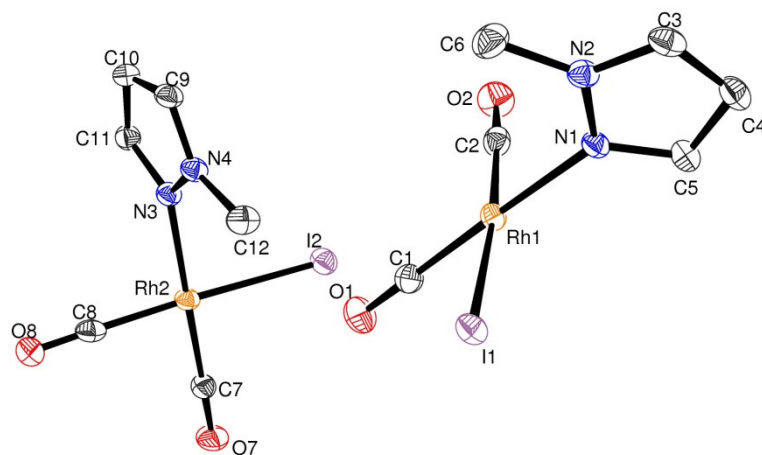


Figure 15. Single crystal X-ray structure of **4f** (asymmetric unit).

Table 15. Bond lengths (Å) and angles (°) for **4f**.

C(1)-O(1) 1.135(5), C(1)-Rh(1) 1.839(5), C(2)-O(2) 1.125(5), C(2)-Rh(1) 1.855(4), C(3)-N(2) 1.337(5), C(3)-C(4) 1.360(6), C(3)-H(3) 0.9500, C(4)-C(5) 1.388(6), C(4)-H(4) 0.9500, C(5)-N(1) 1.332(5), C(5)-H(5) 0.9500, C(6)-N(2) 1.441(5), C(6)-H(6A) 0.9800, C(6)-H(6B) 0.9800, C(6)-H(6C) 0.9800, C(7)-O(7) 1.133(5), C(7)-Rh(2) 1.841(4), C(8)-O(8) 1.140(5), C(8)-Rh(2) 1.847(5), C(9)-N(4) 1.342(5), C(9)-C(10) 1.364(6), C(9)-H(9) 0.9500, C(10)-C(11) 1.384(6), C(10)-H(10) 0.9500, C(11)-N(3) 1.333(5), C(11)-H(11) 0.9500, C(12)-N(4) 1.448(5), C(12)-H(12A) 0.9800, C(12)-H(12B) 0.9800, C(12)-H(12C) 0.9800, Rh(2)-N(3) 2.099(3), Rh(2)-I(2) 2.6568(4), Rh(1)-N(1) 2.099(3), Rh(1)-I(1) 2.6599(4), N(1)-N(2) 1.357(4), N(3)-N(4) 1.353(4).

O(1)-C(1)-Rh(1) 178.4(4), O(2)-C(2)-Rh(1) 177.2(4), N(2)-C(3)-C(4) 109.0(4), N(2)-C(3)-H(3) 125.5, C(4)-C(3)-H(3) 125.5, C(3)-C(4)-C(5) 104.6(4), C(3)-C(4)-H(4) 127.7, C(5)-C(4)-H(4) 127.7, N(1)-C(5)-C(4) 110.7(4), N(1)-C(5)-H(5) 124.6, C(4)-C(5)-H(5) 124.6, N(2)-C(6)-H(6A) 109.5, N(2)-C(6)-H(6B) 109.5, H(6A)-C(6)-H(6B) 109.5, N(2)-C(6)-H(6C) 109.5, H(6A)-C(6)-H(6C) 109.5, H(6B)-C(6)-H(6C) 109.5, O(7)-C(7)-Rh(2) 178.9(4), O(8)-C(8)-Rh(2) 179.0(4), N(4)-C(9)-C(10) 107.3(4), N(4)-C(9)-H(9) 126.3, C(10)-C(9)-H(9) 126.3, C(9)-C(10)-C(11) 106.0(4), C(9)-C(10)-H(10) 127.0, C(11)-C(10)-H(10) 127.0, N(3)-C(11)-C(10) 110.0(4), N(3)-C(11)-H(11) 125.0, C(10)-C(11)-H(11) 125.0, N(4)-C(12)-H(12A) 109.5, N(4)-C(12)-H(12B) 109.5, H(12A)-C(12)-H(12B) 109.5, N(4)-C(12)-H(12C) 109.5, H(12A)-C(12)-H(12C) 109.5, H(12B)-C(12)-H(12C) 109.5, C(7)-Rh(2)-C(8) 90.73(18), C(7)-Rh(2)-N(3) 177.59(15), C(8)-Rh(2)-N(3) 90.48(15), C(7)-Rh(2)-I(2) 87.54(13), C(8)-Rh(2)-I(2) 177.64(12), N(3)-Rh(2)-I(2) 91.31(9), C(1)-Rh(1)-C(2) 90.22(18), C(1)-Rh(1)-N(1) 178.54(15), C(2)-Rh(1)-N(1) 91.14(16), C(1)-Rh(1)-I(1) 87.78(13), C(2)-Rh(1)-I(1) 174.55(12), N(1)-Rh(1)-I(1) 90.91(8), C(5)-N(1)-N(2) 105.9(3), C(5)-N(1)-Rh(1) 129.1(3), N(2)-N(1)-Rh(1) 124.9(2), C(3)-N(2)-N(1) 109.7(3), C(3)-N(2)-C(6) 129.0(4), N(1)-N(2)-C(6) 121.3(3), C(11)-N(3)-N(4) 106.0(3), C(11)-N(3)-Rh(2) 127.6(3), N(4)-N(3)-Rh(2) 126.4(2), C(9)-N(4)-N(3) 110.7(3), C(9)-N(4)-C(12) 128.1(4), N(3)-N(4)-C(12) 121.2(3).

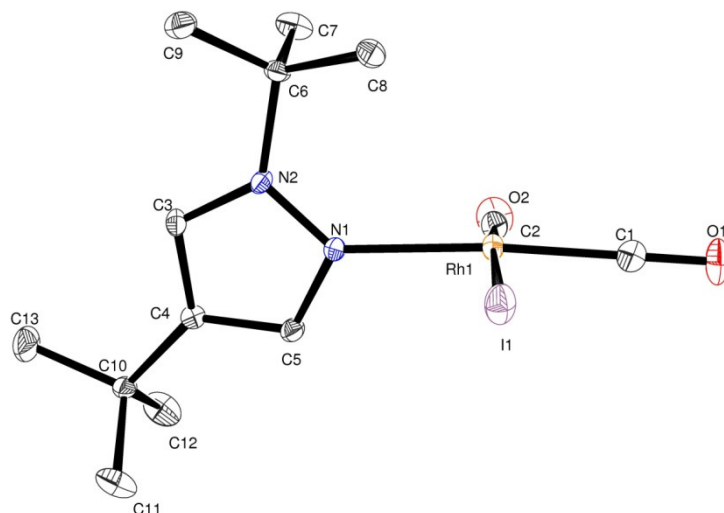


Figure 16. Single crystal X-ray structure of **4h**.

Table 16. Bond lengths (Å) and angles (°) for **4h**.

I(1)-Rh(1) 2.6497(7), Rh(1)-C(1) 1.838(5), Rh(1)-C(2) 1.849(5), Rh(1)-N(1) 2.127(3), O(1)-C(1) 1.123(5), O(2)-C(2) 1.134(5), N(1)-C(5) 1.322(5), N(1)-N(2) 1.344(5), N(2)-C(3) 1.340(5), N(2)-C(6) 1.507(5), C(3)-C(4) 1.370(6), C(3)-H(3) 0.9500, C(4)-C(5) 1.394(5), C(4)-C(10) 1.512(6), C(5)-H(5) 0.9500, C(6)-C(8) 1.510(6), C(6)-C(9) 1.522(6), C(6)-C(7) 1.525(5), C(7)-H(7A) 0.9800, C(7)-H(7B) 0.9800, C(7)-H(7C) 0.9800, C(8)-H(8A) 0.9800, C(8)-H(8B) 0.9800, C(8)-H(8C) 0.9800, C(9)-H(9A) 0.9800, C(9)-H(9B) 0.9800, C(9)-H(9C) 0.9800, C(10)-C(12) 1.511(6), C(10)-C(13) 1.517(6), C(10)-C(11) 1.528(5), C(11)-H(11A) 0.9800, C(11)-H(11B) 0.9800, C(11)-H(11C) 0.9800, C(12)-H(12A) 0.9800, C(12)-H(12B) 0.9800, C(12)-H(12C) 0.9800, C(13)-H(13A) 0.9800, C(13)-H(13B) 0.9800, C(13)-H(13C) 0.9800.

C(1)-Rh(1)-C(2) 91.1(2), C(1)-Rh(1)-N(1) 175.49(17), C(2)-Rh(1)-N(1) 89.99(17), C(1)-Rh(1)-I(1) 86.00(13), C(2)-Rh(1)-I(1) 173.97(16), N(1)-Rh(1)-I(1) 92.54(9), C(5)-N(1)-N(2) 106.3(3), C(5)-N(1)-Rh(1) 118.6(3), N(2)-N(1)-Rh(1) 135.0(3), C(3)-N(2)-N(1) 109.6(4), C(3)-N(2)-C(6) 125.5(3), N(1)-N(2)-C(6) 124.3(3), O(1)-C(1)-Rh(1) 179.3(5), O(2)-C(2)-Rh(1) 177.1(5), N(2)-C(3)-C(4) 109.3(4), N(2)-C(3)-H(3) 125.3, C(4)-C(3)-H(3) 125.3, C(3)-C(4)-C(5) 103.2(4), C(3)-C(4)-C(10) 129.2(4), C(5)-C(4)-C(10) 127.6(4), N(1)-C(5)-C(4) 111.5(4), N(1)-C(5)-H(5) 124.3, C(4)-C(5)-H(5) 124.3, N(2)-C(6)-C(8) 110.0(3), N(2)-C(6)-C(9) 108.4(3), C(8)-C(6)-C(9) 109.5(4), N(2)-C(6)-C(7) 107.4(4), C(8)-C(6)-C(7) 110.7(3), C(9)-C(6)-C(7) 110.7(4), C(6)-C(7)-H(7A) 109.5, C(6)-C(7)-H(7B) 109.5, H(7A)-C(7)-H(7B) 109.5, C(6)-C(7)-H(7C) 109.5, H(7A)-C(7)-H(7C) 109.5, H(7B)-C(7)-H(7C) 109.5, C(6)-C(8)-H(8A) 109.5, C(6)-C(8)-H(8B) 109.5, H(8A)-C(8)-H(8B) 109.5, C(6)-C(8)-H(8C) 109.5, H(8A)-C(8)-H(8C) 109.5, H(8B)-C(8)-H(8C) 109.5, C(6)-C(9)-H(9A) 109.5, C(6)-C(9)-H(9B) 109.5, H(9A)-C(9)-H(9B) 109.5, C(6)-C(9)-H(9C) 109.5, H(9A)-C(9)-H(9C) 109.5, H(9B)-C(9)-H(9C) 109.5, C(12)-C(10)-C(4) 108.9(3), C(12)-C(10)-C(13) 109.9(4), C(4)-C(10)-C(13) 110.1(4), C(12)-C(10)-C(11) 108.9(4), C(4)-C(10)-C(11) 110.1(3), C(13)-C(10)-C(11) 108.9(4), C(10)-C(11)-H(11A) 109.5, C(10)-C(11)-H(11B) 109.5, H(11A)-C(11)-H(11B) 109.5, C(10)-C(11)-H(11C) 109.5, H(11A)-C(11)-H(11C) 109.5, H(11B)-C(11)-H(11C) 109.5, C(10)-C(12)-H(12A) 109.5, C(10)-C(12)-H(12B) 109.5, H(12A)-C(12)-H(12B) 109.5, C(10)-C(12)-H(12C) 109.5, H(12A)-C(12)-H(12C) 109.5, H(12B)-C(12)-H(12C) 109.5, C(10)-C(13)-H(13A) 109.5, C(10)-C(13)-H(13B) 109.5, H(13A)-C(13)-

H(13B) 109.5, C(10)-C(13)-H(13C) 109.5, H(13A)-C(13)-H(13C) 109.5, H(13B)-C(13)-H(13C) 109.5.

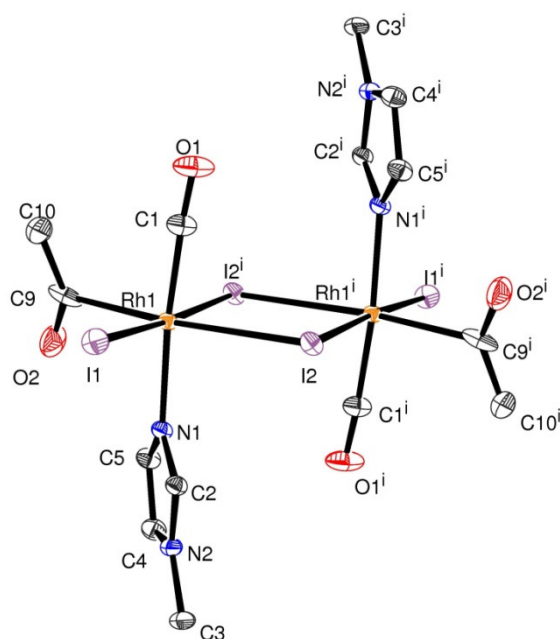


Figure 17. Single crystal X-ray structure of **6d₁**.

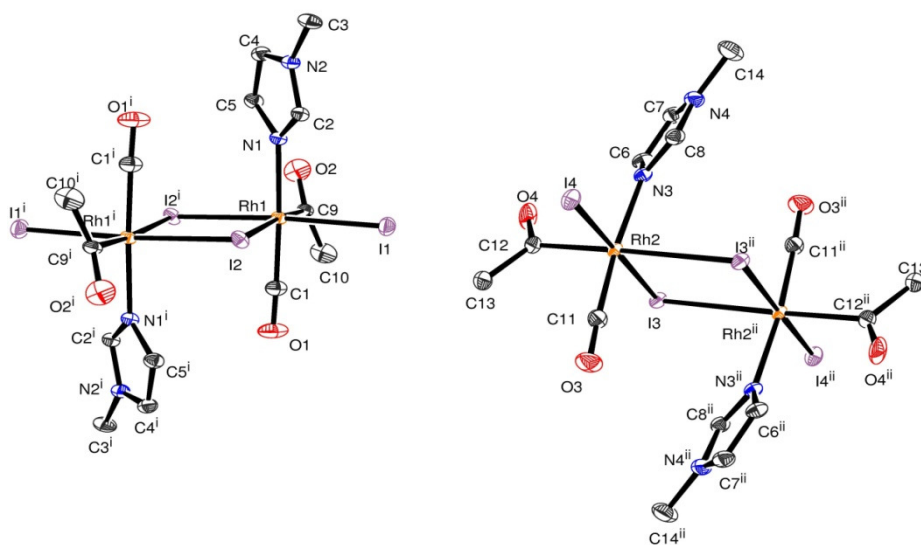


Figure 17. Single crystal X-ray structure of **6d₁** (asymmetric unit).

Table 18. Bond lengths (Å) and angles (°) for **6d₁**.

Rh(1)-C(1) 1.854(4), Rh(1)-N(1) 2.100(3), Rh(1)-C(9) 2.217(6), Rh(1)-I(1) 2.6530(5), Rh(1)-I(2)#1 2.6800(5), Rh(1)-I(2) 2.9581(6), I(2)-Rh(1)#1 2.6799(5), Rh(2)-C(11) 1.859(5), Rh(2)-

C(12) 2.057(5), Rh(2)-N(3) 2.105(3), Rh(2)-I(4) 2.6474(6), Rh(2)-I(3) 2.6694(6), Rh(2)-I(3)#2 2.9780(5), I(3)-Rh(2)#2 2.9780(5), N(1)-C(2) 1.326(5), N(1)-C(5) 1.383(5), C(9)-O(2) 1.149(6), C(9)-C(10) 1.368(8), N(2)-C(2) 1.340(5), N(2)-C(4) 1.367(6), N(2)-C(3) 1.461(5), C(4)-C(5) 1.367(6), C(4)-H(4) 0.9500, C(5)-H(5) 0.9500, C(1)-O(1) 1.121(6), C(2)-H(2) 0.9500, N(3)-C(8) 1.322(5), N(3)-C(6) 1.378(5), N(4)-C(8) 1.351(6), N(4)-C(7) 1.363(6), N(4)-C(14) 1.461(6), C(8)-H(8) 0.9500, O(4)-C(12) 1.142(6), C(12)-C(13) 1.509(6), O(3)-C(11) 1.130(6), C(13)-H(13A) 0.9800, C(13)-H(13B) 0.9800, C(13)-H(13C) 0.9800, C(3)-H(3A) 0.9800, C(3)-H(3B) 0.9800, C(3)-H(3C) 0.9800, C(10)-H(10A) 0.9800, C(10)-H(10B) 0.9800, C(10)-H(10C) 0.9800, C(14)-H(14A) 0.9800, C(14)-H(14B) 0.9800, C(14)-H(14C) 0.9800, C(7)-C(6) 1.356(6), C(7)-H(7) 0.9500, C(6)-H(6) 0.9500.

C(1)-Rh(1)-N(1) 174.69(19), C(1)-Rh(1)-C(9) 91.1(2), N(1)-Rh(1)-C(9) 94.08(15), C(1)-Rh(1)-I(1) 88.81(16), N(1)-Rh(1)-I(1) 92.25(10), C(9)-Rh(1)-I(1) 89.48(11), C(1)-Rh(1)-I(2)#1 87.21(16), N(1)-Rh(1)-I(2)#1 91.76(10), C(9)-Rh(1)-I(2)#1 90.13(11), I(1)-Rh(1)-I(2)#1 175.991(15), C(1)-Rh(1)-I(2) 83.93(16), N(1)-Rh(1)-I(2) 90.85(9), C(9)-Rh(1)-I(2) 175.06(11), I(1)-Rh(1)-I(2) 90.580(17), I(2)#1-Rh(1)-I(2) 89.469(16), Rh(1)#1-I(2)-Rh(1) 90.530(16), C(11)-Rh(2)-C(12) 92.78(19), C(11)-Rh(2)-N(3) 174.42(17), C(12)-Rh(2)-N(3) 92.73(16), C(11)-Rh(2)-I(4) 89.26(15), C(12)-Rh(2)-I(4) 90.96(12), N(3)-Rh(2)-I(4) 91.58(9), C(11)-Rh(2)-I(3) 88.58(15), C(12)-Rh(2)-I(3) 90.59(12), N(3)-Rh(2)-I(3) 90.43(9), I(4)-Rh(2)-I(3) 177.402(14), C(11)-Rh(2)-I(3)#2 86.09(14), C(12)-Rh(2)-I(3)#2 178.06(12), N(3)-Rh(2)-I(3)#2 88.39(9), I(4)-Rh(2)-I(3)#2 90.600(16), I(3)-Rh(2)-I(3)#2 87.815(16), Rh(2)-I(3)-Rh(2)#2 92.185(15), C(2)-N(1)-C(5) 106.0(3), C(2)-N(1)-Rh(1) 124.9(3), C(5)-N(1)-Rh(1) 129.0(3), O(2)-C(9)-C(10) 138.8(7), O(2)-C(9)-Rh(1) 108.3(4), C(10)-C(9)-Rh(1) 112.9(4), C(2)-N(2)-C(4) 108.1(3), C(2)-N(2)-C(3) 125.7(4), C(4)-N(2)-C(3) 126.3(4), C(5)-C(4)-N(2) 106.2(4), C(5)-C(4)-H(4) 126.9, N(2)-C(4)-H(4) 126.9, C(4)-C(5)-N(1) 108.9(4), C(4)-C(5)-H(5) 125.6, N(1)-C(5)-H(5) 125.6, O(1)-C(1)-Rh(1) 176.7(5), N(1)-C(2)-N(2) 110.8(4), N(1)-C(2)-H(2) 124.6, N(2)-C(2)-H(2) 124.6, C(8)-N(3)-C(6) 106.4(4), C(8)-N(3)-Rh(2) 124.4(3), C(6)-N(3)-Rh(2) 128.1(3), C(8)-N(4)-C(7) 107.5(4), C(8)-N(4)-C(14) 124.9(4), C(7)-N(4)-C(14) 127.5(4), N(3)-C(8)-N(4) 110.4(4), N(3)-C(8)-H(8) 124.8, N(4)-C(8)-H(8) 124.8, O(4)-C(12)-C(13) 123.5(4), O(4)-C(12)-Rh(2) 119.1(4), C(13)-C(12)-Rh(2) 117.4(3), O(3)-C(11)-Rh(2) 177.3(5), C(12)-C(13)-H(13A) 109.5, C(12)-C(13)-H(13B) 109.5, H(13A)-C(13)-H(13B) 109.5, C(12)-C(13)-H(13C) 109.5, H(13A)-C(13)-H(13C) 109.5, H(13B)-C(13)-H(13C) 109.5, N(2)-C(3)-H(3A) 109.5, N(2)-C(3)-H(3B) 109.5, H(3A)-C(3)-H(3B) 109.5, N(2)-C(3)-H(3C) 109.5, H(3A)-C(3)-H(3C) 109.5, H(3B)-C(3)-H(3C) 109.5, C(9)-C(10)-H(10A) 109.5, C(9)-C(10)-H(10B) 109.5, H(10A)-C(10)-H(10B) 109.5, C(9)-C(10)-H(10C) 109.5, H(10A)-C(10)-H(10C) 109.5, H(10B)-C(10)-H(10C) 109.5, N(4)-C(14)-H(14A) 109.5, N(4)-C(14)-H(14B) 109.5, H(14A)-C(14)-H(14B) 109.5, N(4)-C(14)-H(14C) 109.5, H(14A)-C(14)-H(14C) 109.5, H(14B)-C(14)-H(14C) 109.5, C(6)-C(7)-N(4) 106.8(4), C(6)-C(7)-H(7) 126.6, N(4)-C(7)-H(7) 126.6, C(7)-C(6)-N(3) 108.8(4), C(7)-C(6)-H(6) 125.6, N(3)-C(6)-H(6) 125.6.

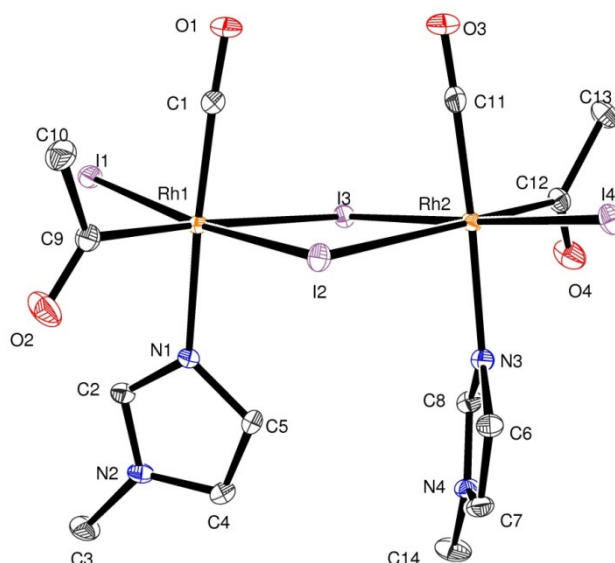


Figure 18. Single crystal X-ray structure of **6d₂**.

Table 19. Bond lengths (Å) and angles (°) for **6d₂**.

C(1)-O(1) 1.120(7), C(1)-Rh(1) 1.863(6), C(2)-N(1) 1.323(7), C(2)-N(2) 1.325(7), C(2)-H(2) 0.9500, C(3)-C(4) 1.342(8), C(3)-N(2) 1.376(7), C(3)-H(3) 0.9500, C(4)-N(1) 1.373(7), C(4)-H(4) 0.9500, C(5)-N(2) 1.472(7), C(5)-H(5A) 0.9800, C(5)-H(5B) 0.9800, C(5)-H(5C) 0.9800, C(10)-O(2) 1.194(7), C(10)-C(11) 1.501(9), C(10)-Rh(1) 2.037(6), C(11)-H(11A) 0.9800, C(11)-H(11B) 0.9800, C(11)-H(11C) 0.9800, C(12)-O(3) 1.133(7), C(12)-Rh(2) 1.860(6), C(6)-N(3) 1.321(8), C(6)-N(4) 1.352(7), C(6)-H(6) 0.9500, C(7)-C(8) 1.346(9), C(7)-N(4) 1.372(8), C(7)-H(7) 0.9500, C(8)-N(3) 1.371(7), C(8)-H(8) 0.9500, C(9)-N(4) 1.449(8), C(9)-H(9A) 0.9800, C(9)-H(9B) 0.9800, C(9)-H(9C) 0.9800, C(13)-O(4) 1.174(7), C(13)-C(14) 1.512(8), C(13)-Rh(2) 2.044(5), C(14)-H(14A) 0.9800, C(14)-H(14B) 0.9800, C(14)-H(14C) 0.9800, N(1)-Rh(1) 2.106(4), N(3)-Rh(2) 2.101(5), Rh(1)-I(1) 2.6624(5), Rh(1)-I(2) 2.6797(5), Rh(1)-I(3) 2.9595(5), Rh(2)-I(4) 2.6397(5), Rh(2)-I(3) 2.6796(5), Rh(2)-I(2) 3.0672(5).

O(1)-C(1)-Rh(1) 176.5(5), N(1)-C(2)-N(2) 110.9(5), N(1)-C(2)-H(2) 124.5, N(2)-C(2)-H(2) 124.5, C(4)-C(3)-N(2) 105.9(5), C(4)-C(3)-H(3) 127.0, N(2)-C(3)-H(3) 127.0, C(3)-C(4)-N(1) 109.6(5), C(3)-C(4)-H(4) 125.2, N(1)-C(4)-H(4) 125.2, N(2)-C(5)-H(5A) 109.5, N(2)-C(5)-H(5B) 109.5, H(5A)-C(5)-H(5B) 109.5, N(2)-C(5)-H(5C) 109.5, H(5A)-C(5)-H(5C) 109.5, H(5B)-C(5)-H(5C) 109.5, O(2)-C(10)-C(11) 122.2(5), O(2)-C(10)-Rh(1) 119.6(5), C(11)-C(10)-Rh(1) 118.2(4), C(10)-C(11)-H(11A) 109.5, C(10)-C(11)-H(11B) 109.5, H(11A)-C(11)-H(11B) 109.5, C(10)-C(11)-H(11C) 109.5, H(11A)-C(11)-H(11C) 109.5, H(11B)-C(11)-H(11C) 109.5, O(3)-C(12)-Rh(2) 177.1(5), N(3)-C(6)-N(4) 111.1(5), N(3)-C(6)-H(6) 124.4, N(4)-C(6)-H(6) 124.4, C(8)-C(7)-N(4) 106.6(5), C(8)-C(7)-H(7) 126.7, N(4)-C(7)-H(7) 126.7, C(7)-C(8)-N(3) 109.9(5), C(7)-C(8)-H(8) 125.1, N(3)-C(8)-H(8) 125.1, N(4)-C(9)-H(9A) 109.5, N(4)-C(9)-H(9B) 109.5, H(9A)-C(9)-H(9B) 109.5, N(4)-C(9)-H(9C) 109.5, H(9A)-C(9)-H(9C) 109.5, H(9B)-C(9)-H(9C) 109.5, O(4)-C(13)-C(14) 123.4(5), O(4)-C(13)-Rh(2) 118.2(4), C(14)-C(13)-Rh(2) 118.4(4), C(13)-C(14)-H(14A) 109.5, C(13)-C(14)-H(14B) 109.5, H(14A)-C(14)-H(14B) 109.5, C(13)-C(14)-H(14C) 109.5, H(14A)-C(14)-H(14C) 109.5, H(14B)-C(14)-H(14C) 109.5, C(2)-N(1)-C(4) 105.7(5), C(2)-N(1)-Rh(1) 126.3(3), C(4)-N(1)-Rh(1) 127.8(4), C(2)-N(2)-C(3) 107.8(5), C(2)-N(2)-C(5)

125.7(5), C(3)-N(2)-C(5) 126.5(5), C(6)-N(3)-C(8) 105.7(5), C(6)-N(3)-Rh(2) 127.1(4), C(8)-N(3)-Rh(2) 126.3(4), C(6)-N(4)-C(7) 106.7(5), C(6)-N(4)-C(9) 126.8(5), C(7)-N(4)-C(9) 126.4(5), C(1)-Rh(1)-C(10) 93.5(2), C(1)-Rh(1)-N(1) 175.3(2), C(10)-Rh(1)-N(1) 91.1(2), C(1)-Rh(1)-I(1) 86.89(18), C(10)-Rh(1)-I(1) 89.43(16), N(1)-Rh(1)-I(1) 92.71(12), C(1)-Rh(1)-I(2) 86.52(18), C(10)-Rh(1)-I(2) 90.20(16), N(1)-Rh(1)-I(2) 93.93(12), I(1)-Rh(1)-I(2) 173.36(2), C(1)-Rh(1)-I(3) 88.95(18), C(10)-Rh(1)-I(3) 177.15(16), N(1)-Rh(1)-I(3) 86.39(12), I(1)-Rh(1)-I(3) 92.113(16), I(2)-Rh(1)-I(3) 88.549(14), C(12)-Rh(2)-C(13) 93.1(2), C(12)-Rh(2)-N(3) 173.9(2), C(13)-Rh(2)-N(3) 92.8(2), C(12)-Rh(2)-I(4) 88.11(18), C(13)-Rh(2)-I(4) 89.43(16), N(3)-Rh(2)-I(4) 90.61(13), C(12)-Rh(2)-I(3) 89.08(18), C(13)-Rh(2)-I(3) 91.01(16), N(3)-Rh(2)-I(3) 92.16(13), I(4)-Rh(2)-I(3) 177.18(2), C(12)-Rh(2)-I(2) 86.83(17), C(13)-Rh(2)-I(2) 177.34(16), N(3)-Rh(2)-I(2) 87.30(12), I(4)-Rh(2)-I(2) 93.226(15), I(3)-Rh(2)-I(2) 86.338(13), Rh(1)-I(2)-Rh(2) 90.897(14), Rh(2)-I(3)-Rh(1) 93.279(16).

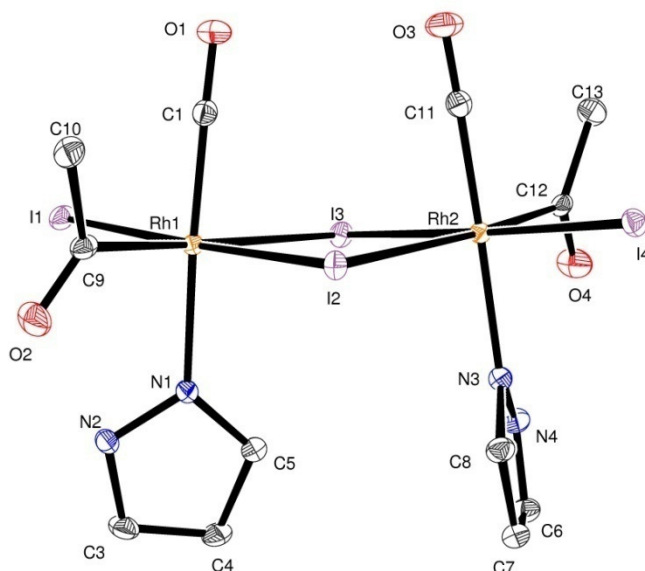


Figure 19. Single crystal X-ray structure of **6e**.

Table 20. Bond lengths (Å) and angles (°) for **6e**.

I(1)-Rh(1) 2.6543(3), I(3)-Rh(2) 2.6815(3), I(3)-Rh(1) 3.0019(3), I(2)-Rh(1) 2.6707(3), I(2)-Rh(2) 2.9562(3), I(4)-Rh(2) 2.6471(3), Rh(1)-C(1) 1.856(3), Rh(1)-C(9) 2.064(3), Rh(1)-N(1) 2.104(3), Rh(2)-C(11) 1.868(3), Rh(2)-C(12) 2.088(3), Rh(2)-N(3) 2.107(3), O(1)-C(1) 1.133(4), O(2)-C(9) 1.165(4), O(3)-C(11) 1.128(4), O(4)-C(12) 1.163(4), N(1)-C(5) 1.339(4), N(1)-N(2) 1.345(4), N(2)-C(3) 1.341(4), N(2)-H(2A) 0.878(10), N(3)-C(8) 1.340(4), N(3)-N(4) 1.348(4), N(4)-C(6) 1.333(4), N(4)-H(4A) 0.875(10), C(9)-C(10) 1.490(4), C(10)-H(10A) 0.9800, C(10)-H(10B) 0.9800, C(10)-H(10C) 0.9800, C(5)-C(4) 1.394(5), C(5)-H(5) 0.9500, C(4)-C(3) 1.364(5), C(4)-H(4) 0.9500, C(3)-H(3) 0.9500, C(8)-C(7) 1.384(5), C(8)-H(8) 0.9500, C(7)-C(6) 1.368(5), C(7)-H(7) 0.9500, C(6)-H(6) 0.9500, C(12)-C(13) 1.476(5), C(13)-H(13A) 0.9800, C(13)-H(13B) 0.9800, C(13)-H(13C) 0.9800.

Rh(2)-I(3)-Rh(1) 91.939(9), Rh(1)-I(2)-Rh(2) 93.175(9), C(1)-Rh(1)-C(9) 92.11(13), C(1)-Rh(1)-N(1) 174.91(12), C(9)-Rh(1)-N(1) 92.91(11), C(1)-Rh(1)-I(1) 87.58(10), C(9)-Rh(1)-I(1) 87.66(9), N(1)-Rh(1)-I(1) 91.78(7), C(1)-Rh(1)-I(2) 89.62(10), C(9)-Rh(1)-I(2) 90.21(9), N(1)-Rh(1)-I(2) 91.20(7), I(1)-Rh(1)-I(2) 176.422(11), C(1)-Rh(1)-I(3) 85.48(10), C(9)-Rh(1)-I(3) 176.13(9), N(1)-Rh(1)-I(3) 89.56(7), I(1)-Rh(1)-I(3) 95.243(9), I(2)-Rh(1)-I(3) 86.760(9), C(11)-Rh(2)-C(12) 92.33(13), C(11)-Rh(2)-N(3) 173.29(12), C(12)-Rh(2)-N(3) 93.72(11), C(11)-Rh(2)-I(4) 88.02(10), C(12)-Rh(2)-I(4) 91.31(8), N(3)-Rh(2)-I(4) 88.92(7), C(11)-Rh(2)-I(3) 89.61(10), C(12)-Rh(2)-I(3) 88.15(8), N(3)-Rh(2)-I(3) 93.50(7), I(4)-Rh(2)-I(3) 177.544(12), C(11)-Rh(2)-I(2) 84.49(10), C(12)-Rh(2)-I(2) 174.62(8), N(3)-Rh(2)-I(2) 89.70(7), I(4)-Rh(2)-I(2) 92.909(9), I(3)-Rh(2)-I(2) 87.499(9), C(5)-N(1)-N(2) 104.9(3), C(5)-N(1)-Rh(1) 130.0(2), N(2)-N(1)-Rh(1) 124.4(2), C(3)-N(2)-N(1) 111.8(3), C(3)-N(2)-H(2A) 134(3), N(1)-N(2)-H(2A) 114(3), C(8)-N(3)-N(4) 104.7(3), C(8)-N(3)-Rh(2) 129.4(2), N(4)-N(3)-Rh(2) 125.9(2), C(6)-N(4)-N(3) 111.8(3), C(6)-N(4)-H(4A) 130(3), N(3)-N(4)-H(4A) 117(3), O(1)-C(1)-Rh(1) 177.6(3), O(2)-C(9)-C(10) 124.9(3), O(2)-C(9)-Rh(1) 118.1(2), C(10)-C(9)-Rh(1) 117.0(2), C(9)-C(10)-H(10A) 109.5, C(9)-C(10)-H(10B) 109.5, H(10A)-C(10)-H(10B) 109.5, C(9)-C(10)-H(10C) 109.5, H(10A)-C(10)-H(10C) 109.5, H(10B)-C(10)-H(10C) 109.5, N(1)-C(5)-C(4) 110.8(3), N(1)-C(5)-H(5) 124.6, C(4)-C(5)-H(5) 124.6, C(3)-C(4)-C(5) 105.0(3), C(3)-C(4)-H(4) 127.5, C(5)-C(4)-H(4) 127.5, N(2)-C(3)-C(4) 107.4(3), N(2)-C(3)-H(3) 126.3, C(4)-C(3)-H(3) 126.3, N(3)-C(8)-C(7) 111.0(3), N(3)-C(8)-H(8) 124.5, C(7)-C(8)-H(8) 124.5, C(6)-C(7)-C(8) 105.1(3), C(6)-C(7)-H(7) 127.5, C(8)-C(7)-H(7) 127.5, N(4)-C(6)-C(7) 107.4(3), N(4)-C(6)-H(6) 126.3, C(7)-C(6)-H(6) 126.3, O(3)-C(11)-Rh(2) 177.2(3), O(4)-C(12)-C(13) 125.4(3), O(4)-C(12)-Rh(2) 117.4(3), C(13)-C(12)-Rh(2) 117.1(2), C(12)-C(13)-H(13A) 109.5, C(12)-C(13)-H(13B) 109.5, H(13A)-C(13)-H(13B) 109.5, C(12)-C(13)-H(13C) 109.5, H(13A)-C(13)-H(13C) 109.5, H(13B)-C(13)-H(13C) 109.5.

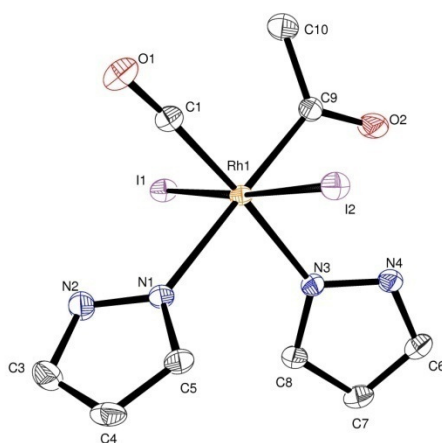


Figure 20. Single crystal X-ray structure of **8e**.

Table 21. Bond lengths (Å) and angles (°) for **8e**.

I(1)-Rh(1) 2.6743(4), I(2)-Rh(1) 2.6685(4), Rh(1)-C(1) 1.864(4), Rh(1)-C(9) 2.042(4), Rh(1)-N(3) 2.107(3), Rh(1)-N(1) 2.245(3), O(1)-C(1) 1.127(4), O(2)-C(9) 1.204(4), N(1)-C(5) 1.322(4), N(1)-N(2) 1.343(4), N(2)-C(3) 1.351(5), N(2)-H(2A) 0.880(10), N(3)-C(8) 1.331(4), N(3)-N(4) 1.345(4), N(4)-C(6) 1.328(5), N(4)-H(4A) 0.874(10), C(9)-C(10)

1.478(5), C(10)-H(10A) 0.9800, C(10)-H(10B) 0.9800, C(10)-H(10C) 0.9800, C(3)-C(4) 1.346(6), C(3)-H(3) 0.9500, C(4)-C(5) 1.375(5), C(4)-H(4) 0.9500, C(5)-H(5) 0.9500, C(8)-C(7) 1.382(5), C(8)-H(8) 0.9500, C(7)-C(6) 1.370(5), C(7)-H(7) 0.9500, C(6)-H(6) 0.9500.

C(1)-Rh(1)-C(9) 92.16(15), C(1)-Rh(1)-N(3) 174.59(13), C(9)-Rh(1)-N(3) 93.06(13), C(1)-Rh(1)-N(1) 88.61(13), C(9)-Rh(1)-N(1) 179.23(13), N(3)-Rh(1)-N(1) 86.17(11), C(1)-Rh(1)-I(2) 87.42(11), C(9)-Rh(1)-I(2) 87.73(10), N(3)-Rh(1)-I(2) 91.35(8), N(1)-Rh(1)-I(2) 92.22(7), C(1)-Rh(1)-I(1) 90.22(11), C(9)-Rh(1)-I(1) 87.88(10), N(3)-Rh(1)-I(1) 91.41(8), N(1)-Rh(1)-I(1) 92.20(7), I(2)-Rh(1)-I(1) 174.925(13), C(5)-N(1)-N(2) 104.7(3), C(5)-N(1)-Rh(1) 129.3(3), N(2)-N(1)-Rh(1) 125.9(2), N(1)-N(2)-C(3) 111.3(3), N(1)-N(2)-H(2A) 119(3), C(3)-N(2)-H(2A) 129(3), C(8)-N(3)-N(4) 104.6(3), C(8)-N(3)-Rh(1) 129.5(3), N(4)-N(3)-Rh(1) 125.2(2), C(6)-N(4)-N(3) 112.1(3), C(6)-N(4)-H(4A) 129(3), N(3)-N(4)-H(4A) 119(3), O(1)-C(1)-Rh(1) 175.6(3), O(2)-C(9)-C(10) 120.2(4), O(2)-C(9)-Rh(1) 120.0(3), C(10)-C(9)-Rh(1) 119.8(3), C(9)-C(10)-H(10A) 109.5, C(9)-C(10)-H(10B) 109.5, H(10A)-C(10)-H(10B) 109.5, C(9)-C(10)-H(10C) 109.5, H(10A)-C(10)-H(10C) 109.5, H(10B)-C(10)-H(10C) 109.5, C(4)-C(3)-N(2) 106.9(4), C(4)-C(3)-H(3) 126.6, N(2)-C(3)-H(3) 126.6, C(3)-C(4)-C(5) 105.7(3), C(3)-C(4)-H(4) 127.2, C(5)-C(4)-H(4) 127.2, N(1)-C(5)-C(4) 111.5(3), N(1)-C(5)-H(5) 124.3, C(4)-C(5)-H(5) 124.3, N(3)-C(8)-C(7) 111.2(4), N(3)-C(8)-H(8) 124.4, C(7)-C(8)-H(8) 124.4, C(6)-C(7)-C(8) 105.0(3), C(6)-C(7)-H(7) 127.5, C(8)-C(7)-H(7) 127.5, N(4)-C(6)-C(7) 107.1(3), N(4)-C(6)-H(6) 126.4, C(7)-C(6)-H(6) 126.4.

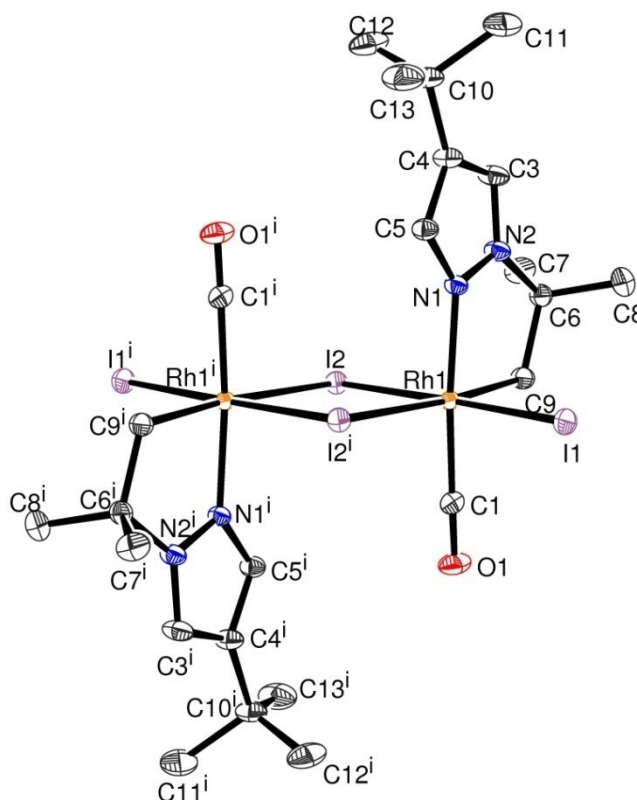


Figure 21. Single crystal X-ray structure of **9h**.

Table 22. Bond lengths (Å) and angles (°) for **9h**.

C(1)-O(1) 1.129(3), C(1)-Rh(1) 1.860(2), C(3)-N(2) 1.348(3), C(3)-C(4) 1.379(3), C(3)-H(3) 0.9500, C(5)-N(1) 1.335(3), C(5)-C(4) 1.394(3), C(5)-H(5) 0.9500, C(6)-N(2) 1.479(3), C(6)-C(8) 1.521(3), C(6)-C(7) 1.524(3), C(6)-C(9) 1.546(3), C(7)-H(7A) 0.9800, C(7)-H(7B) 0.9800, C(7)-H(7C) 0.9800, C(8)-H(8A) 0.9800, C(8)-H(8B) 0.9800, C(8)-H(8C) 0.9800, C(9)-Rh(1) 2.074(2), C(9)-H(9A) 0.9900, C(9)-H(9B) 0.9900, C(4)-C(10) 1.517(3), C(10)-C(13) 1.476(6), C(10)-C(12) 1.515(6), C(10)-C(11) 1.589(6), C(11)-H(11A) 0.9800, C(11)-H(11B) 0.9800, C(11)-H(11C) 0.9800, C(12)-H(12A) 0.9800, C(12)-H(12B) 0.9800, C(12)-H(12C) 0.9800, C(13)-H(13A) 0.9800, C(13)-H(13B) 0.9800, C(13)-H(13C) 0.9800, I(1)-Rh(1) 2.6457(2), I(2)-Rh(1) 2.6683(2), I(2)-Rh(1)#1 2.8148(2), N(1)-N(2) 1.346(2), N(1)-Rh(1) 2.0455(16), Rh(1)-I(2)#1 2.8148(2), Cl(1)-C(14) 1.517(13), C(14)-Cl(2) 1.575(12), C(14)-H(14A) 0.9900, C(14)-H(14B) 0.9900.

O(1)-C(1)-Rh(1) 178.4(2), N(2)-C(3)-C(4) 108.53(19), N(2)-C(3)-H(3) 125.7, C(4)-C(3)-H(3) 125.7, N(1)-C(5)-C(4) 110.70(19), N(1)-C(5)-H(5) 124.6, C(4)-C(5)-H(5) 124.6, N(2)-C(6)-C(8) 108.18(19), N(2)-C(6)-C(7) 107.79(18), C(8)-C(6)-C(7) 110.8(2), N(2)-C(6)-C(9) 109.49(16), C(8)-C(6)-C(9) 110.01(19), C(7)-C(6)-C(9) 110.48(19), C(6)-C(7)-H(7A) 109.5, C(6)-C(7)-H(7B) 109.5, H(7A)-C(7)-H(7B) 109.5, C(6)-C(7)-H(7C) 109.5, H(7A)-C(7)-H(7C) 109.5, H(7B)-C(7)-H(7C) 109.5, C(6)-C(8)-H(8A) 109.5, C(6)-C(8)-H(8B) 109.5, H(8A)-C(8)-H(8B) 109.5, C(6)-C(8)-H(8C) 109.5, H(8A)-C(8)-H(8C) 109.5, H(8B)-C(8)-H(8C) 109.5, C(6)-C(9)-Rh(1) 112.70(14), C(6)-C(9)-H(9A) 109.1, Rh(1)-C(9)-H(9A) 109.1, C(6)-C(9)-H(9B) 109.1, Rh(1)-C(9)-H(9B) 109.1, H(9A)-C(9)-H(9B) 107.8, C(3)-C(4)-C(5) 104.19(19), C(3)-C(4)-C(10) 127.5(2), C(5)-C(4)-C(10) 128.3(2), C(13)-C(10)-C(12) 113.9(4), C(13)-C(10)-C(4) 111.5(3), C(12)-C(10)-C(4) 109.3(3), C(13)-C(10)-C(11) 107.3(4), C(12)-C(10)-C(11) 106.4(4), C(4)-C(10)-C(11) 108.0(3), C(10)-C(11)-H(11A) 109.5, C(10)-C(11)-H(11B) 109.5, H(11A)-C(11)-H(11B) 109.5, C(10)-C(11)-H(11C) 109.5, H(11A)-C(11)-H(11C) 109.5, H(11B)-C(11)-H(11C) 109.5, C(10)-C(12)-H(12A) 109.5, C(10)-C(12)-H(12B) 109.5, H(12A)-C(12)-H(12B) 109.5, C(10)-C(12)-H(12C) 109.5, H(12A)-C(12)-H(12C) 109.5, H(12B)-C(12)-H(12C) 109.5, C(10)-C(13)-H(13A) 109.5, C(10)-C(13)-H(13B) 109.5, H(13A)-C(13)-H(13B) 109.5, C(10)-C(13)-H(13C) 109.5, H(13A)-C(13)-H(13C) 109.5, H(13B)-C(13)-H(13C) 109.5, Rh(1)-I(2)-Rh(1)#1 92.721(8), C(5)-N(1)-N(2) 106.67(16), C(5)-N(1)-Rh(1) 137.86(14), N(2)-N(1)-Rh(1) 115.28(12), N(1)-N(2)-C(3) 109.92(17), N(1)-N(2)-C(6) 120.28(16), C(3)-N(2)-C(6) 129.64(18), C(1)-Rh(1)-N(1) 173.03(8), C(1)-Rh(1)-C(9) 91.31(9), N(1)-Rh(1)-C(9) 81.72(7), C(1)-Rh(1)-I(1) 88.89(7), N(1)-Rh(1)-I(1) 91.21(5), C(9)-Rh(1)-I(1) 92.30(7), C(1)-Rh(1)-I(2) 90.59(7), N(1)-Rh(1)-I(2) 89.62(5), C(9)-Rh(1)-I(2) 90.27(7), I(1)-Rh(1)-I(2) 177.383(7), C(1)-Rh(1)-I(2)#1 92.92(7), N(1)-Rh(1)-I(2)#1 94.05(5), C(9)-Rh(1)-I(2)#1 175.13(6), I(1)-Rh(1)-I(2)#1 90.183(8), I(2)-Rh(1)-I(2)#1 87.280(7), Cl(1)-C(14)-Cl(2) 128.2(9), Cl(1)-C(14)-H(14A) 105.2, Cl(2)-C(14)-H(14A) 105.2, Cl(1)-C(14)-H(14B) 105.2, Cl(2)-C(14)-H(14B) 105.2, H(14A)-C(14)-H(14B) 106.0.

V-2 Experimental section: Chapter III

V-2-1 Instrumentation and materials

FT-IR spectra were collected on a Perkin-Elmer Spectrum One FT spectrophotometer with a 0.1 mm cell equipped with CaF₂ windows. All NMR spectra data were recorded on Bruker DRX 300 or Avance 300-500 spectrometers with TMS as external reference for ¹H and ¹³C and phosphoric acid for ³¹P. Chemical shifts are reported in ppm and coupling constants (*J*) are given in Hertz. Spectral assignments were made by means of routine one and two dimensional NMR experiments when appropriate. Mass spectra analyses were performed on a NERMAC R10-10 (FAB negative mode, gas: Xe). The major *m/z* peak was reported with the intensity as a percentage of the base peak between brackets. Elemental analyses were measured with a precision superior to 0.3% at the Microanalysis Laboratory of the LCC in Toulouse. X-ray structures were determined on an Oxford Diffraction Xcalibur CCd diffractometer.

V-2-2 Synthesis

All experiments were carried out under an atmosphere of argon using Schlenk techniques or glovebox. Solvents were obtained from a Solvent Purification System (MB SPS-800). CD₂Cl₂ was dried using activated molecular sieves. RhCl₃.x H₂O salt was supplied by Johnson Matthey, RhI₃.xH₂O from the Celanese Plant at Clearlake (Texas, USA). Tetramethyl iodide, tetraethyl iodide, lithium iodide salts were used as received from Aldrich. PPnCl (bis-triphenylphosphoranylidene chloride) was re-crystallized in MeOH/ter-butyl methyl ether before used. Butylmethylimidazolium iodide (BMIMI) and 1-Propyl-2,3-dimethylimidazolium iodide (PrMMIMI) ionic liquids were purchased from Solvionic and Iolitec, respectively and used as received. N-heterocyclic solid amine compounds (imidazole

and pyrazole) were used as received. Amine precursors (1-methylimidazole, 1-methylpyrazole, pyridine) were dried and distilled over KOH and degassed prior to use. Methyl and ethyl iodide (Aldrich) were distilled over calcium hydride and stored in foil-wrapped Schlenk tubes under argon to prevent formation of I₂. Hydriodic acid 57% in H₂O solution (Aldrich) was used as received and stored at the shelter of light.

V-2-3 Alkyl iodide NMR data

Methyl iodide CH₃I: ¹³C{¹H} NMR (298 K, 75.47 MHz, AcOH-*d*₄, ppm): δ -23.4 (s, 1C, CH₃).

Ethyl iodide CH₃CH₂I: ¹H NMR (298 K, 300.13 MHz, AcOH-*d*₄, ppm): δ 3.23 (q, 2H, ³J_{H-H} = 7.5 Hz, ICH₂CH₃), 1.85 (t, 3H, ³J_{H-H} = 7.5 Hz, ICH₂CH₃). ¹³C{¹H} NMR (298 K, 75.47 MHz, AcOH-*d*₄, ppm): δ 20.6 (s, 1C, ICH₂CH₃), -1.2 (s, 1C, ICH₂CH₃).

V-2-4 Synthesis of imidazolium and pyridinium iodide salt precursors

To a dichloromethane solution (V = 15 mL) of imidazole/1-methylimidazole (1/1 g, 14.7/12.2 mmol) was added 1.2 molar eq. of 57% hydriodic acid in a H₂O solution (4.0/3.3 g, 30.9/25.7 mmol) under vigorous stirring for 8 hours at 273 K. The reaction mixture was slowly warmed to room temperature and excess of HI, CH₂Cl₂ and water were removed under vacuum. The white precipitate was washed three times with dry diethyl ether (20 mL) at 273 K. HHIMI/MHIMI salts were obtained with good yields (89/93%), dried under vacuum and stored under argon at 255 K prior to use.

To an acetone solution (V = 20 mL) of 1-methylimidazole (4 g, 48.7 mmol) was added drop wise 5 molar eq. of methyl iodide/ethyl iodide (34.6/38.0 g, 243.6/243.6 mmol) at room temperature under vigorous stirring. After complete addition the reaction was gently heated to reflux for 12 hours. A white solid precipitated in solution and after vacuum removal of

solvent and reagent excess, MMIMI/EMIMI salts were recovered, washed three times with dry diethyl ether (20 mL), dried under vacuum (96/91 %) and stored under argon at 255 K prior to use.

To an acetone solution ($V = 20$ mL) of pyridine (4 g, 50.6 mmol) was added drop wise 5 molar eq. of methyl iodide (35.9 g, 253.2 mmol) at room temperature under vigorous stirring. After complete addition the reaction was gently heated to reflux for 12 hours. A white solid was obtained after vacuum removal of solvent and reagent excess. MePyI was obtained, washed three times with dry diethyl ether (20 mL), dried under vacuum (90 %) and stored under argon at 255 K prior to use.

1-methyl-imidazolium iodide MHIMI: ^1H NMR (298 K, 400.13 MHz, DMSO, ppm): δ 9.08 (s, 1H, ring-NCHN), 7.70 (d, 1H, $^3J_{\text{H-H}} = 1.6$ Hz, ring-NCHCHN), 7.66 (d, 1H, $^3J_{\text{H-H}} = 1.6$ Hz, ring-NCHCHN), 3.88 (s, 3H, NCH₃).

1,3-dimethyl-imidazolium iodide MMIMI: ^1H NMR (298 K, 300.13 MHz, DMSO, ppm): δ 9.09 (s, 1H, ring-NCHN), 7.70 (s, 2H, ring-NCHCHN), 3.86 (s, 6H, NCH₃-CH-NCH₃). $^{13}\text{C}\{^1\text{H}\}$ NMR (298 K, 75.47 MHz, DMSO, ppm): δ 137.5 (s, 1C, ring-NCHN), 123.9 (s, 2C, ring-NCHCHN), 36.3 (s, 2C, NCH₃-CH-NCH₃).

1-propyl-2-methyl-3-methyl imidazolium iodide PrMMIMI: ^1H NMR (298 K, 400.13 MHz, CD₂Cl₂, ppm): δ 7.62 (d, 1H, $^3J_{\text{H-H}} = 6.8$ Hz, ring-NCHCHN), 7.52 (d, 1H, $^3J_{\text{H-H}} = 6.8$ Hz, ring-NCHCHN), 4.18 (t, 2H, $^3J_{\text{H-H}} = 7.6$ Hz, NCH₂CH₂CH₃), 3.97 (s, 3H, NCH₃), 2.78 (s, 3H, CCH₃), 1.90 (m, 2H, NCH₂CH₂CH₃), 1.02 (m, 3H, NCH₂CH₂CH₃).

1-buthyl-3-methyl imidazolium iodide BMIMI: ^1H NMR (298 K, 400.13 MHz, CD₂Cl₂, ppm): δ 9.91 (s, 1H, ring-NCHN), 7.59 (t, 1H, $^3J_{\text{H-H}} = 1.6$ Hz, ring-NCHCHN), 7.55 (t, 1H, $^3J_{\text{H-H}} = 2.0$ Hz, ring-NCHCHN), 4.32 (t, 2H, $^3J_{\text{H-H}} = 7.6$ Hz, NCH₂CH₂CH₂CH₃), 4.00 (s, 3H, NCH₃), 1.90 (m, 2H, $^3J_{\text{H-H}} = 5.6$ Hz, NCH₂CH₂CH₂CH₃), 1.38 (m, 2H, $^3J_{\text{H-H}} = 7.6$ Hz, NCH₂CH₂CH₂CH₃), 0.95 (t, 3H, $^3J_{\text{H-H}} = 7.2$ Hz, NCH₂CH₂CH₂CH₃). ^1H NMR (298 K,

300.13 MHz, AcOH- d_4 , ppm): δ 9.27 (s, 1H, ring-NCHN), 7.81 (t, 1H, $^3J_{\text{H-H}} = 1.8$ Hz, ring-NCHCHN), 7.73 (t, 1H, $^3J_{\text{H-H}} = 1.5$ Hz, ring-NCHCHN), 4.38 (t, 2H, $^3J_{\text{H-H}} = 7.2$ Hz, NCH₂CH₂CH₂CH₃), 4.00 (s, 3H, NCH₃), 1.90 (m, 2H, $^3J_{\text{H-H}} = 7.5$ Hz, NCH₂CH₂CH₂CH₃), 1.36 (m, 2H, $^3J_{\text{H-H}} = 7.5$ Hz, NCH₂CH₂CH₂CH₃), 0.92 (t, 3H, $^3J_{\text{H-H}} = 7.5$ Hz, NCH₂CH₂CH₂CH₃). $^{13}\text{C}\{^1\text{H}\}$ NMR (298 K, 75.47 MHz, AcOH- d_4 , ppm): δ 136.5 (s, 1C, ring-NCHN), 123.8 (s, 1C, ring-NCHCHN), 122.5 (s, 1C, ring-NCHCHN), 49.5 (s, 1C, NCH₃), 36.9 (s, 1C, NCH₂CH₂CH₂CH₃), 31.9 (s, 1C, NCH₂CH₂CH₂CH₃), 19.2 (s, 1C, NCH₂CH₂CH₂CH₃), 13.2 (s, 1C, NCH₂CH₂CH₂CH₃).

V-2-5 Synthesis of ammonium iodide salt precursors

To an anhydrous and degassed triethylamine/diethylamine (1.5/1 g, 14/13.6 mmol) solution was added 1.2 molar eq. of 57% hydriodic acid in water (3.97/3.66 g, 31/28.6 mmol) under vigorous stirring for 8 hours at 273 K. The reaction mixture was slowly warmed to room temperature and excess of HI and water were removed under vacuum. A white solid precipitated that was washed three times with dry diethyl ether (20 mL) at 273 K. The corresponding salts HNEt₃I/H₂NEt₂I were obtained in good yields (~ 90%), dried under vacuum and stored under argon at 255 K prior to use. Salts were used in the following days because they revealed to be unstable for long term period.

Tetramethyl ammonium iodide NMe₄I: ^1H NMR (298 K, 400.13 MHz, D₂O, ppm): δ 3.14 (s, 12H, N(CH₃)₄). $^{13}\text{C}\{^1\text{H}\}$ NMR (298 K, 75.47 MHz, D₂O, ppm): δ 55.4 (t, 4C, N(CH₃)₄). $^{13}\text{C}\{^1\text{H}\}$ NMR (298 K, 75.47 MHz, DMSO, ppm): δ 54.9 (t, 4C, N(CH₃)₄).

Tetraethyl ammonium iodide NEt₄I: Low solubility in CH₂Cl₂. ^1H NMR (298 K, 400.13 MHz, CD₂Cl₂, ppm): δ 3.41 (q, 8H, $^3J_{\text{H-H}} = 7.2$ Hz N(CH₂CH₃)₄), 1.40 (t, 12H, $^3J_{\text{H-H}} = 6.4$ Hz N(CH₂CH₃)₄). $^{13}\text{C}\{^1\text{H}\}$ NMR (298 K, 75.47 MHz, CD₂Cl₂, ppm): δ 53.0 (s, 4C, N(CH₂CH₃)₄), 7.8 (s, 4C, N(CH₂CH₃)₄).

Triethyl ammonium iodide HNEt₃I: ¹H NMR (298 K, 400.13 MHz, CD₂Cl₂, ppm): δ 8.10 (br s, 1H, HN(CH₂CH₃)₃), 3.17 (q, 6H, ³J_{H-H} = 7.2 Hz, HN(CH₂CH₃)₃), 1.47 (t, 9H, ³J_{H-H} = 7.2 Hz, HN(CH₂CH₃)₃). ¹³C{¹H} NMR (298 K, 100.62 MHz, CD₂Cl₂, ppm): δ 46.4 (s, 3C, HN(CH₂CH₃)₃), 8.6 (s, 3C, HN(CH₂CH₃)₃).

Diethyl ammonium iodide H₂NEt₂I: ¹H NMR (298 K, 400.13 MHz, CD₂Cl₂, ppm): δ 7.20 (br s, 2H, H₂N(CH₂CH₃)₂), 2.10 (q, 4H, ³J_{H-H} = 7.2 Hz, H₂N(CH₂CH₃)₂), 0.50 (t, 6H, ³J_{H-H} = 7.2 Hz, H₂N(CH₂CH₃)₂). ¹³C{¹H} NMR (298 K, 100.62 MHz, CD₂Cl₂, ppm): δ 42.9 (s, 2C, H₂N(CH₂CH₃)₂), 11.1 (s, 2C, H₂N(CH₂CH₃)₂).

V-2-6 *Synthesis of pyrazolium and sulfonium iodide salt precursors*¹²

To a dichloromethane solution (V = 15 mL) of pyrazole/1-methylpyrazole (1/1 g, 14.7/12.2 mmol) was added 1.2 molar eq. of 57% hydriodic acid in water (4.1/3.1 g, 32.1/24.4 mmol) under vigorous stirring for 8 hours at 273 K. The reaction mixture was slowly warmed to room temperature and excess of HI, CH₂Cl₂ and water were removed under vacuum. The white solid that precipitated was washed three times with dry diethyl ether (20 mL) at 273 K. HHPYI/MHPYI salts were obtained in good yields (91/96%), dried under vacuum and stored under argon at 255 K prior to use.

To an acetone solution (V = 15 mL) of 1-methylpyrazole (4 g, 48.7 mmol) was added drop wise 5 molar eq. of methyl iodide (34.6 g, 243.6 mmol) at room temperature under vigorous stirring. After complete addition the reaction was gently heated to reflux for 12 hours. A white solid precipitated in solution and after vacuum removal of solvent and reagent excess, MMPYI was recovered, washed three times with dry diethyl ether (20 mL), dried under vacuum (95%) and stored under argon at 255 K prior to use.

(12) Paulsson, H.; Hagfeldt, A.; Kloo, L. *J. Phys. Chem. B* **2003**, *107*, 13665.

To an acetone solution ($V = 50$ mL) of diethylsulfide (23.3 g, 258.4 mmol) was added drop wise 5 molar eq. of methyl iodide (183.4 g, 1292.0 mmol) at room temperature under vigorous stirring. After complete addition the reaction was gently heated to reflux for 12 hours. After full evaporation under vacuum and after washes in acetone (20 mL) at 273 K and diethyl ether (50 mL) at RT, a yellow oil was dried and recovered (90%). SEt_2MeI was stored under argon at 255 K prior to use.

1-methyl pyrazolium iodide MHPYI: ^1H NMR (298 K, 300.13 MHz, CD_2Cl_2 , ppm): δ 8.08 (br d, 1H, $^3J_{\text{H-H}} = 2.7$ Hz, ring- $\text{HN}=\text{CH}-\text{CH}$), 8.07 (br d, 1H, $^3J_{\text{H-H}} = 2.7$ Hz, ring- $\text{NCH}_3-\text{CH}-\text{CH}$), 7.97 (br s, 1H, ring- $\text{N}(\text{CH}_3)-\text{NH}$), 6.72 (t, 1H, $^3J_{\text{H-H}} = 1.2$ Hz, ring- $\text{NCH}_3-\text{CH}=\text{CH}$), 4.45 (s, 3H, ring- $\text{N}(\text{CH}_3)-\text{NH}$).

1,3-dimethyl pyrazolium iodide MMPYI: ^1H NMR (298 K, 300.13 MHz, $(\text{CD}_3)_2\text{CO}$, ppm): δ 8.63 (s, 2H, $^3J_{\text{H-H}} = 3.0$ Hz, ring- $\text{CH}_3\text{N}=\text{CH}-\text{CH}=\text{CH}$), 6.88 (t, 1H, $^3J_{\text{H-H}} = 3.0$ Hz, ring- $\text{CH}_3\text{N}=\text{CH}-\text{CH}=\text{CH}$), 4.43 (s, 6H, ring- $\text{N}(\text{CH}_3)-\text{N}(\text{CH}_3)$). $^{13}\text{C}\{^1\text{H}\}$ NMR (298 K, 75.47 MHz, $(\text{CD}_3)_2\text{CO}$, ppm): δ 137.8 (s, 2C, ring- $\text{CH}_3\text{N}=\text{CH}-\text{CH}=\text{CH}$), 107.0 (s, 1C, ring- $\text{CH}_3\text{N}=\text{CH}-\text{CH}=\text{CH}$), 36.9 (s, 2C, ring- $\text{N}(\text{CH}_3)-\text{N}(\text{CH}_3)$).

Diethyl-methyl sulfonium iodide SEt_2MeI : ^1H NMR (298 K, 300.13 MHz, CD_2Cl_2 , ppm): δ 3.78 (q, 4H, $^3J_{\text{H-H}} = 7.5$ Hz, $\text{CH}_3\text{S}(\text{CH}_2\text{CH}_3)_2$), 3.24 (s, 3H, $\text{CH}_3\text{S}(\text{CH}_2\text{CH}_3)_2$), 1.53 (t, 6H, $^3J_{\text{H-H}} = 5.7$ Hz, $\text{CH}_3\text{S}(\text{CH}_2\text{CH}_3)_2$). $^{13}\text{C}\{^1\text{H}\}$ NMR (298 K, 75.47 MHz, CD_2Cl_2 , ppm): δ 35.5 (s, 2C, $\text{CH}_3\text{S}(\text{CH}_2\text{CH}_3)_2$), 22.1 (s, 1C, $\text{CH}_3\text{S}(\text{CH}_2\text{CH}_3)_2$), 9.1 (s, 2C, $\text{CH}_3\text{S}(\text{CH}_2\text{CH}_3)_2$).

V-2-7 Synthesis of anionic cis-dicarbonyl-diiodo-rhodium(I) ammonium/sulfonium/lithium salt complexes

To a dichloromethane solution ($V = 25$ mL) of $[\text{Rh}(\mu\text{-I})(\text{CO})_2]_2$ **2** (500 mg, 0.87 mmol) under stirring was added via canulation a solution of 2 molar eq. of iodide salt in dichloromethane ($V = 5$ mL) at 263 K. The reaction mixture was slowly warmed to room

temperature and vigorously stirred during 6 hours. After solvent removal under vacuum, the compounds **10a-27a** were washed (x3) with pentane (20 mL), dried under vacuum and stored under argon at 255 K prior to use. Complex **26a** was unstable and only characterized by FT-IR and complex **27a** was prepared in the presence of a minimum of CH₃OH to solubilize the LiI starting salt. For ¹³C{¹H} NMR measurements of **10a-25a,27a** ¹³CO-labeled [Rh(μ -I)(CO)₂]₂ was used as the precursor. For complexes **10a-27a**, when solvent was removed under vacuum, additional CO bubbling on the concentrated product increased the final product yield due to better stabilization.

[RhI₂(CO)₂](HHIM) 10a: Light brown-red powder (Yield 89%). FT-IR (ν_{CO} , cm⁻¹): 2068.0 (s), 1998.4 (s) (CH₂Cl₂).

[RhI₂(CO)₂](MHIM) 11a: Dark brown-red oil (Yield 89%). FT-IR (ν_{CO} , cm⁻¹): 2066.8 (s), 1996.9 (s) (CH₂Cl₂). **11a-¹³CO:** ¹H NMR (298 K, 300.13 MHz, CD₂Cl₂, ppm): δ 11.89 (t, 1H, ¹J_{H-N} = 51.0 Hz, ring=NH-), 8.93 (s, 1H, ring-NCHN), 7.60 (s, 1H, ring-H₃CNCH=CHNH), 7.40 (s, 1H, ring-H₃CNCH=CHNH), 4.06 (s, 3H, ring-H₃CNCH=CHNH). ¹³C{¹H} NMR (298 K, 75.468 MHz, CD₂Cl₂, ppm): δ 183.0 (d, 2C, CO ¹J_{CO-Rh} = 71.2 Hz), 134.6 (s, 1C, ring-H₃CNCHNH), 123.1 (s, 1C, ring-H₃CNCH=CHNH), 120.1 (s, 1C, ring-H₃CNCH=CHNH), 37.2 (s, 1C, ring-H₃CNCH=CHNH).

[RhI₂(CO)₂](MMIM) 12a: Dark green microcrystalline product (Yield 92%). Crystals ready for X-ray analysis were obtained in CH₂Cl₂/toluene at 255 K. FT-IR (ν_{CO} , cm⁻¹): 2062.5 (s), 1991.6 (s) (CH₂Cl₂); (ν_{CO} , cm⁻¹): 2014 (s), 1946 (s) (CH₂Cl₂); (ν_{CO} , cm⁻¹): 2001 (s), 1938 (s) (solid KBr). **12a-¹³CO:** ¹H NMR (298 K, 300.13 MHz, CD₂Cl₂, ppm): δ 9.22 (s, 1H, ring-NCHN), 7.37 (d, 2H, ¹J_{H-H} = 1.5 Hz, ring-NCH-CHN), 4.05 (s, 6H, ring-NCH₃). ¹³C{¹H} NMR (298 K, 75.47 MHz, CD₂Cl₂, ppm): δ 183.3 (d, 2C, CO, ¹J_{CO-Rh} = 72.2 Hz), 136.3 (s, 1C, ring-NCHN), 123.6 (s, 2C, ring-NCHCHN), 37.2 (s, 2C, ring-NCH₃).

[RhI₂(CO)₂](EMIM) 13a: Dark green powder (Yield 88%). FT-IR (ν_{CO} , cm^{-1}): 2062.4 (s), 1991.5 (s) (CH_2Cl_2). **13a-¹³CO:** ¹H NMR (298 K, CD_2Cl_2 , 400.13 MHz, ppm): δ 9.20 (s, 1H, ring-NCHN), 7.43 (t, 1H, ¹ $J_{\text{H-H}} = 1.6$ Hz, ring-NCHCHN), 7.40 (t, 1H, ¹ $J_{\text{H-H}} = 1.6$ Hz, ring-NCHCHN), 4.38 (q, 2H, ¹ $J_{\text{H-H}} = 7.2$ Hz, NCH_2CH_3), 4.06 (s, 3H, NCH_3), 1.63 (t, 3H, ¹ $J_{\text{H-H}} = 7.6$ Hz, NCH_2CH_3). ¹³C{¹H} NMR (298 K, CD_2Cl_2 , 100.61 MHz, ppm): δ 183.3 (d, 2C, CO, ¹ $J_{\text{CO-Rh}} = 71.8$ Hz), 135.3 (s, 1C, ring-NCHN), 123.8 (s, 1C, ring-NCHCHN), 122.0 (s, 1C, ring-NCHCHN), 45.7 (s, 1C, NCH_2CH_3), 37.3 (s, 1C, NCH_3), 15.3 (s, 1C, NCH_2CH_3).

[RhI₂(CO)₂](PrMMIM) 14a: Dark brown-green powder (Yield 90%). FT-IR (ν_{CO} , cm^{-1}): 2062.0 (s), 1989.6 (s) (CH_2Cl_2); 2056.2 (s), 1984.4 (s) (CH_3I). **14a-¹³CO:** ¹H NMR (298 K, CD_2Cl_2 , 300.13 MHz, ppm): δ 7.34 (d, 1H, ¹ $J_{\text{H-H}} = 2.1$ Hz, ring-CH=CH-), 7.32 (d, 1H, ¹ $J_{\text{H-H}} = 2.4$ Hz, ring-CH=CH-), 4.11 (t, 2H, ¹ $J_{\text{H-H}} = 7.5$ Hz, $\text{NCH}_2\text{CH}_2\text{CH}_3$), 3.91 (s, 3H, NCH_3), 2.74 (s, 3H, CCH_3), 1.92 (m, 2H, ¹ $J_{\text{H-H}} = 7.5$ Hz, $\text{NCH}_2\text{CH}_2\text{CH}_3$), 1.04 (t, 3H, ¹ $J_{\text{H-H}} = 7.2$ Hz, $\text{NCH}_2\text{CH}_2\text{CH}_3$). ¹³C{¹H} NMR (298 K, CD_2Cl_2 , 100.61 MHz, ppm): δ 183.5 (d, 2C, CO, ¹ $J_{\text{CO-Rh}} = 72.1$ Hz), 143.7 (s, 1C, ring-NC(CH₃)=N-), 122.8 (s, 1C, ring-CH=CH-), 121.2 (s, 1C, ring-CH=CH-), 50.7 (s, 1C, $\text{CH}_3\text{CH}_2\text{CH}_2\text{N}$), 36.4 (s, 1C, NCH_3), 23.2 (s, 1C, $\text{CH}_3\text{CH}_2\text{CH}_2\text{N}$), 11.2 (s, 1C, -CH₃, ring-NC(CH₃)=N-), 10.8 (s, 1C, $\text{CH}_3\text{CH}_2\text{CH}_2\text{N}$).

[RhI₂(CO)₂](BMIM) 15a: Dark brown oil (Yield 87%). FT-IR (ν_{CO} , cm^{-1}): 2062.7 (s), 1991.8 (s) (CH_2Cl_2). **15a-¹³CO:** ¹H NMR (298 K, CD_2Cl_2 , 400.13 MHz, ppm): δ 9.20 (s, 1H, ring-NCHN), 7.42 (d, 2H, ¹ $J_{\text{H-H}} = 1.5$ Hz, ring-CH=CH), 4.30 (t, 2H, ¹ $J_{\text{H-H}} = 7.5$ Hz, 2H, $\text{NCH}_2\text{CH}_2\text{CH}_2\text{CH}_3$), 4.05 (s, 3H, NCH_3), 1.95 (m, 2H, ¹ $J_{\text{H-H}} = 6.0$ Hz, $\text{NCH}_2\text{CH}_2\text{CH}_2\text{CH}_3$), 1.43 (m, 2H, ¹ $J_{\text{H-H}} = 7.5$ Hz, $\text{NCH}_2\text{CH}_2\text{CH}_2\text{CH}_3$), 1.00 (t, 3H, ¹ $J_{\text{H-H}} = 7.2$ Hz, $\text{NCH}_2\text{CH}_2\text{CH}_2\text{CH}_3$). ¹³C{¹H} NMR (298 K, CD_2Cl_2 , 75.47 MHz, ppm): δ 183.3 (d, 2C, ¹ $J_{\text{CO-Rh}} = 72.5$ Hz, CO), 135.4 (s, 1C, ring-NCHN), 123.7 (s, 1C, ring-CH=CH-), 122.4 (s, 1C,

ring-CH=CH-), 50.2 (s, 1C, NCH₂CH₂CH₂CH₃), 37.3 (s, 1C, NCH₃), 32.0 (s, 1C, NCH₂CH₂CH₂CH₃), 19.5 (s, 1C, NCH₂CH₂CH₂CH₃), 13.3 (s, 1C, NCH₂CH₂CH₂CH₃).

[RhI₂(CO)₂](NMe₄) 16a: Dark brown powder (Yield 91%). FT-IR (ν_{CO} , cm⁻¹): 2062.4 (s), 1991.4 (s) (CH₂Cl₂); 2060.5 (s), 1990.1 (s) (CH₃OH); 2058.8 (s), 1987.5 (s) (CH₃I). **16a-¹³C**: ¹H NMR (298 K, 500.33 MHz, CD₂Cl₂, ppm): δ 3.39 (s, 12H, N(CH₃)₄). ¹³C{¹H} NMR (298 K, 125.82 MHz, CD₂Cl₂, ppm): δ 183.4 (d, 2C, ¹J_{CO-Rh} = 71.7 Hz, CO), 57.1 (s, 4C, N(CH₃)₄).

[RhI₂(CO)₂](NEt₄) 17a: Dark brown powder (Yield 90%). FT-IR (ν_{CO} , cm⁻¹): 2060.7 (s), 1988.8 (s) (CH₂Cl₂). **17a-¹³C**: ¹H NMR (298 K, 500.33 MHz, CD₂Cl₂, ppm): δ 3.31 (q, 8H, ³J_{H-H} = 7.5 Hz N(CH₂CH₃)₄), 1.36 (t, 12H, ³J_{H-H} = 7.5 Hz N(CH₂CH₃)₄). ¹³C{¹H} NMR (298 K, 125.82 MHz, CD₂Cl₂, ppm): δ 183.4 (d, 2C, ¹J_{CO-Rh} = 70.5 Hz, CO), 53.1 (s, 4C, N(CH₂CH₃)₄), 8.0 (s, 4C, N(CH₂CH₃)₄).

[RhI₂(CO)₂](PPN) 18a: Light yellow microcrystalline product (Yield 94%). Crystals ready for X-ray analysis were obtained in CH₂Cl₂/pentane at 255 K. FT-IR (ν_{CO} , cm⁻¹): 2058.0 (s), 1986.1 (s) (CH₂Cl₂); 2059.6 (s), 1989.2 (s) (CH₃OH); 2051.2 (s), 1979.2 (s) (CH₃I); 2058.4 (s), 1986.7 (s) (CH₃CN); 2055.9 (s), 1985.6 (s), 1956.1 (w) (solid KBr). **18a-¹³C**: ¹H NMR (298 K, 300.13 MHz, CD₂Cl₂, ppm): δ 7.71 (m, 6H, N(PPh₃)₂), 7.56 (m, 24H, N(PPh₃)₂). ¹³C{¹H} NMR (298 K, CD₂Cl₂, 75.47 MHz, ppm): δ 183.8 (d, 2C, ¹J_{CO-Rh} = 72.1 Hz, CO), 133.8 (s, 6C, N(PPh₃)₂), 132.2 (m, 12C, N(PPh₃)₂), 129.5 (m, 12C, N(PPh₃)₂), 127.8 (d, 3C, ¹J_{C-P} = 106.5 Hz, N(PPh₃)₂), 126.3 (d, 3C, ¹J_{C-P} = 106.5 Hz, N(PPh₃)₂). ¹³C{¹H}{³¹P} NMR (298 K, CD₂Cl₂, 75.47 MHz, ppm): δ 183.8 (d, 2C, ¹J_{CO-Rh} = 72.1 Hz, CO), 133.8 (s, 6C, N(PPh₃)₂), 132.2 (s, 12C, N(PPh₃)₂), 129.5 (s, 12C, N(PPh₃)₂), 127.1 (s, 6C, N(PPh₃)₂). ³¹P{¹H} NMR (298 K, CD₂Cl₂, 125.50 MHz, ppm): δ 21.07 (s, 2P, N(PPh₃)₂). ¹³C NMR (298 K, solid, 100.50 MHz, ppm): δ 182.6 (s, 2C, CO), 131.3 (m, 36C, N(PPh₃)₂).

[RhI₂(CO)₂](HNEt₃) 19a: Dark brown oil (Yield 86%). FT-IR (ν_{CO} , cm⁻¹): 2067.1 (s), 1997.3 (s) (CH₂Cl₂); 2059.7 (s), 1990.7 (s) (CH₃OH); 2062.4 (s), 1993.6 (s) (CH₃I). **19a-¹³C**O: ¹H NMR (298 K, 500.33 MHz, CD₂Cl₂, ppm): δ 7.40 (br s, 1H, HN(CH₂CH₃)₃), 3.35 (q, 6H, ³J_{H-H} = 7.5 Hz, HN(CH₂CH₃)₃), 1.46 (t, 9H, ³J_{H-H} = 7.5 Hz, HN(CH₂CH₃)₃). ¹³C{¹H} NMR (298 K, 125.82 MHz, CD₂Cl₂, ppm): δ 183.1 (d, 2C, ¹J_{CO-Rh} = 73.0 Hz, CO), 47.4 (s, 3C, HN(CH₂CH₃)₃), 9.1 (s, 3C, HN(CH₂CH₃)₃).

[RhI₂(CO)₂](H₂NEt₂) 20a: Dark brown oily-solid (Yield 88%). FT-IR (ν_{CO} , cm⁻¹): 2070.4 (s), 2003.5 (s) (CH₂Cl₂); 2060.1 (s), 1989.9 (s) (CH₃OH); 2065.8 (s), 2001.2 (s) (CH₃I). **20a-¹³C**O: ¹H NMR (298 K, 500.33 MHz, CD₂Cl₂, ppm): δ 6.95 (br s, 2H, H₂N(CH₂CH₃)₂), 3.37 (q, 4H, ³J_{H-H} = 7.5 Hz, H₂N(CH₂CH₃)₂), 1.57 (t, 6H, ³J_{H-H} = 7.5 Hz, H₂N(CH₂CH₃)₂). ¹³C{¹H} NMR (298 K, 125.82 MHz, CD₂Cl₂, ppm): δ 182.7 (d, 2C, ¹J_{CO-Rh} = 73.0 Hz, CO), 43.6 (s, 2C, H₂N(CH₂CH₃)₂), 11.6 (s, 2C, H₂N(CH₂CH₃)₂).

[RhI₂(CO)₂](HHPY) 21a: Brown-red powder (Yield 87%). FT-IR (ν_{CO} , cm⁻¹): 2071.9 (s), 2003.1 (s) (CH₂Cl₂). **21a-¹³C**O: ¹H NMR (298 K, 300.13 MHz, CD₂Cl₂, ppm): δ not detected (br s, 2H, ring-HN-NH), 8.02 (br s, 2H, ring-HN=CH-CH=CH), 6.74 (br s, 1H, ring-HN=CH-CH=CH). ¹³C{¹H} NMR (298 K, 75.47 MHz, CD₂Cl₂, ppm): δ 182.9 (d, 2C, ¹J_{CO-Rh} = 72.1 Hz, CO), 136.4 (br s, 2C, ring-HN=CH-CH=CH), 108.2 (s, 1C, ring-HN=CH-CH=CH).

[RhI₂(CO)₂](MHPY) 22a: Dark brown-red oil (Yield 87%). FT-IR (ν_{CO} , cm⁻¹): 2068.3 (s), 1999.1 (s) (CH₂Cl₂); 2073.2 (s), 1776.1 (s), 1754.6 (sh), 1743.9 (sh) (CH₃I).

[RhI₂(CO)₂](MMPY) 23a: Dark brown powder (Yield 91%). FT-IR (ν_{CO} , cm⁻¹): 2062.4 (s), 1990.5 (s) (CH₂Cl₂). **23a-¹³C**O: ¹H NMR (298 K, 300.13 MHz, CD₂Cl₂, ppm): δ 8.20 (d, 2H, ³J_{H-H} = 3.0 Hz, ring-CH₃N=CH-CH=CH), 6.81 (t, 1H, ³J_{H-H} = 3.0 Hz, ring-CH₃N=CH-CH=CH), 4.31 (s, 6H, ring-N(CH₃)-N(CH₃)). ¹³C{¹H} NMR (298 K, 75.47 MHz, CD₂Cl₂,

ppm): δ 183.3 (d, 2C, $^1J_{\text{CO-Rh}} = 71.7$ Hz, CO), 138.1 (s, 2C, ring-CH₃N=CH-CH=CH), 108.0 (s, 1C, ring-CH₃N=CH-CH=CH), 38.6 (s, 2C, ring-N(CH₃)-N(CH₃)).

[RhI₂(CO)₂](MePy) 24a: Yellow microcrystalline product (Yield 93%). FT-IR (ν_{CO} , cm⁻¹): 2062.3 (s), 1990.9 (s) (CH₂Cl₂). **24a-¹³CO:** ¹H NMR (298 K, 500.33 MHz, CD₂Cl₂, ppm): δ 8.91 (d, 4H, ring-CH-N-CH), 8.57 (t, 2H, ring-CH=CH-N=CH-CH), 8.17 (t, 1H, ring-CH=CH-CH=CH-CH), 4.57 (s, 3H, N-CH₃). ¹³C{¹H} NMR (298 K, 125.82 MHz, CD₂Cl₂, ppm): δ 183.3 (d, 2C, $^1J_{\text{CO-Rh}} = 71.7$ Hz, CO), 145.7 (s, 2C, ring-CH-N-CH), 145.0 (s, 2C, ring-CH=CH-N=CH-CH), 128.9 (s, 1C, ring-CH=CH-CH=CH-CH), 49.8 (s, 1C, N-CH₃).

[RhI₂(CO)₂](SEt₂Me) 25a: Brownish oily-solid (Yield 85%). FT-IR (ν_{CO} , cm⁻¹): 2063.1 (s), 1992.1 (s) (CH₂Cl₂). **25a-¹³CO:** ¹H NMR (298 K, 300.13 MHz, CD₂Cl₂, ppm): δ 3.60 (q, 4H, $^3J_{\text{H-H}} = 7.4$ Hz, CH₃S(CH₂CH₃)₂), 3.08 (s, 3H, CH₃S(CH₂CH₃)₂), 1.56 (t, 6H, $^3J_{\text{H-H}} = 7.5$ Hz, CH₃S(CH₂CH₃)₂). ¹³C{¹H} NMR (298 K, 75.47 MHz, CD₂Cl₂, ppm): δ 183.3 (d, 2C, $^1J_{\text{CO-Rh}} = 72.1$ Hz, CO), 35.8 (s, 2C, CH₃S(CH₂CH₃)₂), 22.3 (s, 1C, CH₃S(CH₂CH₃)₂), 9.2 (s, 2C, CH₃S(CH₂CH₃)₂).

[RhI₂(CO)₂](H) 26a: (*in situ*) FT-IR (ν_{CO} , cm⁻¹): 2065.6 (s), 1995.9 (s) (CH₂Cl₂); 2059.3 (s), 1989.7 (s) (CH₃OH).

[RhI₂(CO)₂](Li) 27a: Dark brown oil (Yield 86%). FT-IR (ν_{CO} , cm⁻¹): 2068.7 (s), 1999.3 (s) (CH₂Cl₂); 2061.2 (s), 1990.2 (s) (CH₃OH). **27a-¹³CO:** ¹³C{¹H} NMR (298 K, 75.47 MHz, CD₂Cl₂, ppm): δ 182.4 (d, 2C, $^1J_{\text{CO-Rh}} = 73.0$ Hz, CO). ⁷Li NMR (298 K, 194.45 MHz, CD₂Cl₂, ppm): δ -0.41 (s, 1Li, Li⁺).

V-2-8 Synthesis of anionic dimeric rhodium(III) ammonium/sulfonium/lithium salt complexes

To a solution of MeI (12 mL) was added *cis*-[C][RhI₂(CO)₂] **11a-12a**, **14a-20a**, **23a** (100 mg) at room temperature. The solution was allowed to react at RT under vigorous stirring for 12 hours (in order to make sure that the oxidative addition was complete). During this time, all solutions turned dark red. After removal of MeI excess under vacuum, the compounds **11b-12b**, **14b-20b**, **23b** obtained were washed with pentane (10 mL) or ether (10 mL), dried under vacuum and stored under argon at 255 K prior to use.

[Rh(μ -I)I₂(COCH₃)(CO)]₂(MHIM)₂ **11b: Dark brown oil (Yield 86%). ¹H NMR (298 K, 300.13 MHz, CD₂Cl₂, ppm): δ 13.27 (br, 2H, ring-NH), 8.81 (s, 2H, ring-NCHN), 7.54 (br, 2H, ring-H₃C-NCH=CHNH), 7.38 (br t, 2H, ³J_{H-H} = 1.5 Hz, ring-H₃CNCH=CHNH), 4.06 (s, 6H, ring-N(CH₃)CH=CHNH), 3.13 (br, 6H, CH₃CO). ¹³C{¹H} NMR (298 K, 75.47 MHz, CD₂Cl₂, ppm): δ 210.9 (m, 2C, COCH₃), 183.6 (d, 1C, ¹J_{CO-Rh} = 57.3 Hz, CO), 182.0 (d, 1C, ¹J_{CO-Rh} = 69.9 Hz, CO), 134.9 (s, 2C, ring-NCHN), 123.0 (s, 2C, ring-NCHCHN), 120.5 (s, 2C, ring-NCHCHN), 49.7 (br s, 1C, COCH₃), 47.2 (br s, 1C, COCH₃), 36.8 (s, 2C, NCH₃).**

[Rh(μ -I)I₂(COCH₃)(CO)]₂(MMIM)₂ **12b: Dark brown powder (Yield 88%). ¹H NMR (298 K, 300.13 MHz, CD₂Cl₂, ppm): δ 9.08 (s, 2H, ring-NCHN), 7.36 (d, 4H, ³J_{H-H} = 1.8 Hz, ring-NCHCHN), 4.05 (d, 12H, NCH₃), 3.13 (br s, 6H, COCH₃). ¹³C{¹H} NMR (298 K, 75.47 MHz, CD₂Cl₂, ppm): δ 214.6 (m, 2C, COCH₃), 183.3 (d, 2C, ¹J_{CO-Rh} = 71.9 Hz, CO), 136.4 (s, 2C, ring-NCHN), 123.6 (s, 4C, ring-NCHCHN), n. d. (2C, COCH₃), 37.1 (s, 2C, NCH₃).**

[Rh(μ -I)I₂(COCH₃)(CO)]₂(PrMMIM)₂ **14b: Dark brown powder (Yield 89%). FT-IR (ν_{CO} , cm⁻¹): 2079.5 (s), 1737.1 (m, sh), 1720.4 (m, br) (CH₂Cl₂); 2078.6 (s), 2067.6 (sh), 1742.5 (m, br), 1736.5 (sh), 1727.7 (m, br) (CH₃OH); 2073.2 (s), 2063.5 (sh), 1737.7 (m, sh), 1719.6 (m, br) (CH₃I). ¹H NMR (298 K, CD₂Cl₂, 400.13 MHz, ppm): δ 7.47 (d, 2H, ³J_{H-H} = 2.0 Hz, ring-**

$CH=CH-$), 7.42 (d, 2H, $^3J_{H-H} = 2.4$ Hz, ring- $CH=CH-$), 4.14 (t, 4H, $^3J_{H-H} = 7.6$ Hz, ring- $NCH_2CH_2CH_3$), 3.93 (s, 6H, NCH_3), 3.09 (s, 6H, $COCH_3$), 2.75 (s, 6H, ring- CCH_3), 1.89 (m, 4H, ring- $NCH_2CH_2CH_3$), 0.99 (t, 6H, $^3J_{H-H} = 7.6$ Hz, $NCH_2CH_2CH_3$).

[Rh(μ -I) $_2$ (COCH $_3$)(CO)] $_2$ (BMIM) $_2$ 15b: Dark brown oil (Yield 84%). FT-IR (ν_{CO} , cm^{-1}): 2077.0 (s), 1717.1 (m, br) (CD_2Cl_2); 2076.4 (sh), 2064.3 (s), 1722.0 (m, br) (CH_2Cl_2). 1H NMR (298 K, CD_2Cl_2 , 400.13 MHz, ppm): δ 9.24 (s, 2H, ring- $CH=$, $NCHN$), 7.46 (d, 2H, $^3J_{H-H} = 1.6$ Hz, ring- $CH=CH-$), 7.44 (d, 2H, $^3J_{H-H} = 1.6$ Hz, ring- $CH=CH-$), 4.34 (t, 4H, $^3J_{H-H} = 7.6$ Hz, $NCH_2CH_2CH_2CH_3$), 4.09 (s, 6H, NCH_3), 3.14 (br s, 6H, $COCH_3$), 1.93 (m, 4H, $^3J_{H-H} = 7.6$ Hz, $NCH_2CH_2CH_2CH_3$), 1.42 (m, 4H, $^3J_{H-H} = 7.6$ Hz, $NCH_2CH_2CH_2CH_3$), 0.99 (t, 3H, $^3J_{H-H} = 7.2$ Hz, $NCH_2CH_2CH_2CH_3$). $^{13}C\{^1H\}$ NMR (298 K, CD_2Cl_2 , 100.61 MHz, ppm): δ 210.8 (br s, $COCH_3$), 185-181 (CO, main d at 182.2, $^1J_{CO-Rh} = 68.5$ Hz), 135.4 (s, 2C, ring- $NCHN$), 123.8 (s, 2C, ring- $CH=CH-$), 122.4 (s, 2C, ring- $CH=CH-$), 50.1 (s, 2C, $NCH_2CH_2CH_2CH_3$), 48.7 (br s, 2C, $COCH_3$), 37.3 (s, 2C, NCH_3), 32.1 (s, 2C, $NCH_2CH_2CH_2CH_3$), 19.5 (s, 2C, $NCH_2CH_2CH_2CH_3$), 13.4 (s, 2C, $NCH_2CH_2CH_2CH_3$).

[Rh(μ -I) $_2$ (COCH $_3$)(CO)] $_2$ (NMe $_4$) $_2$ 16b: Dark brown oil (Yield 88%). FT-IR (ν_{CO} , cm^{-1}): 2070.1 (s), 1719.6 (m, br) (CH_2Cl_2); 2062.3 (s), 2044.9 (sh), 1734.5 (m, br), 1719.0 (sh) (CH_3OH); 2076.6 (s), 2065.8 (sh), 1736.0 (sh), 1720.2 (m, br) (CH_3I). 1H NMR (298 K, CD_2Cl_2 , 400.13 MHz, ppm): δ 3.39 (s, 24H, $N(CH_3)_4$), 3.15 (br s, 3H, $COCH_3$), 3.05 (br s, 3H, $COCH_3$). $^{13}C\{^1H\}$ NMR (298 K, 100.62 MHz, CD_2Cl_2 , ppm): δ n. d. (d, 2C, $COCH_3$), 182.1 (d, 2C, $^1J_{CO-Rh} = 71.0$ Hz, CO), 57.1 (s, 8C, $N(CH_3)_4$) 47.3 (br s, 1C, $COCH_3$), 46.4 (br s, 1C, $COCH_3$).

[Rh(μ -I) $_2$ (COCH $_3$)(CO)] $_2$ (NEt $_4$) $_2$ 17b: Dark brown oil (Yield 84%). FT-IR (ν_{CO} , cm^{-1}): 2078.1 (sh), 2049.3 (s), 1739.6 (m, br), 1736.4 (sh) (CH_2Cl_2); 2074.5 (s), 2059.7 (sh), 1738.0 (m, br), 1728.8 (w, br) (CH_3I). 1H NMR (298 K, CD_2Cl_2 , 300.13 MHz, ppm): δ 3.31 (q, 16H,

$^3J_{\text{H-H}} = 7.2$ Hz $\text{N}(\text{CH}_2\text{CH}_3)_4$, 3.08 (br s, 3H, COCH_3), 3.01 (br s, 3H, COCH_3), 1.38 (t, 24H, $^3J_{\text{H-H}} = 7.2$ Hz $\text{N}(\text{CH}_2\text{CH}_3)_4$). $^{13}\text{C}\{^1\text{H}\}$ NMR (298 K, 75.47 MHz, CD_2Cl_2 , ppm): δ n. d. (d, 2C, COCH_3), n. d. (d, 2C, CO), 52.7 (s, 8C, $\text{N}(\text{CH}_2\text{CH}_3)_4$), 46.6 (br s, 2C, COCH_3), 7.5 (s, 8C, $\text{N}(\text{CH}_2\text{CH}_3)_4$).

[Rh(μ -I)I₂(COCH₃)(CO)]₂(PPN)₂ 18b: Brown-red powder (Yield 90%). FT-IR (ν_{CO} , cm^{-1}): 2074.8 (sh), 2063.7 (s), 1736.5 (m, br), 1714.8 (sh) (CH_2Cl_2); 2077.3 (sh), 2063.9 (s), 1742.3 (m, br), 1726.4 (m, br) (CH_3OH); 2071.6 (s), 2057.3 (sh), 1735.7 (m, br), 1715.3 (w, br) (CH_3I). **18b- ^{13}C** : ^1H NMR (298 K, CD_2Cl_2 , 300.13 MHz, ppm): δ selected 3.15 (s, COCH_3), 3.13 (s, COCH_3). $^{13}\text{C}\{^1\text{H}\}$ NMR (298K, CD_2Cl_2 , 75.47 MHz, ppm): δ selected 211.3 (d, $^1J_{\text{COMe-Rh}} = 20.2$ Hz, COCH_3), 204.1 (d, $^1J_{\text{COMe-Rh}} = 20.5$ Hz, COCH_3), 182.4 (d, $^1J_{\text{CO-Rh}} = 71.0$ Hz, CO), 182.0 (d, $^1J_{\text{CO-Rh}} = 66.7$ Hz, CO), 49.7 (br s, 1C, COCH_3), 46.5 (br s, 1C, COCH_3). Anal. Calcd. for $\text{C}_{76}\text{H}_{66}\text{I}_6\text{N}_2\text{O}_4\text{P}_4\text{Rh}_2$: C 42.81; H 3.02; N 1.28. Found: C 42.62; H 2.92; N 1.33.

[Rh(μ -I)I₂(COCH₃)(CO)]₂(HNEt₃)₂ 19b: Dark brown oil (Yield 83%). FT-IR (ν_{CO} , cm^{-1}): 2075.3 (s), 1738.7 (sh), 1722.4 (sh), 1717.9 (m, br) (CH_2Cl_2); 2078.0 (s), 2066.8 (sh), 1742.5 (m, br), 1736.4 (sh), 1727.0 (m, br) (CH_3OH); 2077.2 (sh), 2066.6 (s), 1737.0 (m, br), 1727.0 (sh) (CH_3I).

[Rh(μ -I)I₂(COCH₃)(CO)]₂(H₂NEt₂)₂ 20b: Dark brown oil (Yield 85%). FT-IR (ν_{CO} , cm^{-1}): 2079.1 (sh), 2068.3 (s), 1739.9 (m, br), 1733.1 (sh) (CH_3I).

[Rh(μ -I)I₂(COCH₃)(CO)]₂(MMPY)₂ 23b: Brown solid (Yield 87%). FT-IR (ν_{CO} , cm^{-1}): 2065.8 (s), 1738.4 (sh), 1719.9 (m, br) (CH_2Cl_2). ^1H NMR (298 K, CD_2Cl_2 , 400.13 MHz, ppm): δ 8.25 (d, 4H, $^3J_{\text{H-H}} = 3.2$ Hz, ring- $\text{CH}_3\text{N}=\text{CH}-\text{CH}=\text{CH}$), 6.78 (t, 2H, $^3J_{\text{H-H}} = 3.2$ Hz, ring- $\text{CH}_3\text{N}=\text{CH}-\text{CH}=\text{CH}$), 4.28 (s, 12H, ring- $\text{N}(\text{CH}_3)-\text{N}(\text{CH}_3)$), 3.59 (s, 3H, COCH_3), 3.13 (br

s, 3H, COCH₃). ¹³C{¹H} NMR (298 K, 100.62 MHz, CD₂Cl₂, ppm): δ n. d. (d, 2C, CO), n. d. (d, 2C, CO), 138.0 (s, 4C, ring-CH₃N=CH-CH=CH), 107.8 (s, 2C, ring-CH₃N=CH-CH=CH), 49.5 (br s, 2C, COCH₃), 37.5 (s, 4C, ring-N(CH₃)-N(CH₃)).

V-2-9 Catalytic batch experiments

Neutral *cis*-rhodium(I) complexes **4** bearing N-containing ligands were synthesized, isolated and fully characterized before batch tested under catalytic working conditions. Experiments were all carried out in the following catalytic medium: Rh metal: 0.1 wt % (1000 ppm), [H₂O]: 5 wt %, [AcOCH₃]: 35 wt %, [CH₃I]: 10 wt % and [AcOH]: balance. For each batch run, the total reaction solution volume was of ~ 60 mL (The catalytic solution total weight was 60 g for each batch). The [RhI(CO)₂(L)] complex **4** was loaded together with acetic acid/water and flushed (x5) with CO in a sealed 100 mL hastelloy[®] B2 reactor (Figure 1). The reactor was heated to 190 °C and CO pressurized to 10 bar. Methyl iodide and methyl acetate were both separately loaded in a hastelloy[®] B2 50 mL liquid vessel which was over-pressurized and fed to the reactor under vigorous stirring (1200 rpm). At this very moment, stopwatch turned on, the reaction total pressure was adjusted to 30 bar and fed continuously. CO pressure decrease due to CO consumption for carbonylation reaction was measured from the CO reservoir (110 mL/150 bar) every minute during a total 10 minute batch run. Carbonylation rates were calculated according to gas-chromatography analyses by determination of acetic acid, methyl acetate, water and CH₃I concentrations at the end of each run.



Figure 1. Hastelloy[®] B2 100 mL reactor for batch experiments (TOP INDUSTRIE).

V-2-10 High pressure variable temperature NMR experiments

All HP-VT-NMR experiments were carried out at the EPFL in Lausanne Switzerland supervised. These experiments were supervised by Professor Gabor Laurency. The reactions were carried out in high pressure sapphire 10 mm NMR tubes (pressure < 120 bar) and were followed by NMR spectroscopy (Figure 2). ^1H and $^{13}\text{C}\{^1\text{H}\}$ NMR spectra were recorded on a Bruker DRX 400 NMR spectrometer. 3-(trimethylsilyl)-1-propane sulfonic acid sodium salt (TSPSA) was used as reference for the ^1H (400.13 MHz) and $^{13}\text{C}\{^1\text{H}\}$ (100.62 MHz) NMR measurements. The spectra were fitted with WINNMR and NMRICMA/MATLAB programs (non-linear least square fit to determine the spectral parameters). The samples were pressurized with CO up to 100 bar in 10 mm high pressure sapphire NMR tubes. The tube was thermostated to the desired temperature (< 100 °C) in the NMR spectrometer and the reactions were followed by multinuclear NMR techniques.

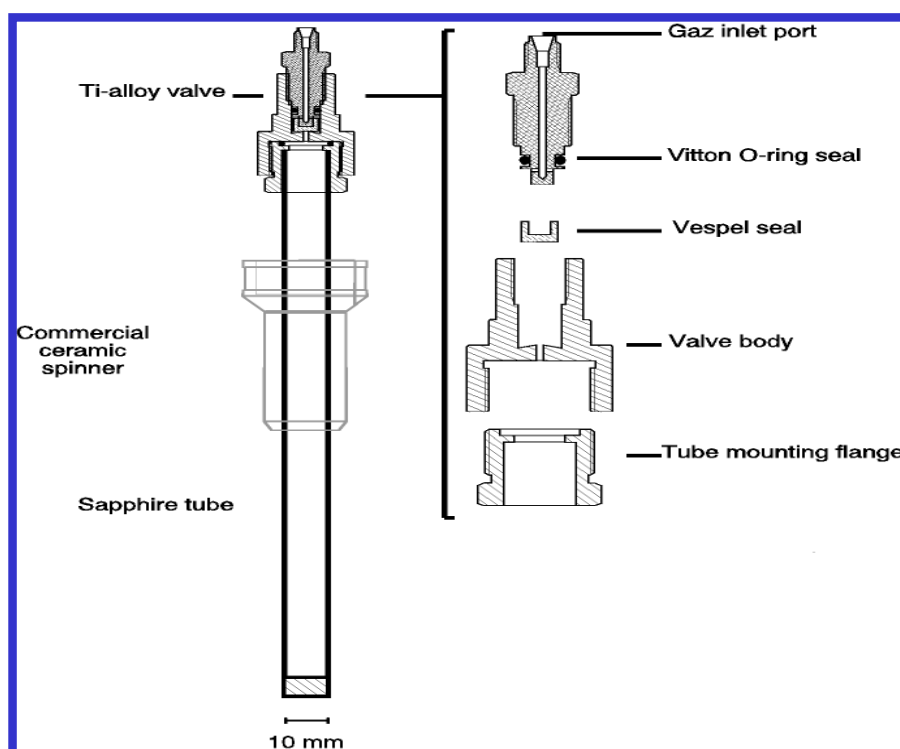


Figure 2. HP-NMR sapphire tube components.

Experiment 1 details: In a 10 mm sapphire NMR tube the total volume for the reaction medium was limited to the range ~ 2-3 mL (~ 2-3 g) in order to obtain a good resolution. To further gain in resolution reactant quantities were increased x3 in comparison to Celanese AO process quantities and the total volume was fixed to 2 mL: 0.3 wt % of Rh catalyst $^{13}\text{CO-4d}$ (MW: 367.9-369.9 $\text{g}\cdot\text{mol}^{-1}$) was introduced (0.022 g), 30 wt % of CH_3I (0.60 g) and $\text{AcOH-}d_4$ to complete as the balance (1.40 g). Further on was added 9 wt % of pure H_2O (~ 0.18 mL).

Experiment 2 details: The total volume was fixed to 3 mL: 0.153 wt % of Rh catalyst $^{13}\text{CO-4d}$ (MW: 367.9-369.9 $\text{g}\cdot\text{mol}^{-1}$) was introduced (0.005 g), 10 wt % of CH_3I (0.51 g), 1 wt % of HI (57 % HI in water solution) (0.087 g), 35 wt % of AcOMe (1.80 g), 3 wt % of pure H_2O (0.15 g – 0.04 g provided by HI solution = 0.11 g) and $\text{AcOH-}d_4$ to complete as the balance (0.75 g).

V-2-11 Conductivity measurements

The conductivity was determined with a conductivity cell (LTA 1, WTW, cell constant $K = 1$, platinized platinum electrode) using alternating voltage. The apparatus was calibrated with 0.01 m KCl standard solution ($\kappa = 1.413 \text{ mS/cm}$ at 298 K). All samples were kept in a thermostat prior to and during the measurement to guarantee isothermal conditions.

V-2-12 Ionic chromatography

Analyses were performed on a Metrohm apparatus with a cationic column (metrosep C4 250 / 4.0) packed of silica gel with carboxyl groups. Samples were prefiltered ($0.45 \mu\text{m}$). The eluent was prepared with tartaric acid (15 mmol.L^{-1}), acetone (10 %) and water. The pressure fed through the column was of 15 MPa with a recommended flow of 0.9 mL.min^{-1} . The retention time range for the salts used was 5 to 30 minutes. The chromatography control and data acquisition system was performed with IC net 2.3 software.

V-2-13 X-ray structure determination (for complex 12a)

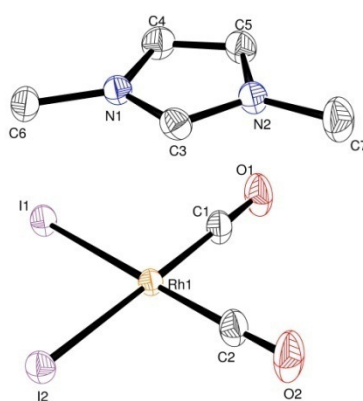


Figure 3. Single crystal X-ray structure of **12a**.

Table 1. Bond lengths (Å) and angles (°) for **12a**.

N(1)-C(3) 1.318(3), N(1)-C(4) 1.367(3), N(1)-C(6) 1.463(3), N(2)-C(3) 1.320(2), N(2)-C(5) 1.364(3), N(2)-C(7) 1.471(3), C(3)-H(3) 0.9500, C(4)-C(5) 1.352(3), C(4)-H(4) 0.9500, C(5)-H(5) 0.9500, C(6)-H(6A) 0.9800, C(6)-H(6B) 0.9800, C(6)-H(6C) 0.9800, C(7)-H(7A) 0.9800, C(7)-H(7B) 0.9800, C(7)-H(7C) 0.9800, I(1)-Rh(1) 2.6586(2), I(2)-Rh(1) 2.6560(2), Rh(1)-C(2) 1.837(2), Rh(1)-C(1) 1.842(2), O(1)-C(1) 1.135(3), O(2)-C(2) 1.129(3)

C(3)-N(1)-C(4) 108.43(18), C(3)-N(1)-C(6) 124.7(2), C(4)-N(1)-C(6) 126.9(2), C(3)-N(2)-C(5) 108.73(18), C(3)-N(2)-C(7) 124.5(2), C(5)-N(2)-C(7) 126.7(2), N(1)-C(3)-N(2) 108.98(18), N(1)-C(3)-H(3) 125.5, N(2)-C(3)-H(3) 125.5, C(5)-C(4)-N(1) 107.11(19), C(5)-C(4)-H(4) 126.4, N(1)-C(4)-H(4) 126.4, C(4)-C(5)-N(2) 106.76(19), C(4)-C(5)-H(5) 126.6, N(2)-C(5)-H(5) 126.6, N(1)-C(6)-H(6A) 109.5, N(1)-C(6)-H(6B) 109.5, H(6A)-C(6)-H(6B) 109.5, N(1)-C(6)-H(6C) 109.5, H(6A)-C(6)-H(6C) 109.5, H(6B)-C(6)-H(6C) 109.5, N(2)-C(7)-H(7A) 109.5, N(2)-C(7)-H(7B) 109.5, H(7A)-C(7)-H(7B) 109.5, N(2)-C(7)-H(7C) 109.5, H(7A)-C(7)-H(7C) 109.5, H(7B)-C(7)-H(7C) 109.5, C(2)-Rh(1)-C(1) 92.92(10), C(2)-Rh(1)-I(2) 87.58(7), C(1)-Rh(1)-I(2) 179.15(8), C(2)-Rh(1)-I(1) 178.47(7), C(1)-Rh(1)-I(1) 85.61(7), I(2)-Rh(1)-I(1) 93.891(7), O(1)-C(1)-Rh(1) 179.2(3), O(2)-C(2)-Rh(1) 178.6(2).

Crystal data and details of collection and refinement for **12a**:

Empirical formula: C₅ H₉ N₂, C₂ I₂ O₂ Rh

Formula weight: 509.87

Temperature: 180(2) K

Wavelength: 0.71073 Å

Crystal system, space group: monoclinic, P 21/c

Unit cell dimensions: a = 7.5281(3) Å α = 90 deg.
 b = 14.3169(6) Å β = 117.214(2) deg.
 c = 14.2718(5) Å γ = 90 deg.

Volume: 1367.93(9) Å³

Z, Calculated density: 4, 2.476 mg.m⁻³

Absorption coefficient: 5.743 mm⁻¹

F(000): 928

Crystal size: 0.22 x 0.2 x 0.1 mm

θ range for data collection: 2.14 to 30.64 deg.

Limiting indices: -10 ≤ h ≤ 7, -19 ≤ k ≤ 20, -19 ≤ l ≤ 20

Reflections collected / unique: 39265 / 4213 [R(int) = 0.0203]

Completeness to θ : 30.64 99.8 %

Refinement method: Full-matrix least-squares on F^2

Data / restraints / parameters: 4213 / 0 / 129

Goodness-of-fit on F^2 : 1.092

Final R indices: [$I > 2\sigma(I)$]: $R_1 = 0.0166$, $wR_2 = 0.0419$

R indices (all data): $R_1 = 0.0192$, $wR_2 = 0.0432$

Largest diff. peak and hole: 0.549 and -1.079 e. \AA^{-3}

V-3 Experimental section: Chapter IV

V-3-1 Instrumentation and materials

FT-IR spectra were collected on a Perkin-Elmer Spectrum One FT spectrophotometer with a 0.1 mm cell equipped with CaF₂ windows. All NMR spectra data were recorded on Bruker DRX 300 or Avance 300-500 spectrometers with TMS as internal reference for ¹H and ¹³C, 85% phosphoric acid as external reference for ³¹P. Chemical shifts are reported in ppm and coupling constants (*J*) are given in Hertz. Mass spectra analyses were performed on a NERMAC R10-10 (FAB negative mode, gas: Xe). The major *m/z* peak was reported with the intensity as a percentage of the base peak in brackets. Elemental analyses were measured with a precision superior to 0.3% on a Perkin-Elmer 2400 Series II CHNS/O Elemental Analyzer. X-ray structures were determined on an Oxford Diffraction Xcalibur CCd diffractometer.

V-3-2 Synthesis

All experiments were carried out under argon using Schlenk techniques or glovebox. Solvents were obtained from a Solvent Purification System (MB SPS-800). CD₂Cl₂ was dried using activated molecular sieves. RhCl₃.x H₂O salt was supplied from Johnson Matthey, RhI₃.xH₂O from the Celanese Plant at Pardies. Bis-triphenylphosphoranylidene chloride (PPNCl) was purchased from Aldrich and re-crystallized from MeOH/ter-butyl methyl ether before used.

[PPN] *cis*-[RhI₂(CO)₂] 18a¹³: RhI₃.xH₂O (3 g) was added to a mixture of DMF (400 mL) and water (2.5 mL). The resulting suspension was stirred and heated at 160 °C under CO bubbling until the solution became pale yellow. The solution was cooled at room temperature and 1 eq.

(13) Serp. P.; Hernandez, M.; Richard, B.; Kalck, P. *Eur. J. Inorg. Chem.* **2001**, 2327.

of bis-triphenylphosphoranylidene chloride [PPN]Cl, 3.34 g) was added and then water was slowly added at 0 °C in order to precipitate [PPN][RhI₂(CO)₂] as a yellow solid. The product was filtered off, washed several times with cold water and dried under vacuum. Yield 70 %. IR (CH₂Cl₂, cm⁻¹): ν_{CO} = 2057.8(vs); 1987.1(vs). ¹³C{¹H} NMR (298 K, CD₂Cl₂, 75.468 MHz, ppm): δ selected 183.3 (d, ¹J_{CO-Rh} = 71.0 Hz, CO-[Rh]). MS (FAB⁻, MNBA) *m/z*: (%) = 413 (100%) [M]⁺. Anal. Calcd. for C₃₈H₃₀I₂NO₂P₂Rh: C 47.98; H 3.18; N 1.47. Found: C 47.93; H 3.07; N 1.51.

***cis*-[RhI₂(¹³CO)₂][PPN] ¹³CO-18a**: In a 200 ml flask, a solution of [PPN][RhI₂(CO)₂] (1 g) in 20 ml CH₂Cl₂ was stirred for 12 hours under 1 atm. of ¹³CO. The solvent was removed under vacuum giving quantitatively the labelled *cis*-[RhI₂(¹³CO)₂][PPN] **1a-¹³CO**. IR (CH₂Cl₂, cm⁻¹): ν(¹³CO) = 2010.0(vs); 1942.5(vs).

***mer,trans*-[RhI₃(COMe)(CO)₂][PPN] 4a**: Carbon monoxide was bubbled through a solution of [RhI₃(COMe)(CO)₂][PPN]₂ (1.0 g) in dichloromethane (10 mL) for 5 minutes at room temperature. The product was crystallized by addition of *n*-hexane under CO atmosphere. Yield 65 % (0.70 g). IR (CH₂Cl₂, cm⁻¹): ν_{CO} = 2140.4(w), 2083.5(vs); ν_{COMe} = 1704.2(s). NMR (298 K, CD₂Cl₂, 300.13 MHz, ppm): δ selected 2.97 (s, COCH₃-[Rh]). ¹³C{¹H} NMR (298 K, CD₂Cl₂, 75.468 MHz, ppm): δ selected 216.85 (d, ¹J_{COMe-Rh} = 18.2 Hz, COMe-[Rh]), 177.70 (d, ¹J_{CO-Rh} = 54.1 Hz, CO-[Rh]).

V-3-3 High pressure NMR analyses:

All high-pressure NMR experiments were performed on a Bruker DRX-400 spectrometer. The NMR sapphire tube (10 mm e.d.) was charged with *cis*-[PPN][RhI₂(¹³CO)₂] ¹³CO-18a, reactants (AcOMe, MeI, H₂O) and AcOH-*d*₄ as solvent. Once the tube was sealed,

the medium was flushed several times with ^{12}CO then pressurized at the desired pressure with ^{13}CO .

V-3-4 *Kinetic experiments*

The kinetic experiments of reductive elimination reactions were monitored by using IR spectroscopy in a solution cell (0.1 mm path length). Reductive elimination reactions under CO pressure were performed in a glassware reactor (TOP INDUSTRIE) at 298 K. $[\text{PPN}]_2[\text{RhI}_3(\text{COMe})(\text{CO})]_2$ (0.84 g) was dissolved in dichloromethane (45 mL) and the reactor was filled with CO gas up to desired pressures. An aliquot of the reaction mixture was transferred by a syringe into the IR cell. The kinetic measurements were monitored by the decay of ν_{CO} band of complex $[\text{PPN}][\text{RhI}_3(\text{COCH}_3)(\text{CO})_2]$ at 2083.5 cm^{-1} and the growth of the ν_{CO} band of complex $[\text{PPN}][\text{RhI}_2(\text{CO})_2]$ at 2058 cm^{-1} . Spectra were taken at a regular time intervals.

V-3-5 *Conductivity measurements*

Conductivity measurements of water/acetic acid mixture were carried out with a pH/conductometer Consort model C832. The cell constant was determined by using three solutions of KCl for which the specific conductivity was readably known. The calculated cell constant was 1.254 cm^{-1} . Deionized or distilled water was used in all preparations. The concentration of water in solution was successively increased by a stepwise addition of 0.10 or 1 mL of pure water to 50.0 mL of glacial acetic acid solvent being initially placed in a cell for conductivity measurements. After each addition, the solution was stirred to ensure the homogeneous mixing, and then was subjected to the conductivity measurement. The conductivity cell was immersed in a water bath (Fisher Bioblock scientific circulation bath

model 9005-BB) of which the temperature was kept constant (within ± 0.1 °C of a desired temperature using a standard internal controller).

V-3-6 DFT calculations (computational details)

Rhodium was treated with a Stuttgart–Dresden pseudo potential in combination with the appropriate basis sets.^{14,15} The basis sets were augmented by a set of polarization function (f for Rh and d for Si).¹⁶ Carbon, oxygen and hydrogen atoms were described with a 6–31G(d) polarized double- ζ basis set.¹⁷ Calculations were carried out at the DFT level of theory using the hybrid functional B3PW91.^{18,19} Geometry optimizations were carried out without any symmetry restrictions and the nature of the extremes (minima) was verified with analytical frequency calculations. For all transition states, the intrinsic reaction coordinate was followed to verify the direct connection between the transition state and the adducts. All these computations were performed with the Gaussian 03²⁰ suite of programs. Gibbs free energies were obtained at 298.15 K within the harmonic approximation.

(14) Andrae, D.; Haussermann, U.; Dolg, M.; Stoll, H.; Preuss, H. *Theor. Chim. Acta* **1990**, 77, 123.

(15) Moritz, A.; Cao, X.; Dolg, M. *Theor. Chem. Acc.* **2007**, 118, 845.

(16) Ehlers, A. W.; Bohme, M.; Dapprich, S.; Gobbi, A.; Hollwarth, A.; Jonas, V.; Kohler, K. F.; Stegmann, R.; Veldkamp, A.; Frenking, G. *Chem. Phys. Lett.* **1993**, 208, 111.

(17) Hehre, W. J.; Ditchfie, R.; Pople, J. A. *J. Chem. Phys.* **1972**, 56, 2257. (e) Becke, A. D. *J. Chem. Phys.* **1993**, 98, 5648.

(18) Becke, A. D. *J. Chem. Phys.* **1993**, 98, 5648.

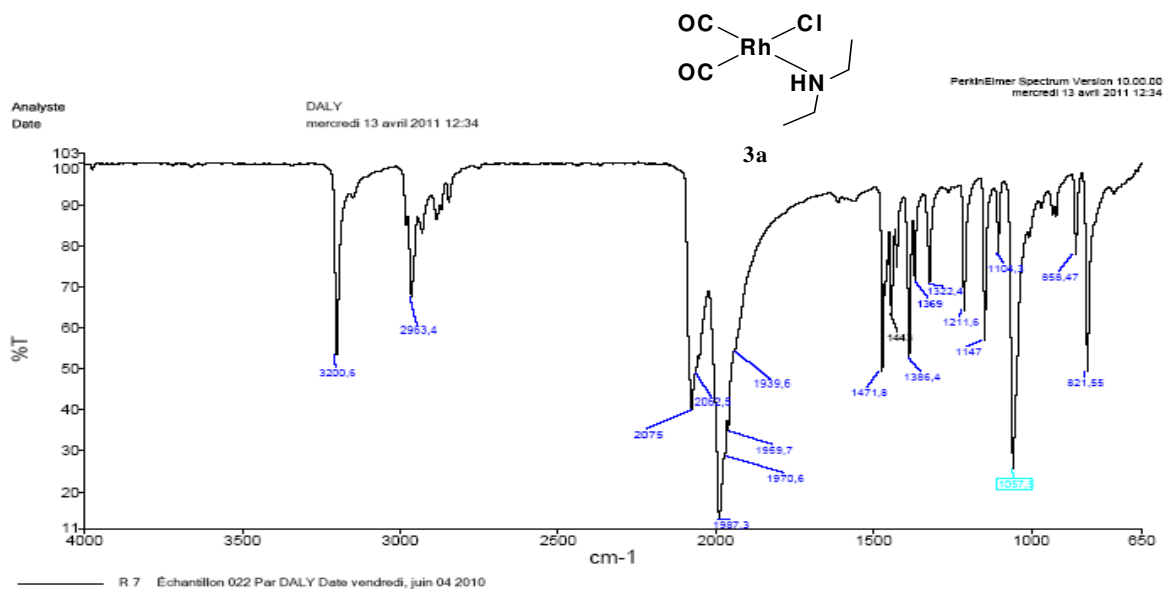
(19) Burke, K. P.; Yang, W. *Electronic Density Functional Theory: Recent Progress and New Directions*, **1998**.

(20) Frisch, M. J. et al. *Gaussian 03, Revision B.05*, Gaussian, Inc., Wallingford CT.

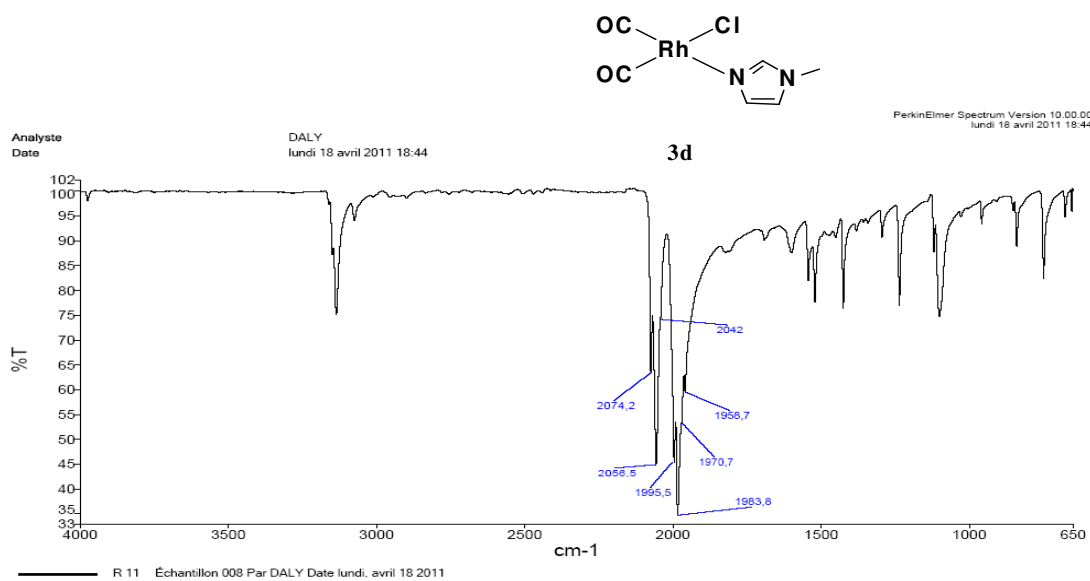
SUPPORTING INFORMATION

CHAPTER II

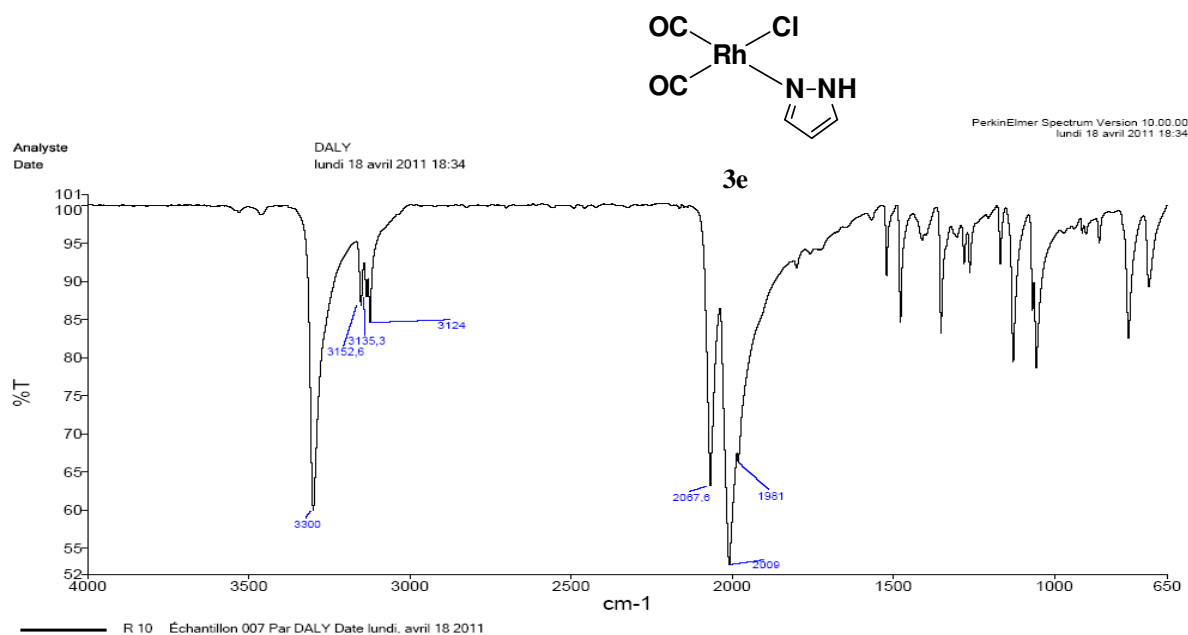
I- ATR-IR Rh(I) SPECTRA

ATR-IR Figure 1. Spectrum of **3a** at 298 K.

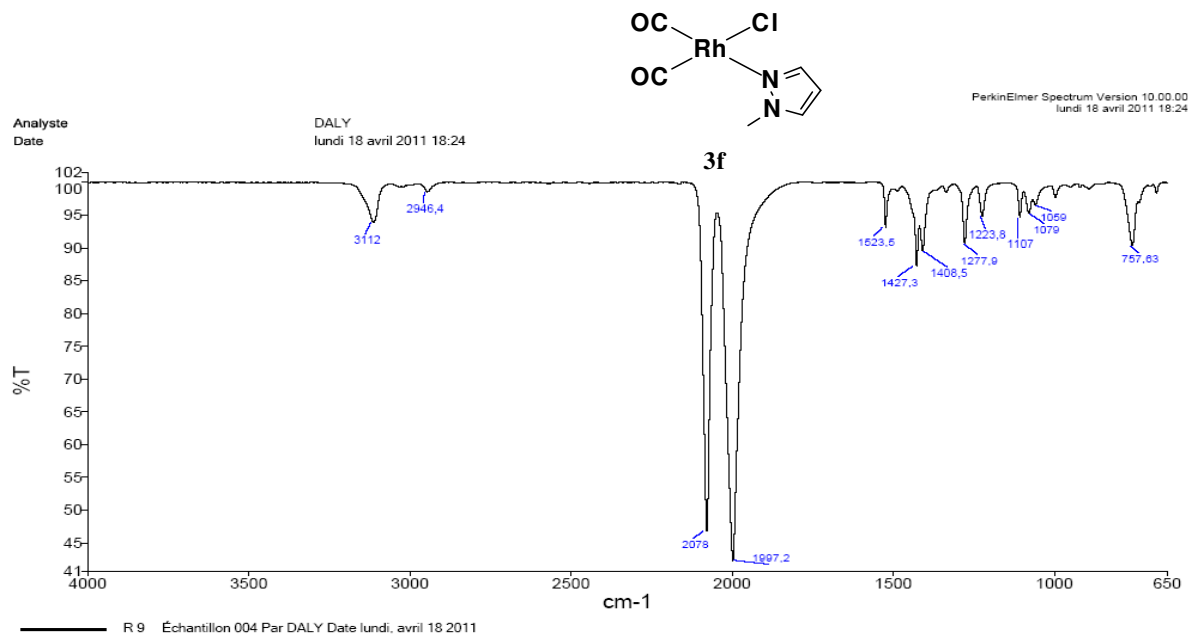
Page 1

ATR-IR Figure 2. Spectrum of **3d** at 298 K.

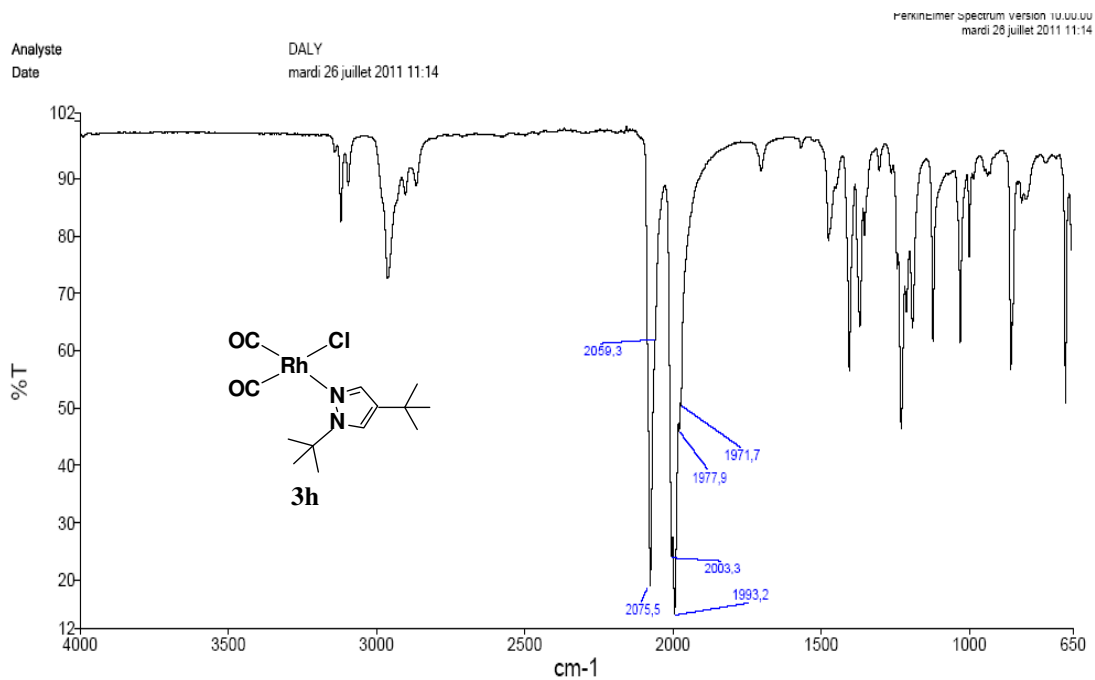
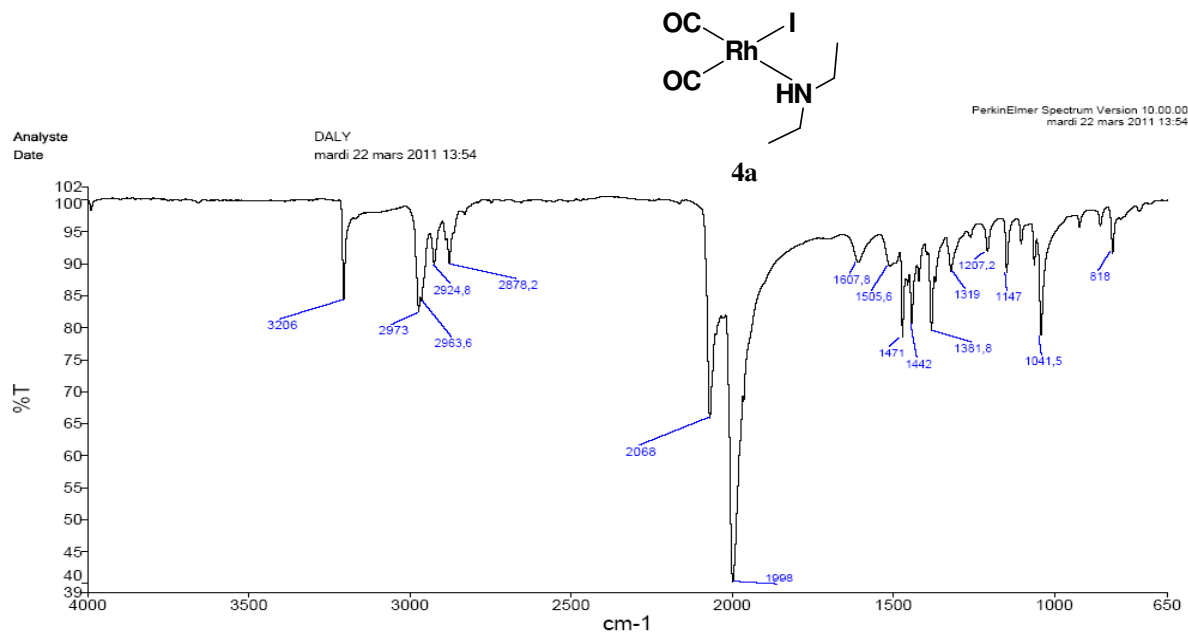
Page 1

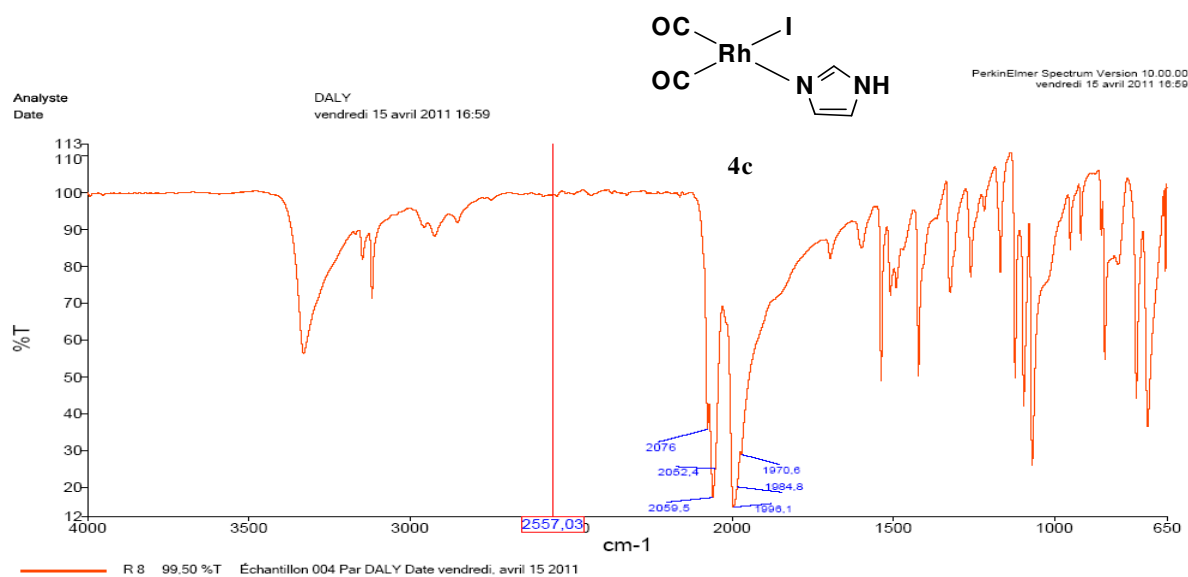
ATR-IR Figure 3. Spectrum of **3e** at 298 K.

Page 1

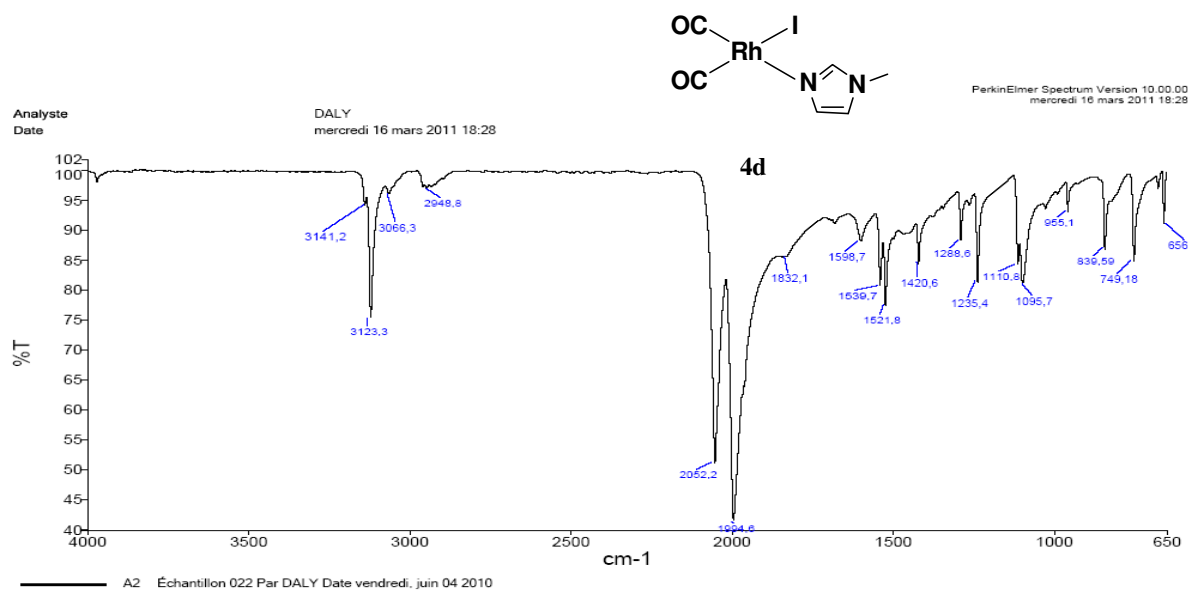
ATR-IR Figure 4. Spectrum of **3f** at 298 K.

Page 1

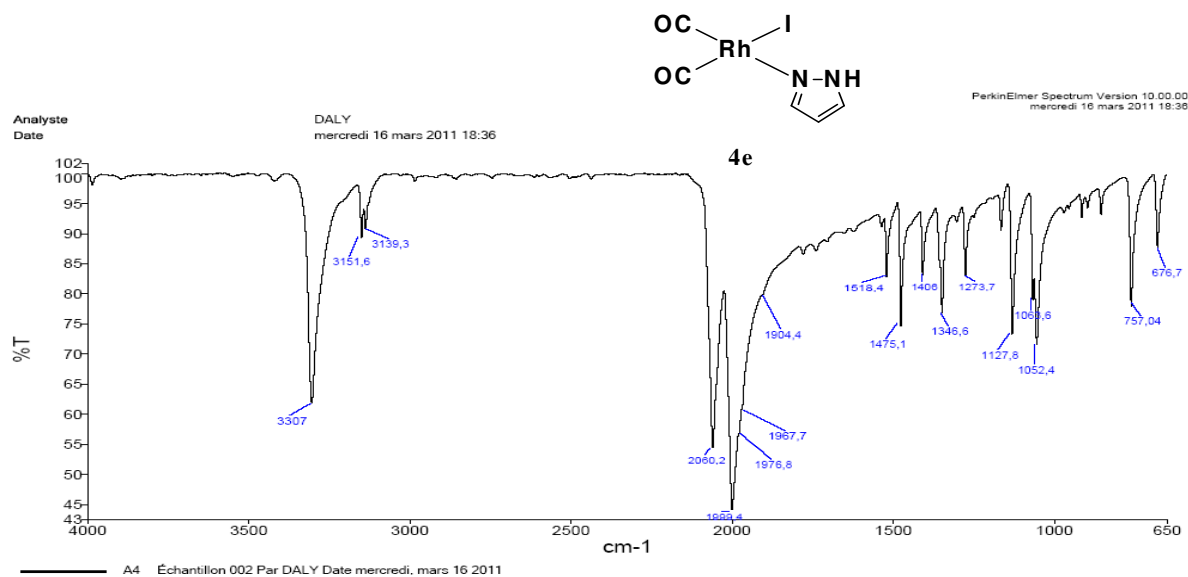
ATR-IR Figure 5. Spectrum of **3h** at 298 K.ATR-IR Figure 6. Spectrum of **4a** at 298 K.

ATR-IR Figure 7. Spectrum of **4c** at 298 K.

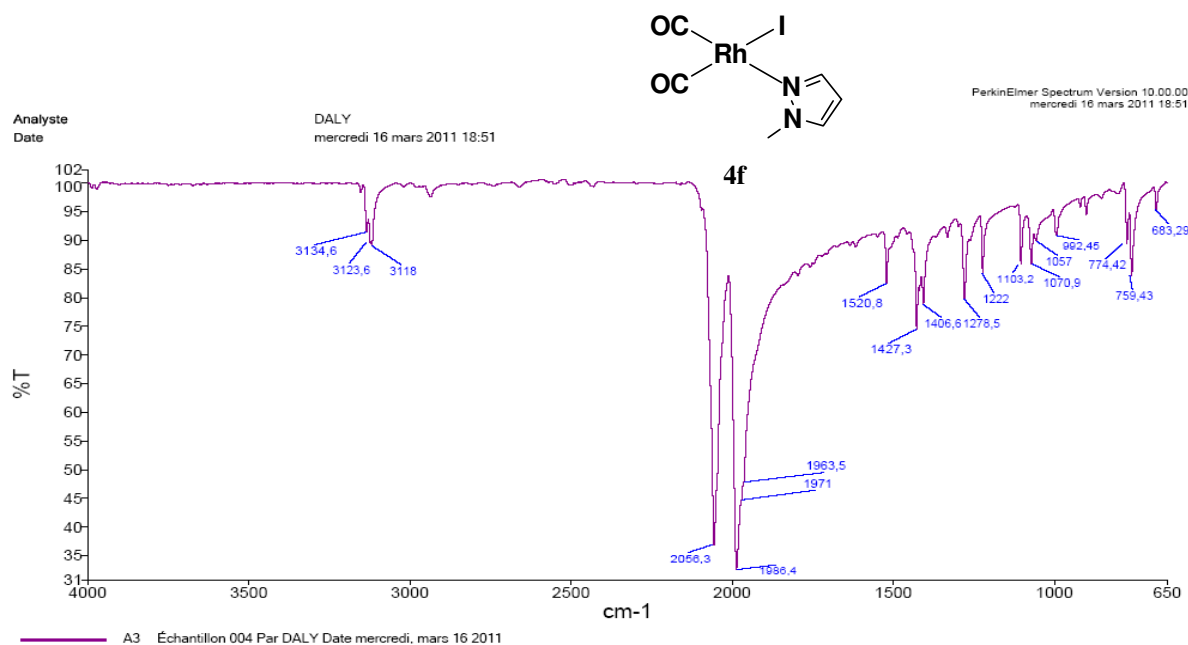
Page 1

ATR-IR Figure 8. Spectrum of **4d** at 298 K.

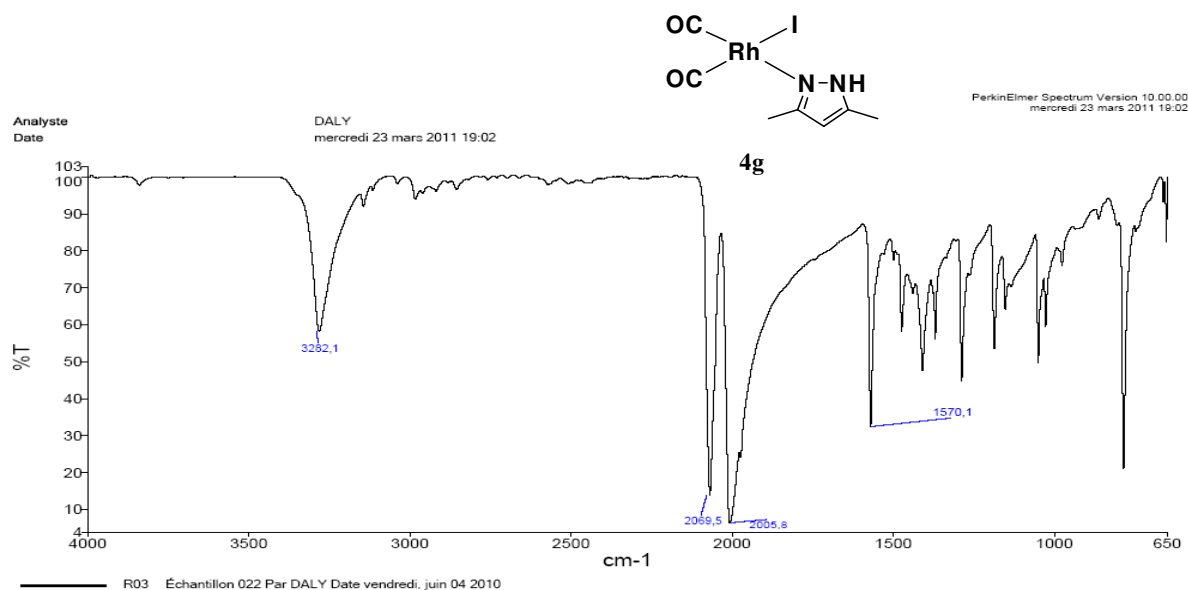
Page 1

ATR-IR Figure 9. Spectrum of **4e** at 298 K.

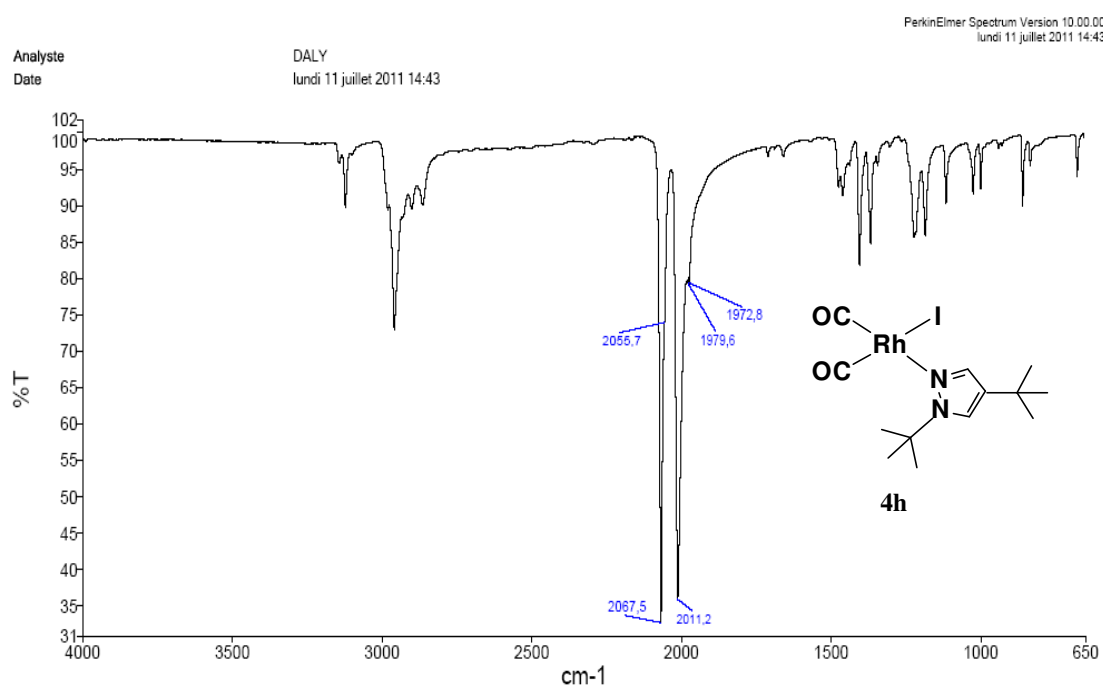
Page 1

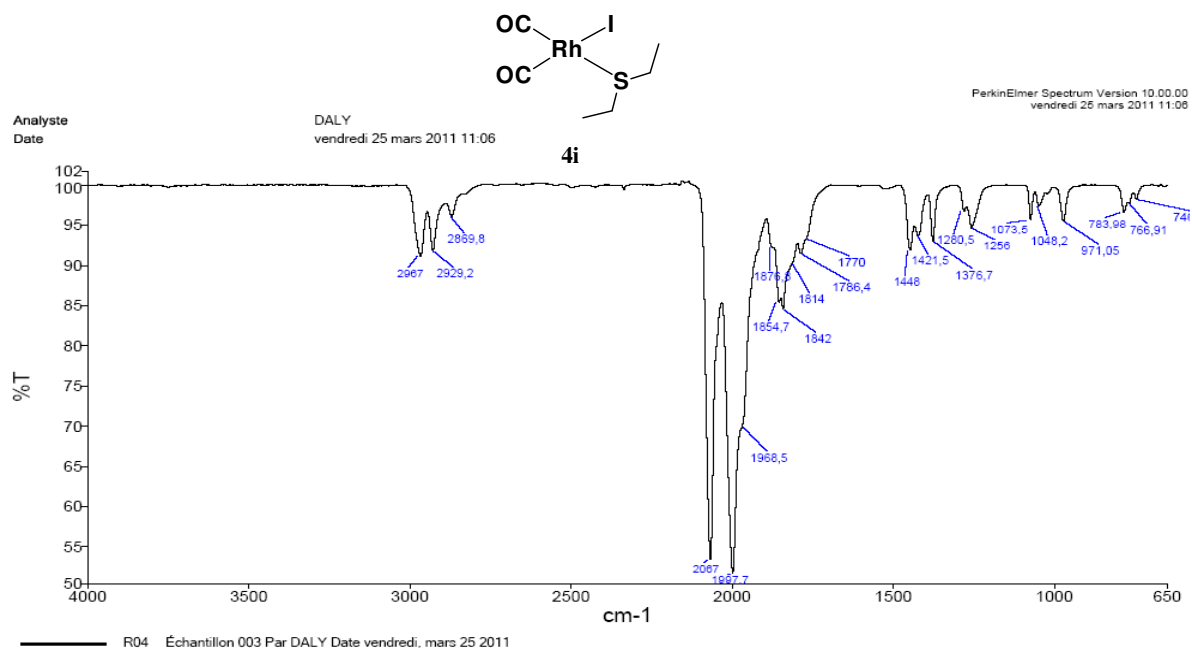
ATR-IR Figure 10. Spectrum of **4f** at 298 K.

Page 1

ATR-IR Figure 11. Spectrum of **4g** at 298 K.

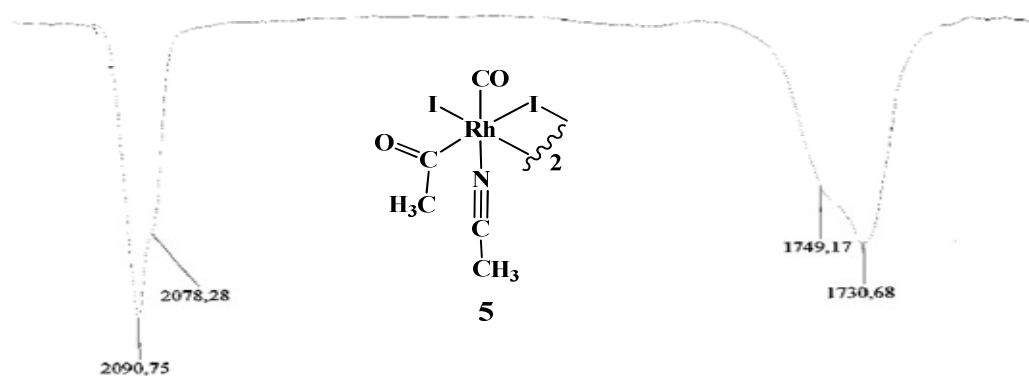
Page 1

ATR-IR Figure 12. Spectrum of **4h** at 298 K.

ATR-IR Figure 13. Spectrum of **4i** at 298 K.

Page 1

II- FT-IR Rh(III) SPECTRA

Figure 1. FT-IR spectrum of **5** at 298 K in CH₂Cl₂. (Poor solubility in CH₂Cl₂).

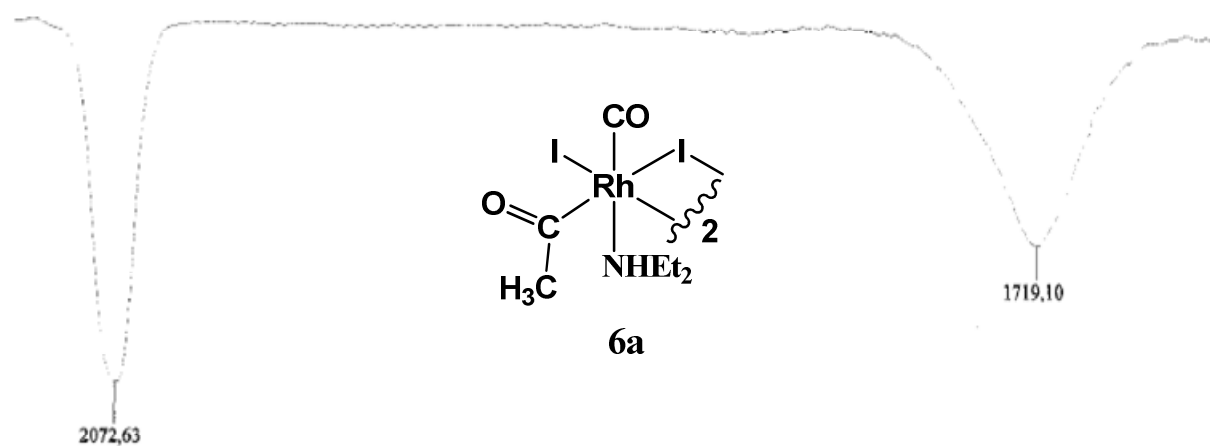


Figure 2. FT-IR spectrum of **6a** at 298 K in CH₂Cl₂.

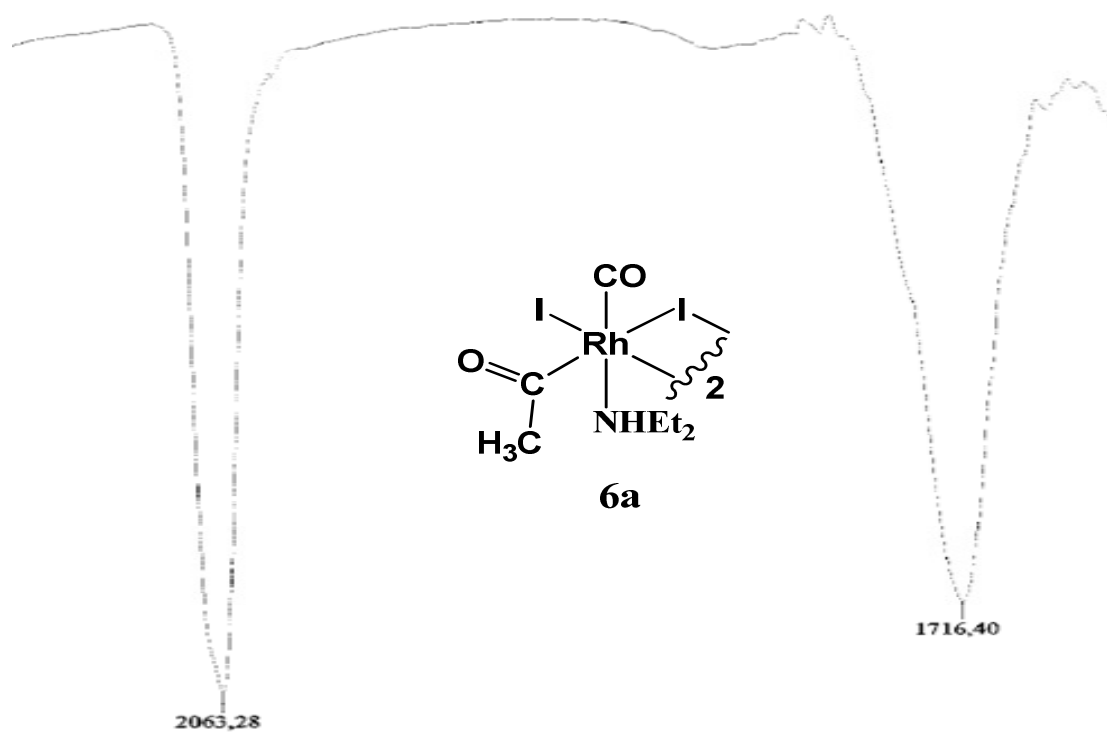


Figure 3. FT-IR spectrum of **6a** at 298 K in CH₃I.

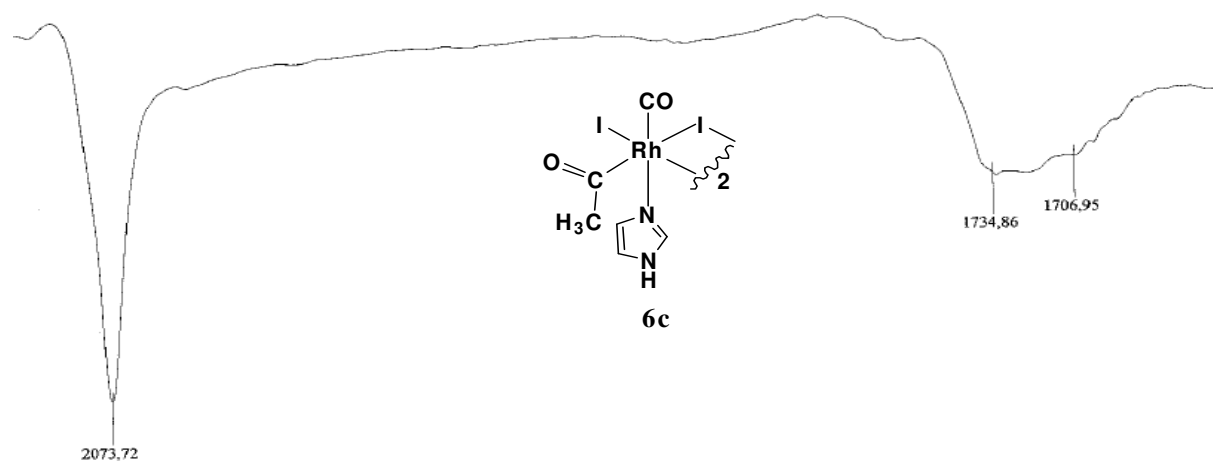


Figure 4. FT-IR spectrum of **6c** at 298 K in CH_2Cl_2 .

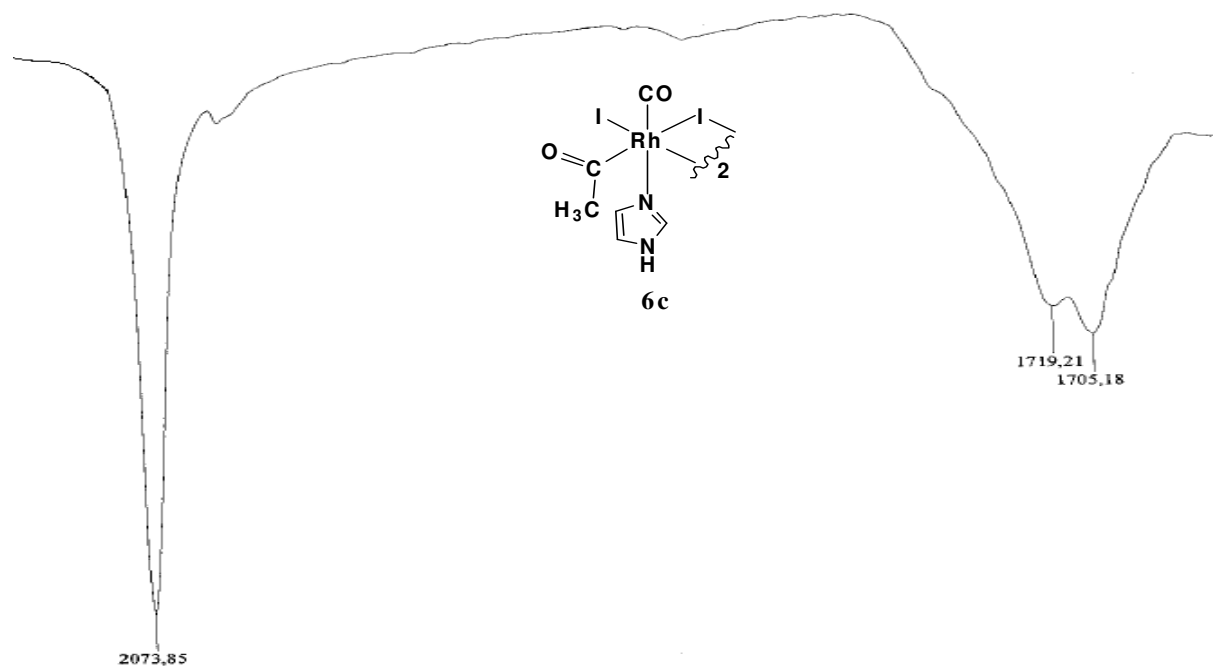


Figure 5. FT-IR spectrum of **6c** at 298 K in CH_3I .

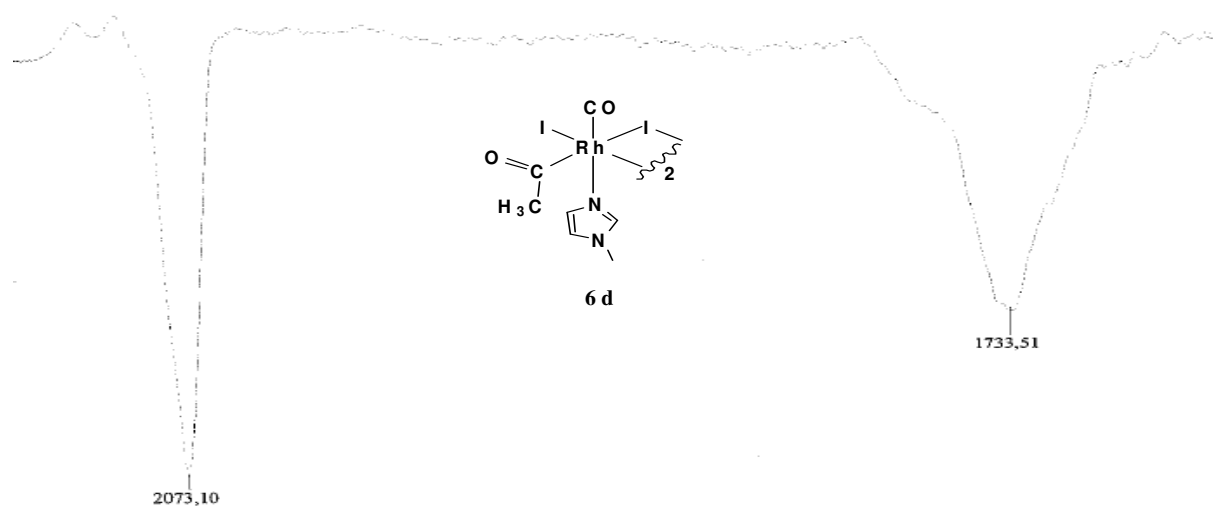


Figure 6. FT-IR spectrum of **6d** at 298 K in CH₂Cl₂.

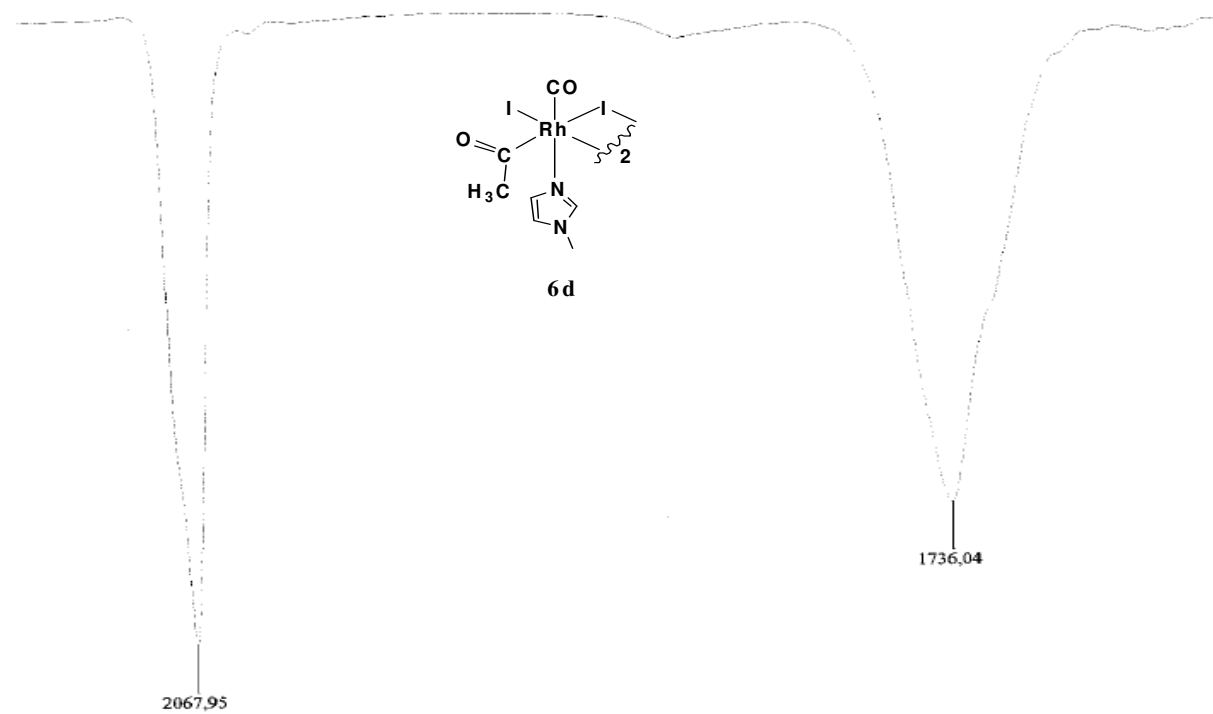


Figure 7. FT-IR spectrum of **6d** at 298 K in CH₃I.

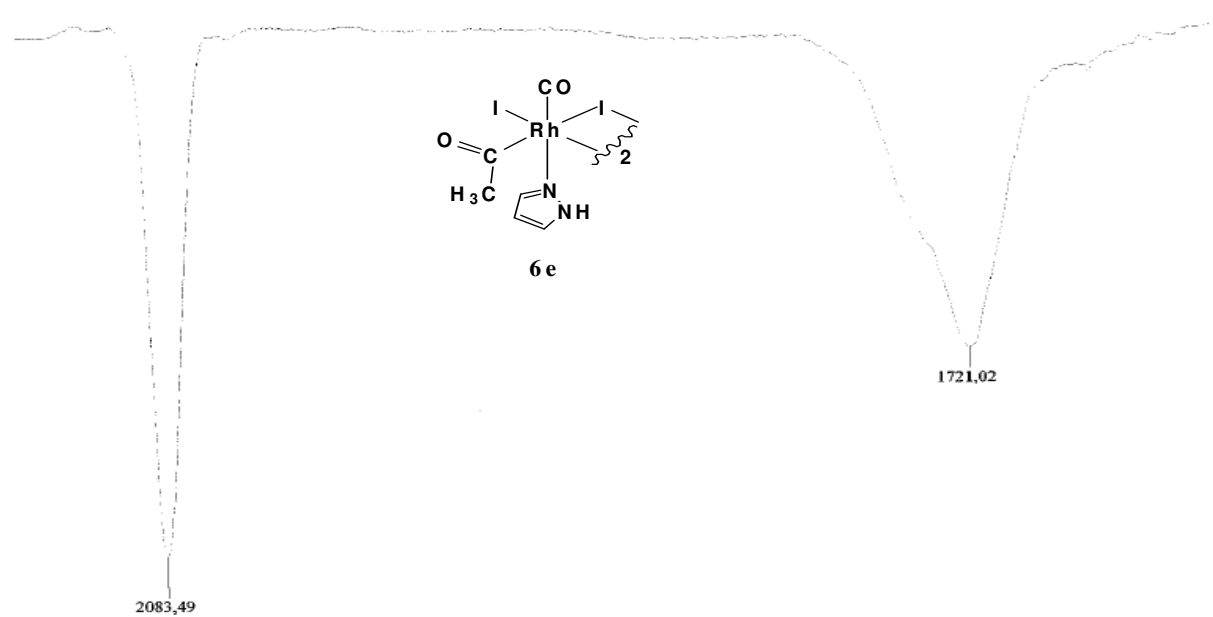


Figure 8. FT-IR spectrum of **6e** at 298 K in CH₂Cl₂.

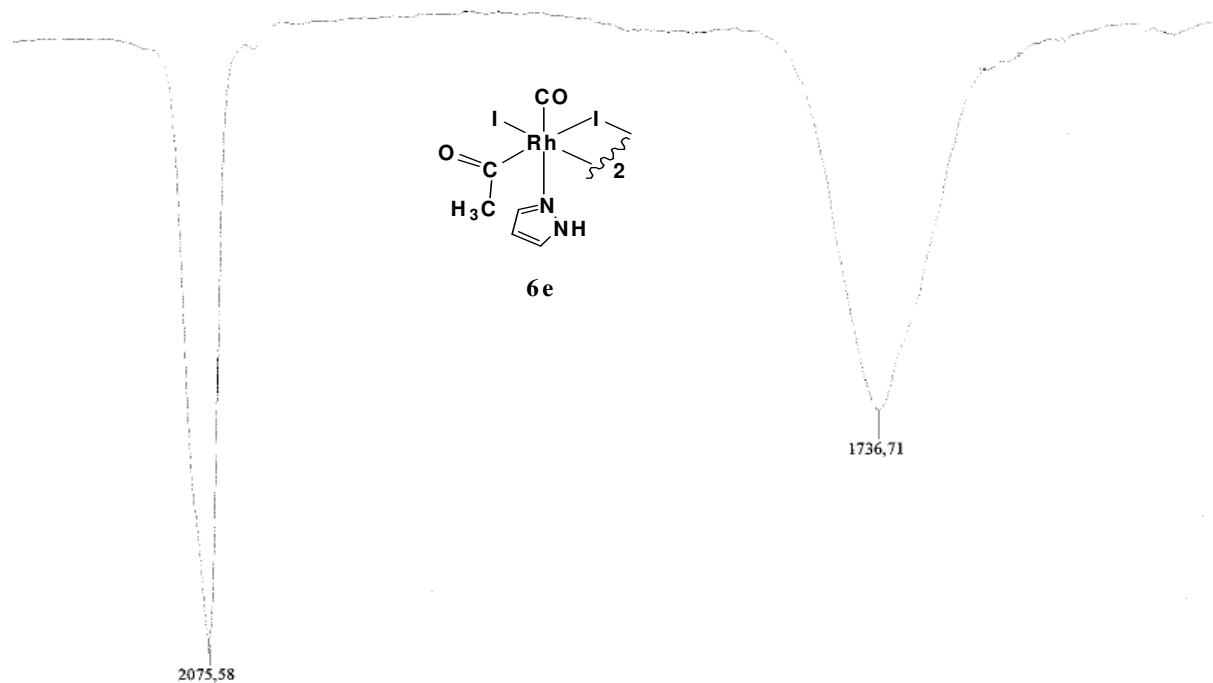


Figure 9. FT-IR spectrum of **6e** at 298 K in CH₃I.

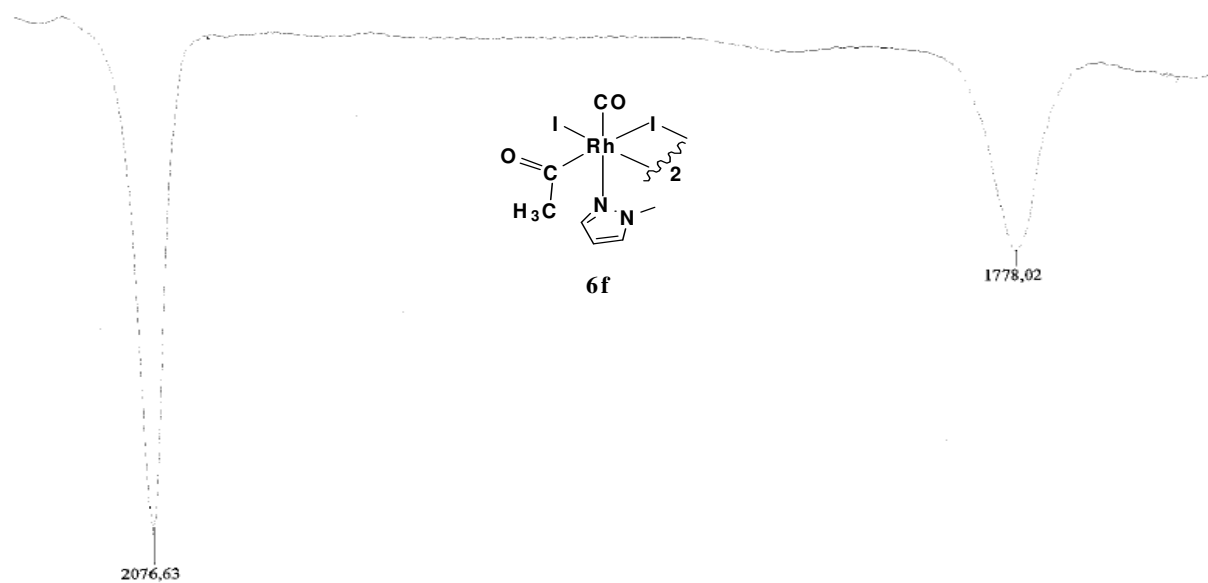


Figure 10. FT-IR spectrum of **6f** at 298 K in CH₂Cl₂.

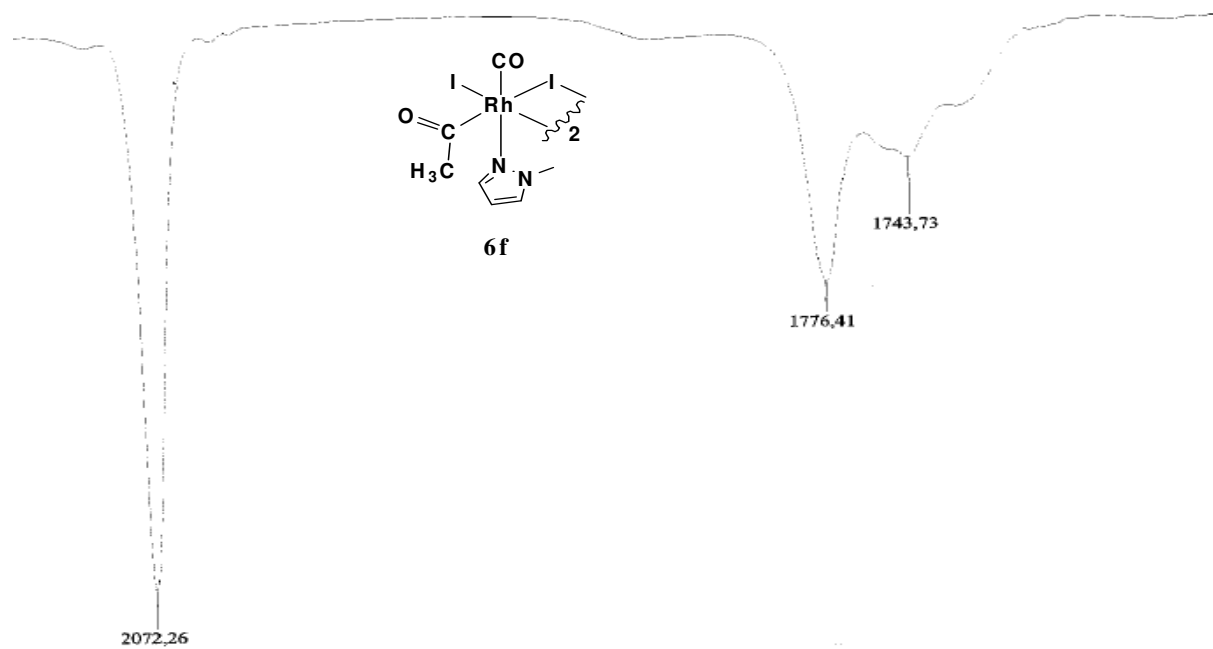


Figure 11. FT-IR spectrum of **6f** at 298 K in CH₃I.

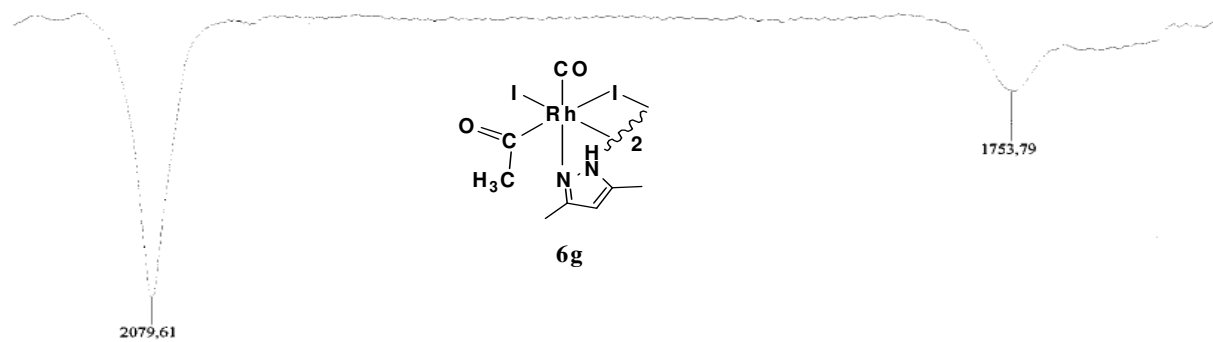


Figure 12. FT-IR spectrum of **6g** at 298 K in CH_2Cl_2 .

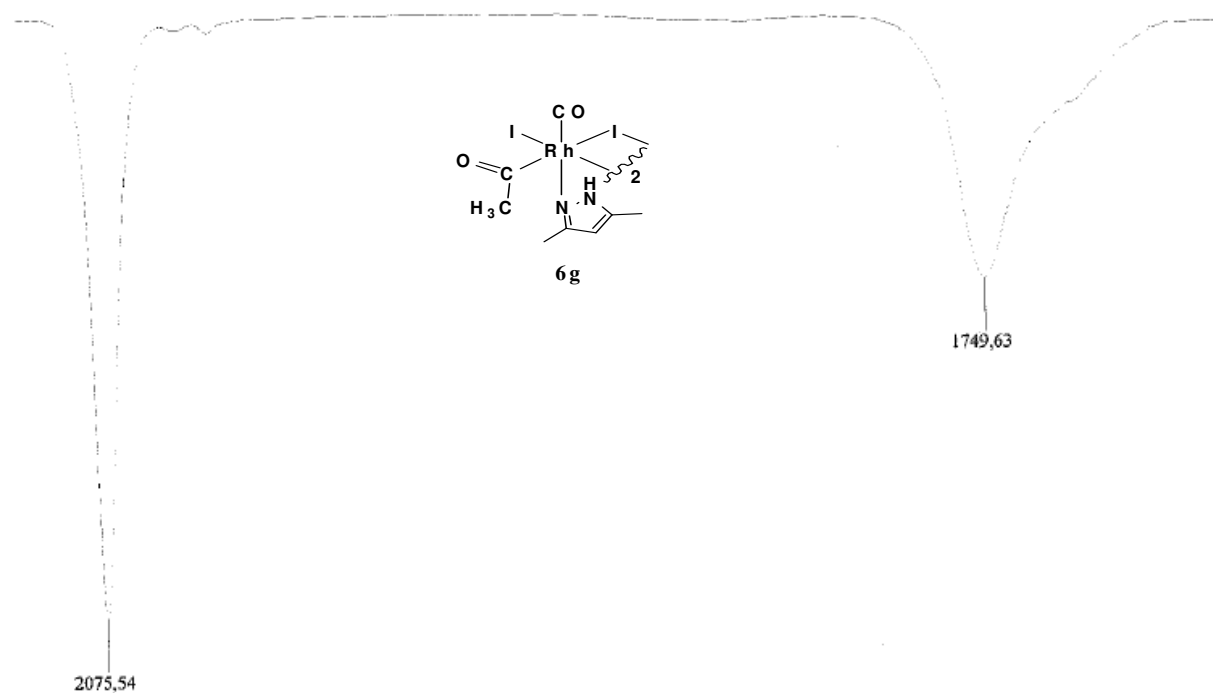


Figure 13. FT-IR spectrum of **6g** at 298 K in CH_3I .

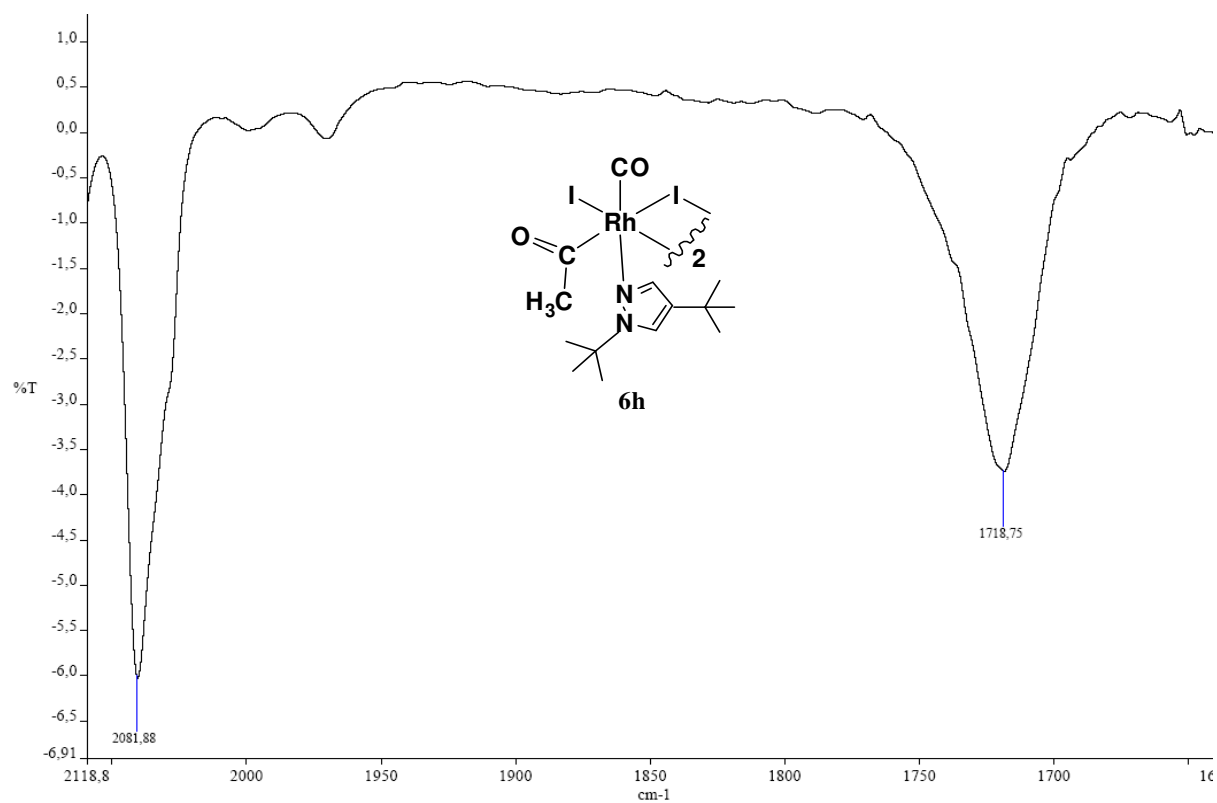


Figure 14. FT-IR spectrum of **6h** at 298 K in CH_2Cl_2 .

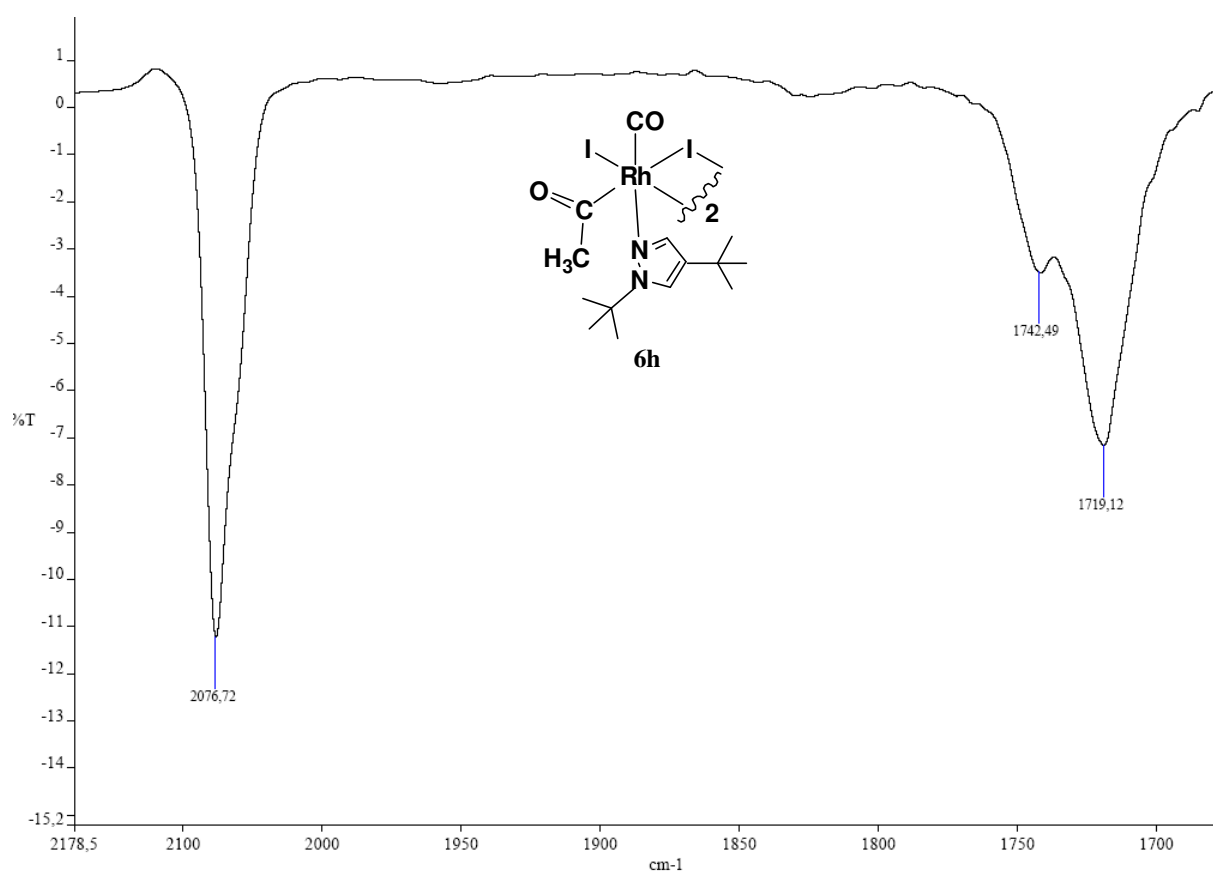


Figure 15. FT-IR spectrum of **6h** at 298 K in CH_3I .

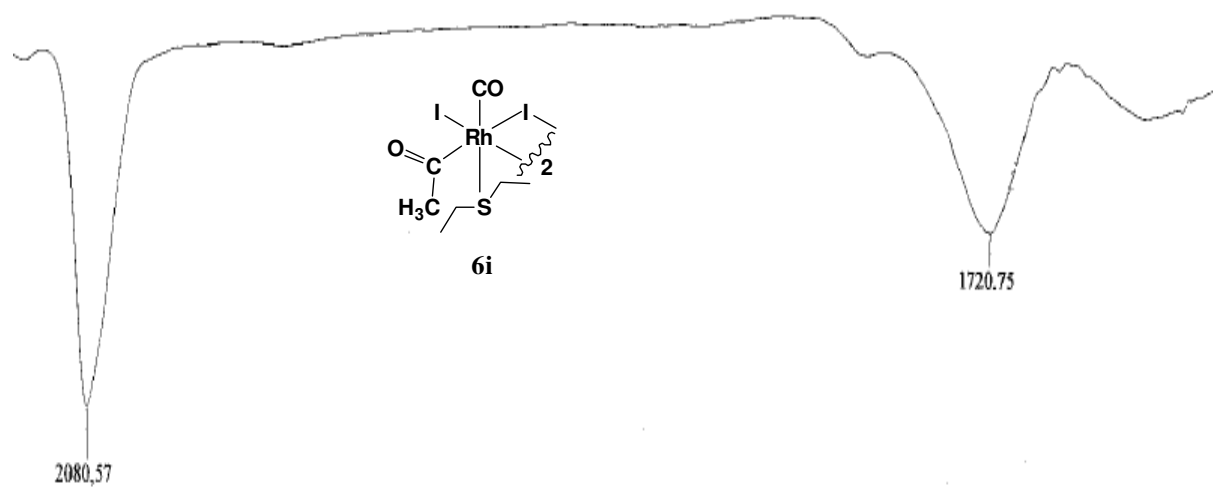


Figure 16. FT-IR spectrum of **6i** at 298 K in CH_2Cl_2 .

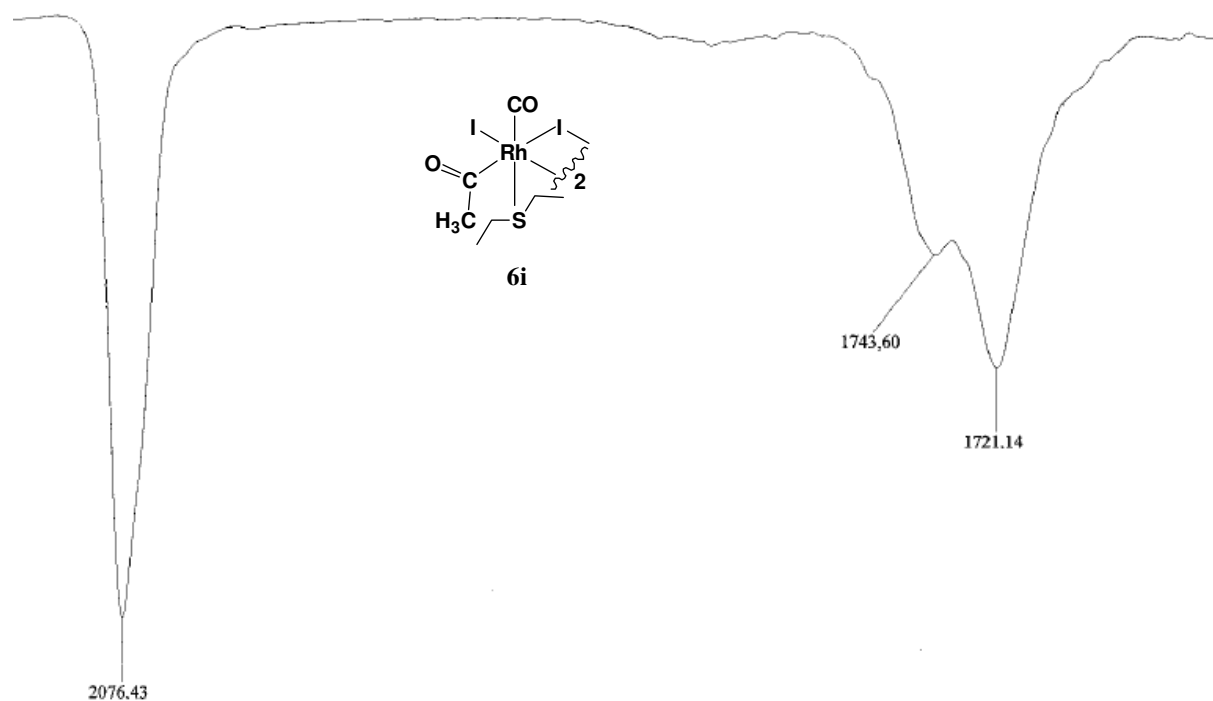


Figure 17. FT-IR spectrum of **6i** at 298 K in CH_3I .

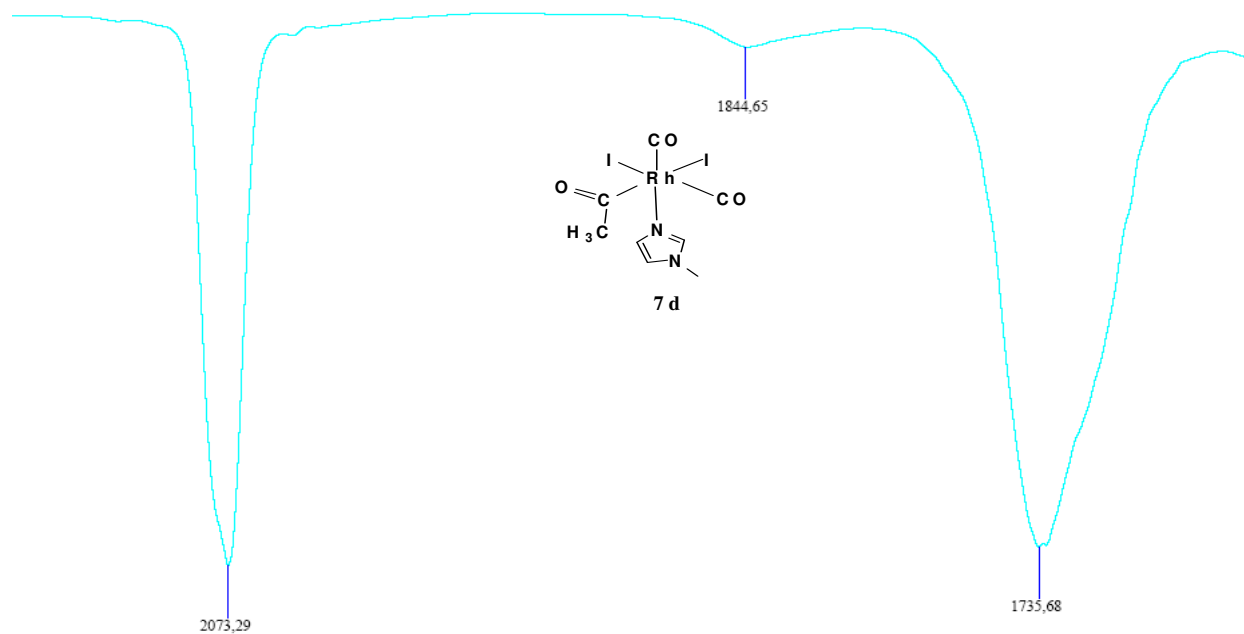


Figure 18. FT-IR spectrum of **7d** at 298 K in CH₂Cl₂.

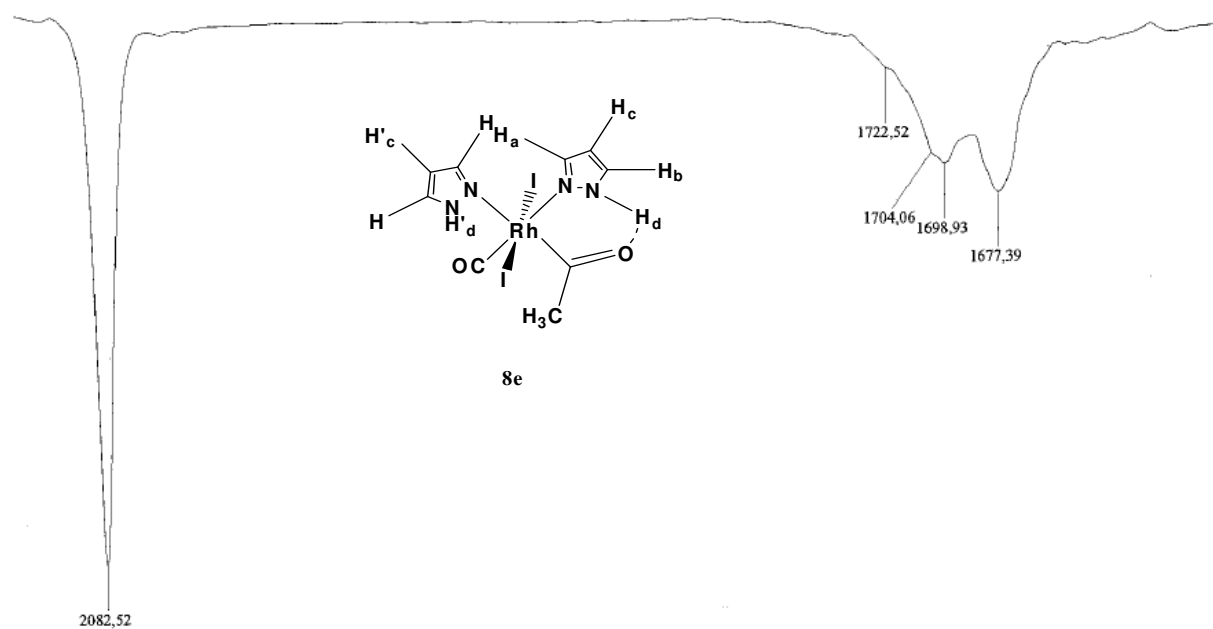
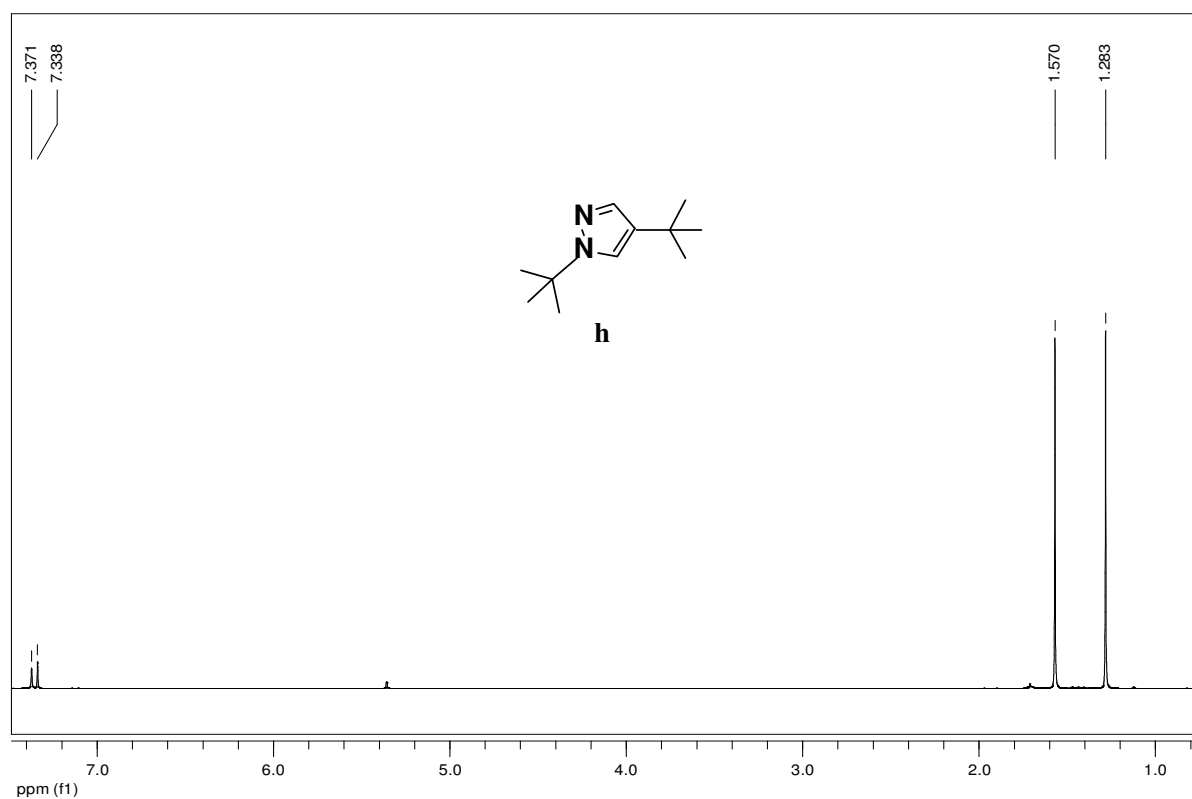
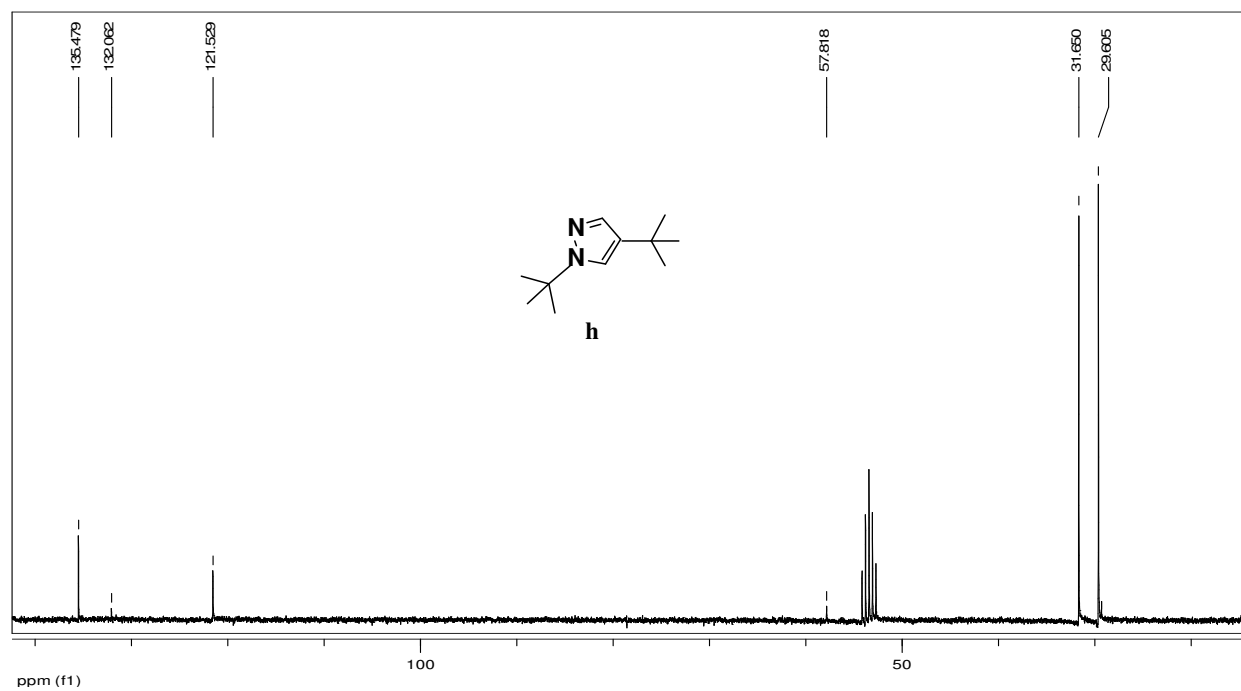


Figure 19. FT-IR spectrum of **8e** at 298 K in CH₂Cl₂.

III- NMR DATA / LIGAND **h** AND SELECTED Rh(I) NMR SPECTRA**Figure 1.** ^1H NMR spectrum of **h** at 298 K in CD_2Cl_2 .**Figure 2.** $^{13}\text{C}\{^1\text{H}\}$ NMR spectrum of **h** at 298 K in CD_2Cl_2 .

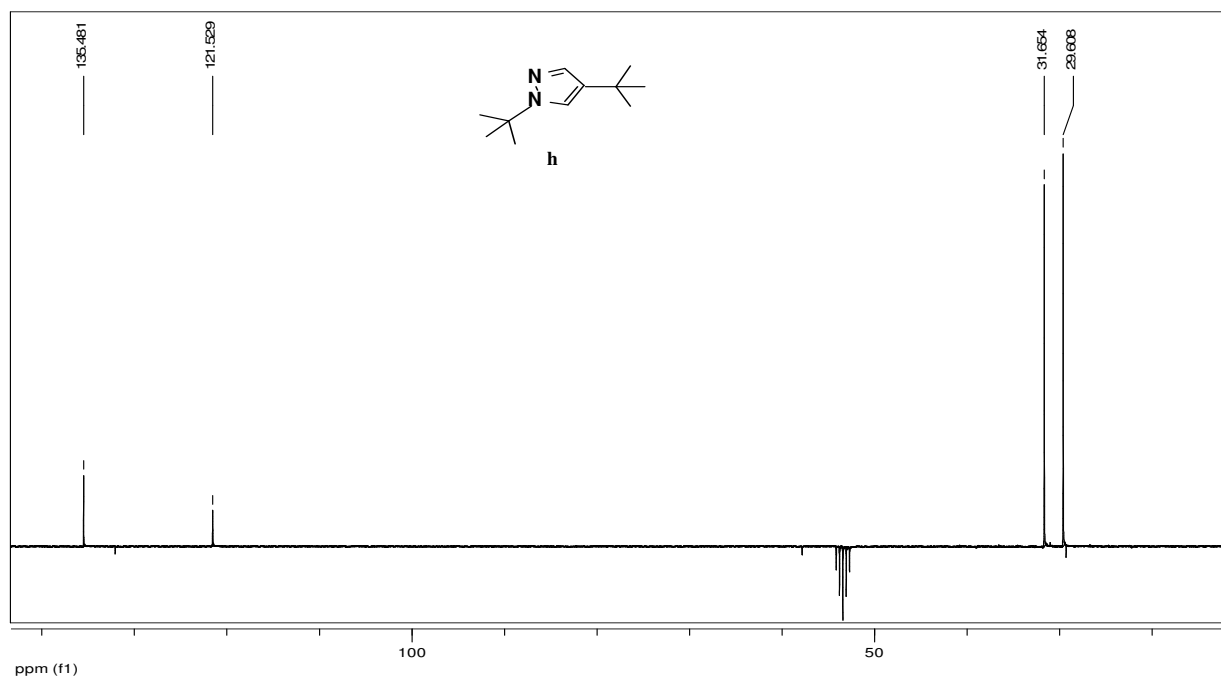


Figure 3. $^{13}\text{C}\{^1\text{H}\}$ (Jmod) NMR spectrum of **h** at 298 K in CD_2Cl_2 .

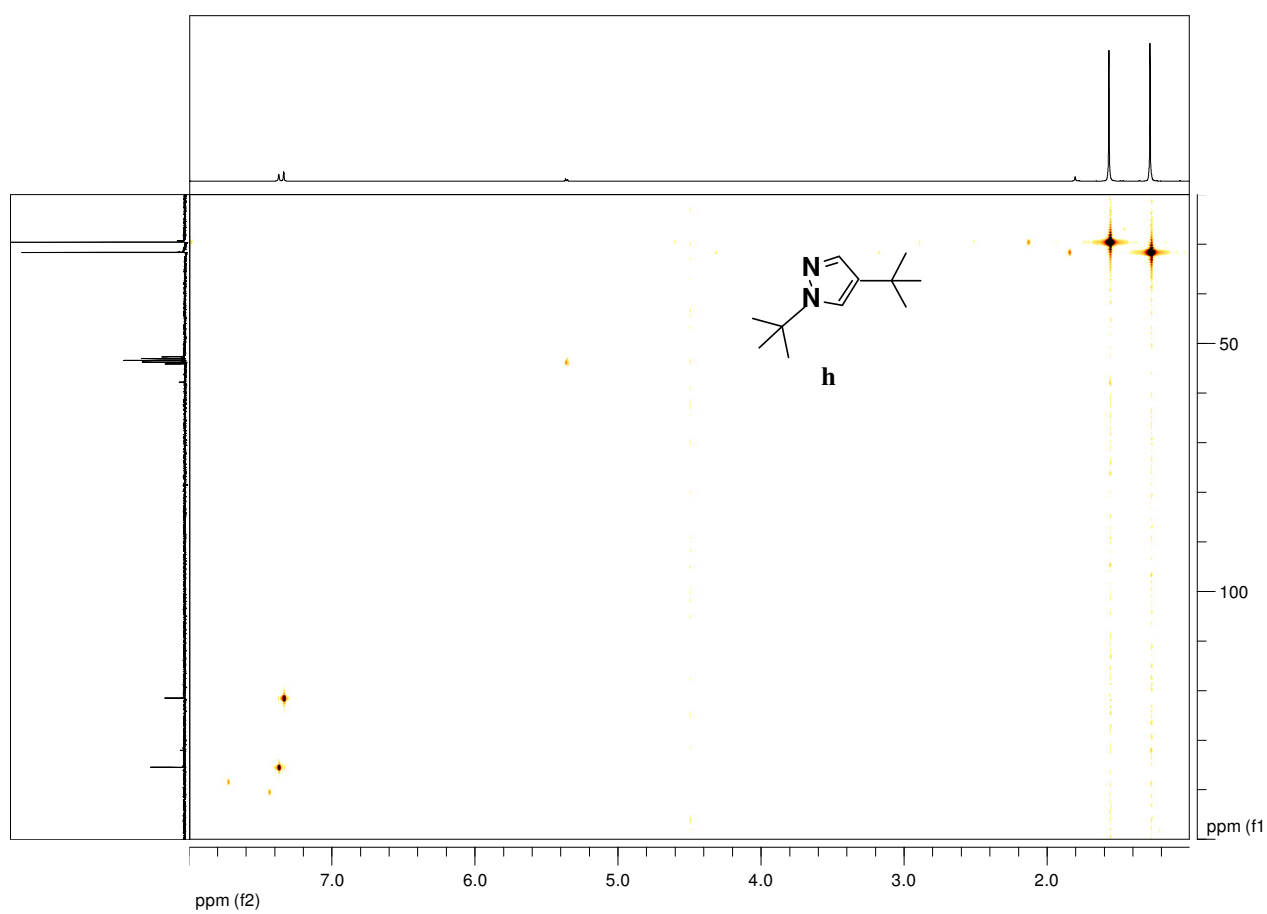


Figure 4. 2D ^1H - ^{13}C HMQC NMR spectrum of **h** at 298 K in CD_2Cl_2 .

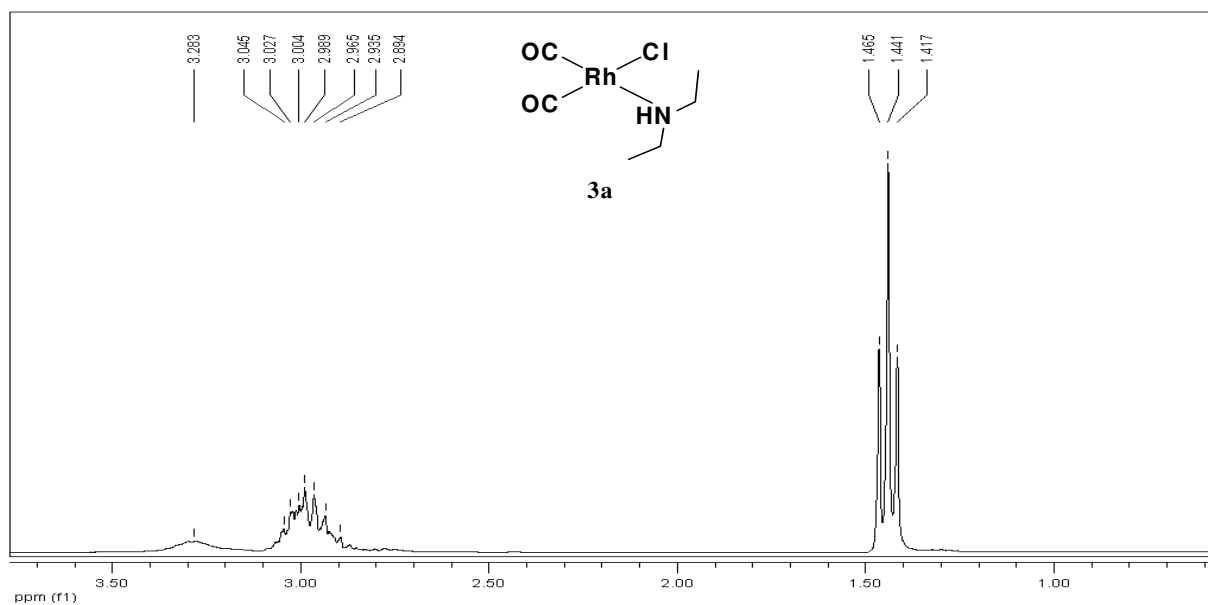


Figure 5. ^1H NMR spectrum of **3a** at 298 K in CD_2Cl_2 .

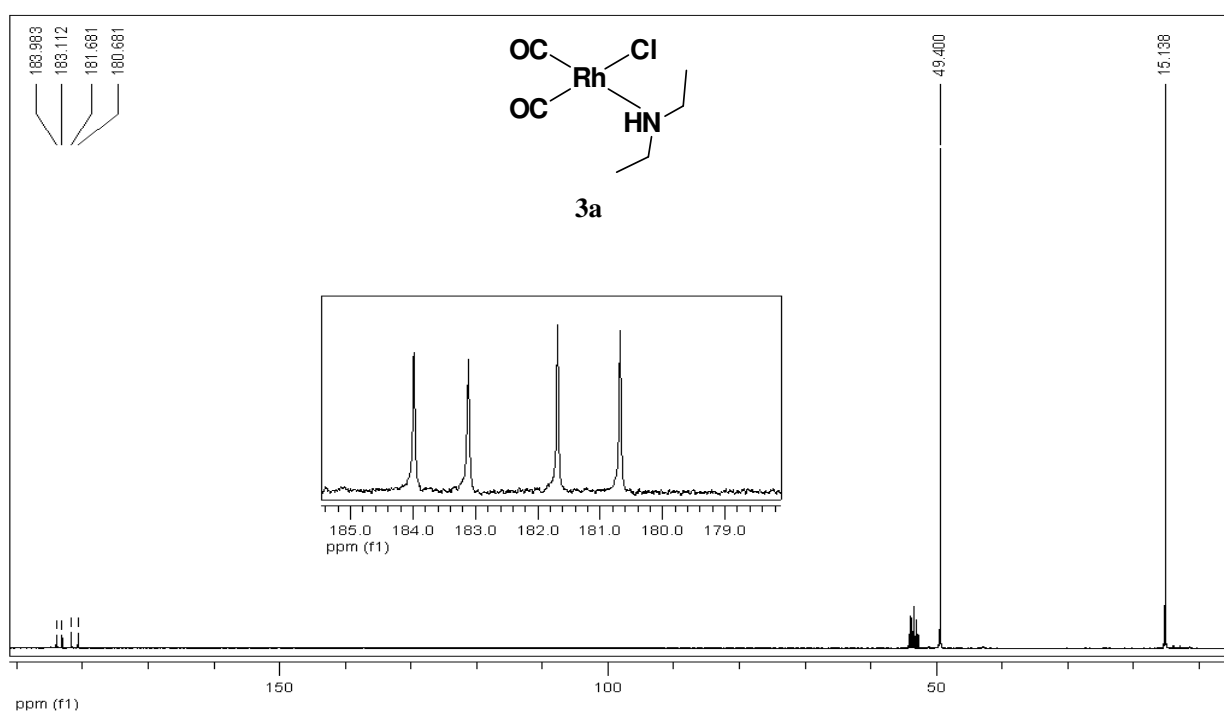


Figure 6. $^{13}\text{C}\{^1\text{H}\}$ NMR spectrum of **3a** at 298 K in CD_2Cl_2 .

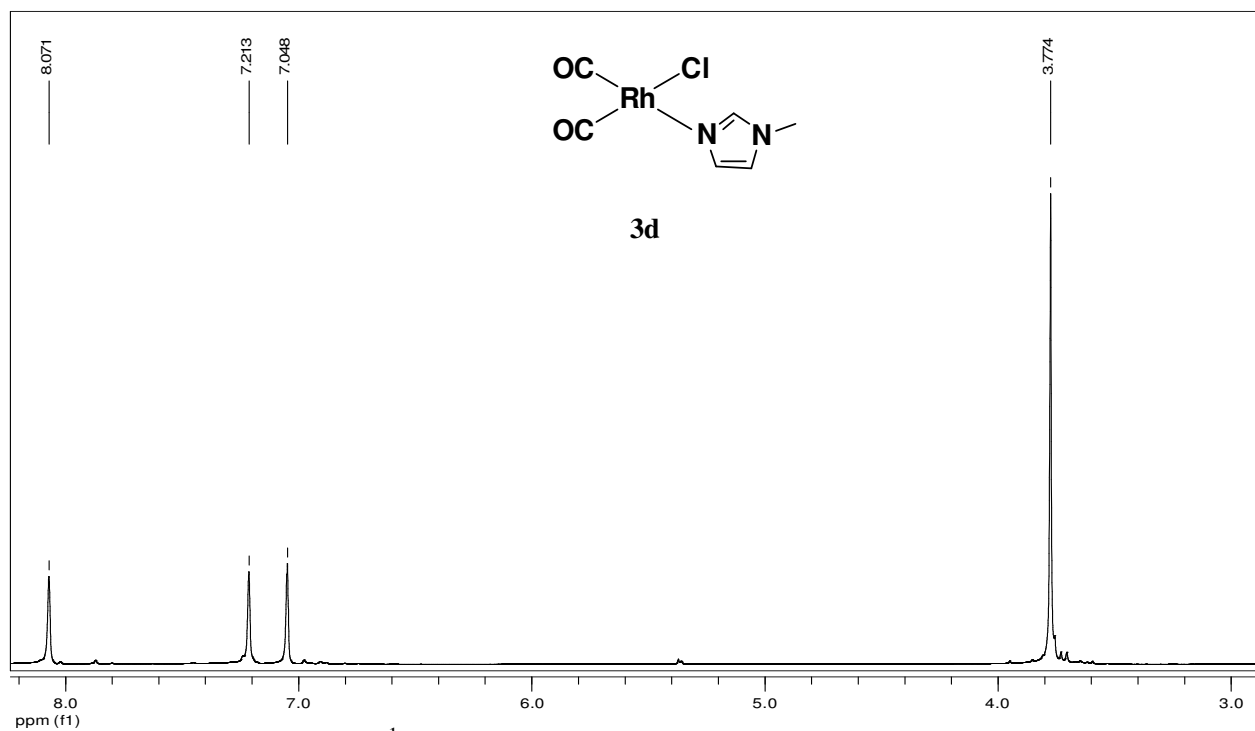


Figure 7. ^1H NMR spectrum of **3d** at 298 K in CD_2Cl_2 .

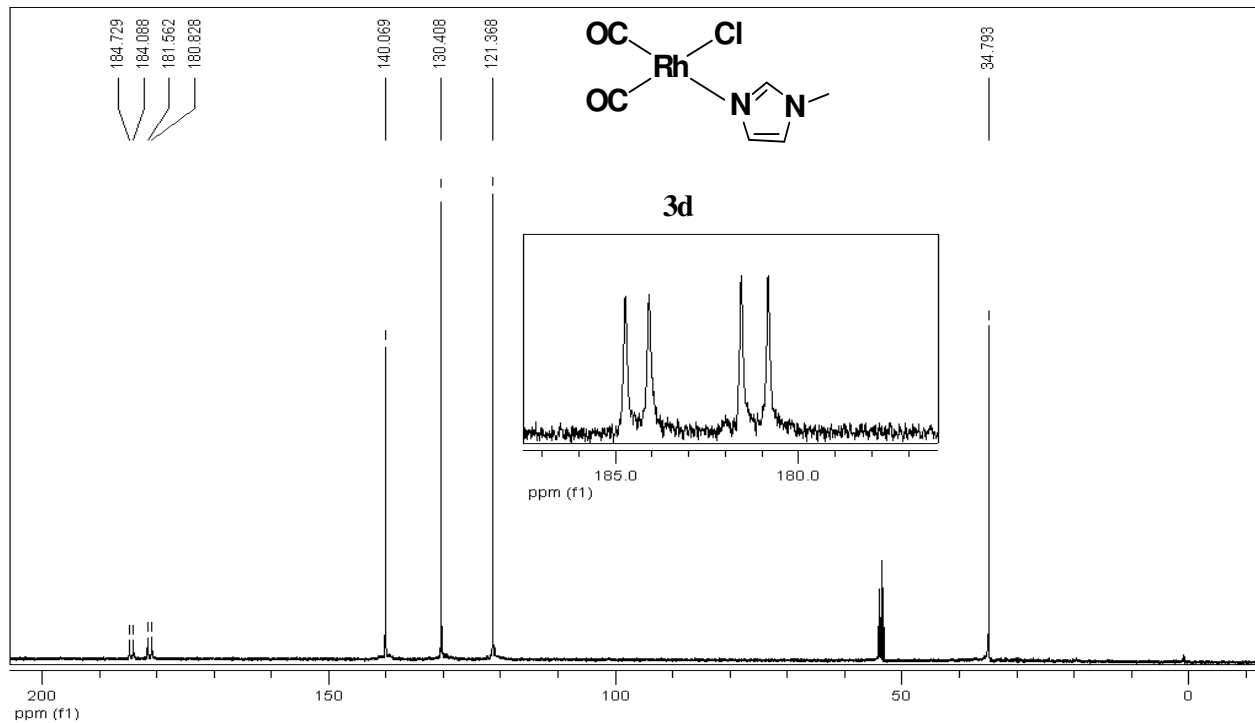


Figure 8. $^{13}\text{C}\{^1\text{H}\}$ NMR spectrum of **3d** at 298 K in CD_2Cl_2 .

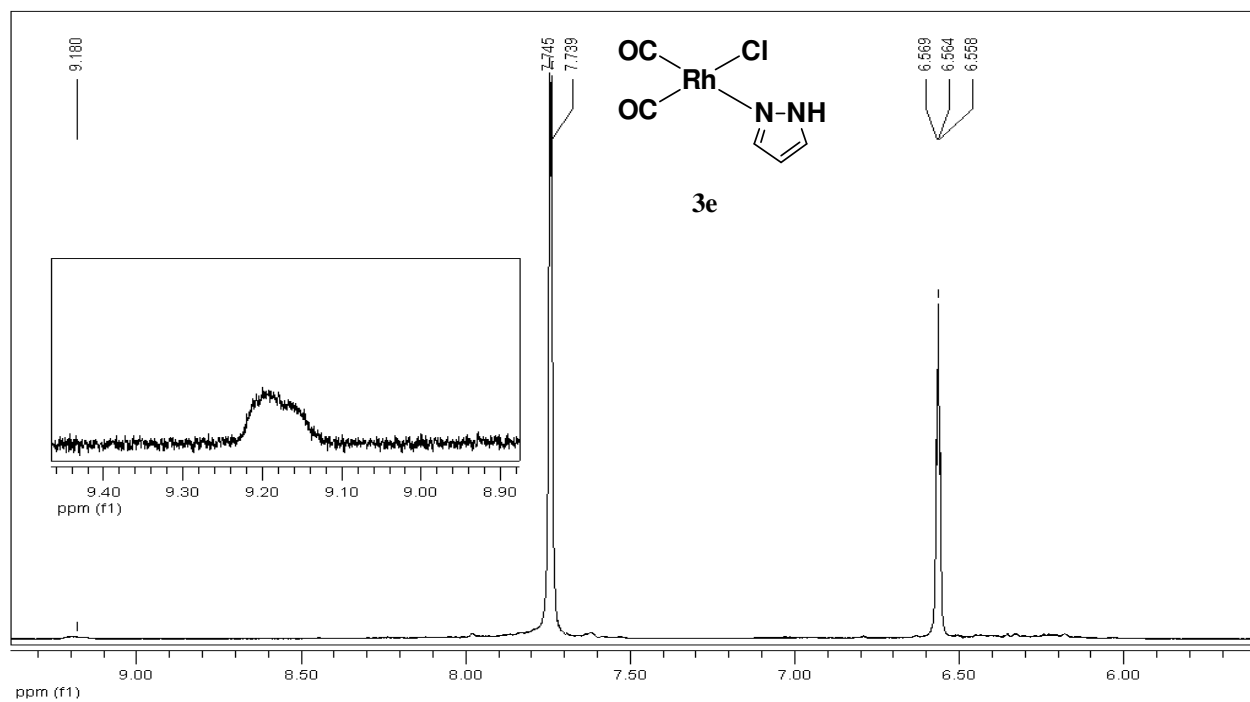


Figure 9. ^1H NMR spectrum of **3e** at 298 K in CD_2Cl_2 .

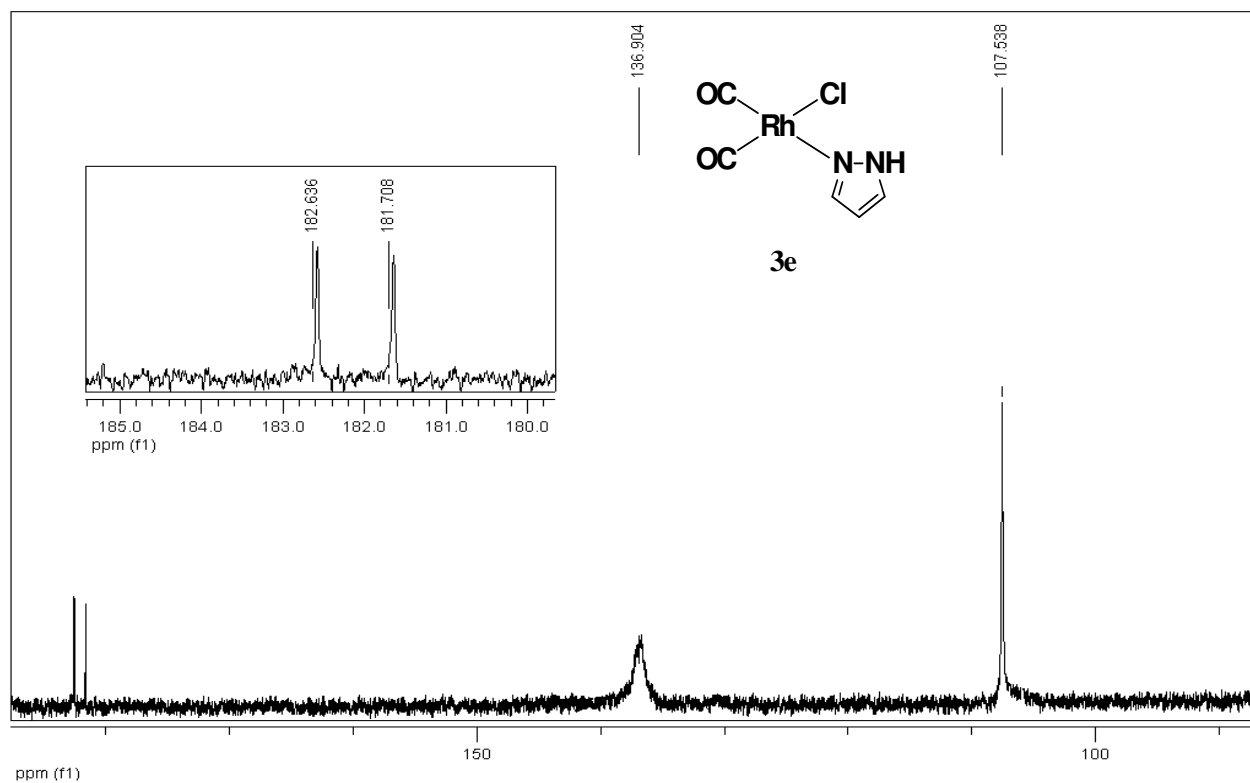


Figure 10. $^{13}\text{C}\{^1\text{H}\}$ NMR spectrum of **3e** at 298 K in CD_2Cl_2 .

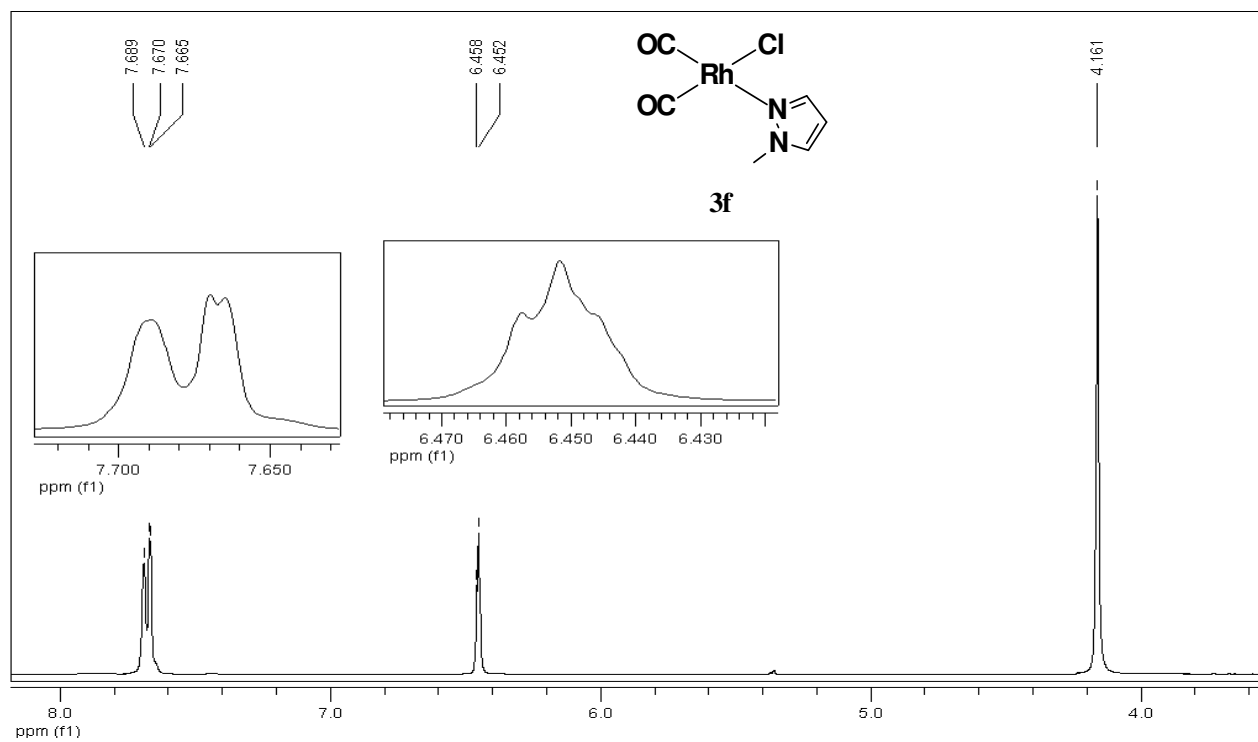


Figure 11. ^1H NMR spectrum of **3f** at 298 K in CD_2Cl_2 .

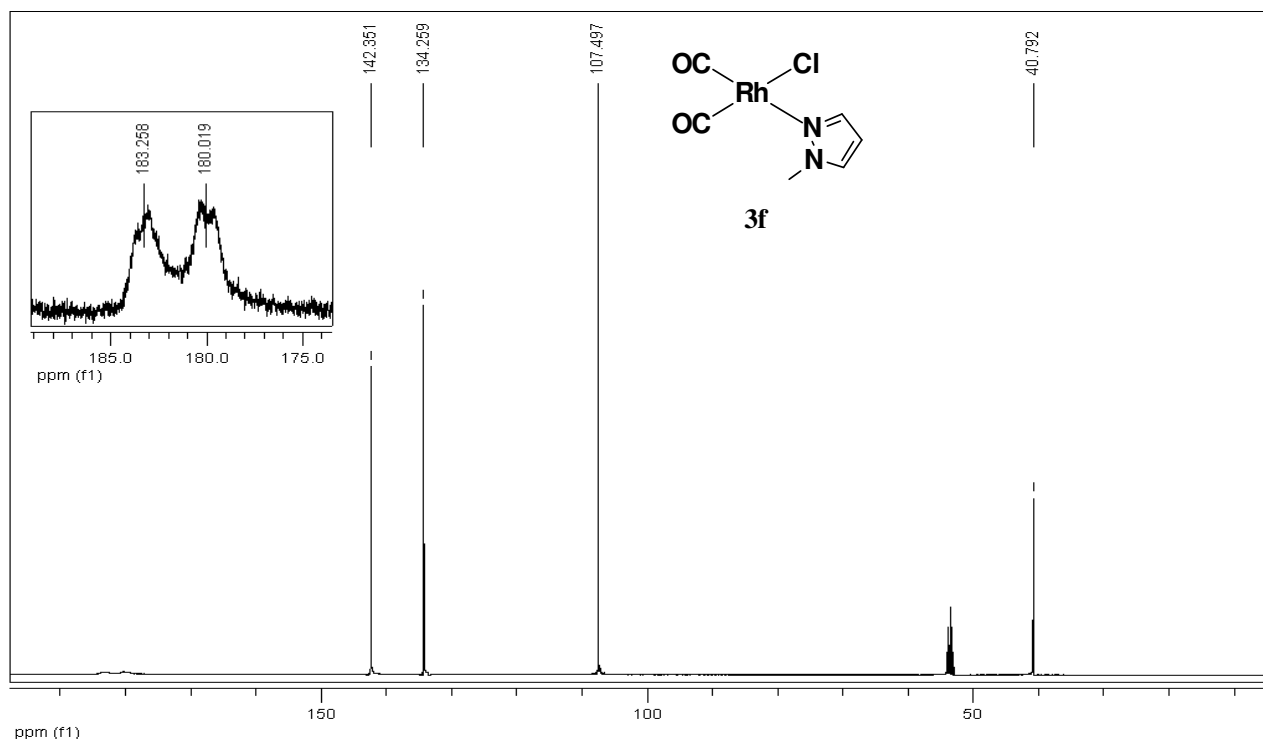


Figure 12. $^{13}\text{C}\{^1\text{H}\}$ NMR spectrum of **3f** at 298 K in CD_2Cl_2 .

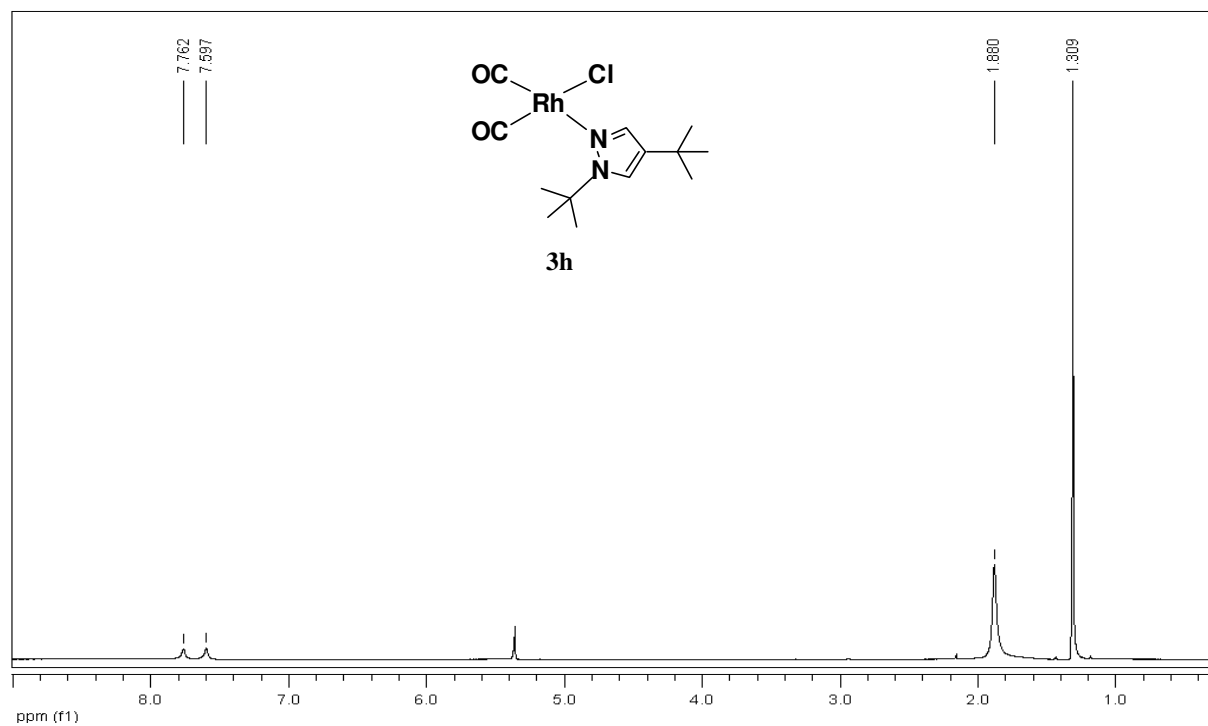


Figure 13. ^1H NMR spectrum of **3h** at 298 K in CD_2Cl_2 .

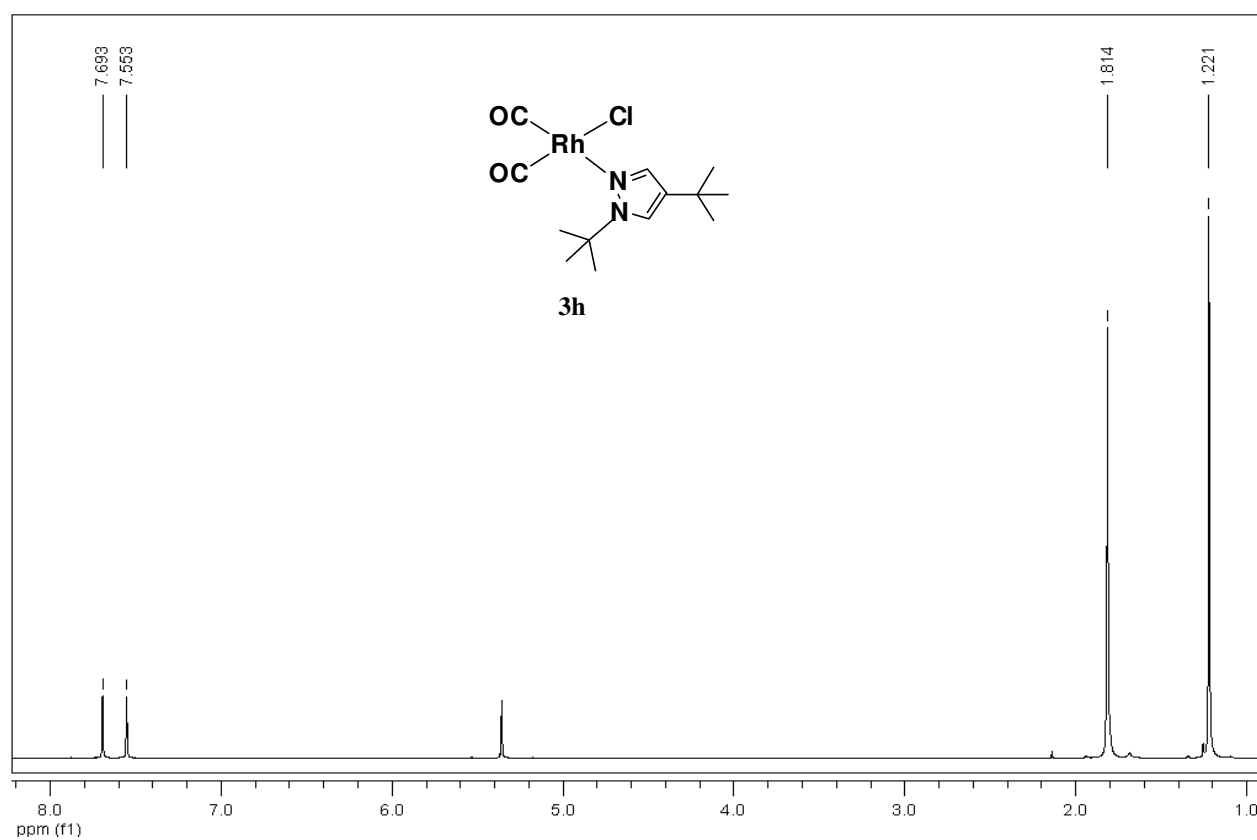


Figure 14. $^{13}\text{C}\{^1\text{H}\}$ NMR spectrum of **3h** at 193 K in CD_2Cl_2 .

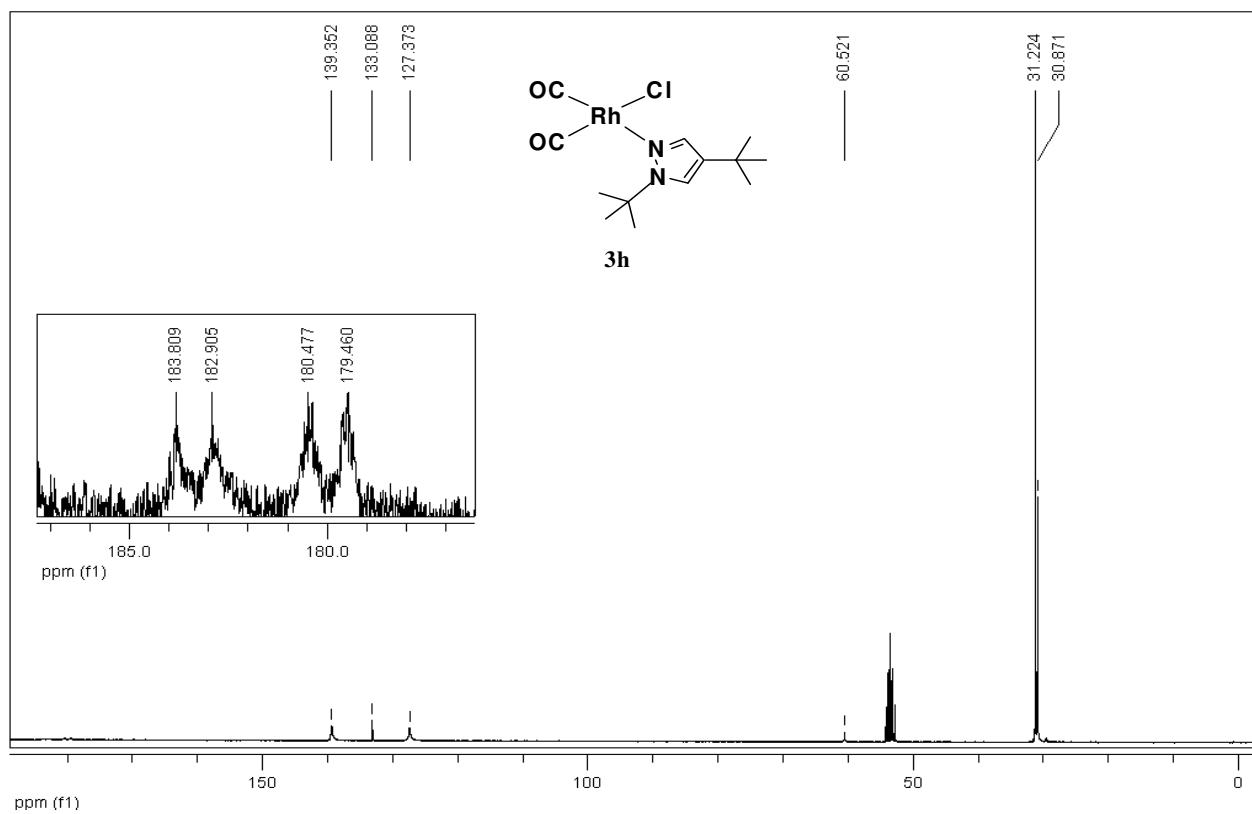


Figure 15. $^{13}\text{C}\{^1\text{H}\}$ NMR spectrum of **3h** at 298 K in CD_2Cl_2 .

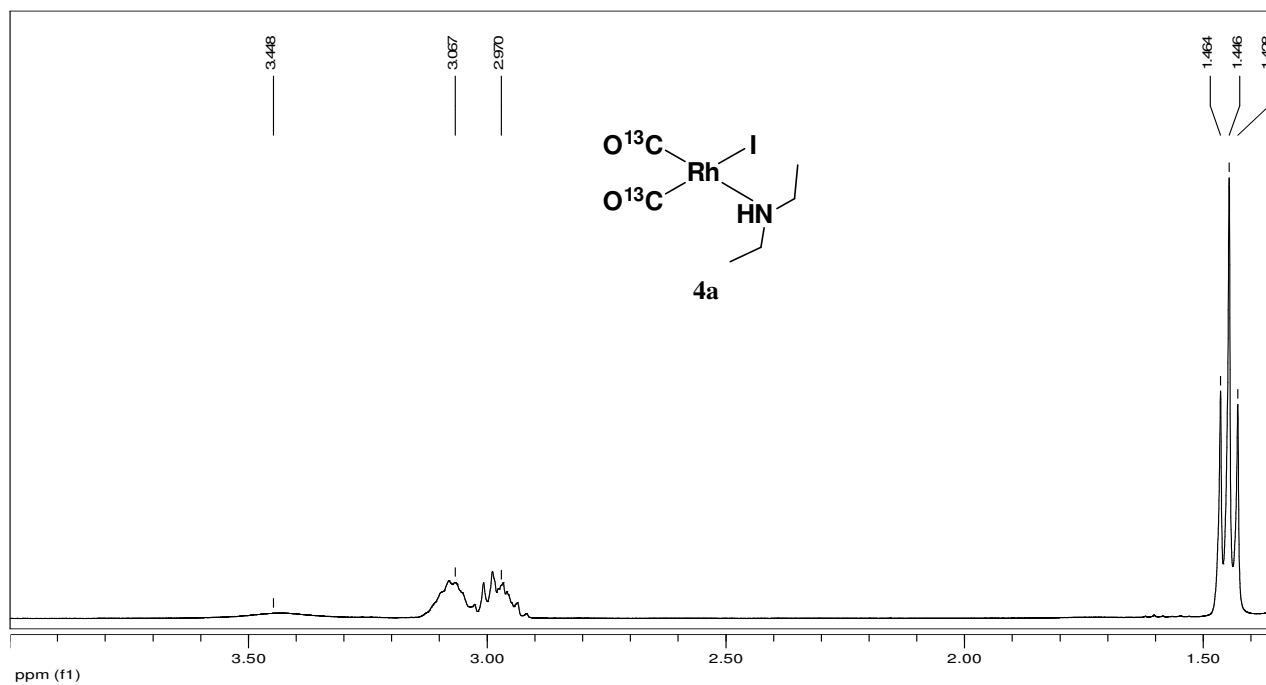


Figure 16. ^1H NMR spectrum of **4a** at 298 K in CD_2Cl_2 .

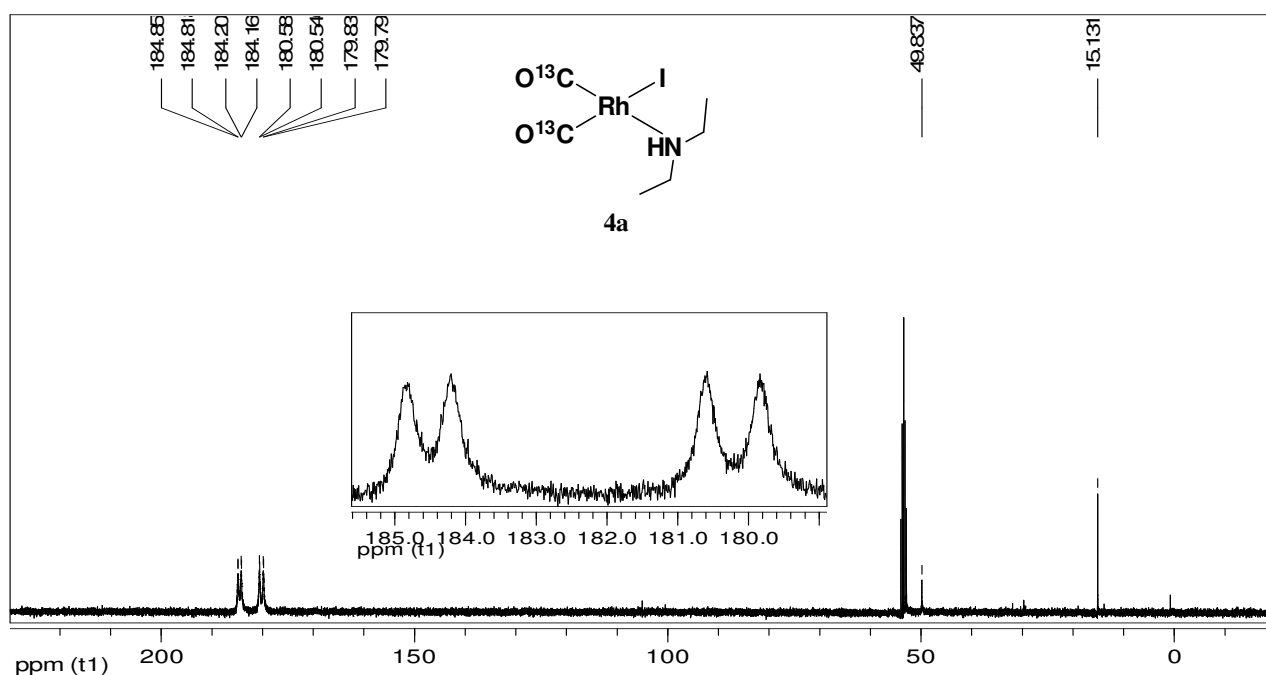


Figure 17. $^{13}\text{C}\{^1\text{H}\}$ NMR spectrum of **4a** at 298 K in CD_2Cl_2 .

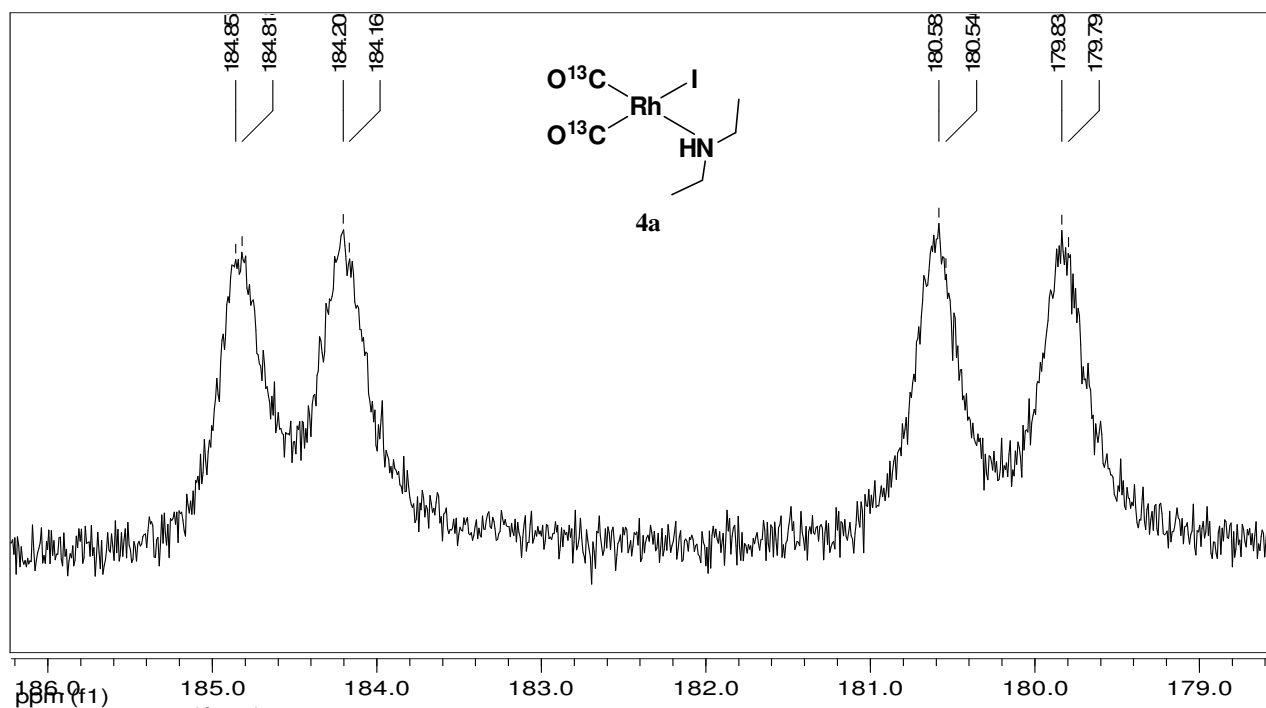


Figure 18. $^{13}\text{C}\{^1\text{H}\}$ NMR spectrum of **4a** at 298 K in CD_2Cl_2 in the carbonyl region. No dynamic ligand-exchange occurs. Two double doublets are represented: $^2J_{^{13}\text{CO}-^{13}\text{CO}} \sim 4$ Hz.

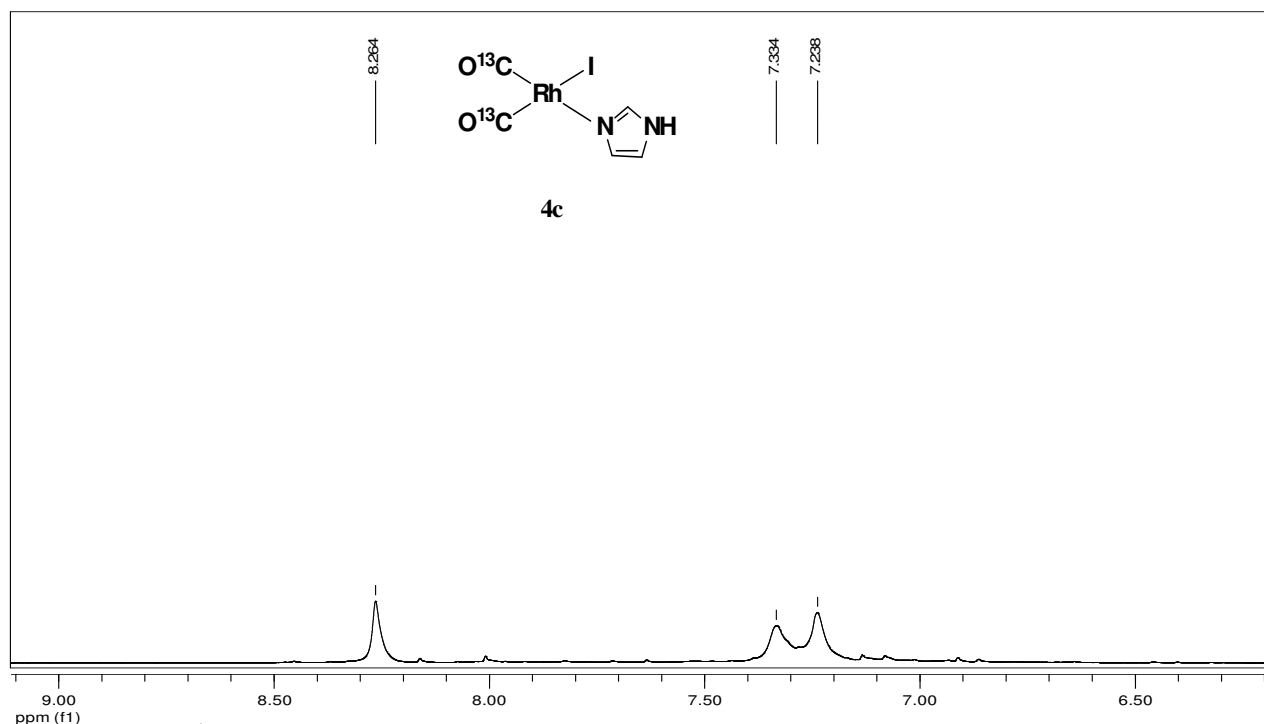


Figure 19. ^1H NMR spectrum of **4c** at 298 K in CD_3OD . (N-H signal was not detected).

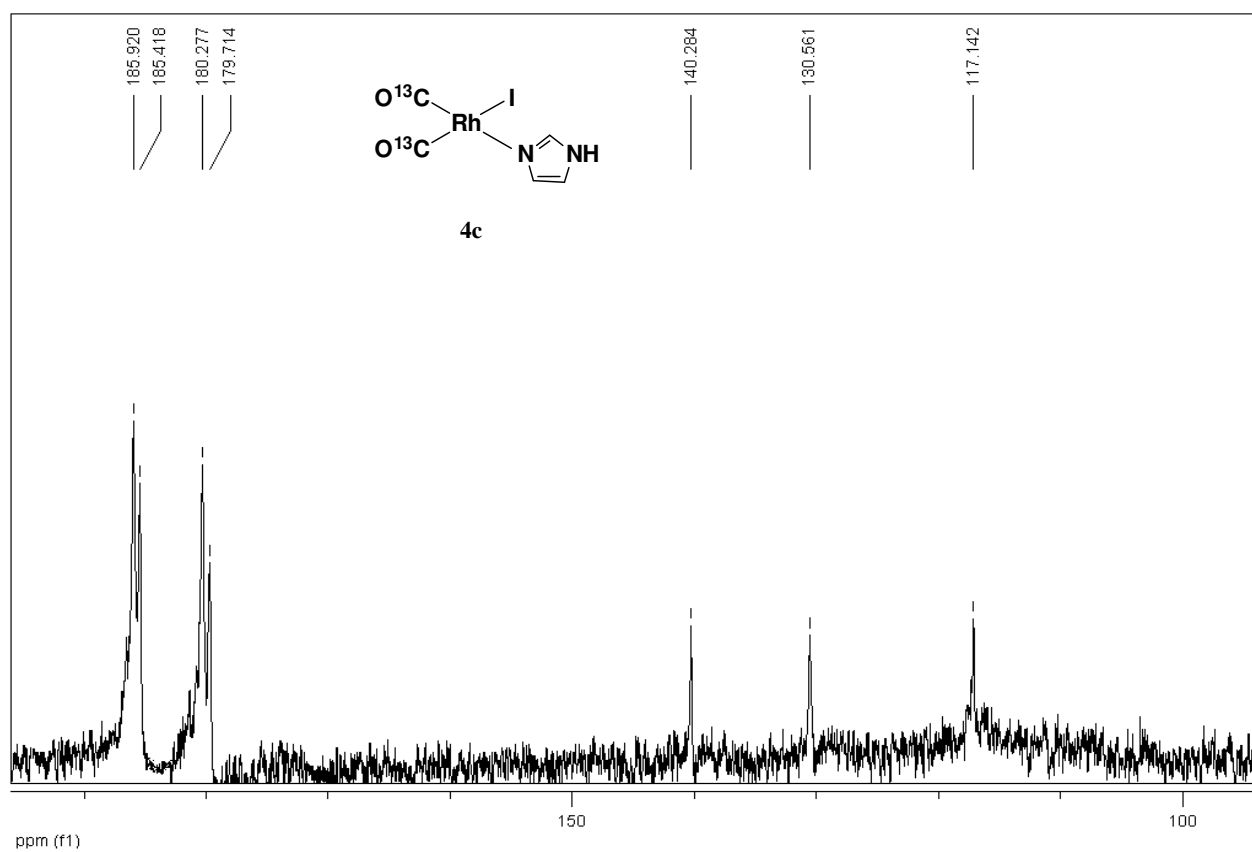


Figure 20. $^{13}\text{C}\{^1\text{H}\}$ NMR spectrum of **4c** at 298 K in CD_3OD .

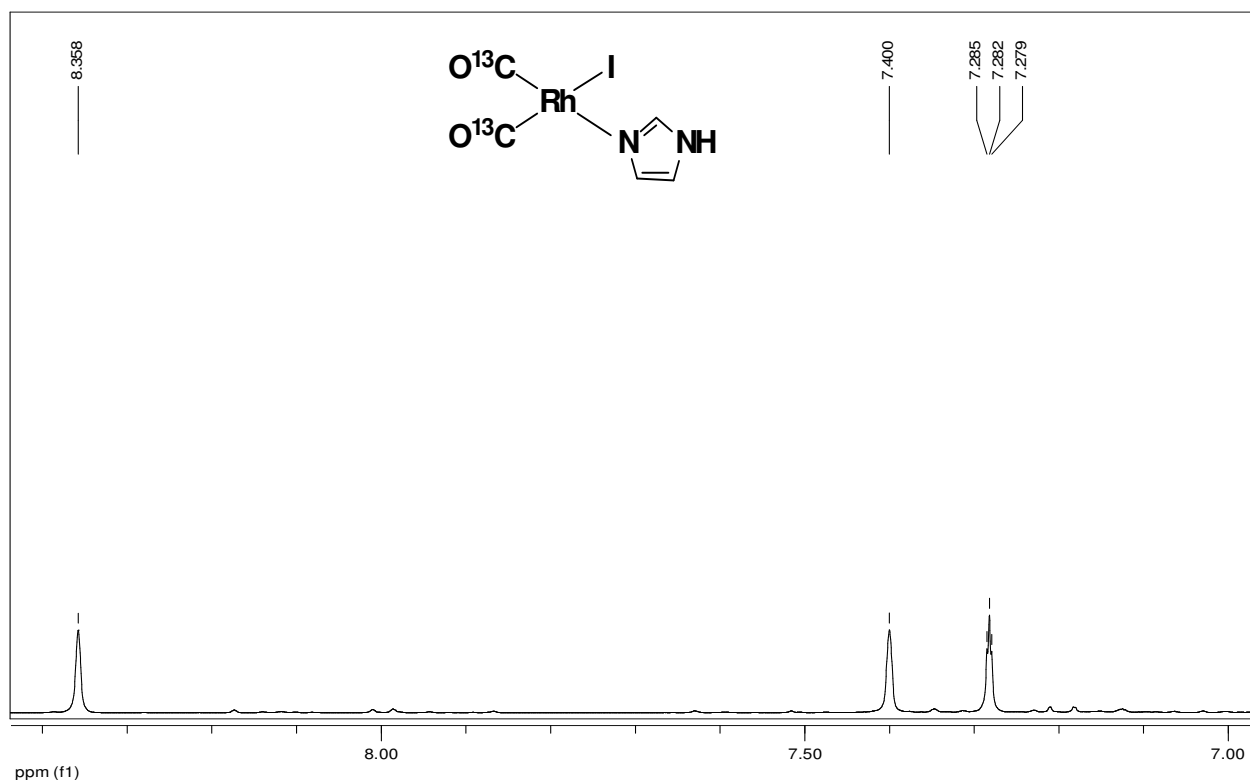


Figure 21. ¹H NMR spectrum of **4c** at 233 K in CD₃OD. (N-H signal was not detected).

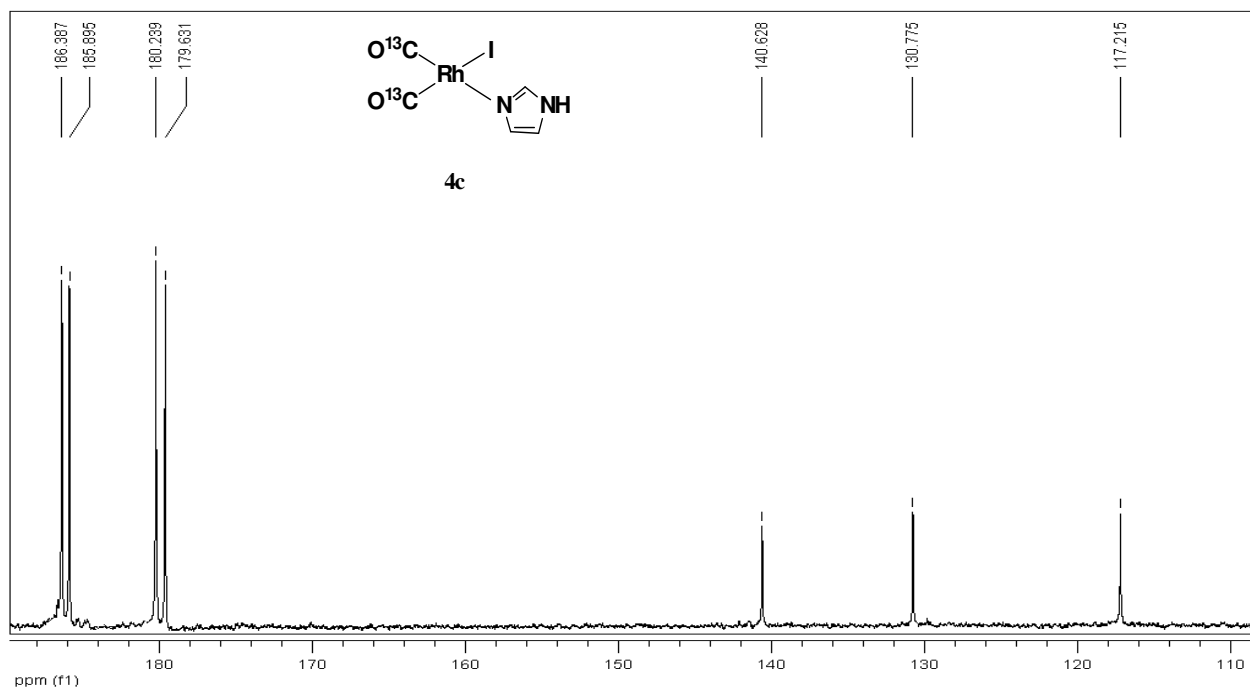


Figure 22. ¹³C{¹H} NMR spectrum of **4c** at 233 K in CD₃OD.

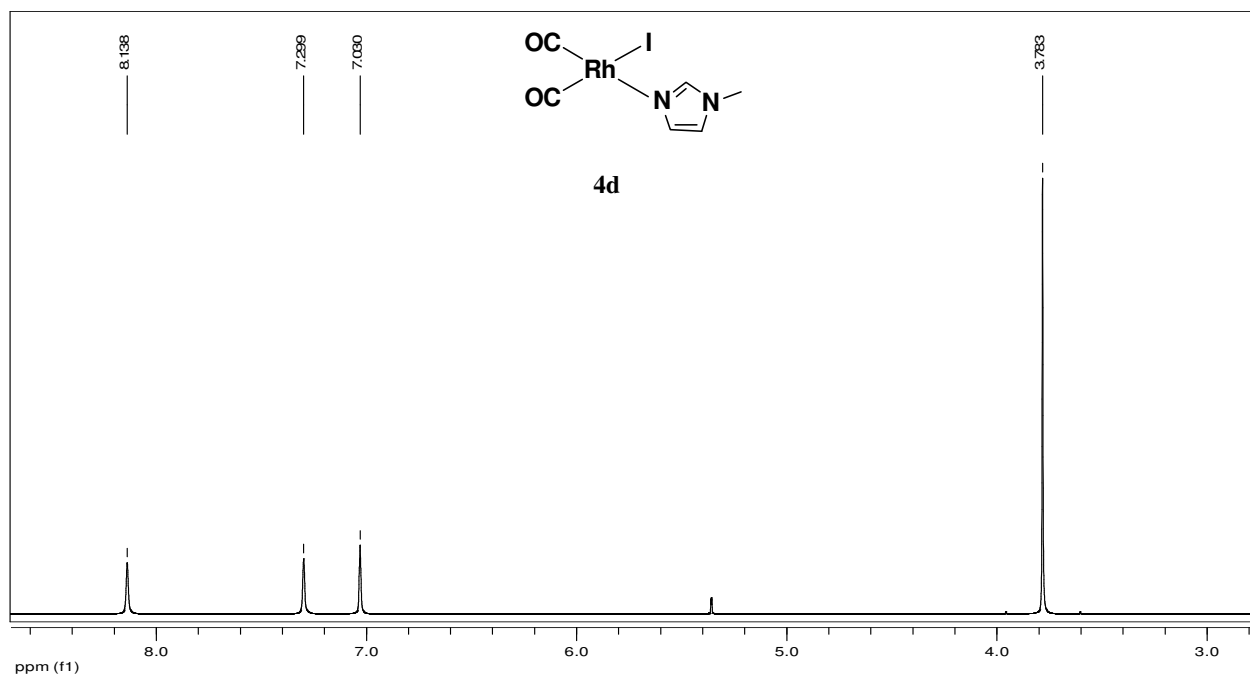


Figure 23. ^1H NMR spectrum of **4d** at 298 K in CD_2Cl_2 .

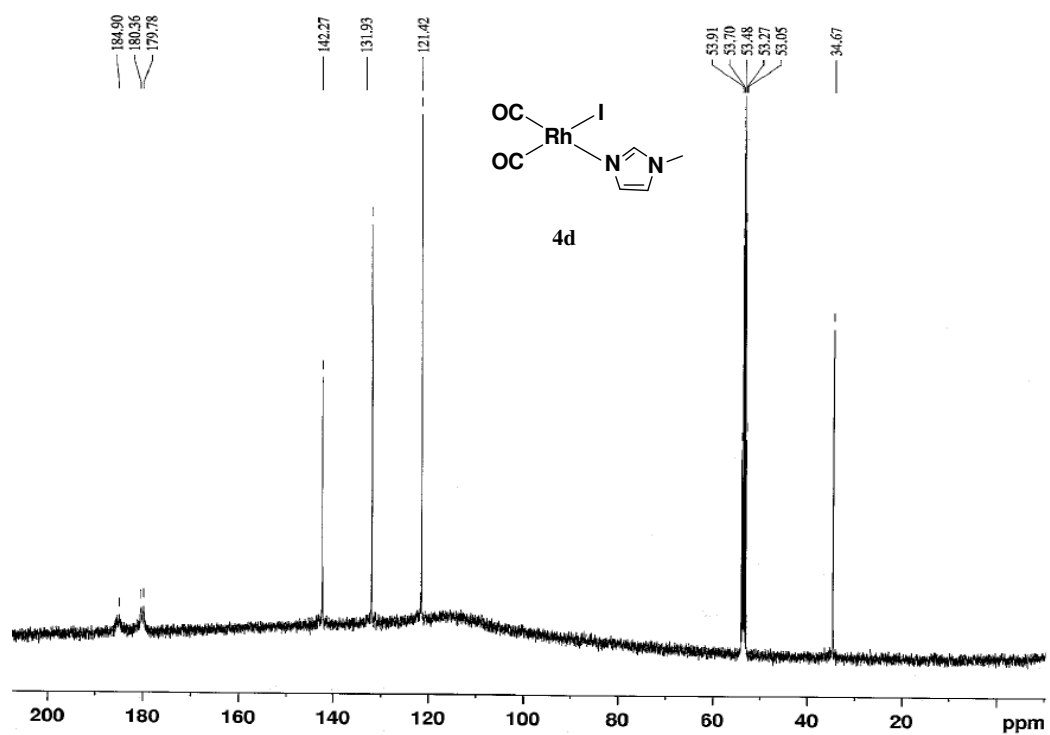


Figure 24. $^{13}\text{C}\{^1\text{H}\}$ NMR spectrum of **4d** at 298 K in CD_2Cl_2 .

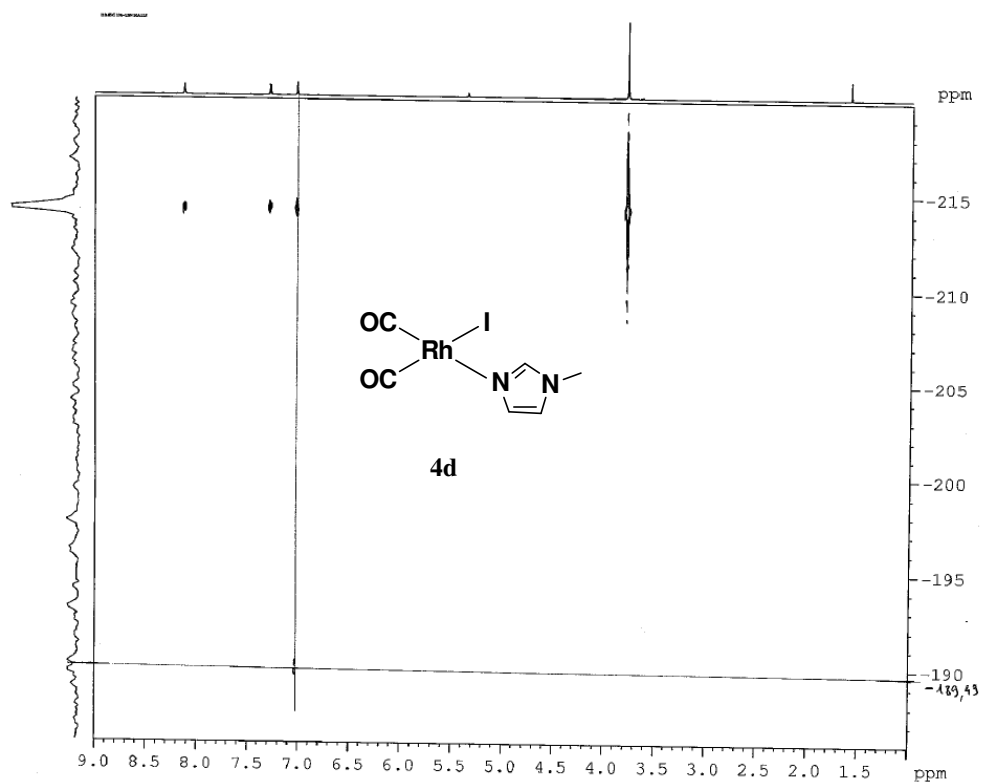


Figure 25. 2D $(^1\text{H}-^{15}\text{N})$ HMBC NMR spectrum of **4d** at 298 K in CD_2Cl_2 .

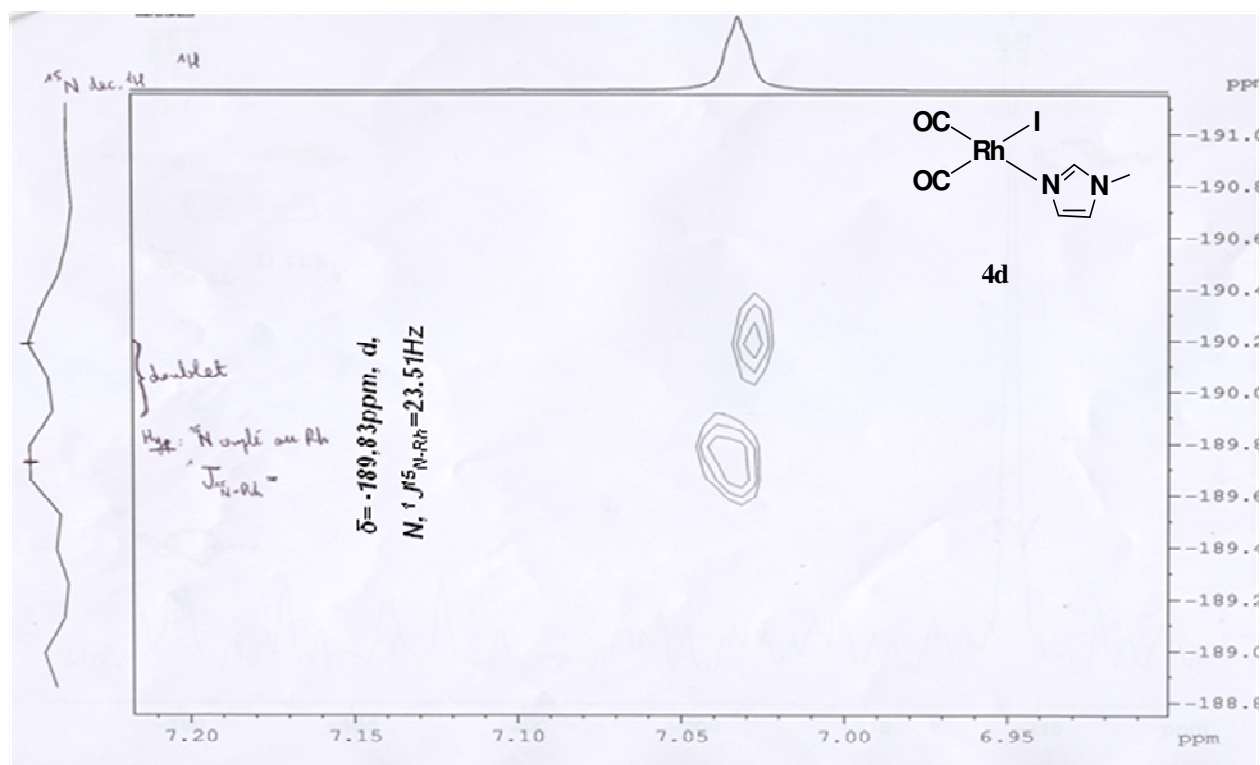


Figure 26. Zoomed 2D $(^1\text{H}-^{15}\text{N})$ HMBC NMR spectrum of **4d** at 298 K in CD_2Cl_2 .

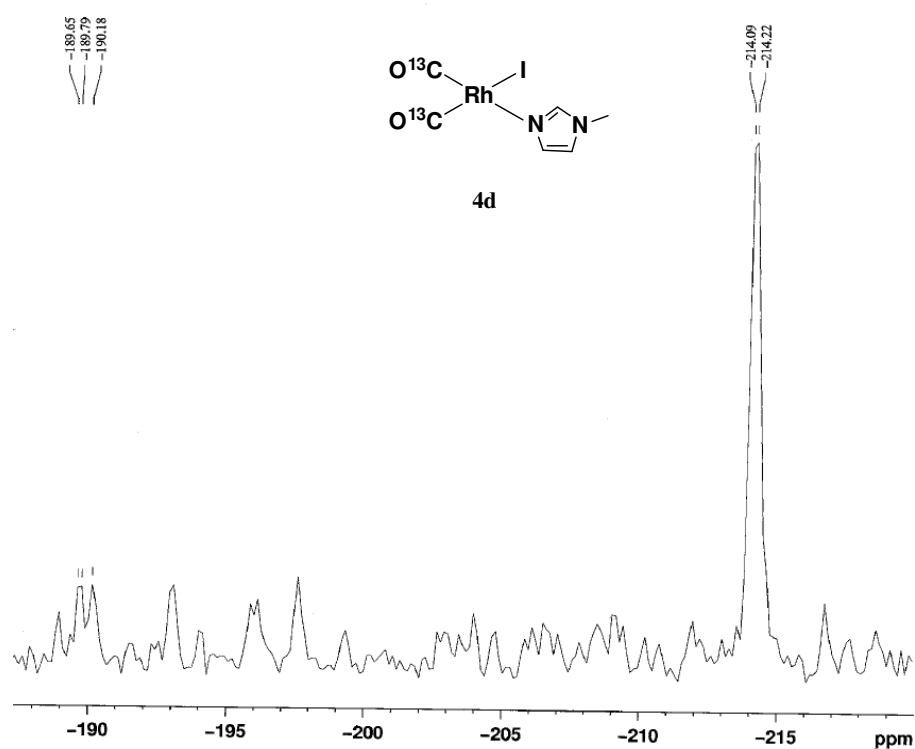


Figure 27. 2D (^1H - ^{15}N) HMBC NMR: ^{15}N projection spectrum of **4d** at 298 K in CD_2Cl_2 .

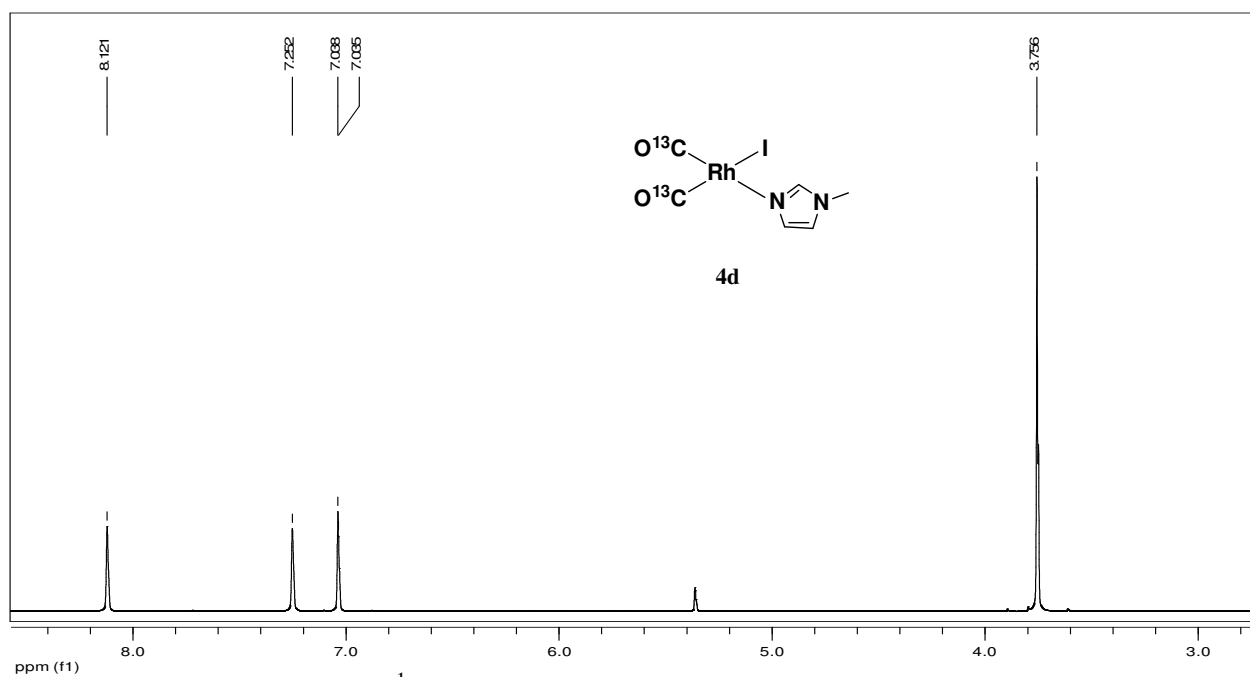


Figure 28. ^1H NMR spectrum of **4d** at 235 K in CD_2Cl_2 .

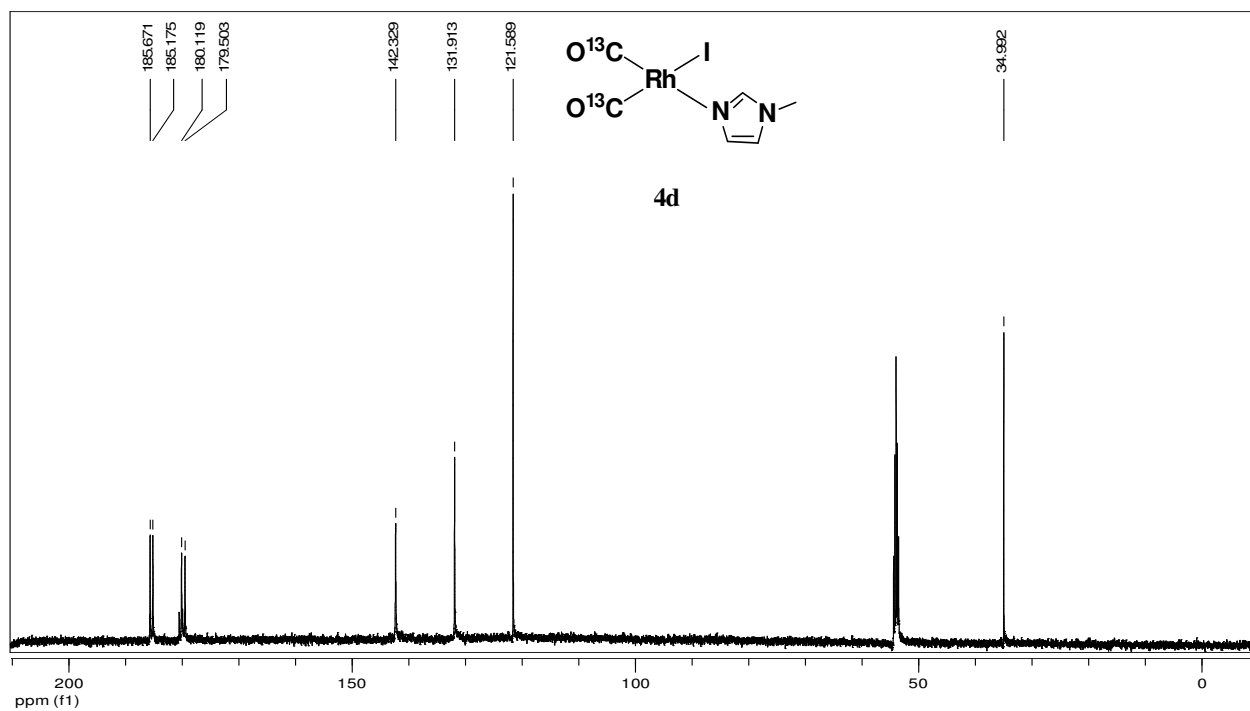


Figure 29. $^{13}\text{C}\{^1\text{H}\}$ NMR spectrum of **4d** at 235 K in CD_2Cl_2 .

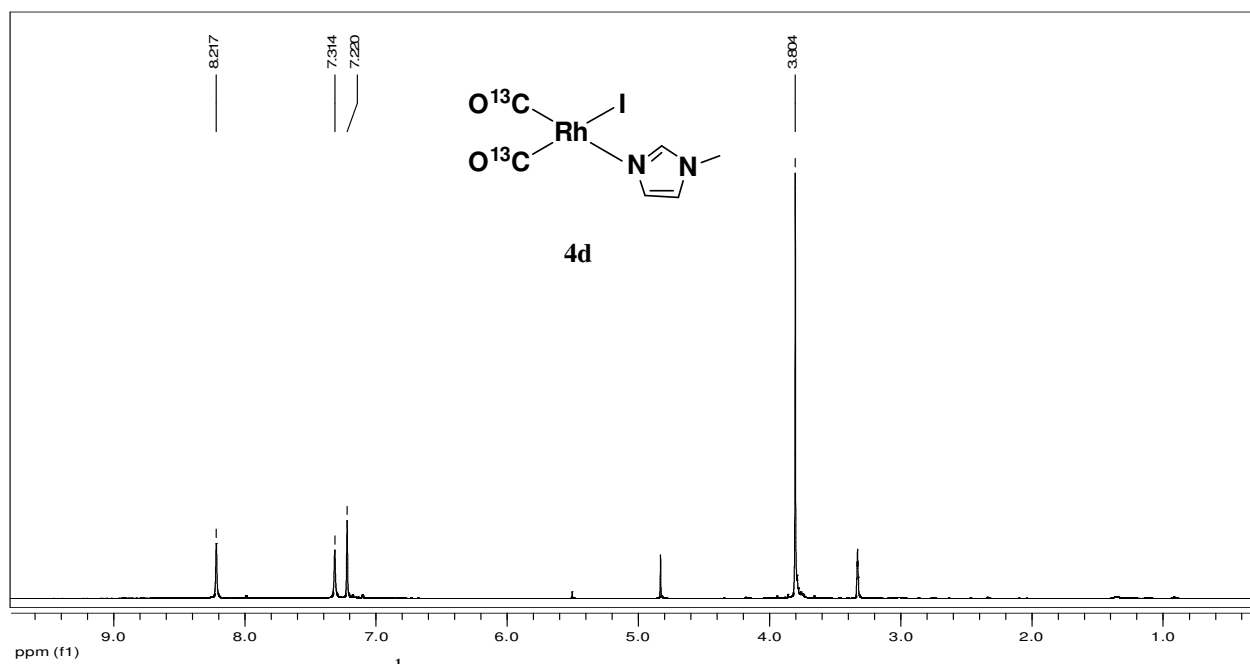


Figure 30. ^1H NMR spectrum of **4d** at 298 K in CD_3OD .

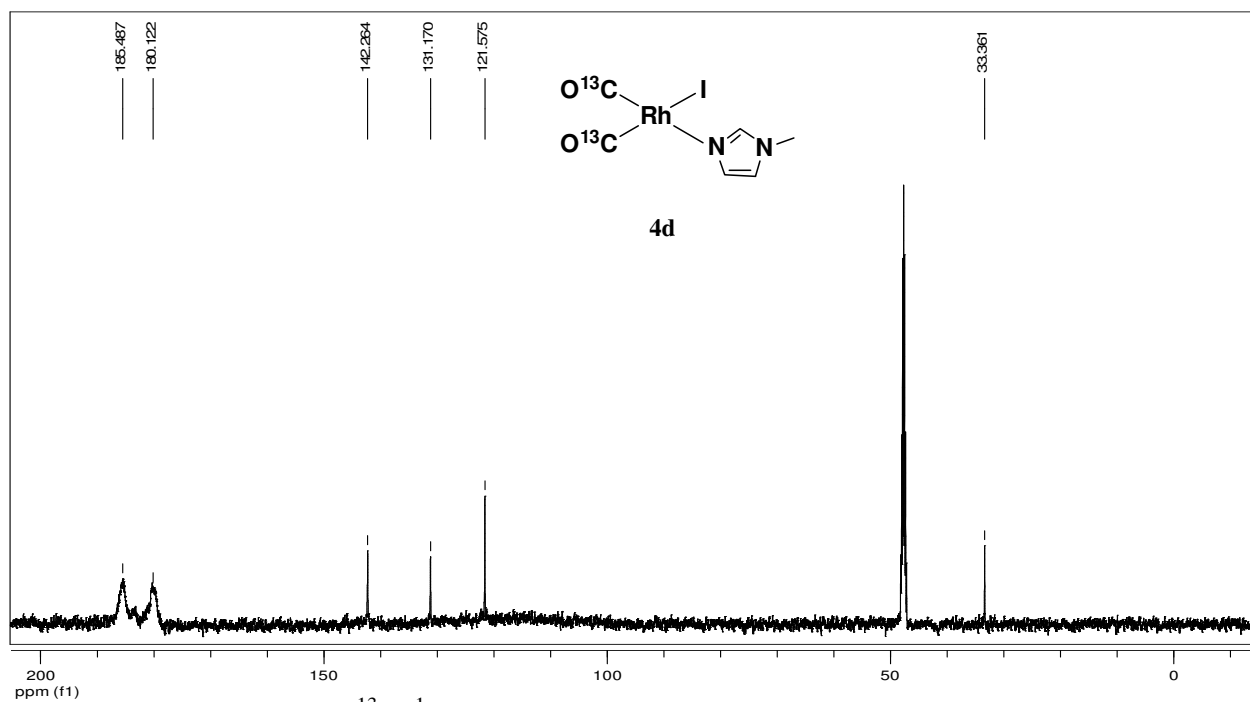


Figure 31. $^{13}\text{C}\{^1\text{H}\}$ NMR spectrum of **4d** at 298 K in CD_3OD .

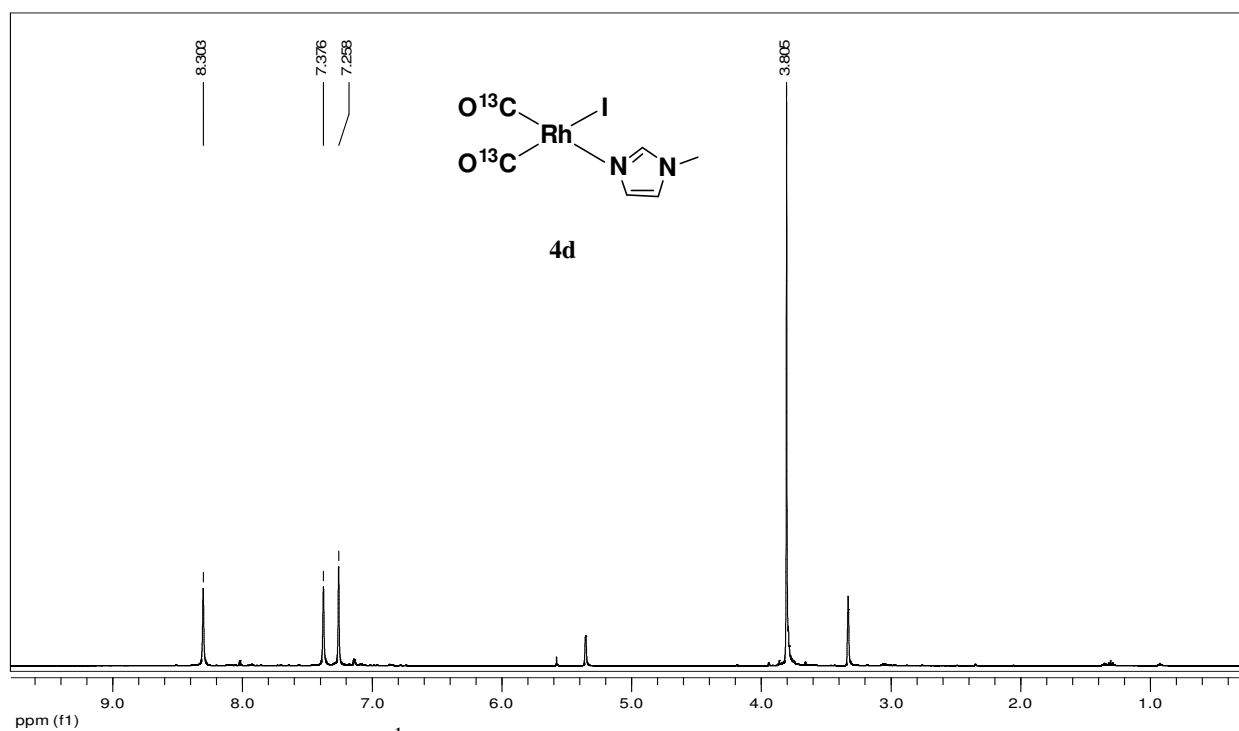


Figure 32. ^1H NMR spectrum of **4d** at 243 K in CD_3OD .

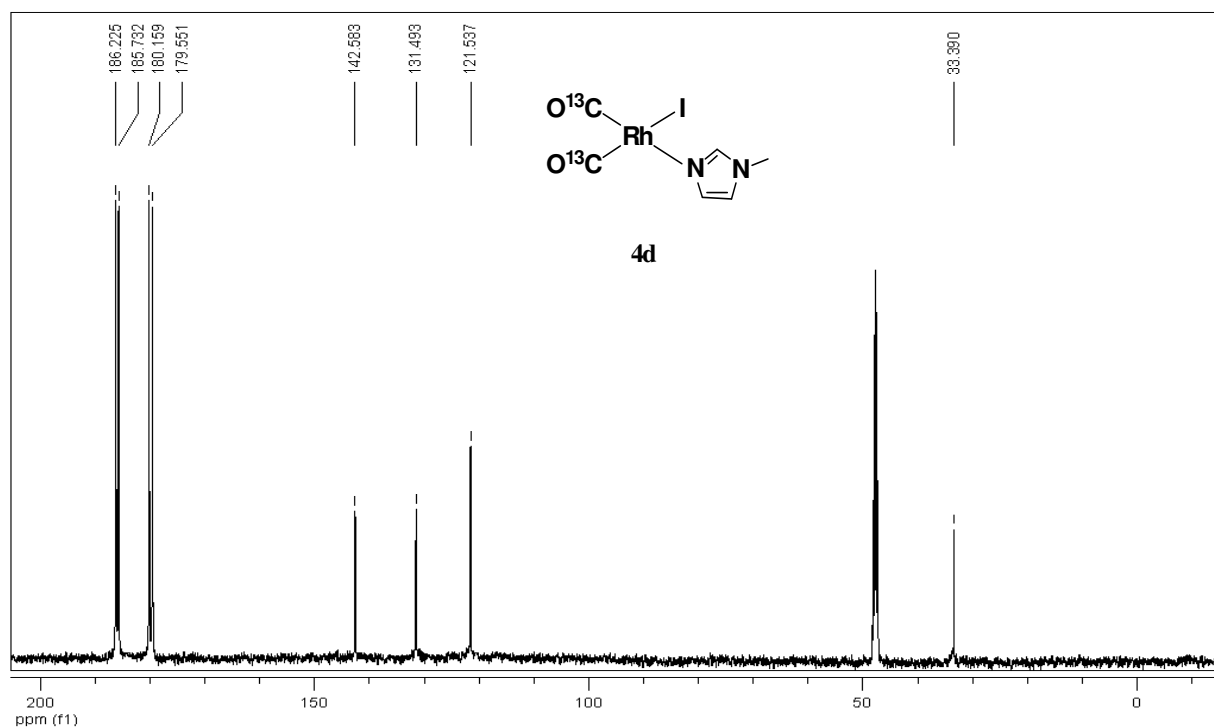


Figure 33. $^{13}\text{C}\{^1\text{H}\}$ NMR spectrum of **4d** at 243 K in CD_3OD .

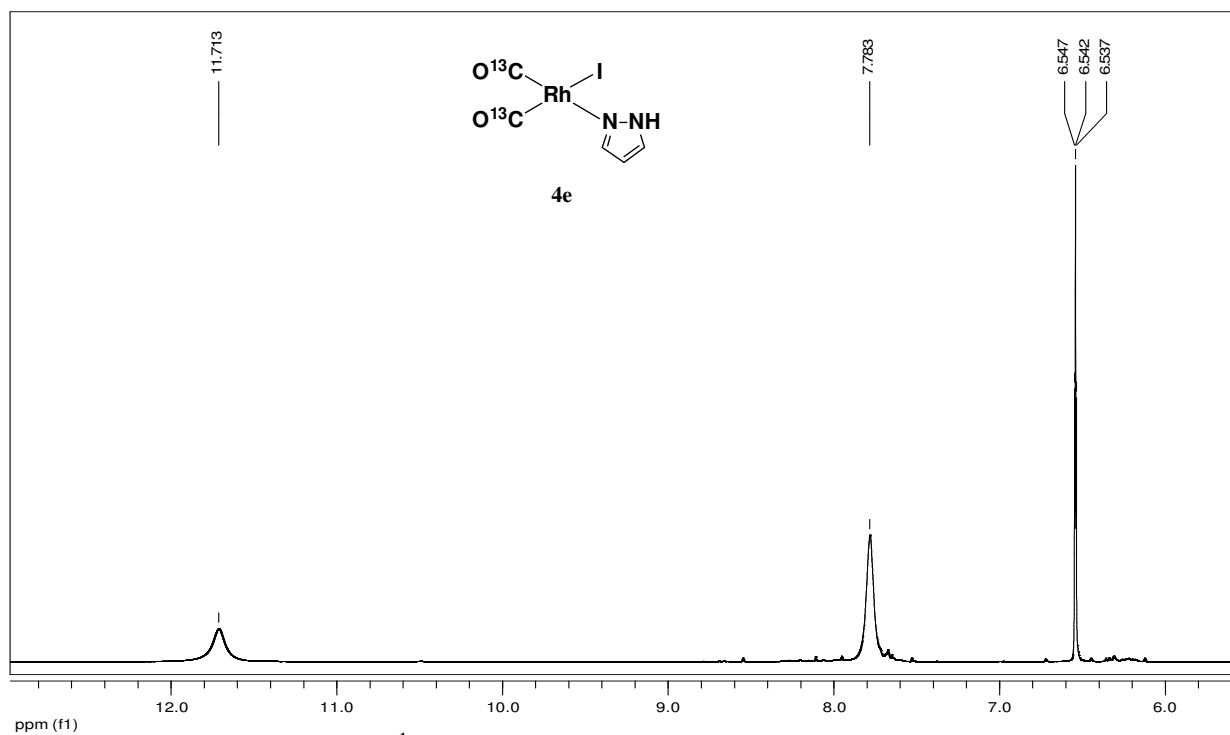


Figure 34. ^1H NMR spectrum of **4e** at 298 K in CD_2Cl_2 .

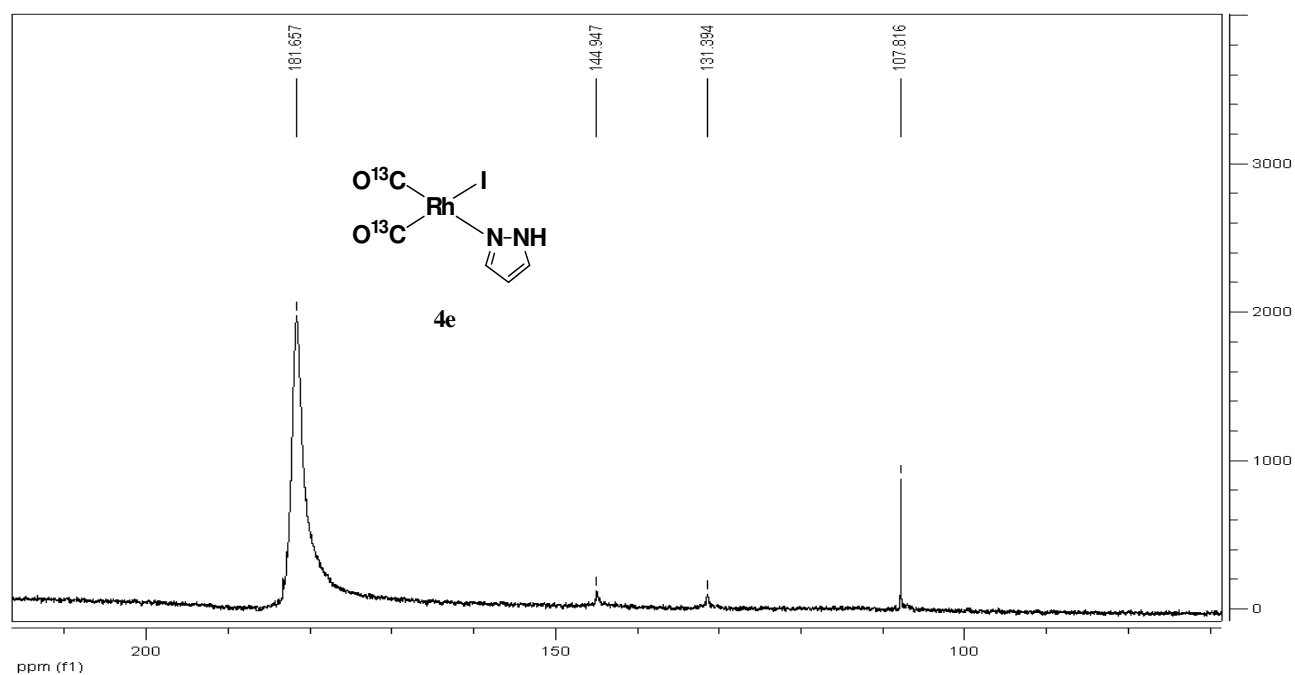


Figure 35. $^{13}\text{C}\{^1\text{H}\}$ NMR spectrum of **4e** at 298 K in CD_2Cl_2 .

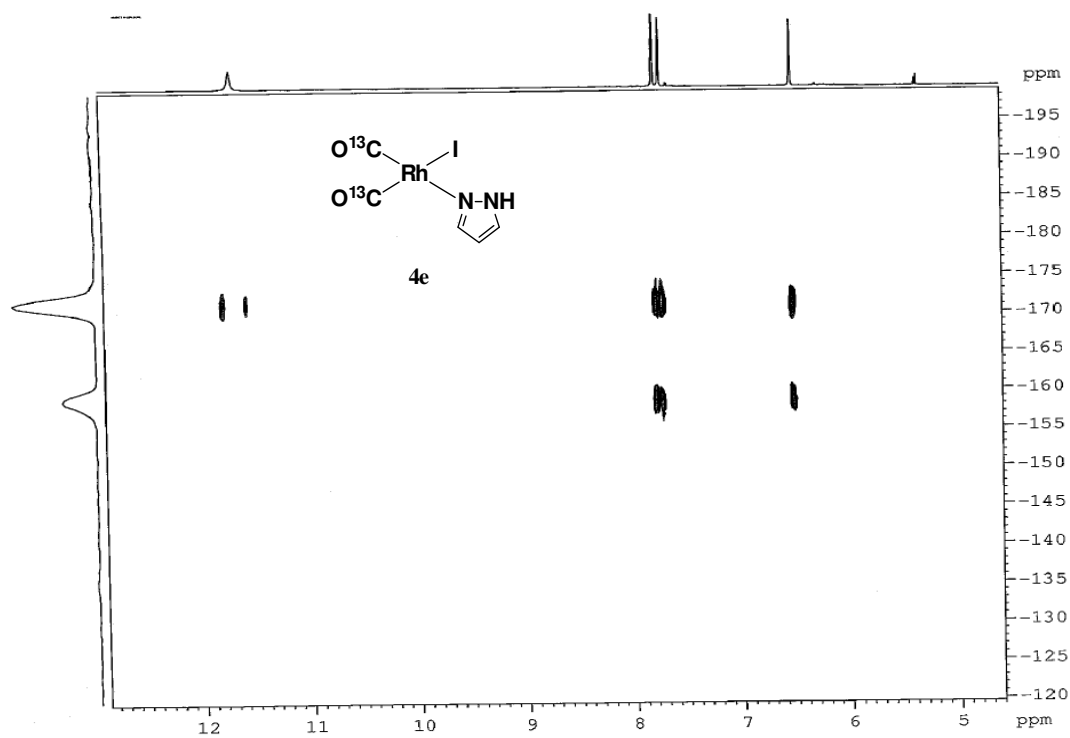


Figure 36. 2D $(^1\text{H}-^{15}\text{N})$ HMBC NMR spectrum of **4e** at 250 K in CD_2Cl_2 .

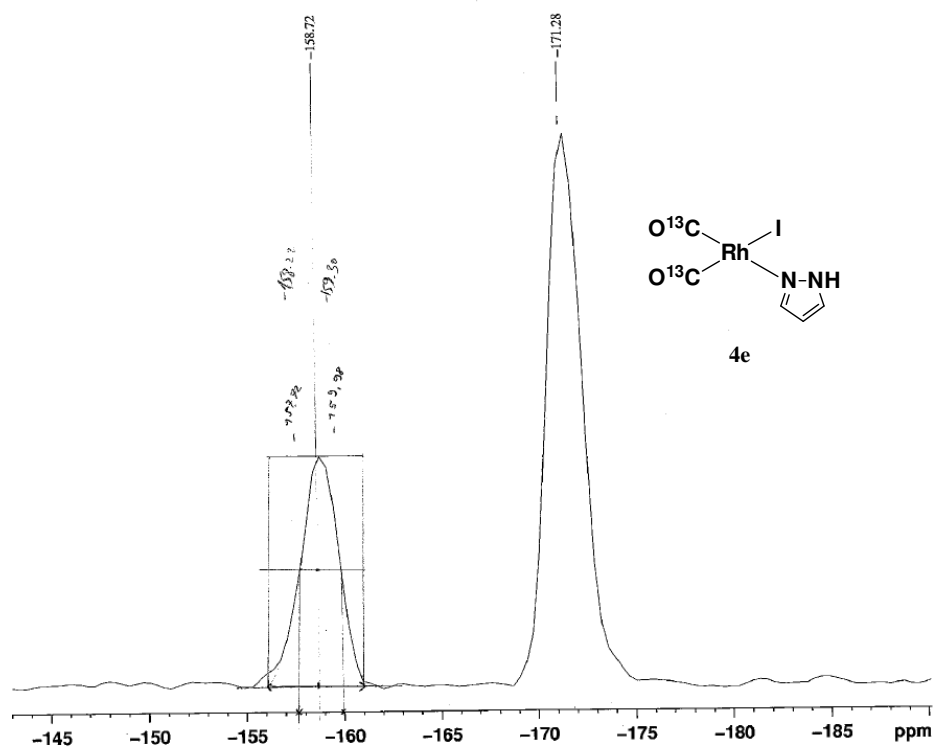


Figure 37. 2D $(^1\text{H}-^{15}\text{N})$ HMBC NMR: ^{15}N projection spectrum of **4e** at 250 K in CD_2Cl_2 .

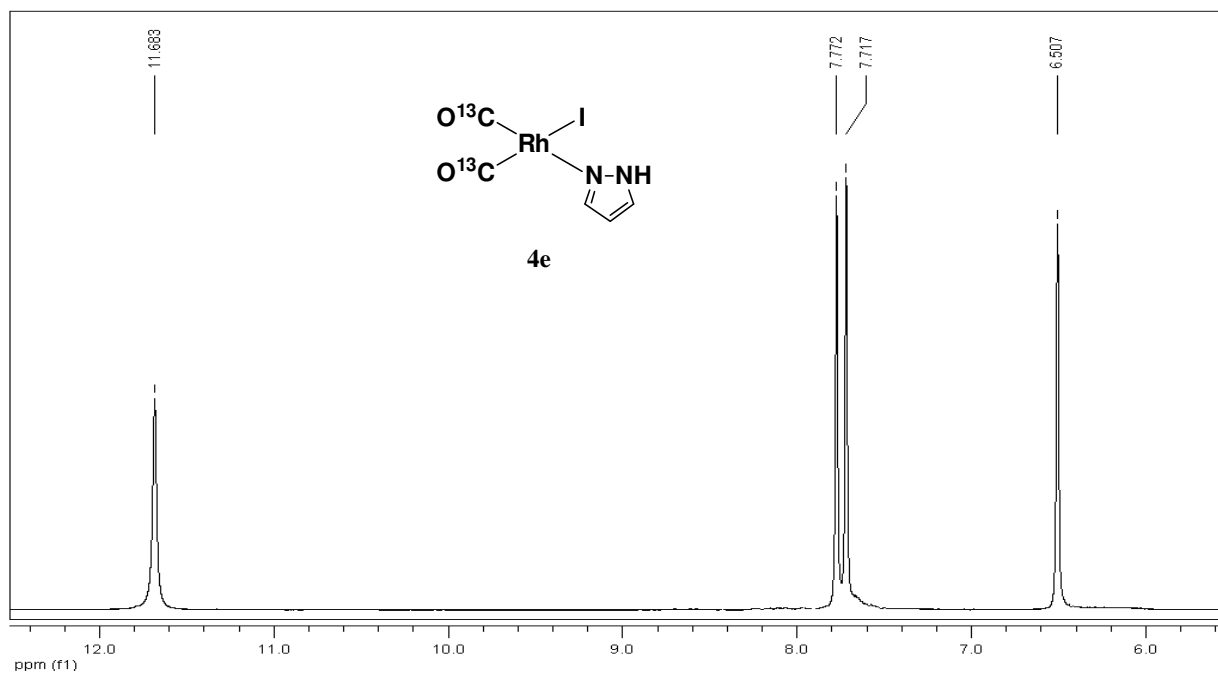


Figure 38. ^1H NMR spectrum of **4e** at 223 K in CD_2Cl_2 .

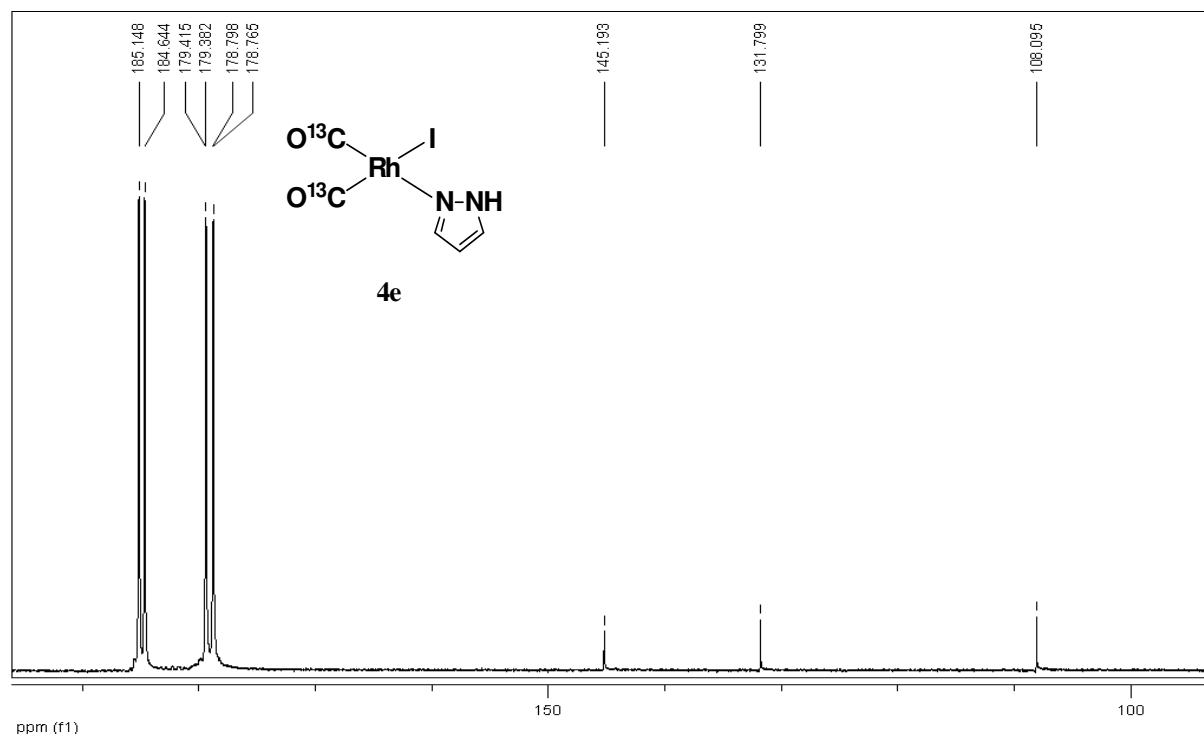


Figure 39. $^{13}\text{C}\{^1\text{H}\}$ NMR spectrum of **4e** at 223 K in CD_2Cl_2 .

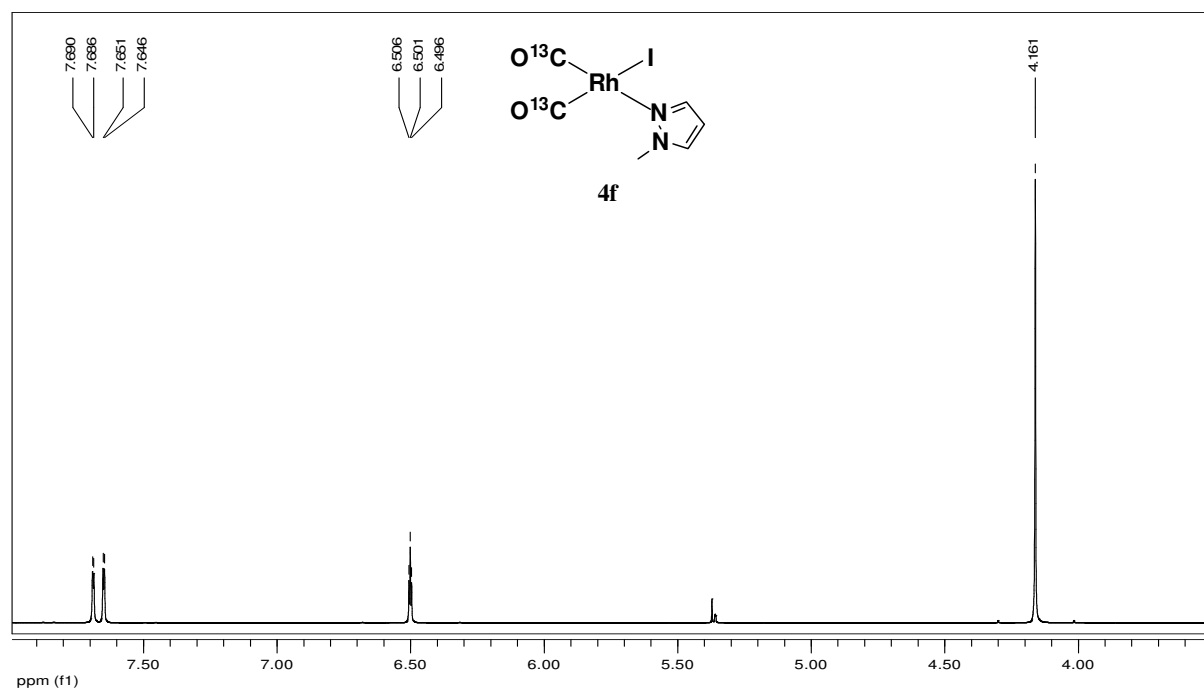


Figure 40. ^1H NMR spectrum of **4f** at 298 K in CD_2Cl_2 .

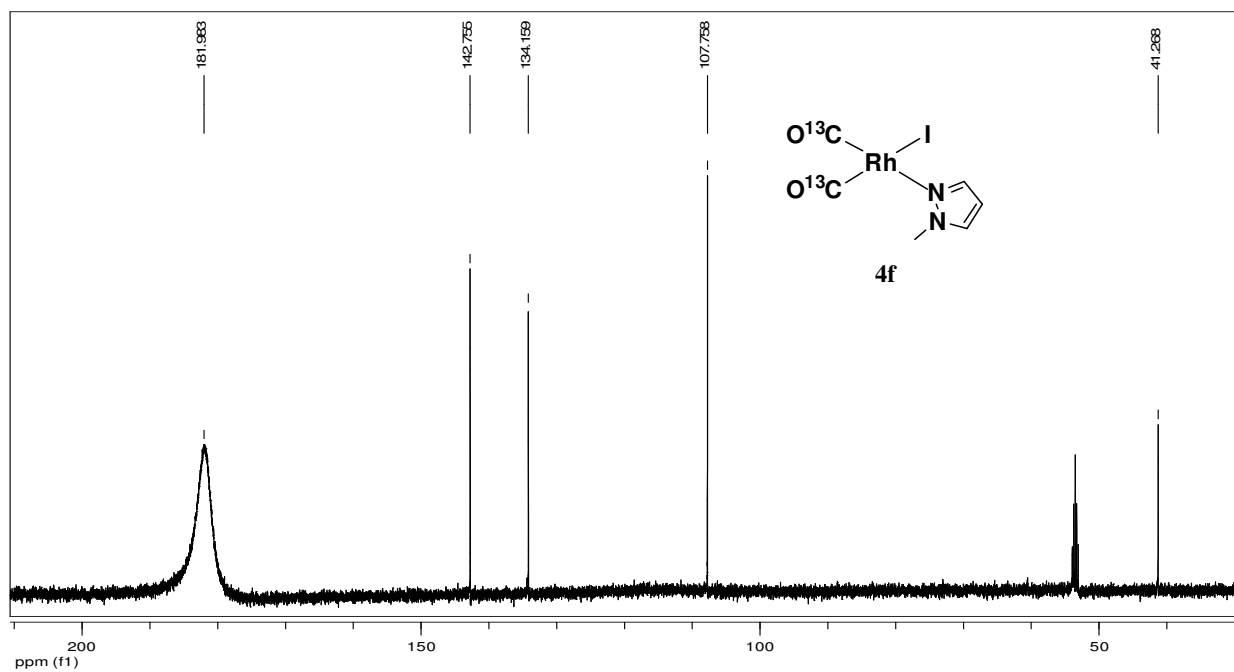


Figure 41. $^{13}\text{C}\{^1\text{H}\}$ NMR spectrum of **4f** at 298 K in CD_2Cl_2 .

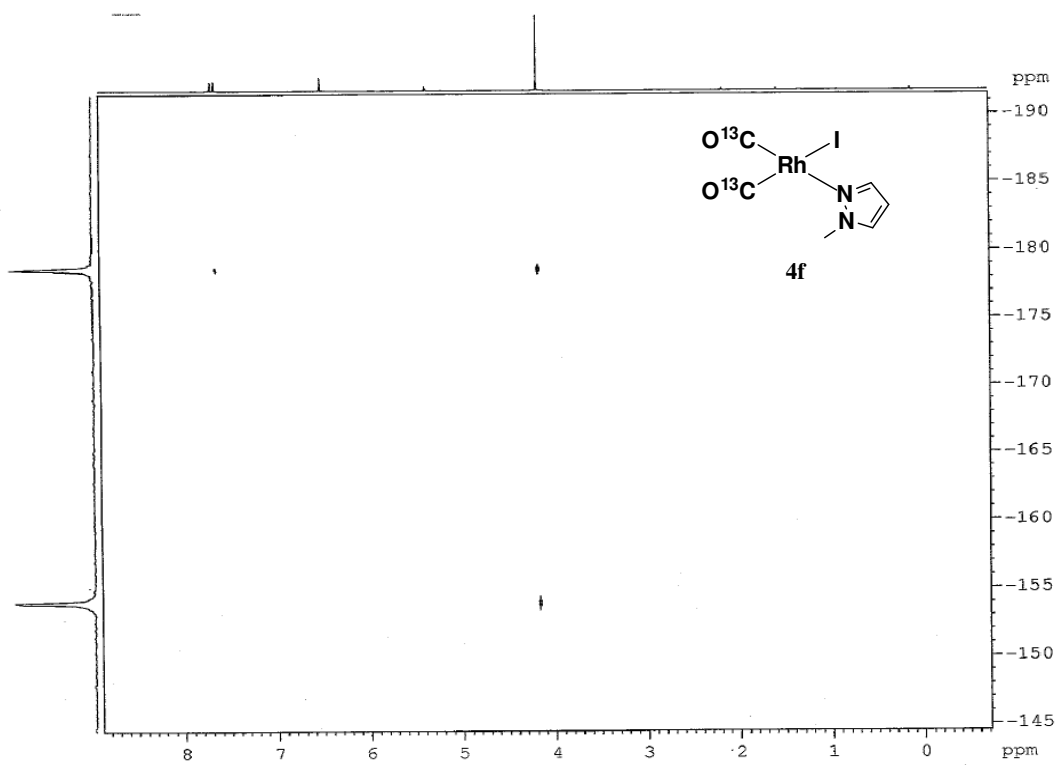


Figure 42. 2D $(^1\text{H}-^{15}\text{N})$ HMBC NMR spectrum of **4f** at 298 K in CD_2Cl_2 .

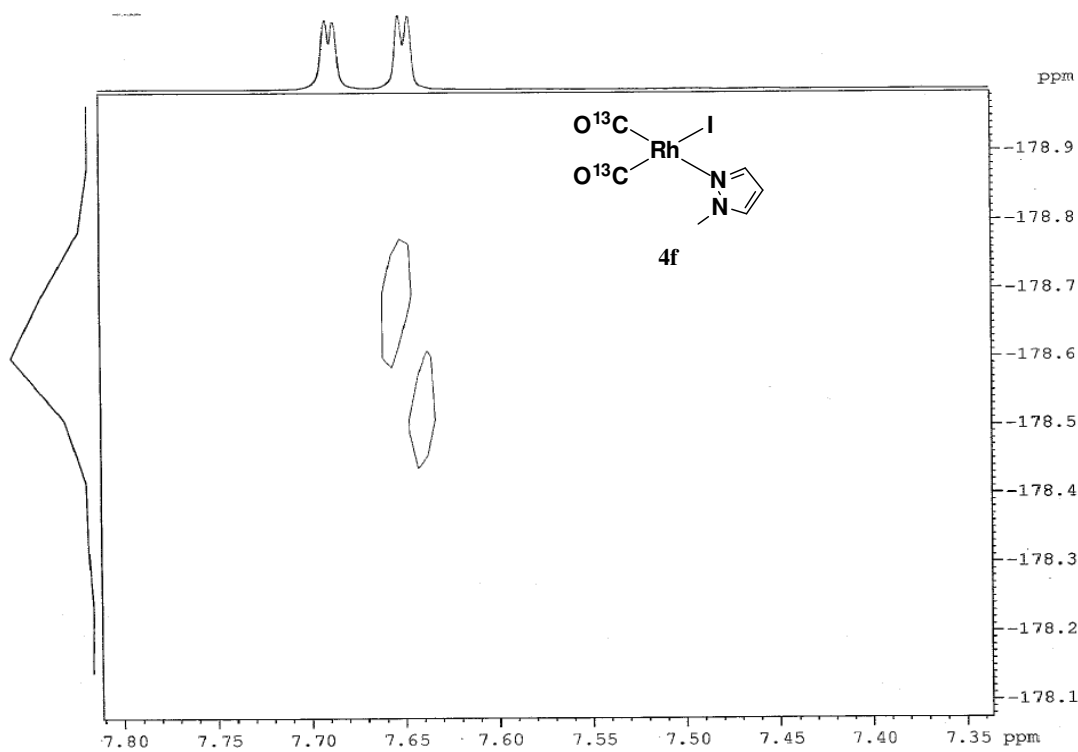


Figure 43. Zoomed 2D ($^1\text{H}-^{15}\text{N}$) HMBC NMR spectrum of **4f** at 298 K in CD_2Cl_2 .

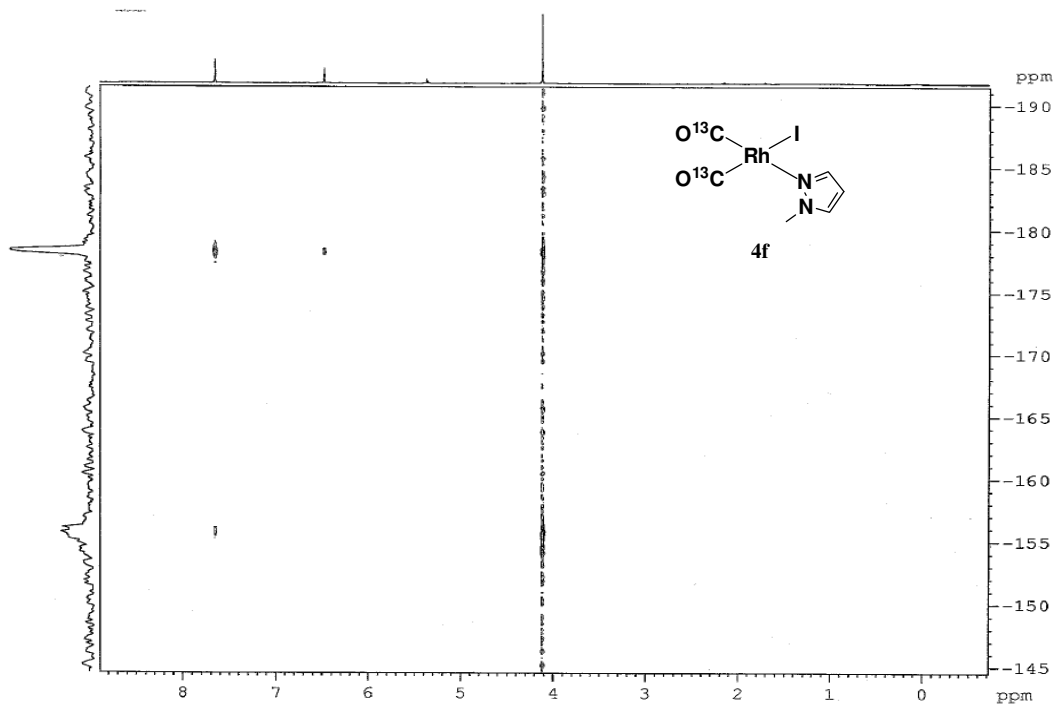


Figure 44. 2D ($^1\text{H}-^{15}\text{N}$) HMBC NMR spectrum of **4f** at 230 K in CD_2Cl_2 .

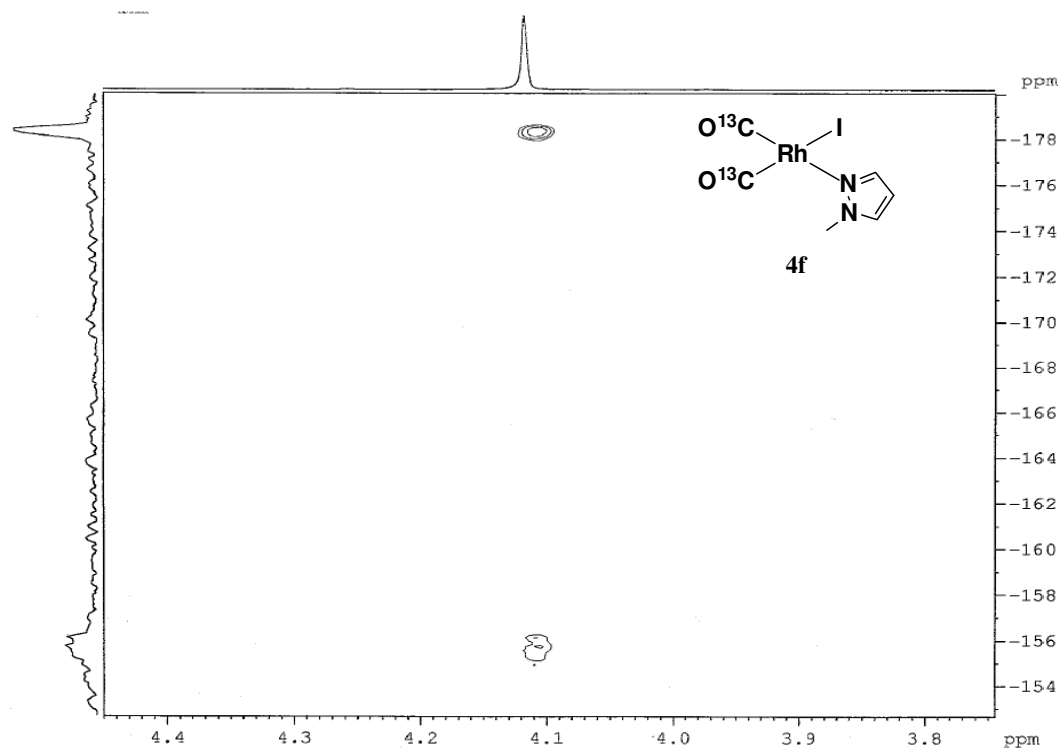


Figure 45. Zoomed 2D (^1H - ^{15}N) HMBC NMR spectrum of **4f** at 230 K in CD_2Cl_2 .

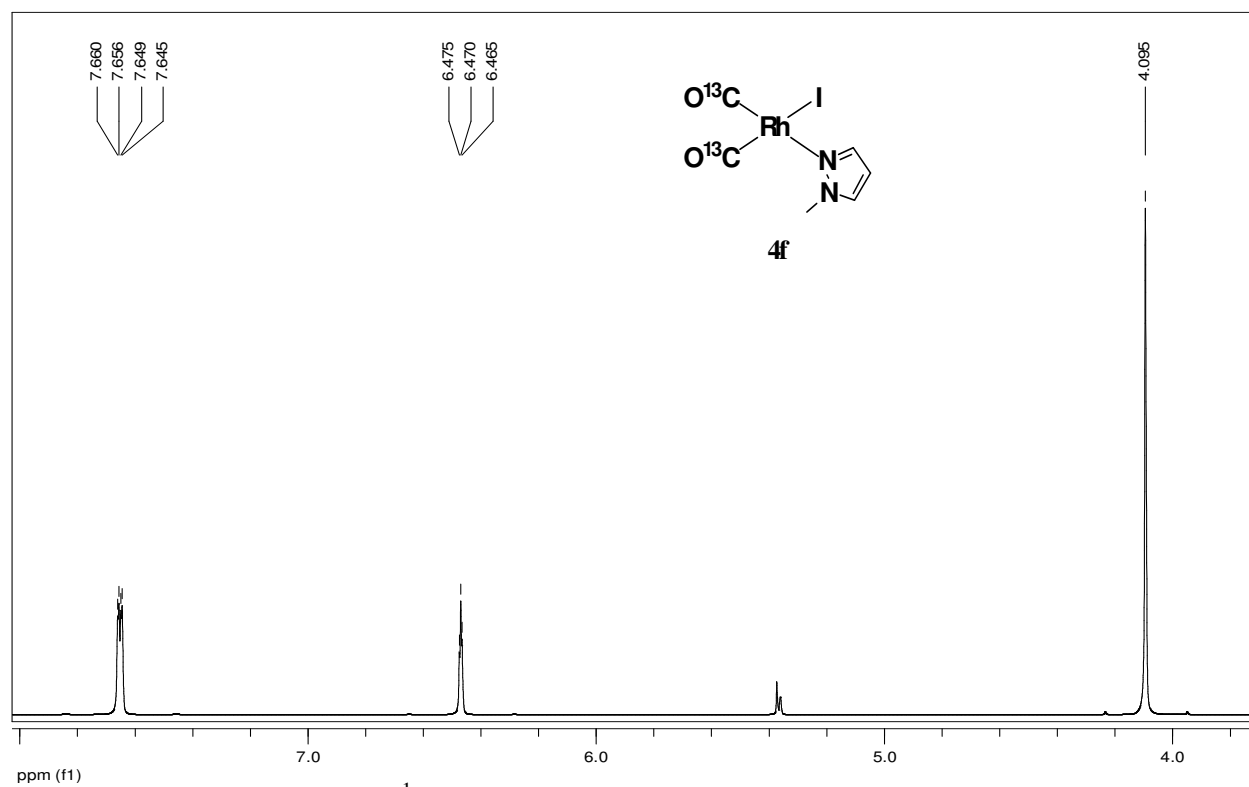


Figure 46. ^1H NMR spectrum of **4f** at 203 K in CD_2Cl_2 .

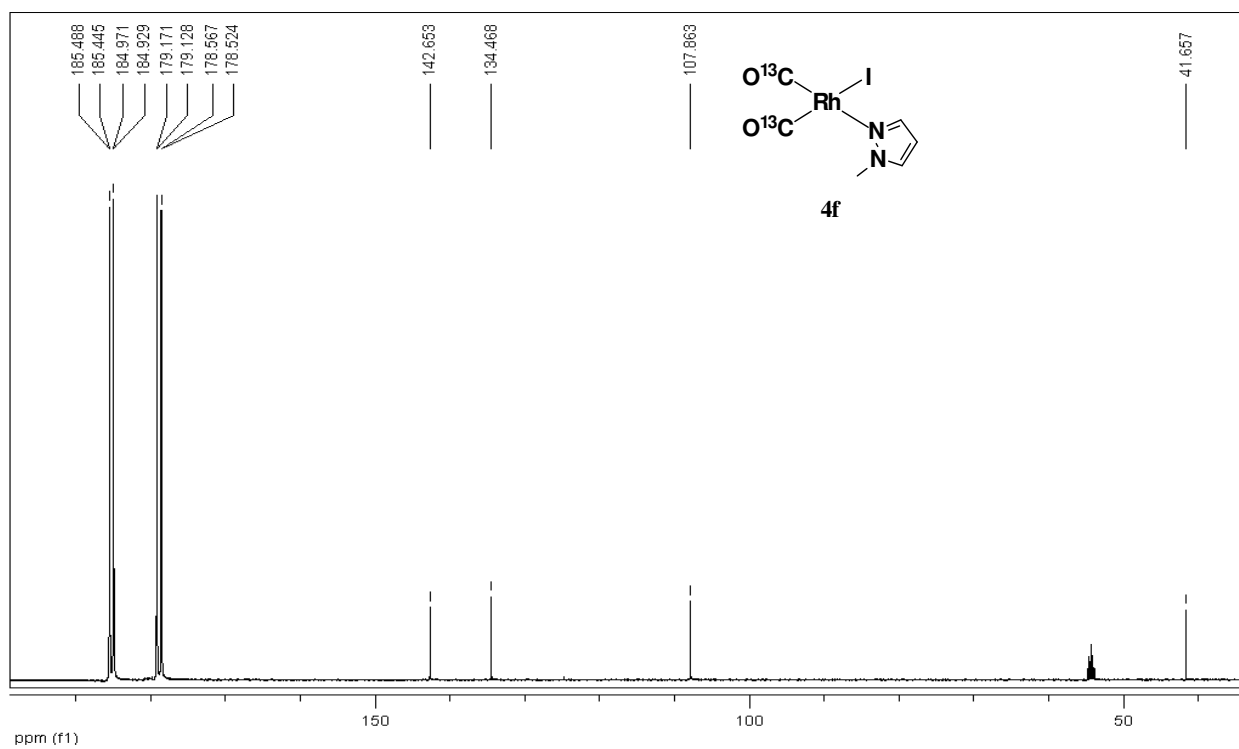


Figure 47. $^{13}\text{C}\{^1\text{H}\}$ NMR spectrum of **4f** at 203 K in CD_2Cl_2 .

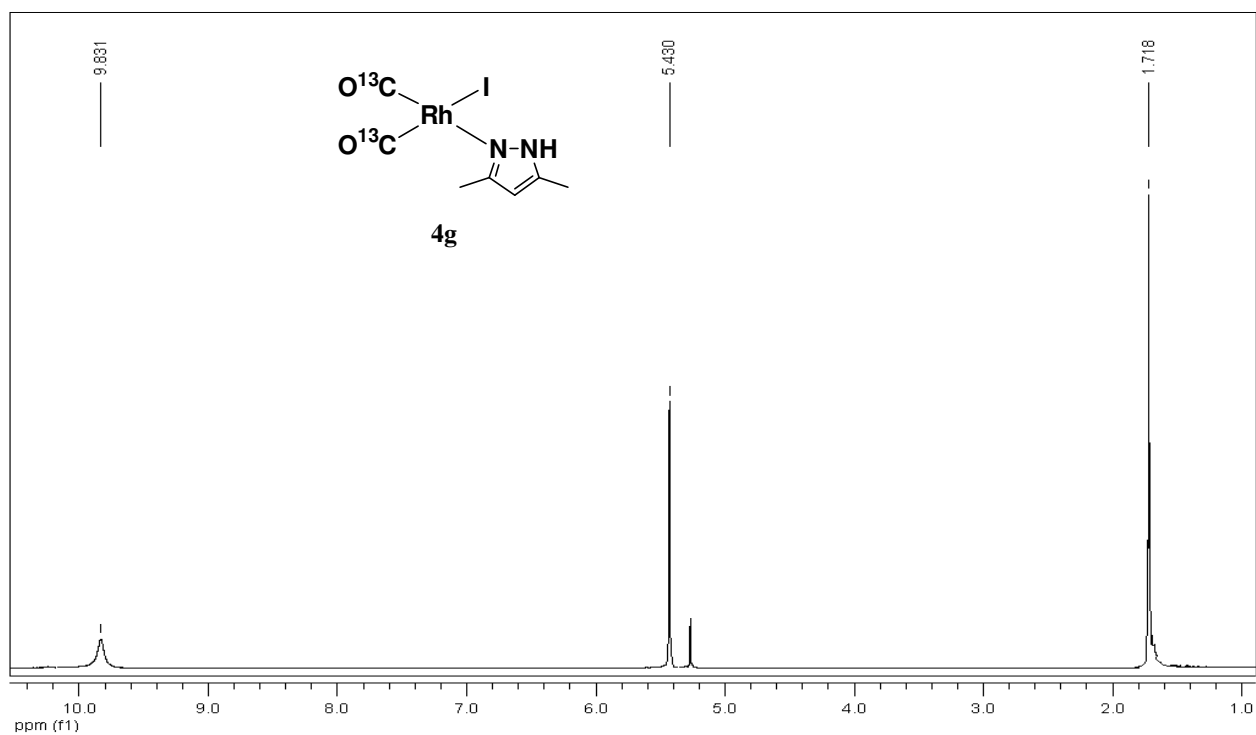


Figure 48. ^1H NMR spectrum of **4g** at 298 K in CD_2Cl_2 .

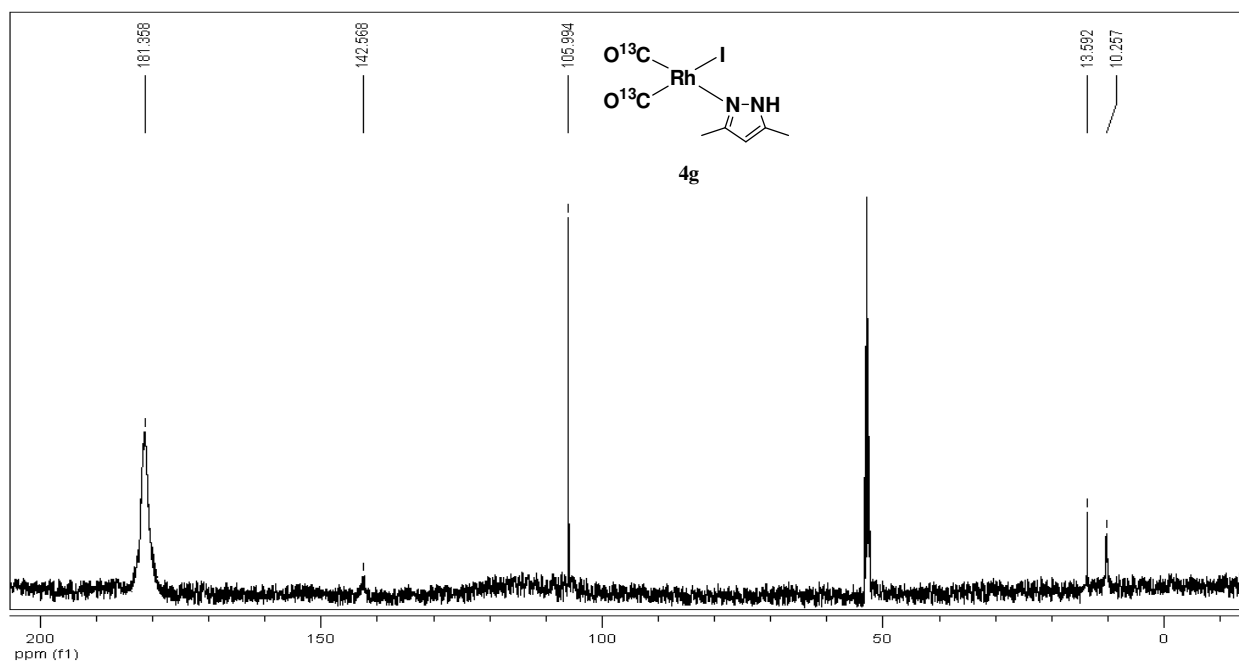


Figure 49. $^{13}\text{C}\{^1\text{H}\}$ NMR spectrum of **4g** at 298 K in CD_2Cl_2 .

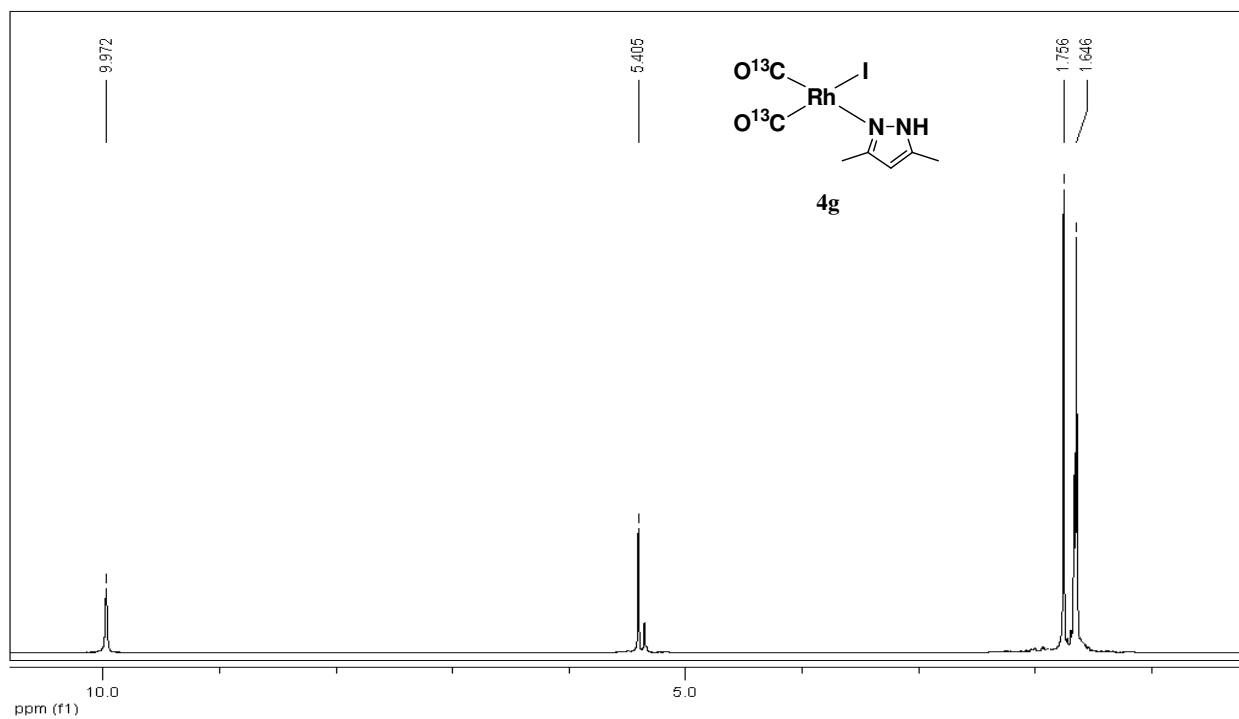


Figure 50. ^1H NMR spectrum of **4g** at 193 K in CD_2Cl_2 .

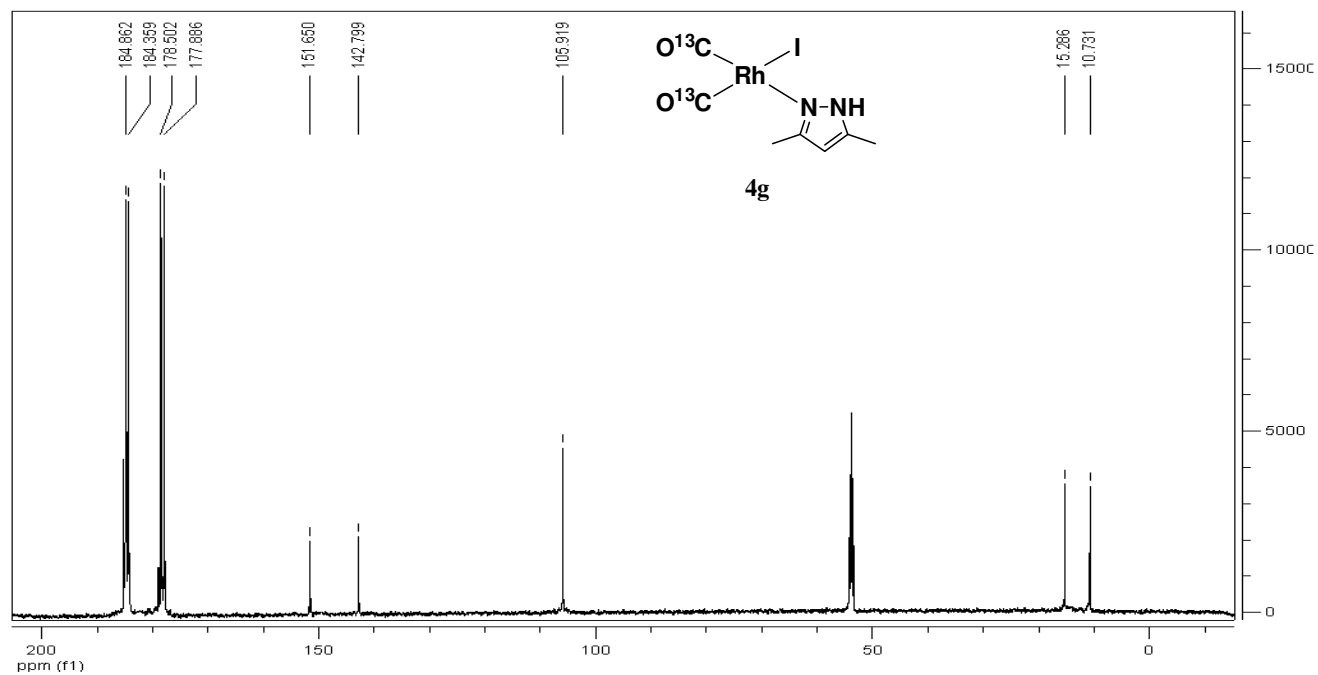


Figure 51. $^{13}\text{C}\{^1\text{H}\}$ NMR spectrum of **4g** at 193 K in CD_2Cl_2 .

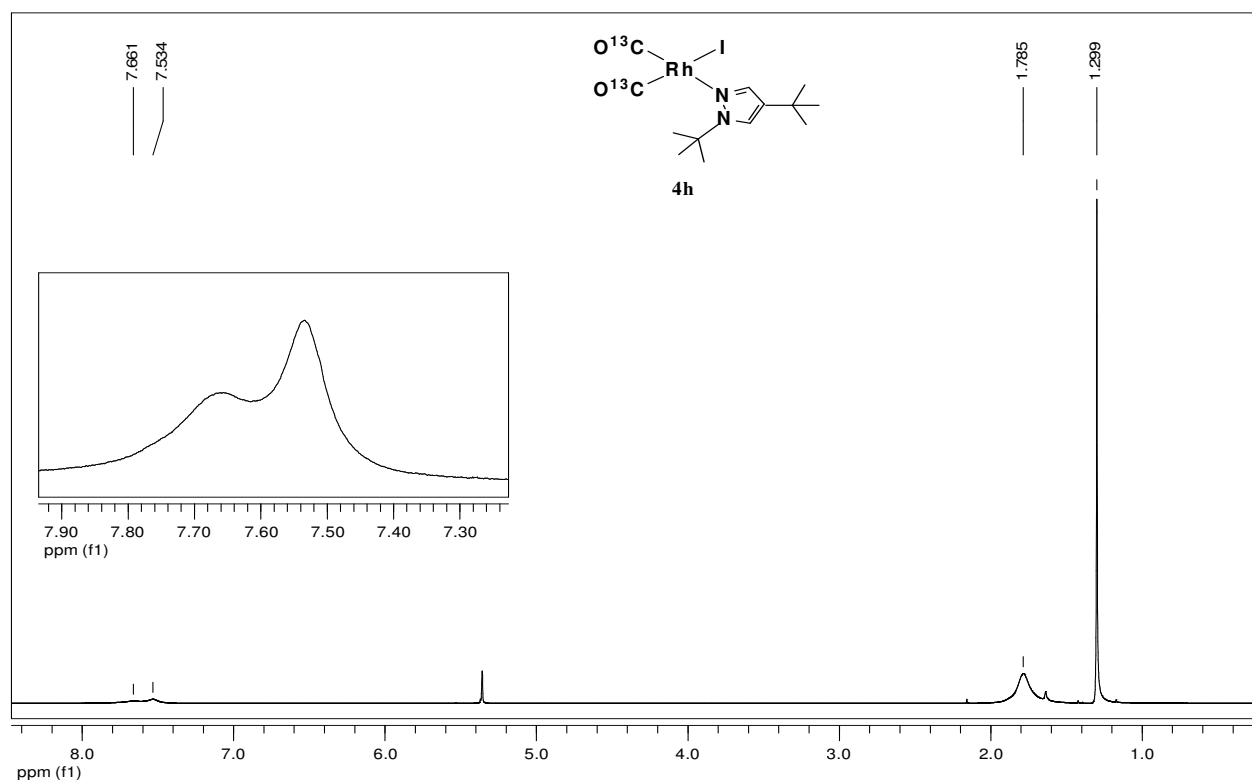


Figure 52. ^1H NMR spectrum of **4h** at 298 K in CD_2Cl_2 .

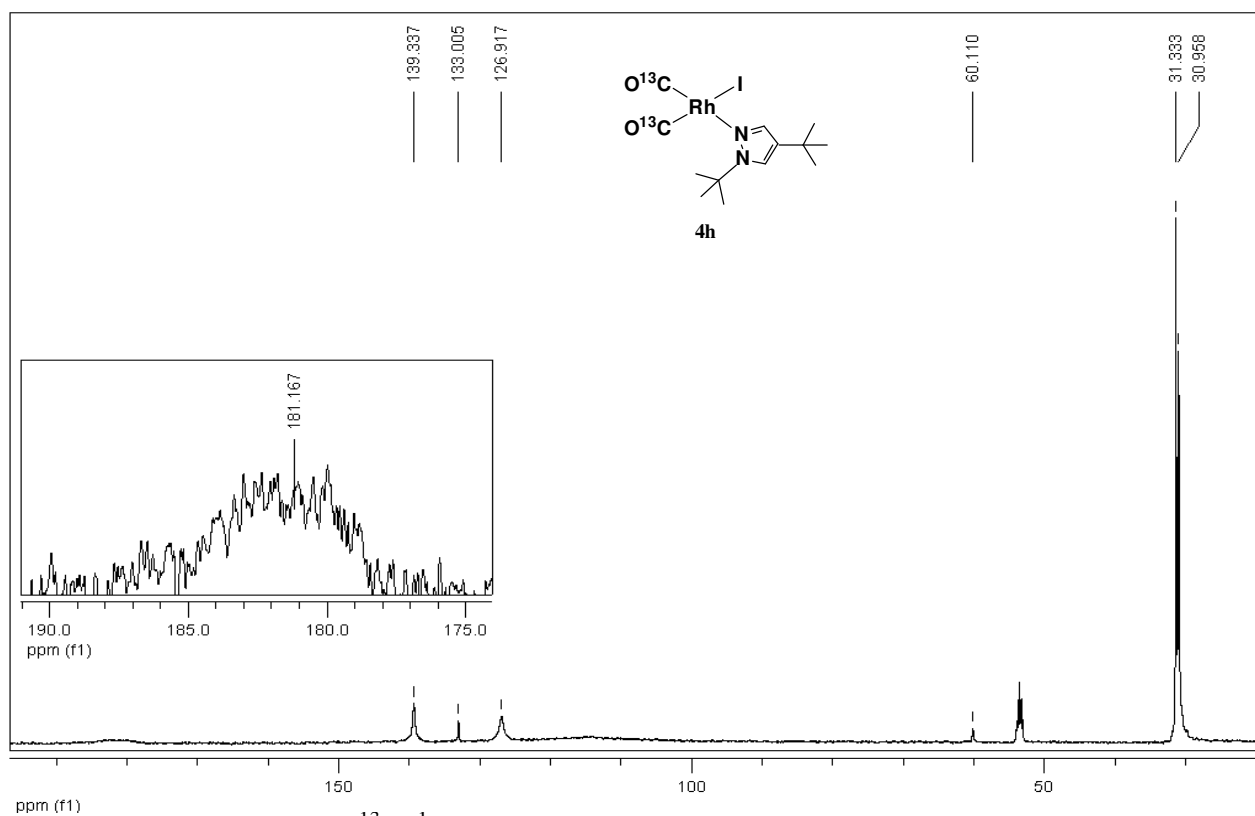


Figure 53. $^{13}\text{C}\{^1\text{H}\}$ NMR spectrum of **4h** at 298 K in CD_2Cl_2 .

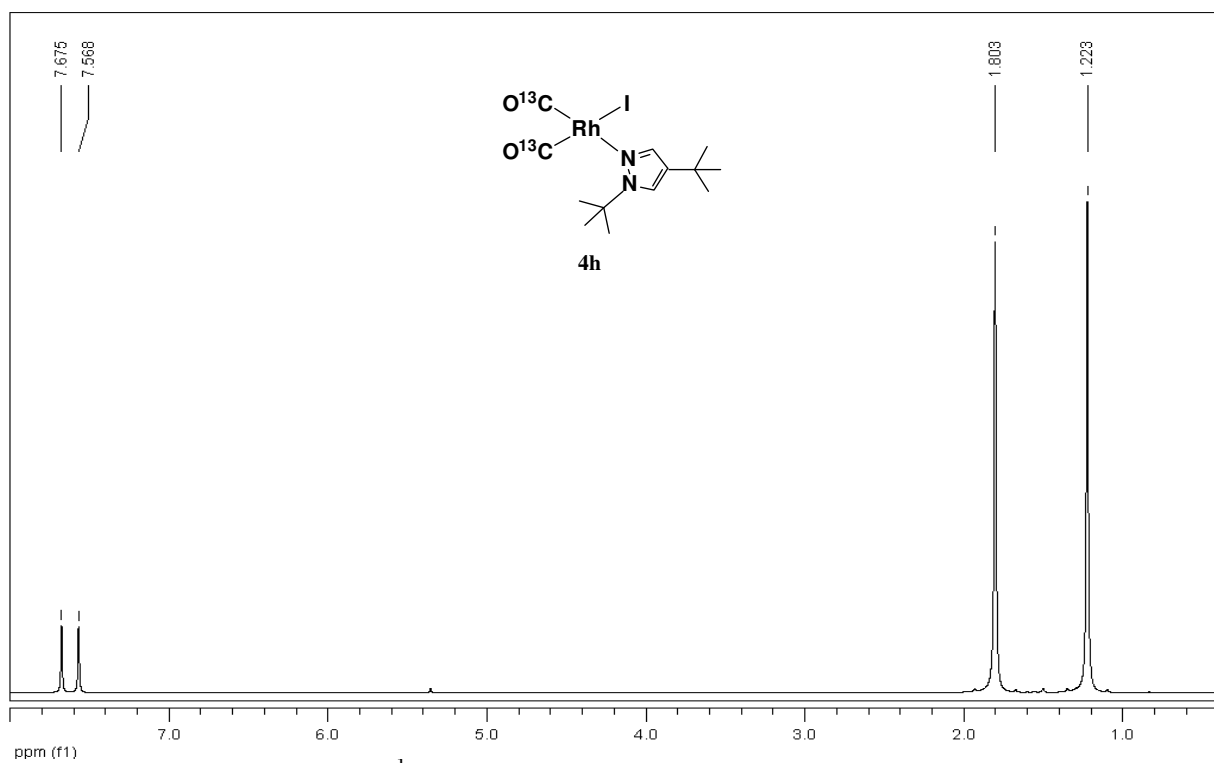


Figure 54. ^1H NMR spectrum of **4h** at 193 K in CD_2Cl_2 .

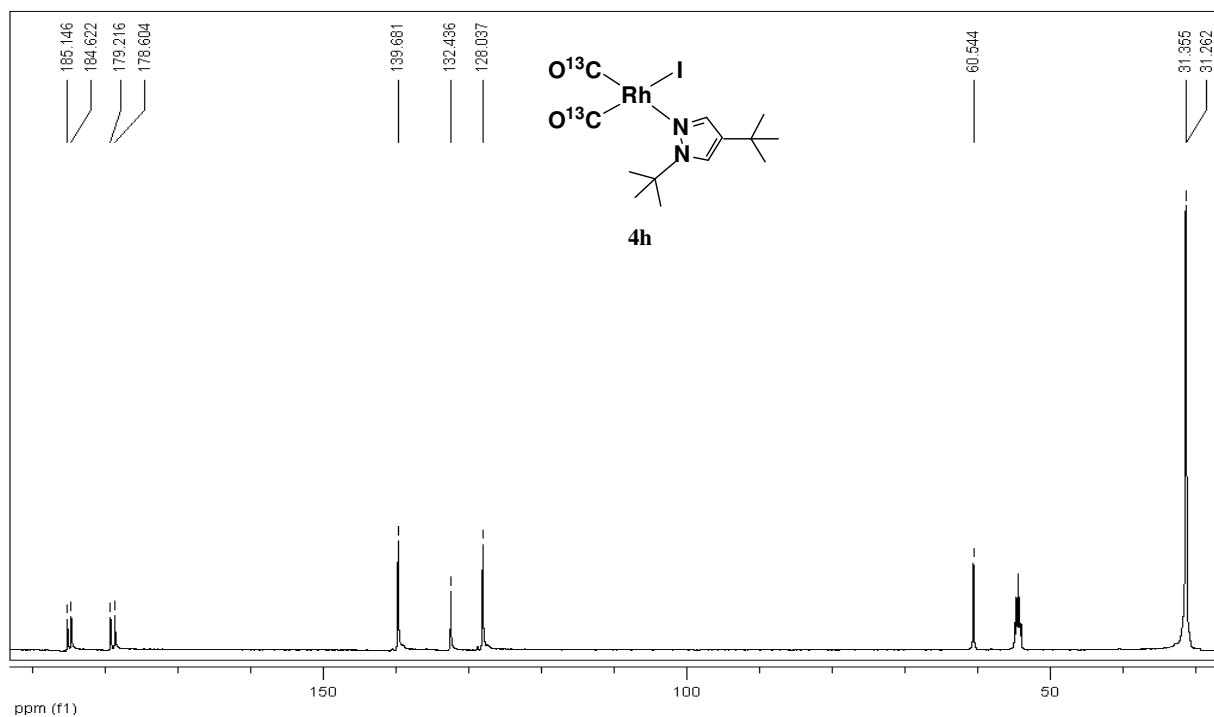


Figure 55. $^{13}\text{C}\{^1\text{H}\}$ NMR spectrum of **4h** at 193 K in CD_2Cl_2 .

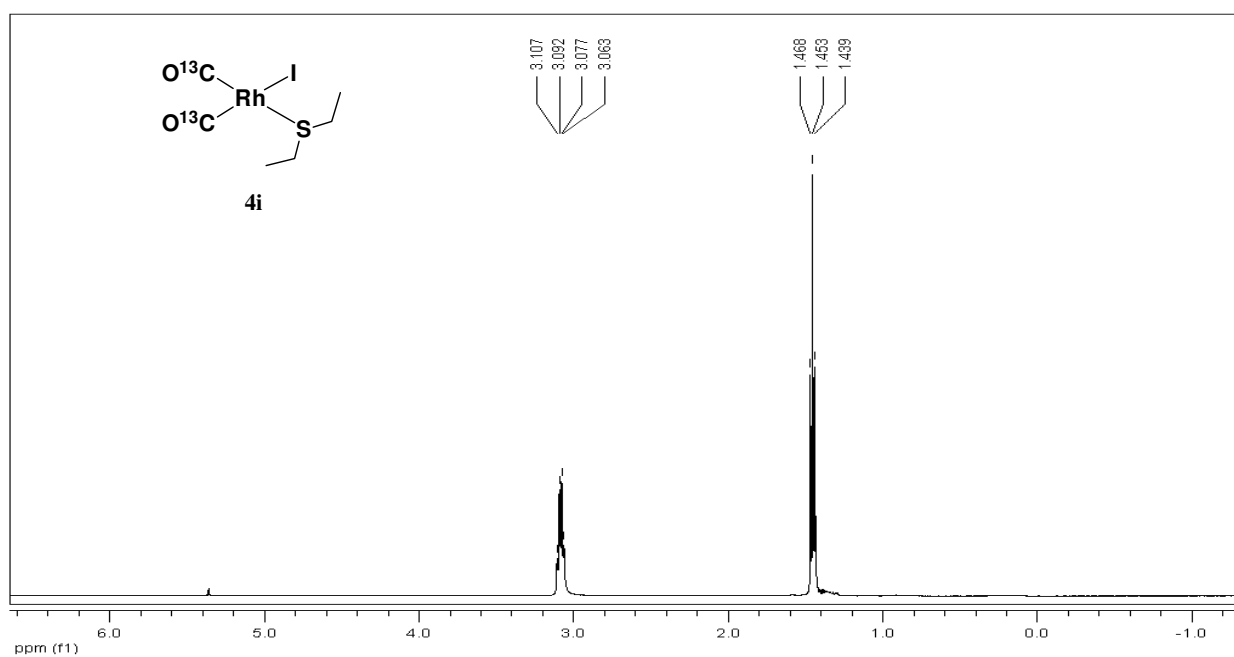


Figure 56. ^1H NMR spectrum of **4i** at 298 K in CD_2Cl_2 .

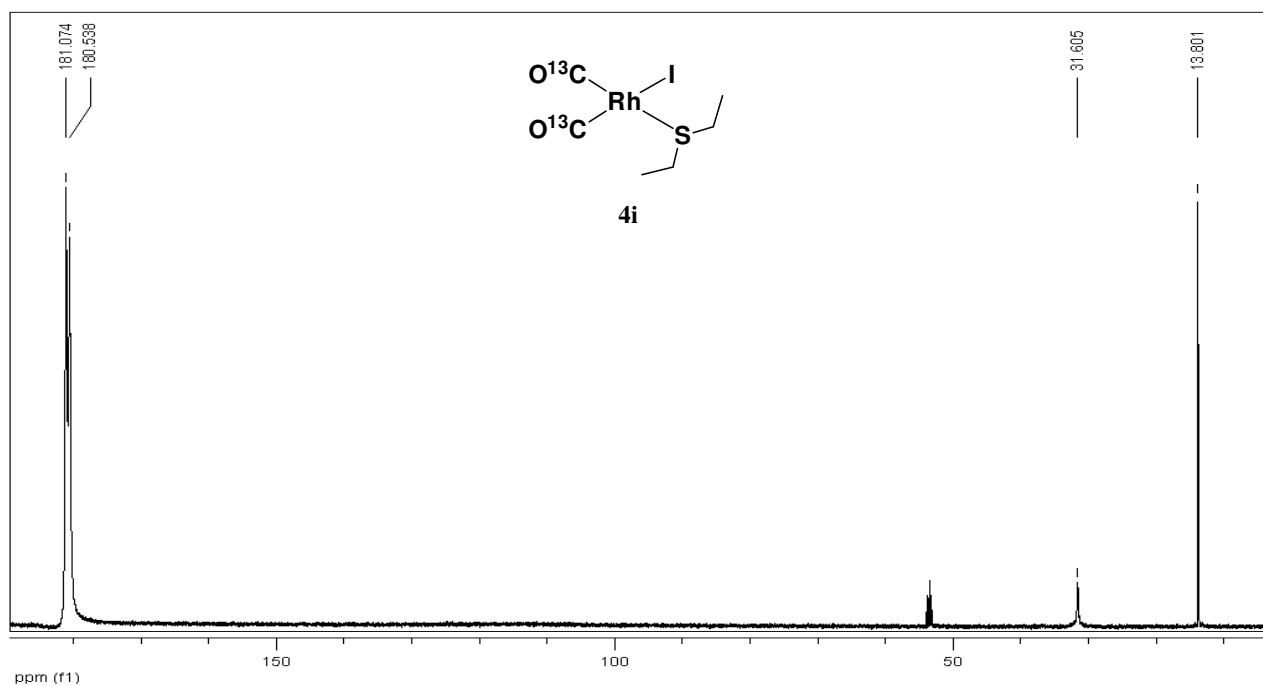


Figure 57. $^{13}\text{C}\{^1\text{H}\}$ NMR spectrum of **4i** at 298 K in CD_2Cl_2 .

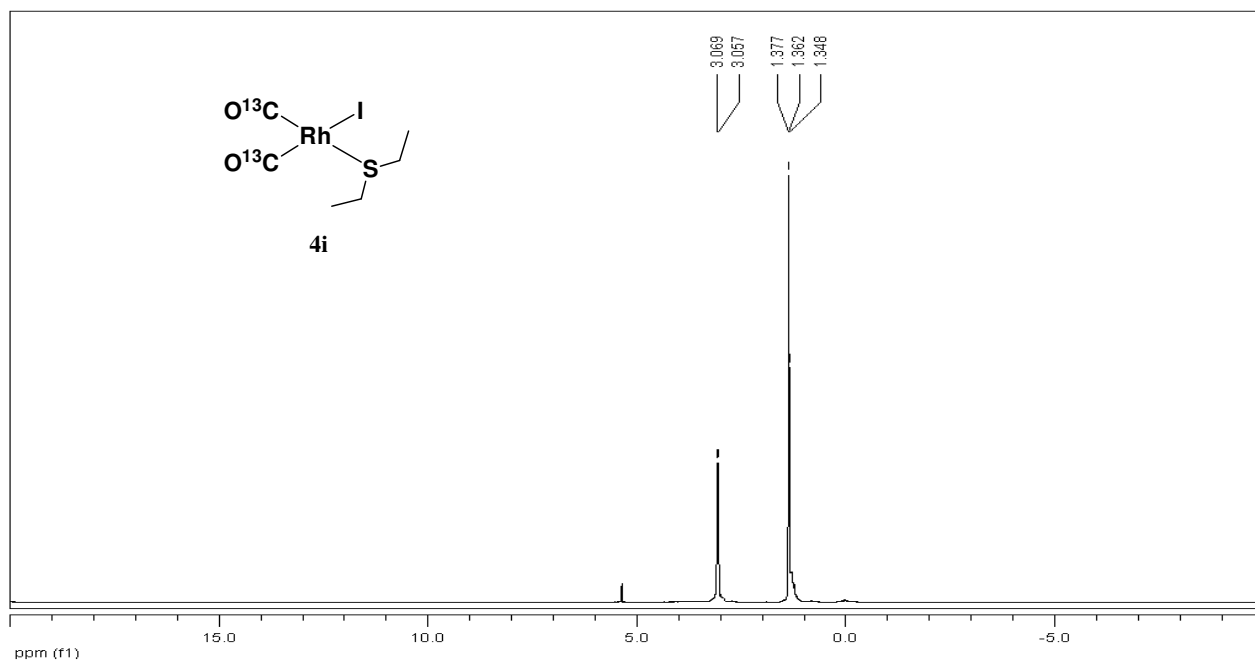


Figure 58. ^1H NMR spectrum of **4i** at 183 K in CD_2Cl_2 .

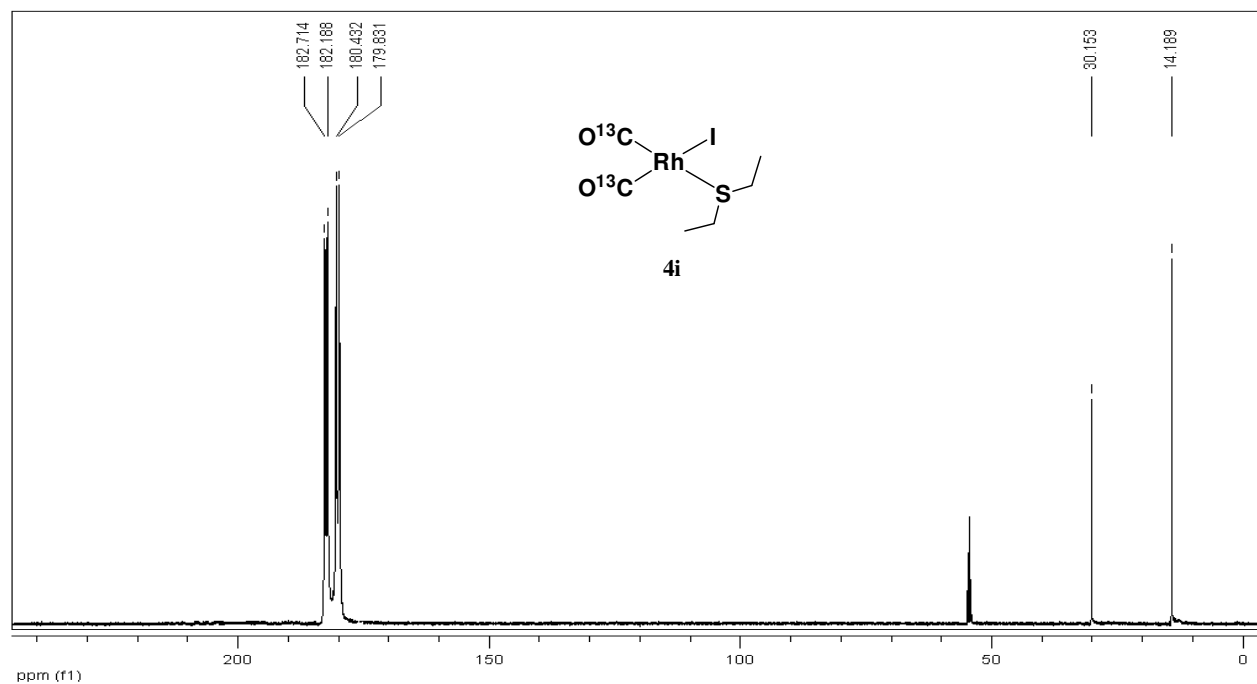


Figure 59. $^{13}\text{C}\{^1\text{H}\}$ NMR spectrum of **4i** at 183 K in CD_2Cl_2 .

IV- SELECTED VT-NMR SPECTRA

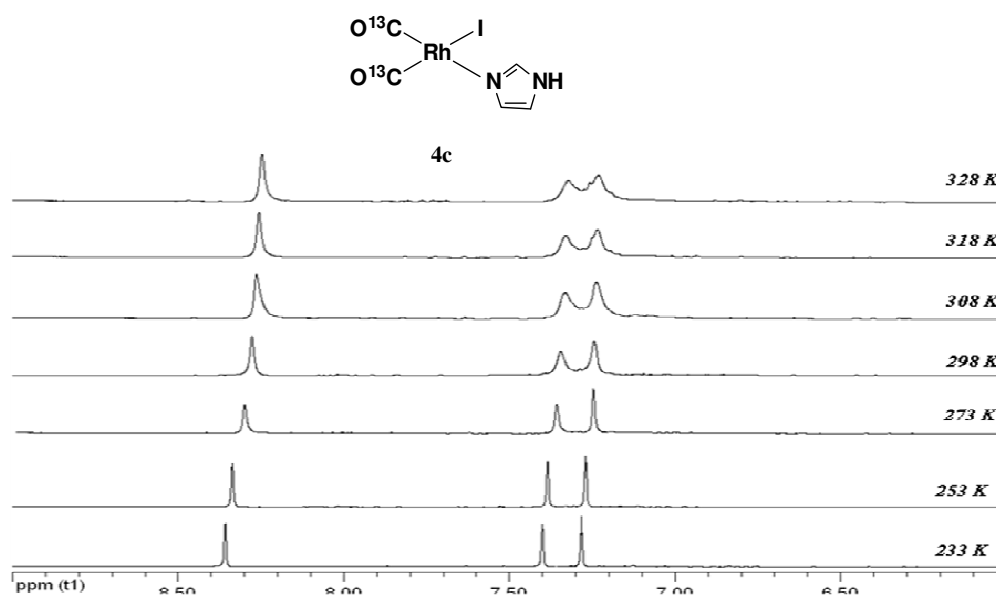


Figure 1. ^1H VT-NMR stacked spectra of **4c** in the 7.00–8.50 ppm region in CD_3OD .

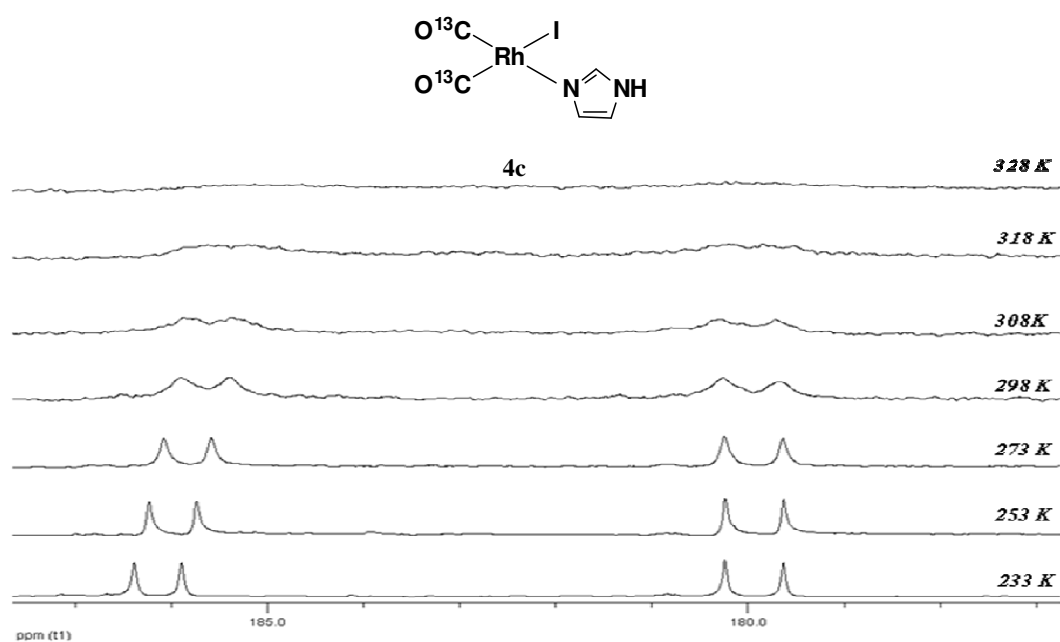


Figure 2. $^{13}\text{C}\{^1\text{H}\}$ VT-NMR stacked spectra of **4c** in the carbonyl region in CD_3OD .

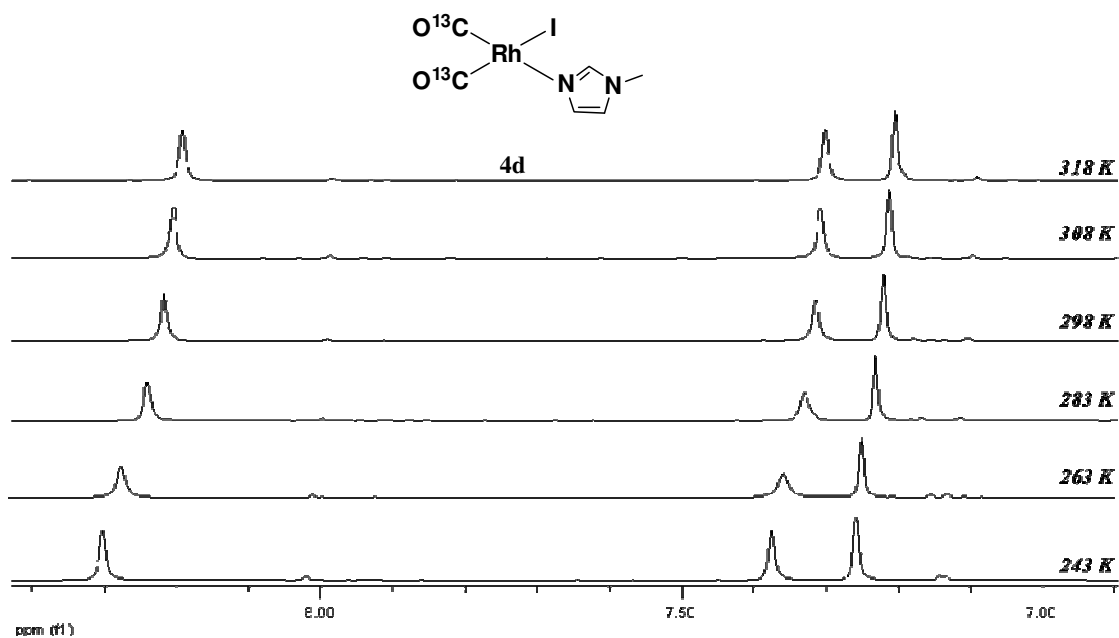


Figure 3. ^1H VT-NMR stacked spectra of **4d** in the 7.00-8.50 ppm region in CD_3OD .

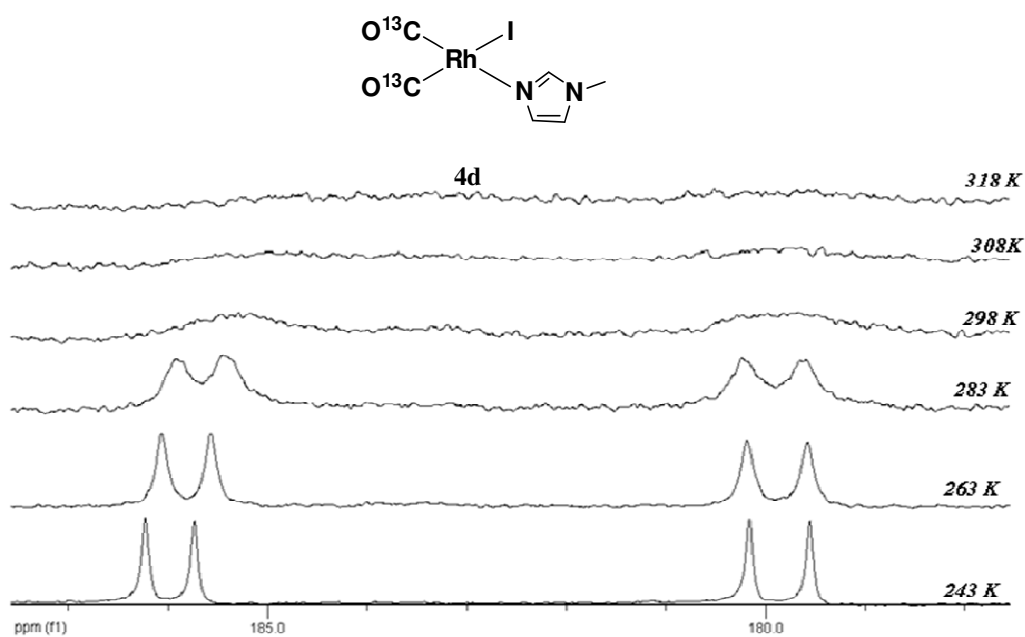


Figure 4. $^{13}\text{C}\{^1\text{H}\}$ VT-NMR stacked spectra of **4d** in the carbonyl region in CD_3OD .

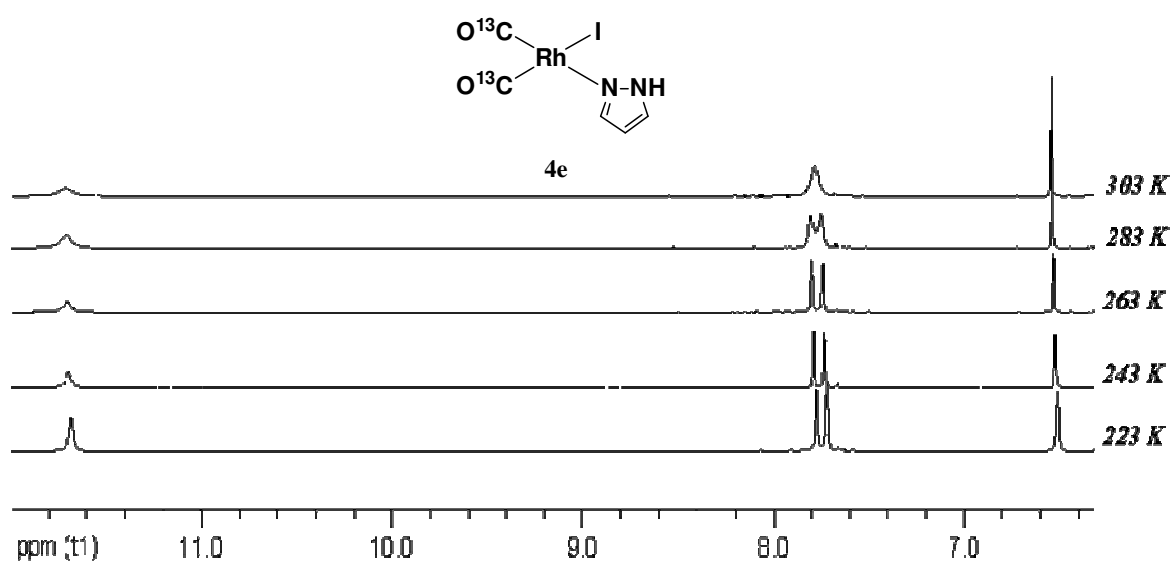


Figure 5. ^1H VT-NMR stacked spectra of **4e** in the 6.00–12.00 ppm region in CD_2Cl_2 .

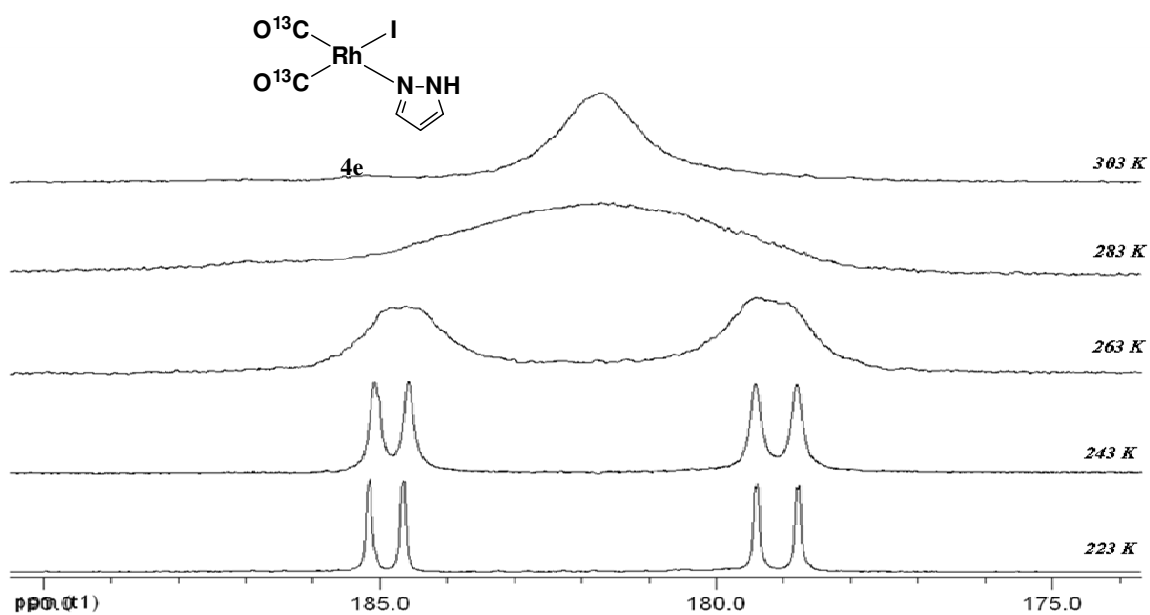


Figure 6. $^{13}\text{C}\{^1\text{H}\}$ VT-NMR stacked spectra of **4e** in the carbonyl region in CD_2Cl_2 .

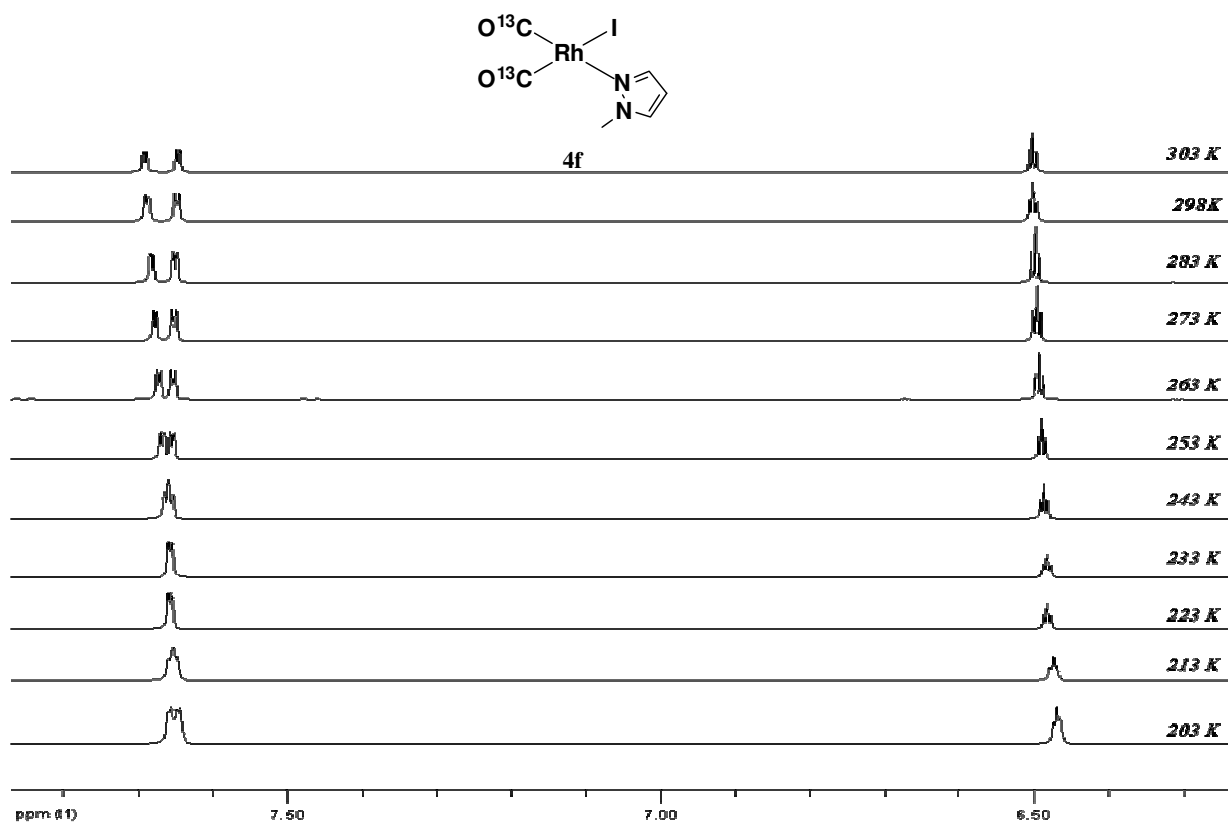


Figure 7. ^1H VT-NMR stacked spectra of **4f** in the 6.00-7.80 ppm region in CD_2Cl_2 .

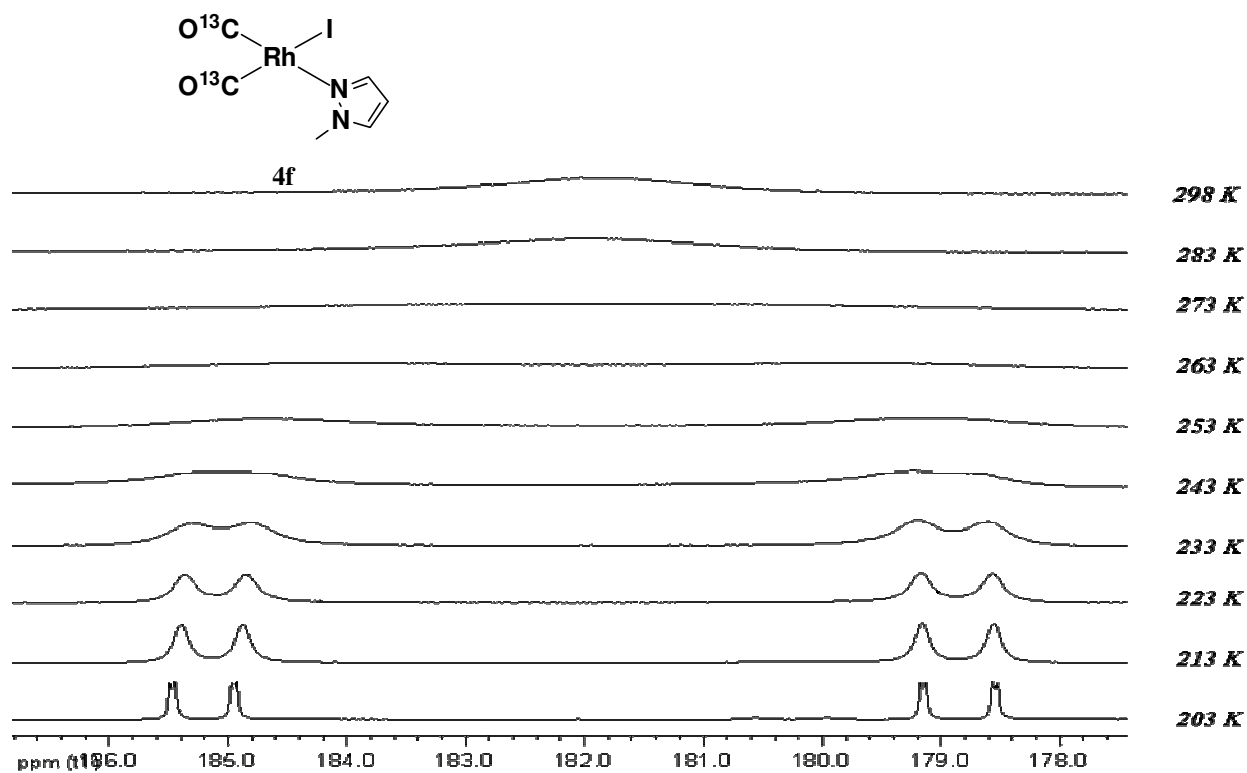


Figure 8. $^{13}\text{C}\{^1\text{H}\}$ VT-NMR stacked spectra of **4f** in the carbonyl region in CD_2Cl_2 .

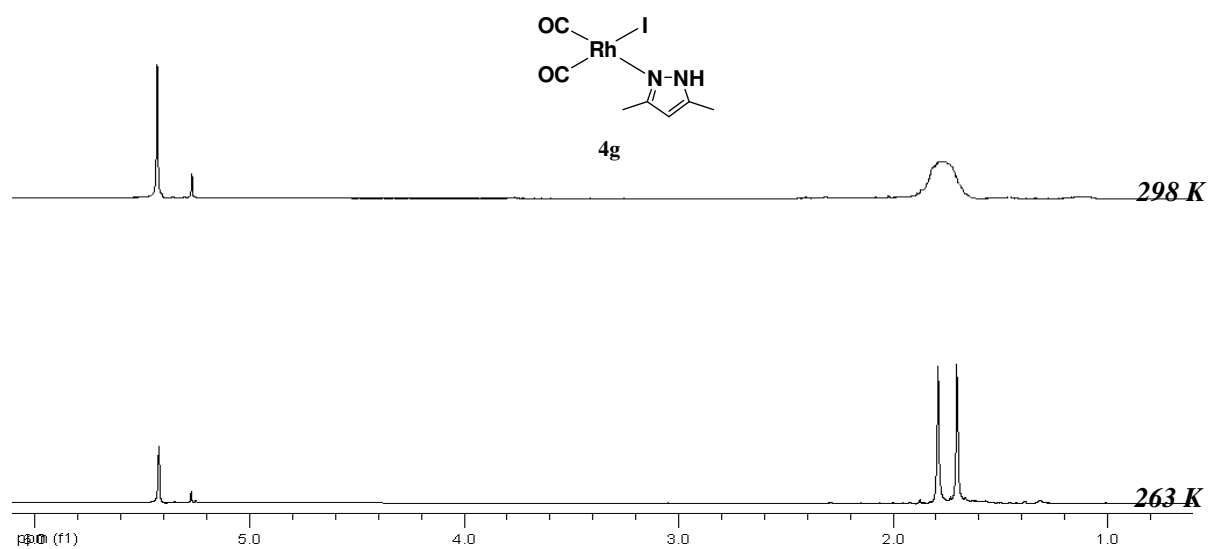


Figure 9. ^1H VT-NMR spectra of **4g** in the 1.00-6.00 ppm region in CD_2Cl_2 .

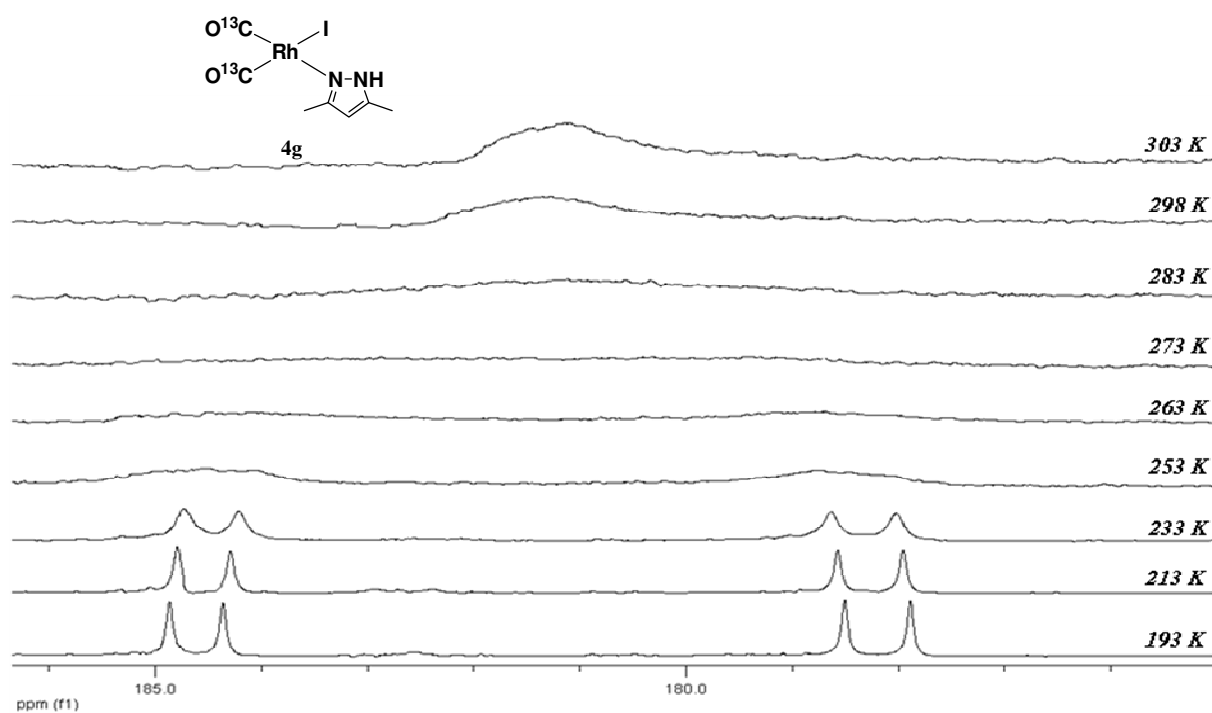


Figure 10. $^{13}\text{C}\{^1\text{H}\}$ VT-NMR stacked spectra of **4g** in the carbonyl region in CD_2Cl_2 .

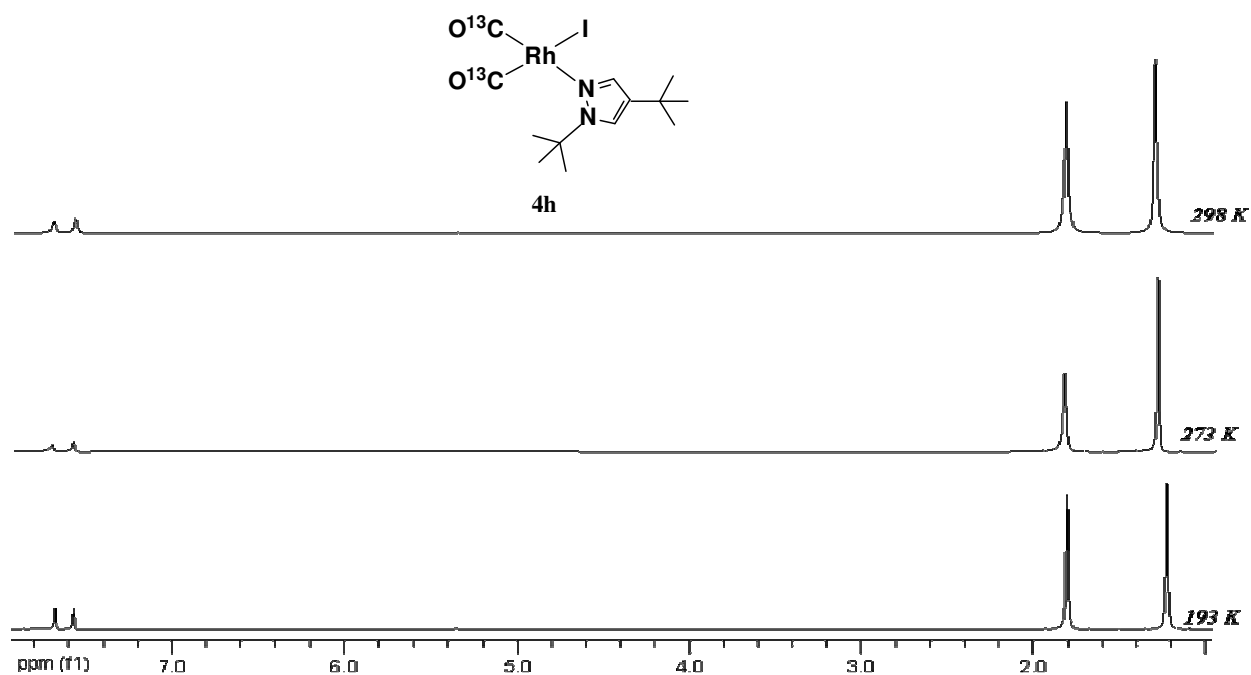


Figure 11. ^1H VT-NMR spectra of **4h** in the 1.00–8.00 ppm region in CD_2Cl_2 .

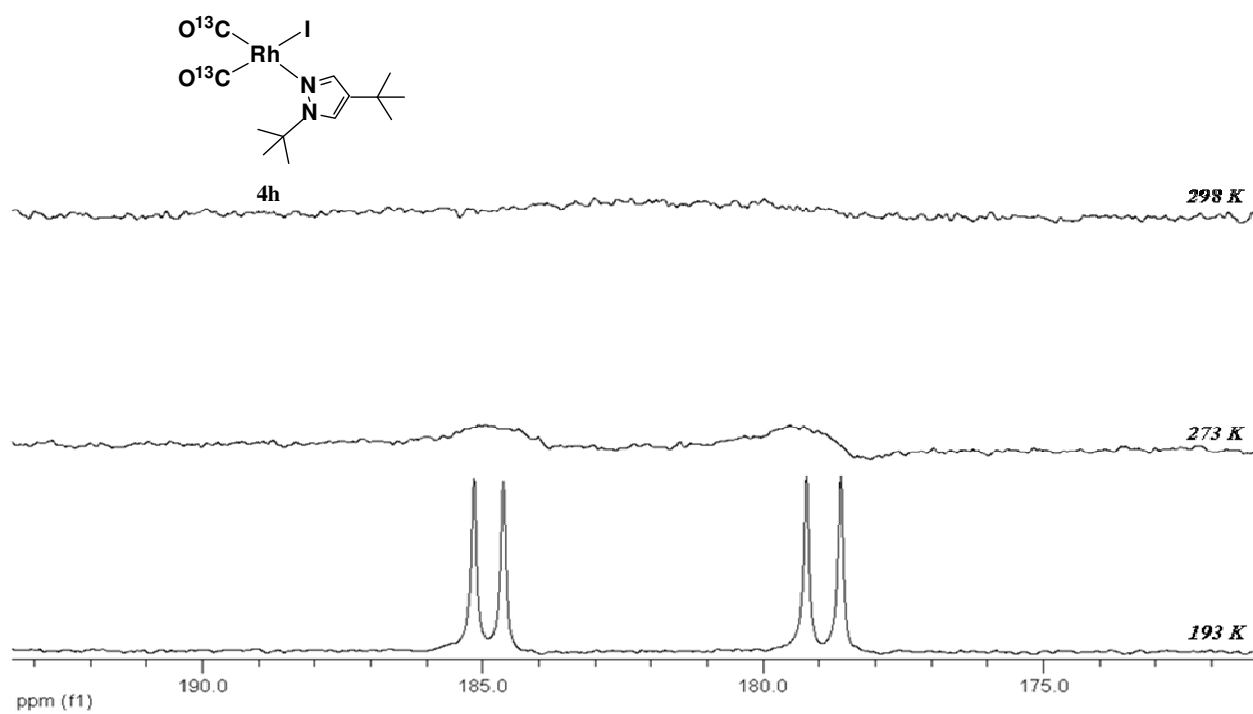


Figure 12. $^{13}\text{C}\{^1\text{H}\}$ VT-NMR stacked spectra of **4h** in the carbonyl region in CD_2Cl_2 .

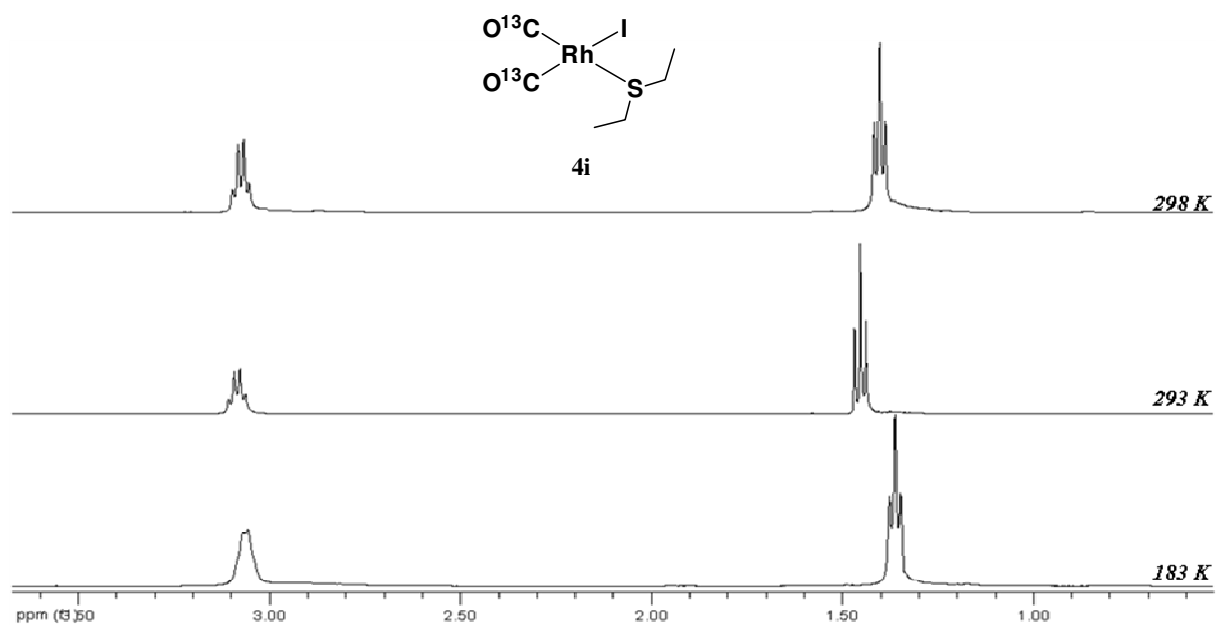


Figure 13. ^1H VT-NMR stacked spectra of **4i** in the 1.00-3.50 ppm region in CD_2Cl_2 .

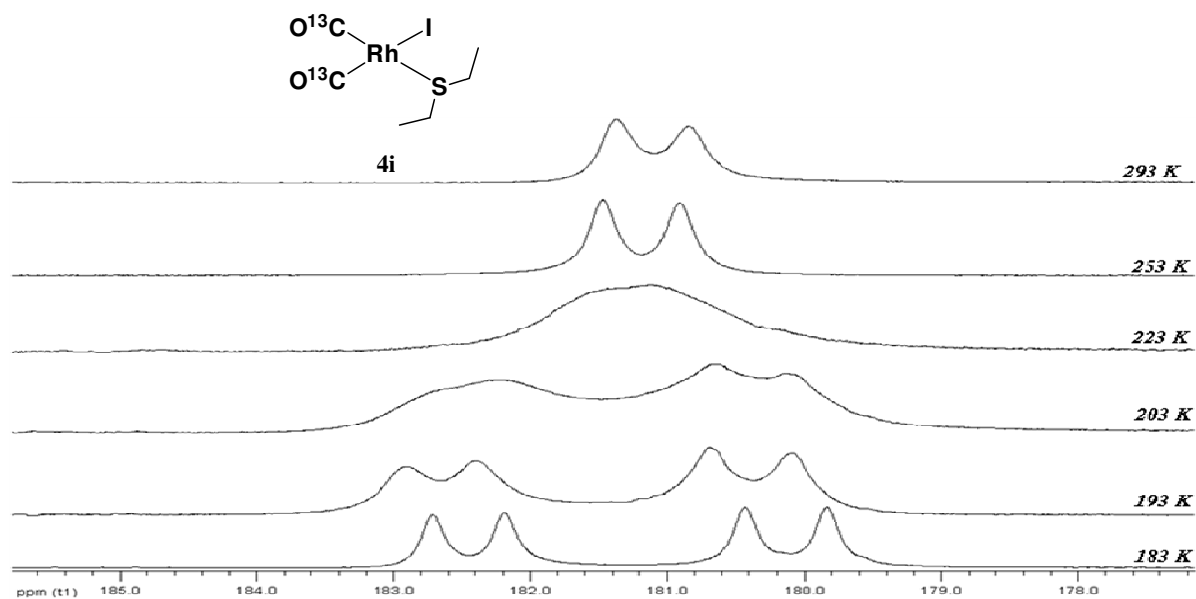


Figure 14. $^{13}\text{C}\{^1\text{H}\}$ VT-NMR stacked spectra of **4i** in the carbonyl region in CD_2Cl_2 .

V- SELECTED Rh(III) NMR SPECTRA

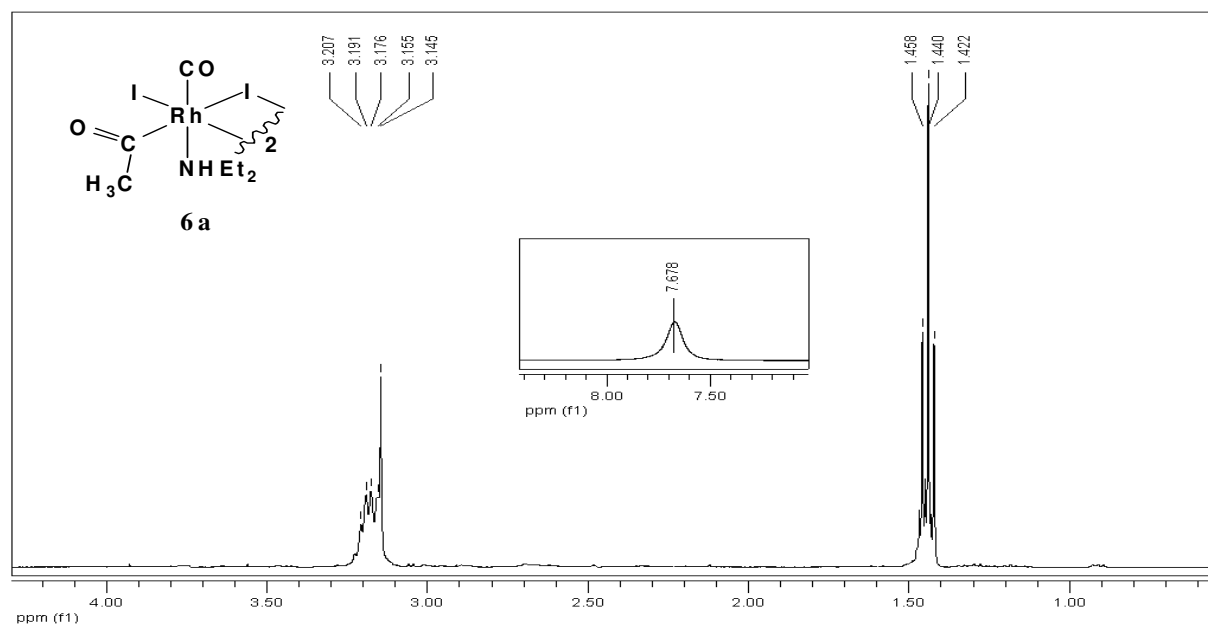


Figure 1. ^1H NMR spectrum of **6a** in the 1.00-3.50 ppm region at 298 K in CD_2Cl_2 .

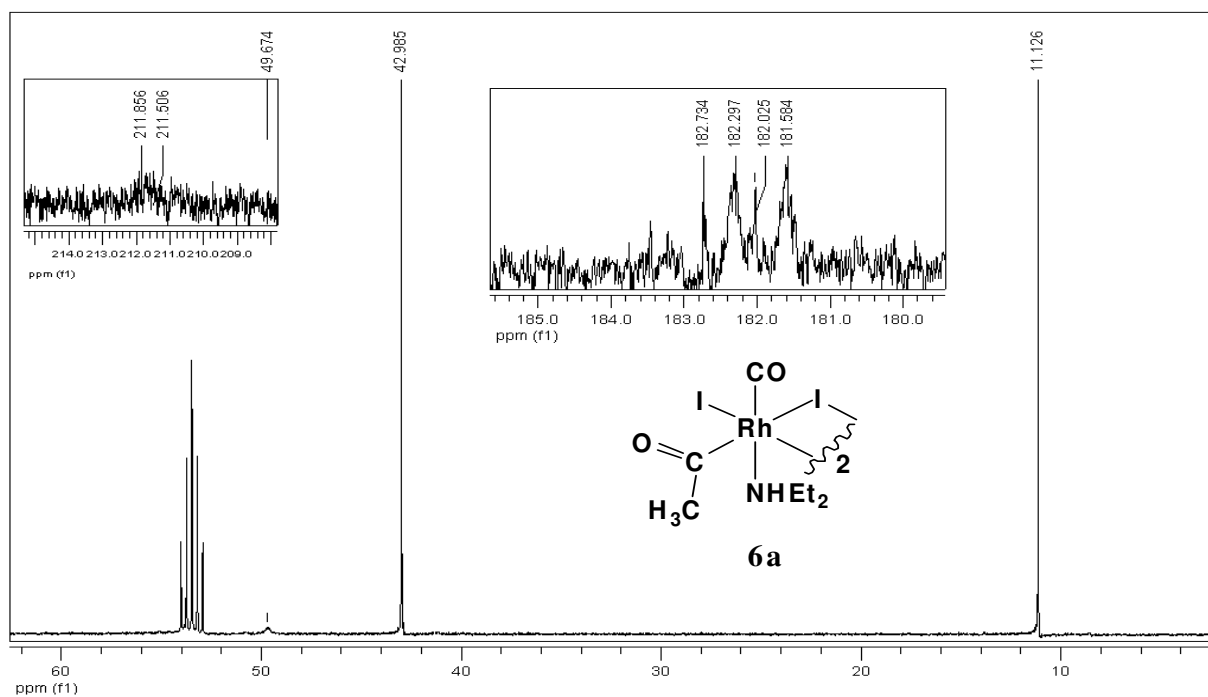


Figure 2. $^{13}\text{C}\{^1\text{H}\}$ NMR spectrum of **6a** at 298 K in CD_2Cl_2 . $-\text{CH}_3\text{CO}$ doublets were hardly detected.

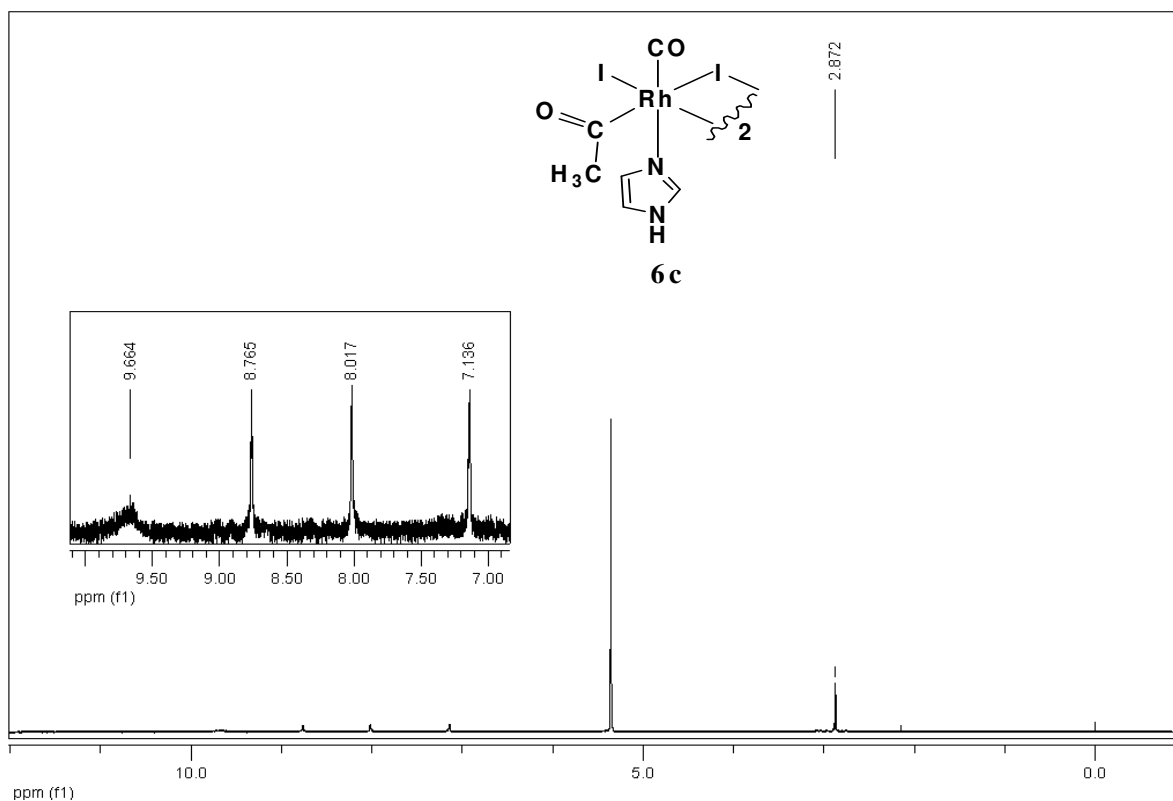


Figure 3. ^1H NMR spectrum of **6c** (poorly soluble) in the -1.00-12.00 ppm region at 298 K in CD_2Cl_2 .

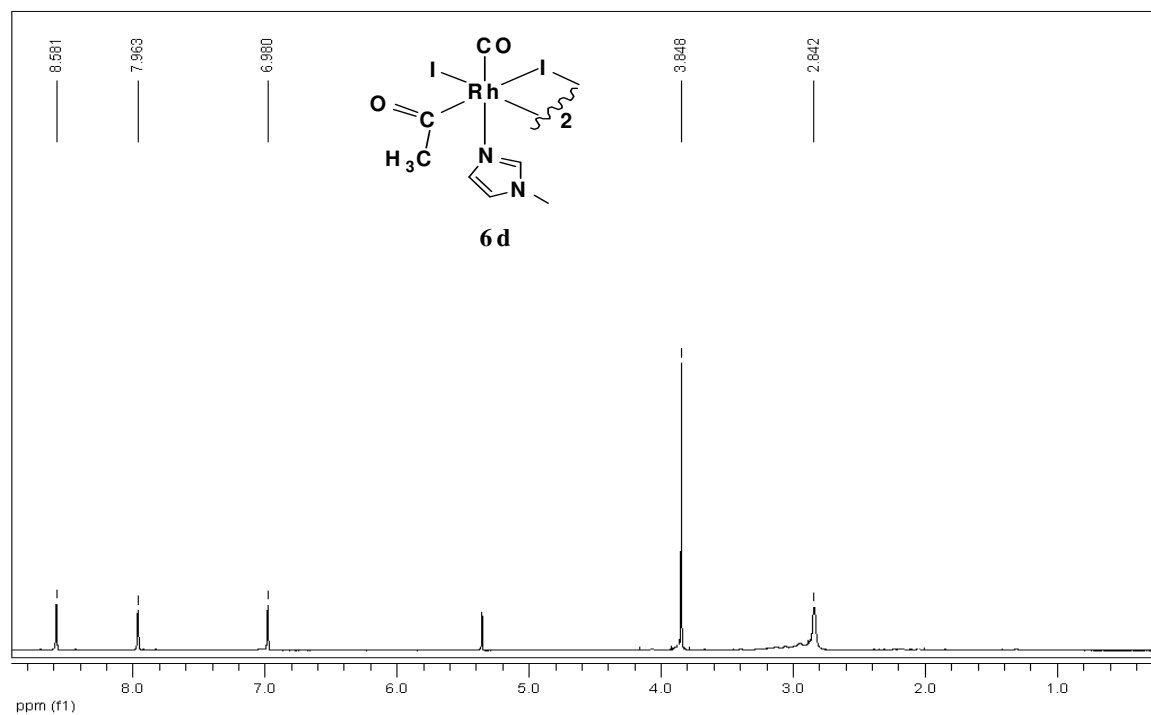


Figure 4. ^1H NMR spectrum of **6d** in the 1.00-9.00 ppm region at 298 K in CD_2Cl_2 .

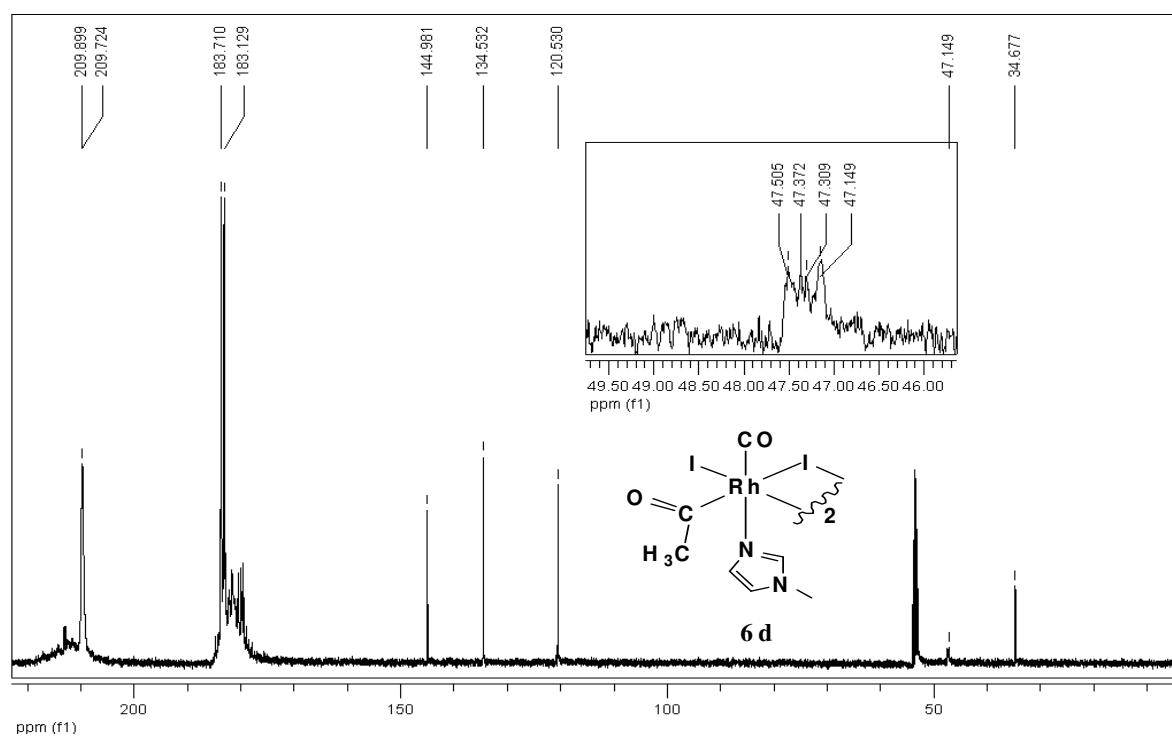


Figure 5. $^{13}\text{C}\{^1\text{H}\}$ NMR spectrum of **6d** at 298 K in CD_2Cl_2 .

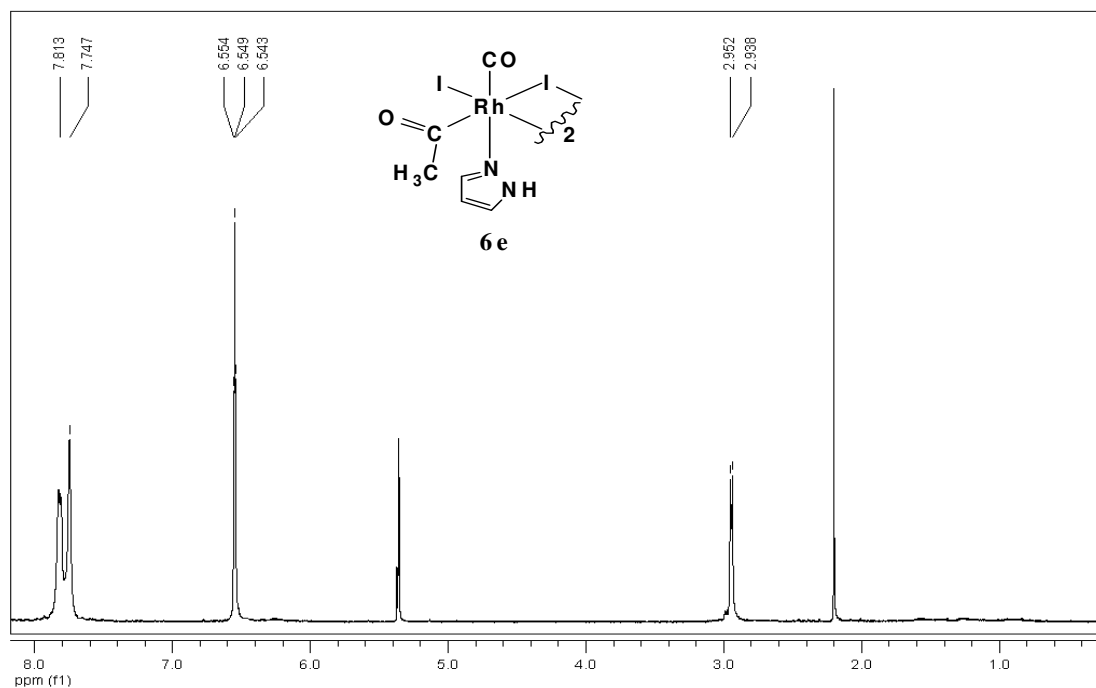


Figure 6. ^1H NMR spectrum of **6e** in the 1.00-8.00 ppm region at 298 K in CD_2Cl_2 . δ (N-H) was omitted for clarity.

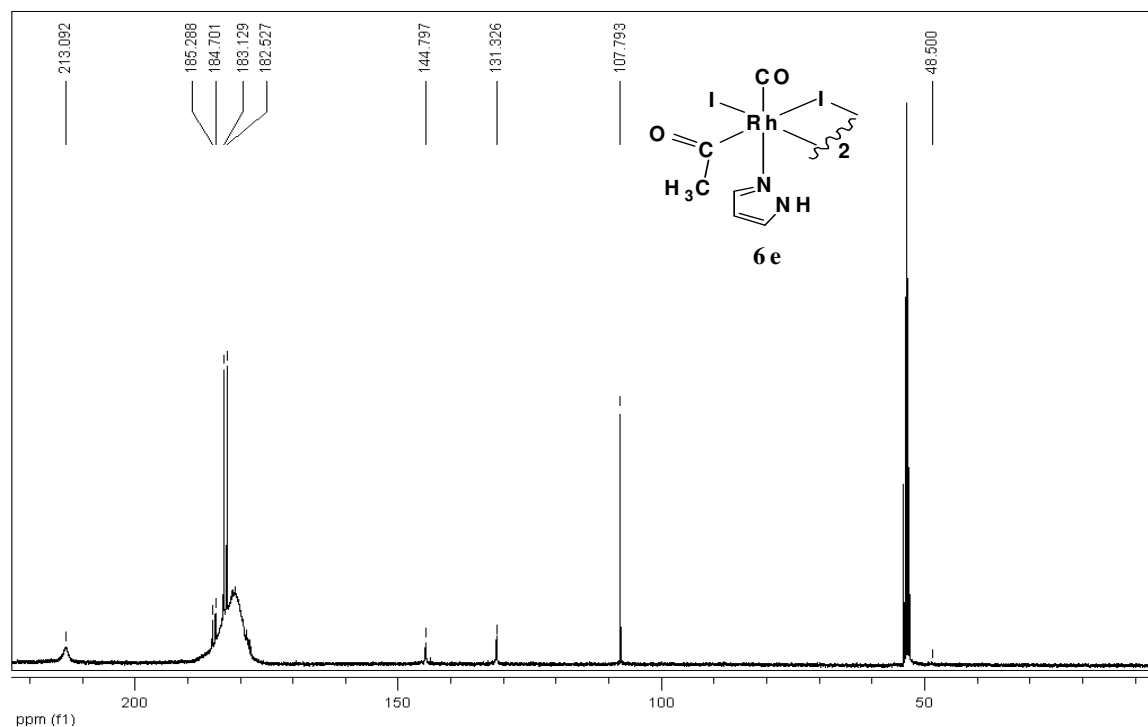


Figure 7. $^{13}\text{C}\{^1\text{H}\}$ NMR spectrum of **6e** at 298 K in CD_2Cl_2 . $-\text{CH}_3\text{CO}$ signal was hardly detected.

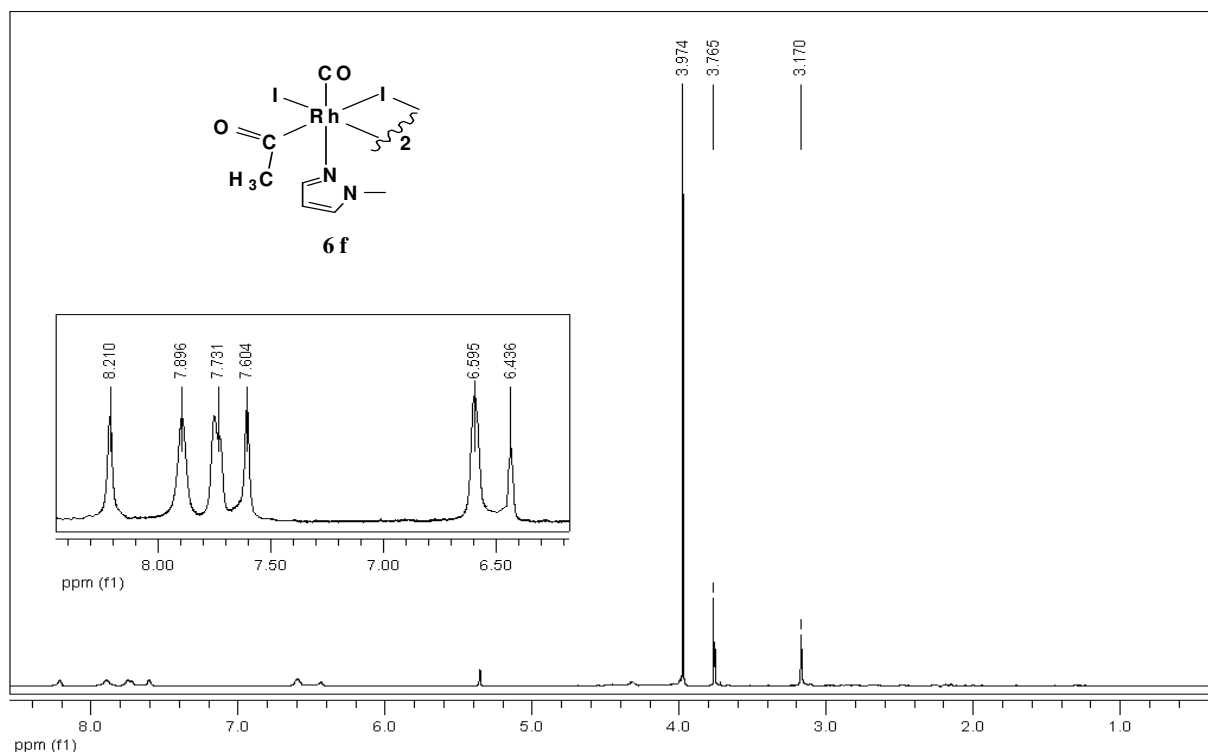


Figure 8. ^1H NMR spectrum of **6f** in the 1.00-9.00 ppm region at 298 K in CD_2Cl_2 .

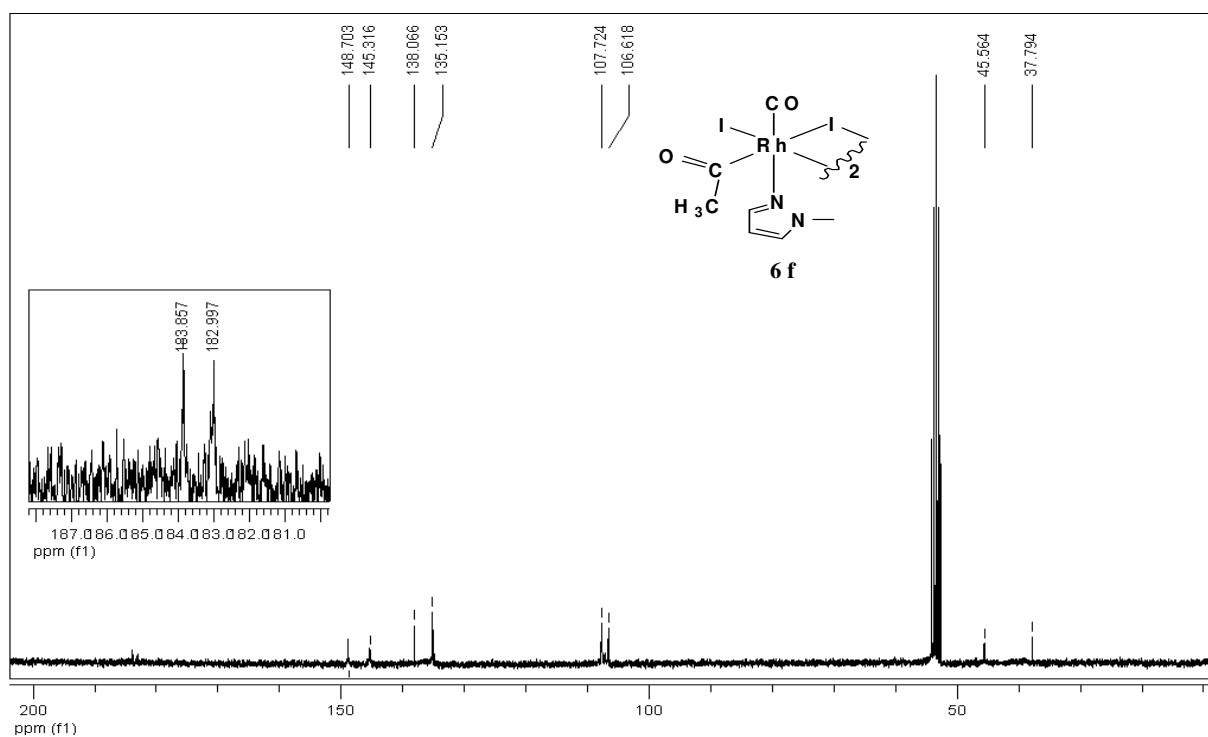


Figure 9. $^{13}\text{C}\{^1\text{H}\}$ NMR spectrum of **6f** at 298 K in CD_2Cl_2 . $-\text{CH}_3\text{CO}$ signals were not detected.

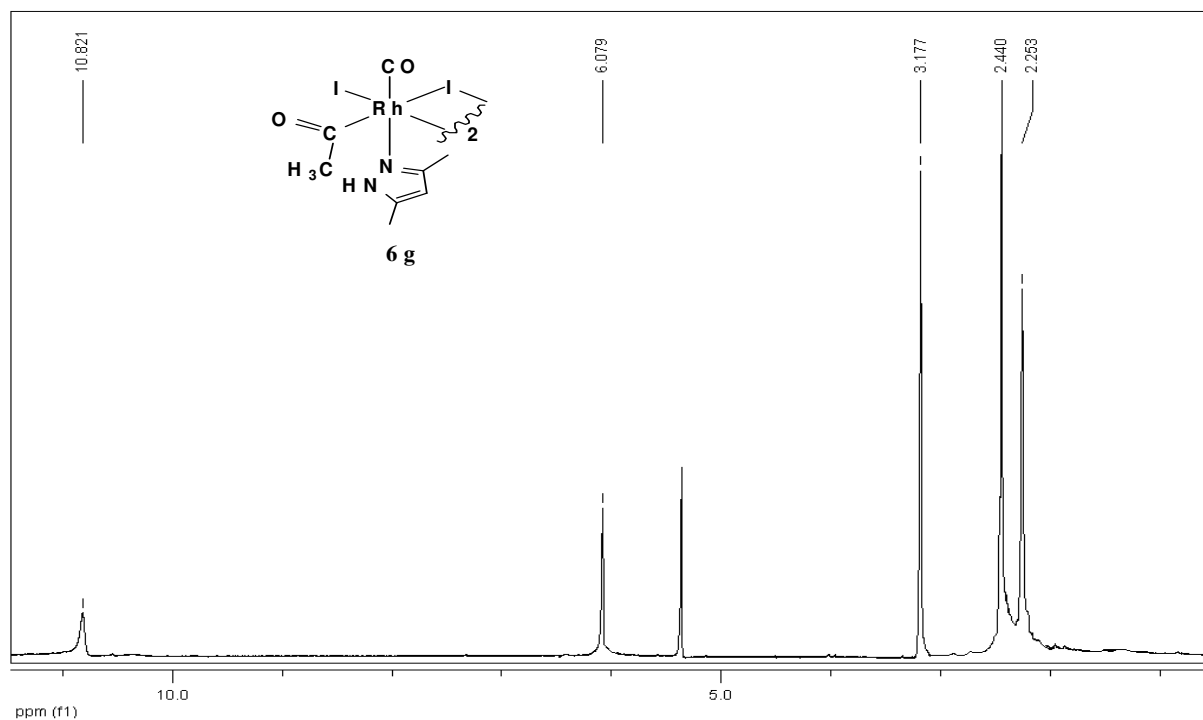


Figure 10. ^1H NMR spectrum of **6g** in the 1.00-11.00 ppm region at 298 K in CD_2Cl_2 .

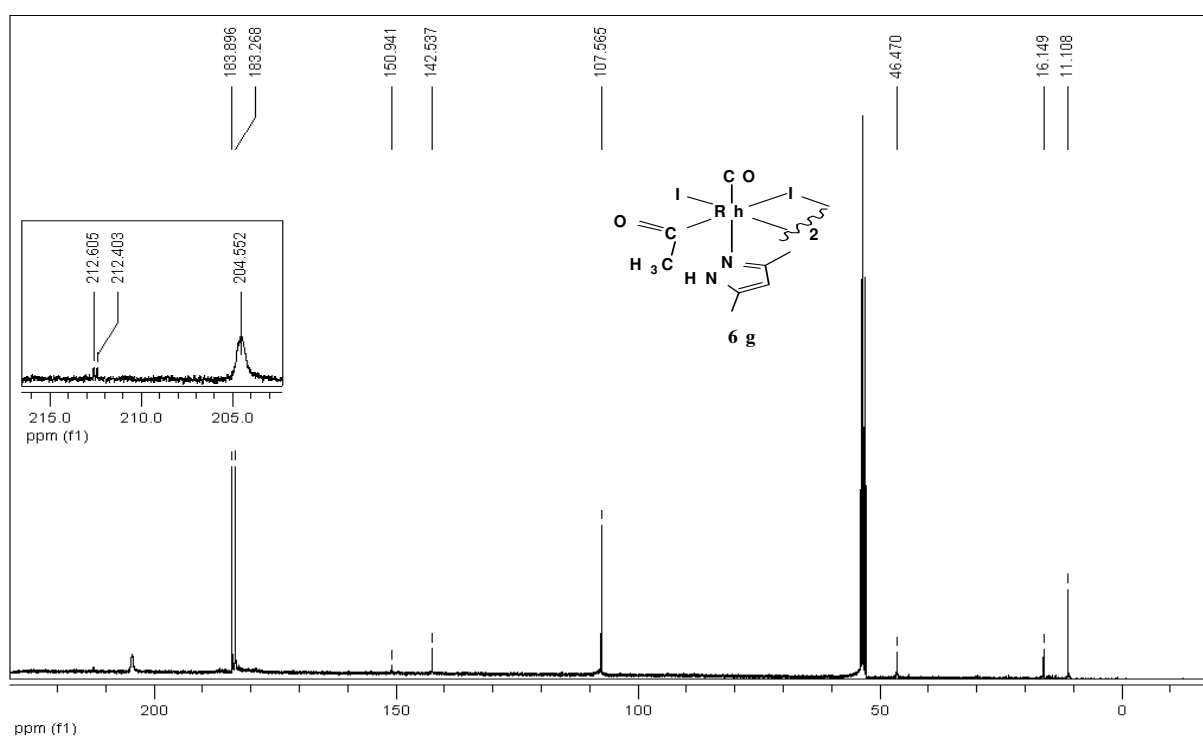


Figure 11. $^{13}\text{C}\{^1\text{H}\}$ NMR spectrum of **6g** at 298 K in CD_2Cl_2 .

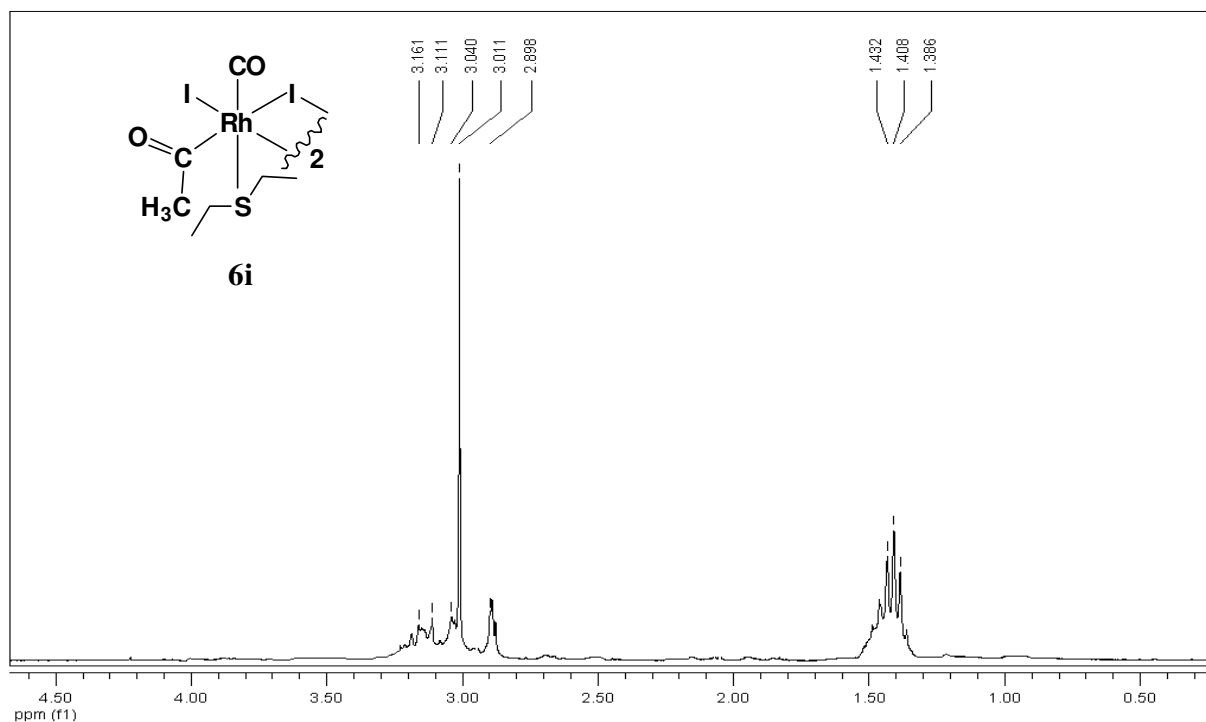


Figure 12. ^1H NMR spectrum of **6i** in the 0.50-4.50 ppm region at 298 K in CD_2Cl_2 .

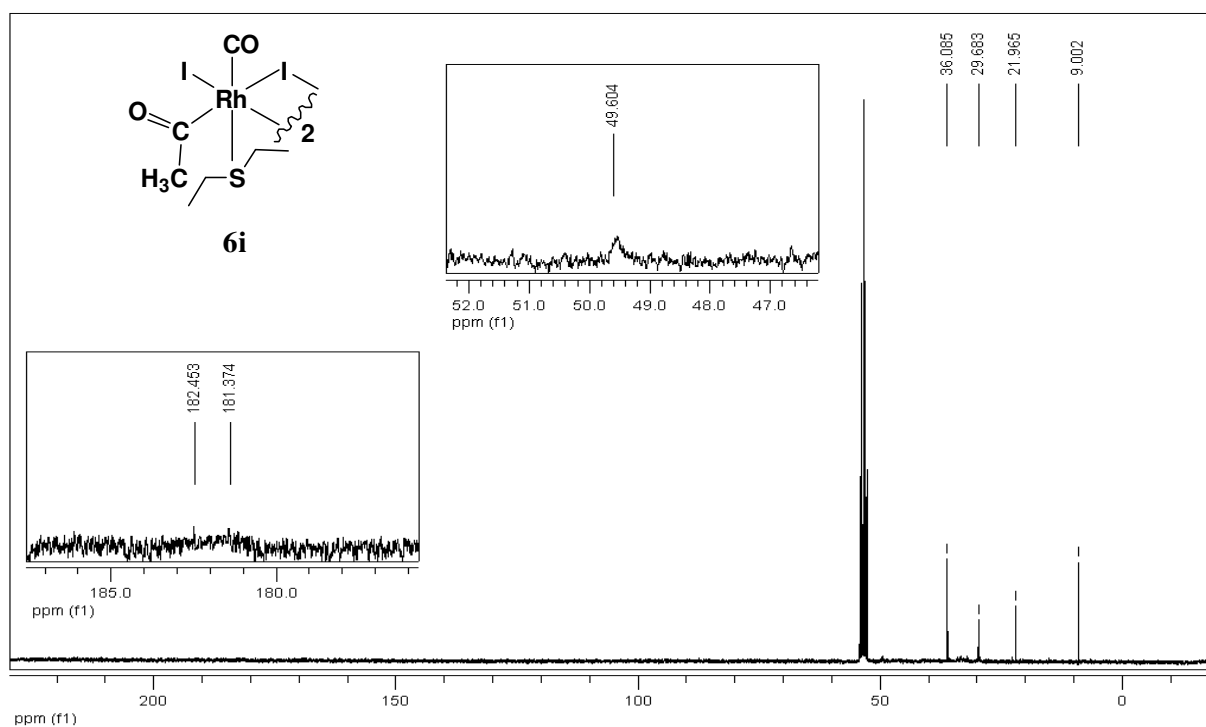


Figure 13. $^{13}\text{C}\{^1\text{H}\}$ NMR spectrum of **6i** at 298 K in CD_2Cl_2 . $-\text{CH}_3\text{CO}$ signals were not detected.

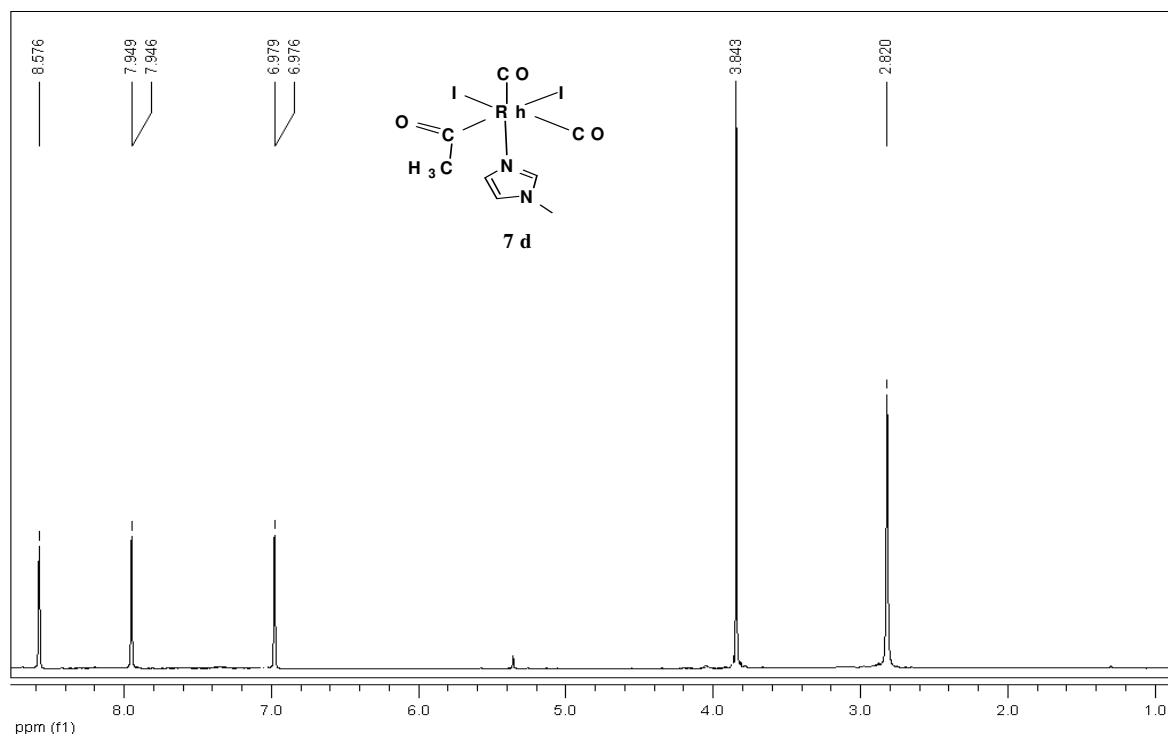


Figure 14. ^1H NMR spectrum of **7d** in the 1.00-8.50 ppm region at 298 K in CD_2Cl_2 .

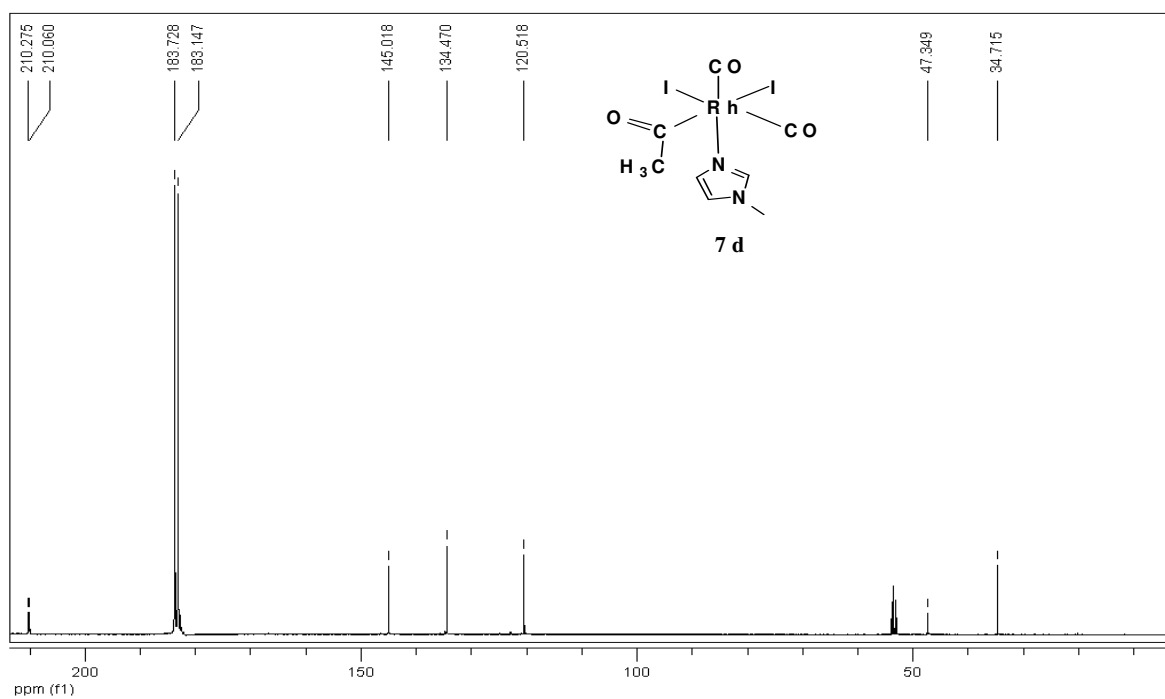


Figure 15. $^{13}\text{C}\{^1\text{H}\}$ NMR spectrum of **7d** at 298 K in CD_2Cl_2 .

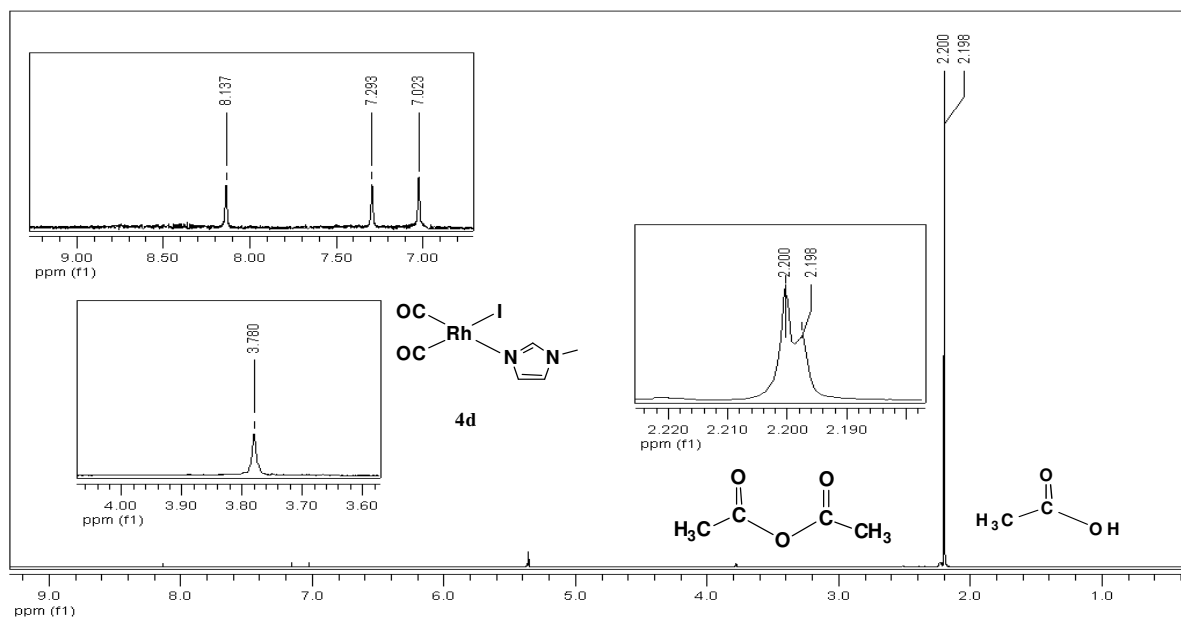


Figure 16. ^1H NMR spectrum in the 1.00-9.00 ppm region at 298 K in CD_2Cl_2 : Under ^{13}CO atm during 36 hours, occurs reductive elimination of **7d** affording **4d**, acetic anhydride δ (2.200) and acetic acid δ (2.198).

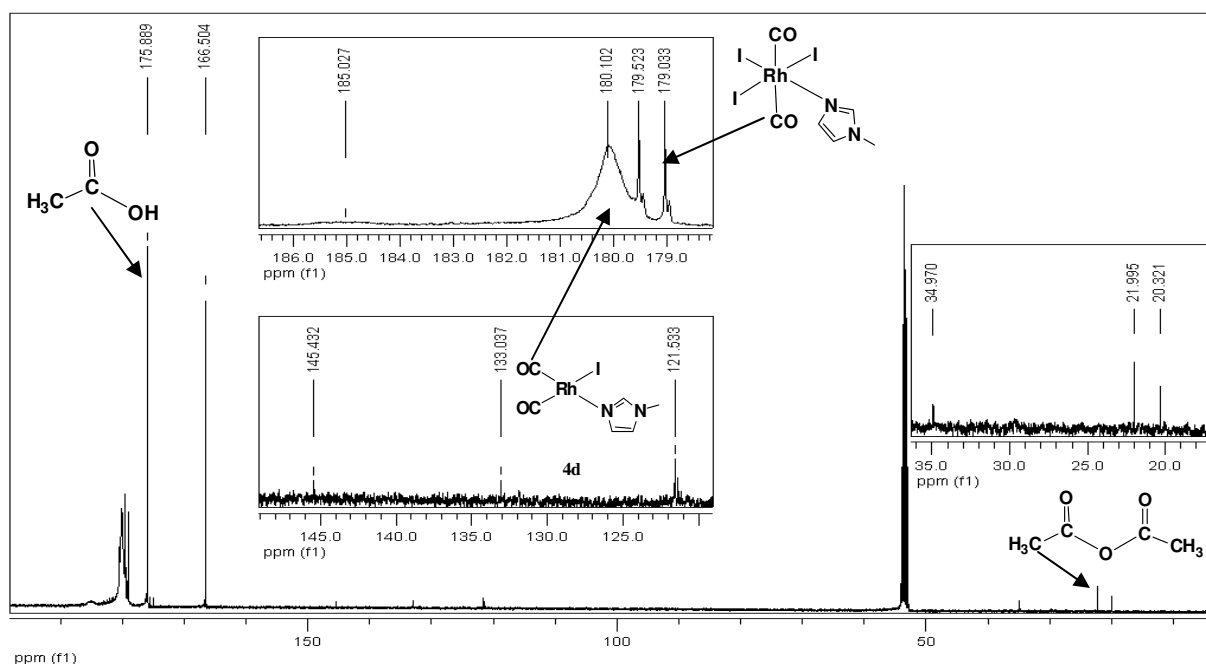


Figure 17. $^{13}\text{C}\{^1\text{H}\}$ NMR spectrum in the 10.0-190.0 ppm region at 298 K in CD_2Cl_2 : Under ^{13}CO atm during 36 hours, occurs reductive elimination of **7d** affording **4d**.

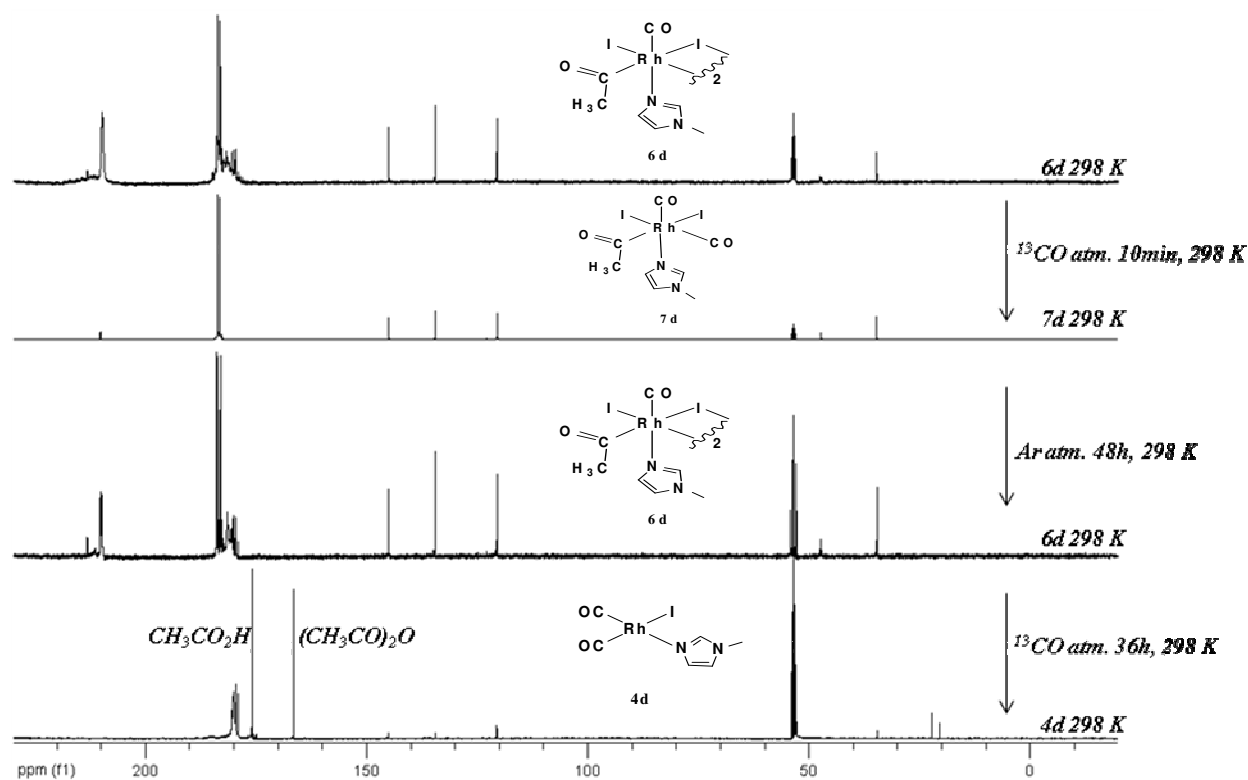


Figure 18. $^{13}\text{C}\{^1\text{H}\}$ NMR stacked spectra of **6d-7d-6d-4d** at 298 K in CD_2Cl_2 .

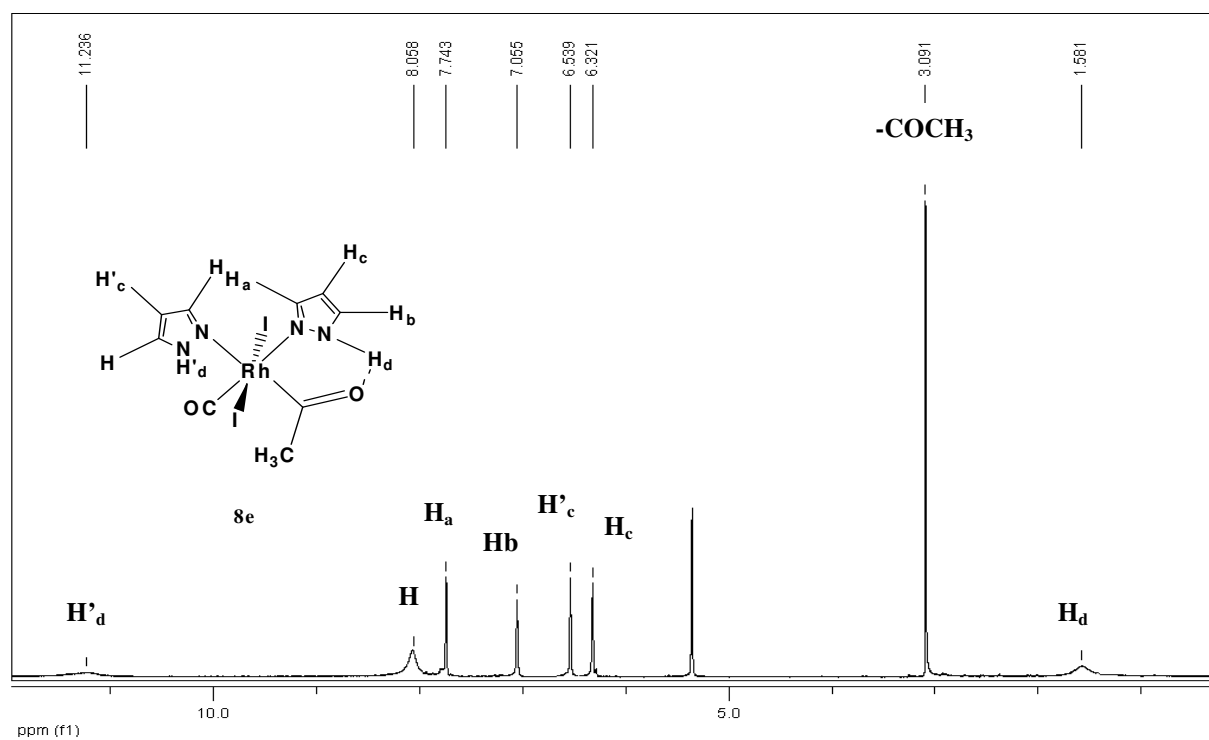


Figure 19. ^1H NMR spectrum of **8e** in the 1.00-12.00 ppm region at 298 K in CD_2Cl_2 .

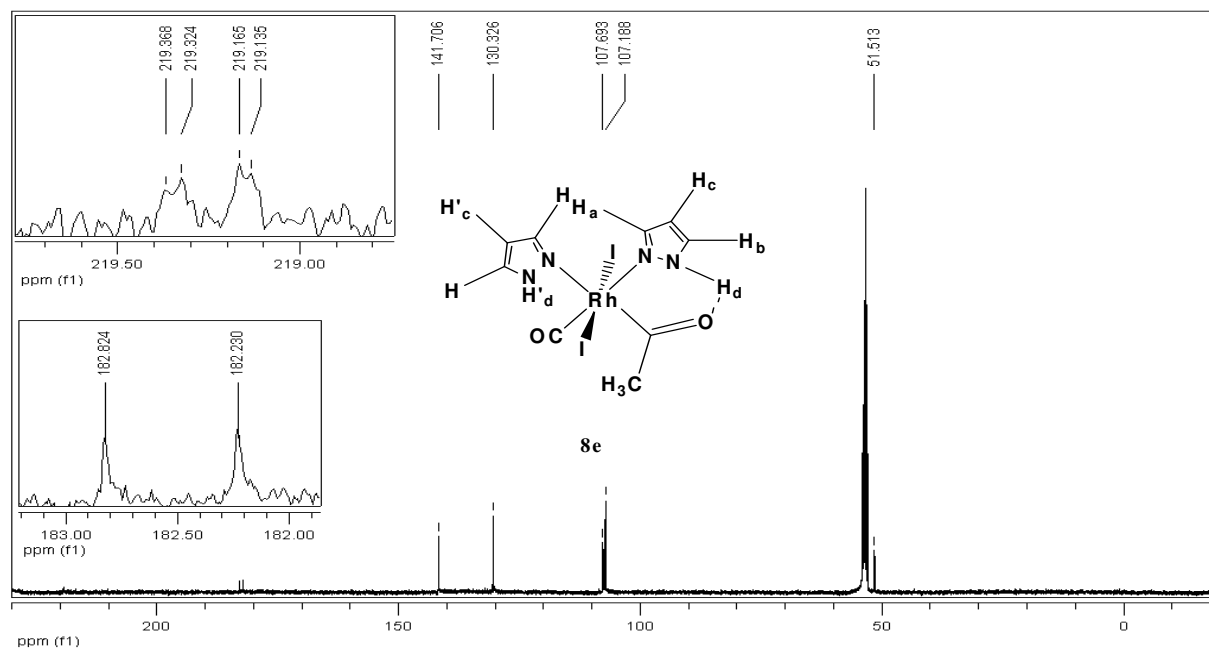


Figure 20. $^{13}\text{C}\{^1\text{H}\}$ NMR spectrum of **8e** at 298 K in CD_2Cl_2 .

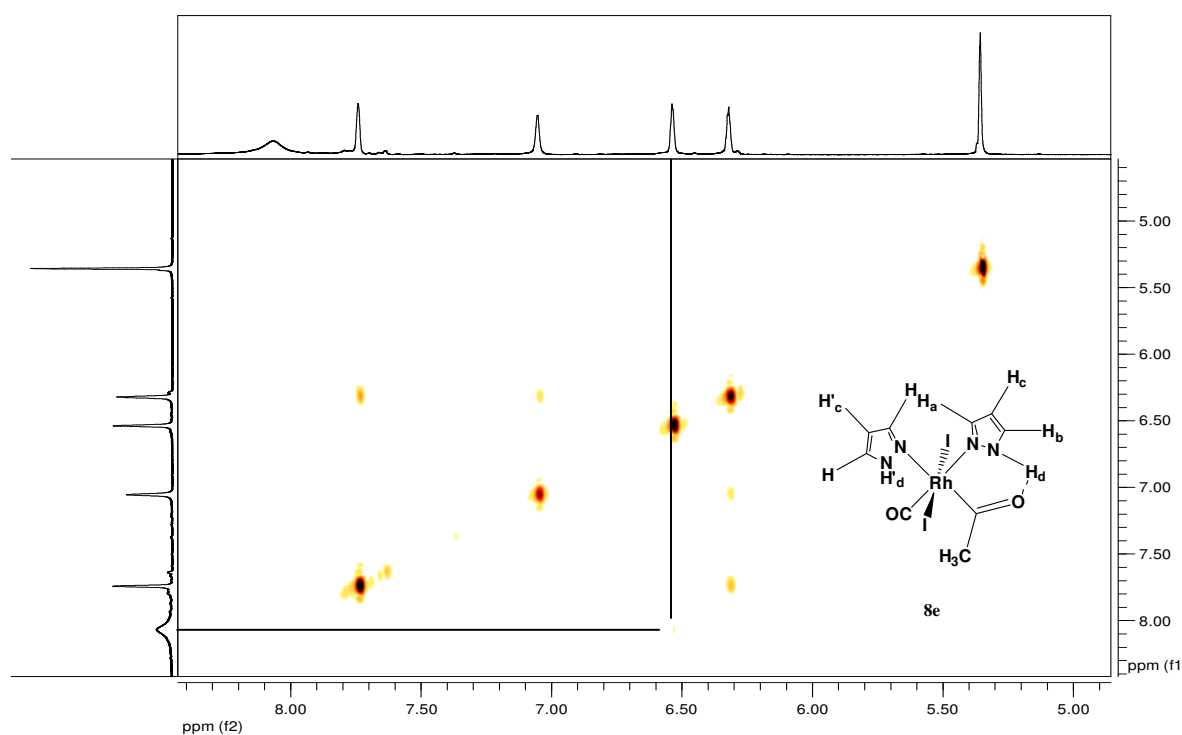


Figure 21. 2D ^1H - ^1H COSY NMR spectrum of **8e** in the 5.00-9.00 ppm region at 298 K in CD_2Cl_2 .

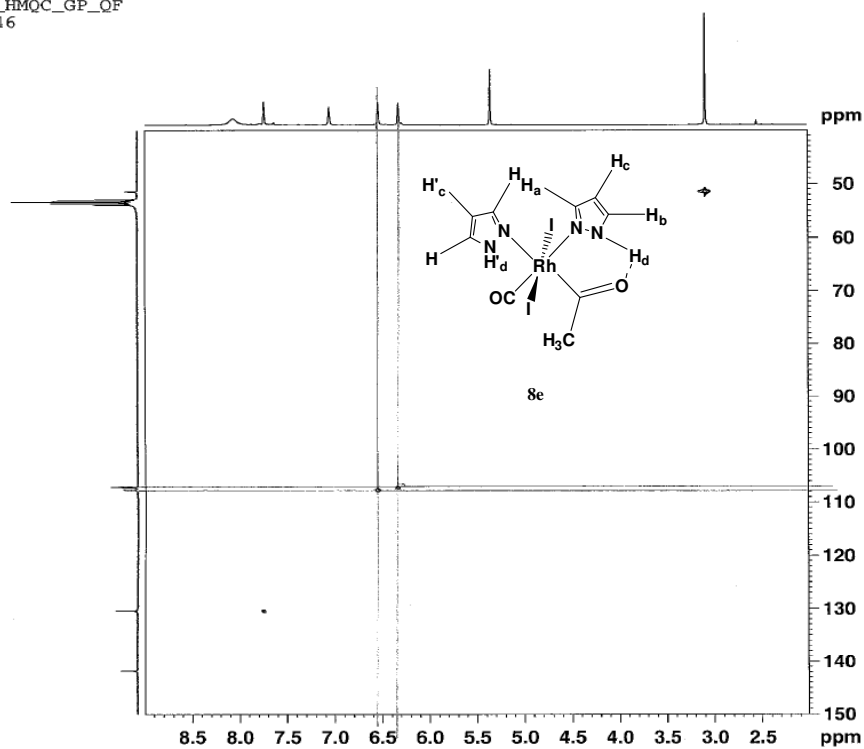
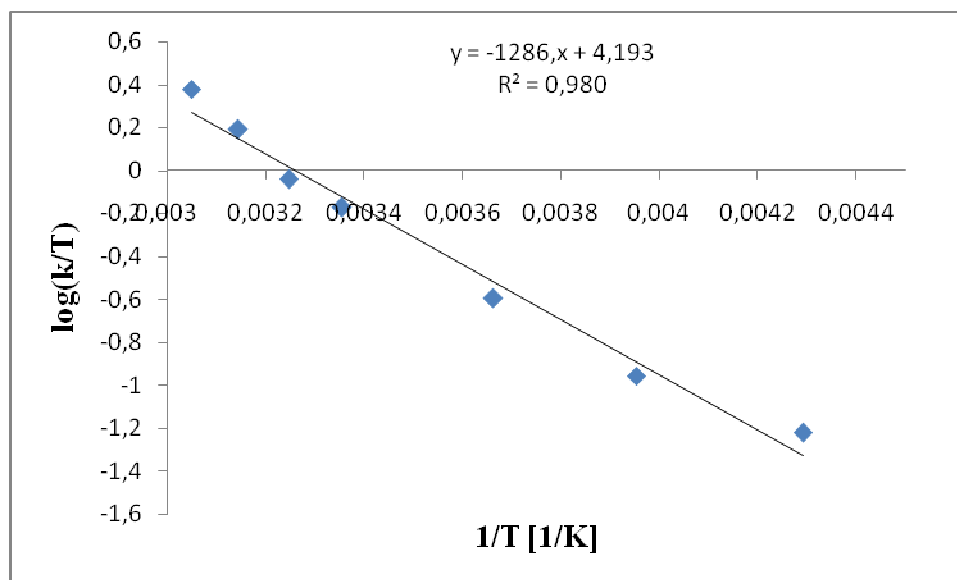
C13_HMQC_GP_QF
RA346

Figure 22. 2D ^1H - ^{13}C HMQC NMR spectrum of **8e** at 298 K in CD_2Cl_2 .

VI- EYRING PLOTS & RELATIVE ACTIVATION PARAMETER

DETERMINATIONS (ΔH^\ddagger ΔS^\ddagger ΔG^\ddagger and E_a) FOR NMR EXCHANGE PROCESSESLigand-exchange parameters of **4c***: (*CD₃OD)

T (Kelvin)	k (s ⁻¹)
328	783
318	495
308	279
298	201
273	69
253	28
233	14

4c* Eyring plot:

Graph 1

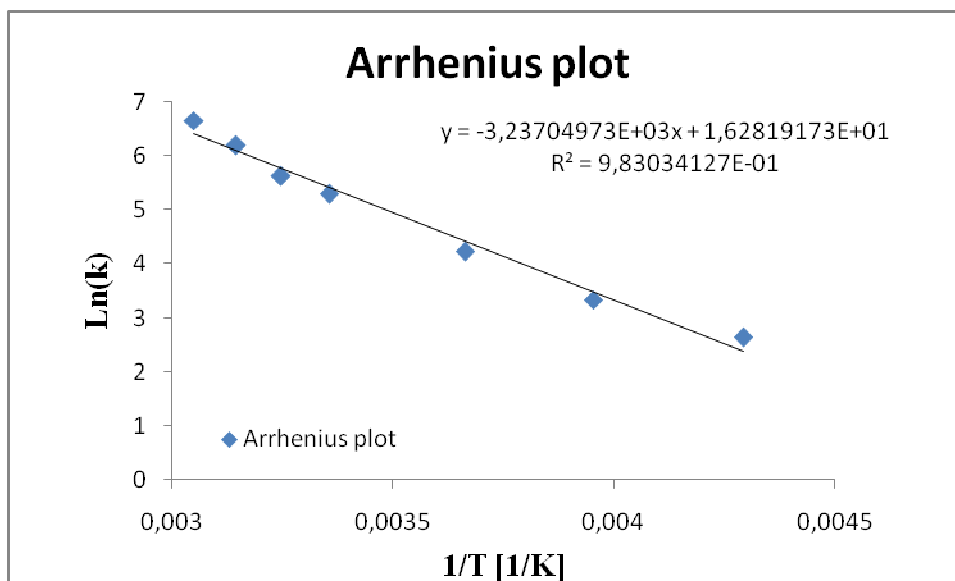
$$\Delta H^\ddagger = 5891 \frac{\text{cal}}{\text{mol}} = 24648 \frac{\text{J}}{\text{mol}} = 24.65 \frac{\text{KJ}}{\text{mol}}$$

$$\Delta S^\ddagger = -28.06 \frac{\text{cal}}{\text{K.mol}} = -117.40 \frac{\text{J}}{\text{K.mol}}$$

4c* coalescence temperature $T_c > 328$ K:

$$\Delta G^\ddagger > 5891 - 328 (-28.06) > 15094.68 \text{ cal.mol}^{-1} > 15.095 \text{ Kcal.mol}^{-1} > 63.156 \text{ KJ.mol}^{-1}$$

$$(1 \text{ cal} = 4.184 \text{ J})$$



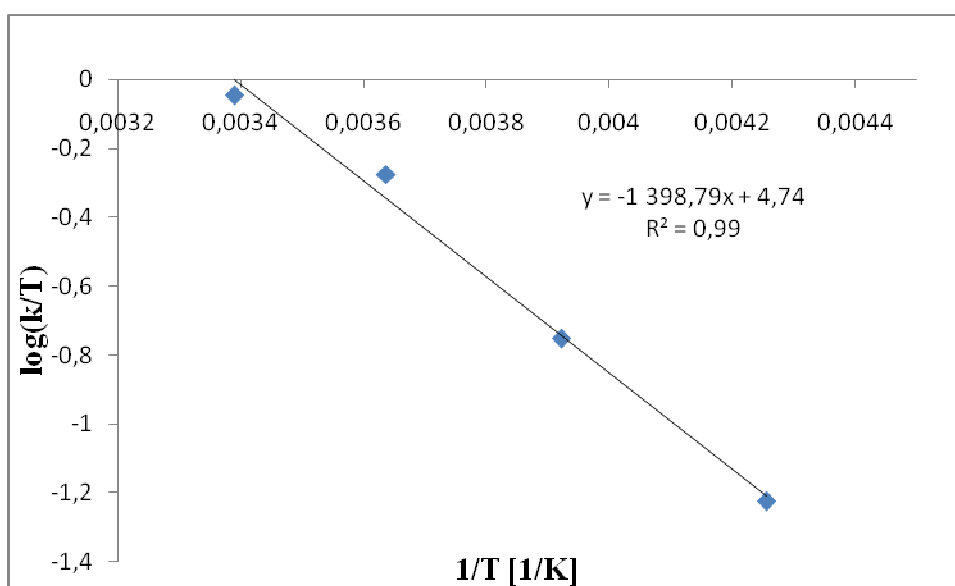
Graph 2

$$E_a = 26912.83 \text{ J.mol}^{-1} = 26.913 \text{ KJ.mol}^{-1}$$

Ligand-exchange parameters of **4d**:

T (Kelvin)	k (s^{-1})
295	265
275	146
255	45
235	14

4d Eyring plot:



Graph 3

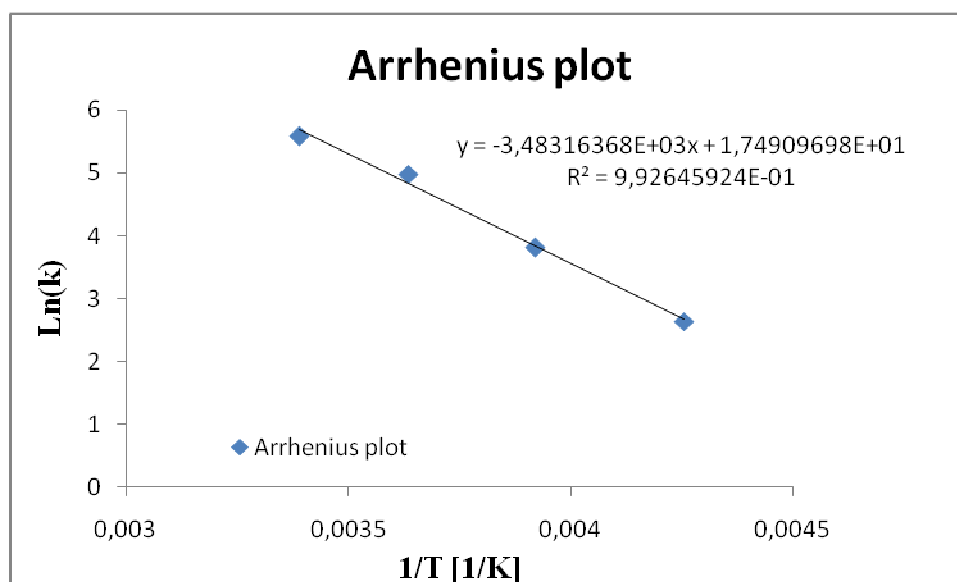
$$\Delta H^\ddagger = 6407 \frac{\text{cal}}{\text{mol}} = 26807 \frac{\text{J}}{\text{mol}} = 26.81 \frac{\text{KJ}}{\text{mol}}$$

$$\Delta S^\ddagger = -25.56 \frac{\text{cal}}{\text{K.mol}} = -106.94 \frac{\text{J}}{\text{K.mol}}$$

4d coalescence temperature $T_c > 295$ K:

$$\Delta G^\ddagger > 6407 - 295 (-25.56) > 13947.20 \text{ cal.mol}^{-1} > 13.947 \text{ Kcal.mol}^{-1} > 58.355 \text{ KJ.mol}^{-1}$$

$$(1 \text{ cal} = 4.184 \text{ J})$$



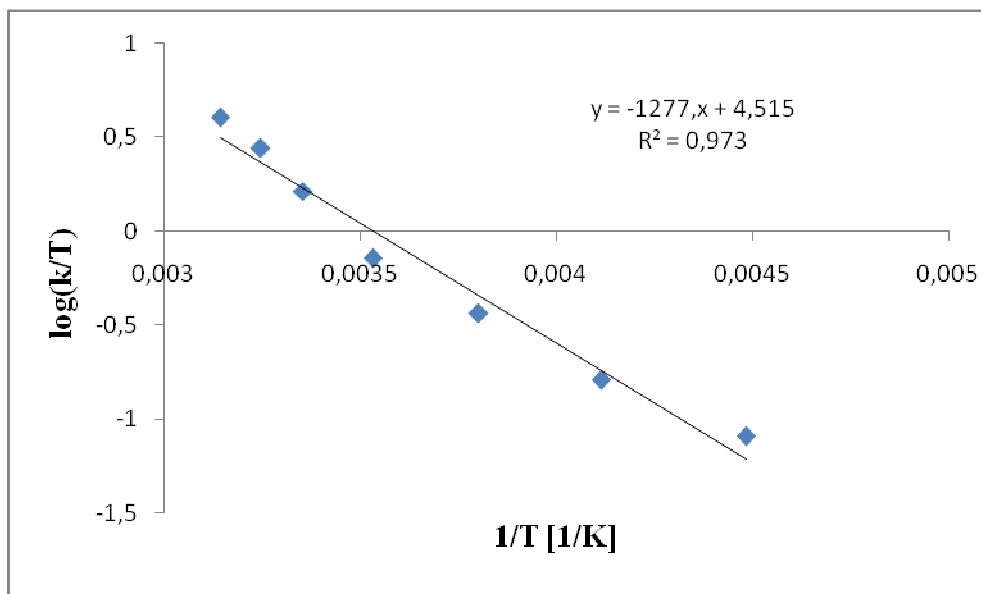
Graph 4

$$E_a = 28959.02 \text{ J.mol}^{-1} = 28.959 \text{ KJ.mol}^{-1}$$

Ligand-exchange parameters of **4d***: (*CD₃OD)

T (Kelvin)	k (s ⁻¹)
318	1278
308	852
298	486
283	203
263	96
243	39
223	18

4d* Eyring plot:



Graph 5

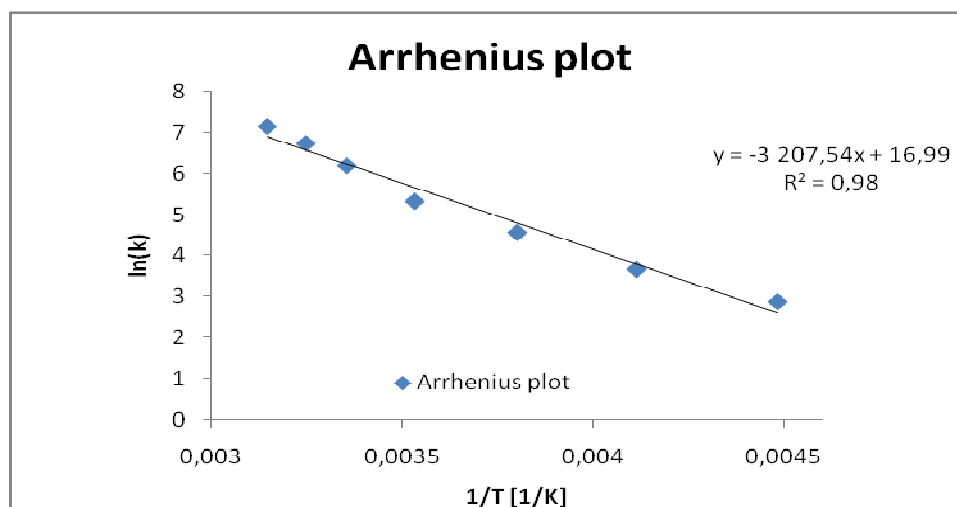
$$\Delta H^\ddagger = 5853 \frac{\text{cal}}{\text{mol}} = 24489 \frac{\text{J}}{\text{mol}} = 24.49 \frac{\text{KJ}}{\text{mol}}$$

$$\Delta S^\ddagger = -26.61 \frac{\text{cal}}{\text{K.mol}} = -111.34 \frac{\text{J}}{\text{K.mol}}$$

4d* coalescence temperature $T_c = 328$ K:

$$\Delta G^\ddagger = 5853 - 328 (-26.61) = 14581.08 \text{ cal.mol}^{-1} = 14.581 \text{ Kcal.mol}^{-1} = 61.007 \text{ KJ.mol}^{-1}$$

$$(1 \text{ cal} = 4.184 \text{ J})$$



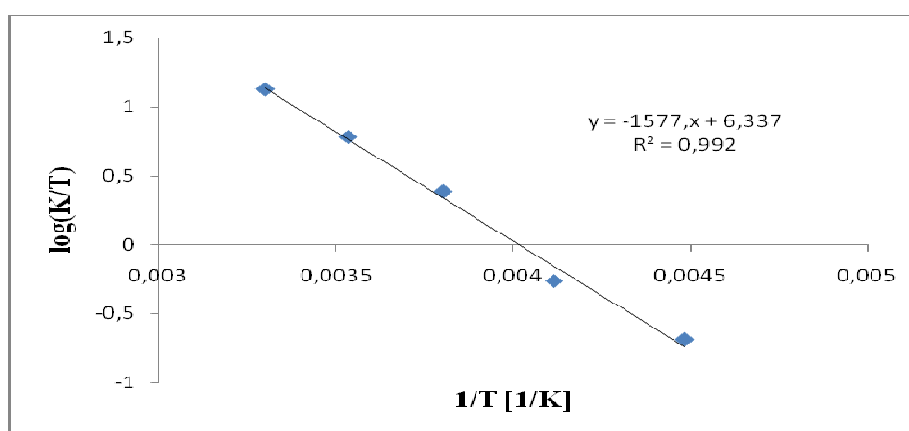
Graph 6

$$E_a = 26667.48 \text{ J.mol}^{-1} = 26.667 \text{ KJ.mol}^{-1}$$

Ligand-exchange parameters of **4e**:

T (Kelvin)	k (s^{-1})
303	4030
283	1710
263	640
243	133
223	46

4e Eyring plot:



Graph 7

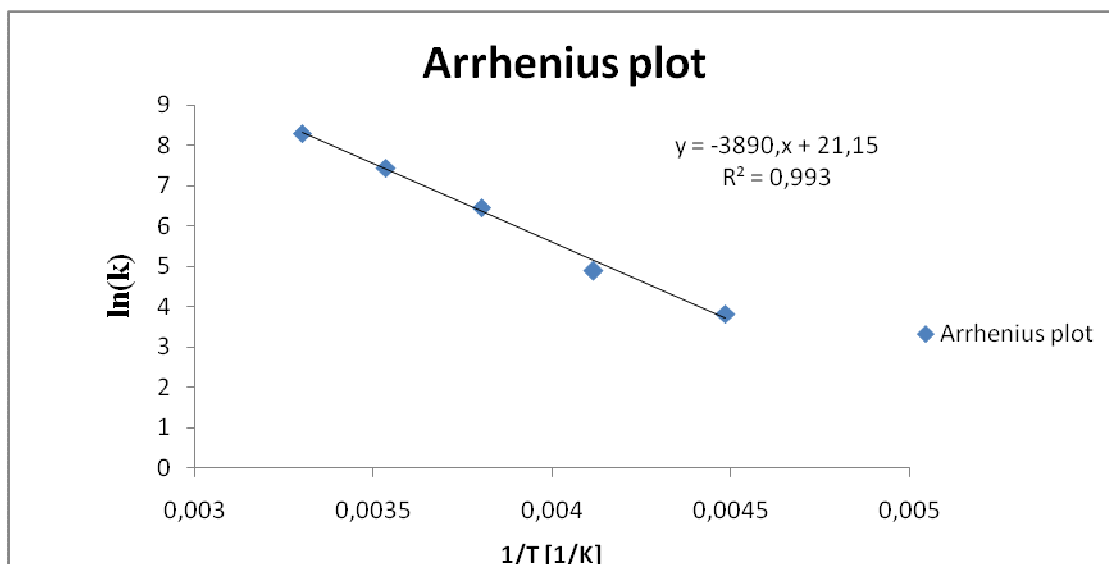
$$\Delta H^\ddagger = 7225.4 \frac{\text{cal}}{\text{mol}} = 30231 \frac{\text{J}}{\text{mol}} = 30.23 \frac{\text{KJ}}{\text{mol}}$$

$$\Delta S^\ddagger = -18.22 \frac{\text{cal}}{\text{K.mol}} = -76.23 \frac{\text{J}}{\text{K.mol}}$$

4e coalescence temperature $T_c = 283 \text{ K}$:

$$\Delta G^\ddagger = 7225.4 - 283 (-18.22) = 12381.66 \text{ cal.mol}^{-1} = 12.382 \text{ Kcal.mol}^{-1} = 51.805 \text{ KJ.mol}^{-1}$$

$$(1 \text{ cal} = 4.184 \text{ J})$$



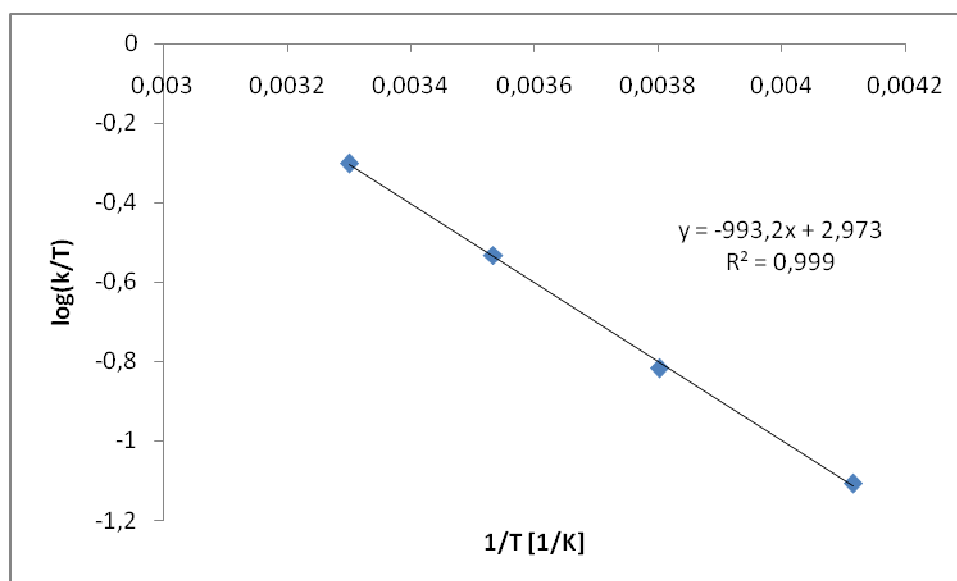
Graph 8

$$E_a = 32349.03 \text{ J.mol}^{-1} = 32.349 \text{ KJ.mol}^{-1}$$

H-exchange parameters of **4e**:

T (Kelvin)	k (s^{-1})
303	151
283	83
263	40
243	19

4e Eyring plot:



Graph 9

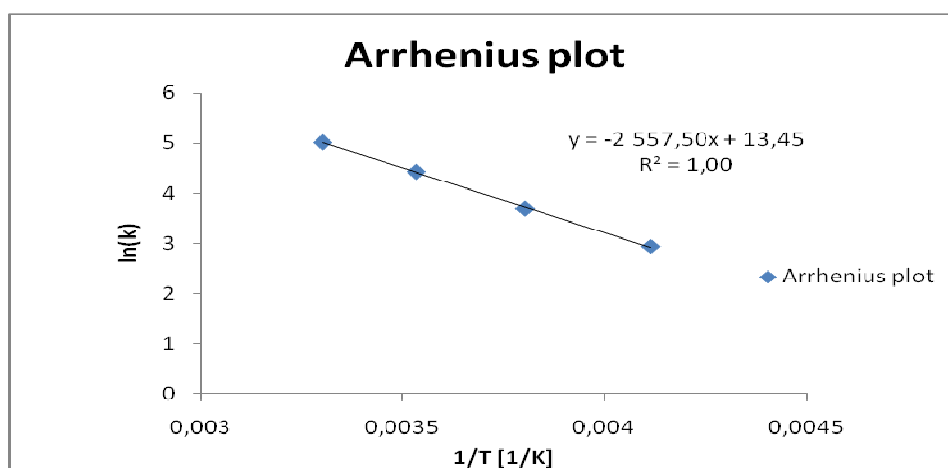
$$\Delta H^\ddagger = 4549.3 \frac{\text{cal}}{\text{mol}} = 19034.27 \frac{\text{J}}{\text{mol}} = 19.034 \frac{\text{KJ}}{\text{mol}}$$

$$\Delta S^\ddagger = -33.66 \frac{\text{cal}}{\text{K.mol}} = -140.83 \frac{\text{J}}{\text{K.mol}}$$

4e coalescence temperature $T_c = 303 \text{ K}$:

$$\Delta G^\ddagger = 4549.3 - 303 (-33.66) = 14748.28 \text{ cal.mol}^{-1} = 14.748 \text{ Kcal.mol}^{-1} = 61.707 \text{ KJ.mol}^{-1}$$

(1 cal = 4.184 J)



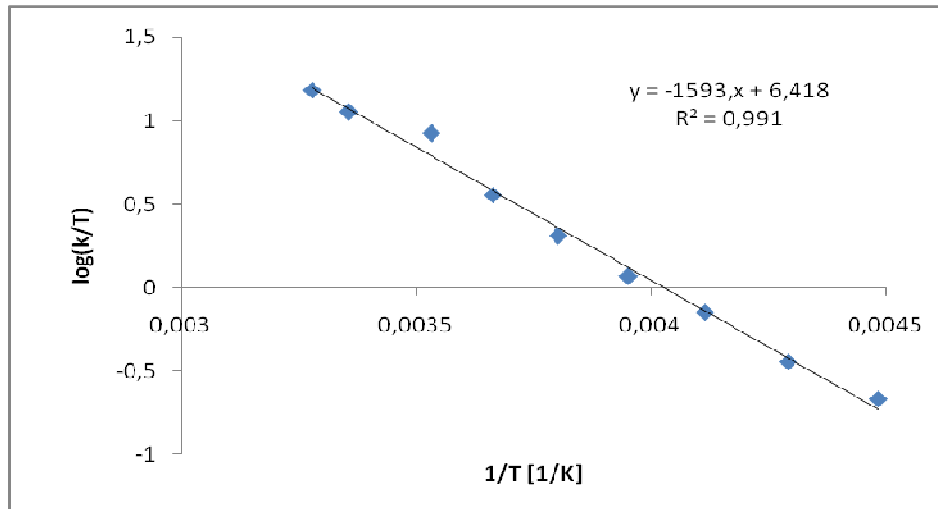
Graph 10

$$E_a = 21263.05 \text{ J.mol}^{-1} = 21.263 \text{ KJ.mol}^{-1}$$

Ligand-exchange parameters of 4f:

T (Kelvin)	k (s^{-1})
305	4664
298	3364
283	2364
273	984
263	534
253	294
243	174
233	84
223	48

4f Eyring plot:



Graph 11

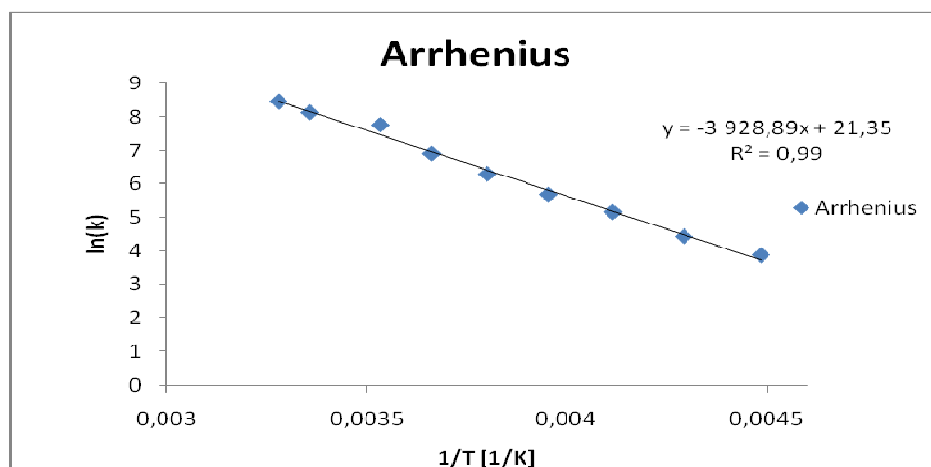
$$\Delta H^\ddagger = 7295.9 \frac{\text{cal}}{\text{mol}} = 30526.05 \frac{\text{J}}{\text{mol}} = 30.526 \frac{\text{KJ}}{\text{mol}}$$

$$\Delta S^\ddagger = -17.86 \frac{\text{cal}}{\text{K.mol}} = -74.726 \frac{\text{J}}{\text{K.mol}}$$

4f coalescence temperature $T_c = 283$ K:

$$\Delta G^\ddagger = 7295.9 - 283 (-17.86) = 12350.28 \text{ cal.mol}^{-1} = 12.350 \text{ Kcal.mol}^{-1} = 51.674 \text{ KJ.mol}^{-1}$$

(1 cal = 4.184 J)



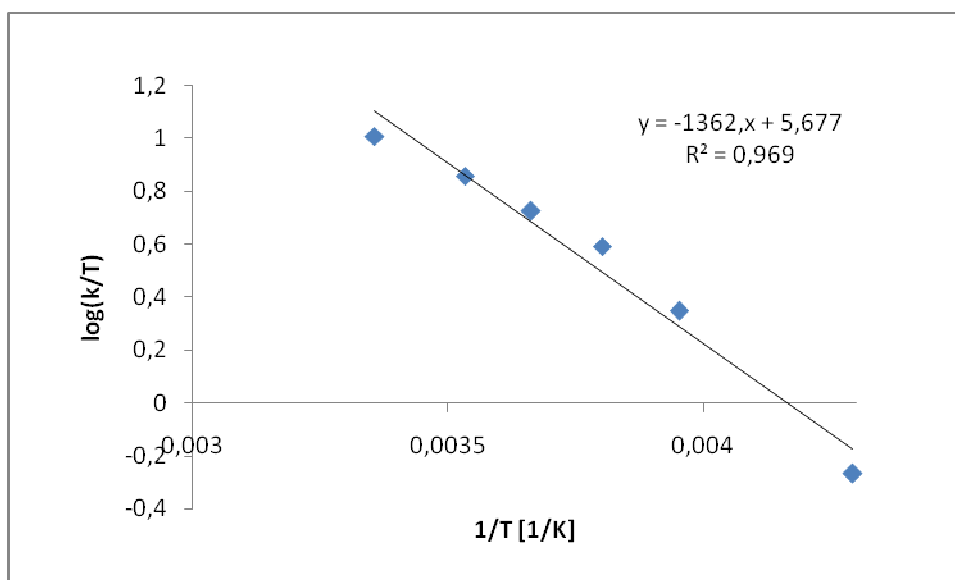
Graph 12

$$E_a = 32664.79 \text{ J.mol}^{-1} = 32.665 \text{ KJ.mol}^{-1}$$

Ligand-exchange parameters of **4g**:

<i>T</i> (Kelvin)	<i>k</i> (s ⁻¹)
298	3039
283	2043
273	1449
263	1026
253	564
233	126

4g Eyring plot:



Graph 13

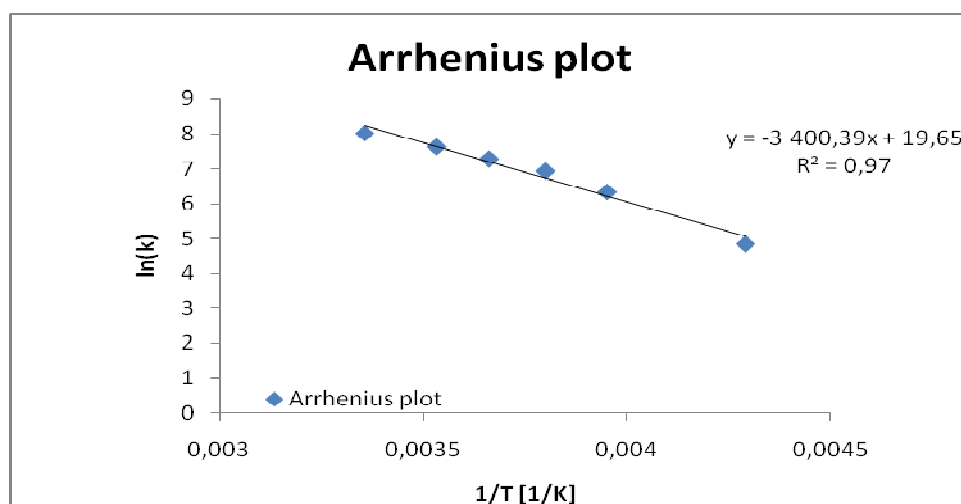
$$\Delta H^\ddagger = 6243 \frac{\text{cal}}{\text{mol}} = 26120.71 \frac{\text{J}}{\text{mol}} = 26.12 \frac{\text{KJ}}{\text{mol}}$$

$$\Delta S^\ddagger = -21.25 \frac{\text{cal}}{\text{K.mol}} = -88.91 \frac{\text{J}}{\text{K.mol}}$$

4g coalescence temperature $T_c = 273 \text{ K}$:

$$\Delta G^\ddagger = 6243 - 273 (-21.25) = 12044.25 \text{ cal.mol}^{-1} = 12.044 \text{ Kcal.mol}^{-1} = 50.393 \text{ KJ.mol}^{-1}$$

$$(1 \text{ cal} = 4.184 \text{ J})$$



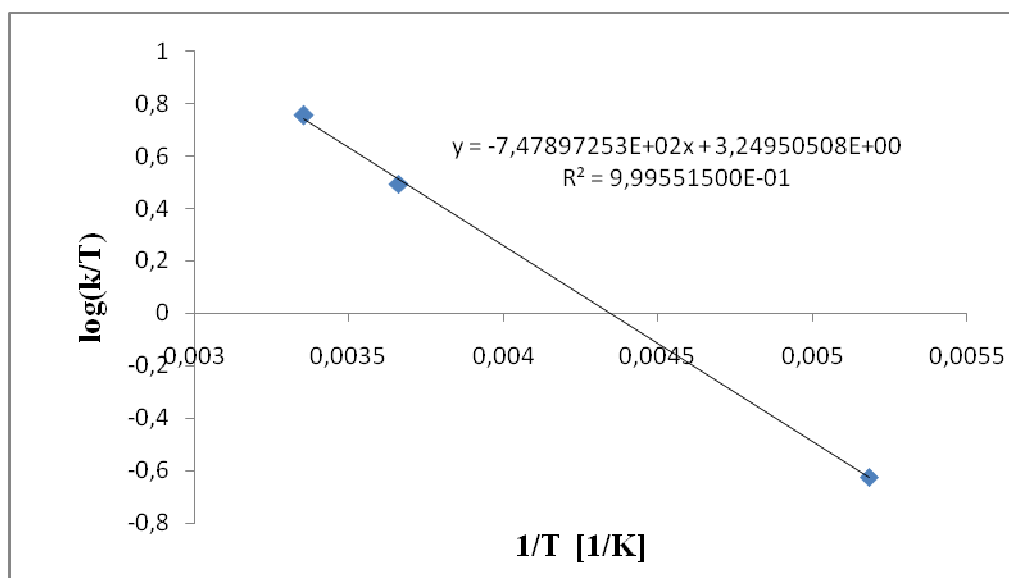
Graph 14

$$E_a = 28270.8 \text{ J.mol}^{-1} = 28.271 \text{ KJ.mol}^{-1}$$

Ligand-exchange parameters of **4h**:

T (Kelvin)	k (s^{-1})
298	1690
273	850
193	46

4h Eyring plot:



Graph 15

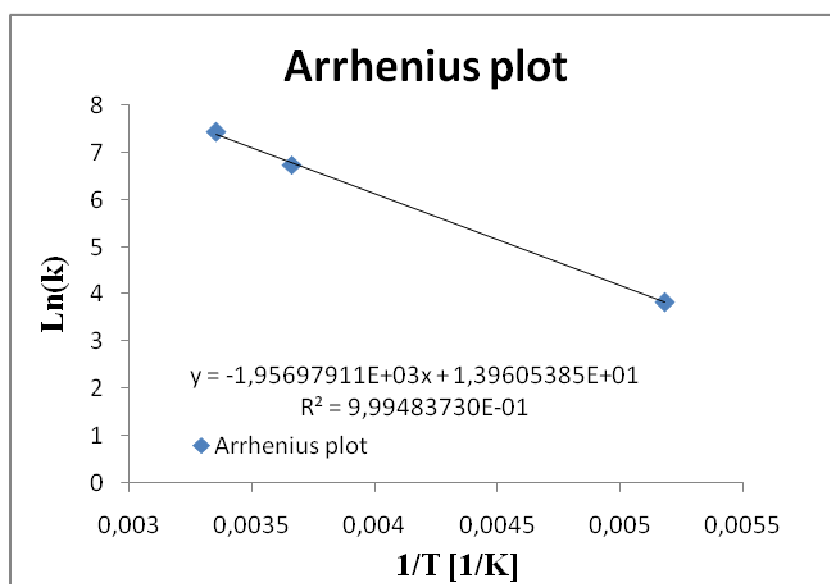
$$\Delta H^\ddagger = 3425.4 \frac{\text{cal}}{\text{mol}} = 14331.87 \frac{\text{J}}{\text{mol}} = 14.33 \frac{\text{KJ}}{\text{mol}}$$

$$\Delta S^\ddagger = -32.38 \frac{\text{cal}}{\text{K.mol}} = -135.48 \frac{\text{J}}{\text{K.mol}}$$

4h coalescence temperature $T_c = 298 \text{ K}$:

$$\Delta G^\ddagger = 3425.4 - 298 (-32.38) = 13074.64 \text{ cal.mol}^{-1} = 13.075 \text{ Kcal.mol}^{-1} = 54.704 \text{ KJ.mol}^{-1}$$

$$(1 \text{ cal} = 4.184 \text{ J})$$



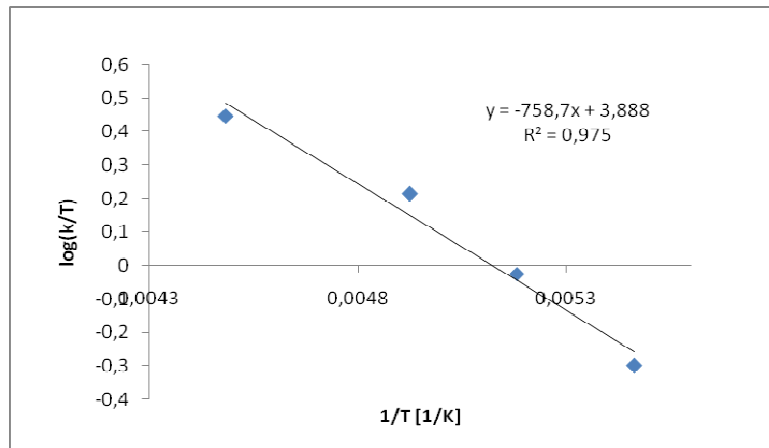
Graph 16

$$E_a = 16270.32 \text{ J.mol}^{-1} = 16.270 \text{ KJ.mol}^{-1}$$

Ligand-exchange parameters of **4i**:

T (Kelvin)	k (s^{-1})
223	623
203	332
193	182
183	92

4i Eyring plot:



Graph 17

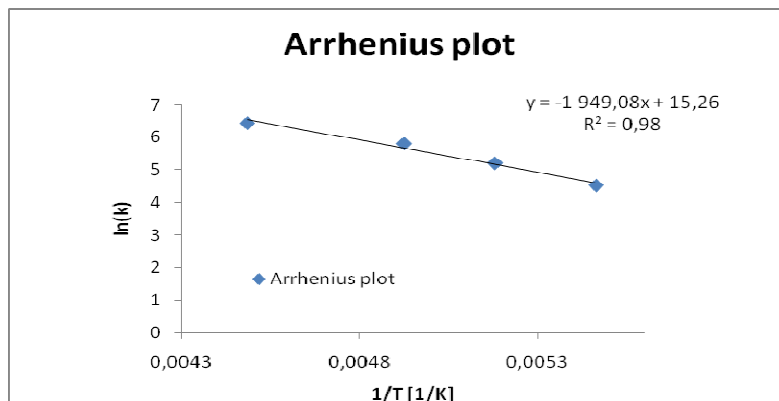
$$\Delta H^\ddagger = 3476.2 \frac{\text{cal}}{\text{mol}} = 14544.42 \frac{\text{J}}{\text{mol}} = 14.54 \frac{\text{KJ}}{\text{mol}}$$

$$\Delta S^\ddagger = -29.45 \frac{\text{cal}}{\text{K.mol}} = -123.22 \frac{\text{J}}{\text{K.mol}}$$

4i coalescence temperature $T_c = 223 \text{ K}$:

$$\Delta G^\ddagger = 3476.2 - 223 (-29.45) = 10043.55 \text{ cal.mol}^{-1} = 10.044 \text{ Kcal.mol}^{-1} = 42.022 \text{ KJ.mol}^{-1}$$

$$(1 \text{ cal} = 4.184 \text{ J})$$



Graph 18

$$E_a = 16204.65 \text{ J.mol}^{-1} = 16.205 \text{ KJ.mol}^{-1}$$

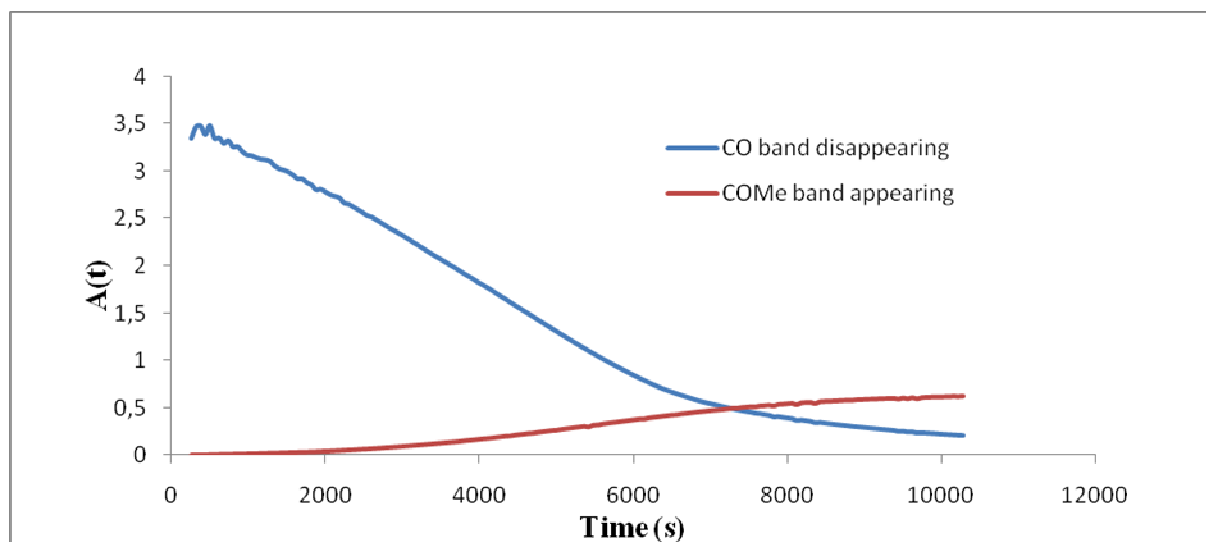
VII- IR-MONITORED KINETIC CH₃I OXIDATIVE ADDITION DATAKinetic data for complex **4a**

Figure 1. Antisymmetric CO band $A(t)$ disappearance for **4a** at 288.4 K.

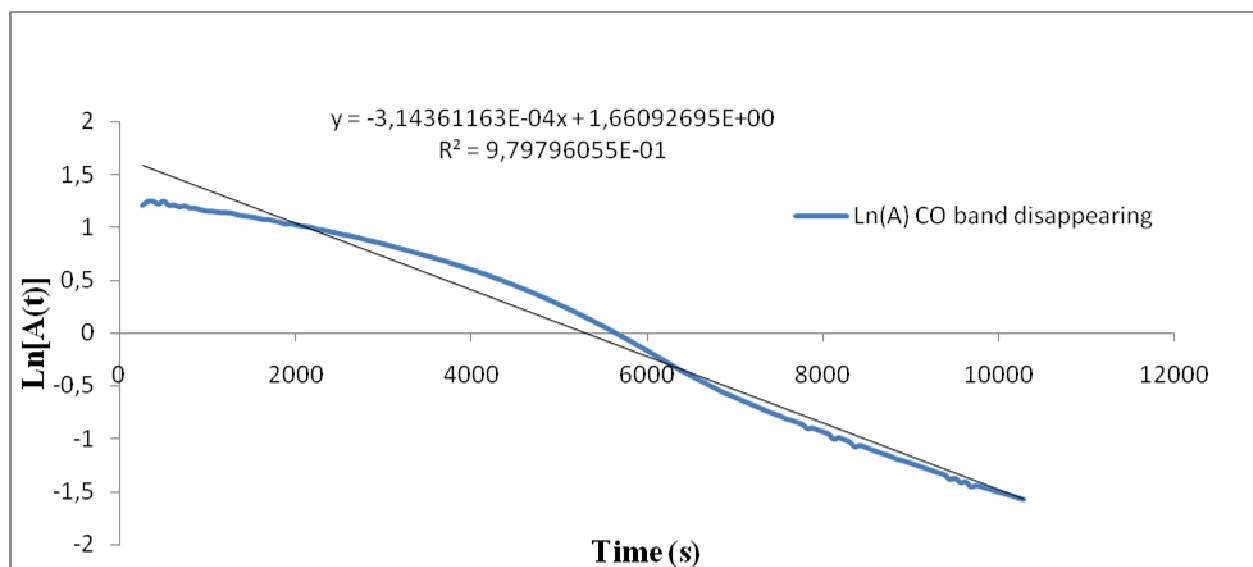


Figure 2. $\ln[A(t)]$ vs. time plot for **4a** at 288.4 K: $k_{288.4}$ determination.

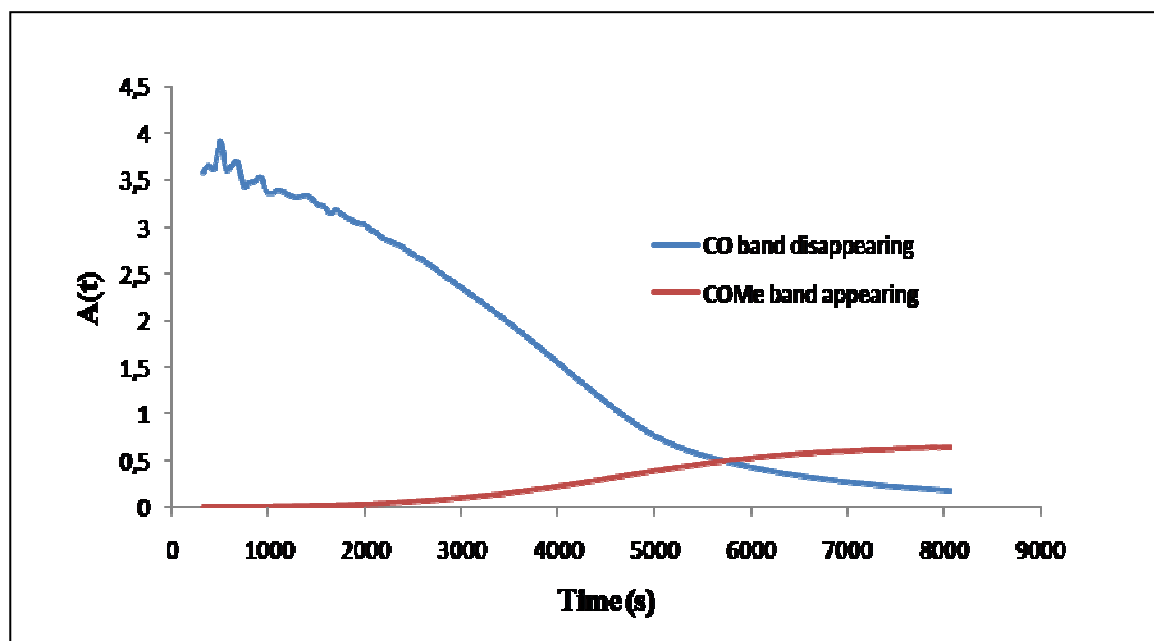


Figure 3. Antisymmetric CO band $A(t)$ disappearance for **4a** at 293 K.

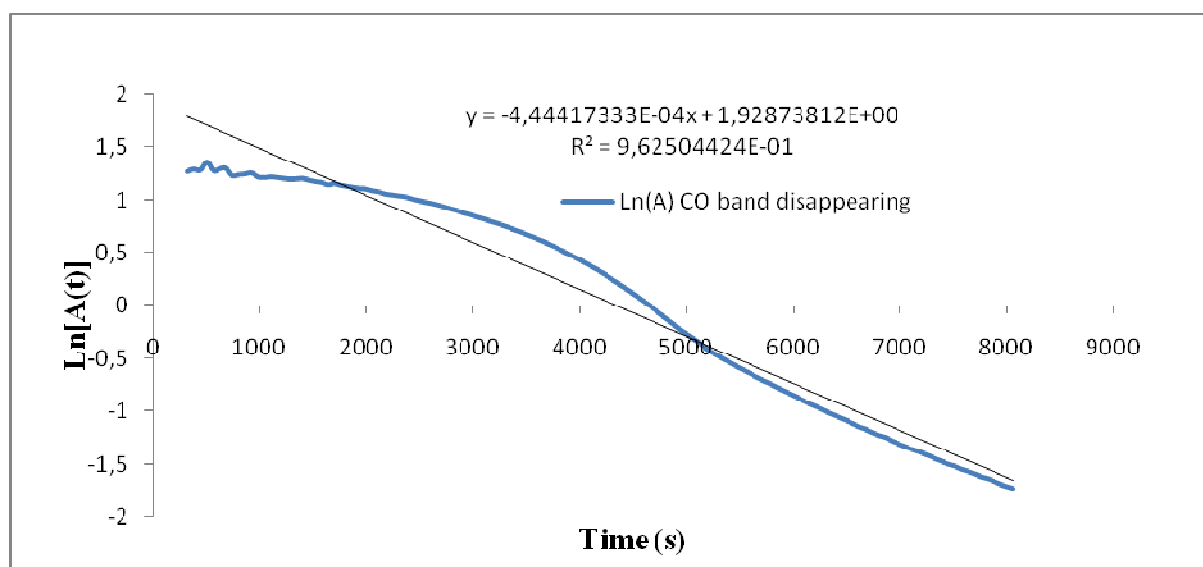


Figure 4. $\ln[A(t)]$ vs. time plot for **4a** at 293 K: k_{293} determination.

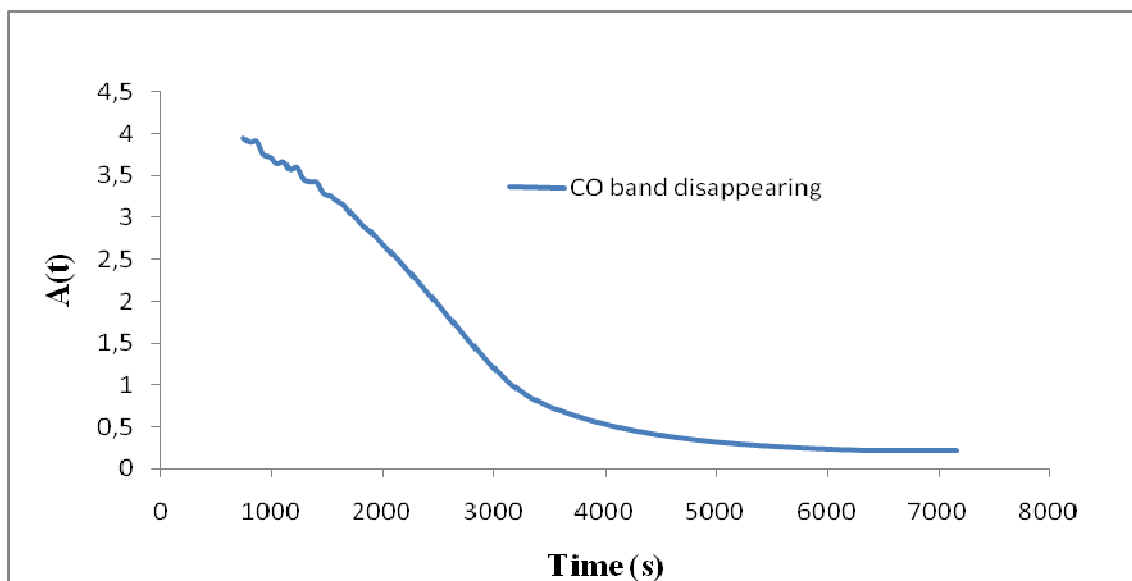


Figure 5. Antisymmetric CO band A(t) disappearance for **4a** at 298.2 K.

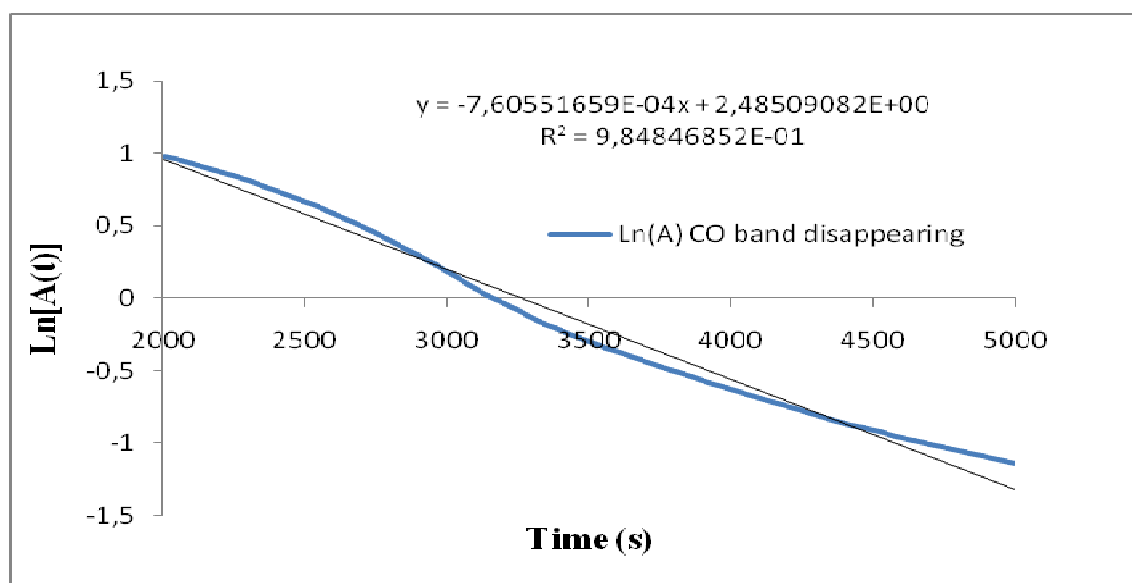


Figure 6. Ln[A(t)] vs. time plot for **4a** at 298.2 K: $k_{298.2}$ determination.

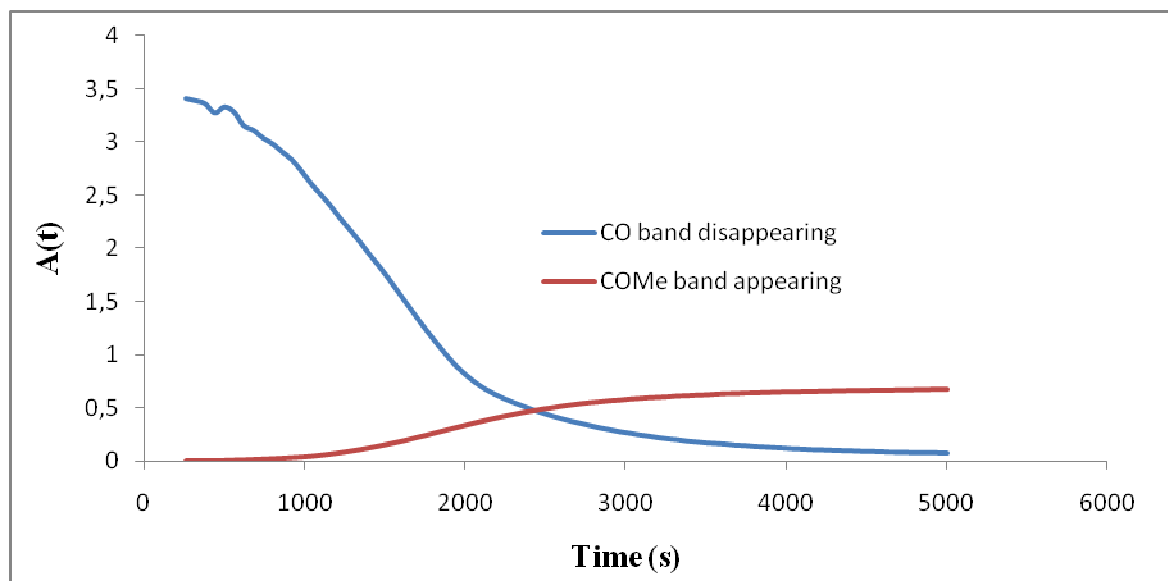


Figure 7. Antisymmetric CO band $A(t)$ disappearance for **4a** at 303 K.

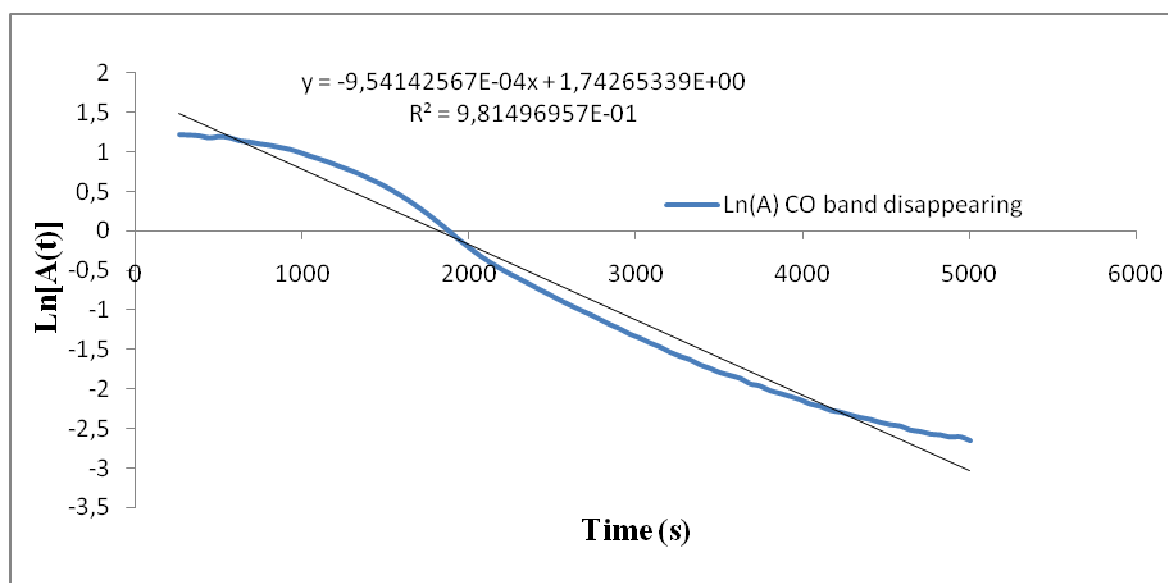
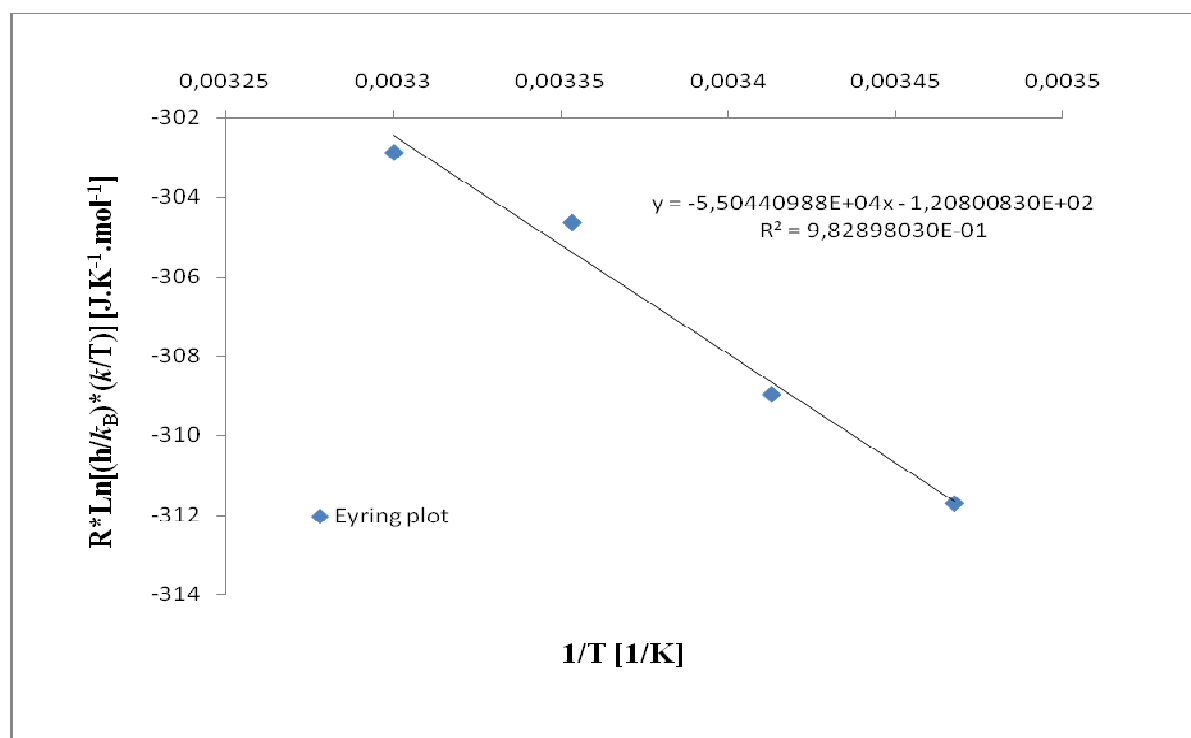


Figure 8. $\ln[A(t)]$ vs. time plot for **4a** at 303 K: k_{303} determination.

Table 1.

$T(^{\circ}\text{C})$	$T(\text{K})$	$1/T$	k	$\text{Ln}(k)$
15.4	288.4	0.00346741	0.00031436116300	-8.064968032
20	293	0.00341297	0.00044441733300	-7.718746498
25.2	298.2	0.003353454	0.0007605516590	-7.181466521
30	303	0.00330033	0.0009541425670	-6.954697456
$\text{Ln}(k/T)$	k/T	$(h/k_B)*(k/T)$	$\text{Ln}[(h/k_B)*(k/T)]$	$R*(\text{Ln}[(h/k_B)*(k/T)])$
-13.72931643780380	0.00000109001790222	$5.231261 \cdot 10^{-17}$	-37.4892942	-311.7036869
-13.39891910682620	0.00000151678270648	$7.279409 \cdot 10^{-17}$	-37.15889687	-308.9566076
-12.87923092322340	0.00000255047504695	$1.224035 \cdot 10^{-16}$	-36.63920869	-304.6356747
-12.66843026189080	0.00000314898536964	$1.511274 \cdot 10^{-16}$	-36.42840802	-302.8829785

h : Planck constant $6.62606957(29) \times 10^{-34} \text{ J}\cdot\text{s}^{-1}$; Boltzmann constant k_B : $1.3806488(13) \times 10^{-23} \text{ J}\cdot\text{K}^{-1}$; R : gaz constant $8.314472 \text{ J}\cdot\text{mol}^{-1}\cdot\text{K}^{-1}$.

**Figure 9.** Eyring plot for 4a: ΔH^\ddagger and ΔS^\ddagger determination.

$$\Delta H^\ddagger = 55044.0988 \text{ J}\cdot\text{mol}^{-1} = 55.0440988 \text{ KJ}\cdot\text{mol}^{-1}$$

$$\Delta S^\ddagger = -120.800830 \text{ J}\cdot\text{K}^{-1}\cdot\text{mol}^{-1}$$

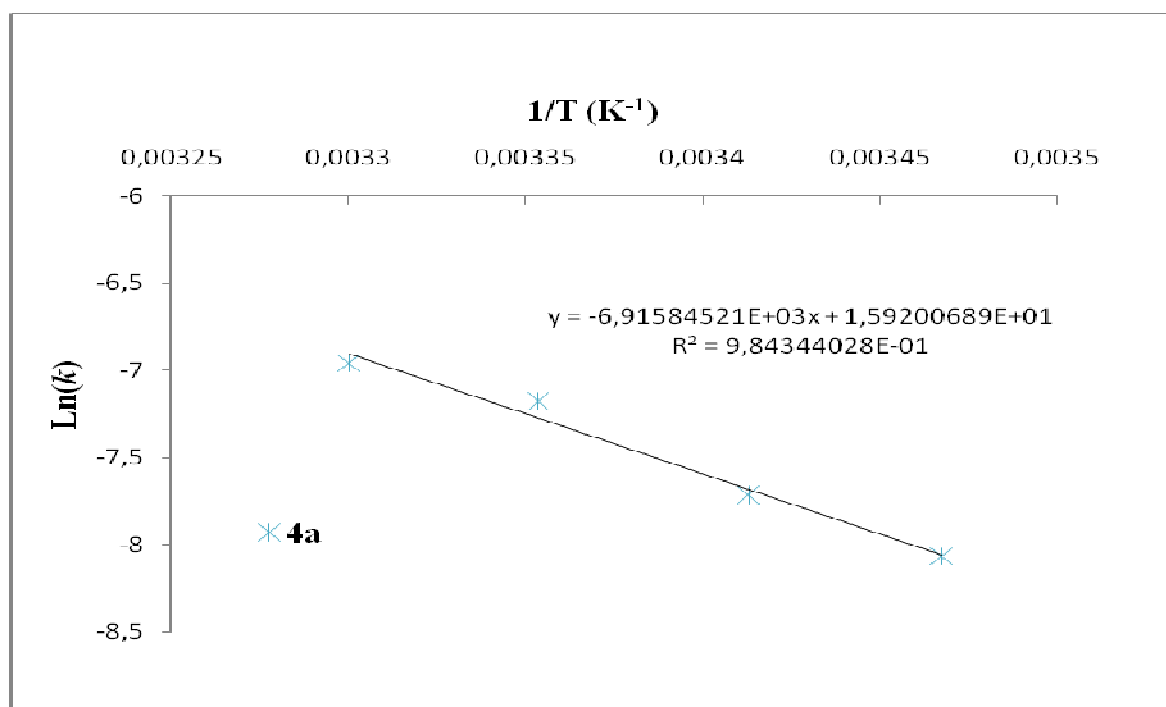


Figure 10. Arrhenius plot for **4a**: E_a determination.

$$E_a = 57498.33707594 \text{ J.mol}^{-1} = 57.49833707594 \text{ KJ.mol}^{-1}$$

Kinetic data for complex **4c**

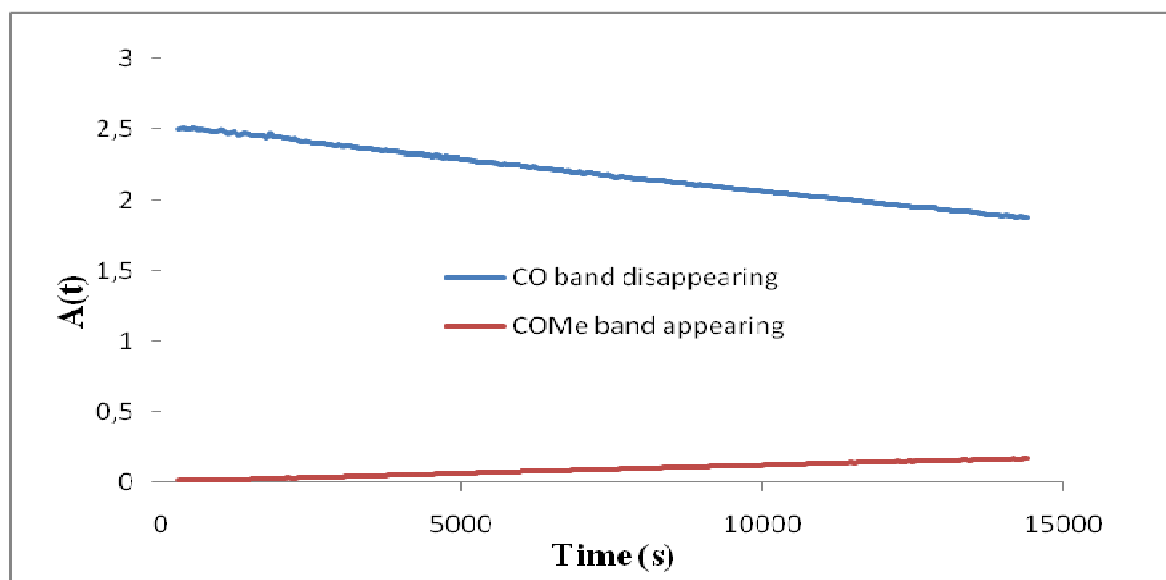


Figure 11. Antisymmetric CO band $A(t)$ disappearance for **4c** at 293.4 K.

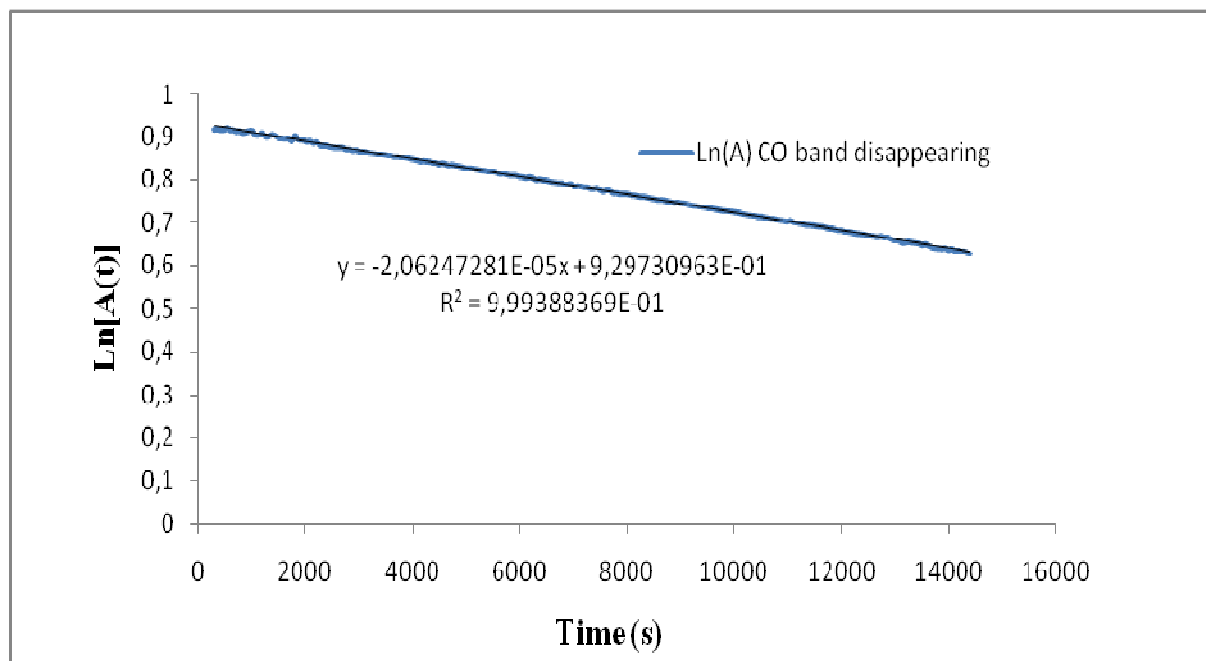


Figure 12. $\text{Ln}[A(t)]$ vs. time plot for **4c** at 293.4 K: $k_{293.4}$ determination.

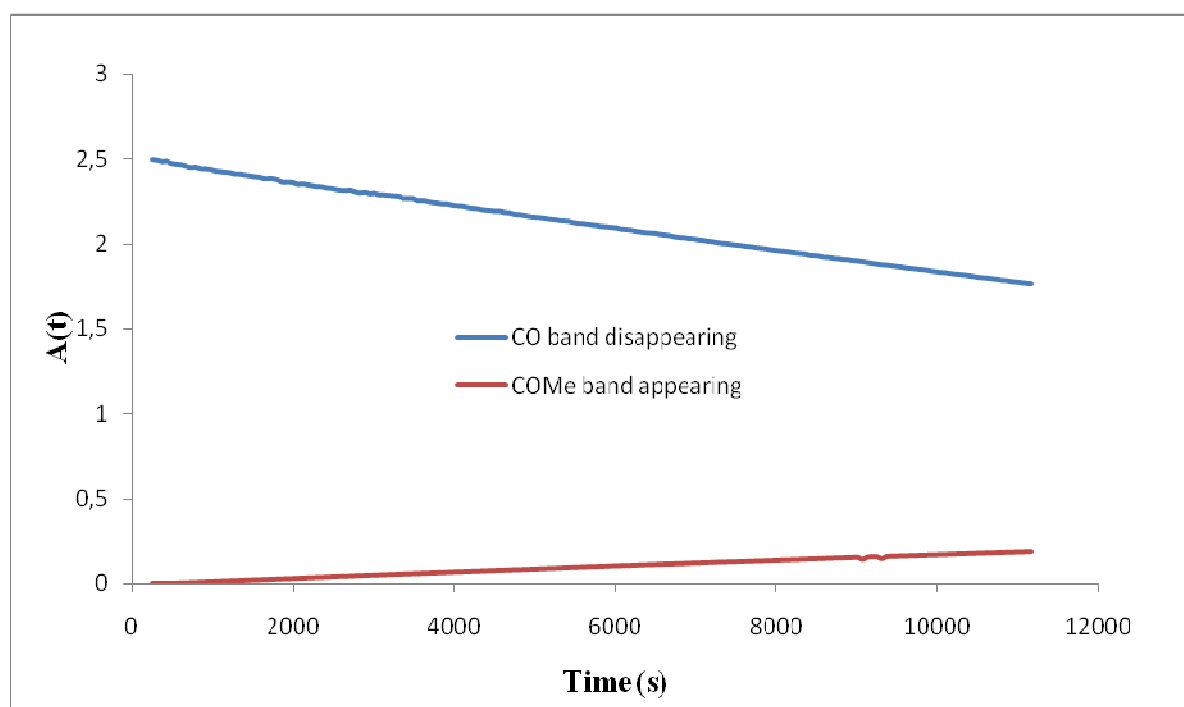


Figure 13. Antisymmetric CO band $A(t)$ disappearance for **4c** at 298 K.

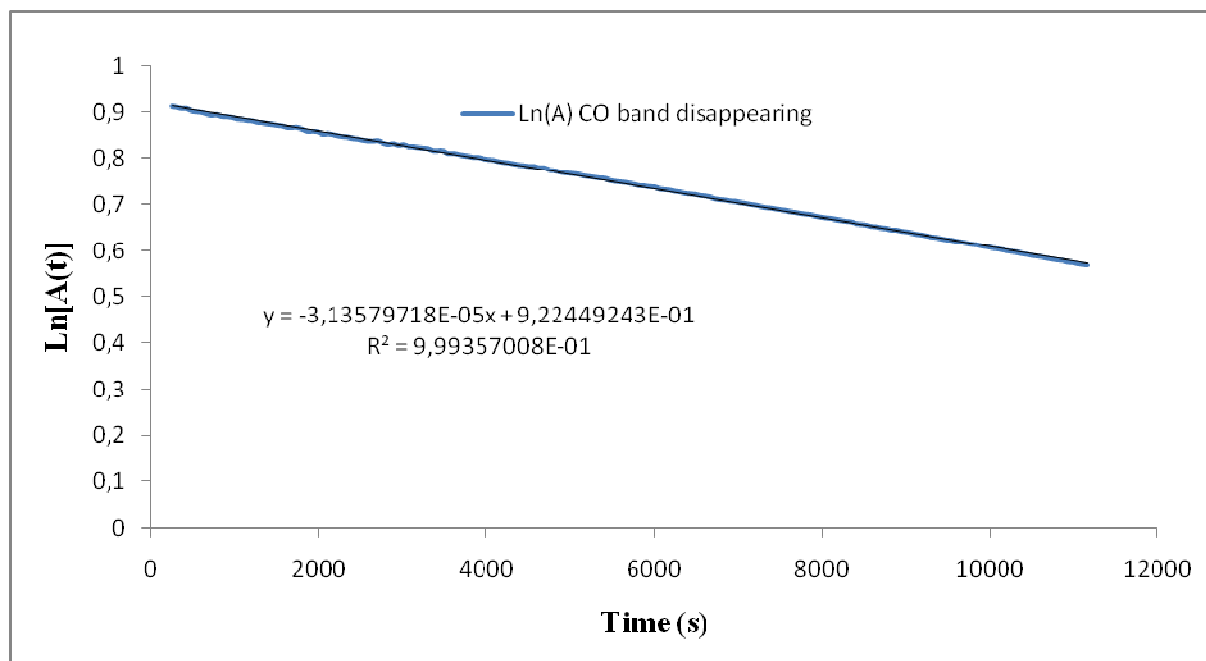


Figure 14. $\text{Ln}[A(t)]$ vs. time plot for **4c** at 298 K: k_{298} determination.

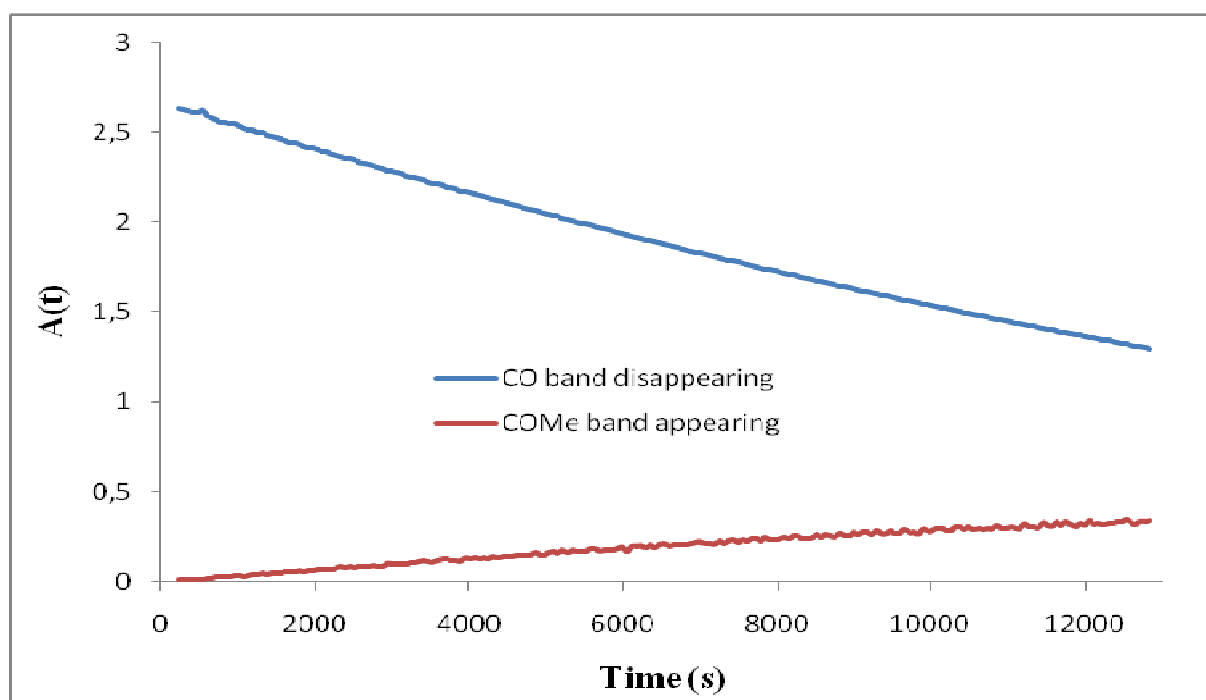


Figure 15. Antisymmetric CO band $A(t)$ disappearance for **4c** at 303 K.

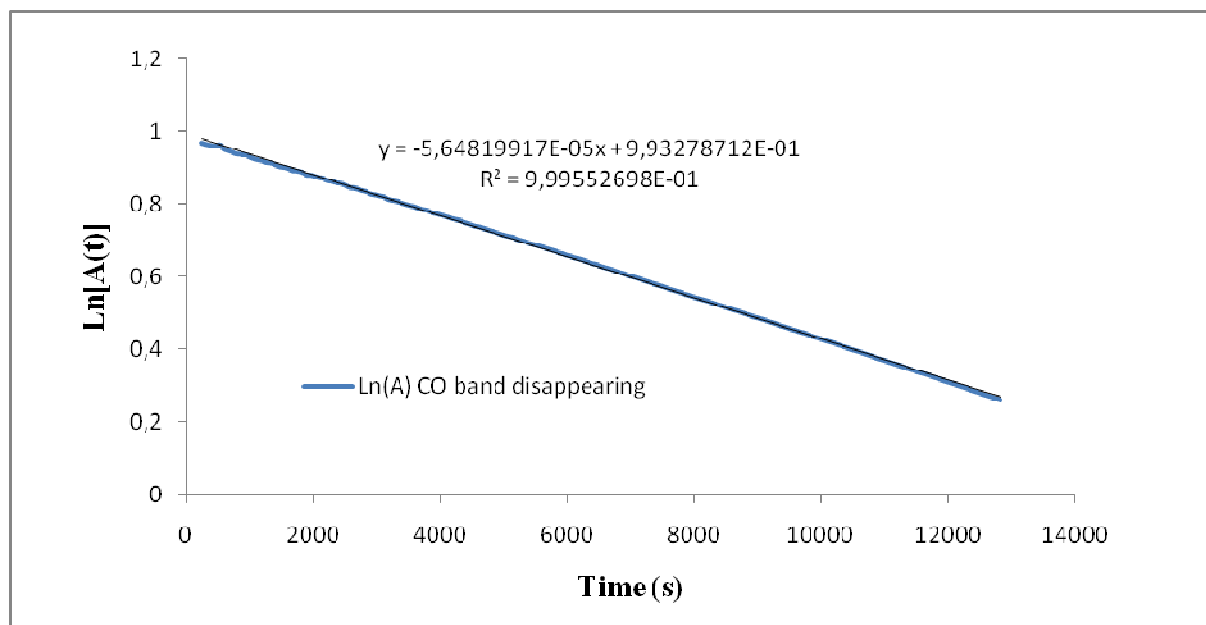


Figure 16. $\text{Ln}[A(t)]$ vs. time plot for **4c** at 303 K: k_{303} determination.

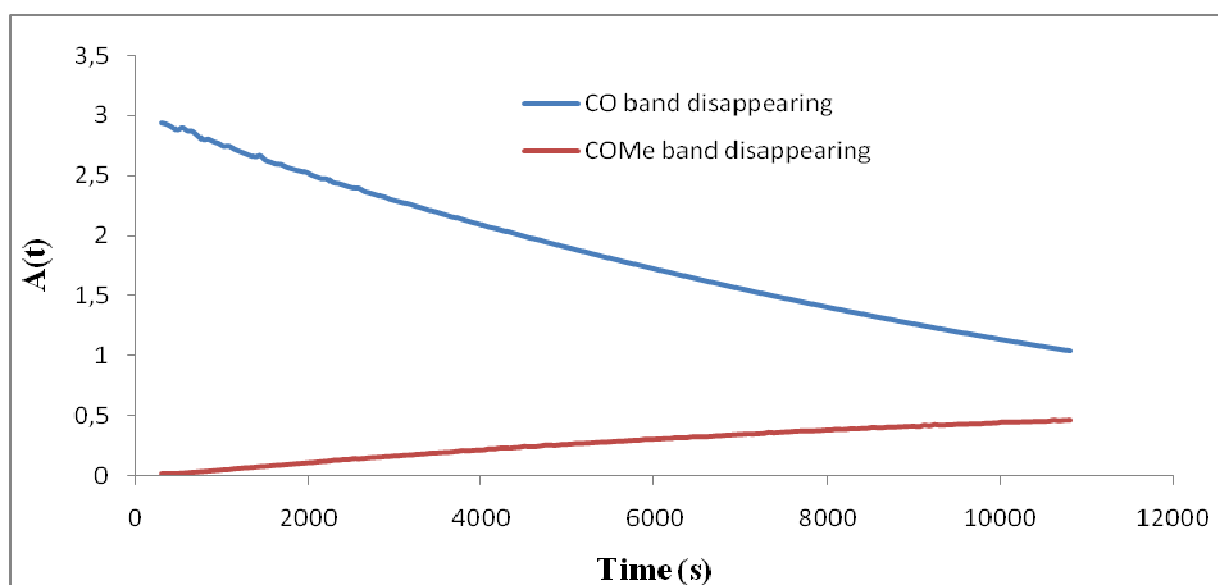


Figure 17. Antisymmetric CO band $A(t)$ disappearance for **4c** at 308 K.

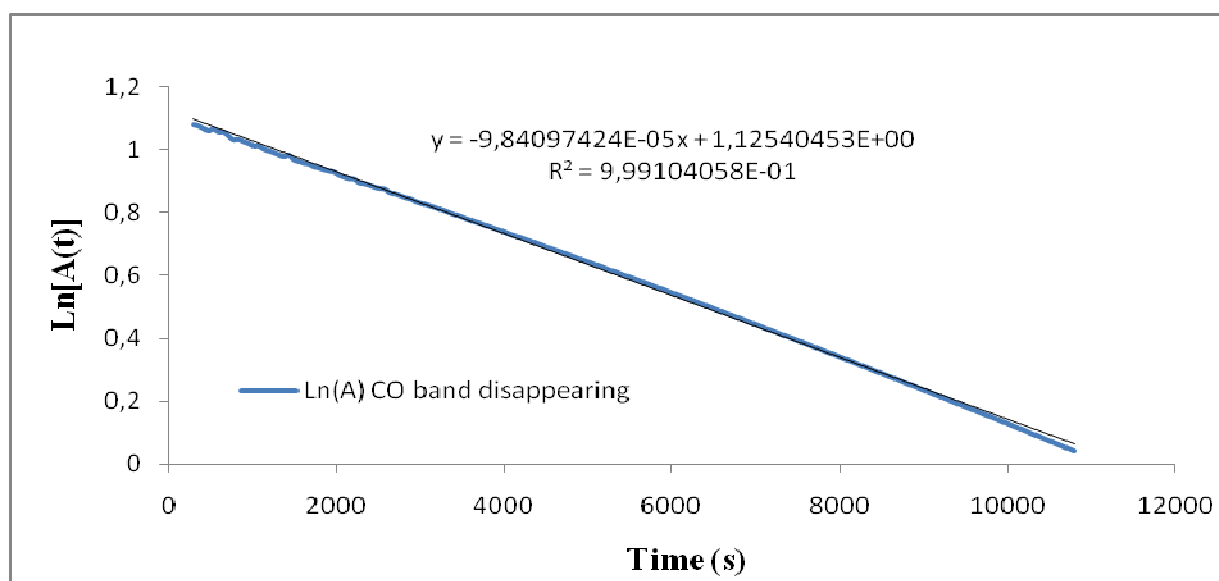


Figure 18. $\ln[A(t)]$ vs. time plot for **4c** at 308 K: k_{308} determination.

Table 2.

$T(^{\circ}\text{C})$	$T(\text{K})$	$1/T$	k	$\ln(k)$
20.4	293.4	0.0034083162	0.00002062472810	-10.78901981
25	298	0.0033557046	0.00003135797180	-10.37004204
30	303	0.0033003300	0.00005648199170	-9.781588702
35	308	0.0032467532	0.00009840974240	-9.226370751
$\ln(k/T)$	k/T	$(h/K_B) \cdot (k/T)$	$\ln[(h/K_B) \cdot (k/T)]$	$R^* (\ln[(h/K_B) \cdot (k/T)])$
-16.47055667456960	0.00000007029559680	$3.373656 \cdot 10^{-18}$	-40.23053444	-334.4956521
-16.06713552582390	0.00000010522809329	$5.050152 \cdot 10^{-18}$	-39.82711329	-331.1414183
-15.49532150710020	0.00000018640921353	$8.946231 \cdot 10^{-18}$	-39.25529927	-326.3870866
-14.95647053365050	0.00000031951215065	$1.533416 \cdot 10^{-17}$	-38.7164483	-321.9068253

h : Planck constant $6.62606957(29) \times 10^{-34} \text{ J}\cdot\text{s}^{-1}$; Boltzmann constant k_B : $1.3806488(13) \times 10^{-23} \text{ J}\cdot\text{K}^{-1}$; R : gas constant $8.314472 \text{ J}\cdot\text{mol}^{-1}\cdot\text{K}^{-1}$.

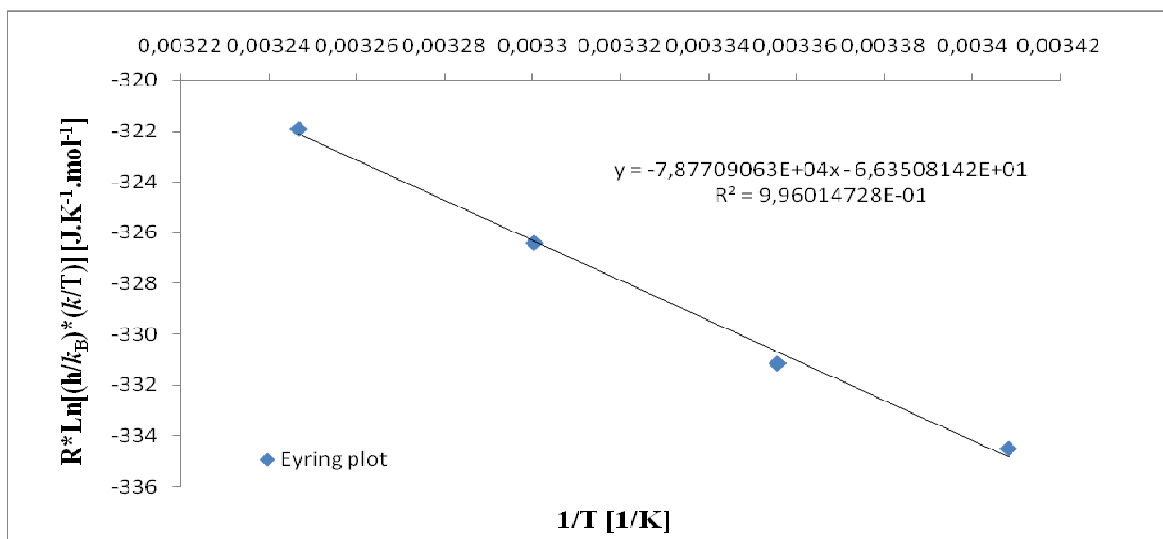


Figure 19. Eyring plot for **4c**: ΔH^\ddagger and ΔS^\ddagger determination.

$$\Delta H^\ddagger = 78770.9063 \text{ J} \cdot \text{mol}^{-1} = 78.7709063 \text{ KJ} \cdot \text{mol}^{-1}$$

$$\Delta S^\ddagger = -66.3508142 \text{ J} \cdot \text{K}^{-1} \cdot \text{mol}^{-1}$$

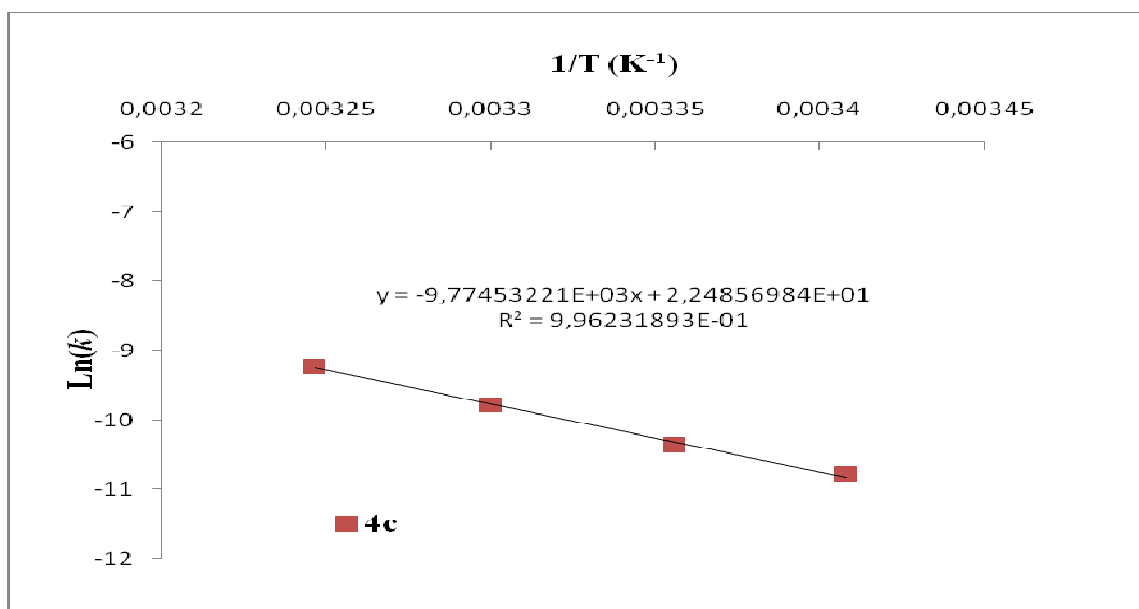


Figure 20. Arrhenius plot for **4c**: E_a determination.

$$E_a = 81265.46079394 \text{ J} \cdot \text{mol}^{-1} = 81.26546079394 \text{ KJ} \cdot \text{mol}^{-1}$$

Kinetic data for complex 4d

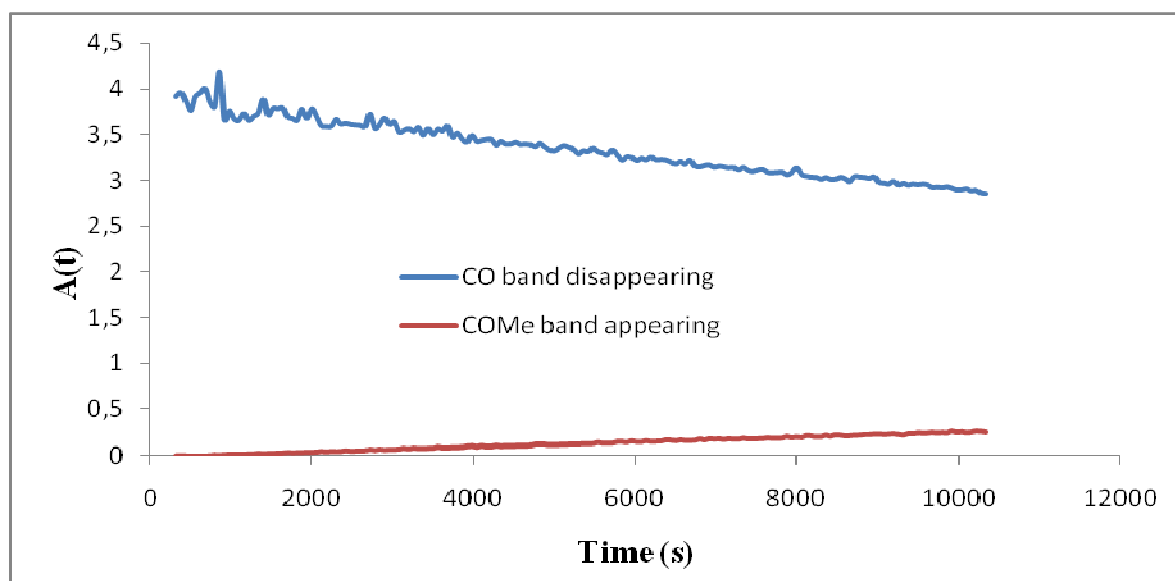


Figure 21. Antisymmetric CO band $A(t)$ disappearance for **4d** at 293.1 K.

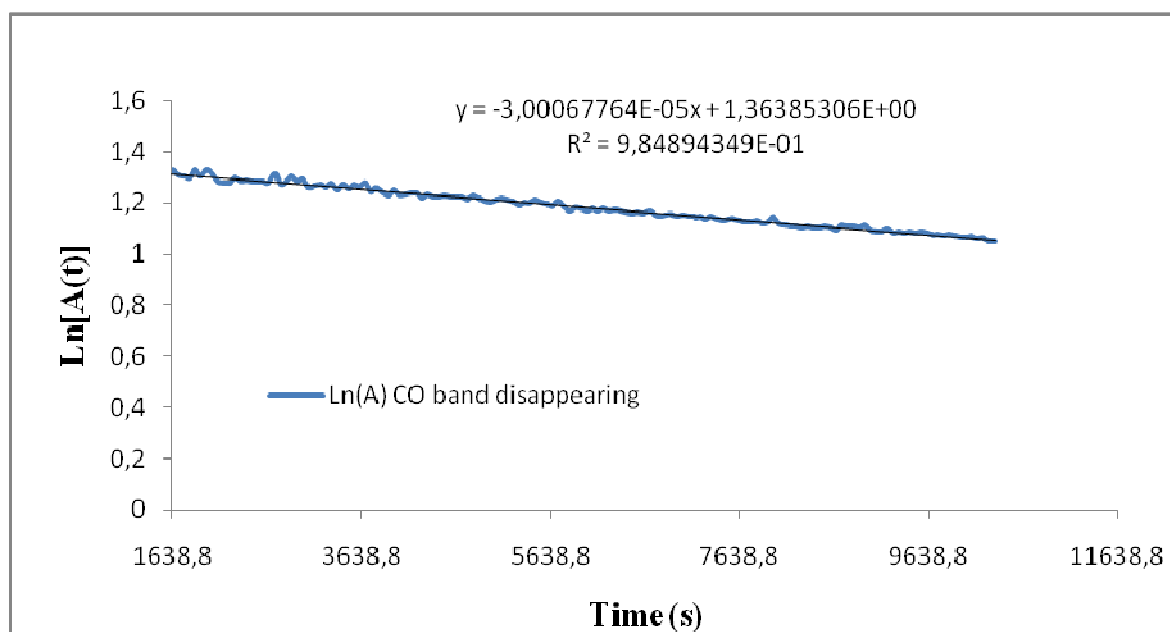


Figure 22. $\ln[A(t)]$ vs. time plot for **4d** at 293.1 K: $k_{293,1}$ determination.

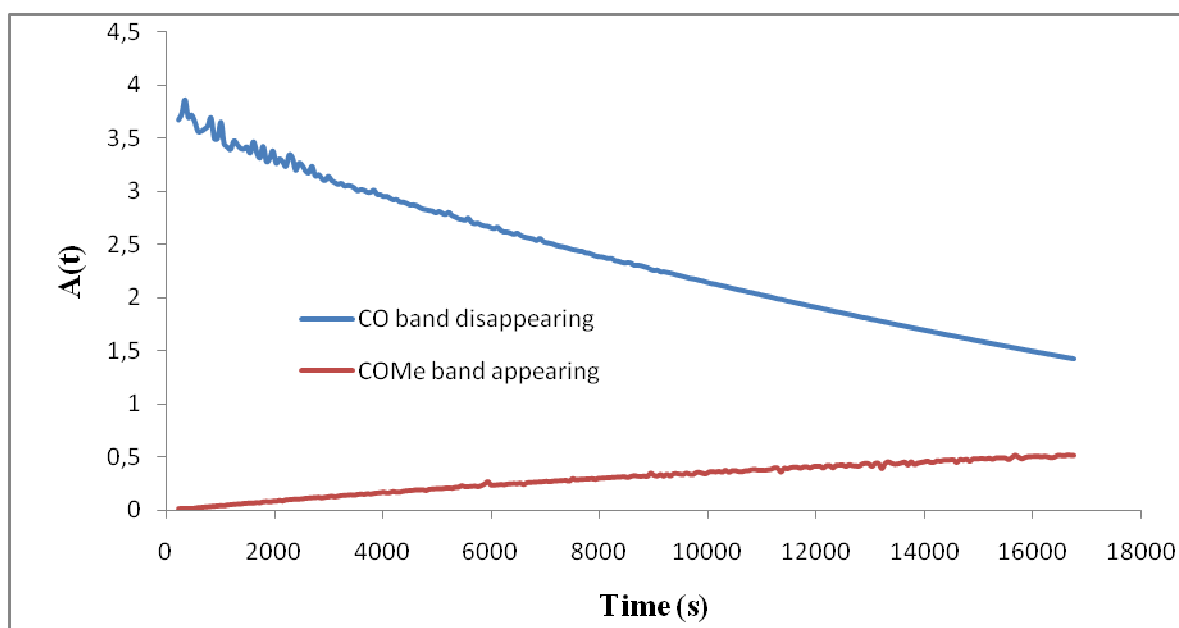


Figure 23. Antisymmetric CO band $A(t)$ disappearance for **4d** at 298.1 K.

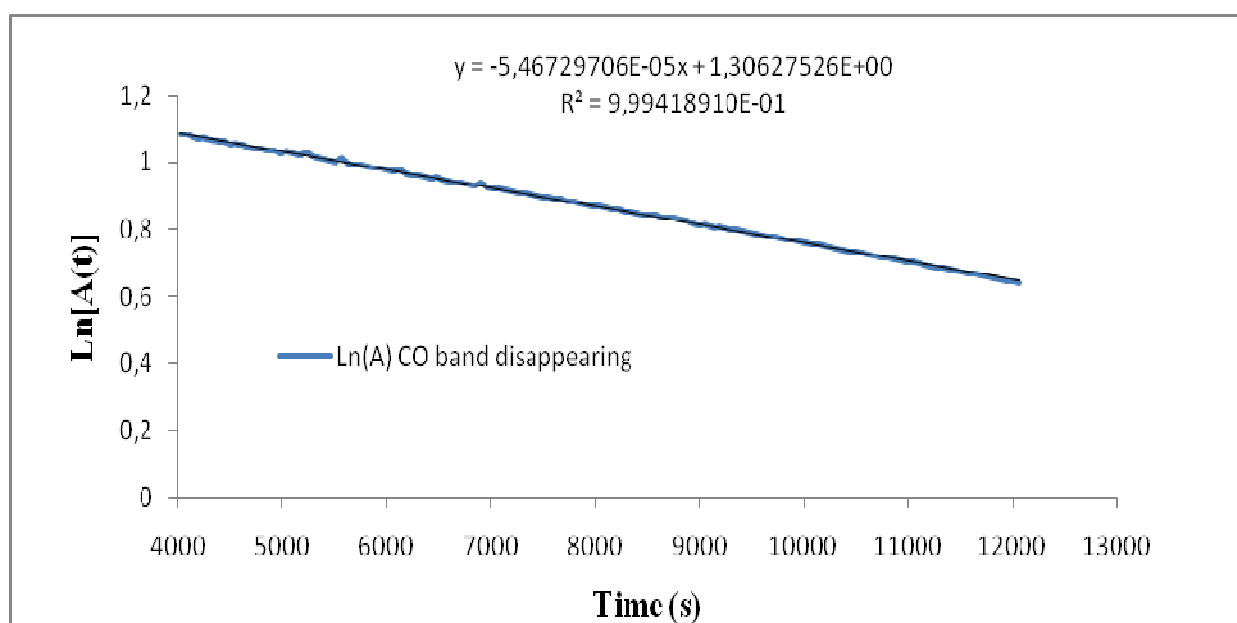


Figure 24. $\ln[A(t)]$ vs. time plot for **4d** at 298.1 K: $k_{298.1}$ determination.

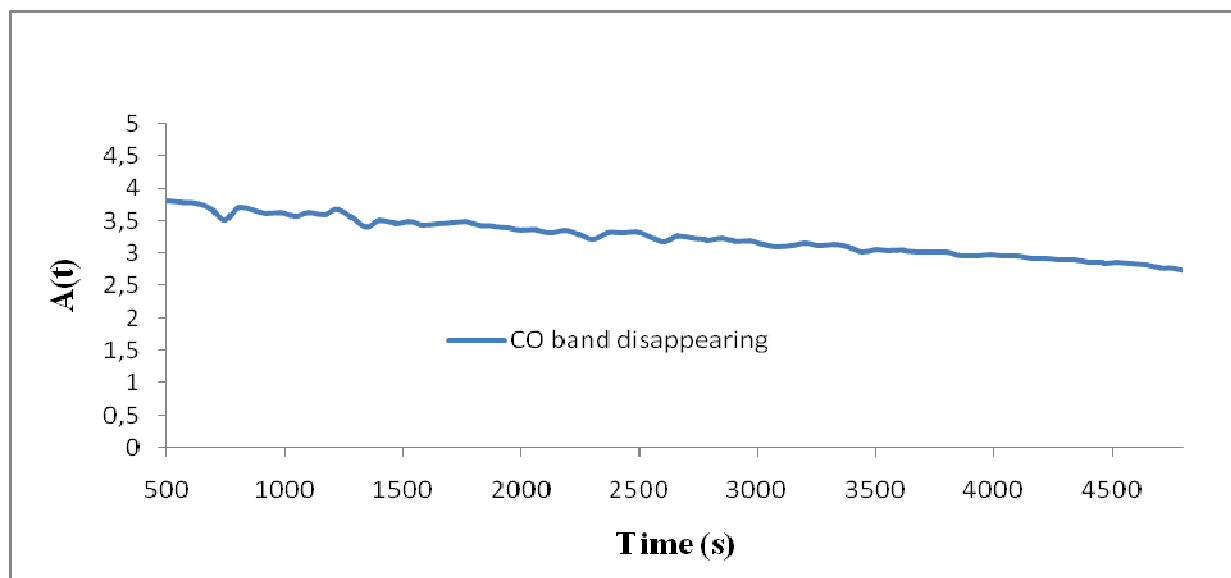


Figure 25. Antisymmetric CO band A(t) disappearance for **4d** at 302.8 K.

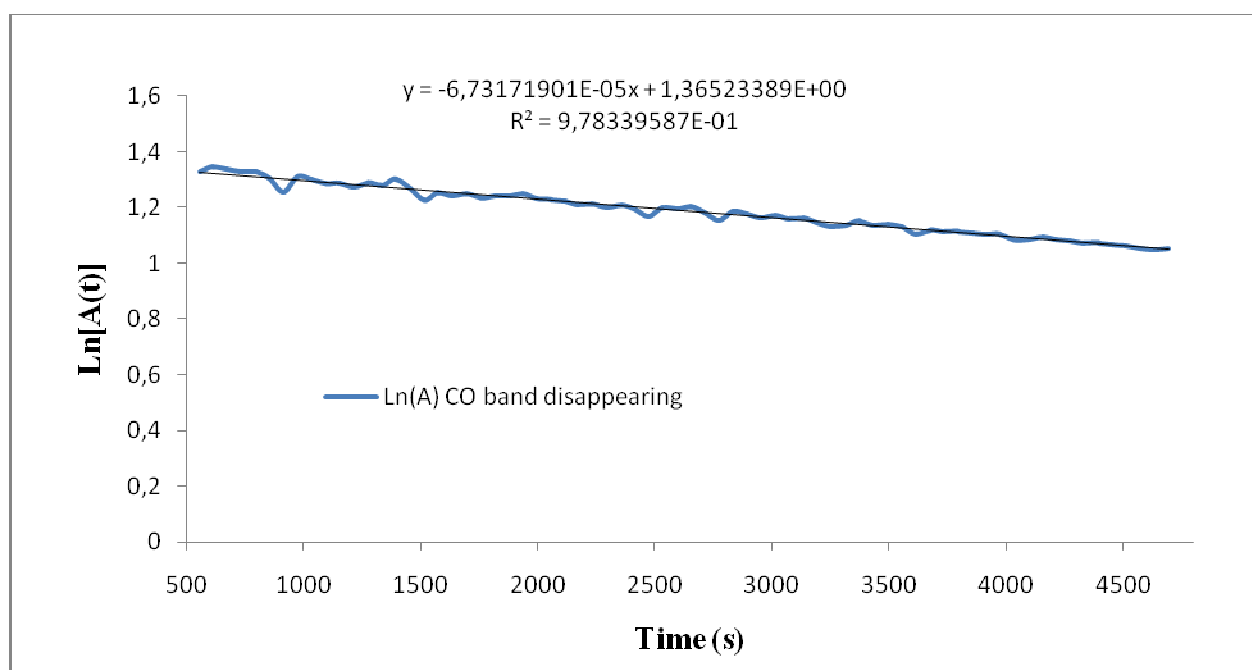


Figure 26. Ln[A(t)] vs. time plot for **4d** at 302.8 K: $k_{302.8}$ determination.

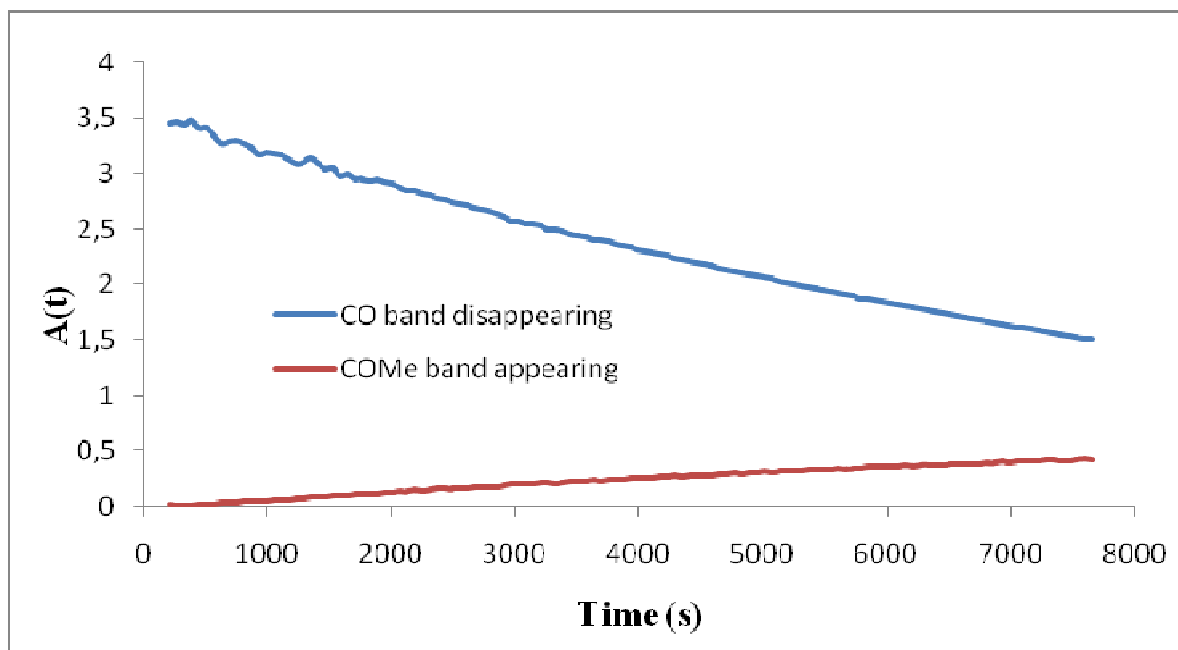


Figure 27. Antisymmetric CO band $A(t)$ disappearance for **4d** at 307.5 K.

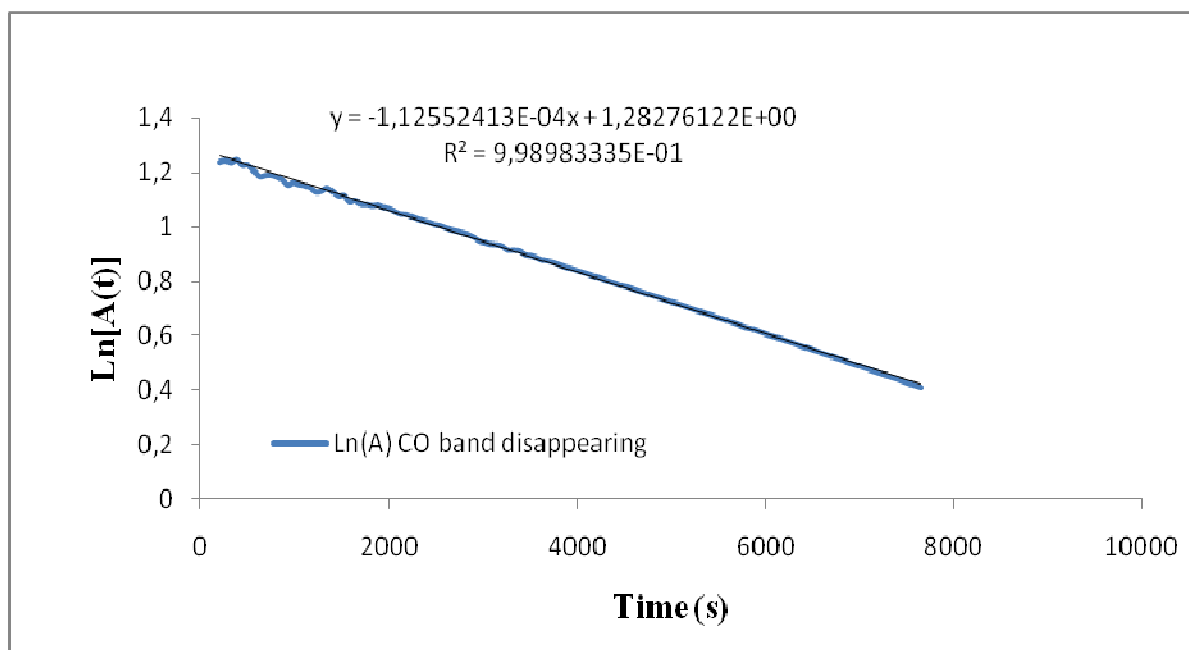


Figure 28. $\text{Ln}[A(t)]$ vs. time plot for **4d** at 307.5 K: $k_{307.5}$ determination.

Table 3.

$T(^{\circ}\text{C})$	$T(\text{K})$	$1/T$	k	$\text{Ln}(k)$
20.1	293.1	0.00341180	0.00003000677640	-10.41205692
25.1	298.1	0.00335458	0.00005467297060	-9.81414111
29.8	302.8	0.00330250	0.00006731719010	-9.606094929
34.5	307.5	0.003252033	0.0001125524130	-9.092091551
$\text{Ln}(k/T)$	k/T	$(h/k_B)^*(k/T)$	$\text{Ln}[(h/k_B)^*(k/T)]$	$R^*(\text{Ln}[(h/k_B)^*(k/T)])$
-16.09460116952600	0.00000010237726510	$4.913334 \cdot 10^{-18}$	-39.85457893	-331.3697806
-15.51157011028690	0.00000018340479906	$8.802042 \cdot 10^{-18}$	-39.27154787	-326.5221852
-15.31916745052940	0.00000022231568725	$1.066947 \cdot 10^{-17}$	-39.07914521	-324.9224587
-14.82056663872760	0.00000036602410732	$1.756638 \cdot 10^{-17}$	-38.5805444	-320.7768562

h : Planck constant $6.62606957(29) \times 10^{-34} \text{ J}\cdot\text{s}^{-1}$; Boltzmann constant k_B : $1.3806488(13) \times 10^{-23} \text{ J}\cdot\text{K}^{-1}$; R : gaz constant $8.314472 \text{ J}\cdot\text{mol}^{-1}\cdot\text{K}^{-1}$.

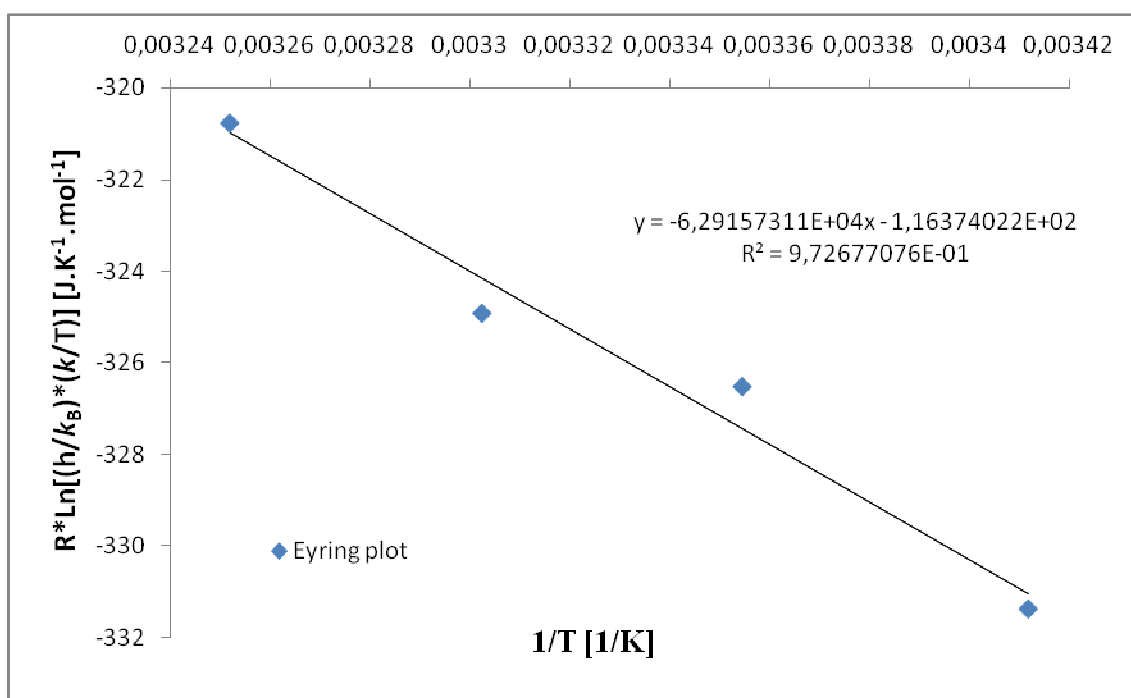


Figure 29. Eyring plot for 4d: ΔH^\ddagger and ΔS^\ddagger determination.

$$\Delta H^\ddagger = 62915.7311 \text{ J}\cdot\text{mol}^{-1} = 62.9157311 \text{ KJ}\cdot\text{mol}^{-1}$$

$$\Delta S^\ddagger = -116.374022 \text{ J}\cdot\text{K}^{-1}\cdot\text{mol}^{-1}$$

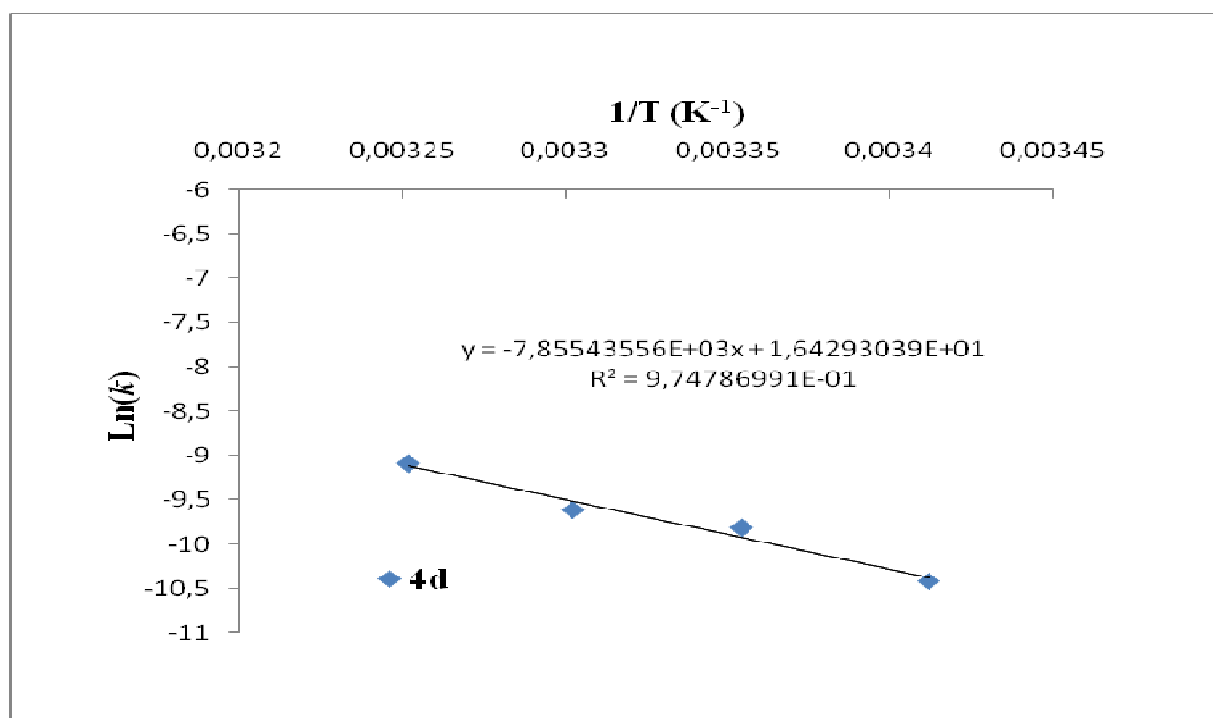


Figure 30. Arrhenius plot for **4d**: E_a determination.

$$E_a = 65310.09124584 \text{ J.mol}^{-1} = 65.31009124584 \text{ KJ.mol}^{-1}$$

Kinetic data for complex **4e**

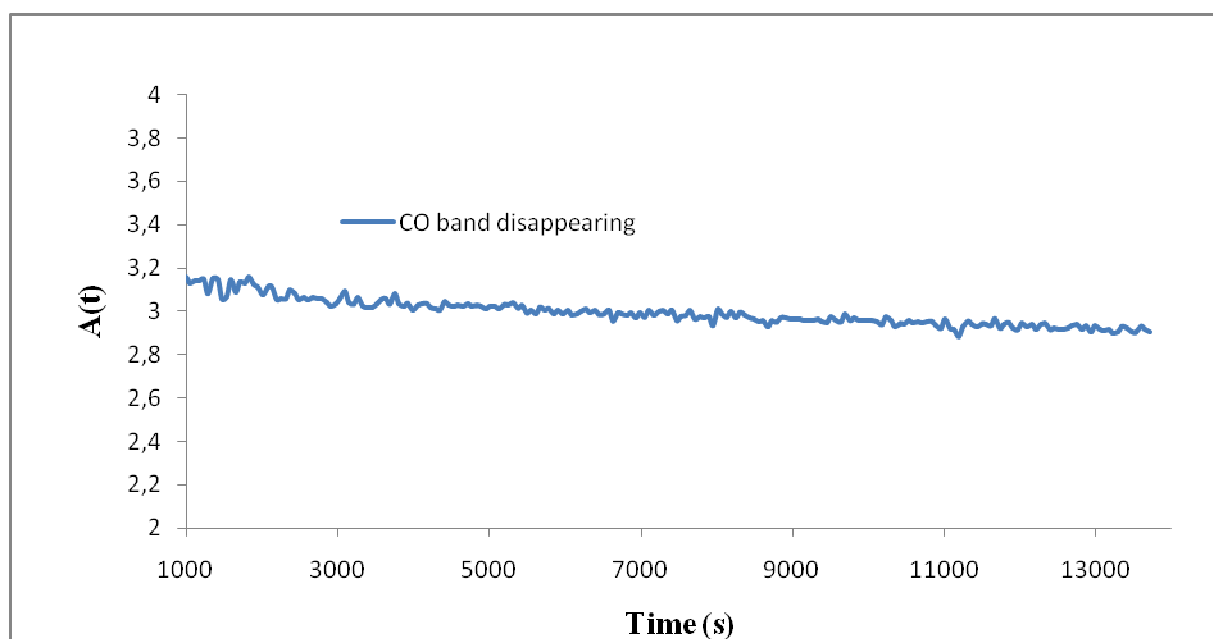


Figure 31. Antisymmetric CO band $A(t)$ disappearance for **4e** at 298.1 K.

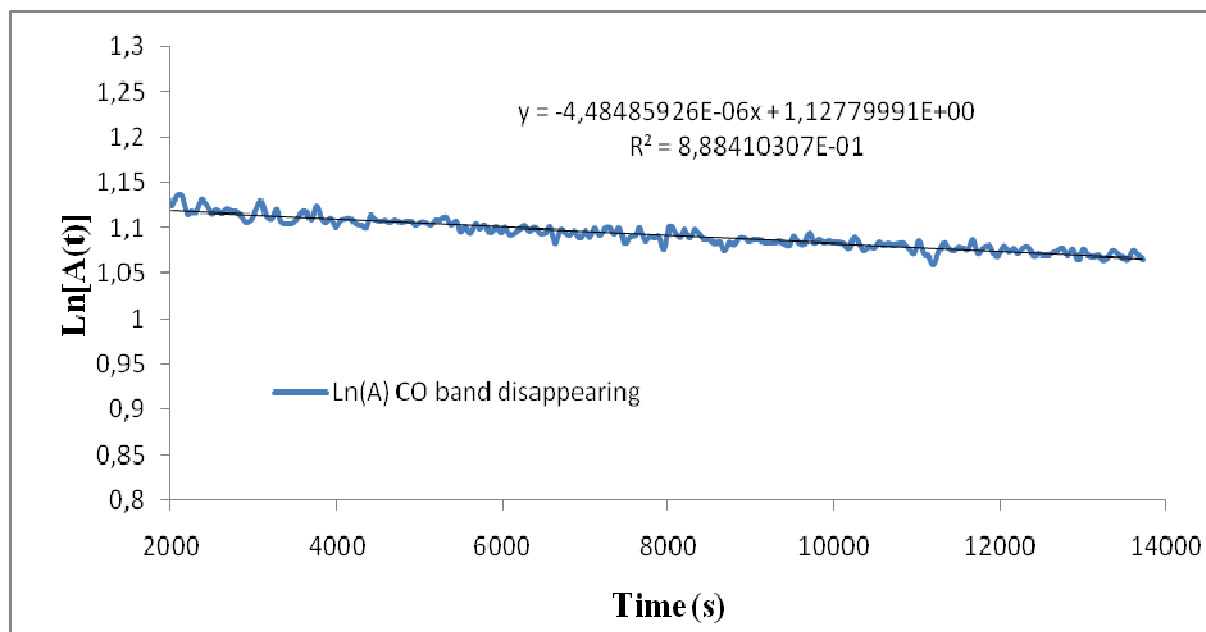


Figure 32. $\text{Ln}[A(t)]$ vs. time plot for **4e** at 298.1 K: $k_{298,1}$ determination.

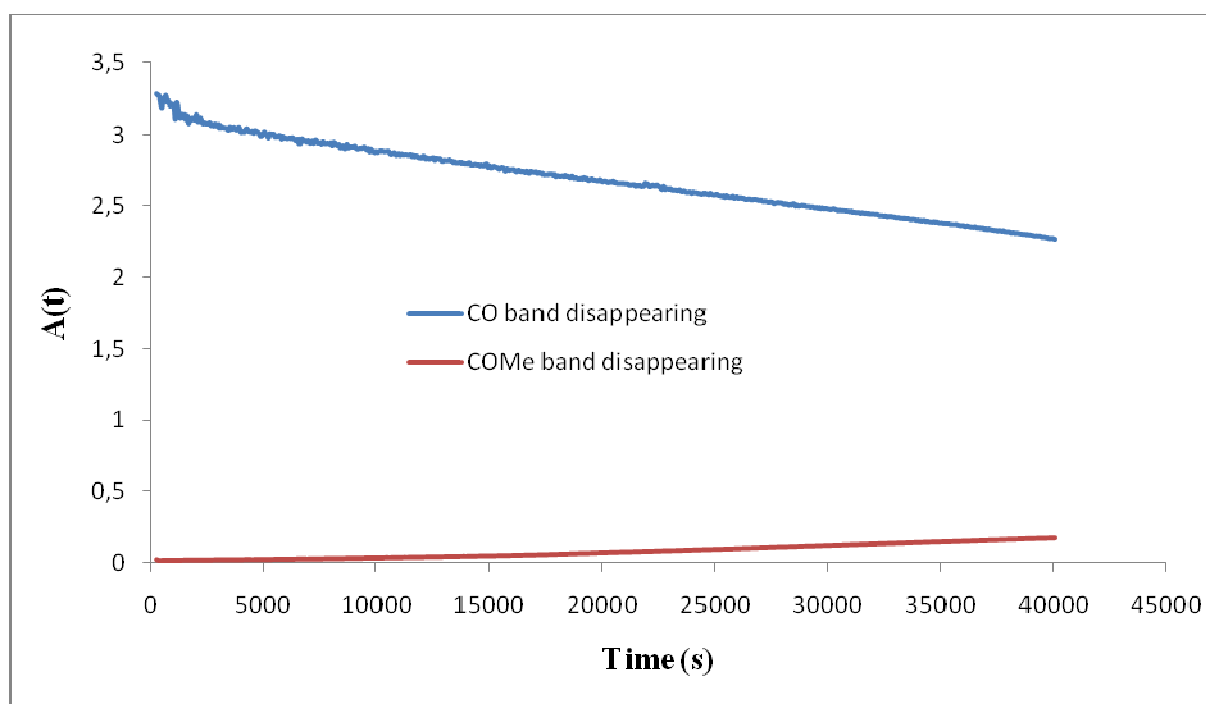


Figure 33. Antisymmetric CO band $A(t)$ disappearance for **4e** at 302.8 K.

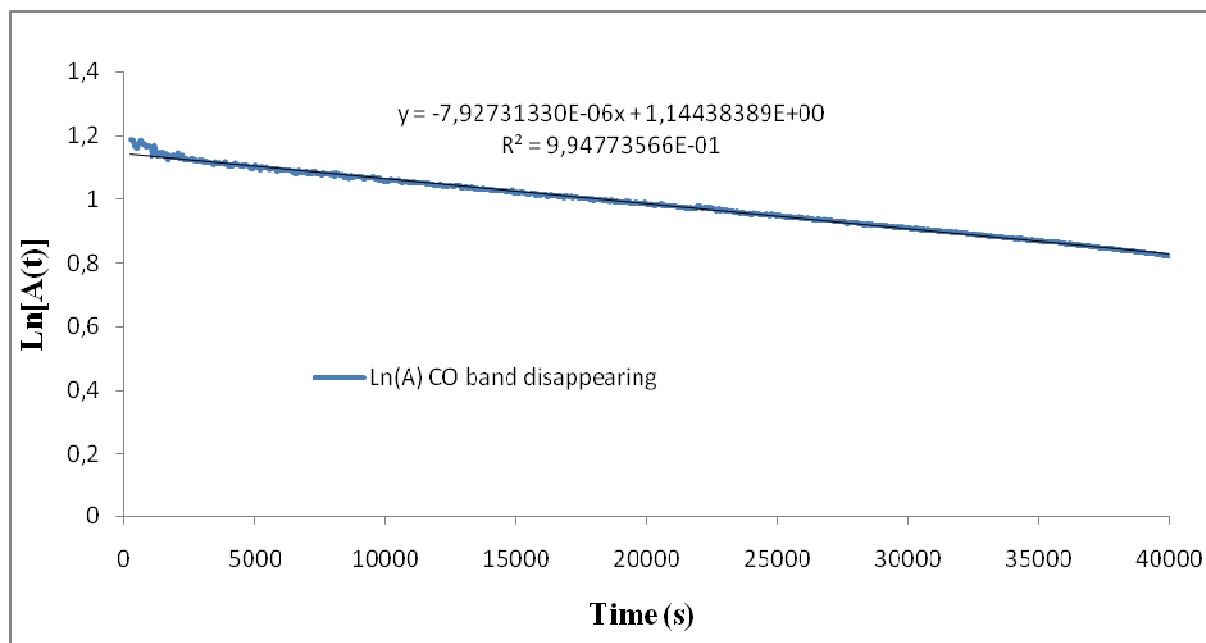


Figure 34. $\ln[A(t)]$ vs. time plot for **4e** at 302.8 K: $k_{302.8}$ determination.

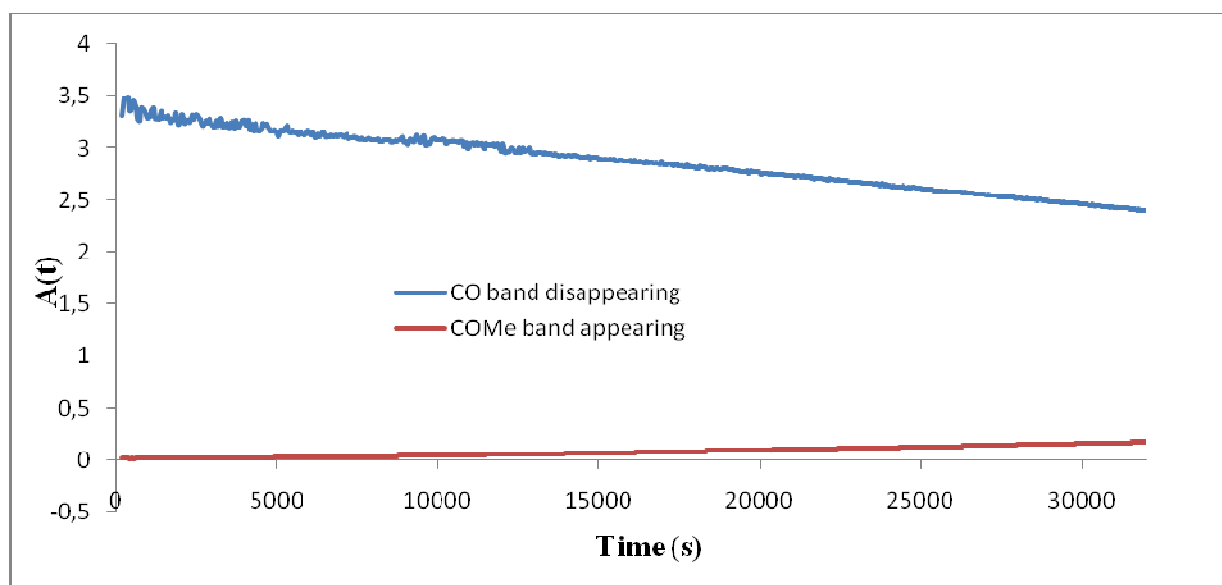


Figure 35. Antisymmetric CO band $A(t)$ disappearance for **4e** at 307.5 K.

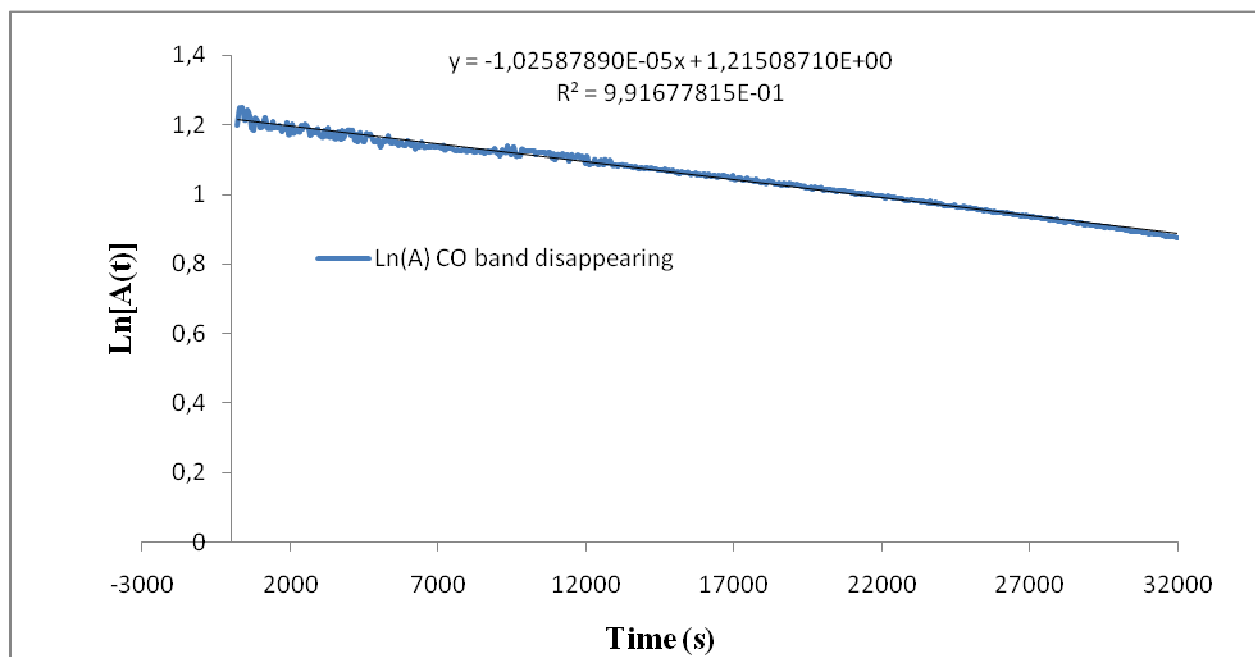


Figure 36. $\text{Ln}[A(t)]$ vs. time plot for **4e** at 307.5 K: $k_{307.5}$ determination.

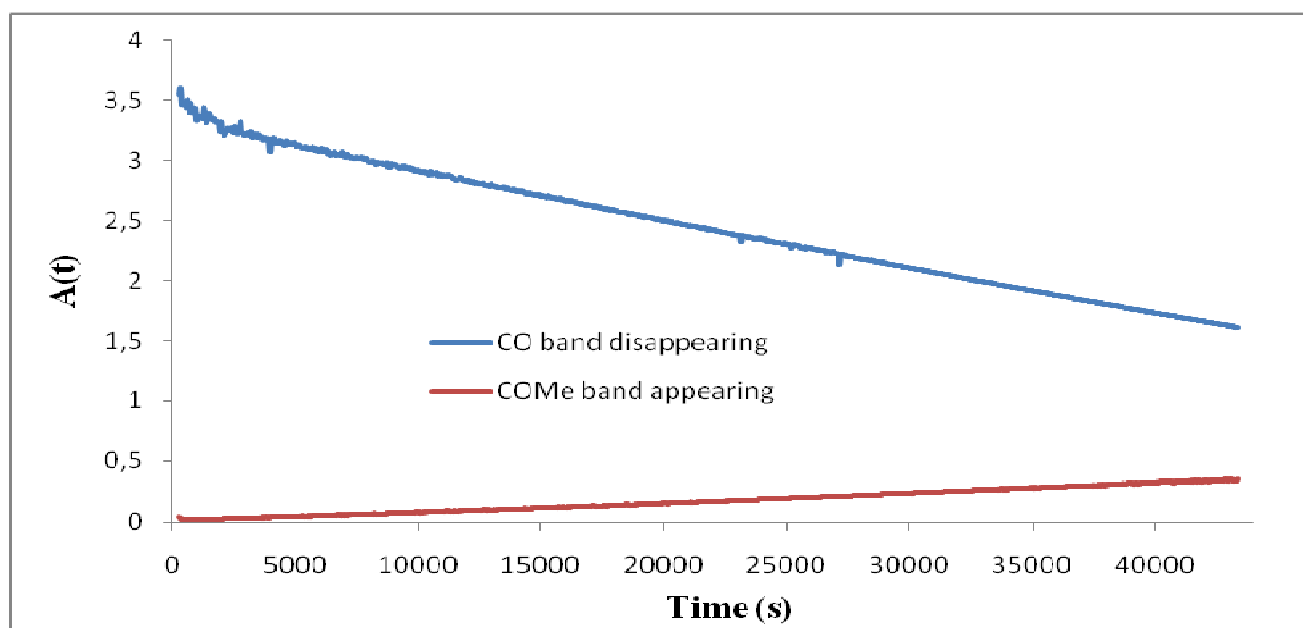


Figure 37. Antisymmetric CO band $A(t)$ disappearance for **4e** at 312.2 K.

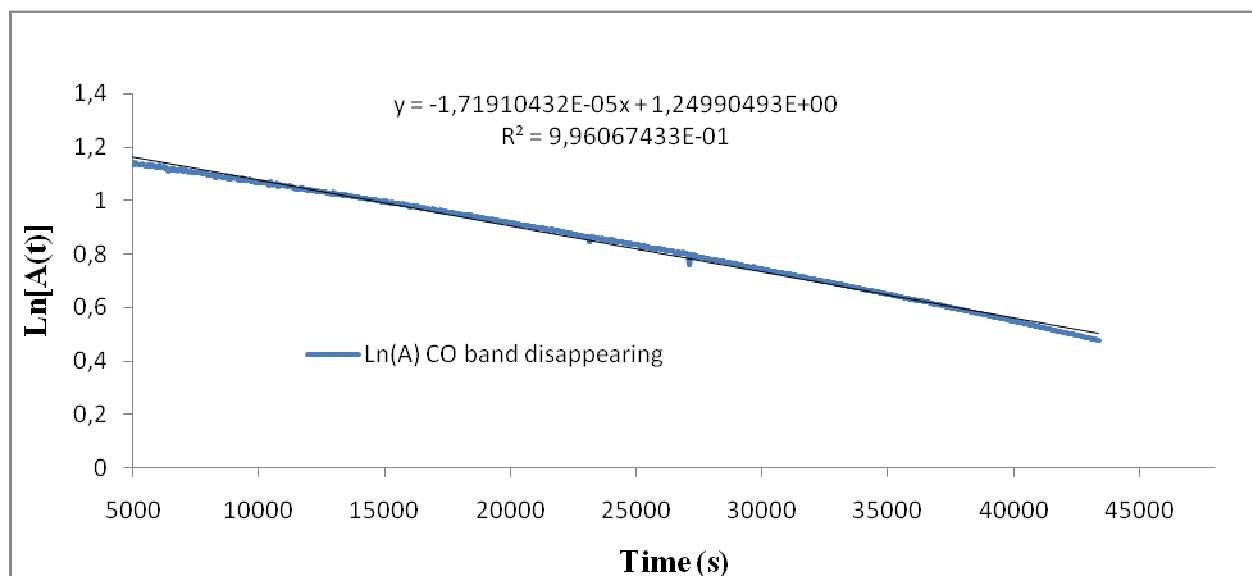


Figure 38. Ln[A(t)] vs. time plot for **4e** at 312.2 K: $k_{312,2}$ determination.

Table 4.

$T(^{\circ}\text{C})$	$T(\text{K})$	$1/T$	k	$\text{Ln}(k)$
25.1	298.1	0.00335458	0.00000448485926	-12.31480344
29.8	302.8	0.00330250	0.00000792731330	-11.74519638
34.5	307.5	0.003252033	0.0000102587890	-11.48737576
39.2	312.2	0.003203075	0.0000171910432	-10.97112205
Ln(k/T)	k/T	(h/k_B)*(k/T)	Ln[(h/k_B)*(k/T)]	R*(Ln[(h/k_B)*(k/T)])
-18.01223244378600	0.00000001504481469	$7.220372 \cdot 10^{-19}$	-41.77221021	-347.3138721
-17.45826890330480	0.00000002618003071	$1.256443 \cdot 10^{-18}$	-41.21824667	-342.7079578
-17.21585084362350	0.00000003336191545	$1.601119 \cdot 10^{-18}$	-40.97582861	-340.6923796
-16.71476606204660	0.00000005506419987	$2.642664 \cdot 10^{-18}$	-40.47474382	-336.5261242

h : Planck constant $6.62606957(29) \times 10^{-34} \text{ J}\cdot\text{s}^{-1}$; Boltzmann constant k_B : $1.3806488(13) \times 10^{-23} \text{ J}\cdot\text{K}^{-1}$; R : gaz constant $8.314472 \text{ J}\cdot\text{mol}^{-1}\cdot\text{K}^{-1}$.

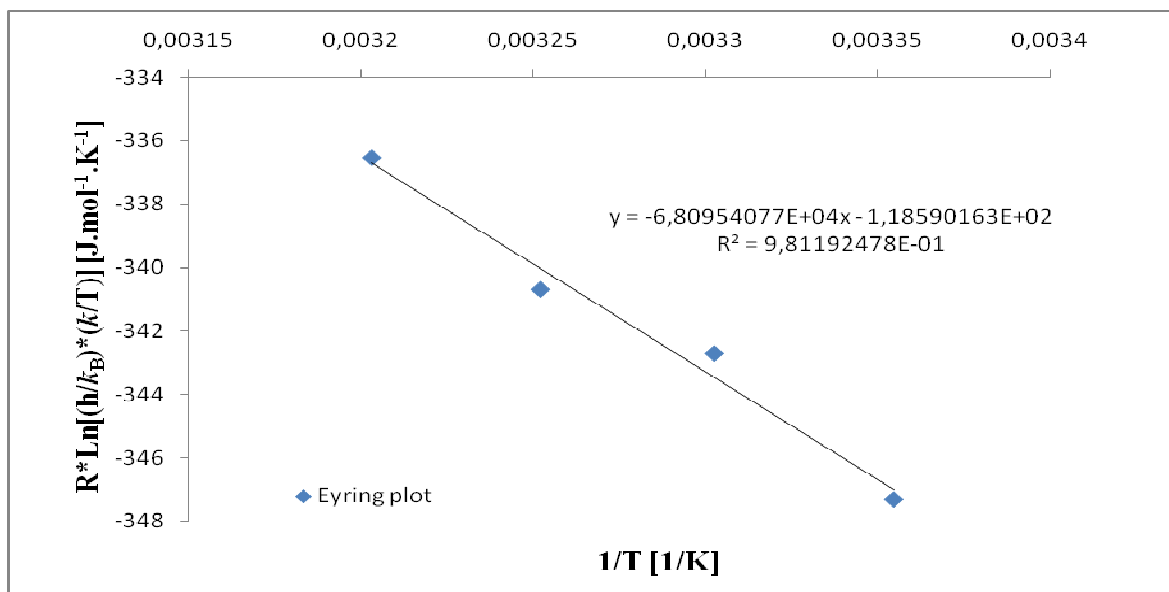


Figure 39. Eyring plot for **4e**: ΔH^\ddagger and ΔS^\ddagger determination.

$$\Delta H^\ddagger = 68095.4077 \text{ J.mol}^{-1} = 68.0954077 \text{ KJ.mol}^{-1}$$

$$\Delta S^\ddagger = -118.590163 \text{ J.K}^{-1}.\text{mol}^{-1}$$

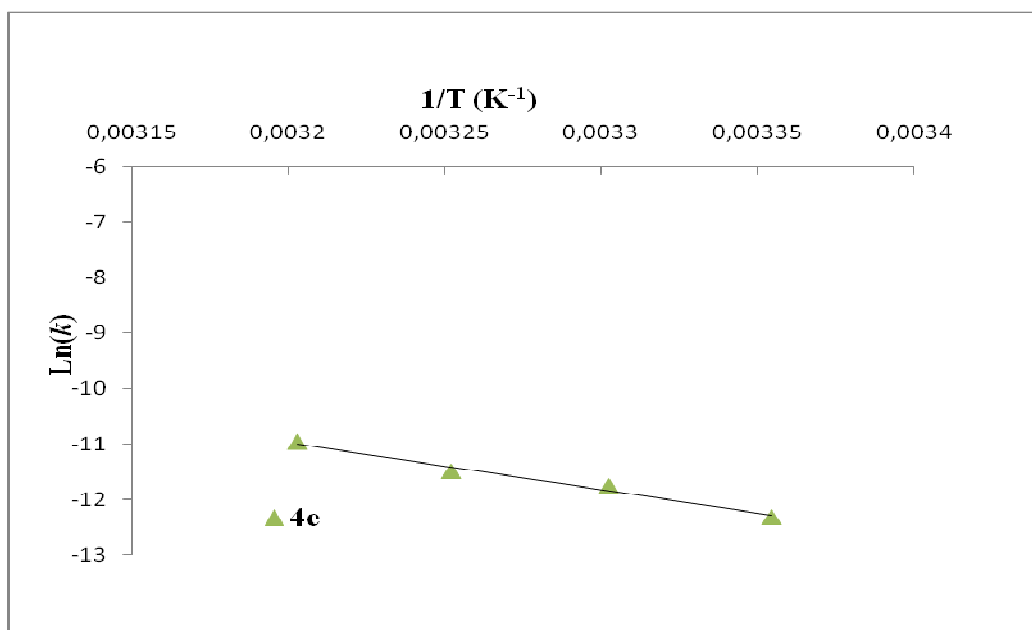


Figure 40. Arrhenius plot for **4e**: E_a determination.

$$E_a = 70627.54315354 \text{ J.mol}^{-1} = 70.62754315354 \text{ KJ.mol}^{-1}$$

Kinetic data for complex 4f

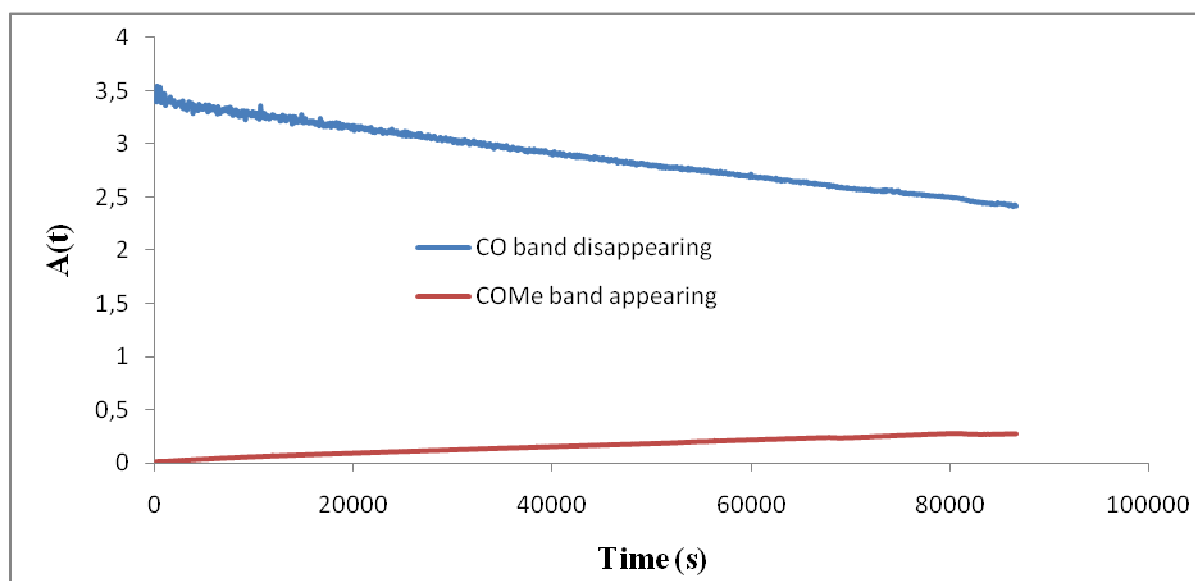


Figure 41. Antisymmetric CO band $A(t)$ disappearance for 4f at 298 K.

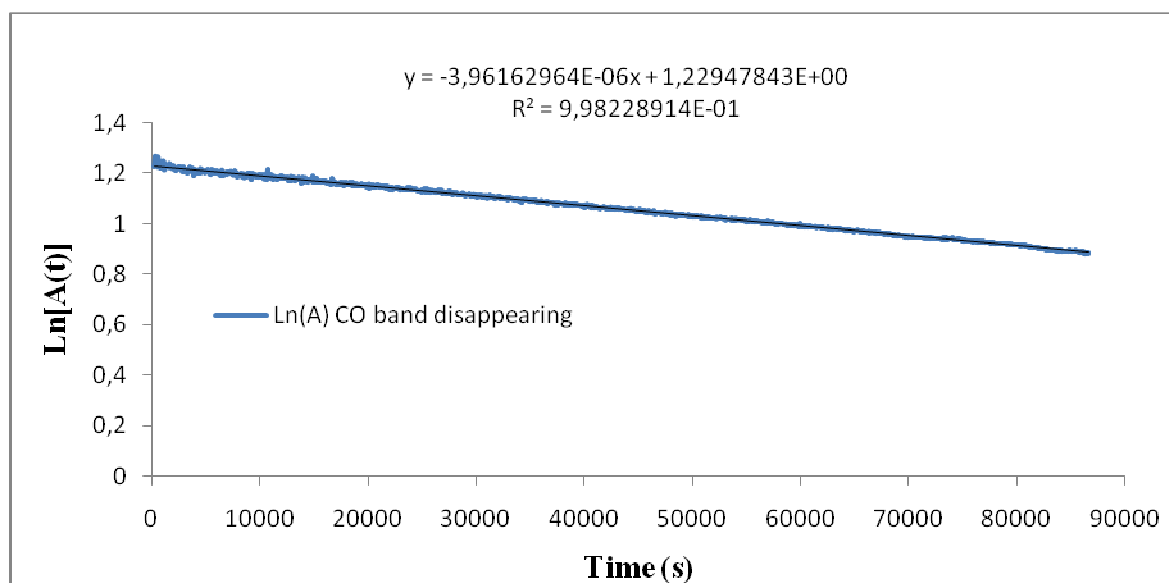


Figure 42. $\text{Ln}[A(t)]$ vs. time plot for 4f at 298 K: k_{298} determination.

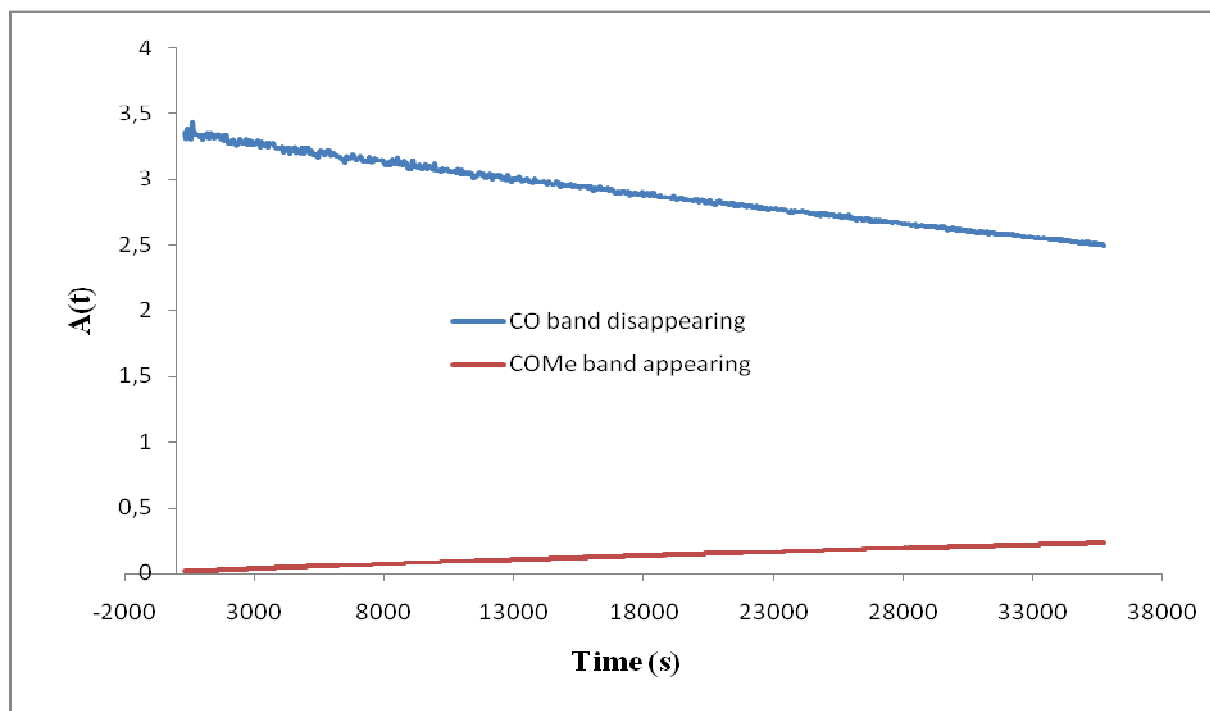


Figure 43. Antisymmetric CO band $A(t)$ disappearance for **4f** at 302.8 K.

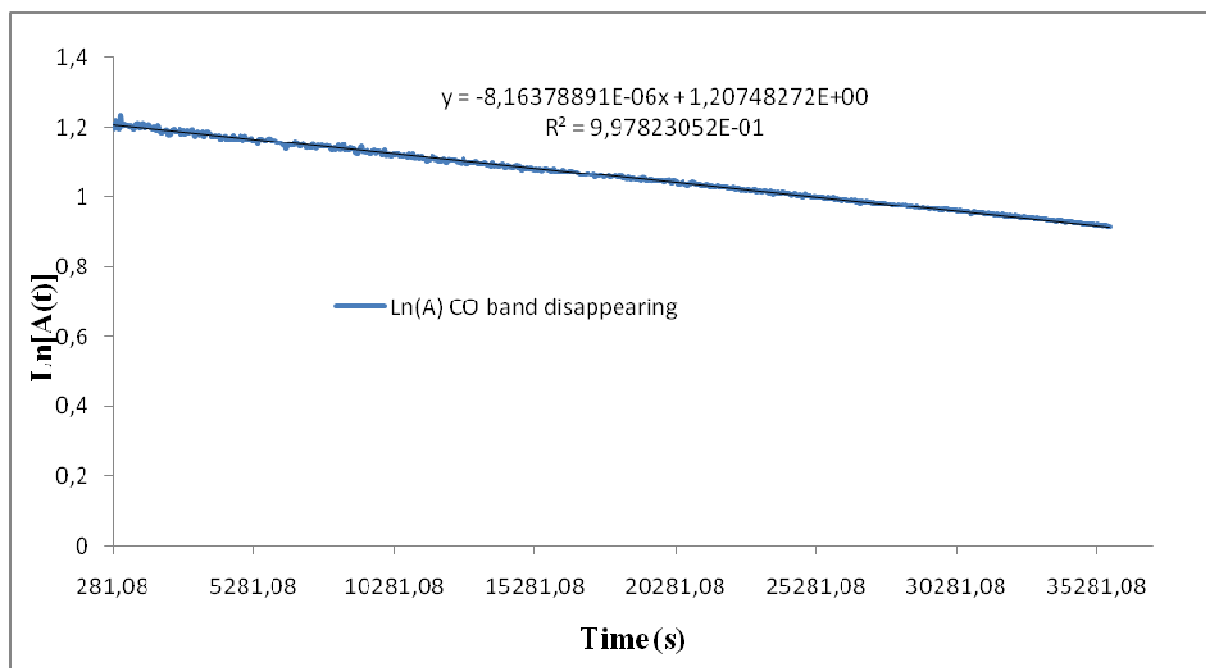


Figure 44. $\ln[A(t)]$ vs. time plot for **4f** at 302.8 K: $k_{302.8}$ determination.

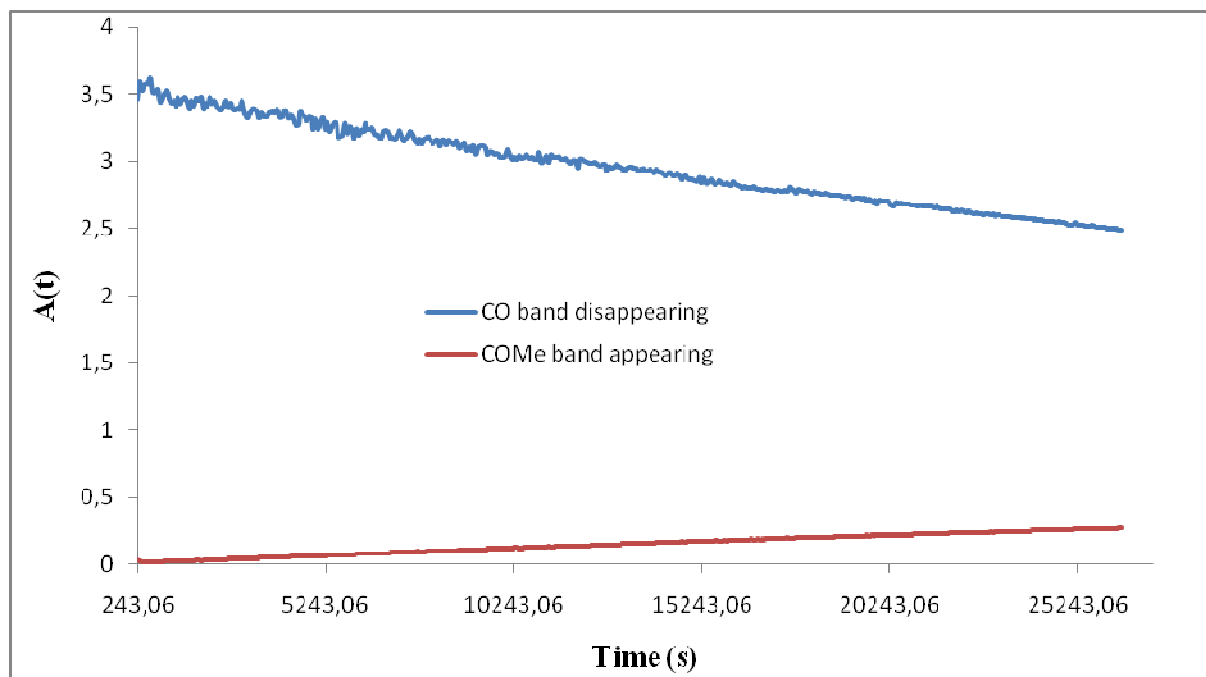


Figure 45. Antisymmetric CO band $A(t)$ disappearance for **4f** at 307.5 K.

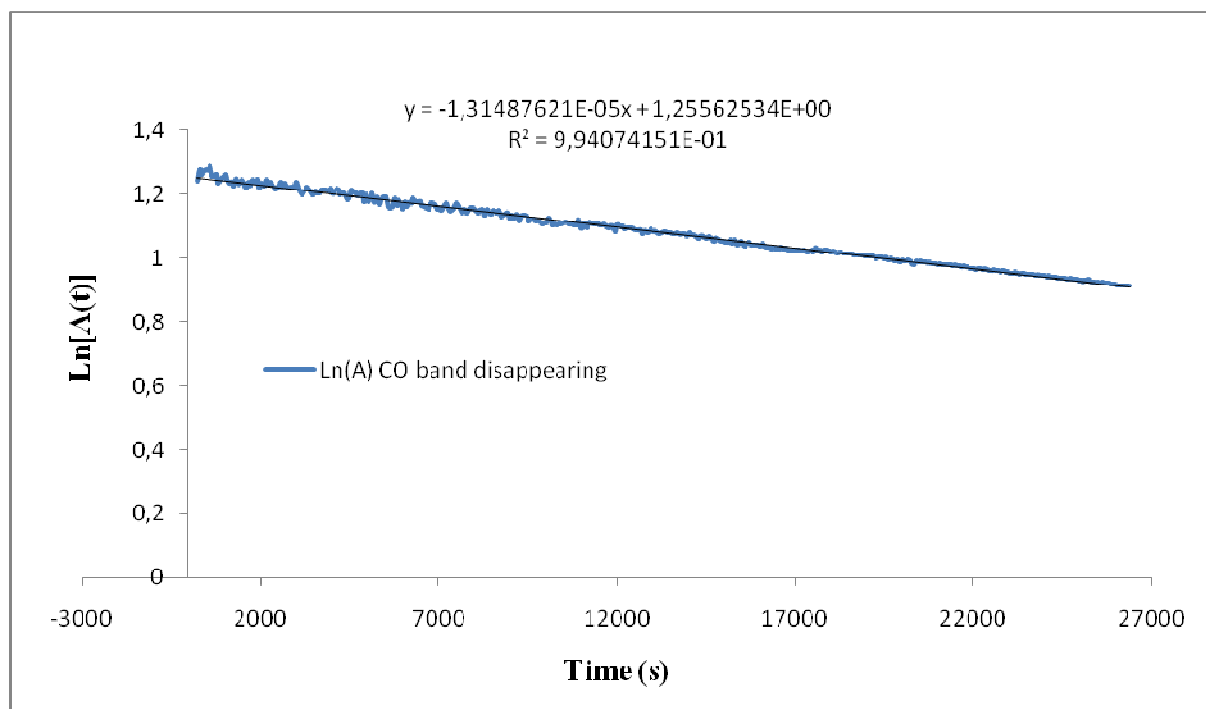


Figure 46. $\text{Ln}[A(t)]$ vs. time plot for **4f** at 307.5 K: $k_{307.5}$ determination.

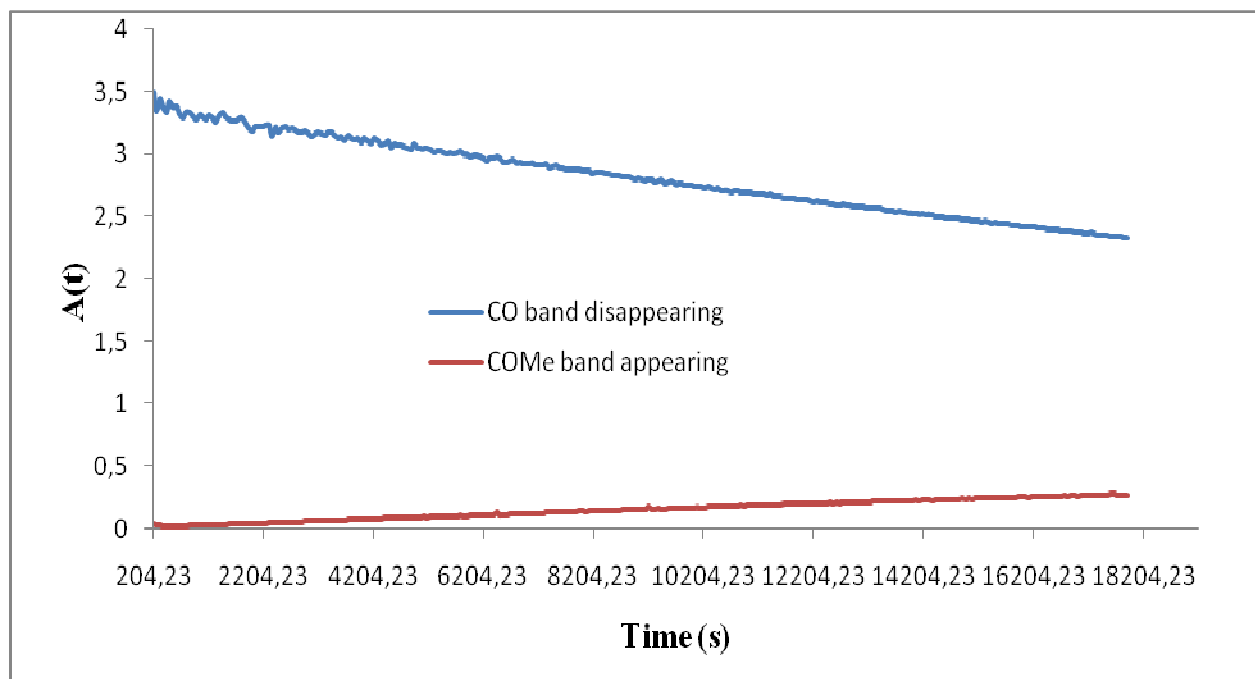


Figure 47. Antisymmetric CO band $A(t)$ disappearance for **4f** at 312.2 K.

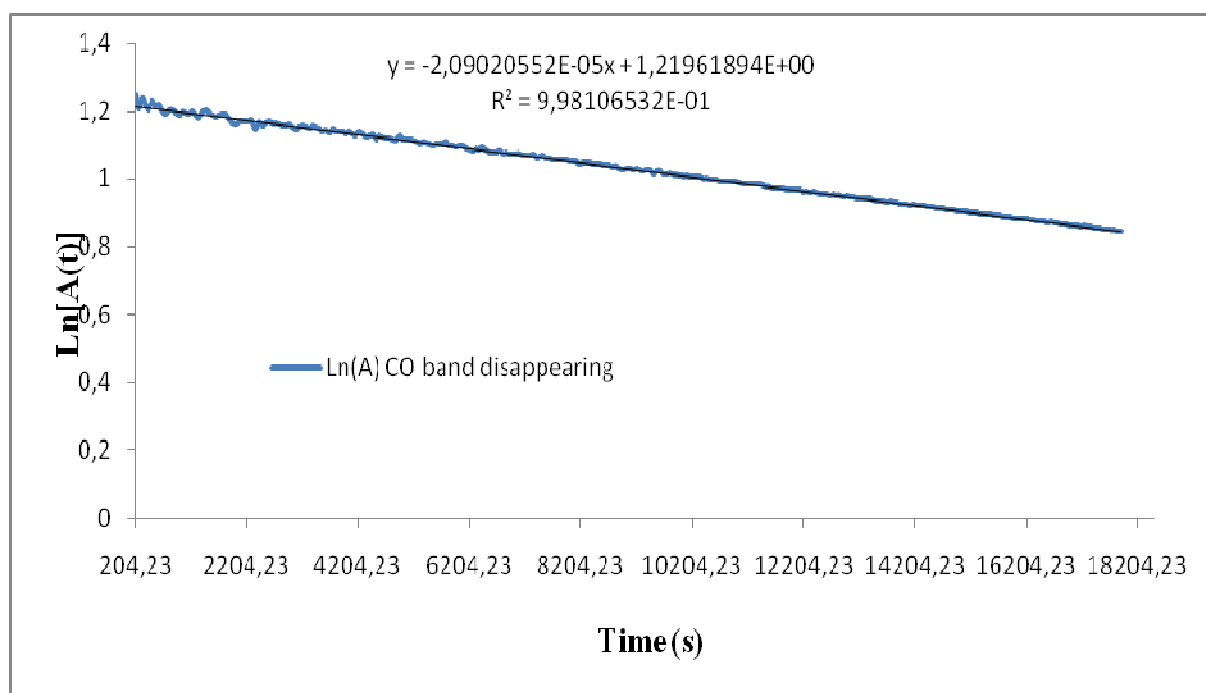


Figure 48. $\ln[A(t)]$ vs. time plot for **4f** at 312.2 K: $k_{312,2}$ determination.

Table 5.

$T(^{\circ}C)$	$T(K)$	$1/T$	k	$Ln(k)$
25	298	0.00335570	0.00000396162964	-12.43885509
29.8	302.8	0.00330250	0.00000816378891	-11.71580217
34.5	307.5	0.003252033	0.0000131487621	-11.23918294
39.2	312.2	0.003203075	0.0000209020552	-10.77566307
$Ln(k/T)$	k/T	$(h/k_B)*(k/T)$	$Ln[(h/k_B)*(k/T)]$	$R*(Ln[(h/k_B)*(k/T)])$
-18.13594857860410	0.00000001329405919	$6.380142 \cdot 10^{-19}$	-41.89592634	-348.3425065
-17.42887469111220	0.00000002696099376	$1.293923 \cdot 10^{-18}$	-41.18885245	-342.4635604
-16.96765802790040	0.00000004276020195	$2.052166 \cdot 10^{-18}$	-40.72763579	-338.6287874
-16.51930707698120	0.00000006695084946	$3.213134 \cdot 10^{-18}$	-40.27928484	-334.900986

h : Planck constant $6.62606957(29) \times 10^{-34} \text{ J}\cdot\text{s}^{-1}$; Boltzmann constant k_B : $1.3806488(13) \times 10^{-23} \text{ J}\cdot\text{K}^{-1}$; R : gaz constant $8.314472 \text{ J}\cdot\text{mol}^{-1}\cdot\text{K}^{-1}$.

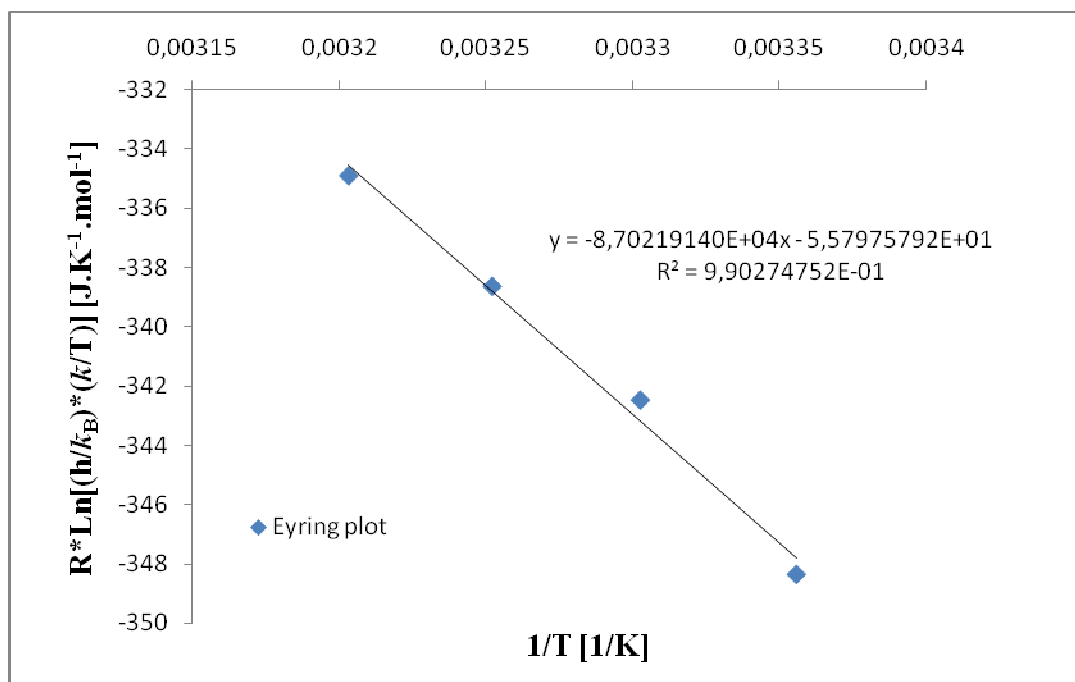


Figure 49. Eyring plot for 4f: ΔH^{\ddagger} and ΔS^{\ddagger} determination.

$$\Delta H^{\ddagger} = 87021.9140 \text{ J}\cdot\text{mol}^{-1} = 87.0219140 \text{ KJ}\cdot\text{mol}^{-1}$$

$$\Delta S^{\ddagger} = -55.7975792 \text{ J}\cdot\text{K}^{-1}\cdot\text{mol}^{-1}$$

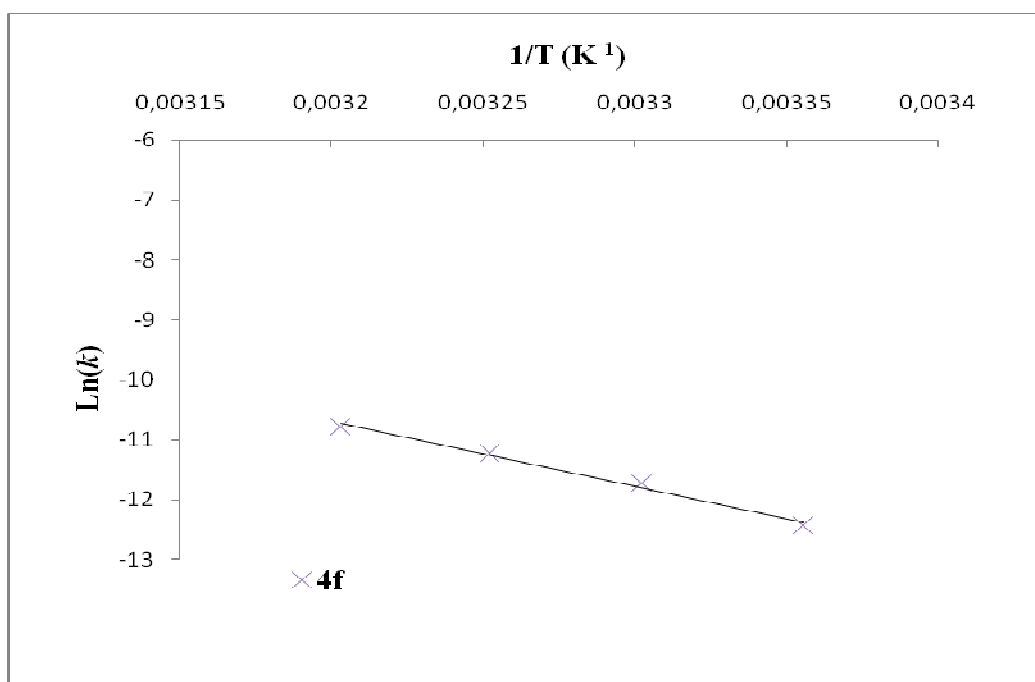


Figure 50. Arrhenius plot for 4f: E_a determination.

$$E_a = 89552.4984088 \text{ J}\cdot\text{mol}^{-1} = 89.5524984088 \text{ KJ}\cdot\text{mol}^{-1}$$

Kinetic data for complex 4g

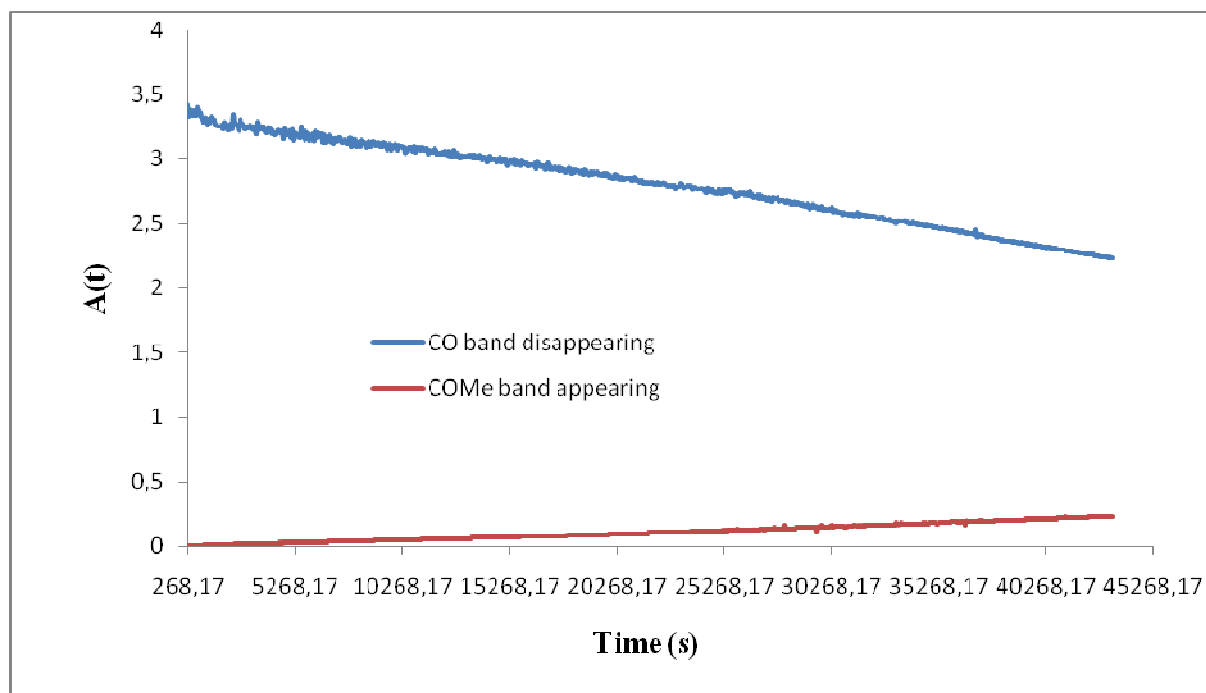


Figure 51. Antisymmetric CO band $A(t)$ disappearance for 4g at 298 K.

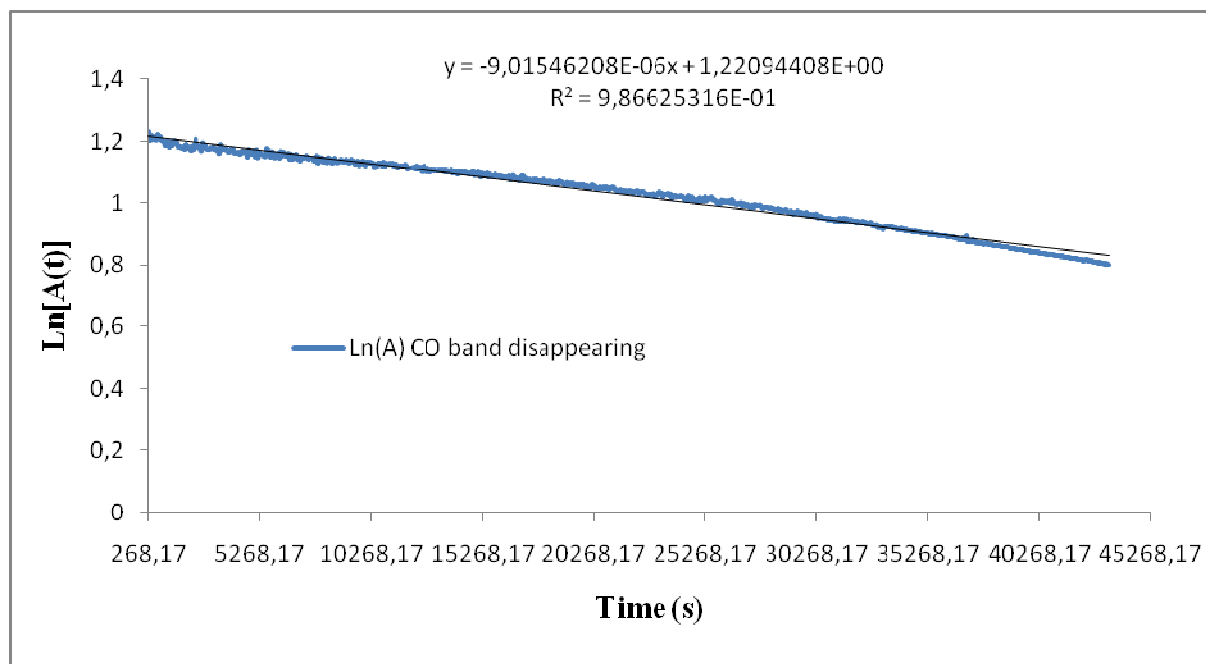


Figure 52. $\text{Ln}[A(t)]$ vs. time plot for **4g** at 298 K: k_{298} determination.

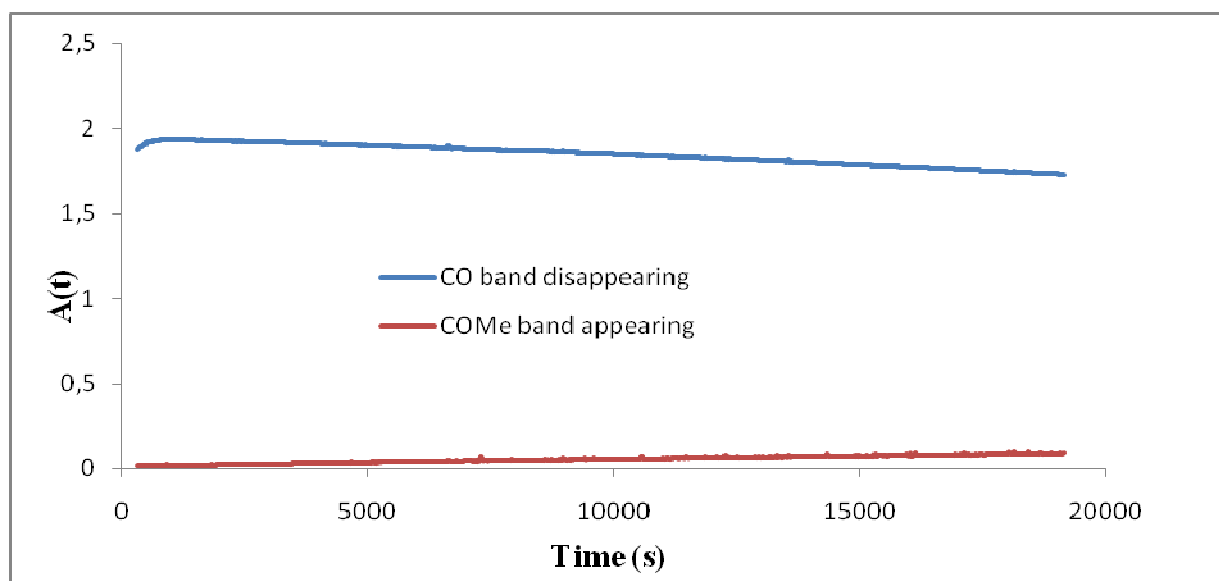


Figure 53. Antisymmetric CO band $A(t)$ disappearance for **4h** at 298 K.

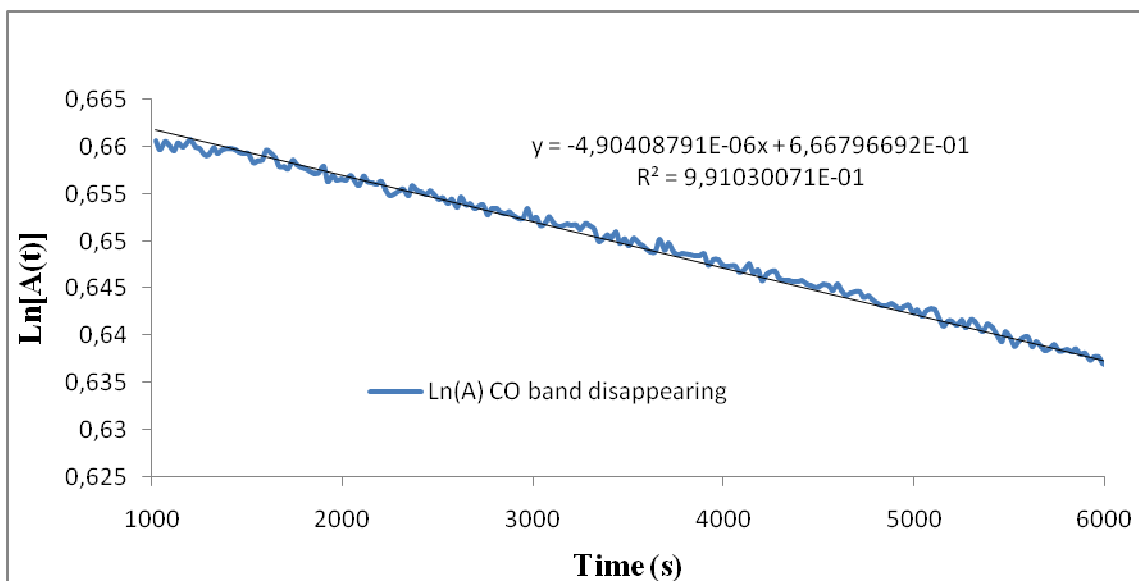
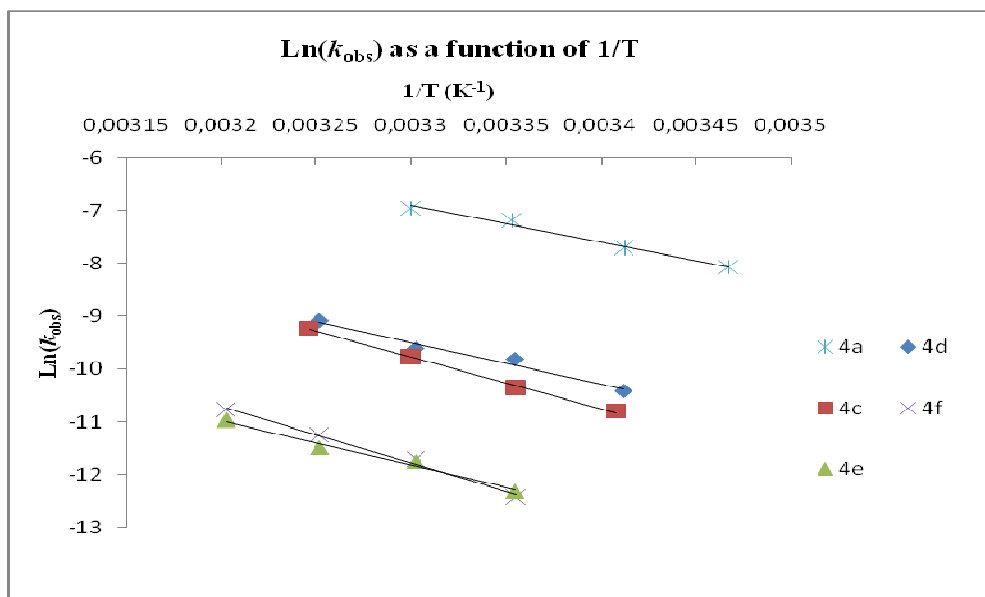


Figure 54. $\text{Ln}[A(t)]$ vs. time plot for **4h** at 298 K: k_{298} determination.

Kinetic data summary



CHAPTER IV

I- DFT-Computational details

Cartesian coordinates of the optimized structures:

trans-[RhI₃(CO)₂(COCH₃)]⁻, *mer,trans*-18c₁

Free energy: G = -524.970056 a.u.

Total energy: E = -381.506576 a.u.

H	1.372873	1.118453	-2.255707
C	1.142696	0.298637	-1.566794
H	1.242172	-0.650612	-2.103018
H	1.832393	0.321927	-0.716472
C	-0.284858	0.451888	-1.068331
O	-0.532289	0.597263	0.101771
Rh	-1.778953	0.408195	-2.468644
I	-1.769828	-2.309638	-2.096465
C	-3.122170	0.634708	-1.100132
C	-0.685945	0.180217	-4.022255
I	-1.417404	3.121350	-2.645241
O	-0.061243	0.043181	-4.971773
O	-3.937296	0.767235	-0.312290
I	-3.956496	0.358847	-4.359177

***cis*-[RhI₃(CO)₂(COCH₃)]⁻, *fac,cis*-18c₂**

Free energy: G = -524.964891 a.u.

Total energy: E = -524.9815613 a.u.

I	3.591231	-0.603974	-1.144864
Rh	1.286077	0.240013	-2.379388
I	-0.358662	0.156143	0.051765
I	0.493397	-2.269645	-3.187904
O	-1.279756	1.131282	-3.719214
C	-0.317550	0.769237	-3.212363
C	2.382354	0.635417	-4.100340
O	2.443784	1.769125	-4.508131
C	3.063784	-0.502208	-4.832417
O	2.048019	2.954436	-1.267629
C	1.772355	1.917204	-1.665791
H	3.819711	-0.080730	-5.504208
H	3.504725	-1.216475	-4.135597
H	2.302936	-1.034366	-5.413833

Acetate

Free energy: G = -228.386556 a.u.

Total energy: E = -228.4074791 a.u.

C	0.207514	0.000000	0.020718
O	-0.203020	0.000000	1.206000
O	1.381550	0.000000	-0.424329
C	-0.903923	0.000000	-1.088345

H	-1.915865	0.000000	-0.663312
H	-0.788155	0.880248	-1.737761
H	-0.788155	-0.880248	-1.737761

TS CH₃OI formation: *mer,trans*-[RhI₃(CO)₂(CH₃CO)][†]

Free energy: G = -524.928692 a.u.

Total energy: E = -524.9434054 a.u.

O	-0.495913	0.335586	-5.347212
C	-0.903060	0.271258	-4.277597
O	-3.452671	-0.634017	-0.127843
C	-2.781754	-0.363501	-1.018314
I	-0.754394	-2.519299	-2.497455
I	-3.412137	2.082562	-3.104393
Rh	-1.723913	0.029383	-2.564776
C	-0.065319	1.184291	-1.091063
C	1.026368	0.165147	-0.877925
H	1.824579	0.681307	-0.328434
H	1.414792	-0.219275	-1.817486
H	0.623163	-0.654406	-0.275490
O	-0.787707	1.661010	-0.274886
I	0.920980	2.792655	-2.685246

TS CH₃OI formation: *mer,trans*-[RhI₃(CO)₂(CH₃CO)]⁻ intermediate

Free energy: G = -524.937455 a.u.

Total energy: E = -524.95203 a.u.

O	-0.422426	0.320205	-5.099046
C	-0.531214	0.574260	-3.976701
O	-3.798235	-0.821516	-0.363923
C	-2.980977	-0.471801	-1.086280
I	-0.807327	-2.506050	-2.477235
I	-3.222764	2.218680	-2.863316
Rh	-1.668989	0.068135	-2.360599
C	-0.474858	0.673647	-0.865981
C	0.957092	0.186346	-0.920755
H	1.585437	0.925215	-0.415143
H	1.309742	0.022163	-1.935471
H	0.972580	-0.767369	-0.378101
O	-0.943612	1.293897	0.038328
I	1.175160	2.687313	-3.479351

TS CH₃OI formation: *cis,fac*-[RhI₃(CO)₂(CH₃CO)]⁻

Free energy: G = -524.924071 a.u.

Total energy: E = -524.9398943 a.u.

I	-0.496111	2.895401	-1.518990
Rh	-1.813463	0.154690	-2.429438

C	-1.550937	-1.577159	-1.882045
C	-0.685860	0.069259	-3.898405
O	0.018610	-0.048367	-4.804937
I	-3.799977	0.116906	-0.553419
I	-3.371169	1.577540	-4.293243
C	0.026999	0.629519	-0.756691
O	-0.313502	0.346365	0.345189
C	1.333765	0.236169	-1.408151
H	2.140184	0.650677	-0.791015
H	1.426080	0.613548	-2.423639
H	1.406225	-0.857268	-1.395031
O	-1.399946	-2.698175	-1.641833

CH₃COI

Free energy: G = -164.608532 a.u.

Total energy: E = -164.6253835 a.u.

I	3.836170	-0.412422	-0.850753
C	1.699639	-0.228807	-0.110560
O	1.413901	0.615585	0.663629
C	0.819111	-1.272650	-0.727446
H	1.205563	-2.266365	-0.481899
H	0.838963	-1.168799	-1.816428
H	-0.198980	-1.150317	-0.347037

I

Free energy: $G = -11.558441$ a.u.

Total energy: $E = -11.5415927$ a.u.

Compound 18d₁

Free energy: $G = -741.821174$ a.u.

Total energy: $E = -741.885162$ a.u.

H	-1.944432	2.057856	2.304305
C	-1.055637	2.309411	1.712313
H	-1.362203	2.487541	0.684086
H	-0.574614	3.197328	2.132099
C	-0.087827	1.143787	1.846485
O	0.527967	0.964153	2.865500
Rh	-0.019427	-0.195067	0.286286
I	-2.790667	-0.316754	0.063428
O	0.092085	1.294654	-1.143378
C	-0.129327	-1.555887	1.540265
I	2.716790	-0.477349	0.378500
O	-0.191395	-2.391222	2.325830
C	0.051438	-1.405896	-1.458408
C	0.750817	2.409157	-0.990226
C	0.869901	3.186062	-2.298624
H	1.259441	4.188969	-2.107895
H	1.554089	2.656002	-2.971399
H	-0.101640	3.245961	-2.799772
O	1.236913	2.839482	0.049806

O 0.083241 -1.969702 -2.448674

Compound 18d₂

Free energy: G = -741.836166 a.u.

Total energy: E = -741.9012905 a.u.

H -1.571452 1.262764 2.531162
C -0.829074 2.000894 2.211120
H -1.255166 2.594686 1.395364
H -0.553044 2.647704 3.050971
C 0.405906 1.288312 1.689792
O 1.504693 1.521016 2.132493
Rh 0.174749 -0.010266 0.141996
C -1.675119 0.426508 -0.233163
O 0.967324 1.447019 -1.088826
I -0.702818 -1.868830 1.945840
C 1.965025 -0.699000 0.377527
I 0.009726 -1.756722 -2.166595
C 0.220771 2.442652 -1.440333
C 0.916090 3.387059 -2.409356
H 0.383204 4.339490 -2.455166
H 1.957542 3.544681 -2.115739
H 0.916536 2.929216 -3.405003
O -0.944771 2.645087 -1.084592

O	3.017348	-1.123851	0.499906
O	-2.802281	0.504113	-0.411311

Compound 18d₃

Free energy: G = -741.842082 a.u.

Total energy: E = -741.9080968 a.u.

H	-2.073487	2.260735	-1.011108
C	-1.944122	2.704086	-0.022421
H	-1.129670	3.435918	-0.081132
H	-2.859732	3.202026	0.313128
C	-1.562266	1.647584	0.998461
O	-2.058582	1.621176	2.097596
Rh	-0.105178	0.314296	0.435538
I	-2.107686	-1.050654	-0.863819
O	0.279144	1.345283	-1.299907
C	-0.460367	-0.789052	1.896918
C	1.247668	1.328569	1.365165
O	-0.661803	-1.458900	2.804025
I	2.026267	-1.560418	-0.211918
C	1.184806	2.249295	-1.262516
C	1.555682	2.838785	-2.608002
H	0.674153	2.917382	-3.249335
H	2.033987	3.812830	-2.484412
H	2.262757	2.155812	-3.092524

O	1.772468	2.642086	-0.234363
O	1.920243	1.673251	2.234475

Compound TS_A

Free energy: G = -741.797783 a.u.

Total energy: E = -741.8639242 a.u.

H	-1.536542	1.550101	2.448231
C	-1.071515	2.244302	1.746105
H	-1.709999	2.339264	0.869560
H	-0.955882	3.224710	2.230991
C	0.321068	1.760720	1.419097
O	1.189652	1.558694	2.221216
Rh	-0.081181	-0.320384	-0.029558
I	-2.845048	-0.201197	-0.145715
O	0.155937	1.261739	-1.472798
C	-0.210718	-1.305377	1.472182
I	2.638199	-0.702840	-0.037597
O	-0.298809	-1.933336	2.441579
C	-0.201650	-1.835670	-1.576755
C	0.607086	2.337598	-1.053231
C	1.036207	3.403100	-2.028965
H	0.774342	4.398769	-1.661861
H	2.126470	3.354333	-2.130319
H	0.582063	3.217516	-3.003857

O	0.800138	2.651603	0.188368
O	-0.307430	-2.971972	-1.722514

Compound TS_B

Free energy: G = -741.800395 a.u.

Total energy: E = -741.864796 a.u.

H	-0.670133	1.355965	2.877974
C	-0.746090	2.131288	2.115294
H	-1.695367	2.031757	1.589784
H	-0.700459	3.121760	2.593650
C	0.428776	2.021792	1.187774
O	1.591465	1.932582	1.493837
Rh	-0.008133	-0.358735	-0.082514
C	-1.791202	0.075516	-0.534547
O	0.860228	1.215555	-1.454863
I	-1.005632	-1.622726	2.121984
C	1.717081	-0.977838	0.478308
I	0.062109	-2.172917	-2.397358
C	0.615858	2.389834	-1.200314
C	0.828970	3.489679	-2.202599
H	-0.050949	4.138987	-2.244964
H	1.678485	4.104307	-1.883733
H	1.031855	3.060317	-3.184356
O	0.125628	2.813646	-0.048332

O	2.742996	-1.369606	0.810754
O	-2.882381	0.329696	-0.803930

Compound TS_C

Free energy: G = -741.814615 a.u.

Total energy: E = -741.8813816 a.u.

H	-0.639585	1.352224	2.964062
C	-0.672437	2.081170	2.151364
H	-1.620853	2.008764	1.619086
H	-0.566205	3.089055	2.578972
C	0.508853	1.844856	1.244470
O	1.662842	1.754910	1.602481
Rh	-0.016435	-0.235455	-0.067885
I	-2.545939	0.546010	-0.788184
O	0.779916	1.189214	-1.463965
C	-0.815588	-1.138932	1.306769
C	1.680393	-0.880049	0.375425
O	-1.301882	-1.734816	2.168247
I	0.308401	-2.399041	-2.168507
C	0.625132	2.381707	-1.158617
C	0.750026	3.450667	-2.206626
H	-0.250400	3.649777	-2.608190
H	1.145346	4.375859	-1.781150
H	1.381899	3.091970	-3.021264

O	0.306164	2.806044	0.025799
O	2.718346	-1.275278	0.667658

***trans*-[RhI₂(CO)₂]⁻**

Free energy: G = -360.349404 a.u.

Total energy: E = -360.3254375 a.u.

I	-0.070896	3.467937	-0.050032
Rh	-0.000863	0.770842	-0.205554
C	-1.886512	0.704373	-0.016932
C	1.884637	0.801156	-0.007575
I	0.068248	-1.908299	-0.552954
O	3.019498	0.811931	0.188424
O	-3.021403	0.656858	0.173395

***cis*-[RhI₂(CO)₂]⁻**

Free energy: G = -360.360612 a.u.

Total energy: E = -360.3386107 a.u.

C	0.103837	0.000000	1.994387
Rh	0.164786	0.000000	0.162815
I	-2.563210	0.000000	0.281369
C	1.996167	0.000000	0.095236
I	0.273577	0.000000	-2.565530
O	3.153660	0.000000	0.095759

O 0.108618 0.000000 3.151866

Acetic anhydride

Free energy: G = -381.506576 a.u.

Total energy: E = -381.5744095 a.u.

C 0.087310 0.000000 -0.164490

O 0.258837 0.000000 1.216974

C 1.504121 0.000000 1.839175

C -1.389965 0.000000 -0.455631

C 1.286192 0.000000 3.329010

O 2.559762 0.000000 1.276600

O 0.969588 0.000000 -0.972237

H 2.252553 0.000000 3.834362

H 0.708980 0.881987 3.625699

H 0.708980 -0.881987 3.625699

H -1.544299 0.000000 -1.535175

H -1.862087 -0.881987 -0.010325

H -1.862087 0.881987 -0.010325

TS *trans*-[RhI₃(CO)₂COMe]⁻ + H₂O

Free energy : G = -601.277063 a.u.

Total energy : E = -601.313938 a.u.

C	-0.075171	1.262380	-1.957769
Rh	-2.747506	-0.007499	-2.866662
I	-3.021707	-0.159940	-0.115548
C	-2.677490	-1.912035	-2.915566
O	-2.688018	-3.062122	-2.960480
I	-1.852344	-0.028212	-5.455107
C	-2.809197	1.893960	-2.856307
O	-2.887961	3.042220	-2.867346
O	0.051506	-0.451061	-1.504886
O	-0.215415	1.971688	-1.028966
C	0.711189	1.369688	-3.212085
H	-0.624844	-0.742031	-2.194510
H	0.457008	2.322297	-3.683861
H	0.496050	0.564523	-3.913846
H	1.774139	1.370868	-2.931930
H	-0.547628	-0.446820	-0.705218
I	-5.548987	-0.153566	-3.467452

H₂O

Free energy : G = -76.376814 a.u.

Total energy : E = -76.379837 a.u.

H	-0.083344	1.258629	-1.977581
O	-0.928497	0.856651	-2.217992
H	-1.340928	0.652960	-1.368267

HOCOMe

Free energy : $G = -228.956754$ a.u.

Total energy : $E = -228.991697$ a.u.

O	1.217819	1.437882	-1.693282
C	0.114473	1.025075	-1.966186
C	-0.957379	0.643410	-0.982955
H	-0.601048	0.820439	0.032027
H	-1.864508	1.227207	-1.169538
H	-1.218736	-0.412766	-1.106943
O	-0.300290	0.849014	-3.242167
H	0.450222	1.115801	-3.803244

HI

Free energy : $G = -12.048498$ a.u.

Total energy : $E = -12.033394$ a.u.

I	-0.316975	0.000000	0.000000
H	1.316975	0.000000	0.000000